FRACTURE MECHANICS OF CARBON FIBRE REINFORCED PLASTICS TO Ti-ALLOY ADHESIVE JOINTS

Diego Álvarez Feito

October 2012

Mechanics of Materials

Department of Mechanical Engineering

Imperial College London

A thesis submitted for the degree of Doctor of Philosophy of

Imperial College London and the Diploma of Imperial College

Abstract

Adhesive bonding has emerged as an appealing technique to join carbon fibre-reinforced plastics (CFRP) to other structural parts. The advantages that adhesive bonding offers include an even stress distribution, weight saving and superior fatigue resistance when compared to more traditional methods of joining. However, despite these advantages, the uncertainties regarding their durability have confined them largely to use in secondary structures. In the present work, a fracture mechanics methodology has been followed using both experimental and FE methods to predict the service-life of a CFRP-titanium alloy adhesive joint intended for use in a turbofan application. The methodology utilises the concept of the cohesive zone model to evaluate the performance of a simplified but representative structure, i.e. a Ti-to-CFRP tapered double-lap joint.

The adhesive bondline was modelled by a layer of newly-developed cohesive elements, the kinematics and topology of which have been optimised to improve the mixed-mode behaviour and reduce the mesh-dependency. Their damage evolution has been enhanced to incorporate high-cycle fatigue degradation. Additionally, a simplified version of this formulation, specifically designed to predict only the fatigue threshold, has also been developed.

To determine the various input parameters required for the models, a series of fracture mechanics specimens manufactured with a commercial film adhesive were tested quasi-statically in various modes and in mode I fatigue. Various data reduction schemes were evaluated and a version of corrected beam theory employing an effective crack length approach was found to be optimum for all tests. The fracture energies determined in the various modes were partitioned according to the theories proposed by Williams (Global) and by Davidson's crack tip element singular field (CTE/SF) and non singular field (CTE-NSF) theories. The CTE-NSF partitioning strategy was found to be most suitable for the system under investigation. Fatigue tests were performed under wet and dry conditions, to investigate the effect of moisture on the joint performance. The fatigue results were fitted to a modified version of the Paris law and the required fatigue parameters were determined.

The response of the various test specimens was simulated using the numerical scheme and good agreement with the experimental results was obtained. Significantly, the results obtained with a quadratic version of the cohesive element have been found to be independent of the element size, at least with respect to the global response. Finally, both the quasi-static and fatigue responses of the double lap joints were simulated using the cohesive element formulation and conservative predictions of the service life were obtained, in accordance with expectation, as only mode I fatigue data (lower bound G_c) was inputted into the model.

A mis abuelos, Cesar y Juan

Acknowledgements

I would like to express my deepest gratitude to my academic supervisors, Dr Bamber Blackman and Professor Tony Kinloch for giving me the opportunity to undertake this project. Their patience, guidance, and support have made this a hugely rewarding experience, whilst their vast knowledge and stimulating discussion have kept me focused on the important questions. Special thanks go to Bamber for his encouragement during the later stages of this PhD, and for his relentless effort to make this a better thesis. I am also grateful to my industrial sponsor, Rolls Royce, for funding this research, and particularly to Dr Stephen Osiyemi, whose passion for Fracture Mechanics has always been inspiring.

Many thanks go to Professor Felicity Guild for her advice and invaluable help with the numerical side of this project. My appreciation also goes to those who helped with the testing programme, including Amit Choda, Hugh MacGillivray and Joseph Meggyesi. For her continuous assistance in the preparation of specimens and for sharing her technical expertise with me, I am specially indebted to Dr Sabine Frenz. I would also like to thank Dr Michael Brett and Dr Jibumon Babu for the useful discussions regarding the FE models.

For their contributions to this thesis, the technical advice, the productive discussions and, mainly, for the all the laughs, I am extremely grateful to all my colleagues in Room 393. Ed, Hari, Idris, Kunal, Nanke, Paul, Tim and Yatish, it has been a real pleasure to share office and "coffee-breaks" with you. Thank you!

My most heartfelt gratitude goes to the entire Birrell family. You have welcomed me in your home and made these years in the UK so much more enjoyable. In particular, thanks to Laura and James for putting up with me for so long!

Last but not least, Gracias a mi familia por tantos años de apoyo incondicional, por vuestra infinita paciencia, por aguantar mis manías y rutinas y por animarme en los momentos más bajos. Gracias de todo corazón.

Contents

List of Figures

Nomenclature

British Alphabet

A	Crack area
A_{CZ}	Cohesive zone area
A_d	Damaged area of the element (or the integration point)
A_e	Area of the element (or the integration point)
a	Crack length (2D problems)
a_e	Effective crack length
$\bar{a}_i$	Average crack length over the cycle interval $[N_i, N_{i+1}]$ (secant method)
$\hat{a}_i$	Crack length approximation (polynomial method)
a_{ij}	Geometrical/material properties used in the analysis of the CTE (Davidson method)
$a_0,\ a_f$	Initial and final crack lengths
a_p	Crack length after pre-cracking
B	Specimen width
b_i,C_i	Fitting coefficients (polynomial method)
C	Specimen compliance
C_0	Initial compliance
C_T	Fitting coefficient modified Paris law (origin ordinate in logarithmic fatigue diagram)
C_{T_i}	Fitting coefficient modified Paris law for mode "i"
C_{T_m}	Fitting parameter controlling the value of C_T in mixed mode
c_1, c_2, c_{12}	Geometrical/material properties used in the analysis of the CTE (Davidson method)

D_{ij}	Interface stiffness tensor
D_{ij}^{0}	Undamaged stiffness tensor
D_{ij}^{TAM}	Consistent tangent stiffness tensor
d	Scalar damage variable ranging between 0 and 1
$d(t)$	Total damage at time t
d_f	Damage due to cyclic fatigue
d_s	Quasi-static component of the damage variable
$dA, \Delta A$	Incremental increase in the crack area
$da, \Delta a$	Incremental increase in the crack length
$\frac{da}{dN}, \frac{\partial A}{\partial N}$	Fatigue crack growth rate
E	Young's modulus
E_a	Young's modulus of the adhesive
E_e	Back-calculated flexural modulus
E_i	Elastic modulus in the direction "i"
E_s	Flexural modulus of the substrate material in the longitudinal direction
E'	Equivalent elastic modulus for orthotropic materials
$E'_{II,slender}$	Reduced Young's modulus
F	Frequency of the fatigue cyclic load
F_v	Correction factor for large displacements
G_c	Critical strain-energy release rate or fracture energy
G_i	Strain-energy release rate for mode "i"
G_{ic}	Critical strain-energy release rate or fracture energy for mode "i"
G_{ij}	Shear modulus in the "i-j" plane
G_{II}/G	Mixed-mode ratio in energy terms

$(G_c)_{initiation}$	Initiation values of the critical strain energy release rate
G_{th}	Fatigue threshold fracture energy
G_{th_i}	Threshold fracture energy for mode "i"
$(G_{th})_{crit}$	Critical value of the threshold fracture energy
$(G_{th})_{exp}$	Experimental value of the threshold fracture energy
G_{max}	Maximum strain energy release rate applied in the fatigue cycle
$G_{Total}^{Will.}, G_{Total}^{Dav.}$	Total fracture energy calculated with Williams or Davidson methods
H_V	Hardness (Vickers)
h	Laminate half thickness or substrate thickness
h_1, h_2	Substrate thicknesses in asymmetric test specimens
h_0, x_0	Height and length of the straight section of the TDCB substrates
I	Second moment of area of half the un-cracked laminate or joint
J	Non-linear energy release rate (i.e. value of the J-integral along the contour path Υ)
J_{ext}	Value of the J-integral along the external boundaries of the test specimen
J_R	Fracture resistance of the material
K_c	Critical stress intensity factor (i.e, the fracture toughness)
k_{eff}	Effective penalty stiffness
K_i	Stress intensity factor for mode "i"
K_{ic}	Critical stress intensity factor (i.e, the fracture toughness) for mode "i"
k_I, k_{II}	Penalty stiffness for opening (mode I) and shear (mode II) modes
L	Free length (ELS, FRMM and AFRMM test) or half-span length (ENF tests)
l_{CZ}	Cohesive zone length (two-dimensional problems)
l_e^i	Length of the cohesive element *"i"*

M	Correction factor for the analytical estimates of the cohesive zone length
M_1, M_2, M_3	Bending moments acting on the tip elements used for mode decomposition. (when using plate theory – Davidson –, they are the resultant per unit width).
M_c	Concentrated crack tip moment
M_I, M_{II}	Bending moments in pure mode I and II (William mode decomposition)
m	Fitting parameter for modified Paris law (gradient linear regime)
m_b	TDCB parameter
m_i	Fitting parameter for modified Paris law (gradient linear regime) for mode "i"
m_m	Fitting parameter controlling the value of m in mixed mode
N	Number of cycles
N_1, N_2, N_3	Axial loads acting on the tip elements used for mode decomposition (when using plate theory – Davidson –, they are the resultant per unit width).
N_c	Concentrated crack tip force
N_{CZ}	Number of cohesive elements within the numerical cohesive zone
N_f	Number of cycles to failure
N_v	Correction factor for the presence of loading blocks
N_{II}	Axial load yielding pure mode II (William decomposition)
$N_k(\xi^*)$	Lagrange shape function associated to node "k" in the isoparametric element
n	Fitting parameter – exponent – for ECM
n_{1i}, n_{2i}	Fitting coefficients of the modified Paris law for mode "i"
P	Load
P_{max}, P_{min}	Maximum and minimum loads during the fatigue tests
$\overline{P_{max_i}}$	Maximum load corresponding to $\bar{a}_i$ (secant method)
p, q	Fitting parameters controlling the values of C_T and m in mixed mode (B-K)

Q_1, Q_2, Q_3	Shear loads acting on the tip elements used for mode decomposition (Williams)
$Q(\lambda)$	Quasi-static damage evolution law
Q_I	Shear load yielding pure mode I (William decomposition)
R	Displacement ratio of the fatigue cyclic load
r	Distance to crack tip
r^t	Damage threshold at time "t"
r_y	Radius of the mode I failure process zone for θ=0
T_g	Glass transition temperature
T_{th}	Fatigue limit or threshold load per unit width
t	Time variable
$\vec{t}, \vec{n}$	Tangent and normal vectors to the mid-surface of the cohesive element
t_a	Initial thickness of the interface
t_0	Time at which the fatigue analysis (i.e. cyclic loading) starts
U_e	Work done by the external forces
U_s	Strain energy stored in the body
u_i^+ , u_i^-	Displacements of any point in the upper and lower surfaces of Γ_d
u_i^k	Displacement of the node "k" in the direction "i"
X_i^+ , X_i^-	Initial coordinates of any point in the upper and lower surfaces of Γ_d
X_i^k	Initial coordinate "i" of the node "k"
X_{1l}, Z_{1l}	Crack tip forces used in VCCT
$\vec{x}_i$	Position vector of point "i"
x_i^+ , x_i^-	Deformed coordinates of any point in the upper and lower surfaces of Γ_d
$\bar{x}_i$	Coordinates of the mid-surface $\bar{\Gamma}_d$

$\bar{x}_{i,\xi^*}$	Derivative of the coordinates of the mid-surface with respect to ξ^*
w_j	Gauss weighting factor associated with integration point "j"

Greek Alphabet

α	Thickness ratio for asymmetric test specimens
α_i	Fitting parameters used in the fracture criteria
β	Mode-mixity parameter in displacement terms
Γ	Geometry/material parameter used in Davidson' crack tip element
Γ_d	Two-dimensional interface
$\Gamma_d{}^+$, $\Gamma_d{}^-$	Upper and lower surfaces of the interface Γ_d
$\bar{\Gamma}_d$	Mid-surface of the interface Γ_d, equidistant from the top and bottom surfaces
γ	Thickness ratio (Davidson mode decomposition)
γ_m	Surface energy needed to create the new surfaces
γ_p	Energy dissipated by plastic deformation in the near-tip region
Δ_{clamp}	Clamp correction factor
Δ_i	Displacement jump in the local reference system at a generic point of the interface
$\Delta_{implied}$	Implied crack length correction factor (obtained from CBTE)
Δ_i^0	Displacement at damage initiation for mode "i"
Δ_i^f	Displacement for a fully damaged interface (d=1) for mode "i"
Δ^{th}	Threshold displacement jump norm
Δ_I	Crack length correction factor for mode I (CBT)
Δ_{II}	Crack length correction factor for mode II (CBT)
ΔE	Energy release calculated with VCCT
$\Delta d_{\max}$	Maximum damage increment allowed

$\Delta d_s(t, t+\Delta t)$	Increase in damage due to the change in λ between t and $t+\Delta t$
ΔG	Variation of the energy release rate in the fatigue cycle
Δt_{max}	Upper limit for the time increment permitted at each step
ΔU	Change in energy
Δu_{i}	Displacement jumps across the interface Γ_d in global coordinates
$\Delta u_l, \Delta w_l$	Crack opening displacements at the released nodes used in VCCT
δ	Applied displacement
δ_C	Displacement for completely damaged element
$\bar{\delta}_{ij}$	Kronecker delta
δ_n	Normal crack opening displacement
δ_n^*	End-opening of the failure process zone
δ_0	Displacement at damage initiation
δ_t	Tangential crack opening displacement
δ_t^*	End-sliding of the failure process zone
ε^0	Mid-surface strain (plate theory)
ϵ_U	Ultimate tensile strain (at break)
ϵ_Y	Tensile strain at plastic deformation
η	Mixed mode parameter in the B-K criterion
Θ_{mi}	Rotation tensor (global to local coordinate systems)
θ	Angular coordinate of polar coordinate system with origin in the crack tip
θ_{i}	Coefficients of the correction factors F_v and N_v
κ	Mid-surface curvature (plate theory)
λ	Norm of the displacement jump tensor or equivalent displacement jump norm
λ_{max}	Maximum applied displacement jump norms in the fatigue cycle

λ_{min}	Minimum applied displacement jump norms in the fatigue cycle
μ	Fitting parameter for ECM (slope in $log(C)$-$log\,(a)$ plot)
ν	Poisson's ratio
ν_{ij}	Poisson's ratio corresponding to a contraction in the direction "j" when an extension is applied in the "i" direction
Ξ	Energy dissipated in the element
ξ	Thickness ratio (Williams's mode partitioning method)
ξ^*, η^*	Coordinates of the isoparametric element configuration
ρ	Dimensionless material parameter in Davidson's crack tip element
σ	Stress in the process zone
σ_c	Maximum stress of the traction-separation law
σ_{ij}	Stress field around the crack tip
σ_n	Normal cohesive stress
σ_t	Tangential cohesive stress
σ_U	Ultimate tensile strength
σ_Y	Yield stress
σ_{yy}	Normal stress
σ_{xx}	Tangential stress
τ_i	Cohesive tractions in the local coordinate system
τ_i^0	Interfacial strength for mode "i"
Υ	Contour going around the crack counter clockwise (J-integral)
$\Phi(\alpha)$	Mixed mode ratio as a function of the thickness parameter
χ	Beam elastic parameter
ψ	Mixed mode parameter (Williams mode partitioning method)

Ω	Mixed mode parameter (Davidson's mode partitioning method)
Ω^*	Two dimensional domain divided in two parts by an interface Γ_d
Ω^+, Ω^-	Top and bottom parts into which the interface Γ_d divides the domain Ω^*
Ω_{NSF}	Effective mixed mode parameter (Davidson CTE/NSF)
ω	Mixed mode parameter (Hutchinson and Suo mode partitioning method)

Acronyms and Abbreviations

4ENF	Four-Point Bending End-Notched Flexure
ACM	Adaptive Cohesive Model
ADCB	Asymmetric Double Cantilever Beam
AF163-2OST	AF163-2 supported "One side tacky"
AF163-2U	AF163-2 unsupported
AFRMM	Asymmetric Fixed Ratio Mixed Mode
ASTM	American Society for Testing and Materials
B-K	Benzeggagh and Kenane
BS	British Standard
BSI	British Standard Institution
CAE	Chromic Acid Etching
CBT	Corrected Beam Theory
CBTE	Corrected Beam Theory with Effective Crack Length
CFRP	Carbon Fibre Reinforced Composites
CTE	Crack Tip Element
CTE/NSF	Crack Tip Element/Non-Singular Field
CTE/SF	Crack Tip Element/Singular Field
CZM	Cohesive Zone Model
DCB	Double Cantilever Beam
DIC	Digital Image Correlation

ECM	Experimental Compliance Method
ELS	End-Loaded Split
ENF	End-Notched Flexure
ESIS	European Structural Integrity Society
FEA	Finite Element Analysis
FOD	Foreign Object Damage
FPZ	Failure Process Zone
FRMM	Fixed Ratio Mixed Mode
GB	Grit-blasting
GBD	Grit-blasting and Drying
GLARE	Glass Laminate Aluminium Reinforced Epoxy
ISO	International Organization for Standardization
LEFM	Lineal Elastic Fracture Mechanics
NL	Non-linear criterion for initiation
MAX/5%	Maximum load point or 5% increase in compliance initiation criterion
MMB	Mixed Mode Bending
MMF	Mixed Mode Flexure
PTFE	Polytetrafluoroethylene
RH	Relative Humidity
SBT	Simple Beam Theory
SEM	Scanning Electron Microscope
SHA	Sodium Hydroxide Anodising
SLB	Single Leg Bending

TDCB	Tapered Double Cantilever Beam
TDLJ	Tapered Double Lap Joint
UD	Unidirectional
VCCT	Virtual Crack Closure Technique
VIS	Visual criterion for initiation
VRMM	Varying Ratio Mixed Mode
WPPD	Wet Peel Ply and Drying
XFEM	Extended Finite Element Method

1. Introduction

1.1 Introduction: CFRP-Ti Fan Blade

Weight has been a major concern for the aerospace industry since the very beginning, as pointed out by Emanuel Swedenborg back in 1716 when referring to one of the earliest flying machine concept designs: "It seems easier to talk of such machine than put it to actuality, for it requires greater force and less weight than exists in a human body" [1]. Only the invention of the combustion engine and a better understanding of aerodynamics allowed aviation to take off. Nonetheless, even though aircraft have experienced a dramatic transformation since the Wright Flyer I took to the air for the first time in 1903 (see Figure 1.1), lightness has remained both a top priority and a driving force in their evolution. However, a renewed interest in the subject has emerged in recent times spurred on by a never-ending increase in fuel prices and a growing environmental impact awareness.

Engine manufacturers have not been indifferent to these issues. Whilst advances in fluid mechanics, combustion and high temperature super-alloys have opened the door to considerable efficiency improvements, the adoption of new material technologies and manufacturing processes has contributed to the creation of lighter power plants. In this respect, the high values of stiffness-to-weight and strength-to-weight ratios of carbon fibre reinforced plastics (CFRP) have found application in the aerospace sector, where composites have become the material of choice for many structural components.

(a) (b)

Figure 1.1. (a) Wright Flyer I takes off at Kill Devil Hills (North Carolina, USA) on December the 17th 1903 [2]; (b) the Airbus A380-800, which entered service in 2007, is one of the most advanced passenger aircrafts to date [3].

Confined to non-critical elements at first, fibre-reinforced materials are gradually finding their way into primary structures. The fan blades are a good example of this transition. Traditionally made from titanium alloy, they are the ideal candidates for the use of CFRP due to the relatively low temperatures at the entrance of the engine. Not only would CFRP aerofoils offer a significant weight advantage compared to their metallic counterparts, but their lower density would also induce smaller inertia forces. As a result bigger blades and higher engine speeds could be employed, improving the aerodynamic efficiency of the fan and therefore reducing fuel consumption. In addition, shifting to CFRP aerofoils would enable further weight savings since the fan case, which is designed to contain the debris in the event of blade detachment or failure, could be also made from lighter materials.

Despite their numerous benefits, the use of fibre-reinforced composites imposes a number of challenges: they have low damage tolerance and damage can be difficult to detect visually, limited non-destructive test methods are available, they are prone to manufacturing variability, potential degradation when subjected to heat or radiation and complex failure mechanisms. These are particularly important in an industry where any new technology has to undergo extensive and costly testing and must finally pass a rigorous certification process prior to entering service.

Because it represents a major threat to flight safety, the so-called “bird-strike” or “bird-ingestion” test is possibly the most stringent of all the certification tests that any new turbofan must go through. To comply with the regulations (e.g.[4]), manufacturers have to demonstrate that the engine will continue to produce at least 75% of maximum thrust after ingesting a flock of small or medium size birds. Similarly, fan integrity requirements stipulate that the power plant cannot catch fire or disintegrate after being struck by a single 4lb bird.

These tests are carried out at full power, using a gas cannon to fire birds of appropriate weight (from 3oz to 4lb) at representative operational speeds, typically between 100 and 225m/s (see Figure 1.2).

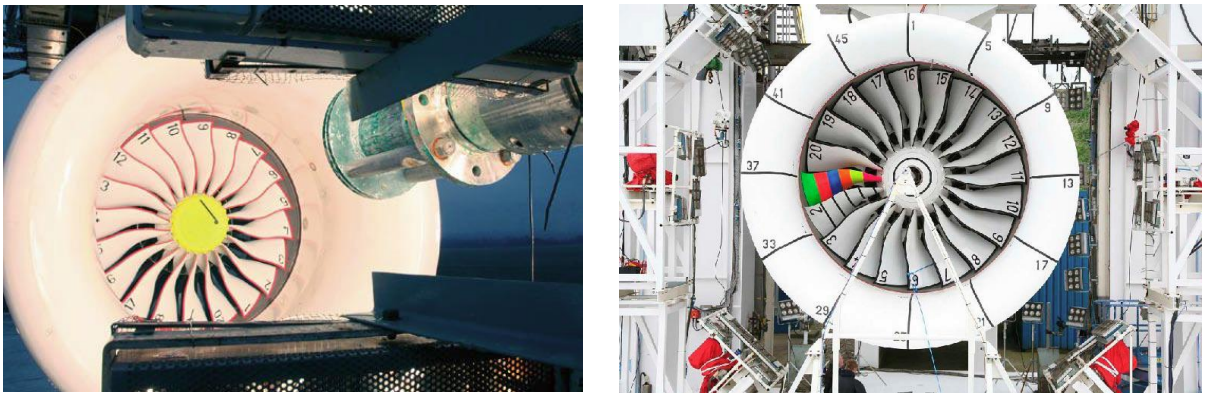

(a) (b)

Figure 1.2. Rolls Royce Trent 1000 ready for (a) bird-ingestion and (b) fan blade containment tests [5].

Carbon fibre composites have been proven to be very effective for absorbing impact energy (e.g. [6-8]). However, due to their intrinsic brittle nature, the energy of the impact is mainly dissipated by creating new surfaces through a sequence of fracture mechanisms involving fibre rupture, matrix crazing and cracking, fibre-matrix debonding, delamination and ply separation [9]. Whilst shattering of the CFRP may be advantageous in case of a blade detachment, it compromises the integrity of the fan during bird-ingestion incidents and therefore hinders fulfilment of the airworthiness requirements. These difficulties became evident during the certification phase of the ill-fated RB211 Hyfil blade in the 1970's.

Covering both the leading and tailing edges of the aerofoil with titanium alloy strips has been suggested as a possible way to overcome these issues without introducing a significant weight penalty (see Figure 1.3). The metalwork would enhance the resistance of the CFRP blade to foreign object damage (FOD) as well as improve its durability. However, this approach introduces a new question: How to join the two parts together?

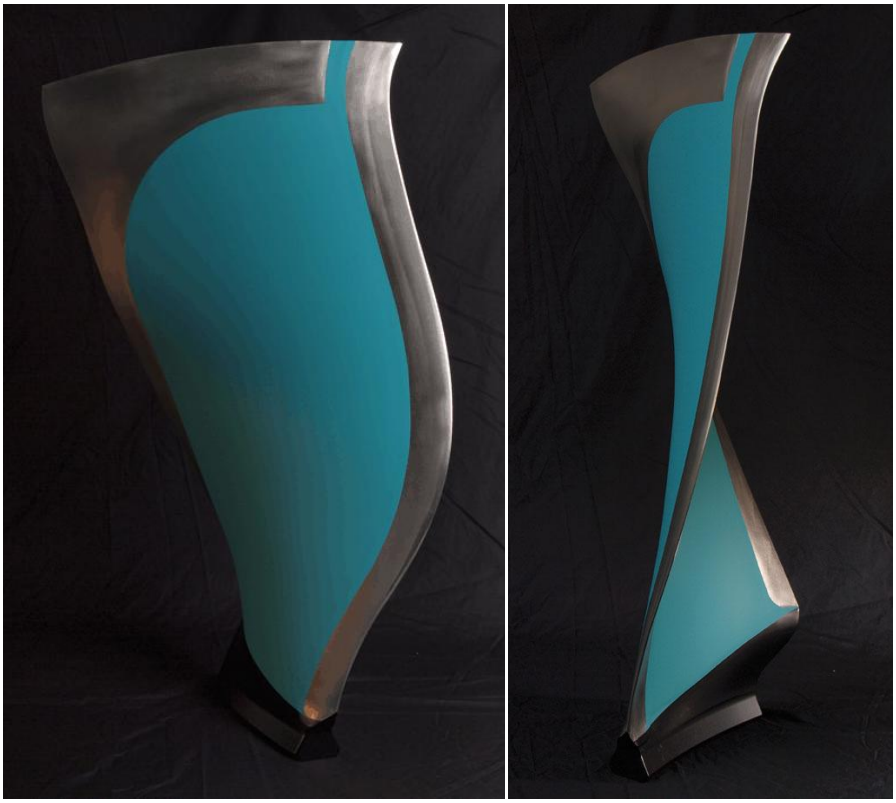

Figure 1.3. Prototype of the CFRP fan blade featuring titanium metalwork in the leading and tail edges [10].

Advances in polymer science, and particularly the development of tougher structural adhesives, have positioned adhesive bonding as an appealing technique to join composite parts to the rest of the structure. The characteristics of the fan blade make this the perfect choice for this application. Not only does it offer additional weight savings, but it also has been shown to improve the fatigue performance compared to mechanically fastened structures. The large areas and the geometrical complexity involved are ideally suited to the design flexibility, repeatability and the possibility of automation offered by this technique. Furthermore, adhesive bonding produces a smooth surface finish, facilitating the overall aerodynamic performance of the blade. Unfortunately, despite their numerous advantages, the industrial application of adhesively-bonded joints has been limited by their susceptibility to environmental attack. Specifically, the presence of moisture coupled with relatively high temperatures has been shown to significantly reduce the service life of bonded components. The uncertainties regarding their durability have confined them largely to use in secondary structures.

These issues must be addressed before adhesives can be safely employed in critical areas of the engine such as the fan blades. A better understanding of the behaviour of bonded components under different loading conditions and methodologies to predict their service life

are also required. Similarly, the design process of new joints, currently based on expensive and time-consuming experimental programs, could also greatly benefit from computer-aided tools. For example, suitable modelling techniques such as Finite Element Analysis would allow engineers to evaluate the performance of several configurations in a short period of time, drastically cutting the development times and facilitating the constructions of optimised adhesively-bonded structures. The present thesis focuses on a number of these questions.

1.2 Aims and Objectives

The primary aim of this research has been to develop a methodology for the optimisation of adhesive joints formed by bonding a titanium alloy to carbon fibre reinforced epoxy composites. Following a fracture mechanics approach, both experimental and numerical techniques have been used to assess the influence of various aspects on the joint performance, including geometry, type and mode of loading and service environment. In addition, empirical and Finite Element methods have been combined to generate a tool capable of predicting the service life of bonded components and accounting for the effects of the above variables. Such a tool has great potential to reduce the development time and associated costs of new adhesively-bonded structures, and has been validated using the experimental data obtained for a representative structure.

Although they can be very accurate in some cases, many of the existing FE methods for the analysis of fracture in adhesive joints are inadequate for industrial applications due to their complexity and level of detail. Furthermore, these methods often require problem-dependent tuning and extremely fine meshes, making them less appealing for the study of large and complicated components. A key objective of this thesis has been to devise a more efficient and flexible modelling approach, particularly for cyclic fatigue problems.

The work undertaken within this project focuses on a commercially-available structural adhesive. Its fracture behaviour under different loading modes has been studied using different test geometries and substrate materials in order to derive a suitable fracture criterion. Since mixed-mode fracture criteria (and their partition) remain controversial, various criteria and partitioning schemes have been investigated and a suitable scheme is recommended.

This project overlapped with the work of another researcher (Dr Sabine Frenz), who focussed on the selection of the optimum surface treatments for the adhesive bonding of titanium alloys to CFRP. The findings of that research have been utilised in the experimental

programme described in the present thesis, using the results obtained from testing optimally bonded joints as input parameters to the finite element models created for the prediction of service life.

1.3 Structure of the Thesis

This thesis is divided into eleven chapters. The core research topic and the fundamental aims and objectives are introduced here. Chapter 2 reviews the basic notions of adhesion and fracture mechanics, providing a critical overview of the numerical techniques which have been reported on to model bonded structures.

A modelling approach to simulate the response of adhesively bonded joints is presented in Chapter 3. Two different methodologies to predict their fatigue performance are introduced. Based on the concept of the Cohesive Zone, they both use specialized cohesive element formulations, the details of which are described in Chapter 3. The application of these methods requires a considerable amount of experimental input data. Additionally, a number of tests performed with an independent geometry, in this case a CFRP-to-titanium double lap joint, are needed for validation.

Chapter 4 details the adhesive and substrate materials employed in this research. The manufacturing and testing procedures for the various types of joint investigated are also outlined. The data reduction schemes employed for the analysis of the results obtained with the fracture mechanics specimens are described in Chapter 5. This includes the application of three different mode decomposition theories for the specific test configurations used to study mixed mode fracture.

Chapter 6 discusses the results obtained for the fracture specimens tested quasi-statically. The critical strain energy release rates measured for different mixed mode ratios are then combined in the first part of Chapter 7 to define an appropriate failure criterion for the adhesive. Approximated by a suitable function, this criterion is subsequently used in the performance prediction of the double lap joint. The outcomes of the fracture mechanics fatigue tests are presented at the end of Chapter 7, deriving crack growth rate diagrams also required for the simulations.

The potential of the cohesive zone formulation is investigated in Chapter 8 using 2D models of the bonded joints tested both quasi-statically and in fatigue. The results of a parametric study carried out to evaluate the effects of the elastic properties of the adhesive layer on the mode mix seen by the cohesive elements are discussed. The response of the joints is then

simulated, assessing the accuracy of the numerical predictions by direct comparison with the experimental results. Various aspects, including the size of the process zone and stress distribution along the bondline, are examined in detail to gain a better understanding of the fracture process.

In order to assess its predictive capability, the methodology proposed in Chapter 3 is then applied to the CFRP-to-titanium double lap joint. A comparison between the numerical and experimental results is presented in Chapter 9. Chapter 10 focuses on a very specific characteristic of cohesive elements: mesh-dependency. The conclusions of a mesh-sensitivity analysis carried out using the various test configurations studied experimentally are discussed, considering the effects of the element order, size and topology.

Finally, the main findings of this research are summarized in Chapter 11. In addition to the main conclusions, a number of potential areas for future work are identified, making recommendations for possible lines of future investigation.

2. Literature Review

2.1 Introduction

Since the middle of the 1940s, when major advances in polymer science opened the door to their use in demanding engineering applications [11], adhesives and adhesive bonding have attracted attention from numerous scientists and engineers. This growing interest has not been exclusively limited to their chemistry, albeit subsequent developments in the field have widened their range of applicability even further (e.g. [12-14]). Instead, the research lines have covered very diverse aspects, including mechanical characterization (e.g. [15-17]), optimization of joint design (e.g. [18-20]), environmental degradation (e.g. [18-20]) or performance prediction (e.g. [21-23]).

A summary of the more significant findings to date is presented next, focusing on those particularly relevant for the present study. The basic principles of the theory of adhesion and fracture mechanics are reviewed first, followed by a brief survey of the numerical techniques proposed for simulating the response of adhesively bonded joints. Some of the cited references deal with delamination in fibre-reinforced composites rather than fracture in adhesive joints. However, the well-known similarities between failure in these materials made them pertinent for the purposes of this work.

2.2 Adhesive Bonding and Adhesively-Bonded Joints

2.2.1 Introduction: Mechanisms of Adhesion

Adhesively-bonded joints consist of two or more substrates joined together with an adhesive material which resists separation and allows load transfer. It is widely accepted that the establishment of an intimate molecular contact between adhesive and substrate is essential to produce strong joints [24].

Fulfilment of this requirement is subjected to the ability of the glue to spread across the surface to be bonded, which depends on the surface energy of the substrate-adhesive interface and increases if the adhesive has low viscosity at the moment of application. Typical polymeric adhesives have low surface energies and therefore tend to wet metallic substrates with relative ease. Nevertheless, the removal of contaminants and surface roughing to increase the contact area facilitate the process [25]. In contrast, the hydrophobic character of most plastics often results in poor adhesion, calling for specific surface treatments to enhance their wettability prior to bonding [26, 27].

Despite its importance, the attainment of intimate adhesive-substrate contact is not sufficient to ensure good adhesion. Instead, it is the formation of intrinsic forces acting across the interface and their magnitude that will define the strength and stability of the bond. However, the complexity associated with these forces and the difficulties to measure them have led to some controversy regarding their nature [24]. Various theories have been proposed over the years in an attempt to explain the origin of the intrinsic adhesion forces, namely: (i) mechanical interlocking, (ii) diffusion theory, (iii) electronic theory and (iv) adsorption theory (see [24] for a detailed review).

The adsorption theory, based on the establishment of primary and secondary bonds between the atoms and molecules in the surfaces of adhesive and substrates, has became the most popular and widely accepted mechanism of adhesion. Furthermore, it offers the possibility of correlating the strength of bonded joints with the thermodynamic work of adhesion [28, 29]. Nevertheless, the other mechanisms can also contribute to the intrinsic adhesion forces under certain circumstances. Take for instance mechanical interlocking: for many years seen as the primary source of adhesion, this concept has led to the development of numerous surface treatments aimed at enhancing the roughness of the substrates [30, 31]. Not only have these operations been found to remove contaminants and weak layers, but they also improve the wettability by increasing the contact area [24, 32, 33].

2.2.2 Surface Pre-Treatments

Some form of surface pre-treatment is usually required if the performance of the joint is to be maximized. Ranging from simple mechanical abrasion operations (e.g. [32]) to complex multi-step chemical procedures (e.g.[31, 34]), these treatments are designed to maximise the intrinsic adhesion forces either by enhancing the intimate interfacial contact or facilitating the formation of stronger and more durable bonds across the interface. Overall, if selected and applied properly, they should steer the fracture path away from the interface.

As discussed in [24, 35, 36], a considerable number of surface pre-treatments have been developed, mostly empirically, over the years. However, their suitability for a particular case will depend on the nature of the adhesive/substrate system and the application of interest. Plastics and fibre reinforced polymers typically require pre-treatments to increase their inherently low surface energy [27]. On the other hand, metallic adherends with high surface energies tend to attract contamination in the form of oils, grease or other weak layers which must be removed prior to bonding. In other cases, formation of a specific surface topography could promote secondary mechanisms of adhesion (i.e. interlocking or chemisorption) [30, 37].

Depending on the nature of the operations involved, the surface pre-treatments could be divided into: (i) Mechanical, such as hand abrasion, “dry” or “wet” grit-blasting [32, 38, 39] and the use of peel plies [40-43]; (ii) Chemical, including solvent cleaning, acid etching [31, 44], anodising [45-48] and sol-gel processes [49, 50]; (iii) Physical, as plasma and flame treatments [26, 51, 52] or corona discharge [53, 54]; and (iv) Coatings like silane-based primers which have been shown to improve dramatically the durability and environmental resistance of bonded joints [55-58]. For the purposes of the present work, reviews of the specific options available for titanium alloys and carbon reinforced composites can be found in [59-61] and [59, 62] respectively.

2.2.3 Types of Adhesives and Toughening Mechanisms

A very wide range of polymeric materials can be used as adhesives. They admit various classifications, depending on their end-use, load carrying capability, in-service temperature, method of application, environmental suitability etc. Nevertheless, most of these characteristics are directly related to their molecular structure and the nature of their polymeric bonds, according to which they can be divided into thermoplastic and thermosetting adhesives.

The molecules making up the thermoplastics have a linear structure with no reactive lateral bonds which can link them strongly with other molecules. Consequently they do not suffer

chemical reactions upon heating and often can be reprocessed. Their mechanical properties change dramatically above the glass transition temperature (T_g) and, even though these changes may be reversed upon cooling, this characteristic makes them unsuitable for severe service conditions (i.e. high temperature or radiation). In contrast, in the presence of a hardener, thermosetting resins undergo irreversible transformations which result in three-dimensional molecular networks. Unlike the thermoplastics, they exhibit high modulus and strength and good creep resistance, constituting the basis for many high load and temperature applications [63].

Despite their many advantages, the highly cross-linked molecular structure of thermosetting adhesives often translates into brittle behaviour. Caused by the poor mobility of the polymeric chains, this poor fracture resistance would be unacceptable for many demanding engineering applications. However, the addition of a second phase, typically in the form of rubber particles, has been shown to radically increase their toughness without substantially damaging other important characteristics [11, 14, 64]. This approach has been particularly successful with epoxy resins, as demonstrated by the adhesives used in the present work.

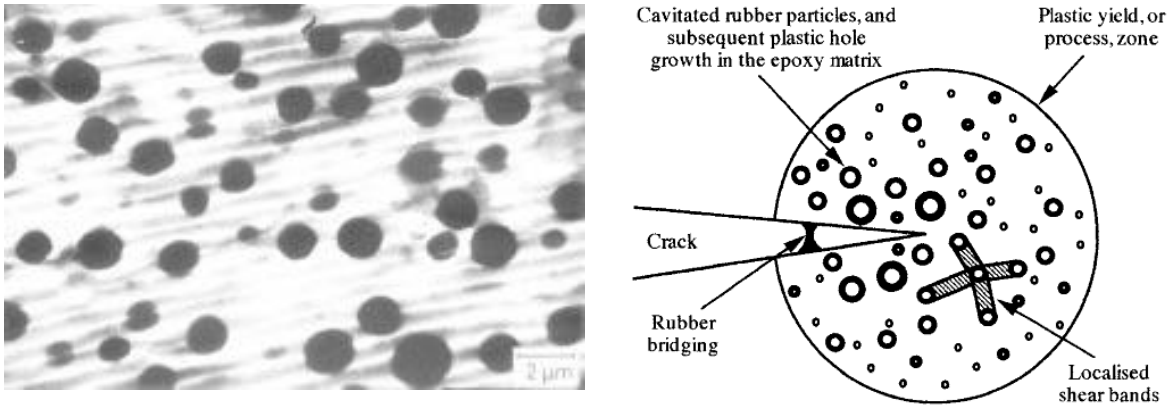

(a) (b)

Figure 2.1. (a) Example of dual microstructure and (b) a schematic representation of the toughening mechanisms in a rubber-toughened epoxy adhesive [11].

The resulting two-phase microstructure, illustrated in Figure 2.1-a, has considerable repercussions on the processes which take place in the failure process zone (FPZ) developed ahead of the crack tip. Specifically, the presence of the rubbery phase enables three energy dissipation mechanisms which contribute to enhance the fracture toughness, namely: (i) localized shear yielding, (ii) plastic void growth or cavitation and (iii) rubber particles bridging the crack faces (see Figure 2.1-b). Out of these, which are reviewed in [65-68], the first two are considered the most important ones.

Acting as stress concentrators, the rubber particles promote localized shear yielding of the matrix between particles. In addition, they debond from the polymeric resin due to the triaxial stress state in the near-tip region. The newly created holes then grow and deform plastically, absorbing energy in a process also favoured by the stress triaxiality. Detailed studies of this phenomenon using numerical techniques have also revealed a particle size effect [69].

2.2.4 Joint Design

Other factors besides the level of intrinsic adhesion and the mechanical properties of the adhesive material influence the strength of the bonded joints. In particular, the geometry design and loading conditions play a major role, as they define the stress state along the bondline. Typically, four types of stresses are considered in adhesive joints: normal, shear, cleavage and peel stresses (see Figure 2.2). While the first two correspond to the classic components in any two-dimensional problem, cleavage and peel stresses arise when there is a bending moment or one of the substrates is flexible respectively [24, 70].

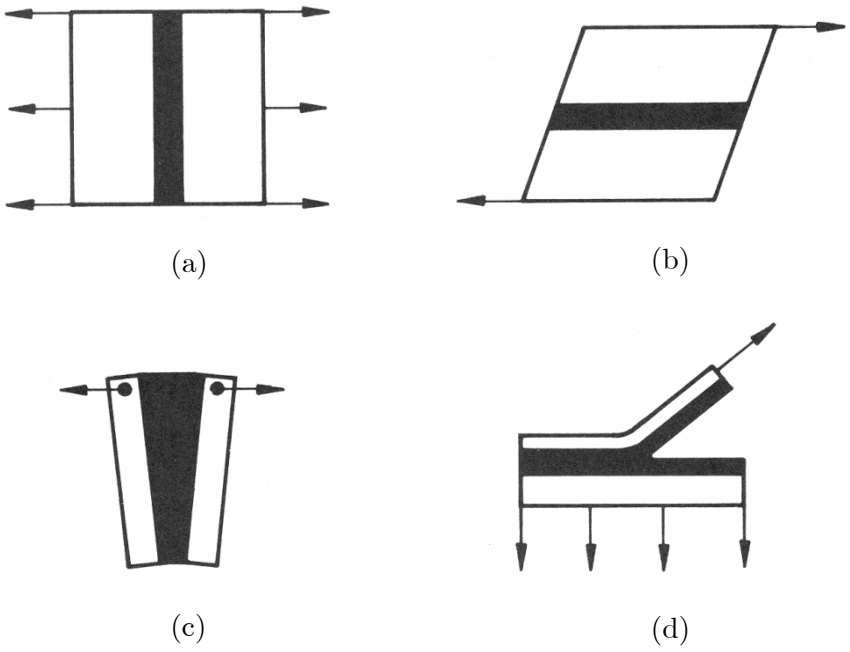

Figure 2.2. Types of stresses acting in adhesive layers: (a) normal, (b) shear, (c) cleavage and (d) peel stresses [24].

Bearing in mind the superior strength of polymeric adhesives in compression or shear compared to tension, peel or cleavage, minimizing the latter is always a priority when designing a new bonded joint. For the same reason, eliminating any potential stress concentrations as well as avoiding misalignments of the substrates and loading eccentricities

are also good practices. Figure 2.3 illustrates some common joint configurations aimed at fulfilling these criteria.

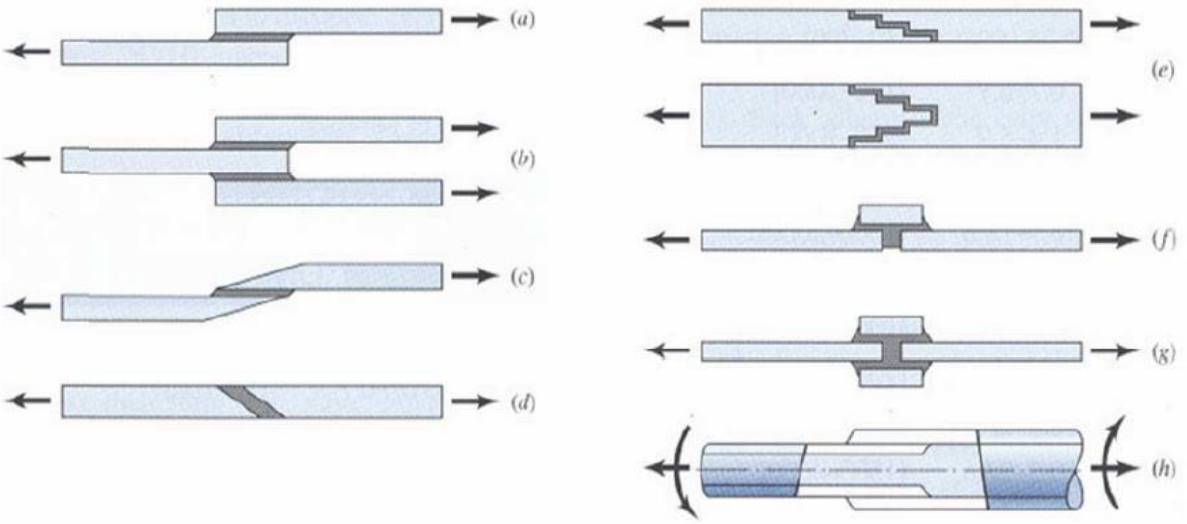

Figure 2.3. Schematic representation of various typical joint designs [71].

Optimisation of adhesive joints has attracted the attention of numerous researchers and engineers. They have used experimental, analytical and numerical techniques to study the effects of a variety of aspects such as substrate geometry, overlap length, spew fillets, tapers, etc. Nevertheless, the roots of most of these investigations can be traced back to the original work of Olaf Volkersen [72, 73], who proposed a simple analytical model to estimate the stress distributions along the adhesive layer in single lap joints. Assuming linear-elastic behaviour, Volkersen concluded that the shear stresses reach their peak values near the ends of the overlap and expressed the stress concentration factor in terms of the geometrical and mechanical properties of the substrates and the adhesive. Goland and Reissner [74] subsequently modified the original model to account for the tensile stresses caused by non-linear geometry (i.e. bending of the substrates due to eccentricity in the loading), while Hart-Smith identified the key role played by the overlap-to-thickness ratio on the structural efficiency of the joints [75, 76]. Further refinements included the incorporation of plasticity in the adhesive [75, 77, 78] and shear deformation in the adherends [79].

Equivalent approaches have also been applied to the analysis of double lap joints. The analytical solutions proposed by Volkersen [73, 80], Adams and Peppiatt [81] and many others [77, 82-85] indicated the superior performance of this configuration over the single lap, not only because of the increase in bonded area but also due to the smaller geometrical non-linearity. The reduced bending in the substrates produces lower transverse normal stresses in the overlap, and consequently higher joint strengths are attained.

Taking into account the important lessons learned from these studies, many authors have proposed techniques to minimize the transverse stresses along the bondline. Adhesive fillets and tapered substrates have become particularly popular methods to alleviate the stress concentrations at the ends of the overlap, and both their optimal design and effect on the performance of the joints have been widely discussed in the literature. For example, in an experimental investigation with CFRP-to-steel double lap joints, Adams et al. [86] showed that the strength was augmented if the inside adhered was tapered. Similar results were obtained by Sancaktar and Nirantar [87] for single lap joints with metallic substrates. Moreover, they used finite element analysis to demonstrate that the reductions in the tensile stresses at the ends of the overlap increased for sharper tapers. The semi-analytical solution proposed by Oterkus et al. [88] corroborated the same trend for composite joints, but indicated that the chamfers do not affect significantly the distribution of shear stresses. With low temperature applications in mind, Da Silva and Adams [89] combined numerical and experimental techniques to asses other unusual configurations to reduce peel stresses and increase the strength in titanium-to-CFRP double lap joints. According to this study, the beneficial effects of an internal taper with adhesive fillet depend on the properties of the adhesive, particularly its tensile strength. However, this joint configuration could be detrimental at low temperatures, in which case the performance would improve if the composite were used as the outer adherends.

Adhesive fillets, which help attenuating the stress concentrations at the ends of the overlap and yield more uniform distributions of transverse stresses along the bondline, have also been found to enhance the load-carrying capability of both single and double lap joints [86, 90, 91]. Confirmed experimentally, the gain in strength varies with the geometry of the fillets. A number of studies, often carried out employing numerical techniques, deal with the optimal shape [92-94]. The general consensus is that smaller spew angles produce larger reductions of the peak stresses. However, as noticed by Belingardi et al. [95], the inclusion of the fillets could lead to secondary stress peaks further inside the overlap. Since the magnitude of these secondary peaks could exceed that of the primary ones for very small spew angles, they concluded that 45° fillets represent the most favourable solution for metal-composite joints. Nonetheless, the difficulties to obtain reproducible spew profiles together with their susceptibility to external damage and environmental attack call into question the dependability of adhesive fillets for stress relief [90, 96].

The effects of the overlap length and the bondline thickness have also received considerable attention in the literature. Despite leading to higher shear stress concentrations, longer overlaps often yield lower average stresses and, particularly for ductile adhesives, they tend to attenuate the eccentricity of the load path. Consequently, the ultimate strength of the

joint increases with the overlap length up to a plateau value [24, 76, 87, 97]. With regard to the bondline thickness, several numerical and theoretical models, including Volkersen's theory, predict an improvement in the load carrying capability for thicker adhesive layers. In contrast, extensive experimental evidence suggests that the strength of the joints decreases with increasing bondline thickness [98, 99].

2.3 Fracture Mechanics

A stress-based approach has been traditionally followed to study the behaviour and to estimate the strength of adhesively-bonded joints [100-102]. The peel and shear stresses (or strains) in the adhesive layer are calculated using beam-bending analysis to predict failure, which is assumed to occur when these stresses (or strains) reach a critical value. As discussed before, this technique has been successfully applied to optimize different geometrical aspects of the joint, such as chamfer angle, overlap length or spew fillets [89, 93, 95]. However, since adhesive joints usually fail by initiation and propagation of flaws [103] which the stress-based method cannot account for, other methodologies such as fracture mechanics have become popular [22, 104, 105].

Fracture mechanics dates back to the 1920s, when Griffith recognized the influence of cracks on the strength of any material or structure [106]. Orowan [107, 108] and Irwin [109] extended Griffith's initial work to account for the effects of plasticity at the crack tip. They stated that a crack will grow if the available elastic energy exceeds the energy needed to create the new crack surfaces plus the energy dissipated during the plastic deformation. The critical elastic strain energy release rate required to propagate a crack – the fracture energy – is given the symbol G_c, after Griffith.

Irwin [110, 111] subsequently proposed an alternative stress criterion describing fracture based on the characterization of the stress field at the crack tip using a single parameter K, also known as stress intensity factor. According to this criterion, a crack will propagate when a critical stress state exists ahead of the crack tip, or when the stress intensity factor reaches a critical value K_c (i.e, the fracture toughness). Provided that the plastic zone is small, i.e. as long as Linear Elastic Fracture Mechanics (LEFM) is applicable, both the energy and the stress criteria are equivalent and a mathematical relationship between G_c and K_c exists.

The ability of fracture mechanics to deal with the effects of cracks and flaws make it ideally suited to study the behaviour and failure of adhesive joints, chiefly those derived from the energy-based criterion (G_c). This approach has gradually become more popular since the pioneering work of Ripling et al. [112] and Mostovoy et al. [113] to determine the fracture

toughness of metallic joints. Not only has it been proven to be a viable tool for static problems (e.g. [114, 115]), it has also found extensive use in fatigue and durability studies [55, 116-119]. Furthermore, the use of cyclic-fatigue tests based on a fracture mechanics approach, has been shown to provide an excellent accelerated test method for assessing joint durability [55].

2.3.1 Linear Elastic Fracture Mechanics (LEFM)

2.3.1.1 Stress Analysis of Cracks: The Stress Intensity Factor, K_c

Assuming isotropic, linear-elastic behaviour, several authors have presented analytical solutions for the stress field in various cracked bodies [110, 120]. These adopt the general form:

$$\sigma_{ij} = \left(\frac{K}{\sqrt{2\pi r}}\right) f_{ij}(\theta) + \sum_{s=0}^{\infty} A_s r^{\frac{s}{2}} g_{ij}^{s}(\theta) \tag{2.1}$$

where r and θ are polar coordinates with the origin at the crack tip, A_s is a constant and f_{ij} and g_{ij} are dimensionless functions. The dominant term $(1/\sqrt{r})$ approaches infinity as $r \rightarrow 0$, leading to a stress singularity at the tip. The stress intensity factor K defines the amplitude of the singularity or the manner in which $\sigma \rightarrow \infty$, and therefore the conditions near the crack tip.

2.3.1.2 Energy Balance: The Fracture Energy, G_c

Early results by Inglis [121] had previously implied the possibility of a stress singularity for infinitely sharp cracks. This issue encouraged Griffith to pursue a global energy approach rather than one based on local stresses. His original work started from the premise that, for a crack to nucleate or grow, the total energy of the system must either decrease or remain constant. The resulting energy balance for an incremental increase in the crack area dA establishes that the difference between the work done by the external forces (U_e) and the strain energy stored in the body (U_s) will be equal to the surface energy needed to create the new surfaces (γ_m):

$$\frac{d(U_e - U_s)}{da} \geq \gamma_m \frac{dA}{da} \tag{2.2}$$

Subsequently, Irwin modified the balance to include the energy dissipated by plastic deformation in the near-tip region (γ_p). For a crack propagating under equilibrium conditions, the corrected criterion could be expressed as:

$$\frac{1}{B}\frac{d(U_e - U_s)}{da} = 2(\gamma_m + \gamma_p) \tag{2.3}$$

The right hand term of the previous equation is often referred to as energy release rate, G. Crack propagation takes place when G reaches its critical value, G_c, thus:

$$\frac{1}{B}\left(\frac{dU_e}{da} - \frac{dU_s}{da}\right) \geq G_c \tag{2.4}$$

The so-called critical strain energy release rate or fracture energy quantifies the net change in potential energy that accompanies an increment in crack extension [122]. It is considered a material parameter, dependent not only on the intrinsic molecular forces but also on all the different energy dissipating mechanisms acting in the fracture process zone (FPZ) [11]. For that reason, G_c is particularly well-suited to characterize the global fracture behaviour of bonded joints and is currently used for adhesive development. However, its value would be expected to vary with the loading conditions (test rate [123-126], temperature [127-129] and environment [18-20, 130, 131]) and the locus of failure, that is, whether failure occurred at the adhesive-substrate interface or within the adhesive layer (i.e. cohesively).

Using a crack closure analysis, Irwin also demonstrated that, under LEFM assumptions, G_c and K_c may be related. For example, for an infinite plate with a through-thickness crack subjected to uniform tension, this relationship is given by:

$$G_c = \begin{cases} \dfrac{K_c^2}{E} & \text{for plane stress} \\ \dfrac{K_c^2}{E}(1-\nu^2) & \text{for plane strain} \end{cases} \tag{2.5}$$

where E and ν are the Young's modulus and the Poisson's ratio respectively.

2.3.1.3 Fracture Modes

In a general case, the stress distribution around a crack is the result of superimposing three basic types of loading, namely: opening, in-plane shear and out-of-plane or antiplane shear (modes I, II and III respectively, see Figure 2.4).

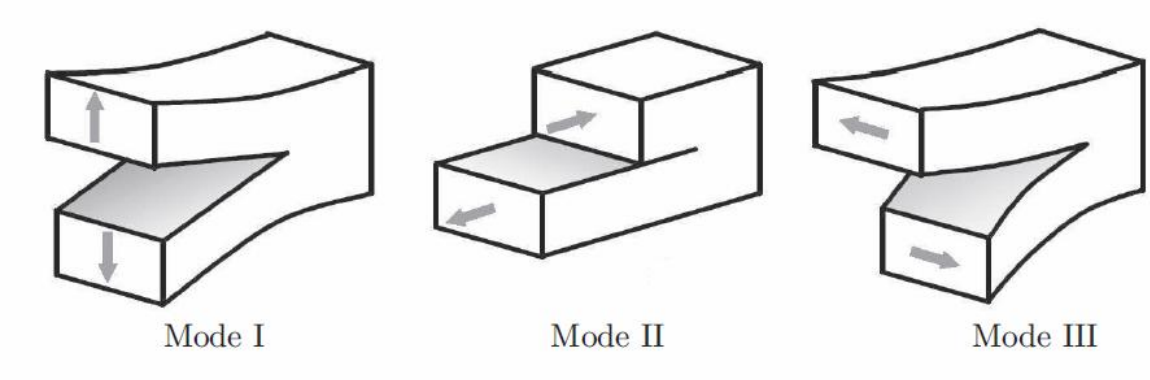

Figure 2.4. Modes of loading that can be applied to a crack [132].

The opening mode or mode I is the most damaging type of loading for the interface, and therefore it has been the main focus of numerous studies (e.g. [133-135]). In addition, since the mode I critical energy release rate (G_{Ic}) very often corresponds to the lowest value of the fracture energy, bonded joints are typically designed to minimize this component. Furthermore, some authors [136-138] maintain that crack propagation only occurs under pure mode I conditions (at least at the very local level). According to this view, the sliding and antiplane shear modes do not lead to fracture themselves, but instead they induce a local opening component ultimately responsible for crack propagation. Nevertheless, mode II has recently became an important topic among the fracture mechanics community [139-142]. However, very few publications to date deal with adhesive joints subjected to mode III [143-145].

There exists considerable experimental evidence that suggests that the value of G_c generally depends on the fracture mode [146-149]. Moreover, the type of loading has been found to affect the crack propagation path or loci of failure. For example, investigating the behaviour of adhesively-bonded CFRP joints, Blackman et al. [125] reported that mixed mode I/II tends to drive the crack towards the interface and, if the transverse tensile strength of the laminate was low enough, fracture could take place in the composite arms.

2.3.1.4 Plastic Zone

In contrast to the predictions of the analytical solutions, the stresses at the crack tip in real materials are finite. Plastic deformation in the vicinity of the tip causes the crack to blunt, and other inelastic processes such as crazing or voiding can lead to further stress relaxation. Nonetheless, if the non-linear behaviour were confined to a sufficiently small region, the theoretical stress field given by equation (2.1) would not be greatly disturbed and LEFM would still be valid (i.e. K_c would still uniquely characterize the crack-tip conditions).

Given that the fracture energy encompasses all viscoelastic and plastic energy dissipated in the near-tip region, its shape and size could have important repercussions on the ultimate value of G_c. Indeed, optimizing the dissipation mechanisms and widening the volume of material in which they act are key aspects in the development of new, tougher adhesives [11]. Irwin [150, 151] proposed a first approximation to the size of the plastic zone. Assuming a homogeneous and isotropic material which plastifies when the normal stress reaches the uniaxial yield stress σ_Y, the radius of the mode I zone for θ=0 (i.e. r_y) is given by:

$$r_y = \begin{cases} \frac{1}{2\pi}\left(\frac{K_{Ic}}{\sigma_Y}\right)^2 & \text{for plane stress} \\ \frac{1}{6\pi}\left(\frac{K_{Ic}}{\sigma_Y}\right)^2 & \text{for plane strain} \end{cases} \tag{2.6}$$

However, the applicability of this result to bonded joints is the subject of some controversy. As pointed out in [24, 129], the volume of the plastic zone developing in the relatively thin adhesive layers may be restricted by the presence of high modulus and high yield strength substrates. At the same time, the stiff adherends induce higher normal stresses than in the homogeneous case ahead of the tip, potentially leading to longer plastic zones. Overall, it is the relative importance of these two phenomena that will define the ultimate shape and size of the plastic zone. In fact, their interaction has been suggested as a possible explanation for the variation of the fracture energy with the bondline thickness observed for some toughened adhesives [129, 152], see Figure 2.5.

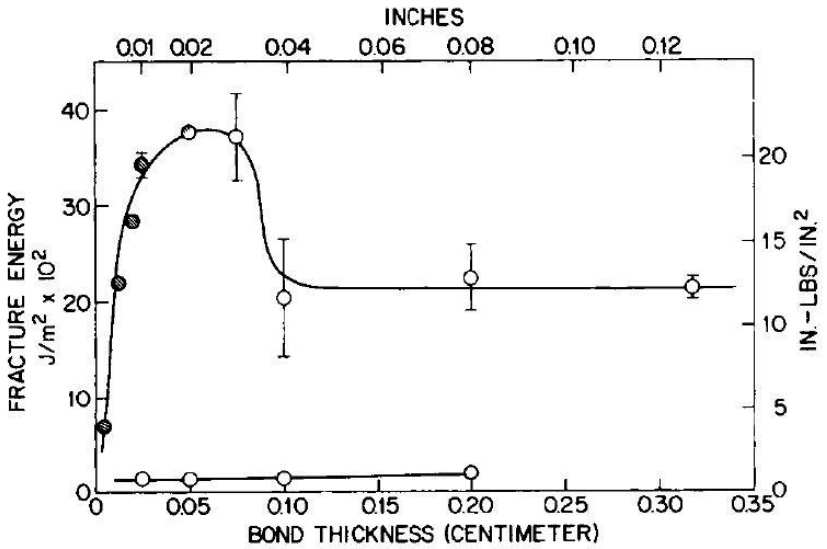

Figure 2.5. Mode I adhesive fracture energy as a function of the bondline thickness for joints consisting of aluminium alloy substrates bonded with a rubber-toughened epoxy [152].

2.3.1.5 Level of Constraint: Triaxial Stress State around the Crack tip

The stress field given in equation (2.1) represents a two-dimensional approximation. Hence any subsequent relationships derived from this result (e.g. equations (2.5) or (2.6)) would be valid only under those conditions. However, a 2D approach might not be always acceptable. For example, as shown by Narashimhan and Rosakis [153] using a three-dimensional elastic-plastic finite element analysis, the stress distribution near a crack the tip in a plate with finite thickness subjected to in-plane loading is a complex function of the x, y and z coordinates. Loaded to higher normal stresses σ_{yy} than in the surroundings, the material in the vicinity of the tip would try to contract in the x and y directions. These contractions would be prevented by the adjacent material, inducing a triaxial stress state in the near-tip region. As seen in Figure 2.6, the level of constraint and therefore of triaxiality would vary across the width of the plate and with the distance to the crack [122].

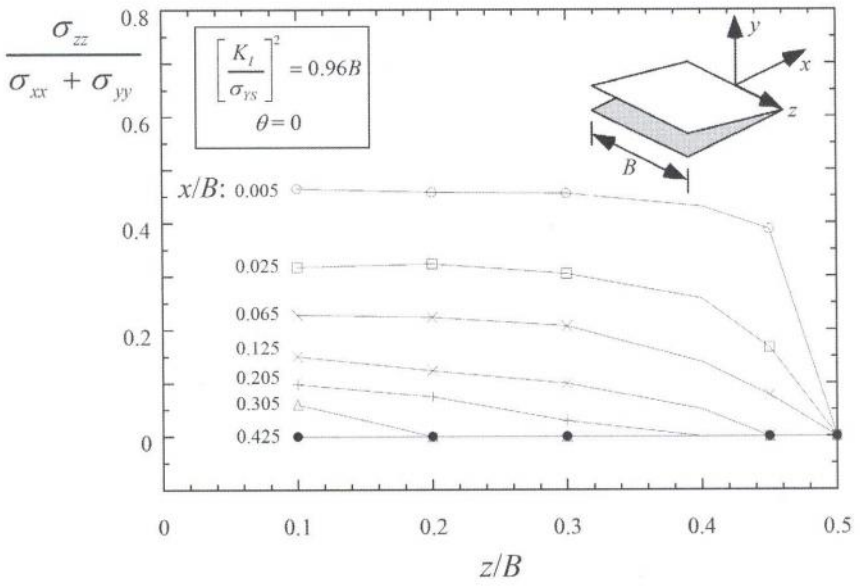

Figure 2.6. Transverse stress across the width of a plate with thickness *B* as a function of the distance from the crack tip [122].

In bonded joints, the deformation of the substrates imposes additional constraints on the adhesive layer [129]. This effect, which is a function of the thickness and mechanical properties of the adherends (e.g. see [154]), combined with the influence of the finite bondline thickness complicates the problem even further [155].

The resulting stress state can have important repercussions on the fracture response. Particularly, the crack front constraint has been found to impact on the yielding behaviour of the adhesive [156], affecting the shape and size of the plastic zone and therefore the fracture

energy. Triaxial stresses have also been found to assist certain energy dissipation and fracture mechanisms, some of which are particularly important in rubber-toughened epoxies (e.g. debonding of rubber particles and cavitation) [24, 69]. This, together with the changes in the triaxility state across the width of the joint, has been used to explain the complex phenomenon of crack tunnelling [122].

Finally, it has been previously suggested that one-parameter fracture mechanics struggles to describe the constraint effects [155, 157]. Furthermore, the geometrical dependency of many of these aspects could compromise the transferability of the results obtained with standardized test specimens to real structures (e.g. [155, 158]).

2.3.2 Determination of the Fracture Energy: Analysis Methods

A number of methods for the experimental determination of the fracture resistance of structural adhesive joints are reviewed in this section. Based upon LEFM, they all consider a crack of width B and length a between two linear-elastic bodies which would propagate if the strain energy release rate reaches its critical value, G_c.

2.3.2.1 The Area Method

This method is a direct application of the energy balance proposed by Irwin [159]. For a small crack extension Δa, equation (2.4) could be re-written in its incremental form:

$$G_c = \frac{1}{B}\left(\frac{\Delta U_e - \Delta U_s}{\Delta a}\right) = \frac{1}{B}\frac{\Delta U}{\Delta a} \tag{2.7}$$

Valid for any type of elastic behaviour (linear or non-linear), the previous expression can be directly used to determine G_c experimentally by loading a specimen to propagate its initial defect from a to $a + \Delta a$ and then unloading (see Figure 2.7). In that case, the change in energy ΔU can be calculated as the area enclosed by the loading and unloading paths and the propagation section of the P-δ trace (area $\widehat{012}$). As illustrated by equation (2.8) computing this area is simple in the linear case, whereas numerical integration could be employed if non-linear behaviour were observed (as suggested in [160]).

$$\Delta U = \frac{P_1\delta_2 - P_2\delta_1}{2} \longrightarrow G_c = \frac{1}{2B}\left(\frac{P_1\delta_2 - P_2\delta_1}{\Delta a}\right) \tag{2.8}$$

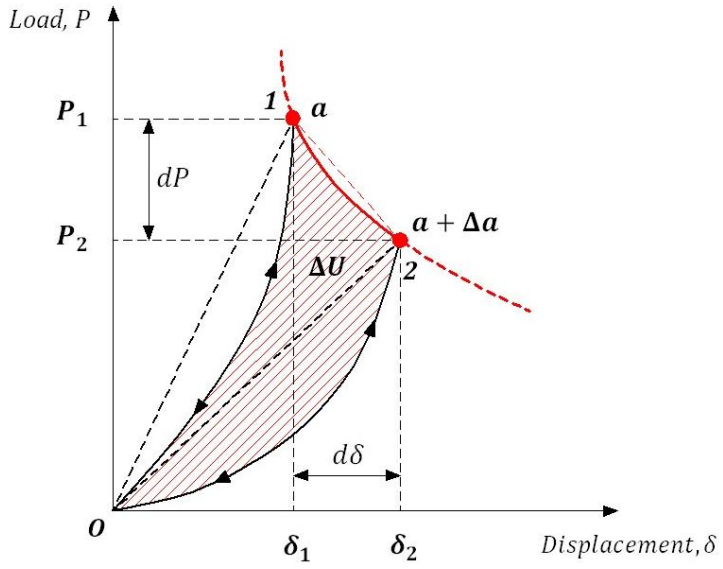

Figure 2.7. Graphical definition of G_c using the area method.

It should be noted that, despite being derived from an exact definition of G_c, the area method is not exempt from inaccuracies. Most of these are associated with the approximation of the derivatives in (2.4) by the difference between two finite measurements, effectively yielding an average G_c value over a given crack extension Δa. Additional problems may arise from relatively common phenomena occurring during the unloading phase, such as hysteresis and not perfectly-closed cracks due to local plasticity or debris (see [147]). Furthermore, if linear behaviour is not assumed, the actual experimental procedure is quite time-consuming as numerous loading-unloading cycles for small crack length increments are required for each specimen in order to obtain representative estimates.

2.3.2.2 The Compliance Method

Initially proposed by Berry [161] for self-propagating cracks in linear-elastic materials, this method circumvents the averaging nature of the area approach by conveniently introducing the specimen compliance C (inverse of the stiffness) as a function of the crack length a.

$$C(a) = \delta/P \longrightarrow \Delta\delta = P\Delta C + C\Delta P \tag{2.9}$$

Using the information in Figure 2.7, (2.8) can be re-written as:

$$\left.\begin{matrix} P_2 = P_1 + \Delta P \\ \delta_2 = \delta_1 + \Delta\delta \end{matrix}\right\} \longrightarrow G_c = \frac{1}{2B}\left(\frac{P_1\delta_2 - P_2\delta_1}{\Delta a}\right) = \frac{1}{2B}\left(\frac{P_1\Delta\delta - \delta_1\Delta P}{\Delta a}\right) \tag{2.10}$$

which combined with (2.9) gives

$$G_c = \frac{P^2}{2B}\frac{\Delta C}{\Delta a} = \frac{P^2}{2B}\frac{dC}{da} \tag{2.11}$$

Note that the same expression, also known as the Irwin-Kies equation, could be obtained directly from (2.4) if linear loading and unloading paths are assumed (see [122]).

For practical applications, the function $C = C(a)$ must be determined experimentally. This requires recording the load P, displacement δ and crack length a throughout the test, and fitting the results to a suitable curve, usually of the form:

$$C = C_0 + \mu a^n \tag{2.12}$$

where C_0 and μ are constants. As suggested in [162-164], the exponent n is typically 3, although in a general case its value could be determined by plotting the logarithm of the compliance versus the logarithm of the crack length [165]. Equation (2.12) can be easily differentiated and introduced in (2.11) to estimate G_c.

Regarded as highly accurate by many authors [160, 162], Berry's method does not require knowledge of the elastic modulus of the substrates. However, it relies heavily on precise crack length measurements, which can prove difficult to obtain when non self-similar or unstable propagation occurs. Similar difficulties may arise in mode II and mixed mode testing of tough systems, where the large damage zones develop ahead of the continuous crack and could lead to ambiguous length readings.

2.3.2.3 Beam Analysis

Originally developed by Williams [146] for delamination problems in fibre-reinforced composites, this method uses classical beam theory for the analysis of the asymmetric cracked laminate illustrated Figure 2.8 and relates the total energy release rate to the in-plane local loads and moments.

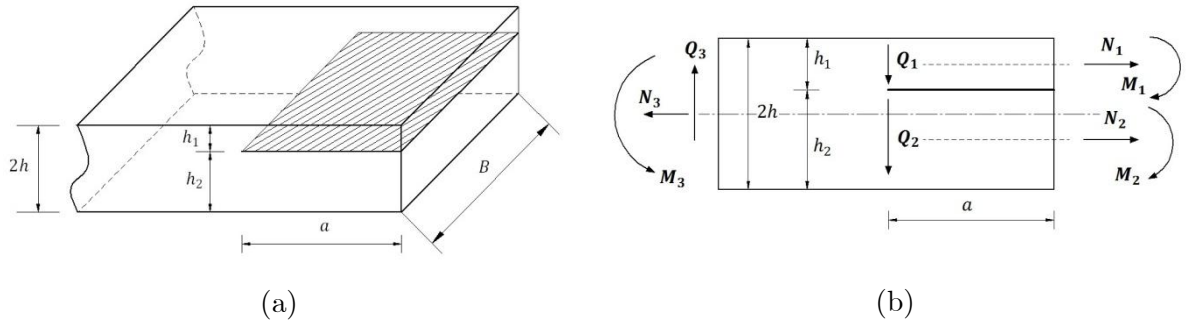

(a) (b)

Figure 2.8. (a) Schematic representation of the asymmetric laminate considered by Williams and (b) the corresponding in-plane loading (uniform across the width of the specimen) for a general case.

Starting from Irwin's energy balance and assuming uniform loading across the width of the specimen (B) and self-similar crack propagation, it can be demonstrated that the strain energy release rate induced when only bending moments are applied is given by

$$G = \frac{1}{16BEI}\left[\frac{{M_1}^2}{\xi^3} + \frac{{M_2}^2}{(1-\xi)^3} - (M_1 + M_2)^2\right] \tag{2.13}$$

where E and I are the elastic modulus parallel to the crack and the second moment of area of half the un-cracked laminate ($I = Bh^3/12$) respectively. The bending moments M_1 and M_2 are taken as positive if they have the directions shown in Figure 2.8-b, while the thickness ratio is accounted for via the parameter ξ:

$$\xi = \frac{h_1}{h_1 + h_2} \tag{2.14}$$

Equivalent expressions have been obtained for axial loads (N_1 and N_2) and shear forces (Q_1 and Q_2) [146] (taken as positive in the directions shown in Figure 2.8-b):

$$G = \frac{1}{4BEA}\left[\frac{{N_1}^2}{\xi} + \frac{{N_2}^2}{(1-\xi)} - (N_1 + N_2)^2\right] \tag{2.15}$$

$$G = \frac{3(1+\upsilon)}{5BEA}\left[\frac{1}{\xi}\left(\frac{dM_1}{da}\right)^2 + \frac{1}{(1-\xi)}\left(\frac{dM_2}{da}\right)^2 - \left(\frac{dM_1}{da} + \frac{dM_2}{da}\right)^2\right] \tag{2.16}$$

where A is the cross-sectional area of the half-laminate ($A = Bh$) and υ is the Poisson's ratio. A quadratic shear stress distribution has been presupposed in the derivation of (2.16), in

which the shear forces arise from the bending moment gradients (i.e. $Q_i = dM_i/da$). In a general problem the contribution of the various loading types would be added by superposition, i.e. the total value of G would be obtained from the combination of equations (2.13), (2.15) and (2.16).

The strength of these results lies in the possibility of calculating the strain energy release rate from the loads applied to the upper and lower arms (top and bottom substrates in adhesive joints) regardless of what happens in the rest of the specimen. Furthermore, correction factors for large displacements have been derived for the most common test geometries [137, 147, 166, 167], broadening the validity of this approach.

For practical applications, a simple beam analysis would provide relationships between the applied forces, the crack length and the quantities M_1, M_2, N_1, etc. These could be substituted into equations (2.13), (2.15) and (2.16) to obtained a function of the form $G = G(load, a)$, which could then be integrated with respect to the crack length and introduced into Irwin-Kies equation to calculate the compliance $C = C(a)$. Finally, this information could be combined with the propagation part of the load-displacement trace to calculate $G_c = G_c(a)$. Examples of this procedure for the DCB, ELS, ENF, AFRMM and MMB can be found in be found in [146, 147, 168].

In line with the original formulation, this analysis ignores the presence of the adhesive layer. Consequently its contribution to the overall compliance of the joint is also neglected. Given the typically low modulus of these materials compared to that of the substrates, this has proven a reasonable simplification for bondline thicknesses between 0.1 and 1.0mm (see [133, 165]).

Suo and Hutchinson [169, 170] have also employed beam theory to investigate the propagation of a semi-infinite interface crack between two finite isotropic, elastic layers. However, the use of superposition led them to conclude that the fracture process and hence the total energy release rate could be characterized using only two loading parameters (a bending moment and an axial force). Nevertheless, it is possible to prove that their expression for the total G_c is equivalent to that proposed by Williams for the usual test geometries if shear contributions are omitted in the latter analysis. Such demonstration is not included in this thesis, but it would be similar to that shown in Appendix D, where the equivalence is established between Williams approach and the method proposed by Schapery and Davidson [171] in terms of the total G.

2.3.2.4 Plate Analysis: Davidson´s Crack Tip Element (CTE)

Working in parallel with Suo and Hutchinson [169, 170], Schapery and Davidson [171] also showed that the total energy release rate for two-dimensional crack propagation processes is a function of only two independent load parameters. However, they reached this conclusion using classical plate theory, which allowed the expression of G to be written in terms of the concentrated crack tip force and moment (N_c and M_c respectively). Applying a modified version of Irwin's virtual crack closure method [110] to the crack-tip element (CTE) illustrated in Figure 2.9, they proposed the following relationship:

$$G = \frac{1}{2}\left[c_1 {N_c}^2 + c_2 {M_c}^2 + 2c_{12} N_c M_c\right] \tag{2.17}$$

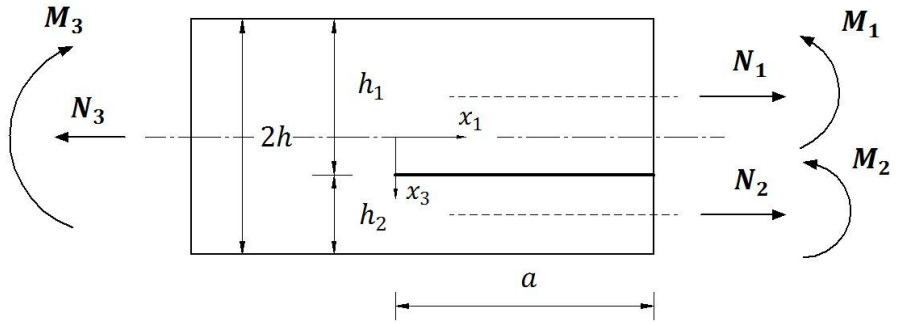

Figure 2.9. Crack Tip Element and external loading for Davidson´s plate analysis of a cracked laminate (note that for subsequent comparisons with the Williams method, the nomenclature shown here is different from that employed in the original formulations [171, 172]).

N_c and M_c occur naturally to enforce displacement compatibility ahead of the crack tip along the plane $x_3 = 0$, and could be obtained from the remote loading employing equilibrium considerations (see equations (2.18) and (2.19)). Furthermore, these quantities fully characterize the fracture loading conditions at the crack tip regardless of the damage state, which could prove advantageous for the subsequent mix mode partitioning [172].

$$\begin{cases} N_3 = N_1 + N_2 \\ M_3 = M_1 + M_2 + N_2 \dfrac{h_1}{2} - N_1 \dfrac{h_2}{2} \end{cases} \tag{2.18}$$

$$\begin{cases} N_c = -N_1 + a_{11} N_3 + a_{12} M_3 \\ M_c = M_1 - N_1 \dfrac{h_1}{2} + \left(a_{11} \dfrac{h_1}{2} - a_{21}\right) N_3 + \left(a_{12} \dfrac{h_1}{2} - a_{22}\right) M_3 \end{cases} \tag{2.19}$$

In line with plate theory, all the forces and moments that appear in equations (2.17)-(2.19) are resultants per unit width (B) taken as positive in the directions shown in Figure 2.9. The constants c_1, c_2, c_{12} and a_{ij} depend only on geometric and material properties and their definition for a general problem as well as simplifications for the isotropic and orthotropic cases are given in Appendix C.

In contrast to the Williams method, the CTE proposed by Schapery and Davidson does not account for transverse shear effects. However it can be demonstrated that, if those were omitted in the former, both analyses result in the same expressions for the total energy release rate (and hence the same compliance) when applied to the typical test geometries (see Appendix D).

$$G_{Total}^{Williams} = G_{Total}^{Davidson} \tag{2.20}$$

Finally, it is worth noting that Davidson's method was also originally conceived for delamination in fibre-reinforced composites. Hence, the contribution of the bondline is again neglected when this technique is employed for the study of adhesive joints.

2.3.3 Mode Partitioning or Decomposition Strategies

As mentioned above, there exists considerable experimental evidence to suggest that the value of G_c obtained with any of the methods described in the previous section generally varies with the type of loading [146-149]. Therefore, it would be sensible to separate the total energy release rate into its individual components which, in a two-dimensional problem, would correspond to the opening and in-plane shear modes. Assuming no interaction between them [136]:

$$G = G_I + G_{II} \tag{2.21}$$

The same reasoning is applicable to the fracture criterion. However, "mode interaction" is usually accepted in this case, resulting in a much more complex expression that adopts the general form $G_c = G_c(G_{II}/G)$. As opposed to the equivalent "failure locus curve" (plot of the mode I component of G_c against the corresponding mode II value) favoured by some authors [137], this representation of the fracture criterion originally suggested by O'Brian et al. [173] uses independent variables. Since testing all possible mixed mode ratios is not practical, the definition of a law which extrapolates the fracture energy to any mode combination from the results obtained in a limited number of experiments is essential to predict crack propagation

accurately. A series of fracture mechanics specimens exhibiting a range of mode mixities are typically tested and the measured values fitted to a suitable function in order to define $G_c = G_c(G_{II}/G)$. Some of the most common test geometries are discussed in section 2.3.4, while a brief review of the analytical models developed to approximate the experimental data can be found in section 2.3.5 (see [174] for a summary).

In light of the above, it is essential to have a method that can accurately decompose the energy release rate into its individual components. Not only will this be crucial to obtain the appropriate failure criterion (that is, to determine the mode mix of the various fracture mechanics specimens), but also to analyse the structural configuration and loading case of interest in order to compare the applied energy release rate with the correct critical value.

This is not a trivial problem and has drawn the attention of many researchers. A number of partitioning schemes have been suggested in the literature, and while the majority give identical results when the crack is located symmetrically in the specimen (geometrically and in terms of the material properties below and above the propagation path), their mode-mix predictions differ for the asymmetric cases [136, 175]. Based in analytical solutions, numerical techniques or a combination of both, most of them can be split up into two groups according to [136, 137]: "local" and "global" methods.

Those strategies belonging to the first category, e.g. as proposed by Suo and Hutchinson [169, 170], assume the existence of a local singularity near the crack tip. As a result, the stress and displacement fields in this region and therefore the mode I and II components of G are obtained from the corresponding stress intensity factors (K_I and K_{II}). The Virtual Crack Closure Technique (VCCT) [176] or any other numerical method derived from classical LEFM (e.g. [177]) also fall within this group. For obvious reasons, the validity of these decompositions is subject to the presence of the so-called "K-dominated area", and more specifically to its relative size compared to that of the damage zone developed ahead of the crack tip [136, 160, 162, 175, 178]. In fact, the large process zones reported for many composites and structural adhesives suggests that the fracture process is not always controlled by the singularity, questioning the suitability of the local methods in those situations.

However, even in those cases in which the singularity is not dominant, the global energy balance is still applicable and can be employed to decompose the total strain energy release rate into its individual components. Such is the case with the Williams partitioning scheme [146, 168], where modes I and II are simply identified as pure crack opening and sliding modes respectively. In contrast to the local approach, this scheme does not require local symmetry of deformation at the crack tip, hence implicitly obviating the singular field.

Hashemi et al. [175] compared Williams decomposition strategy with the local method using mixed-mode delamination data obtained for unidirectional thermosetting and thermoplastic carbon-fibre composites. The fixed and varying ratio mixed mode test geometries (FRMM and VRMM respectively) were employed in that study, and it was concluded that the global approach was the more appropriate partitioning scheme for these materials. Equivalent results on similar PEEK- and epoxy-based laminates were reported by Kinloch et al. [137] using a modified version of the MMB specimen. In both cases the superiority of the global partitioning was attributed to a small K-dominated area, most likely masked by local damage in the near-tip region.

Unfortunately, the universal applicability of the Williams method has been also called into question. In an attempt to define an initiation criterion for delamination in glass-epoxy composites, Ducept et al. [179] pointed to the local approach as the most suitable option for the analysis of such materials. However, they proposed that these observations were not necessarily in contradiction with previous findings, suggesting that the thicker resin layers observed in glass fibre composites (which scales the radius of the singular field) could result in larger singular regions ahead of the crack tip.

The partitioning method proposed by Davidson and co-workers [171, 172] also deserves special attention. They recommended a definition of the mode mixity based on quantities that, while fully characterizing the near-tip loading conditions, were insensitive to the local damage state. Maintaining the crack-tip element (CTE) introduced in section 2.3.2.4, they suggested the use of the concentrated crack tip force N_c and moment M_c. Furthermore, in line with Suo and Hutchinson [170], they concluded that neither beam analysis nor plate theory provide enough information to define the mixed mode ratio in two dimensional problems. Instead, an additional parameter dependent on the geometry and the material properties but insensitive to the type of loading is required to fully characterize the fracture process. Referred to as the "mixed mode parameter, Ω" (ω in the formulation by Suo and Hutchinson), it does not affect the calculation of the total G and could be determined by solving one particular loading case.

In its original formulation, Davidson et al. proposed a finite element analysis of the CTE employing VCCT to obtain Ω. Hence the resulting decomposition, designated here as CTE/SF, indirectly assumed a near-tip singularity and consequently coincided with the partitioning proposed in [170]. The equivalence between Ω and ω, which Suo and Hutchinson extracted from the numerical solution of integral equations, can be found in [172]. That is, the singular field solution is a particular case of Davidson's method, which would not produce realistic results unless the damage zone is small compared with the K-dominated area.

Nonetheless, the shortcomings of the of the CTE/SF decomposition were highlighted by Davidson et al. [162]. After determining the fracture criterion for a unidirectional carbon-epoxy laminate using various symmetric test specimens (for which the mode mixity is independent of the partitioning scheme employed), they compared various decomposition strategies on the basis of their delamination predictions for various unbalanced configurations. Both the Williams method and the local approach (represented by the CTE/SF and the FE version of the VCCT) failed to produce a criterion where the fracture energy was a single-valued function of the mode mixity. On the other hand, an effective mixed mode parameter (Ω_{NSF}) was derived from that experimental data so that specimens with the same mixed mode ratio would produce the same fracture toughness values. The resulting partitioning scheme, from now on referred to as CTE/NSF (making reference to the disregard of the singularity), was later proved valid for the prediction of delamination in multidirectional composites with relatively small zones of K-dominance near the crack tip [160, 178].

Other authors have also addressed the mode partitioning issue. Xu and Tippur [180] examined a large mismatch PMMA/aluminium bi-material system using analytical, numerical and optical techniques. Employing an asymptotic crack tip field expansion instead of K-dominance terms alone to account for the contribution of non-singular stresses, they were able to improve both the experimentally measured stress intensity factors as well as the mode-mixity predictions. The resulting variation of toughness with the mixed mode ratio agreed well with that previously obtained by Tevergaard and Hutchinson [181], who embedded a fracture process zone in their computational models in order to take into consideration the influence of the crack tip plasticity. However, despite the unquestionable potential of the last method to circumvent the problem of exceedingly small singularity-dominated zones, they anticipated that its accuracy would be inevitably linked to the definition of sufficiently realistic traction-separation laws.

Additional efforts have been directed to improve the original partitioning schemes. For example, Li et al. [182] tried refined the method proposed by Suo and Hutchinson by incorporating transverse shear effects extracted from FE analyses, while Point and Sacco [183] adopted a model based on adhesion theory to enhance the global approach. Two new versions of the global decomposition using beam theory have been recently published by Wang and Harvey [184-186]. Developed separately using both Euler-Bernoulli and Timoshenko beam theories, these new approaches employ orthogonal pairs of pure modes to carry out the mixed mode partitioning. The same authors have also proposed a third solution which, obtained as the average of the two extreme cases, is reported to recover the singularity at the crack tip.

Initially validated only against FE simulations, the Wang-Harvey methodologies have been recently used to analyse experimental delamination data measured with asymmetric DCB and FRMM test geometries for unidirectional CFRP [186]. In contrast with the complex shape obtained in [136] with the Williams method, the Euler version was found to produce a fairly linear failure criterion. On the other hand, Timoshenko's theory produced inadequate results due to the large length-to-thickness aspect ratio of the specimens, while the averaged decomposition was predictably equivalent to that by Suo and Hutchinson. In conclusion, despite the promising initial results and the potential of Wang-Harvey theories to help explain some of the particulars of the controversial subject of mode partitioning, further experimental evaluation and a better understanding of their implications are still required.

Finally, it should be noted that most of these decompositions, including both Williams and Davidson's, were originally developed for delamination in fibre-reinforced composites and therefore neglect the presence of the bondline when applied to adhesive joints. Such hypothesis is considered acceptable for the calculation of the total energy release rate if the contribution of the adhesive layer to the overall compliance of the system is small. However, whether the influence of the bondline on the mixed mode ratio can be ignored still remains an open question. Alfredsson and Högberg [187, 188] proposed a specific methodology for the study of these problems. The so-called "beam/adhesive-layer" or "b/a" model incorporates the effects of transverse forces and the flexibility of the constrained adhesive layer, thus replacing the crack-tip singularity with a stress concentration zone. In line with most partitioning schemes reviewed above, the resulting strategy seems to agree well with the local approach for specimens in which the crack propagation path is a plane of symmetry. Conversely, the mode-mix solution for unbalanced cases is found to be strongly dependent on the substrate/adhesive relative stiffness.

Further details of both the Williams and Davidson mode decompositions, which have been used in the present work to analyse the experimental fracture mechanics data obtained for various test specimens, are given next.

2.3.3.1 Williams Mode Decomposition

Employing the beam analysis introduced in section 2.3.2.3, Williams proposed a partitioning scheme based on identifying the particular loading conditions responsible for each pure mode [146]. Take for instance the case shown in Figure 2.8, where only bending moments are applied: while the opening mode only requires equal but opposing moments (i.e. $M_1 = -M_I$ and $M_2 = M_I$), pure mode II is obtained when the resulting curvature in both the lower and

upper arms is the same (i.e. $M_1 = M_{II}$ and $M_2 = \psi M_{II}$). Any general loading condition could therefore be expressed in terms of M_I and M_{II} by invoking the principle of superposition:

$$\begin{cases} M_1 = M_{II} - M_I \\ M_2 = \psi M_{II} + M_I \end{cases} \rightarrow \begin{cases} M_I = \dfrac{M_2 - \psi M_1}{1 + \psi} \\ M_{II} = \dfrac{M_1 + M_2}{1 + \psi} \end{cases} \tag{2.22}$$

where ψ is a geometric parameters given by:

$$\psi = \left(\frac{1 - \xi}{\xi}\right)^3 \tag{2.23}$$

Substituting (2.22) into (2.13) leads to an expression of G with no cross product terms of M_I and M_{II} which can be easily combined with (2.21) to carry out the mode decomposition:

$$G = G_I + G_{II} \begin{cases} G_I = \dfrac{{M_I}^2}{16BEI} \dfrac{(1 + \psi)}{(1 - \xi)^3} \\ G_{II} = \dfrac{3{M_{II}}^2}{16BEI} \dfrac{(1 - \xi)(1 + \psi)}{\xi^2} \end{cases} \tag{2.24}$$

The mixed mode ratio as defined in the typical failure criterion (i.e. G_{II}/G) can be written as:

$$\frac{G_{II}}{G} = \frac{G_{II}}{G_I + G_{II}} = \frac{3{M_{II}}^2 (1 - \xi)^4}{\xi^2 {M_I}^2 + 3{M_{II}}^2 (1 - \xi)^4} \tag{2.25}$$

Equivalent results can be obtained for axial forces and transverse stresses using equations (2.15) and (2.16), although Williams suggested that they would only contribute to pure modes II and I respectively [146]:

$$\begin{cases} G_I = \dfrac{3(1 + \upsilon){Q_I}^2}{5BEA} \left[\dfrac{1}{\xi} + \dfrac{1}{1 - \xi}\right] \\ G_{II} = \dfrac{3{N_{II}}^2}{4BEA} \dfrac{(1 - 2\xi)^2 (1 + \psi)}{\xi (1 - \xi)} \end{cases} \tag{2.26}$$

where Q_I and N_{II} are calculated from the remote applied loading using the relevant superposition:

$$\begin{cases} Q_I = \xi Q_2 - (1-\xi)Q_1 = \xi \dfrac{dM_2}{da} - (1-\xi)\dfrac{dM_1}{da} \\ N_{II} = -\left[\dfrac{\xi N_2 - (1-\xi)N_1}{(1-\xi)}\right] \end{cases} \tag{2.27}$$

2.3.3.2 Davidson Mode Decomposition

As shown in [171, 172], the classical plate analysis of the CTE illustrated in Figure 2.9 can be extended to address the issue of mode partitioning. Such decomposition is best carried out in terms of the concentrated crack tip force and moment (N_c and M_c respectively) and the so-called mixed mode parameter, Ω [160, 162, 172]. Unobtainable from beam or plate theory, Ω must be therefore determined from a separate continuum analysis of a particular loading case or using experimental data.

Even though N_c and M_c do not depend on the existence of a singularity at the crack tip, the original partitioning of the total strain energy release rate was performed using the complex stress intensity factor. Therefore it is necessary to discriminate between cases with oscillatory and non-oscillatory singularities. Taking into account the configuration of all the fracture mechanics specimens tested in the present work, only the latter was considered here. The mixed mode ratio as predicted by Davidson's method for problems where the same material is below and above the crack plane (i.e. non-oscillatory singularities) can be expressed as:

$$\frac{G_{II}}{G} = \frac{[N_c\sqrt{c_1}\cos\Omega + M_c\sqrt{c_2}\sin(\Gamma+\Omega)]^2}{c_1{N_c}^2 + c_2{M_c}^2 + 2\sqrt{c_{12}}N_cM_c\sin\Gamma} \tag{2.28}$$

The general expressions for the quantities c_1, c_2, c_{12} and $\sin\Gamma$ (dependent only on geometrical and material properties) are given in Appendix C, whereas the values of N_c and M_c can be computed from the remote loads applied to the CTE using equilibrium equations (2.18) and (2.19). The conditions assumed at the crack tip, specifically whether dominated by a singularity or localized damage, play a major role in the determination of Ω and consequently would give raise to two different versions of this partitioning scheme, namely: the singular and non-singular field decompositions (CTE/SF and CTE/NSF respectively). Both alternatives are described next. Note that, as for the total energy release rate obtained with plate theory (i.e. equation (2.17)), neither of these can account for the contribution of transverse shear stresses to the mode-mixity.

2.3.3.2.1 Singular Field Mode Decomposition (CTE/SF)

For cases in which the stress and strain fields near the crack tip exhibit the singular behaviour predicted by LEFM (i.e. the radius of the K-dominated zone is larger than that of the damage zone), the mixed mode parameter can be derived from a local analysis of the near-tip region. In their original formulation, Davidson et al. [172] suggested a finite element analysis of the CTE employing a form of the virtual crack closure technique. After an exhaustive numerical investigation carried out over a wide range of arm thicknesses and mechanical properties, they proposed general functions for Ω which were valid for non-oscillatory singularities. These were in excellent agreement with the solution presented in [170]. For any given isotropic or orthotropic material, the variation of Ω with the arm thickness ratio (i.e. h_2/h_1) can be estimated with a reasonable accuracy interpolating linearly (at fixed γ) between the following curves:

$$\begin{cases} \Omega^{\circ}(\gamma, \rho = 1) = 23.529\gamma - 6.8406\gamma^3 + 1.0706\gamma^5 \\ \Omega^{\circ}(\gamma, \rho = 2) = 24.158\gamma - 7.9834\gamma^3 + 1.6055\gamma^5 \\ \Omega^{\circ}(\gamma, \rho = 4) = 24.375\gamma - 8.1897\gamma^3 + 1.6650\gamma^5 \\ \Omega^{\circ}(\gamma, \rho = 8) = 24.382\gamma - 8.2627\gamma^3 + 1.6924\gamma^5 \end{cases} \tag{2.29}$$

where $\gamma = \log_{10}(h_2/h_1)$ and ρ is a function of the elastic properties which is equal to 1 for isotropic materials and defined as follows for the orthotropic case (see Figure 2.9 for details of the coordinate system):

$$\rho = \frac{1}{2}\sqrt{E_1 E_3}\left(\frac{1}{G_{13}} - \frac{2\upsilon_{13}}{E_3}\right) \tag{2.30}$$

2.3.3.2.2 Non-Singular Field Mode Decomposition (CTE/NSF)

When the concept of the singular-field is not applicable, as in the cases where the damage zone ahead of the crack tip was large compared to the K-dominated area, the decomposition given by CTE/SF does not reflect the physics of the problem and so it predicts unrealistic mixed mode ratios (e.g. [137, 160, 162, 178]). Given the insensitivity of N_c and M_c to the local damage state in the near-tip region, equation (2.28) would still be valid in those situations, but a different value of Ω would be required.

Using experimental data obtained for delamination in unidirectional carbon-fibre composites exhibiting large process zones, Davidson et al. [162] calculated an "effective" Ω (Ω_{NSF}) so that the toughness would be a single-valued function of the mode mixty. The validity of this

"global" or "non-classical" definition was also verified for fracture in multidirectional configurations [160], proving its applicability to problems with different materials on either side of the crack plane.

$$\Omega_{\mathrm{NSF}}(^\circ) = \begin{cases} -24.0 & \gamma < -0.468 \\ 60.409\gamma - 41.738\gamma^3 & -0.468 < \gamma < 0.468 \\ 24.0 & \gamma > 0.468 \end{cases} \tag{2.31}$$

The resulting approach is equivalent to define the mode mix in terms of the ratio of N_c to M_c, with the effective Ω providing the necessary scaling normalization (since N_c/M_c is not dimensionless). It should be also noted that both CTE/SF and CTE/NSF produce the same solution for symmetric specimens, as $\Omega_{\mathrm{SF}}(^\circ) = \Omega_{\mathrm{NSF}}(^\circ) = 0$ when $h_1 = h_2$. Furthermore, in those cases they both agree with Williams´ decomposition.

2.3.4 Fracture Mechanics Test Specimens

Several test specimens based on LEFM have been developed over the years to determine the fracture energy (G_c) of adhesively bonded joints for the pure loading modes or their combination (i.e. mixed mode). The most significant examples for each case are briefly reviewed in this section.

2.3.4.1 Mode I Tests

The importance of G_{Ic} is justified from an engineering point of view: associated with the most damaging type of loading for the interface, this parameter is often used to characterize the performance of the entire adhesive system (i.e. adhesive + surface treatment) rather than just that of the adhesive. The double cantilever beam (DCB) or the tapered double cantilever beam (TDCB) specimens are widely accepted for mode I testing, see Figure 2.10. Numerous studies have focused on these geometries, leading to the publications of several standards [165, 189, 190]. More detail on the analysis methods and correction factors pertinent to these configurations can be found in references [133] and [134] respectively.

The "wedge-cleavage" specimen represents another alternative for mode I testing. Due to its simplicity, it has became very popular in industry to study high rate fracture and to assess the susceptibility of the joints to environmental attack [191]. Finally, despite being widely used for measuring adhesive fracture energies and evaluating failure of flexible laminates between polymeric or metallic films, the "peel" test (e.g. [192, 193]) has important limitations which derive from the complex deformation of the substrate-peeling arm: it does not assess

the toughness of the adhesive directly, nor does it measure the intrinsic adhesion of the joint or laminate [11]. Furthermore, it is not clear yet whether this configuration produces pure mode I conditions at the crack tip.

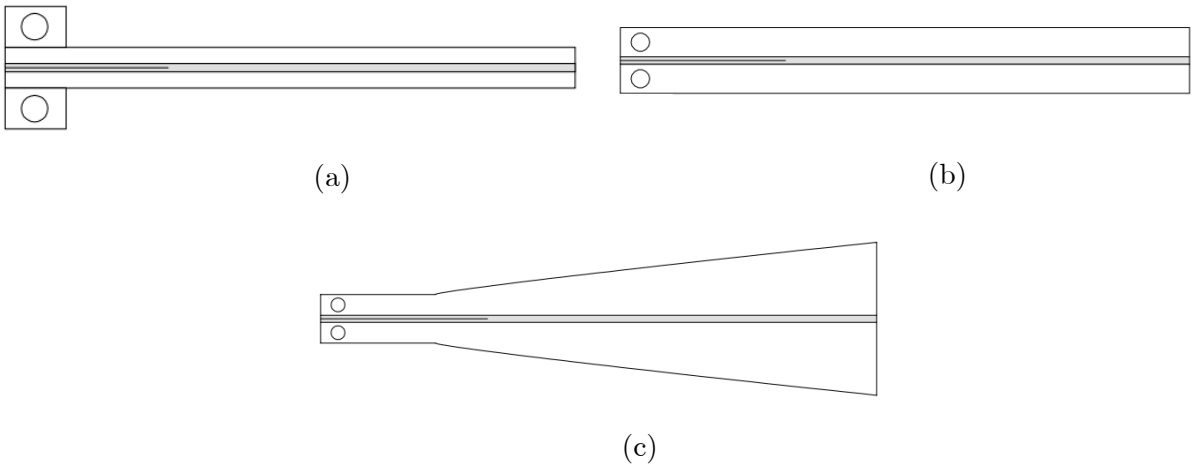

Figure 2.10. Joint configurations for mode I testing: (a) DCB joint with load-blocks, (b) DCB joint with drill-holes and (b) TDCB specimen with drill holes [133].

2.3.4.2 Mode II Tests

There are many difficulties associated with the determination of the mode II fracture energy of adhesively-bonded joints. The stability of the test, the frictional effects and, chiefly, whether the induced conditions at the crack tip truly correspond to in-plane shear are to name but a few (see [139, 194, 195]). An intense debate still surrounds the most appropriate testing configuration and, while the fracture mechanics community assesses the advantages and shortcomings of the various types of specimens proposed thus far, no standardized geometry has yet been agreed [141]. Nonetheless, the end-notched flexure (ENF), the four point ENF (4-ENF) and the end loaded split (ELS) are probably the most widely used specimens (see Figure 2.11).

The basic ENF, which uses a three-point bend rig, has been found to be unstable and therefore yields only initiation values of G_{IIc} [194, 196]. Various procedures to stabilize the test via feedback control of the testing machine have been implemented with some success, but they resulted in complex setups (e.g. [197, 198]). Martin and Davidson [199] suggested the use of a four-point loading variant (i.e. 4-ENF). However, despite the improved stability, this configuration introduces higher friction than the traditional three-point bend rig [140, 200]. Lastly, even though the ELS specimen results in stable crack growth if the geometry is carefully selected (ratio of the crack length to the free length greater than 0.55), it is not free

of disadvantages as it raises questions regarding measurement of the crack length due to bending in the substrates and clamp-induced effects [139, 141, 164].

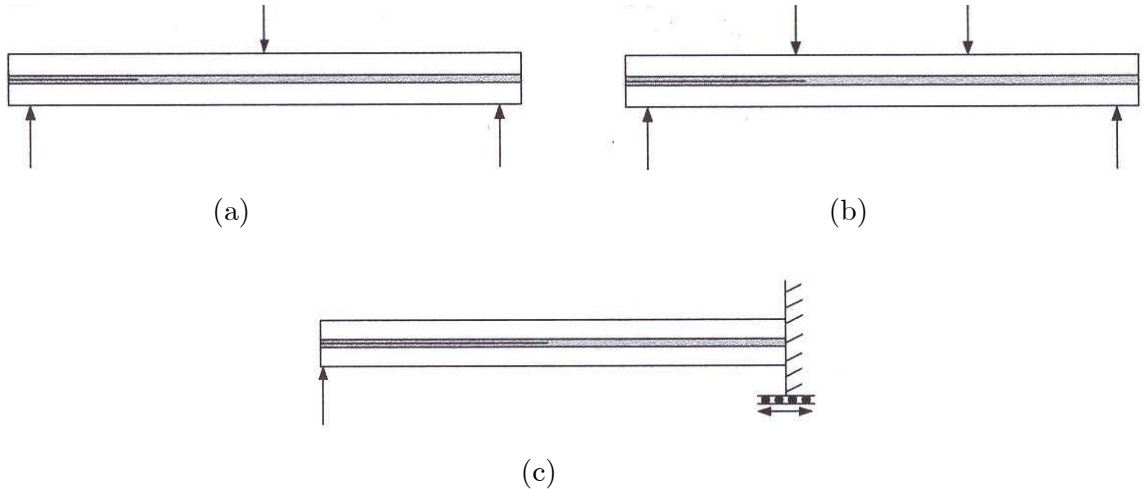

Figure 2.11. Mode II test configurations: (a) The three-point end-notched flexure (ENF) test, (b) the four-point end notched flexure (4-ENF) test and (c) the end-loaded split (ELS) test (from [141]).

2.3.4.3 Mixed Mode I/II Tests

Most real adhesively-bonded structures fail under a combination of opening, in-plane and out-of plane shear loads (macroscopically at least) rather than under pure mode conditions. The Ti-CFRP fan blade which stimulated this study and the simplified TDLJ used in the present work are examples. This highlights the importance of determining the variation of G_c with the mode mix, particularly if the performance of complex bonded structures is to be predicted accurately. Accordingly, fracture under mixed mode I/II conditions has received considerable attention in recent times. Four test configurations stand out amongst the many different alternatives proposed to date for the $G_{I/IIc}$ determination, namely: the mixed mode bending test (MMB), the fixed ratio mixed mode test (FRMM), the mixed mode flexure test (MMF) and the asymmetric DCB test (ADCB) specimens (see Figure 2.12). The Arcan fixture has also been adapted for its use with adhesives [103], but it has not been as widespread as the other configurations.

The MMB test, first proposed by Reeder and Crews [201] and subsequently modified to overcome some of the problems of the early rig design [202], combines the main features of both the DCB and ENF geometries to produce mixed mode conditions at the crack tip. Virtually any mixed mode ratio can be obtained using symmetric specimens by simply changing the loading moment arm. However, the loading apparatus introduces non-linear

effects which make the analysis of the data difficult and could compromise the accuracy of the results obtained with this method [137].

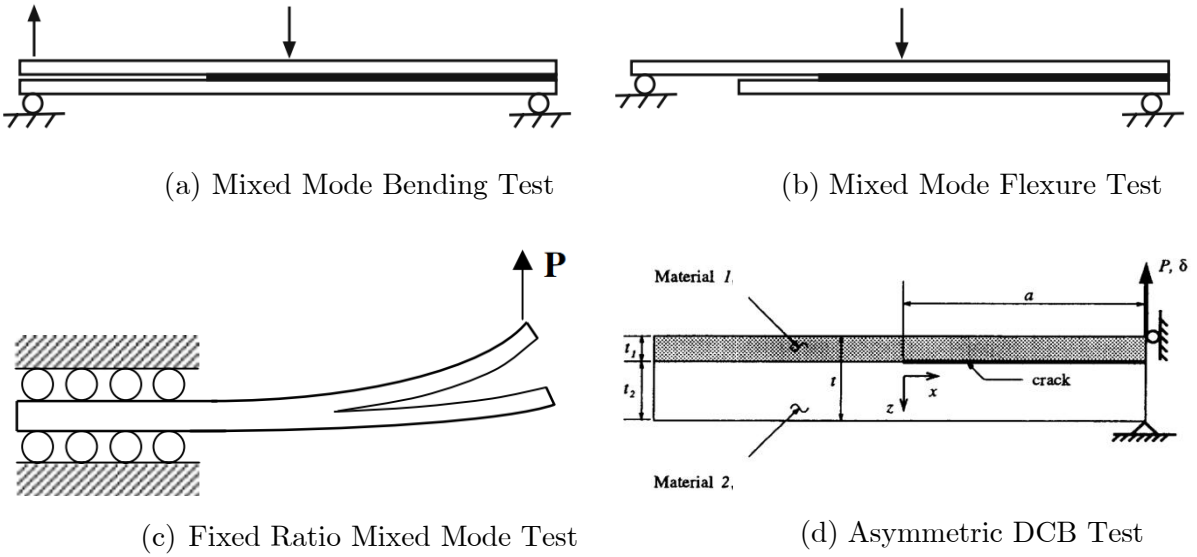

(a) Mixed Mode Bending Test (b) Mixed Mode Flexure Test

(c) Fixed Ratio Mixed Mode Test (d) Asymmetric DCB Test

Figure 2.12. Mixed mode I/II test configurations: (a) the mixed mode bending (MMB), (b) the mixed mode flexure (MMF) [188], (c) the fixed ratio mixed mode (FRMM) [178] and (d) the asymmetric DCB (ADCB) [203] specimens.

The FRMM geometry employs the same clamping arrangement as the mode II ELS test, but only one arm is loaded in this case [175, 204-206]. The resulting mixed mode ratio is almost independent of the crack length, although the actual value is a function of the mechanical properties and relative thickness of the substrates [146, 147]. For the symmetric case, G_{II}/G is equal to 3/7. As pointed out for the pure mode II case, the clamp fixture requires calibration and errors may arise in the crack length measurements because of bending in the loaded substrates [149, 207].

Also referred to as single leg bending test (SLB), the MMF configuration is very similar to the ENF test. It uses a three-point bending rig, but at one end the load is applied only to the upper arm. In contrast to the MMB test, symmetric specimens yield a unique mixed mode ratio, which concurs with that in the FRMM case (i.e. $G_{II}/G = 3/7$). A wider range of mixities can be attained by introducing geometrical or material asymmetry in the joint [160, 208]. However, the deliberate use of unbalanced specimens, which is also the principle behind the ADCB test [136, 188, 203], may cause difficulties as it raises the issue of mode decomposition. Nevertheless, due to its simplicity and robustness, the MMF test has became very popular for the study of mixed mode fracture at high rates (e.g. [125, 148, 209]).

2.3.4.4 Mode III Tests

Out-of-plane shear testing in adhesive joints is still in the very early stages of development. Driven by the work on mode III delamination in fibre composites, some specimen configurations have been proposed (see [143, 210-212]). Nevertheless, no standardized geometry has been agreed yet for this loading case, and the same applies to mixed mode cases including a mode III component.

2.3.5 Fracture Criteria

As it has been stated previously, the value of G_c generally depends on the mode mix [137, 162, 175, 213, 214]. It is impractical to test all possible ratios. Instead, the fracture behaviour is extrapolated from the values measured for a small number of cases, requiring an appropriate function to fit the experimental data. The accuracy of any subsequent predictions will depend on that of the individual measurements as well as on the suitability of the function chosen to approximate them.

Many fracture criteria have been suggested in the literature, some of which are based on certain physical phenomena [136, 215, 216]. However, since the mechanisms that control the values of $G_{I/IIc}$ are not yet well established, they should be viewed as mere curve fits to the experimental fracture results [174, 217]. Hence, their mathematical expression should be considered to be of secondary importance, provided that they can describe the experimental data points adequately [174]. No single criterion would be able to capture all possible material behaviour, and their versatility would be linked to the number of fitting parameters employed. Additionally, some other aspects must be taken into account when selecting the most appropriate fit or law in each case, for example: the potential to provide realistic response in the regions where little or no information is available, theoretical consistency and the ease of use and implementation.

Table 2.1 contains the mathematical expressions for some of the most widely-employed mixed mode criteria for two and three dimensional problems. A comprehensive review of these, including information on the type of responses modelled in each case, can be found in [174, 213, 217, 218]. A discussion concerning the most suitable criteria to apply to the joints considered in this project is presented in Chapter 7.

Table 2.1. Summary of mixed mode fracture criteria proposed in the literature [174].

Two-Dimensional Fracture Criteria	
Simple Mode Critical Criterion [219, 220]	Mode I critical: $G_I/G_{Ic} \geq 1$ Mode II critical: $G_{II}/G_{IIc} \geq 1$
Linear Criterion [215, 221]	$(G_I/G_{Ic}) + (G_{II}/G_{IIc}) \geq 1$
Power Law Criterion [219, 222]	$(G_I/G_{Ic})^{\alpha_1} + (G_{II}/G_{IIc})^{\alpha_2} \geq 1$
Polynomial Interaction [223]	$\frac{G}{G_{Ic} + \alpha_1(G_{II}/G) + \alpha_2(G_{II}/G)^2} \geq 1$
Hackle Criterion [216]	$\frac{G}{(G_{Ic} - \alpha_1) + \alpha_1\sqrt{1 + (G_{II}/G_I)\sqrt{E_{11}/E_{22}}}} \geq 1$
Exponential Hackle Criterion [215]	$\frac{G}{(G_{Ic} - G_{IIc}) + e^{\alpha_1\left(1-\sqrt{1+(G_{II}/G_I)\sqrt{E_{11}/E_{22}}}\right)}} \geq 1$
Mixed Mode Interaction Criterion [175]	$\frac{G_I}{G_{Ic}} + \left(\alpha_1 - 1 + \alpha_2\left(\frac{G_I}{G}\right)\right)\frac{G_I}{G_{Ic}}\frac{G_{II}}{G_{IIc}} + \frac{G_I}{G_{IIc}} \geq 1$
B-K Criterion [224, 225]	$\frac{G}{G_{Ic} + (G_{IIc} - G_{Ic})(G_{II}/G)^{\alpha_1}} \geq 1$
Modified B-K Criterion [217]	$\frac{G_I}{G_{Ic} + (G_{Ic} - G_{IIc})\left(\frac{G_I}{G}\right)^{\alpha_1}} + \frac{G_{II}}{G_{Ic} + (G_{IIc} - G_{Ic})\left(\frac{G_{II}}{G}\right)^{\alpha_2}} \geq 1$
Three-Dimensional Fracture Criteria	
3D Linear Criterion [217]	$(G_I/G_{Ic}) + (G_{II}/G_{IIc}) + (G_{III}/G_{IIIc}) \geq 1$
3D Power Law Criterion [226]	$(G_I/G_{Ic})^{\alpha_1} + (G_{II}/G_{IIc})^{\alpha_2} + (G_{II}/G_{IIc})^{\alpha_3} \geq 1$
3D B-K Criterion [174]	$\frac{G}{G_{Ic} + \left((G_{IIc} - G_{Ic})\frac{G_{II}}{G} + (G_{IIIc} - G_{Ic})\frac{G_{III}}{G}\right)\left(\frac{G_{II} + G_{III}}{G}\right)^{\alpha_1}} \geq 1$

2.4 Fatigue Behaviour and Lifetime of Adhesively-Bonded Joints

The fatigue resistance of adhesively-bonded joints is usually far superior to that of mechanically fastened structures. The enhancement in fatigue performance derives from a reduction in local stress concentrations produced by a more even distribution of stresses across the width of the joint. However, the long-term service life of adhesively joints is still a major concern due to their susceptibility to environmental attack. The presence of moisture coupled with relatively high temperatures has been found to significantly reduce the fatigue life-time of adhesive joints, limiting their industrial applications. At the same time, harsh environments can be combined with cyclic loads to artificially simulate accelerated ageing during the design stages [11].

Since bonded components subjected to cyclic loading can fail at stress levels considerably lower than those they can withstand monotonically, extensive research has been carried out over the years to gain a better understanding of their fatigue response. Just as in the quasi-static case, fracture mechanics has proven valuable identifying the failure mechanisms involved. The influence of various parameters on the fatigue performance has been studied, including that of the loading mode [23, 116, 227-230], amplitude and load ratio [231], the frequency [232] and the environmental conditions [23, 55, 70]. Furthermore, as discussed in section 2.6, on their own or combined with numerical techniques, the methods or fracture mechanics have been widely employed to predict the durability of adhesive joints.

Experimental fracture mechanics data usually adopts one of two formats. For specimens with no initial crack (e.g. single or double lap joints), the applied load (or stress) range per unit width may be plotted against the number of cycles to failure (N_f), see Figure 2.13a. The so-called S-N curves often exhibit a threshold level or endurance limit below which the fatigue life of the joint is infinite. Conversely, when the crack length can be monitored during the test, the results may be presented as logarithmic plots of the crack growth rate (da/dN) versus the maximum strain energy release rate applied in the cycle (G_{max}). Generally, G_{max} is favoured over $\Delta G = G_{max} - G_{min}$ to avoid closure problems during the unloading part of the cycle [11].

As illustrated in Figure 2.13b, a typical log-log diagram is sigmoidal in shape, featuring three clearly defined regions (I, II and III respectively). The growth rates in region I are very low, and no crack propagation takes place below a threshold value G_{th} [233]. Region II, characterized by an increasing da/dN with G_{max}, corresponds to the linear regime. Finally, in

the rapid growth region the crack accelerates as the strain energy release rate approaches the static fracture energy.

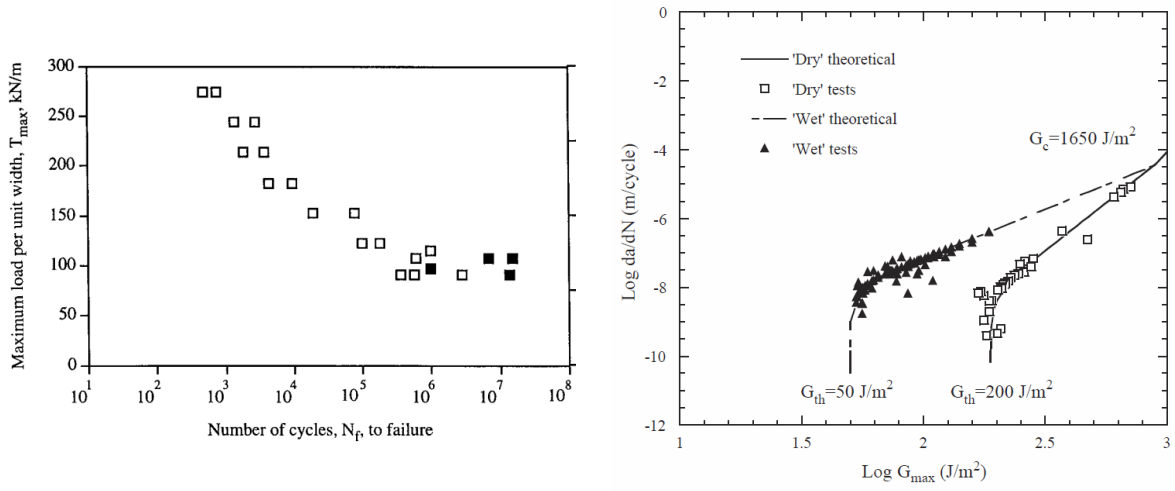

(a) (b)

Figure 2.13. (a) Typical experimental S-N data obtained for single lap joints manufactured with a rubber-toughened epoxy (black points indicate where the test was stopped prior to joint failure) [234]; (b) Typical logarithmic crack growth rate per cycle versus logarithmic G_{max} obtained for aluminium TDCB specimens tested under "dry" and "wet" conditions [23].

A number of functions have been proposed to describe the fatigue crack growth rate (see [235] for an overview). The Paris power law for the linear region [236, 237] and its modified version to capture the entire curve [238] have become the most recognizable (equations (2.32) and (2.33) respectively):

$$\frac{dA}{dN} = C_T(G_{max})^m \tag{2.32}$$

$$\frac{dA}{dN} = C_T(G_{max})^m \left\{ \frac{1-\left(\frac{G_{th}}{G_{max}}\right)^{n_1}}{1-\left(\frac{G_{max}}{G_C}\right)^{n_2}} \right\} \tag{2.33}$$

where A is the crack area instead of the crack length. The $dA/dN = dA/dN\,(G_{max})$ graphs, and therefore the fitting coefficients in equations (2.32) and (2.33), are considered characteristic of the adhesive system. However, they have been found to vary with the loading mode and the test conditions (e.g. amplitude, load or stress ratio, shape of the loading function, frequency, temperature, environment) [24, 204].

2.5 FE Analysis for Adhesive Joints: Numerical Methods in Fracture Mechanics

Currently based on costly and time consuming testing programs, the design of new adhesive joints would greatly benefit from the versatility of numerical techniques such as Finite Element Analysis (FEA). Despite conventional continuum mechanics methods having serious difficulties describing the mechanisms associated with crack nucleation and growth, some fracture mechanics (based) algorithms have been implemented in the main industrial FE codes (e.g. NASTRAN, Abaqus and LS-DYNA). However, some of those methods, including the Virtual Crack Closure technique (VCCT) and the J-integral, have important drawbacks which limit their application to crack propagation analysis, namely: inability to predict crack nucleation, the need to pre-define the growth path, difficulties when modelling multiple flaws and the computational costs for three-dimensional problems [239, 240].

Cohesive Zone Models (CZM) circumvent most of these limitations, and therefore represent an appealing alternative for adhesive-joints simulation. However, despite their current popularity, the use of CZMs is not without difficulties. In addition to the problems in defining suitable values for the cohesive parameters [239, 241, 242], the material softening behaviour associated with the damage formulation poses significant convergence issues [239, 243]. Nevertheless, it is undoubtedly the requirement for extremely fine meshes along the crack propagation path that most hinders the application of this method to the analysis of large and complex structures [242, 244].

2.5.1 The Virtual Crack Closure Technique

Initially proposed by Rybicki and Kanninen in 1977 [176], the Virtual Crack Closure Technique (VCCT) is a modified version of the "crack closure method". It is based on Irwin's crack closure integral [245] and adopts the following assumptions: (i) The strain energy released when a crack of length a is extended by an amount Δa is identical to the energy required to close the crack by the same amount; (ii) The stress state at the crack tip is not significantly altered by a crack extension of Δa (from a to $a + \Delta a$) if Δa is small compared with the crack length.

In order to apply this method, the crack must be included in the finite element model. In a two-dimensional problem the crack path takes the form of a line of node pairs, whereas in 3D models it is represented by two surfaces. Initially, the nodes at the top and bottom surfaces of the discontinuity are coincident, but are not connected to each other to allow the crack to

open. The section where the structure is still intact is modelled using pairs of coincident nodes with all the degrees of freedom coupled together through multipoint constraints. These constraints can be removed for crack propagation analysis if the imposed load reaches a critical value.

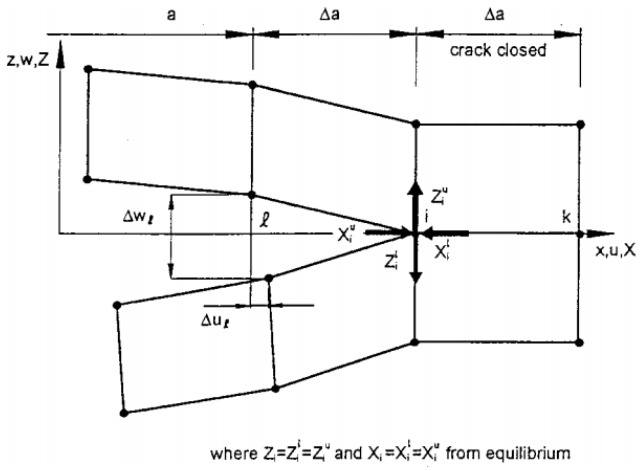

Figure 2.14. Schematic representation of the nodal forces and displacements employed in the Virtual Crack Closure technique [246].

The Virtual Crack Closure Technique provides a simple expression to calculate the energy released (ΔE) when the crack shown in Figure 2.14 propagates Δa from i to k. According to the previous hypotheses, the displacements at node i when the crack tip is located at k are approximately equal to those in l when the crack tip is at i. Similarly, the forces required to close the crack are identical to those acting on the upper and lower surfaces when the crack is closed [246]. Therefore ΔE can be calculated using the nodal forces at the crack tip (X_{1l}, Z_{1l}) and the opening displacements at the released nodes ($\Delta u_l = u_l - u_l^*, \Delta w_l = w_l - w_l^*$). The strain energy release rate (G) can be obtained by dividing ΔE by the crack surface created ΔA ($G = \Delta E / \Delta A$) and then separated into the individual mode components (G_I, G_{II}).

$$\Delta E = \frac{1}{2}\{X_i \cdot \Delta u_l + Z_i \cdot \Delta w_l\} \tag{2.34}$$

$$G_I = \frac{1}{2B\Delta a} Z_i \cdot (w_l - w_l^*) \tag{2.35}$$

$$G_{II} = \frac{1}{2B\Delta a} X_i \cdot (u_l - u_l^*) \tag{2.36}$$

Equations (2.34)-(2.36) are derived for two-dimensional four-noded elements. Similar expressions for other element types (quadrilateral eight-noded, triangular quarter-point) and

three-dimensional problems (with solid, plate and shell elements) can be found in [246]. Corrections for non-linear FE analysis and for the use of elements at the crack tip with different sizes are also included in the same report.

The use of quadrilateral 2D elements with quarter-point nodes at the crack tip (see Figure 2.15) has been proposed in the literature as a method to simulate the $1/\sqrt{r}$ singularity of the stress field at the crack tip [247]. Equivalent triangular elements obtained by collapsing one side of the rectangular elements can be used instead with analogous results ([248, 249]).

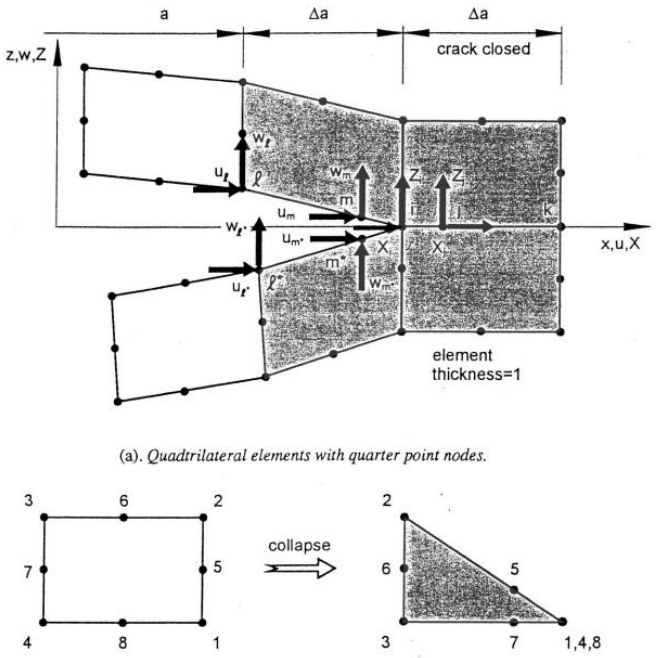

Figure 2.15. Schematic representation of VCCT using quadrilateral elements with quarter-point nodes to simulate the stress singularity at the crack tip [246].

The VCCT has been widely used for calculating energy release rates. As it allows to compute the energy release rate components (G_I, G_{II}, G_{III}) for a generalized load states, this method is especially useful in problems where a mixed-mode fracture criterion is required (e.g. $(G_I/G_{Ic})^{\alpha_1} + (G_{II}/G_{IIc})^{\alpha_2} + (G_{II}/G_{IIc})^{\alpha_3} \geq 1$). Bonhomme et al. [250] used both the VCCT and the "*two-step extension method*" to estimate the strain energy release rate in mode I for inter-laminar fracture of unidirectional CFRP. Davidson et al. [171, 172] used VCCT with standard and crack-tip elements to study mixed-mode delamination in composites. MMELS (i.e. FRMM) test specimens were used by Marannano et al. [251], who studied the crack growth in aluminium/epoxy joints under mixed-mode loading conditions. Taking the displacement and stress distributions determined analytically by the anisotropic laminated plate theory, Yang et al. [252] applied the virtual crack extension to estimate the strain energy release rate of adhesively-bonded composite single-lap joints. Alderliesten [253]

determined the stress intensity factor at the crack tip employing the VCCT in order to predict the fatigue performance of GLARE panels. Similarly, the durability of composite bonded joints was investigated by Johnson et al. [254].

The implementation of the virtual crack closure technique to commercially available FE codes has extended its application to crack propagation analysis. However, its inability to model damage initiation and the need to predefine the crack propagation path represent major limitations compared to alternative techniques such as cohesive elements [240].

2.5.2 The J-Integral

The J-integral was introduced by Rice [255] in 1968 as a parameter to characterize the crack tip conditions in elastic-plastic materials. Assuming that elastic-plastic materials behave as nonlinear elastic solids under monotonically increasing stresses, Rice showed that the nonlinear energy release rate (J) can be expressed as a path independent line integral. Shortly after that, Rice and Rosengren [256] and Hutchinson [257] demonstrated that, in nonlinear materials, the stress and strain fields at the crack tip can be uniquely characterized by the same integral.

$$J = -\frac{\partial \Pi}{\partial A} \rightarrow J = \int_{\Upsilon} \left(W dy - \boldsymbol{T} \cdot \frac{d\boldsymbol{u}}{dx} ds \right) = \int_{\Upsilon} \left(\left(\int_0^{\varepsilon} \sigma_{ij} d\varepsilon_{ij} \right) dy - \sigma_{ij} n_j \frac{du_i}{dx} ds \right) \qquad (2.37)$$

Υ is a contour going around the crack from the lower to the upper crack face counter clockwise, W is the strain energy density, $\boldsymbol{u}$ is the displacement vector, $\boldsymbol{T}$ is the traction vector acting at the boundary, n_j is the outwards normal to the contour and s denotes curve length along Υ.

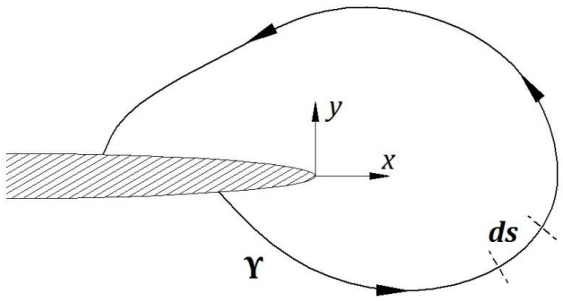

Figure 2.16. An arbitrary contour Υ around crack tip.

J is a more general version of the energy release rate than G [122]. In fact, under Linear Elastic Fracture Mechanics (LEFM) conditions, "*the J-integral coincides with total energy*

release rate, $J = G_I + G_{II} + G_{III}$*, where* G_I*,* G_{II} *and* G_{III} *are the energy release rates associated with the mode I, II and III stress intensity factors*" [103]. Several authors have taken advantage of this fact for their FE analyses of fracture mechanics problems [21, 70, 234].

Some commercially available FE codes (such as Abaqus or ANSYS) incorporate a specific tool to calculate contour integrals. According to the Abaqus User Manual [258], the J-integral can be evaluated both in two and three dimensions (using only quadrilateral or brick elements respectively) along several contours around the crack tip. Each contour is idealized as a ring of elements completely surrounding the crack tip. A new one surrounding all preceding contours is defined recursively by adding a single layer of elements to those that were used to calculate the previous J integral (see Figure 2.17).

Although the latter feature could seem pointless taking into account the theoretical path-independence of the J-integral, it can be extremely useful to obtain accurate estimations with relatively coarse meshes. Due to the approximate nature of the FE solution, the J values obtained for the different contours may vary. This is usually referred to as "*domain or contour dependence*" and could indicate that finer meshes are required to capture the important stress gradients around the crack tip or that the contour does not completely include the plastic zone. Moving away from the crack tip (i.e. increasing the size of Γ) minimizes these problems and provides accurate and robust estimations of J. As in the VCCT, quarter-point eight-noded elements can be employed to reproduce the $1/\sqrt{r}$ singularity predicted by LEFM near the crack tip [248, 249]. The use of these elements greatly improves accuracy and reduces the need for mesh refinement [122, 252, 258]

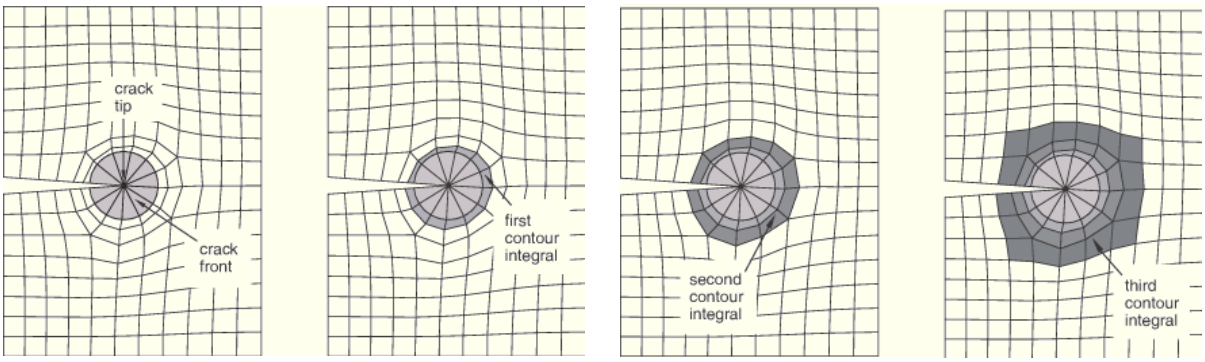

Figure 2.17. Successive contour integrals calculated by adding an extra layer of elements [258].

Finite element analysis using J-integral has been used by several researchers to study the fracture behaviour of adhesively-bonded joints. A contour estimate does not predict how a crack will propagate, but can be useful to study the onset (initiation) of cracking in quasi-static problems. This is particularly useful when LEFM conditions are fulfilled, since under those circumstances the J-integral coincides with total energy release rate (G). Yang et al.

[252] developed an analytical model based on the laminated plate theory to estimate the strain energy release rate of single-lap composite joints, and used both the J-integral and VCCT in order to verify their results. In a numerical investigation on mixed-mode fracture of adhesive joints using modified Arcan specimens, Choupani [103] found that G rises as the adherends become stiffer but diminishes as the bondline thickness and the crack length increase. Curley et al. [234], utilized the J-integral to obtain relationships of the form $G_{max} = G_{max}(T_{max}, a)$ for single lap joints, which they combined with fracture mechanics experimental data to in order to predict fatigue crack growth in bonded joints. Equivalent methodologies were followed by Hadavinia et al. [21] and Daniel Ng [70] in their fatigue lifetime study of aluminium single-lap joints and CFRP/aluminium tapered joints respectively.

2.5.3 Cohesive Zone Modelling (CZM)

2.5.3.1 Introduction

The cohesive zone model overcomes many of the shortcomings of both VCCT and the J-integral. In contrast to these techniques, it was developed within the framework of damage mechanics and relies on the assumption that the damage mechanisms leading to fracture are localized in a thin layer of material ahead of the crack tip referred to as the failure process zone (FPZ) [259]. The concept of the process zone, first introduced by Dugdale to account for yielding in thin steel sheets [260], was used by Hillerborg et al. [261] to study fracture in concrete. They defined a relationship of the form $\sigma = \sigma(\delta)$ to characterize the FPZ, σ and δ being the stress and the separation in the FPZ. Several authors have subsequently made important contributions to further refine the Hillerborg model (also known as "*fictitious crack model*") [262, 263].

Embedded into finite or zero-thickness elements (e.g. [264, 265]), as a contact function connecting two surfaces (e.g. [266]) or combined with finite volume methods (e.g. [267, 268]), the CZM has become one of the most popular approaches to simulate fracture. In particular, cohesive or "interface" elements have been applied to a very wide range of problems involving damage initiation and/or propagation. Among those applications, the study of delamination in fibre-reinforced composites has drawn the attention of many researchers. Blackman et al. [269] used cohesive elements to investigate the response of an unidirectional CFRP DCB specimen. Wimmer et al. [270] used interface elements to analyse an L-shaped structure and a double-lap shear test specimen. De Moura et al. [271] used a cohesive damage model to evaluate the accuracy of the Edge Crack Torsion test for the mode III interlaminar fracture characterization of composite laminates. Harper and Hallett [240] highlighted some of

the limitations of the existing methods to predict delamination, and showed that a minimum number of interface elements is required to obtain accurate load-displacement predictions under mode I, II and mixed mode.

The macroscopic constitutive behaviour of a thin layer, for example an adhesive layer, can also be described using cohesive laws [272]. Martiny et al. [259] used a cohesive zone formulation to investigate the static fracture of adhesively bonded joints in various peel test configurations, obtaining very good agreement with the experimental data. Blackman et al. [134] derived an analytical correction for beam root rotation for the TDCB specimen, and compared the experimental results obtained for different substrate materials with a FE analysis employing CZM. Starting from experimentally determined mode I and II parameters, Li et al. [273] used a cohesive zone approach to model the mixed mode fracture of glass fibre composite joints. For their study on the effects of geometry and plasticity on the fracture of adhesively bonded joints, Kafkalidis and Thouless [241] modelled an aluminium single-lap shear joint with cohesive elements, obtaining excellent agreement with the experimental observations.

2.5.3.2 Traction Separation Law and Cohesive Parameters

The relationship $\sigma = \sigma(\delta)$ is usually referred to as '*cohesive law*' or '*traction-separation law*'. It is commonly assumed that under monotonically increasing loading the stress first increases to a maximum point (σ_c), at which damage initiation ($\delta = \delta_0$) takes place. As damage grows the stress starts decreasing, vanishing when that separation reaches a critical value ($\delta = \delta_C$). A schematic representation of a bilinear traction-separation law is shown in Figure 2.18.

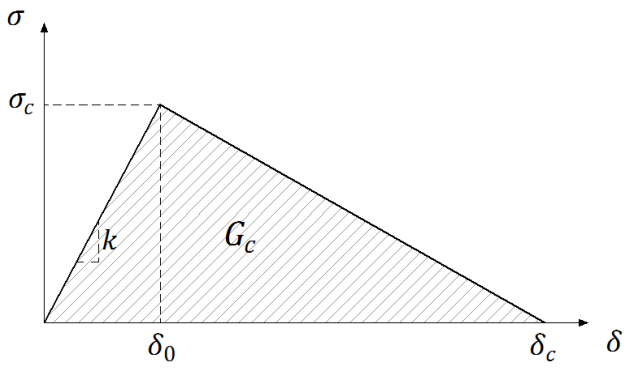

Figure 2.18. Typical traction-separation law for CZM.

In order to combine damage and fracture mechanics concepts, the area under the traction separation law is equated to the critical strain-energy release rate, (G_c) (see equation (2.38)).

Consequently, the CZM employs both strength (σ_c) and energy (G_c) parameters to characterize the failure process, allowing the approach to be of much more general utility than conventional interfacial fracture mechanics [241, 273].

$$G_c = \int_0^{\delta_c} \sigma \cdot d\delta \tag{2.38}$$

For practical applications, the shape of the $\sigma = \sigma(\delta)$ curve is usually predefined (bilinear, cubic, linear with exponential softening, etc). It should be noted that once the shape of the curve is fixed, G_c and δ_C are no longer independent parameters.

Due to its simplicity, the bilinear damage evolution law illustrated in Figure 2.18 has become very popular for crack growth analysis. Even though many other damage evolution laws have been suggested in the literature (e.g. trapezoidal [274], cubic-polynomial [269], exponential [275] or linear-polynomial [276]), several authors have indicated that the form of the traction-separation curve is of secondary importance compared to the critical strain-energy release rate when only the global response of the structure is required [134, 241, 269, 277]. However, some contradictory results have been reported when modelling dynamic phenomena [276, 278] or if mesoscopic scale ductile processes are present [279]. Whether the insensitivity of the solution to the shape of the evolution law applies to mode II and mixed-mode fracture also remains an open question. Further, it has been suggested that the shape of the traction-separation law must reflect the damage mechanisms occurring within the failure process zone (FPZ) if the stress distribution ahead of the crack tip and hence the size of the cohesive zone are to be estimated accurately [240, 280, 281].

2.5.3.3 Cohesive Parameters

In addition to the debate surrounding the shape of the traction-separation law, there is no general consensus on the significance of the parameters that define the cohesive law. While the concept of the strain-energy release rate is relatively well understood, the physical meaning of the maximum stress (σ_c) and the penalty stiffness (the stiffness of the initial linear response – k) remain unclear.

Even though Hillerborg et al. [261] originally stated that the relationship $\sigma = \sigma(\delta)$ is a material property, several researchers [282, 283] have found that the value of the limiting stress in the FPZ (σ_c) is geometry dependent. For adhesive joints, the level of constraint and local triaxial state have been also reported to affect σ_c , potentially compromising transferability between different test configurations [284-286]. In a numerical study of

fracture in composites and adhesively-bonded joints, Blackman et al. [269] concluded that it cannot be stated whether or not σ_c has a physical meaning. Alfano and Crisfield [239] investigated the influence of this parameter on different aspects of the numerical solution, such as convergence and computational efficiency. They found that reducing the value of σ_c lightens the computational burden because it allows for a coarser mesh, although too small a value of σ_c must be avoided since it results in unacceptable errors.

Whether the penalty stiffness has any physical meaning is also an open question. Several authors have shown [239, 287] that a large k value is required to obtain realistic elastic response and pre-initiation behaviour. High values are also desirable from the convergence point of view, since they help to reach the steady-state more quickly [19]. Conversely, an excessive stiffness may result in numerical problems.

In contrast to VCCT, the CZM can also be used when LEFM assumptions are violated [241]. Therefore, the CZM is suited to model problems in which large scale deformation occurs at the FPZ [123], such as those involving important amounts of plasticity. Furthermore, the cohesive zone can alleviate and even obviate the stress singularity at the crack tip, potentially allowing for a coarser mesh around the tip [288]. Nevertheless, the cohesive zone models exhibit a transition to the predictions of LEFM under conditions where these are expected to apply [241]. Alfano and Crisfield [239] studied the influence of σ_c and k on the "smoothness" of this transition, reporting that sufficiently high values of the penalty stiffness and the limiting stress are required to achieve good agreement between the predictions obtained by direct application of LEFM and the interface model.

2.5.3.4 Mixed Mode Behaviour

In its early stages, the CZM was developed for mode I fracture processes, but it was then extended to mode II and ultimately mixed-mode cases [271, 273, 289]. Experimental observations have shown that the micromechanical failure mechanism involved in peel and shear fracture are different, suggesting that the cohesive behaviour and the shape of the traction-separation law are mode dependent [114, 290]. With this in mind, researchers have contemplated various possibilities to deal with mixed mode problems.

In a general two-dimensional case, the normal and tangential cohesive stresses (σ_n and σ_t) would depend on both the local normal and tangential crack opening displacements (δ_n and δ_t respectively):

$$\begin{cases}\sigma_n = \sigma_n(\delta_n, \delta_t) \\ \sigma_t = \sigma_t(\delta_n, \delta_t)\end{cases} \tag{2.39}$$

This type of relationships [291, 292] would describe the fracture behaviour of most engineering materials for any given mixed mode ratio. However, as discussed in section 2.5.3.5.1, their mathematical expression is difficult to determine. Hence, they are often simplified by assuming that $\sigma_n = \sigma_n(\delta_n)$ and $\sigma_t = \sigma_t(\delta_t)$. But even with no cross-terms, the simplified relationships could be consider as uncoupled or coupled modelling [272].

In the first case, $\sigma_n = \sigma_n(\delta_n)$ and $\sigma_t = \sigma_t(\delta_t)$ are assumed to be totally unrelated, but the cohesive parameters could be defined as functions of the mode mix. Each loading mode uses an independent damage variable, defining the individual components of G (i.e. G_I and G_{II}) as the areas under the corresponding traction separation laws. Failure takes place when an energy-based criterion such as the power law [219, 222] (i.e. $(G_I/G_{Ic})^{\alpha_1} + (G_{II}/G_{IIc})^{\alpha_2} \geq 1$) is satisfied. This approach has been used by several authors (e.g. [271, 273, 289]), despite the fact that it can cause sudden drops in the traction before the critical separation is reached [241, 273].

The second technique consists on using coupled cohesive laws. Tevergaard and Hutchinson [263] proposed the use of a dimensionless parameter ($\lambda = \sqrt{\left((\delta_n/\delta_{n_c})^2 + (\delta_t/\delta_{t_c})^2\right)}$) linking the normal and tangential separations (δ_n and δ_t) to couple modes I and II. Using a total of six independent cohesive parameters (three for each pure loading mode), the so-called T-H model predicts the behaviour for any given mixed mode ratio. By adding an additional parameter to quantify G_{II}/G, Högberg [272] developed a similar model capable of accounting for the differences in fracture energy and strength at different mode mixity. Other authors have recently proposed analogous models [293-295].

2.5.3.5 Determination of the Traction-Separation Law

A precise description of the constitutive behaviour of the adhesive layer is required if the strength of adhesively-bonded joints is to be predicted accurately. A small number of studies deal with the direct determination of cohesive laws. In most cases, the law is obtained indirectly using finite element analysis in a long and costly iterative process. The shape is pre-selected (e.g. bilinear, linear-exponential) and an iterative process is followed to determine its characteristic values. The set of parameters that best reproduce the experimental results is identified by direct comparison of the measured response with the predictions of the different models.

However, some authors have proposed experimental approaches to obtain the relation $\sigma = \sigma(\delta)$ directly. Li et al. [296] recommended a procedure based on the J-Integral to experimentally obtain the tension-softening relations in cementitious composites. Subsequently, several researchers [291, 292, 297-300] have applied modified versions of the original method to obtain the constitutive behaviour of adhesive layers. More recently, powerful optical techniques such as DIC have been used with relative success to monitor the strain field in the vicinity of the crack tip [301-303].

2.5.3.5.1 The J-integral approach

Starting from equation (2.39) and assuming that the cohesive stresses are derived from an energy potential (i.e. they do not depend on the opening-path history), it can be shown that:

$$\sigma_n(\delta_n^*, \delta_t^*) = \frac{\partial J_R(\delta_n^*, \delta_t^*)}{\partial \delta_n^*},\ \sigma_t(\delta_n^*, \delta_t^*) = \frac{\partial J_R(\delta_n^*, \delta_t^*)}{\partial \delta_t^*} \tag{2.40}$$

J_R is the fracture resistance of the material, and δ_n^* and δ_t^* are the end-opening and end-sliding of the failure process zone (normal and tangential opening displacement at the original crack tip). For more detail on the mathematical formulation see references [291, 300].

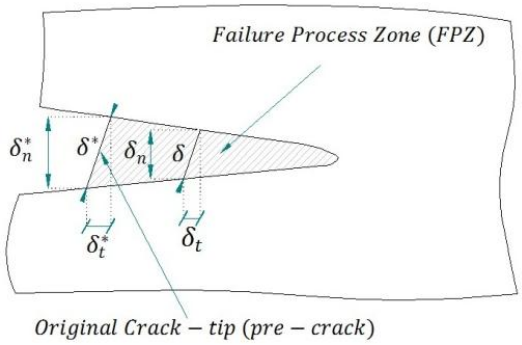

Figure 2.19. Definition of normal and tangential opening displacements – δ_n^* and δ_t^* – at the original crack tip (pre-crack tip).

Equation (2.40) can be used to derive the constitutive relationships of an adhesive layer by simultaneous measurements of J_R, δ_n^* and δ_t^*. For this purpose J_R (which cannot be measured directly) must be related to the applied loads. Several approaches have been suggested to overcome this problem. Li et al. [296] put forward an approximate procedure based on the use of two identical compact tension specimens with slightly different notch lengths (a_1 and a_2). The load (P), load point displacement (Δ) and crack tip separation (δ) are recorded in each test and the J integral is calculated as the area between the two load-displacement curves.

A different solution consists of using a modified test specimen for which the J-integral can be obtained in a closed form along a path along the external boundaries of the test specimen (J_{ext}). Sørensen and Jacobsen [300] suggested a DCB specimen loaded with pure bending moments for pure mode I. A DCB loaded with uneven bending moments (DCB-UBM) was later introduced by Sørensen and Kirkegaard [291] for mixed mode problems. Högberg et al. [292] employed the *Mixed Mode Double Cantilever Beam* (MCB) – described by Högberg and Stigh [289] – to obtain the mixed mode cohesive behaviour of a toughened epoxy adhesive layer. According to their work J_{ext} can be easily calculated for the usual DCB test configuration (loaded with peel forces) if the rotations of the substrates at the crack tip are known. Note that in this case J_{ext} depends on the crack length.

2.5.3.6 Cohesive Zone Length

In any fracture process, irreversible damage occurs ahead of the crack tip within an area usually referred to as FPZ or Cohesive Zone. The actual inelastic micro-mechanisms responsible for this damage vary with the type of material and its microstructure, and depend on the temperature and loading conditions [281]. Accurate predictions of the size of the cohesive zone are often required for mesh design purposes, since the conventional approach to cope with size-dependency of cohesive elements relies on the presence of a minimum number of elements within the FPZ [240, 242]. Furthermore, some special formulation need these estimates to complete the definition of the damage evolution law (e.g. [304, 305]).

Several authors [150, 260, 261, 306] have proposed theoretical expressions to estimate the cohesive zone length (l_{CZ}) in constant-width components with a crack covering the whole width. Derived from the analytical stress field obtained for an infinite cracked body assuming linear elastic behaviour, most of these formulae adopt the form:

$$l_{CZ} = ME\frac{G_c}{(\tau^0)^2} \tag{2.41}$$

E is the Young's modulus of the material, G_c is the critical strain energy release rate, τ^0 is the maximum interfacial strength and M is a parameter that depends on the cohesive zone model (see Table 2.2). Note that these solutions neglect the variation in the stress state across the width of the specimen. As a result, the cohesive zone length is considered to be constant across the width.

Table 2.2. Values of the parameter M for different theoretical models.

	Irwin [150]	Dugdale [260]	Rice [306]	Hillerborg et al.[261]
M	$\frac{1}{\pi}$	$\frac{\pi}{8}$	$\frac{9\pi}{32}$	1

Although these models were originally intended for isotropic materials and infinite bodies loaded in pure mode I, equivalent expressions have been derived for orthotropic materials loaded in pure tension and shear (see [307, 308]). Similarly, suitable equations for slender bodies have been obtained using beam theory analysis (see [240, 307]):

$$\begin{cases} l_{CZ,slender,I} = \left(E_I' \frac{G_{Ic}}{(\tau_I^0)^2} \right)^{\frac{1}{4}} (h)^{\frac{3}{4}} \\ l_{CZ,II} = \sqrt{\left(E_{II,slender}' \frac{G_{IIc}}{(\tau_{II}^0)^2} \right) h} \end{cases} \tag{2.42}$$

where h is the laminate half thickness, whereas details on how to calculate E_I' and E_{II}', which depend on the elastic properties, width and loading conditions are given in [308].

However, as discussed for r_y (see equation (2.6)), the assumptions made to obtain these formulae make their applicability to adhesive joint problems questionable. Any substrate effects are ignored by the first approximation (2.41), whereas (2.42) neglects the presence of the adhesive layer all together. Furthermore, both presume constant traction in the FPZ and neither of them can account for the influence of the bondline thickness or the constraint effects on the adhesive layer.

Regarding numerical simulation using CZM, Harper and Hallet [240] emphasized the importance of distinguishing between the physical cohesive zone and the numerical cohesive zone, i.e. area (length in 2D) ahead of the numerical crack tip over which the interface elements lie on the softening part of the traction-separation law.

2.5.3.7 Mesh Dependency in Cohesive Elements

Although cohesive elements have attained notable popularity and are now frequently used to simulate both delamination and fracture in adhesively-bonded structures, their application to

model large scale problems has been restricted by stringent mesh density requirements [242, 244].

The need for very small cohesive elements has been traditionally justified by the inability of the linear shape functions to reproduce accurately the steep gradients of the stress and displacement fields in the region immediately ahead of the crack tip (i.e. FPZ or cohesive zone) [244, 309]. This problem could be partially circumvented by ensuring a minimum number of elements within the cohesive zone, which given the typical size of the physical FPZ results in very fine meshes along the crack propagation path [240]. Although the minimum number of elements necessary is not yet well established [310-312], the resulting mesh densities are currently holding back the industrial applications of interface elements.

This issue has been extensively discussed in the literature, and several authors have proposed different techniques to alleviate the mesh size restrictions [242, 244, 309]. However, those solutions have been proven only partially effective, allowing the use of slightly coarser meshes and usually involving problem-dependent tuning. A short review of some of these techniques is presented next.

Alfano and Crisfield [239] studied the influence of the cohesive parameters on the numerical efficiency and the mesh requirements, identifying the key role played by the interfacial strength. While sufficiently high values of this parameter are essential to obtain good agreement with LEFM solutions, the higher its value the more refined the required mesh around the crack is to avoid spurious oscillations in the overall response. Information on several methods to address the numerical instability can be found elsewhere [243, 313-316]. However, small values may result in unacceptable errors in the prediction of the overall response.

Turón et al. [242] proposed a simple strategy to artificially increase the cohesive zone length by reducing the interfacial strength. Although the method allows the use of slightly coarser meshes, it calls for problem-dependent tuning of the cohesive parameters and fails to predict accurately both the stress distribution near the crack tip and the global behaviour of the structure. Furthermore, in a study of the minimum number of interface elements needed within the cohesive zone, Harper and Hallett [240] concluded that reductions in the interfacial strength might be acceptable in mode I cases but could cause excessive softening ahead of the crack tip in mode II, resulting in poor predictions of the global load-displacement traces.

In another attempt to mitigate the stringent mesh size requirements, Guiamatsia et al. [244, 309] employed the 'partition of unity' to modify the cohesive element formulation, enriching the nodal displacements with analytical solutions derived from elastic beam theory. Even

though the new element showed encouraging results when applied to mode I and mixed mode problems (DCB and MMB specimens), elements larger than 2mm remain problematic. In addition, the complexity of the approach, the difficulties to derive suitable enrichment functions for mode II and the need to enrich the continuum elements in contact with the interface represent major drawbacks to this method. An analogous approach was investigated by Samimi et al. [317].

With their adaptive cohesive model (ACM), Hu et al. [318] obtained similar results (i.e. good agreement with elements sizes up to 2mm), and at the same time managed to improve the stability of the solution. In this formulation, a pre-softening zone is inserted ahead of the existing traditional softening zone. This is achieved by progressively reducing the stiffness and interface strength according to the effective relative displacements while both the displacement at damage onset and the fracture toughness remain unchanged.

2.5.3.8 Cohesive Contact

Based on the CZM, a penalty contact formulation has been recently derived and used to model problems involving crack initiation and propagation. When the surface-based cohesive formulation or "cohesive contact" is used, the cohesive elements connecting two bodies are substituted by adhesive forces. The opening displacement and the adhesive forces follow a user-defined traction-separation law that incorporates a damage formulation to simulate de-cohesion. According to Abaqus User's Manual [258], the cohesive contact is primarily intended for cases in which the interface thickness is negligibly small. Furthermore, the reduction in the number of elements resulting from neglecting the presence of the interface would potentially contribute to improve the computational efficiency.

Borg et al. [319] implemented this technique in LS-DYNA to model DCB, ENF and MMB test specimens made from a CFRP, obtaining good agreement with experimental data. A similar approach was used to simulate fracture in adhesive layers by Diehl [320], who modelled both a DCB and a single-arm peeling specimens. Borg et al. [321] derived an equivalent formulation suitable for shell elements which they used to predict delamination in mode I, II and mixed mode, and also to study the response of an overlap composite joint.

2.6 Fatigue Lifetime Prediction in Adhesively-Bonded Joints

The development time and associated costs of a new adhesively-bonded structure could be potentially reduced by the use of a fatigue life prediction tool. In this respect, the advantages of combining fatigue data obtained using fracture mechanics with FEA methods to predict the service-life of adhesive joints have been widely demonstrated [21, 23, 70, 234, 322-324]. A number of the most relevant fatigue prediction methodologies are outlined in this section. It should be noted that, although some of these were originally developed for delamination in composite materials, there is every indication that they can be applied to the failure in bonded joints due to the similarities between both phenomena.

Leaving aside total-life methods which use S-N curves, most early approaches to fatigue employed a phenomenological law relating the crack growth rate (da/dN) with the relevant fracture mechanics parameter (i.e. K or G). Suitable specimens would be tested in the relevant environment to obtain da/dN data for the adhesive system of interest. The experimental results would be then fitted to a Paris law (see equations (2.32) and(2.33)), which could be subsequently integrated with respect to the crack length to determine the number of cycles required to propagate an initial defect (a_0) to certain final size (a_f). However, this integration would be possible only if a relationship between the maximum energy release rate (G_{max}), the maximum applied load per unit length (T_{max}) and the crack length (i.e. $G_{max} = G_{max}(T_{max}, a)$) is available for the joint design under consideration. Even though analytical solutions exist for simple configurations, in a general case such a relationship could be extracted from finite element simulations. A model of the joint where a crack is grown quasi-statically according to the expected failure path would be necessary, using VCCT or the J-Integral to compute the value of G_{max} for different applied loads.

$$\frac{da}{dN} = C_T(G_{max})^m \left\{ \frac{1 - \left(\frac{G_{th}}{G_{max}}\right)^{n_1}}{1 - \left(\frac{G_{max}}{G_C}\right)^{n_2}} \right\} \xrightarrow{G_{max}=G_{max}(T_{max},a);\ \int_{a_0}^{a_f}} N_f = N_f(T_{max}, C_T, m, n_1, n_2) \quad (2.43)$$

Curley et al. [119, 234] followed this approach to estimate the durability of two different adhesively-bonded components subjected to cyclic loading: a single lap joint and a bonded top-hat box manufactured with rubber toughened adhesives. Employing fatigue data extracted from TDCB specimens, their methodology yielded conservative predictions in both cases. Similar results were reported in [21] for single lap joints fatigued in “dry” and “wet”

conditions. Additionally, the latter study evaluated the suitability of various analytical expressions proposed elsewhere [22, 325, 326] for $G_{max} = G_{max}(T_{max}, a)$, comparing their accuracy with that that of the function obtained from the simulations. In an attempt to increase its applicability, Wahab et al. [327] implemented this approach in a general FE code. They suggested numerical integration for equation (2.43) and computed the final crack length directly from the FE model. Furthermore, they attributed the conservatism of the predictions in [23, 234] to the use of the total G_{max} as the fatigue-crack-driving parameter, indicating that the best parameter should depend on the local mixed mode ratio.

A slightly modified methodology was presented in [322] to estimate the number of cycles needed to grow a pre-existing defect by certain length in CFRP panels. In this technique the value of G_{max} was calculated using the definition (see equation (2.7), $G = \Delta U/\Delta A$), and then combined with the experimental fracture mechanics fatigue data to deduce the number of cycles until the delamination reached its maximum allowable size. Whilst the change in the delamination area (ΔA) was known beforehand, two FE models of the component (incorporating the original and final defects respectively) were employed to determine the change in the total strain energy release rate.

Despite not requiring the inclusion of cyclic loads in the simulation steps and capturing the threshold with relative success, the previous approaches assumed the existence of an initial crack or defect. Hence they cannot account for the crack initiation period, which can represent a major portion of the fatigue life in bonded joints [328]. Nevertheless, as in the quasi-static case, the use of cohesive elements represents an appealing alternative to overcome this limitation providing that their damage formulation is modified to allow for degradation due to cyclic loading.

The enhanced damage formulation used in fatigue, which typically results in a progressive reduction of either the stiffness or the strength with the number of cycles, could be defined within the framework of damage or fracture mechanics. For example, assuming unloading-reloading hysteresis, Nguyen et al. [329] managed to capture some of the energy dissipation mechanisms associated with fatigue. Starting from a potential function motivated by interatomic potentials, Roe and Siegmund [330] proposed a different irreversible CZM able to accumulate damage during subcritical cyclic loading if damage had already nucleated. The unloading behaviour was analogous to that in an elastic-plastic material, and the two parameters controlling fatigue degradation were somehow related to the endurance limit. Subsequently, this formulation has been applied to the study of various aspects of fatigue with relative success. The resulting formulation has acquired certain popularity, and barely modified versions have been subsequently applied to investigate various aspects of fatigue.

These include the influence of the mean stress, the mode-mix [330], the transient crack growth response to overload cases and abrupt variations in the amplitude and the load ratio [331, 332], the constraint effects induced by T-stress or the bondline thickness [333].

These pioneering studies inspired alternative formulations, such as that presented by Maiti and Geubelle [334, 335]. Even though they also established a two-parameter fatigue degradation scheme, in this case their values could be directly extracted from an experimental Paris-type graph. By combining their damage evolution law with a contact algorithm, the resulting CZM allowed to simulate the crack closure effect during the unloading part of the cycle [335]. Specifically, they were able to evaluate the influence of the induced wedge, its properties and distance to the crack tip on the overall fatigue lifetime. Another technique to study the complex phenomenon of crack retardation was suggested by Ural et al. [336], whose interface model included an additional cohesive parameter which controlled damage healing.

The cycle-by-cycle analysis employed in the previous methodologies is well-suited to simulate in detail some of the local processes associated with fatigue crack propagation. However, it would be computationally unmanageable for high cycle fatigue (HCF) problems where the number of cycles could be of the order of 10^5-10^8. An evolution law expressed in terms of the number of cycles combined with an integration scheme that only calculates the damage state at discrete time intervals (i.e. a cycle jump strategy) would be more appropriate in those situations.

The early work of Peerlings et al. [337] illustrates this last concept very well. Another good example of a methodology intended for HCF can be found in [323, 324]. Following a damage mechanics approach, Robinson and co-workers developed a cohesive element for delamination in composites, demonstrating that it could describe the linear regime of the Paris diagram under mode I, II and I/II. Unfortunately, the resulting law for the total damage growth was an explicit function which had to be linearized and solved iteratively for every increment of the pseudo-time variable. They also noticed that the number of cycles per increment and the size of the interface elements had to be carefully selected in order to avoid spurious oscillations on the overall response. Koutsourelakis et al. [338] suggested a faster extrapolation scheme, which then they combined with a modified version of the hysteresis-based formulation proposed in [329] to study the effects of material uncertainties and pre-existing micro-cracks on the fatigue durability of aircraft fuselages.

Although the various parameters used in [323, 337, 338] are considered material characteristics, their mixed mode dependency and how to extract their values from experimental results are not well-established yet. Taking this into account, a number of

authors have recently proposed methodologies in which the damage accumulation due to the cyclic loading is directly linked to the fatigue crack growth rates measured in fracture mechanics tests. Turón et al. [132, 304] were among the very first to pursue this type of approach by assuming that the crack growth rate was equal to the sum of the damaged area growth rates of all the elements within the FPZ. Moreover, their cycle-jump strategy also simplified integration and, despite only using the linear region of the Paris diagram, they successfully simulated delamination in DCB, 4-ENF and MMB specimens. A very similar model specifically developed for adhesively-bonded joints was included in [305, 339]. These two formulations required an estimate of the cohesive zone length (l_{CZ}) to compute the damage growth rate, employing the analytical formula proposed by Rice [306, 340] in both cases. This issue was further investigated by Harper and Hallett [341], who distinguished between static and fatigue damage lengths and tried to account for mixed mode effects in their own formulation for explicit solvers. Nevertheless, even this last iteration uses a close-form solution for l_{CZ} and relies exclusively on the linear regime of the Paris diagram to define the fatigue degradation.

2.7 Concluding Remarks

An overview of the fundamental aspects of adhesion and fracture mechanics has been presented in this chapter. Various methods for the experimental determination the fracture resistance of structural adhesive joints have been reviewed, paying special attention to the different mode decomposition theories employed to partition the total value of G_c into its individual components. The most popular numerical techniques employed to model bonded structures subjected to static or fatigue loading have been also discussed.

Based on LEFM, the tests specimens used in this project have been drawn from those reported in the literature (see section 2.3.4), as will be fully described in Chapters 4 and 5. The modelling strategy followed employs cohesive zones and incorporates a number of developments which will be described fully in Chapter 3.

3. Performance and Fatigue Life Predictions of Adhesively-Bonded Joints

3.1 Introduction

In recent years cohesive elements have become increasingly popular for simulating both delamination in composite materials and fracture in adhesively-bonded joints. However, even though some models have been proposed for the study of dynamic phenomena [123, 124, 342, 343], their application has been predominantly limited to static problems. This chapter presents two approaches based on the CZM to predict the fatigue performance of bonded structures. Details on the cohesive element formulation employed throughout this work, valid for both quasi-static and cyclic loading cases, are given next. A brief description of the experimental programme required to implement and validate these methodologies can be found in the last section.

It should be noted that, whilst derived from the work of Camanho and co-workers [293, 294], the formulation presented here received a number of significant modifications. Primarily aimed at improving its versatility and reducing the dependence on calibration steps, these covered a wide range of areas including kinematics (quadratic element), topology (user-defined number of integration elements) and the constitutive equations (optimized mixed-mode behaviour for finite-thickness unstrained configuration). The damage evolution was revised as well. In addition to the typical bilinear law, a linear-cubic evolution law similar to that proposed in [276] was implemented.

The improvements also affected the damage degradation due to cyclic loading. Based on the fracture mechanics approach introduced by Turón et al. [304], it was extended for the linear-

cubic case. By using the modified Paris law rather than just the approximation to the linear region, this new version was able to capture the threshold and rapid-growth fatigue regimes. The displacement ratio (R) and frequency were defined as element properties, allowing both the quasi-static and fatigue formulations to be combined in a single user-subroutine. Furthermore, an algorithm to compute the size of the numerical process zone was implemented, eliminating the need for an analytical estimate of the size of the FPZ. Finally, a simplified element formulation to simulate the near-threshold response of adhesive joints was also developed.

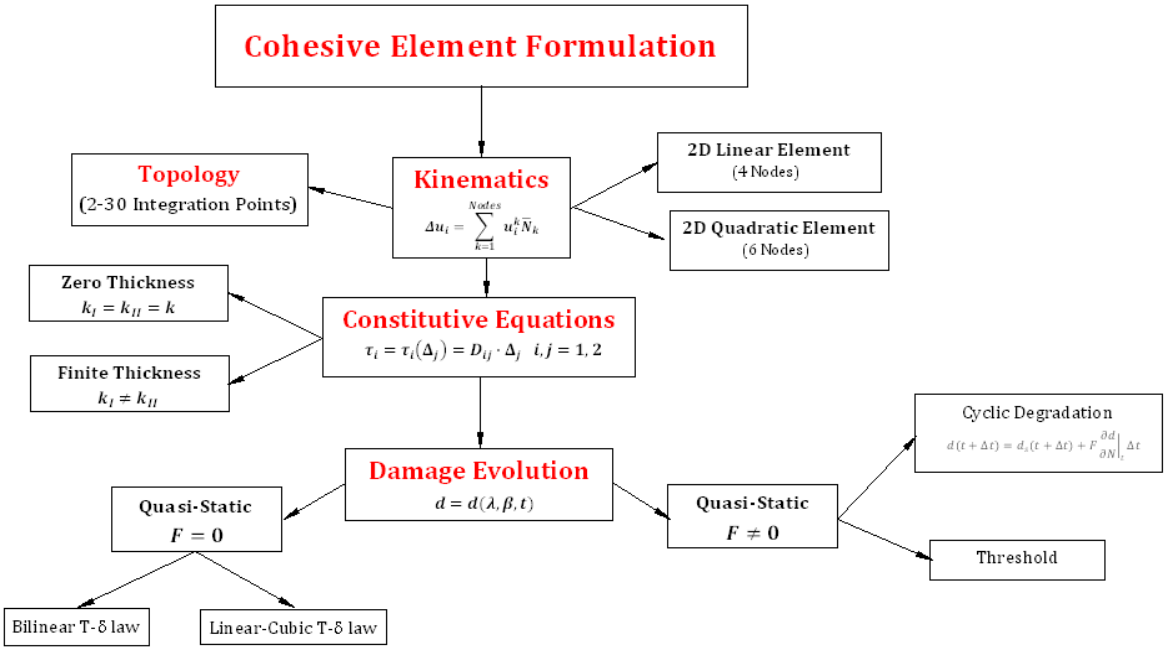

Figure 3.1. Schematic of the cohesive element formulation.

3.2 Proposed Approaches for Fatigue-Lifetime Prediction

The design process of new bonded structures could greatly benefit from the versatility of finite element methods. As discussed in Chapter 2, these are particularly powerful to estimate the service-life of adhesive joints if combined with experimental fracture mechanics data [21, 23, 70, 234, 322-324].

Ideally, any tool devised to predict the fatigue life of adhesively-bonded joints would not have to assume the existence of an initial defect, hence being capable of accounting for crack nucleation. Among the FE techniques for fracture mechanics reviewed in section 2.5, only the CZM meets this requirement. In principle X-FEM [311, 344-346] would also fulfil this condition, but the associated complexity and early stage of development advise against its

use. Consequently, the two methodologies proposed here employ specialized cohesive elements to estimate the fatigue performance of bonded components:

(a) **Methodology A:** Prediction of the T-N_f/S-N_f curve (T: Maximum applied load per unit width; S: Maximum applied stress N_f: Number of fatigue cycles to failure) using modified interface elements in which the damage function has been enhanced to incorporate fatigue degradation due to cyclic loading.

(b) **Methodology B:** Estimation of the fatigue limit or threshold (T_{th}) by combining experimental values of threshold fracture energy G_{th} and a cohesive formulation similar to that employed in quasi-static problems.

Both methods rely heavily on experimental fracture mechanics data: while suitable values of the cohesive parameters (including G_c) can be derived from quasi-static test results, fatigue data is essential to define the accumulated damage function used in the first approach or the value of G_{th} needed in the second one. It is also worth pointing out that "A" and "B" are not mutually exclusive methodologies but are instead complementary. The former uses a relatively complicated formulation to predict the entire fatigue response of the structure. On the other hand, the threshold approach only estimates the fatigue limit, but its simplicity makes it ideally suited for the analysis of big and complex components. Selecting the most suitable methodology for a given application will depend on determining the right balance between several factors, such as the level of detail required, the degree of geometrical complexity involved and the material data and computational resources available.

Described in depth over the next sections, these methods have been applied to estimate the performance of a simplified structure: a titanium-to-CFRP tapered double lap joint (TDLJ – see Figure 3.2). The accuracy of the numerical predictions has been assessed by direct comparison with the experimental results obtained from testing the joint quasi-statically and in fatigue. Details on the geometry, manufacturing process and testing of these joints can be found in chapters 4, 6 and 7 respectively, while the chapter 9 describes the corresponding FE models.

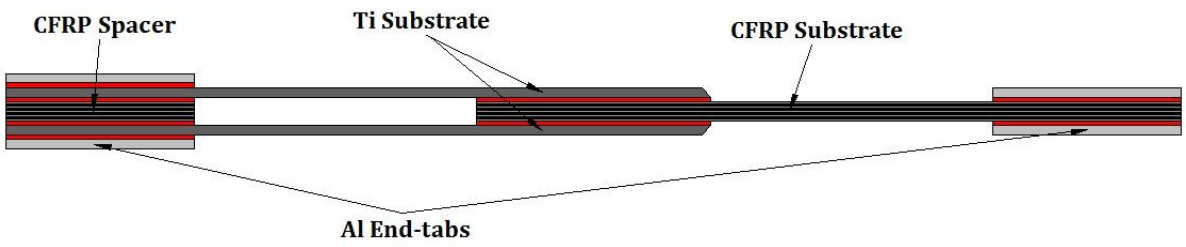

Figure 3.2. Schematic of the CFRP-Titanium Tapered Double Lap Joint (TDLJ) including Al end-tabs and CFRP spacer.

3.2.1 Methodology to predict the T-N Fatigue Response of Adhesive Joints

An interface element formulation to model crack initiation and growth in adhesively bonded joints under mixed-mode loading conditions has been developed. The damage function has been enhanced to incorporate degradation due to cyclic loading, so that the resulting element can be used to predict both the quasi-static and fatigue response of the component. The accumulated damage function introduced in the constitutive law has been derived from experimental fracture mechanics data.

A damage formulation based on the stiffness degradation has been combined with a bilinear or a linear-polynomial constitutive equation to define the quasi-static response of the element. The same traction-separation law represents the starting point in fatigue, but in that case the area under the curve is progressively reduced as the number of cycles increases. Mixed mode is dealt with via a scalar damage variable, defined as a function of a displacement and mixed-mode parameters which account for the contributions of the individual loading modes.

This work is intended for high-cycle fatigue problems (number of cycles $> 10^5$), that would make a cycle-by-cycle analysis computationally intractable. Consequently the sinusoidal load applied to the structure has been replaced in the model by the envelope of its cyclic variation with time (i.e. the decay function of the maximum load values) following the pioneering work by Peerlings et al. [347] and Robinson et al. [323, 324] on delamination of composites. However, for simplicity reasons the jump-cycle strategy proposed by Turón et al. [304] has been used instead of the integration scheme suggested in references [323, 324, 347].

As in [304], the evolution of the damage variable associated with the cyclic loading has been related here to a fracture mechanics description of the fatigue crack growth (i.e. the experimental crack growth rate dA/dN – see Figure 3.3). However, the original formulations [304, 323] only considered the linear fatigue regimen to derive the cumulative damage function, hence neglecting the threshold effects associated with G_{th}. In an attempt to overcome this limitation, the modified Paris law has been employed here to approximate the entire experimental $dA/dN = dA/dN\,(G_{max})$ curve. Developed at NASA and initially published by Forman and Mettu [238] in a slightly different form which considered crack closure effects, the modified Paris law assumed here is:

$$\frac{dA}{dN} = C_T (G_{max})^m \left\{ \frac{1 - \left(\frac{G_{th}}{G_{max}}\right)^{n_1}}{1 - \left(\frac{G_{max}}{G_C}\right)^{n_2}} \right\} \tag{2.33}$$

where G_C , G_{th} and G_{max} are the critical, threshold and maximum energy release rates respectively, and m, C_T, n_1, n_2 are the fitting parameters that define the linear regime and its transitions to the rapid growth and threshold regions. Note that (2.33) is written in terms of the crack area (A) instead of the crack length (a). The fitting parameters of the modified Paris law ($C_T, m, n_1, n_2, G_{th}, G_C$) have been defined as functions of the mixed mode ratio, the frequency (F) and the loading ratio R (quotient between the minimum and maximum applied displacements in the fatigue cycle, see section 3.3.4.1) using experimental data obtained for various loading modes. The maximum energy release rate G_{max} would depend on the maximum applied displacement and has been computed using the constitutive law of the cohesive element.

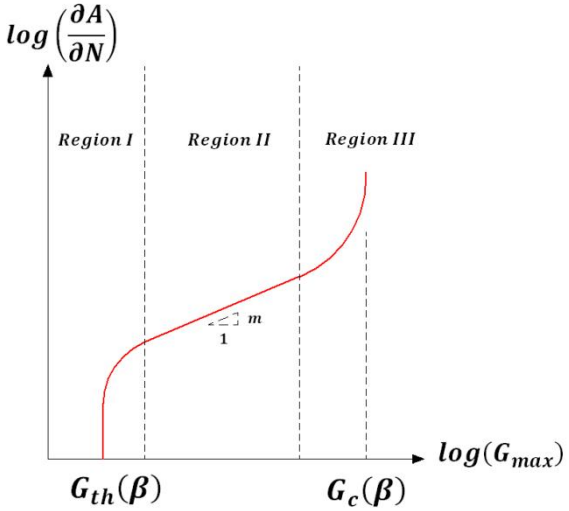

Figure 3.3. Modified Paris law used to approximate the typical experimental fatigue crack growth rate data obtained for a given mixed mode ratio.

3.2.2 Methodology to predict the Fatigue Threshold of Adhesive Joints

A number of drawbacks arise from the previous methodology, chief among which are the mathematical complexity, large amount of experimental data needed and computational costs associated with the enhanced damage function employed to account for cyclic loading. Accordingly, its use would be justified only if those disadvantages were outweighed by the design benefits offered, i.e. provided that the additional information obtained with that modelling tool materialized in the design of superior or improved joints. But even then the applicability of the method would be subjected to certain aspects of the problem under investigation, such as the size and geometry of the component, material data and computational resources available and whether crack growth in the adhesive layer was acceptable from the design point of view.

In order to minimize these difficulties, a second approach using a simplified version of the previous cohesive element is proposed here. The modification to the damage evolution law introduced in the original formulation to account for cyclic fatigue would be omitted in this case. Standard traction-separation laws would be used instead. The area under the traction-separation curve would then be set equal to the experimental value of G_{th} (defined yet again as a function of F, R and the mixed mode ratio), and subsequent static analyses carried out in order to predict the fatigue limit or threshold T_{th} (maximum load per unit width that can be applied in fatigue so that the joint does not experience fatigue crack growth).

As a consequence of this simplification the resulting approach would not predict the whole fatigue response (T-N_f/S-N_f curve) but only the fatigue threshold load or fatigue limit. However, its use is well justified in view of the importance of the threshold in the design of new adhesively-bonded structures, where fatigue crack growth is very often (considered) unacceptable from the design perspective.

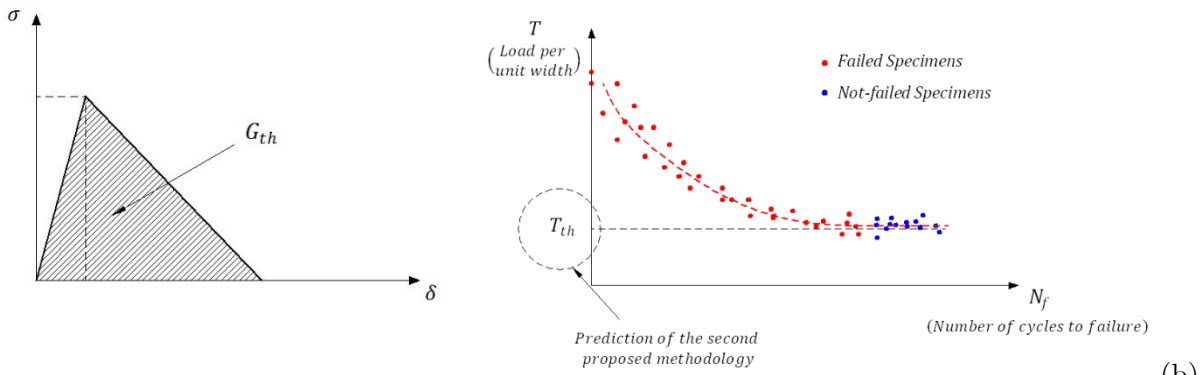

Figure 3.4. Schematic representation of the cohesive law used in (a) the approach proposed for the prediction of the fatigue threshold and (b) typical shape of the experimental T-N_f curve exhibiting a threshold load per unit width T_{th}.

It is worth noting that in this case the shape of the traction-separation law could require small alterations to ensure consistency with the physics of the problem. As no damage should be accumulated below the threshold point, the experimental value of G_{th} should be equal or smaller than the critical area defined by the first triangle of the quasi-static cohesive law (dependent on the penalty stiffness k and the displacement at damage initiation δ_0 – see Figure 3.5). Unfortunately this area cannot be contained under a traditional traction-separation curve while keeping the same cohesive parameters that define the elastic response prior to damage initiation. The solution adopted here to circumvent this problem consists on maintaining the same penalty stiffness used in the quasi-static case and modifying the shape of the cohesive law to accommodate the potentially reduced threshold area. However, it

entails the creation of a specific damage evolution law, which is discussed in depth in the section 3.3.5.

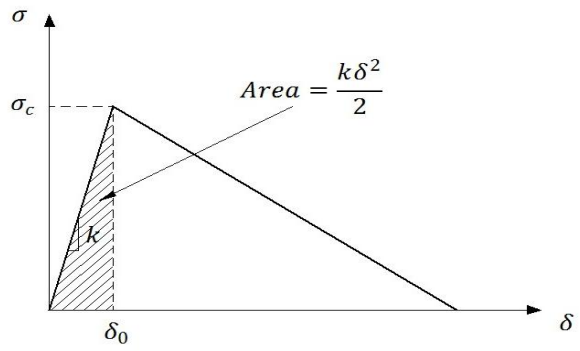

Figure 3.5. Representation of the minimum area defined by the quasi-static cohesive parameters (k and δ_0).

3.3 Cohesive Element Formulation for Crack Propagation Analysis in Adhesive Joints under High-cycle Variable-mode Fatigue Loading

The methodologies presented in the previous section are based on "unconventional" cohesive elements, at least in what refers to the damage evolution law. Consequently a purpose-built element capable of satisfying the particular requirements for the fatigue-life prediction and at the same time suitable for quasi-static problems had to be created.

A two-dimensional interface element formulation to model crack initiation and growth in adhesively bonded joints under quasi-static and cyclic fatigue mixed-mode loading conditions is proposed here. Its quasi-static definition, derived from that in [293, 294], has been considerably revised to improve the mixed-mode behaviour and reduce the dependence on the calibration steps. First of all, the original linear element (4 nodes) has been supplemented with a quadratic version (6 nodes), while the topology has been modified to allow a user-defined number of integration points (between 2 and 30 Gauss-Legendre points). Optimized for a finite thickness unstrained configuration, the constitutive equations now tolerate dissimilar penalty stiffness in tension and shear. Furthermore, a linear cubic damage evolution law similar to that proposed in [276] has been added to the typical bilinear traction-separation law.

The basic damage evolution has been extended to simulate fatigue problems. Following the fracture mechanics approach suggested by Turón et al. [304], both the bilinear and linear-cubic laws have been enhanced to incorporate degradation due to cyclic loading. However, by using a modified Paris law rather than just the approximation to the linear region of the $dA/dN = dA/dN\,(G_{max})$ diagram, the elements presented here could account for the threshold and rapid growth regimes. In addition, an algorithm developed to compute the numerical cohesive zone length has eliminated the dependence of earlier formulations on analytical estimates of the size of the FPZ. Finally, a simplified version of the evolution laws intended only for the prediction of the fatigue threshold has also been devised.

The resulting formulations have been implemented in Abaqus via a user element subroutine UEL. Even though they could be seen as three different elements, the fact that they all share the same kinematics and constitutive equations has allowed to merge them in a single subroutine. Depending on the type of analysis under consideration, the user could select the appropriate element behaviour using various external variables (for example, the frequency value would help distinguishing between quasi-static and fatigue analyses).

A comprehensive description of this element is presented next. The kinematics of the idealised interface is followed by the constitutive equations and various damage evolution laws (for quasi-static problems, cyclic fatigue and threshold determination) and finally the tangent stiffness tensor. For simplicity, only the equations for the bilinear law are included in this chapter. Those corresponding to the linear-cubic case can be found in Appendix A.

3.3.1 Kinematics

Consider a two dimensional domain Ω^* divided in two parts ($\Omega^+$and Ω^-) by an interface Γ_d with a small or negligible initial thickness t_a. The deformed coordinates (x_i^+ and x_i^-, i=1, 2) of any point in the upper and lower surfaces of this interface (${\Gamma_d}^+$and ${\Gamma_d}^-$) can be obtained from their initial coordinates (X_i^+ and X_i^-) and displacements (u_i^+ and u_i^- respectively):

$$x_i^{\pm} = X_i^{\pm} + u_i^{\pm} \tag{3.1}$$

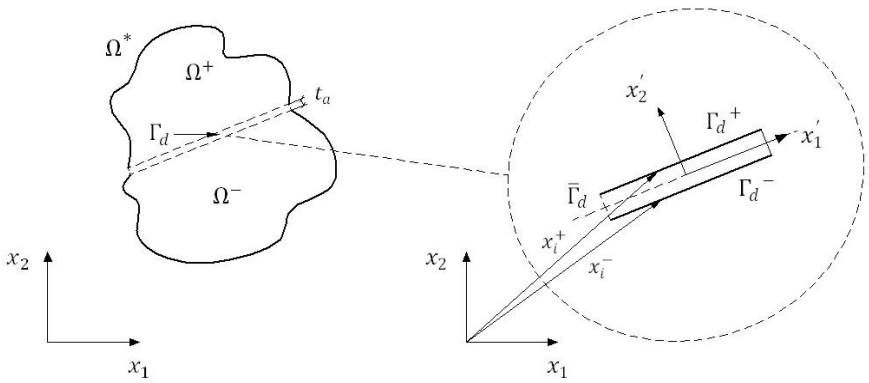

Figure 3.6. Schematic representation of the 2-D interface Γ_d which divides the domain Ω into two parts ($\Omega^+$and Ω^-).

The behaviour of the material linking $\Omega^+$and Ω^- can be characterized in terms of the relative displacements or displacement jumps across the interface (Δu_i), which are evaluated in its mid-surface ($\bar{\Gamma}_d$, equidistant from the top and bottom surfaces) as in the formulations proposed by Turon et al. [294, 304] and Camanho et al. [293]. The displacement jump and the coordinates of the mid-surface ($\bar{x}_i$) can be written as follows:

$$\Delta u_i = u_i^+ - u_i^- \tag{3.2}$$

$$\bar{x}_i = \frac{1}{2}(x_i^+ + x_i^-) = \frac{1}{2}(X_i^+ + X_i^-) + \frac{1}{2}(u_i^+ + u_i^-) \tag{3.3}$$

It is worth noting that these expressions could be further simplified for zero-thickness interfaces, in which case the top and bottom surfaces would coincide in the initial configuration ($X_i^+ = X_i^- = X_i$).

$$\begin{aligned} x_i^\pm &= X_i + u_i^\pm \\ \Delta u_i &= u_i^+ - u_i^- \\ \bar{x}_i &= X_i + \frac{1}{2}(u_i^+ + u_i^-) \end{aligned} \tag{3.4}$$

Two dimensional linear (4-noded) and quadratic (6-noded) cohesive elements have been derived from the previous kinematic description of the interface. The user can choose between finite and zero thickness for the unstained state, whereas a line element (zero-thickness) is adopted for the isoparametric element used in the reference configuration in either case (see Figure 3.7).

Employing a traditional FE discretization, the relative displacements across the interface (Δu_i) in global coordinates ($x_1 - x_2$) can be obtained from the displacement of the nodes at the top and bottom surfaces.

$$\Delta u_i = \sum_{k=1}^{Top\ Nodes} u_i^k N_k - \sum_{k=1}^{Bottom\ Nodes} u_i^k N_k = \sum_{k=1}^{Nodes} u_i^k \overline{N}_k \tag{3.5}$$

where u_i^k is the displacement of the node "k" in the direction "i", and $N_k(\xi^*)$ is the Lagrangian shape function associated to node "k" in the isoparametric element (see Table 3.1). The functions $\overline{N}_k(\xi^*)$ incorporate the right sign and provide a more compact expression for Δu_i.

$$\overline{N}_k = \begin{cases} N_k, & Nodes\ in\ the\ top\ surface\ {\Gamma_d}^+\ (k = 3,4,6) \\ -N_k, & Nodes\ in\ the\ bottom\ surface\ {\Gamma_d}^-\ (k = 1,2,5) \end{cases} \tag{3.6}$$

Table 3.1. Shape functions used in the linear and quadratic cohesive elements (ξ^* and η^* are the coordinates of the element in the isoparametric configuration).

Shape Functions	
Linear element (4 nodes)	**Quadratic element (6 nodes)**
$N_1 = N_4 = \frac{1}{2}(1 - \xi^*)$ $N_2 = N_3 = \frac{1}{2}(1 + \xi^*)$	$N_1 = N_4 = \frac{1}{2}\xi^*(\xi^* - 1)$ $N_2 = N_3 = \frac{1}{2}\xi^*(\xi^* + 1)$ $N_5 = N_6 = 1 - (\xi^*)^2$

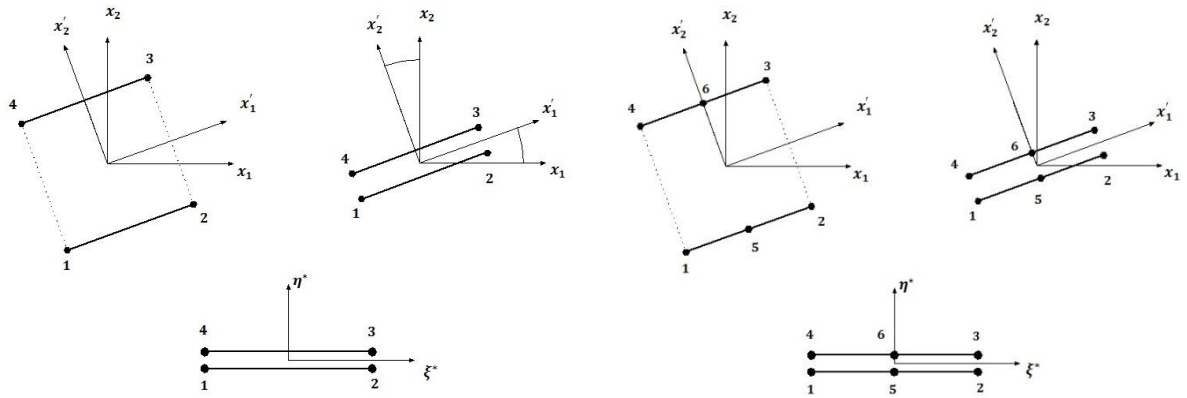

Figure 3.7. Representation of (a) the linear and (b) the quadratic elements with finite and zero thickness in the unstrained state and as a line element in the isoparametric configuration.

For an element with a general orientation in space, the displacement jump Δ_{m} in the local reference system $(x_1' - x_2')$ at a generic point of the interface can be expressed in terms of the nodal displacements in global coordinates using the rotation tensor Θ_{mi} and equation (3.5). Note that the local reference system and that used for defining the isoparametric element are aligned. This relative displacement Δ_{m}, expressed in the local reference system, is used to define the constitutive behaviour of the element.

$$\Delta_{\mathrm{m}} = \Theta_{\mathrm{mi}} \cdot \Delta u_{\mathrm{i}} \tag{3.7}$$

The rotation tensor contains the direction cosines of the local coordinate system to the global one, which coincide with the components of the unit tangent $(\vec{t})$ and normal $(\vec{n})$ vectors of the mid-surface of the element. The tangent vector $(\vec{t})$ can be obtained by differentiating the coordinates of the mid-surface of the element, while the normal vector is orthogonal to the latter.

$$t_i = \frac{\bar{x}_{i,\xi^*}}{\left|\bar{x}_{i,\xi^*}\right|} \rightarrow \vec{t} = \left(\frac{\bar{x}_{1,\xi^*}}{\sqrt{\left(\bar{x}_{1,\xi^*}\right)^2 + \left(\bar{x}_{2,\xi^*}\right)^2}}, \frac{\bar{x}_{2,\xi^*}}{\sqrt{\left(\bar{x}_{1,\xi^*}\right)^2 + \left(\bar{x}_{2,\xi^*}\right)^2}} \right) \tag{3.8}$$

$$\vec{n} = \left(\frac{-\bar{x}_{2,\xi^*}}{\sqrt{\left(\bar{x}_{1,\xi^*}\right)^2 + \left(\bar{x}_{2,\xi^*}\right)^2}}, \frac{\bar{x}_{1,\xi^*}}{\sqrt{\left(\bar{x}_{1,\xi^*}\right)^2 + \left(\bar{x}_{2,\xi^*}\right)^2}} \right) \tag{3.9}$$

Assuming non-linear geometry (i.e. large displacements) the coordinates of the mid-surface can be written as functions of the initial nodal coordinates (X_i^k) and the nodal displacements u_i^k, and then differentiated with respect to ξ^* to obtain the gradients $\bar{x}_{i,\xi^*}$ that appear in equations (3.8) and (3.9):

$$\bar{x}_i = \sum_k \frac{1}{2}\left(X_i^k + u_i^k\right)N_k \;\rightarrow\; \bar{x}_{i,\xi^*} = \sum_k \frac{1}{2}\left(X_i^k + u_i^k\right)N_{k,\xi^*} \tag{3.10}$$

The rotation tensor would then adopt the following expression:

$$\boldsymbol{\Theta} = \frac{1}{\sqrt[2]{\left(\bar{x}_{1,\xi^*}\right)^2 + \left(\bar{x}_{2,\xi^*}\right)^2}}\begin{bmatrix} \bar{x}_{1,\xi^*} & \bar{x}_{2,\xi^*} \\ -\bar{x}_{2,\xi^*} & \bar{x}_{1,\xi^*} \end{bmatrix} \tag{3.11}$$

Previous work [244] has shown that Gauss quadrature is more accurate than nodal integration in cohesive elements. Thus the former has been adopted in this work. Additionally the number of integration points has been defined as an external variable (varying between 2 and 30), so it could be modified by the user to study its effects on the solution. Since the displacement jump is evaluated in its mid-surface, all the integration points lie in that surface (y'=η^*=0).

3.3.2 Constitutive law

The constitutive equations and the damage evolution shared by both the linear and the quadratic cohesive elements are very similar to that introduced by Camanho et al. [293] and subsequently refined by Turón et al. [294]. However they needed to be adapted for the finite thickness case to ensure that the elements would capture the elastic behaviour of the material they represent prior to damage initiation.

The constitutive law describing the behaviour of the elements relates the cohesive tractions (τ_i) to the displacement jump in the local coordinates (Δ_j) through the interface stiffness tensor D_{ij}.

$$\tau_i = \tau_i\left(\Delta_j\right) = D_{ij} \cdot \Delta_j \quad i,j = 1,2 \tag{3.12}$$

A stiffness degradation approach using a scalar damage variable d varying between 0 (undamaged or intact interface) and 1 (complete failure) has been selected as opposed to energy consumed or work done based strategies (see Lopez Armas [348]).

$$\tau_i = (1-d)\, D_{ij}^0\, \Delta_j - d \cdot D_{ij}^0 \bar{\delta}_{2j} \langle -\Delta_2 \rangle \tag{3.13}$$

D_{ij}^0 is the undamaged stiffness tensor, $\bar{\delta}_{ij}$ is the Kronecker delta and $\langle\ \rangle$ represents the MacAuley bracket defined as $\langle \mathrm{x} \rangle = \frac{1}{2}(\mathrm{x} + |\mathrm{x}|)$. The second term of τ_i $(-dD_{ij}^0 \bar{\delta}_{2j} \langle -\Delta_2 \rangle)$ is introduced to prevent interpenetration of the interface surfaces after complete failure by restoring the undamaged penalty stiffness for mode I if $\Delta_2 < 0$. Bear in mind that, unlike negative values of Δ_2, negative values of Δ_1 must be allowed by the model since negative shear deformation does have a physical meaning in fracture problems ($\Delta_1 > 0$ and $\Delta_1 < 0$ represents opposite directions in the applied shear displacement).

Following the work by Tvergaard and Hutchinson [263], a displacement parameter denoted as λ (norm of the displacement jump tensor or equivalent displacement jump norm) is introduced to evaluate the state of the displacement jump as well as to differentiate between loading and unloading conditions in the mixed mode cases. An additional parameter β is introduced to quantify the mode mixity using the relative displacements for mode I and mode II (Δ_2 and Δ_1 respectively).

$$\lambda = \sqrt{(\Delta_1)^2 + (\langle \Delta_2 \rangle)^2} \tag{3.14}$$

$$\beta = \frac{|\Delta_1|}{|\Delta_1| + \langle \Delta_2 \rangle} \rightarrow \begin{cases} \beta = 0 \ \rightarrow Mode\ I \\ \beta = 1 \ \rightarrow Mode\ II \end{cases} \tag{3.15}$$

The undamaged stiffness tensor D_{ij}^0 must be consistent with the unstrained configuration selected for the elements to guarantee a realistic representation of the elastic response and pre-crack behaviour. Zero-thickness interfaces do not represent any physical material, hence a very high but single value of the penalty stiffness is needed. On the other hand, finite thickness elements modelling the response of isotropic materials will require different penalty stiffness values for tension (mode I, $k_2 = k_I$) and shear (mode II, $k_1 = k_{II}$) loading. Finite thickness elements have been employed throughout this work.

$$D_{ij}^0 = \begin{cases} \bar{\delta}_{ij} k & Zero - thickness \\ \bar{\delta}_{ij} k_i & Finite - thickness \end{cases} \tag{3.16}$$

The stiffness tensor can then be written as

$$D_{ij} = D_{ij}^0 \left\{ 1 - d \left(1 + \bar{\delta}_{2j} \frac{\langle -\Delta_j \rangle}{\Delta_j} \right) \right\} \tag{3.17}$$

The constitutive law proposed above is fully defined if the damage function and the mixed mode ratio β are evaluated at every time step.

3.3.3 Damage Evolution Law for Quasi-static problems (F=0)

As indicated in Chapter 2, there is no general consensus regarding the significance of the damage evolution law. Whether its shape affects the overall response still remains an open question, particularly under mixed mode conditions [276-279]. With the aim of investigating this issue further, two different cohesive laws have been implemented here: the traditional bilinear shape (used as baseline) and a linear-cubic form (initially proposed in [276] for explicit solvers). Both laws have been also extended to include cyclic fatigue effects (see section 3.3.4). The equations for the bilinear case are presented in this chapter, whereas those corresponding to the linear-cubic case can be found in Appendix A.

Implemented in the displacement jump space, the cohesive law uses a monotonic scalar function $Q(\lambda)$ ranging from 0 to 1 that controls the damage evolution. This function defines the shape of the traction-separation curve (see Figure 3.8), taking the following expression for the bilinear case:

$$Q_{Bilinear}(\lambda) = \frac{\Delta^f(\lambda - \Delta^0)}{\lambda(\Delta^f - \Delta^0)} \tag{3.18}$$

In both cases the onset of damage occurs at Δ^0, while Δ^f represents a fully damaged interface ($d = 1$). To avoid changes in the damage state during neutral loading (i.e. when the applied displacement remains the same) or unloading situations, the loading history is accounted for via a time-dependent damage threshold r^t. r^t fulfils the relation $r^t \geq r^0$, where $r^0 = \Delta^0$ is the initial damage threshold and t indicates the current time. Consequently the damage variable at the time t ($d(t)$) is defined as follows:

$$d(t) = Q(r^t) \tag{3.19}$$

$$r^t = max\left\{r^0, \max_s \lambda^s\right\} \quad 0 \leq s \leq t \tag{3.20}$$

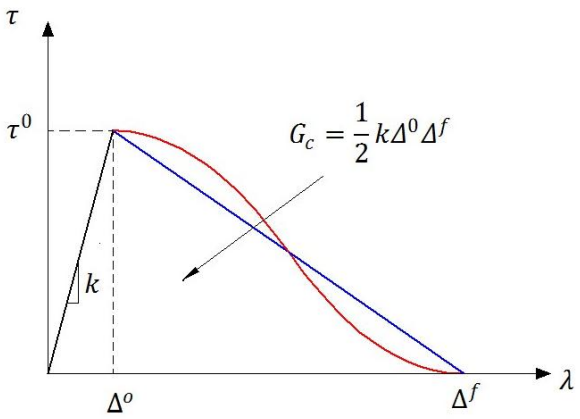

Figure 3.8. Schematic representation of the bilinear (blue) and linear-cubic (red) cohesive laws. The relationship between the cohesive parameters k, Δ^0 and Δ^f and the area under the curve G_c is the same in both cases.

Thanks to its higher-order damage variable, the linear-cubic traction-separation law clearly produces smoother transitions (horizontal tangents) at the points of damage onset and complete decohesion than the bilinear case (see Figure 3.8). Note also that for a constant mixed-mode ratio, both evolution laws produce the same relationship between the area under the traction-separation curve and the cohesive parameters k, Δ^0 and Δ^f, which facilitates enormously their combination in a single subroutine.

$$G_{ic} = \int_0^{\Delta^f} \tau_i(\lambda)\, d\lambda = \int_0^{\Delta^f} (1-d) k_i \lambda\, d\lambda = \frac{1}{2} k_i \Delta^0 \Delta^f \tag{3.21}$$

The values of both Δ^0 and Δ^f depend on the mixed mode ratio (β) and can be derived from the initiation and propagation criteria respectively, which must take into account the interaction between the different loading modes. By defining the damage function in terms of λ and β (indirectly included in $\Delta^0(\beta)$ and $\Delta^f(\beta)$), this formulation can cope with mixed mode problems using a scalar damage function instead of different damage variables for each component of the displacement jump vector. As pointed out by Robinson et al. [323], the latter approach could lead to serious difficulties at complete debonding since in general it does not occur simultaneously in modes I and II.

3.3.3.1 Propagation Criterion

The criterion used to predict crack propagation establishes that crack growth occurs when the total energy release rate G is greater or equal than a critical value G_c. For implementation reasons, it is preferable to express this condition in the displacement jump space through an equivalent definition of the final displacement Δ^f. This can be achieved by equating the area

under the cohesive law to the corresponding critical strain energy release rate G_c. For pure fracture modes I and II this is relatively straightforward, resulting in

$$\begin{cases} G_{Ic} = \frac{1}{2} k_I \Delta_I^0 \Delta_I^f \quad \rightarrow \Delta_I^f = \frac{2 \cdot G_{Ic}}{k_I \Delta_I^0} \\ G_{IIc} = \frac{1}{2} k_{II} \Delta_{II}^0 \Delta_{II}^f \rightarrow \Delta_{II}^f = \frac{2 \cdot G_{IIc}}{k_{II} \Delta_{II}^0} \end{cases} \tag{3.22}$$

where k_I , k_{II} , Δ_I^0 , Δ_{II}^0 , Δ_I^f and Δ_{II}^f are the penalty stiffnesses, onset and final displacement jumps corresponding to pure modes I and II respectively. Usually referred to as "cohesive parameters", these variables unmistakably define the traction-separation laws for pure mode fracture. Even though many authors would consider the fracture toughness for mode I and II (G_{Ic} and G_{IIc}) instead of Δ_I^f and Δ_{II}^f among the set of cohesive parameters, it is worth noting that they are not independent if the shape of the traction-separation law is fixed. Taking into account (3.21), equation (3.22) is valid for both the bilinear and linear-cubic cases.

In contrast, adapting the propagation criterion $G>G_c$ to a mixed mode problem is more complicated, since in that case the values of G_c and G would depend on the mode mixity. While the total energy could be calculated as the sum of the mode I and II contributions ($G = G_I + G_{II}$), one of the many models proposed in the literature (B-K [224], Power law [276], CKWW [136], etc) could be used to fit the experimental data to obtain an relationship between the critical strain energy release rate and the mode mixity. Assuming a general function of the form $G_c = G_c(G_{II}/G)$, where G_{II}/G is the mixed mode ratio in energy terms, the propagation condition could be expressed in the displacement space by equating the area under the cohesive law to the corresponding fracture toughness as in the pure mode cases:

$$G_c(G_{II}/G) = \frac{1}{2} \cdot k_{eff}(\beta) \cdot \Delta^o(\beta) \cdot \Delta^f(\beta) \rightarrow \Delta^f(\beta) = \frac{2 \cdot G_c(G_{II}/G)}{k_{eff}(\beta) \cdot \Delta^o(\beta)} \tag{3.23}$$

Similarly, the mode I and mode II contributions to the total energy can be calculated as the areas under the respective traction-separation laws. Identifying $\Delta_I^0(\beta)$ and $\Delta_{II}^0(\beta)$ as the normal and shear displacement jumps at the onset of damage under mixed mode loading conditions, $\Delta_I^f(\beta)$ and $\Delta_{II}^f(\beta)$ as the normal and shear displacement jumps corresponding to the total de-cohesion, and k_I and k_{II} as the mode I and II penalty stiffness (see Figure 3.9):

$$G = G_I + G_{II} \begin{cases} G_I = \frac{1}{2} k_I \Delta_I^0(\beta) \Delta_I^f(\beta) \\ G_{II} = \frac{1}{2} k_{II} \Delta_{II}^0(\beta) \Delta_{II}^f(\beta) \end{cases} \tag{3.24}$$

The function $\Delta^f(\beta)$ can be derived from (3.23) provided that a relationship between the mixed mode in energy and displacement terms is available. Such relationship can be obtained taking into account (3.24) and the definition of β (see equation (3.15)):

$$\beta = \frac{|\Delta_1|}{|\Delta_1| + \langle\Delta_2\rangle} = \frac{|\Delta_{\mathrm{II}}|}{|\Delta_{\mathrm{II}}| + \langle\Delta_{\mathrm{I}}\rangle} \overset{\Delta_I \geq 0}{\rightleftharpoons} \Delta_{II} = \left(\frac{\beta}{1-\beta}\right)\Delta_I \rightarrow \begin{cases} \Delta_{II}^0(\beta) = \left(\frac{\beta}{1-\beta}\right)\Delta_I^0(\beta) \\ \Delta_{II}^f(\beta) = \left(\frac{\beta}{1-\beta}\right)\Delta_I^f(\beta) \end{cases} \tag{3.25}$$

Using the previous results, the ratio G_{II}/G can be written in terms of β and the penalty stiffness of the pure loading modes (k_I and k_{II}):

$$\frac{G_{II}}{G} = \frac{\mathrm{k}_{II}\Delta_{II}^0(\beta)\Delta_{II}^f(\beta)}{k_I\Delta_I^0(\beta)\Delta_I^f(\beta) + k_{II}\Delta_{II}^0(\beta)\Delta_{II}^f(\beta)} = \frac{k_{II}\beta^2}{k_I - 2k_I\beta + (k_I + k_{II})\beta^2} \tag{3.26}$$

Note that (3.26) can be simplified for zero-thickness elements ($k_I = k_{II} = k$), resulting in the same expression given in [294]:

$$\frac{G_{II}}{G} = \frac{\beta^2}{1 - 2\beta + 2\beta^2} \tag{3.27}$$

An effective penalty stiffness $k_{eff}(\beta)$ is required to calculate the area under the traction-separation curve and therefore to complete the definition of the cohesive parameters for a general mixed mode ratio. While the value used in the undamaged stiffness tensor would be used for zero-thickness elements ($k_{eff}(\beta) = k$), an arbitrary function of β fulfilling the following conditions is chosen for the finite thickness case:

$$\begin{cases} k_{eff}(0) = k_I = k_2 \\ k_{eff}(1) = k_{II} = k_1 \end{cases} \tag{3.28}$$

$$k_{eff}(\beta) = \sqrt{\frac{(k_I\Delta_I)^2 + (k_{II}\Delta_{II})^2}{(\Delta_I)^2 + (\Delta_{II})^2}} = \sqrt{\frac{(1-\beta)^2{k_I}^2 + \beta^2{k_{II}}^2}{(1-\beta)^2 + \beta^2}} \tag{3.29}$$

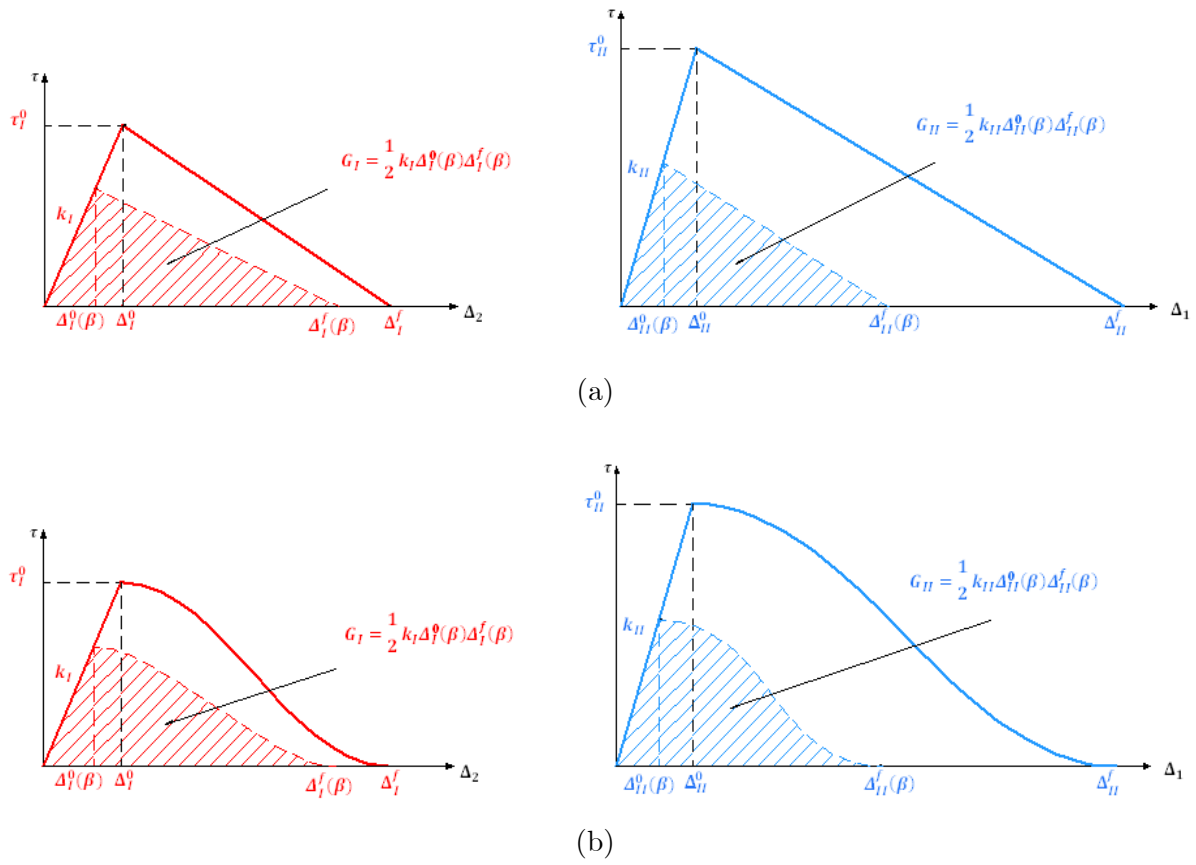

Figure 3.9. Schematic representation of (a) the bilinear and (b) linear-cubic traction-separation laws corresponding to the pure loading modes I (red) and II (blue). The smaller triangles represent the individual contribution of the pure modes in a mixed mode loading case (for a given value of β).

3.3.3.2 Initiation Criterion

The behaviour of the element is completely defined except for the damage initiation criterion, i.e. the value of $\Delta^o(\beta)$. Once again, the contribution of the different loading modes must be taken into account when it comes to define this criterion ($\Delta^o(\beta)$). Several options have been discussed in the literature, with the quadratic separations and the quadratic tractions (Ye's criterion) criteria proving very popular ([258, 293]). Nevertheless, Turón et al. [294] proposed a modified relationship which links the initiation and propagation criteria, allowing a smoother transition from the initial damage to the total failure for any value of β.

Although they have produced good results in previous investigations, these criteria are entirely empirical. A different approach, where the damage initiation parameter (Δ^o) is defined using the interfacial strength (τ^o) and the effective penalty stiffness is used here instead. Although rather general, this method tries to be consistent with the physics of the

problem and at the same time adapting to any material behaviour via a suitable definition of the function $\tau^o(\beta)$.

$$\Delta^o(\beta) = \frac{\tau^o(\beta)}{k_{eff}(\beta)} \rightarrow \begin{cases} \Delta_I^0 = \dfrac{\tau_I^0}{k_I} \;\; Mode\ I\ (\beta = 0) \\ \Delta_{II}^0 = \dfrac{\tau_{II}^0}{k_{II}} \;\; Mode\ II\ (\beta = 1) \end{cases} \tag{3.30}$$

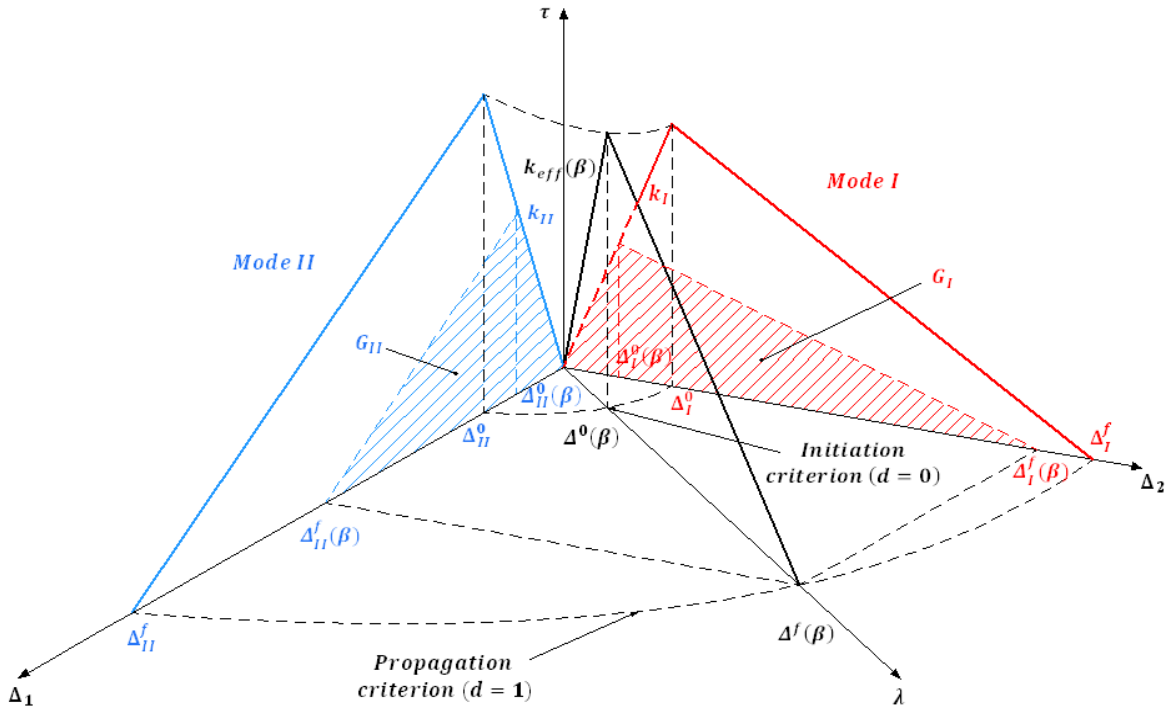

Figure 3.10. Schematic representation of the bilinear traction-separation response for any mixed mode ratio and its connections with the pure loading mode softening laws (assuming general initiation and propagation criteria in the displacement jump space).

3.3.3.3 Selection of the cohesive parameters

It has been indicated before that there is no clear consensus over the physical meaning of the cohesive parameters [19, 239, 269, 282, 283, 287], specifically in what refers to the penalty stiffness and the displacement/traction at damage initiation. However, a precise description of the constitutive behaviour of the adhesive layer (and therefore suitable values of these parameters) is required if the strength of adhesively-bonded joints is to be predicted accurately. Although some authors have proposed experimental techniques based on the J-Integral to obtain the traction-separation law [291, 292, 296, 297, 299, 300], in most cases this relationship is calculated indirectly using finite element analysis (as reviewed by Elices et al.

[349]). A cohesive law shape is pre-selected and an iterative process is followed to determine its characteristic values. The set of parameters that best reproduce the experimental results is identified by direct comparison of the measured response with the predictions of the different models.

Bearing in mind that this iterative process can be long and costly as well as produce results with little or no physical meaning, a different approach is proposed here: the cohesive parameters are derived from the macroscopic mechanical properties of the adhesive material. Firstly, the penalty stiffness for pure modes I and II are obtained from the modulus of elasticity in tension (E) and shear (G_{12}) respectively (divided by the thickness of the unstrained configuration t_a). This would guarantee proper representation of the elastic behaviour of the adhesive layer prior to the onset of damage.

$$k_I = \frac{E}{t_a} \; ; \; k_{II} = \frac{G_{12}}{t_a} \tag{3.31}$$

Establishing the appropriate initiation criterion is more complex though, since the concept of damage onset could be associated to different phenomena (plastic yielding, cavitation in rubber-toughened systems, etc) depending on the type of adhesive material. The relative importance of the various mechanisms in each case could be accounted for via a suitable definition of the interfacial strength $\tau^o(\beta)$ provided that sufficient information were available. Here initiation is assumed to be directly linked to the plastic yielding of the epoxy resin, hence the interfacial strength is set equal to the yield stress σ_Y.

$$\Delta^o(\beta) = \frac{\sigma_Y}{k_{eff}(\beta)} \rightarrow \begin{cases} \Delta_I^0 = \dfrac{\sigma_Y}{k_I} \;\; Mode\ I\ (\beta = 0) \\ \Delta_{II}^0 = \dfrac{\sigma_Y}{k_{II}} \;\; Mode\ II\ (\beta = 1) \end{cases} \tag{3.32}$$

A well-established yielding criterion such as Tresca or Von Mises could be used instead of a constant σ_Y value to define a more physically relevant interfacial strength function of the mixed mode ratio. This solution could prove inconsistent though, as the isotropic behaviour assumption traditionally associated with this criteria clashes with the inherently anisotropic nature of the cohesive element formulation (only two stresses are defined, with $\sigma_{11} = 0$).

Experimental results are directly employed to define the last cohesive parameter, i.e. the area under the traction-separation curve G_c (or Δ^f, since both are linked by equation (3.23)). Various mixed mode ratios are tested and the fracture toughness results fitted to one of the

many models proposed in the literature (see section 2.3.5, [174]) or to a polynomial in order to get a function of the form $G_c = G_c(G_{II}/\mathrm{G})$.

Note that the degree of constraint has been embedded indirectly in the cohesive formulation. The magnitude of the plastic dissipation and therefore the value of G_c have been previously linked with the level of constraint in the adhesive layer [129]. Further, this relationship has been used to justify the variation of the fracture energy with the bondline thickness reported by numerous researchers. Consequently, the use of the experimental fracture energy corresponding to the bondline thickness of interest would partly account for these effects. On the other hand, the potential influence of the triaxial stress state near the crack tip on the yield stress and elastic moduli has been neglected, with the uniaxial values used instead. As suggested by some authors, these simplifications could compromise the transferability of the results to other geometries [284, 350, 351]. However, including such level of detail in the models would clash with the aim of simulating large and complex adhesively-bonded components, which represents the main focus of the present work.

3.3.4 Damage Evolution Law for Cyclic Fatigue problems (F≠0)

In line with the quasi-static formulation, the effects of fatigue loading have been modelled as further reductions in stiffness. In a general problem the additional damage term responsible for the degradation due to the cyclic loading is combined with the quasi-static component. While the quasi-static part is evaluated using the expressions presented in the previous section, the fatigue contribution would be a function of the amplitude and frequency of the applied load and the number of cycles.

3.3.4.1 Loading case of interest

For simplicity, the cyclic load applied to the structure under investigation is assumed to be sinusoidal, positive (i.e. oscillating between positive-traction values) and with a constant frequency F. Displacement control mode is presupposed, although in principle the formulation would also be valid for load control cases. Bearing this in mind the second condition could be rewritten in terms of the load ratio $R = \lambda_{min}/\lambda_{max}$ as $R \geq 0$, where λ_{max} and λ_{min} are the maximum and minimum applied displacement jump norms respectively (see Figure 3.11). Note that the potential contribution of the different loading modes to the applied load is already included in $\lambda(t)$.

Designed for high-cycle fatigue applications, the sinusoidal load is replaced in the model by the envelope of its cyclic variation with time (i.e. the decay function of the maximum load

values) following the work in [304, 323, 324, 347]. The influence of λ_{min} (i.e. the R ratio effects) is then accounted for via a suitable definition of G_{max} (see Section 3.3.3.4.4.2). Furthermore, as suggested by Robinson et al. in [323] the numerical load is initially applied statically up the predefined maximum displacement λ_{max}. The actual fatigue analysis would begin at time t_0 with the introduction of damage accumulation due to cyclic loading (see Figure 3.11).

$$d(t) = \begin{cases} d_{quasi-static} & t \leq t_0 \\ d_{quasi-static} + d_{fatigue} & t > t_0 \end{cases} \tag{3.33}$$

Overall, not only do these simplifications reduce notably the overall computational burden (which would make the method impractical otherwise), but they also bring the nature of the resulting formulation closer to that of a typical static analysis (aside from the additional damage term to account for fatigue degradation).

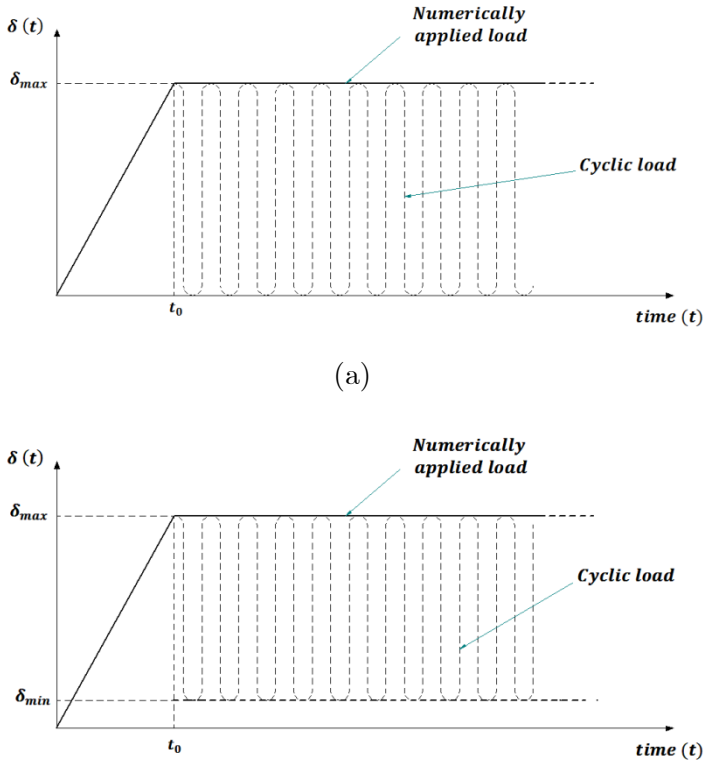

Figure 3.11. Representation of the cyclic displacement jump norm applied to the structure and the decay function of its maximum values that replaces it in the numerical models for a loading ratio (a) $R = 0$ and (b) $R > 0$.

It is worth noting that even if the cyclic loading applied to the structure had constant amplitude and R ratio, the maximum displacement seen by a particular cohesive element

could vary with time. This situation becomes evident in the case of a DCB test specimen, in which the displacement applied at certain distance ahead of the crack tip changes as the crack grows (or as the cohesive zone develops and the material softens) and the compliance decreases. Consequently the formulation has to be able to cope with variable amplitudes. Moreover, by doing so it becomes applicable to cases with changing values of λ_{max} and λ_{min} as long as they vary gradually and not in abrupt steps while remaining positive and defining a constant R ratio. Obviously the accuracy of the solution of such problems would be subjected to the validity of the experimental data employed to define the modified Paris law (see [122]).

3.3.4.2 Damage Accumulation

The damage evolution within an element resulting from a general loading case (cyclic loading with variable amplitude but constant frequency F) can be written as:

$$\frac{\mathrm{d}d}{\mathrm{d}t} = \frac{\partial d}{\partial \lambda}\frac{\partial \lambda}{\partial t} + \frac{\partial d}{\partial N}\frac{\partial N}{\partial t} = \frac{\partial d}{\partial \lambda}\frac{\partial \lambda}{\partial t} + F\frac{\partial d}{\partial N} \tag{3.34}$$

The first term takes into account any variations in the damage due to changes in the displacement jump norm (applied displacement), whereas the second accounts for the increase in the damage variable due to the sinusoidal loading (N is the number of fatigue cycles). The total damage at time $t + \Delta t$ ($d(t + \Delta t)$) could then be obtained by integrating the previous expression between times 0 and $t + \Delta t$.

$$d(t + \Delta t) = \int_0^{t+\Delta t} \frac{\partial d}{\partial t} dt = \int_0^{t} \frac{\partial d}{\partial t} dt + \int_t^{t+\Delta t} \frac{\partial d}{\partial t} dt = d(t) + \int_t^{t+\Delta t} \frac{\partial d}{\partial t} dt \tag{3.35}$$

$$\int_t^{t+\Delta t} \frac{\partial d}{\partial t} dt = \int_{r^t}^{r^{t+\Delta t}} \frac{\partial d}{\partial \lambda} d\lambda + \int_t^{t+\Delta t} F\frac{\partial d}{\partial N} dt = \Delta d_s(t, t + \Delta t) + F\frac{\partial d}{\partial N}\Big|_t \Delta t \tag{3.36}$$

$$d(t + \Delta t) = d(t) + \underbrace{\Delta d_s(t, t + \Delta t)}_{Static\ damage} + \underbrace{F\frac{\partial d}{\partial N}\Big|_t \Delta t}_{Fatigue\ damage} \tag{3.37}$$

where $d(t)$ is the total damage at time t, and $\Delta d_s(t, t + \Delta t)$ corresponds to the increase in damage due to the change in λ between t and $t + \Delta t$, which is evaluated using the equations proposed for the quasi-static case. The last term ($F\frac{\partial d}{\partial N}\Big|_t \Delta t$) represent the contribution of the cyclic loading to the damage variable, and is defined using fracture mechanics data.

In accordance with a jump-cycle strategy [304, 352-354], the integral $\int_t^{t+\Delta t} F \frac{\partial d}{\partial N} dt$ is evaluated here assuming that $\frac{\partial d}{\partial N}$ remains constant and equal to the value corresponding to time t ($\frac{\partial d}{\partial N}\Big|_t$) in the interval $[t, t+\Delta t]$. Although this could have substantial consequences in respect to the accuracy and stability of the solution (both highly sensitive to the value of the time increment Δt, as noted by Armas [348]), it offers important computational advantages compared to the method proposed by Robinson et al. [323]. In the latter that integral is supposed to depend on $d(t+\Delta t)$, resulting in an explicit law for damage accumulation which is in principle more precise but needs to be solved iteratively for each time increment with the subsequent increase in computing burden. Therefore the route followed here represents a compromise between precision and simplicity, so the resultant formulation is applicable to the study of large and complex components. Obviously, this simplification imposes certain accuracy limitations, and the maximum time increment needs to be selected accordingly.

Assuming that the solution up to instant "t" is known, the damage state at the end of the next increment $t+\Delta t$ in a general problem with static and fatigue degradation would be obtained from (3.37). The next sections detail how to evaluate the various terms appearing on the right hand side of that equation. Once $d(t+\Delta t)$ is available, it would be introduced in the constitutive equations presented in section 3.3.2 (see (3.13)) provided that the condition $0 \le d \le 1$ is satisfied. However, the additional fatigue contribution in (3.37) could produce damage values greater than 1 ($d > 1$), so extra precautions must be taken to reject those potential spurious solutions:

$$\tau_i = \begin{cases} (1-d)\, D_{ij}^0\, \Delta_j - d D_{ij}^0 \bar{\delta}_{2j} \langle -\Delta_2 \rangle & \text{if } 0 \le d(t+\Delta t) \le 1 \\ 0 & \text{if } d(t+\Delta t) > 1 \end{cases} \tag{3.38}$$

A very appealing aspect of this formulation is that it could be used to solve quasi-static problems by setting F =0. Consequently, if the frequency is defined as a user-element property (and assigned a suitable value at the beginning of the analysis) the proposed formulation could cope with both quasi-static and fatigue problems without further modifications. Similarly the R-ratio will also be treated as an input parameter.

3.3.4.3 Damage increment due to changes in the applied displacement

The derivative of the damage with respect to the displacement jump norm ($\frac{\partial d}{\partial \lambda}$) could be written in terms of λ using $Q(\lambda)$ (see equations (3.18)) and then integrated analytically between t and $t+\Delta t$ (i.e. r^t and $r^{t+\Delta t}$ to account for the loading history) to obtain Δd_s. For the bilinear evolution law:

$$d_s(t) = Q(r^t) = \frac{\Delta^f(r^t - \Delta^0)}{r^t(\Delta^f - \Delta^0)} \longrightarrow \frac{\partial d_s}{\partial \lambda} = \frac{\Delta^0\Delta^f}{(\Delta^f - \Delta^0)}\frac{1}{\lambda^2} \tag{3.39}$$

$$\Delta d_s(t, t+\Delta t) = \int_{\lambda(t)}^{\lambda(t+\Delta t)} \frac{\partial d_s}{\partial \lambda} d\lambda = \int_{r^t}^{r^{t+\Delta t}} \frac{\Delta^0\Delta^f}{(\Delta^f - \Delta^0)}\frac{1}{\lambda^2} d\lambda = \frac{\Delta^0\Delta^f}{(\Delta^f - \Delta^0)}\left(-\frac{1}{\lambda}\right)\Big|_{r^t}^{r^{t+\Delta t}} \tag{3.40}$$

$$\Delta d_s(t, t+\Delta t) = \frac{\Delta^0\Delta^f}{(\Delta^f - \Delta^0)}\left(\frac{1}{r^t} - \frac{1}{r^{t+\Delta t}}\right) \tag{3.41}$$

As shown in (3.42), by definition the damage thresholds for times t and $t+\Delta t$ (r^t and $r^{t+\Delta t}$ respectively) automatically satisfy the condition $r^{t+\Delta t} \geq r^t$ in both the bilinear and linear-cubic cases. Moreover, for the bilinear law this relationship is enough to ensure that $\Delta d_s(t, t+\Delta t) \geq 0$.

$$\left.\begin{aligned} r^{t+\Delta t} &= max\left\{r^0, \max_s \lambda^s\right\} \;\; 0 \leq s \leq t+\Delta t \\ r^t &= max\left\{r^0, \max_s \lambda^s\right\} \;\; 0 \leq s \leq t \end{aligned}\right\} \longrightarrow r^{t+\Delta t} \geq r^t, with\, r^0 = \Delta^0 \tag{3.42}$$

Evidently, the same expression given in (3.41) (obtained by integration) would be obtained by direct application of the quasi-static evolution laws $Q(\lambda)$ assuming that $\Delta d_s(t, t+\Delta t)$ is the increment in quasi-static damage:

$$\begin{aligned} \Delta d_s = d_s(t+\Delta t) - d_s(t) = Q\left(r^{t+\Delta t}\right) - Q(r^t) &= \frac{\Delta^f\left(r^{t+\Delta t} - \Delta^0\right)}{r^{t+\Delta t}(\Delta^f - \Delta^0)} - \frac{\Delta^f(r^t - \Delta^0)}{r^t(\Delta^f - \Delta^0)} = \cdots \\ &= \frac{\Delta^0\Delta^f}{(\Delta^f - \Delta^0)}\left(\frac{1}{r^t} - \frac{1}{r^{t+\Delta t}}\right) \end{aligned} \tag{3.43}$$

Thus:

$$\Delta d_s(t, t+\Delta t) = \int_{\lambda(t)}^{\lambda(t+\Delta t)} \frac{\partial d_s}{\partial \lambda} d\lambda = \cdots = d_s(t+\Delta t) - d_s(t) = Q\left(r^{t+\Delta t}\right) - Q(r^t) \tag{3.44}$$

Entering with (3.44) in (3.37):

$$\begin{aligned} d(t+\Delta t) &= d(t) + d_s(t+\Delta t) - d_s(t) + F\frac{\partial d}{\partial N}\Big|_t \Delta t \\ &= d(t) + Q\left(r^{t+\Delta t}\right) - Q(r^t) + F\frac{\partial d}{\partial N}\Big|_t \Delta t \end{aligned} \tag{3.45}$$

If the total damage at the end of the increment t ($d(t)$) is expressed in terms of the updated damage threshold r^t (which contains the quasi-static and fatigue contributions accumulated in the interval $[0,t]$), then it is possible to write:

$$d(t+\Delta t) = Q(r^t) + Q\left(r^{t+\Delta t}\right) - Q(r^t) + F\frac{\partial d}{\partial N}\Big|_t \Delta t = Q\left(r^{t+\Delta t}\right) + F\frac{\partial d}{\partial N}\Big|_t \Delta t \tag{3.46}$$

$$d(t+\Delta t) = d_s(t+\Delta t) + F\frac{\partial d}{\partial N}\Big|_t \Delta t \tag{3.47}$$

It becomes apparent in equation (3.47) that the total damage $d(t+\Delta t)$ can be expressed as the sum of the total quasi-static damage ($d_s(t+\Delta t)$) plus the fatigue contribution in the last time increment Δt. The fatigue contribution accumulated in the interval $[0,t]$ is accounted for in the first term via a revised damage threshold, whereas $F\frac{\partial d}{\partial N}\Big|_t \Delta t$ represents the "new fatigue damage". Valid for both the bi-linear and linear-cubic laws, this result matches that presented by Turon et al. [304] and it is theoretically equivalent to that used in [323, 324].

Due to the nature of the jump-cycle scheme, in which the damage state at each integration point is calculated only at certain times and the results extrapolated over the corresponding intervals, the time increments employed must be controlled to ensure the accuracy and stability of the solution. If the desired level of precision is established through a pre-defined value of the maximum damage increment allowed ($\Delta d_{\max}$), then an upper limit for the time increment permitted at each step (Δt_{max}) could be derived from equation (3.47):

$$\Delta t_{max} = \frac{\Delta d_{\max}}{F\frac{\partial d}{\partial N}\Big|_t} \tag{3.48}$$

Note that any potential variation in the damage state due to changes of the mixed mode ratio (β) over time have been so far ignored. The term $\frac{\partial d}{\partial \beta}\frac{\partial \beta}{\partial t}$ has not been included in (3.34), and the variation of the cohesive parameters Δ^0 and Δ^f with time has been neglected in equations (3.40) and (3.41) since the degree of complexity introduced would make analytical

integration impossible. However if the incremental version of Δd_s (3.44) is accepted, these mixed mode effects would be partially absorbed by re-writing the damage threshold after time t (r^t) in terms of the "new" cohesive parameters (corresponding to the mixed mode ratio β at $t+\Delta t$). While this is straightforward in the bilinear case, it requires solving a cubic equation every time step in the linear-polynomial law. Nevertheless it would produce in both cases the same result given in (3.47), which already incorporates the mixed mode effects in $d_s(t+\Delta t)$.

3.3.4.4 Damage accumulation due to the number of cycles ($F\left.\frac{\partial d}{\partial N}\right|_t \Delta t$)

Following Turón et al [304], the damage accumulation due to fatigue is related here to a fracture mechanics description of the fatigue crack growth. For a given element (or integration point within the element), the variation of the damage variable with the number of cycles ($\frac{\partial d}{\partial N}$) can be written as

$$\frac{\partial d}{\partial N} = \frac{\partial d}{\partial A_d}\frac{\partial A_d}{\partial N} \tag{3.49}$$

where A_d represents the damaged area of the element (or the integration point). The ratio between A_d and the area of the element (A_e), usually identified as the damage variable when a consumed energy strategy instead of stiffness degradation approach is employed, is equivalent to the quotient between the dissipated energy (Ξ) and the critical strain energy release rate G_c (see [304, 348]). For a given value of λ, this relationship can be derived using Figure 3.12:

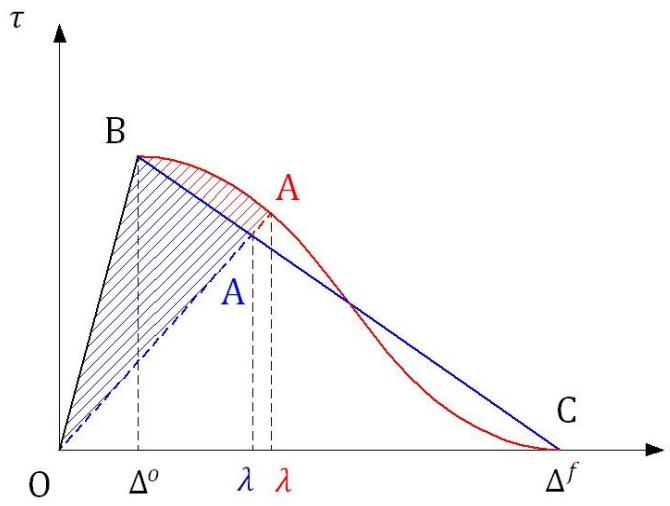

Figure 3.12. Definition of the ratio A_d/A_e for both the bilinear (blue) and linear-cubic (red) cohesive laws using a consumed energy strategy.

$$\frac{A_d}{A_e} = \frac{\Xi}{G_c} = \frac{Area\ \widehat{OBA}}{Area\ \widehat{OBC}} = \frac{G_c - Area\ \widehat{OAC}}{G_c} = 1 - \frac{Area\ \widehat{OAC}}{G_c} \tag{3.50}$$

If a damage evolution law controlled by a function $Q(\lambda)$ similar to that presented in equation (3.18) is employed in the constitutive equations (3.13), and using the (3.21) to relate the area under the traction-separation law and the cohesive parameters, then it is possible to write:

$$\left.\begin{array}{c} G_c = \frac{1}{2} k \Delta^0 \Delta^f \\ Area\ \widehat{OAC} = \frac{1}{2}\lambda\tau(\lambda) + \int_{\lambda}^{\Delta^f} \tau(\lambda) d\lambda \\ \tau(\lambda) = (1 - Q(\lambda)) k \lambda \end{array}\right\} \rightarrow \frac{A_d}{A_e} = f(\lambda) \tag{3.51}$$

Defining $H(\lambda)$ as

$$H(\lambda) = \frac{1}{\frac{\partial f(\lambda)}{\partial \lambda}} \frac{\partial d}{\partial \lambda} \tag{3.52}$$

equation (3.49) can be re-written as

$$\frac{\partial d}{\partial N} = \frac{1}{\frac{\partial A_d}{\partial \lambda}\frac{\partial \lambda}{\partial d}} \frac{\partial A_d}{\partial N} = \frac{1}{A_e \frac{\partial f(\lambda)}{\partial \lambda}} \frac{\partial d}{\partial \lambda}\frac{\partial A_d}{\partial N} = \frac{1}{A_e} H(\lambda) \frac{\partial A_d}{\partial N} \tag{3.53}$$

The functions $f(\lambda)$ and $H(\lambda)$ have different expressions depending on the shape of the traction-separation law (i.e. $Q(\lambda)$). For the bilinear law, in which case λ can be written as a function of the damage variable ($\lambda = \lambda(d)$), the ratio $\frac{A_d}{A_e}$ and hence H could be expressed in terms of d, resulting in the same expressions obtained by Turon et al. [304]:

$$\frac{A_d}{A_e} = f(\lambda) = \frac{\lambda - \Delta^0}{\Delta^f - \Delta^0} = \cdots = \frac{\Delta^0 d}{\Delta^f (1 - d) + \Delta^0 d} \tag{3.54}$$

$$H(\lambda) = \frac{\Delta^0 \Delta^f}{\lambda^2} = \cdots = \frac{\left(\Delta^f (1 - d) + \Delta^0 d\right)^2}{\Delta^0 \Delta^f} \tag{3.55}$$

It is worth noting that equations (3.54) and (3.55) differ from those presented by Pirondi and Moroni [305], as in their formulation $\frac{A_d}{A_e}$ is linked to the damage variable corresponding to stiffness degradation (instead of consumed energy).

To evaluate the last term that appears in equations (3.49) and (3.53) (i.e. $\frac{\partial A_d}{\partial N}$), the increase of crack area with the number of cycles ($\frac{\partial A}{\partial N}$) is supposed to be equivalent to the increase of the damaged area ahead of the crack tip with the number of cycles as suggested in [304]. Taking into account the contribution of each damaged cohesive elements ahead of the crack tip $\frac{\partial A_d^e}{\partial N}$ (i.e. all the elements within the cohesive zone area A_{CZ}), the crack growth rate can be expressed as:

$$\frac{\partial A}{\partial N} = \sum_{e \in A_{CZ}} \frac{\partial A_d^e}{\partial N} \tag{3.56}$$

Given the difficulties to theoretically estimate or experimentally measure the variation of the damaged area growth rate along the cohesive zone, the previous sum is computed using its mean value multiplied by the number of elements within A_{CZ} (assuming an average element size A_e, the quotient A_{CZ}/A_e would represent the number of cohesive elements within the process zone):

$$\frac{\partial A}{\partial N} = \sum_{e \in A_{CZ}} \frac{\partial A_d^e}{\partial N} = \frac{A_{CZ}}{A_e} \frac{\partial A_d}{\partial N} \tag{3.57}$$

Rearranging (3.57) to obtain $\frac{\partial A_d}{\partial N}$ and introducing the result in (3.53):

$$\frac{\partial A_d}{\partial N} = \frac{A_e}{A_{CZ}} \frac{\partial A}{\partial N} \tag{3.58}$$

$$\frac{\partial d}{\partial N} = \frac{1}{A_{CZ}} H(\lambda) \frac{\partial A}{\partial N} \tag{3.59}$$

In accordance with the hypothesis made in section 3.3.4.2 ($\frac{\partial d}{\partial N}$ is assumed to remain constant in the interval $[t, t + \Delta t]$), equation (3.59) must be particularized for the instant t before using it in (3.37) and (3.47):

$$\left.\frac{\partial d}{\partial N}\right|_t = \frac{1}{A_{CZ}(t)} H(r^t) \left.\frac{\partial A}{\partial N}\right|_t \tag{3.60}$$

The loading history is taken into account through the latest damage threshold r^t, whereas suitable expressions for the evaluation of A_{CZ} and $\frac{\partial A}{\partial N}$ are provided in the next sections to complete the element formulation.

Finally, note that (3.59) could be integrated in time within the interval $[t, t+\Delta t]$ without the hypothesis mentioned above. However the result would be a function of $d(t+\Delta t)$ (or $\lambda(t+\Delta t)$), imposing the use of an iterative process like that proposed in [323] to solve the problem stated in (3.35).

Important note:

Even though the damage evolution law presented would be valid for three-dimensional problems, it is combined in this work with 2D kinematics. Assuming a constant-width component with a crack covering the whole width B, the crack area (A) and the area of the cohesive zone A_{CZ} could be written in terms of the crack length (a) and the cohesive zone length (l_{CZ}):

$$\begin{cases} A = B \cdot a \\ A_{CZ} = B \cdot l_{CZ} \end{cases} \tag{3.61}$$

Bearing this in mind (3.60) could be written in length form (only valid for 2D problems):

$$\left.\frac{\partial d}{\partial N}\right|_t = \frac{1}{B \cdot l_{CZ}(t)} H(r^t) \left.\frac{\partial (B \cdot a)}{\partial N}\right|_t = \frac{1}{l_{CZ}(t)} H(r^t) \left.\frac{\partial a}{\partial N}\right|_t \tag{3.62}$$

3.3.4.4.1 Crack growth rate: the modified Paris law

Unlike the models proposed in [304, 323], which only account for the fatigue crack propagation in the linear regime (Region II), the element formulation presented here includes both the threshold and rapid growth regimens. This is achieved by approximating the crack growth rate under fatigue loading with a modified Paris law:

$$\frac{\partial A}{\partial N} = C_T (G_{max})^m \left\{ \frac{1 - \left(\frac{G_{th}}{G_{max}}\right)^{n_1}}{1 - \left(\frac{G_{max}}{G_c}\right)^{n_2}} \right\} \tag{2.33}$$

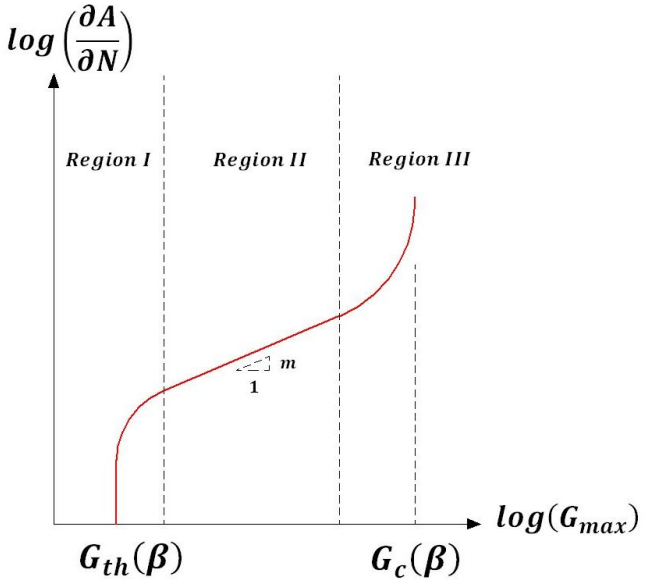

Figure 3.13. Typical shape of the modified Paris law used to approximate experimental fatigue data exhibiting the linear regime (Region II) and the rapid growth (Region III) and threshold (Region I) regions (G_c and G_{th} exhibit at least a dependence on the mixed mode ratio β).

To ensure that no fatigue crack growth occurs if $G_{max} < G_{th}$, the actual expression employed in the UEL subroutine is:

$$\frac{\partial A}{\partial N} = \begin{cases} 0 & \text{if } G_{max} < G_{th} \\ C_T (G_{max})^m \left\{ \dfrac{1 - \left(\dfrac{G_{th}}{G_{max}}\right)^{n_1}}{1 - \left(\dfrac{G_{max}}{G_c}\right)^{n_2}} \right\} & \text{if } G_{max} > G_{th} \end{cases} \tag{3.63}$$

The parameters used to define this law ($C_T, m, n_1, n_2, G_{th}, G_c$) have been shown to be material properties, which depend on the loading conditions (loading mode, frequency F and R ratio). Therefore in a general formulation they could be defined as functions of the mixed mode ratio β and in some cases also of F and R:

$$\begin{cases} C_T = C_T(\beta, F, R) \\ m = m(\beta, F, R) \\ n_1 = n_1(\beta, F, R) \\ n_2 = n_2(\beta, F, R) \\ G_{th} = G_{th}(\beta, F, R) \end{cases} \tag{3.64}$$

Obviously each of these functions and their respective arguments would vary with the nature of the material under investigation. Take for instance the slope of the linear regime (which is controlled by m): while it has been found to be insensitive to the R ratio in some toughened

thermoplastics, the same does not apply to their un-toughened versions (see Moskala [355]) or to most metals (see [122]).

Special attention is needed for the critical strain energy release rate. In this formulation G_c is assumed to depend only on the mixed mode ratio and for consistency is defined using (3.21):

$$G_c = \frac{1}{2} k(\beta) \Delta^o(\beta) \Delta^f(\beta) \tag{3.21}$$

where $\Delta^o(\beta)$ and $\Delta^f(\beta)$ correspond to the initiation and propagation criteria introduced in section 3.3.3.

Albeit the general formulation leaves the door open for any potential dependence, the influence of the different variables on each parameter should be individually assessed in each case using relevant experimental data. The fatigue response of each material within the range of interest (for β, F and R) would be characterized using a series of fracture mechanics tests carried out under the appropriate loading conditions. The results would then be fitted to suitable functions and inputted into the subroutine.

The selection of the most suitable function in each case should be made yet again on a case-by-case basis. A review of some of the expression proposed in the literature can be found in [204]. In the present study, both the frequency and R remained constant in all the experiments, hence leaving β as the only argument in equations (3.64). Under these conditions the expressions proposed by Blanco et al. [206] and Kenane and Benzeggagh [225] to model the variation of C_T and m with the mixed mode ratio would be applicable (equations (3.65) and (3.66) respectively). While in both cases they use the value of the parameters for pure loading modes ($C_{T_I}, C_{T_{II}}, m_I, m_{II}$) plus an additional variable to control the mixed mode behaviour ($C_{T_m}, \mathrm{p}, m_m, \mathrm{q}$), the former option is favoured as it allows non-monotonic variations with β.

$$\begin{cases} \log\left(C_T(\beta)\right) = \log\left(C_{T_I}\right) + \log\left(C_{T_m}\right)\left(\frac{G_{II}}{G}(\beta)\right) + \log\left(\frac{C_{T_{II}}}{C_{T_I} C_{T_m}}\right)\left(\frac{G_{II}}{G}(\beta)\right)^2 \\ m(\beta) = m_I + m_m\left(\frac{G_{II}}{G}(\beta)\right) + (m_{II} - m_I - m_m)\left(\frac{G_{II}}{G}(\beta)\right)^2 \end{cases} \tag{3.65}$$

$$\begin{cases} \ln\left(C_T(\beta)\right) = \ln\left(C_{T_{II}}\right) + \left(\ln\left(C_{T_I}\right) - \ln\left(C_{T_{II}}\right)\right)\left(1 - \left(\frac{G_{II}}{G}(\beta)\right)\right)^p \\ m(\beta) = m_I + (m_{II} - m_I)\left(\frac{G_{II}}{G}(\beta)\right)^q \end{cases} \tag{3.66}$$

The relationship $\frac{G_{II}}{G} = \frac{G_{II}}{G}(\beta)$ is given by (3.26). Following a similar principle, Turon et al. [304] adapted the quasi-static B-K failure criterion [224] for the variation of the threshold fracture energy with β:

$$G_{th}(\beta) = G_{th_I} + \left(G_{th_{II}} - G_{th_I}\right)\left(\frac{G_{II}}{G}(\beta)\right)^{\eta} \tag{3.67}$$

where G_{th_I} and $G_{th_{II}}$ correspond to the threshold fracture energies in pure modes I and II, and η governs the mixed mode behaviour. Conversely, as no equivalent expressions for n_1 and n_2 have been found in the literature, the use of polynomials is suggested here as a possible solution. The order of those polynomials would depend on the experimental data available (i.e. number of mixed-mode ratios tested in fatigue). For example if only the values of the parameters for pure modes I and II ($n_{1_I}, n_{1_{II}}, n_{2_I}, n_{2_{II}}$) were available, the functions would adopt the form:

$$\begin{cases} n_1 = \left(n_{1_{II}} - n_{1_I}\right)\dfrac{G_{II}}{G}(\beta) + n_{1_I} \\ n_2 = \left(n_{2_{II}} - n_{2_I}\right)\dfrac{G_{II}}{G}(\beta) + n_{2_I} \end{cases} \tag{3.68}$$

Finally, it is worth noting that the influence of the frequency and load ratio could be easily re-introduced in equations (3.65)-(3.68) by defining the pure mode parameters ($C_{T_I}, C_{T_{II}}, m_I, m_{II}, G_{th_I}, G_{th_{II}}, n_{1_I}, n_{1_{II}}, n_{2_I}, n_{2_{II}}$) as functions of F and R (both treated as analysis inputs in this user element):

$$\begin{cases} C_{T_I} = C_{T_I}(F,R), C_{T_{II}} = C_{T_{II}}(F,R) \\ m_I = m_I(F,R), m_{II} = m_{II}(F,R) \\ G_{th_I} = G_{th_I}(F,R), G_{th_I} = G_{th_I}(F,R) \\ n_{\mathrm{i}_I}(F,R) = n_{\mathrm{i}_I}(F,R), n_{\mathrm{i}_{II}}(F,R) = n_{\mathrm{i}_{II}}(F,R) \end{cases} \tag{3.69}$$

Note that the threshold fracture energy G_{th} defines a critical displacement jump norm ($\Delta^{th}(\beta,F)$) below which there is no crack growth propagation due to fatigue. The proposed element would be able to identify that value and behave accordingly even if it were smaller than Δ^0.

3.3.4.4.2 Maximum applied G_{max}(t)

The modified Paris law (2.33) needs to be evaluated at the instant t, as shown in (3.60). Apart from the definition of the parameters $C_T, m, n_1, n_2, G_{th}, G_C$, this requires an estimate of

the maximum energy release rate G_{max} applied to the cohesive element. This value would be a function of the local maximum displacement and it is computed using the relevant traction-separation law.

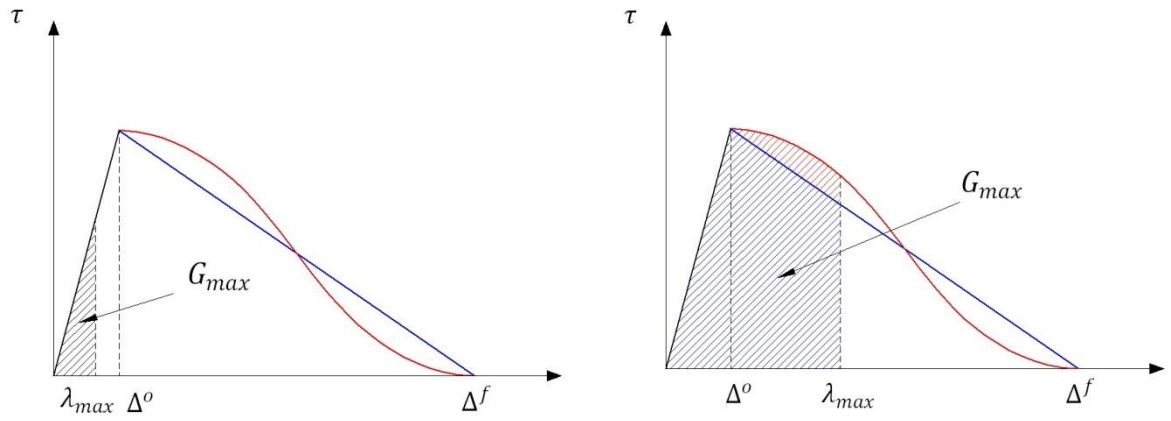

Figure 3.14. Graphic definition of G_{max} when (a) $\lambda_{max} < \Delta^0$ and (b) $\Delta^0 < \lambda_{max} \leq \Delta^f$ for the bilinear (blue) and linear-cubic (red) traction-separation laws.

As shown in Figure 3.14, G_{max} can be seen as the area under the cohesive law up to λ_{max} (the maximum displacement jump norm applied to the element):

$$G_{max}(t) = \int_0^{\lambda_{max}(t)} \tau(\lambda)\, d\lambda = \int_0^{\lambda_{max}(t)} \big(1 - d(\lambda)\big) k\lambda\, d\lambda \tag{3.70}$$

The cohesive stress $\tau(\lambda)$ is given in equation (3.13). Taking into account the different regions of the traction-separation law, this results in

$$G_{max}(t) = \begin{cases} \dfrac{1}{2} k\big(\lambda_{max}(t)\big)^2 & \lambda_{max}(t) \leq \Delta^0 \\ \dfrac{1}{2} k(\Delta^0)^2 + S\big(\lambda_{max}(t)\big) & \Delta^0 < \lambda_{max}(t) \leq \Delta^f \\ \dfrac{1}{2} k\Delta^0\Delta^f & \lambda_{max}(t) > \Delta^f \end{cases} \tag{3.71}$$

where $S\big(\lambda_{max}(t)\big)$ depends on the damage evolution law ($d(t) = Q\big(\lambda(t)\big)$, see equation (3.18)) and is defined as

$$S\big(\lambda_{max}(t)\big) = \int_{\Delta^0}^{\lambda_{max}(t)} \big(1 - Q(\lambda)\big) k\lambda\, d\lambda \tag{3.72}$$

For the bilinear law it adopts expression (3.73):

$$S_{Bilinear}\left(\lambda_{max}(t)\right) = \frac{1}{2}k\Delta^0\left[\left(\Delta^{\mathrm{f}} - \Delta^0\right) - \frac{\left(\Delta^f - \lambda_{max}\right)^2}{\left(\Delta^f - \Delta^0\right)}\right] \tag{3.73}$$

In accordance with the hypotheses made in (3.35), where the integral $\int_t^{t+\Delta t}\frac{\partial d}{\partial N}dt$ was approximated by $F\frac{\partial d}{\partial N}\Big|_t \Delta t$, λ_{max} and hence G_{max} are assumed to remain constant and equal to the values at time t ($\lambda_{max}(t)$ and $G_{max}(t)$ respectively) within the interval $[t, t+\Delta t]$.

Note also that the damage state of the element is not taken into account in the calculation of G_{max}, as this is a measure of the externally applied energy. Nevertheless, the influence of the accumulated damage is included in $H(r^t)$, which in terms multiplies the crack growth rate obtained from the modified Paris law (see equations (3.60) and (3.62)).

Important note:

So far the crack growth rate has been calculated assuming that the applied displacement varies between λ_{max} and 0. However if the minimum displacement jump norm was not zero (i.e. $R \neq 0$), the formulation would need some adjustments. Assuming that λ_{min} is positive ($R > 0$) and that R remains constant, those changes would be relatively small. The modified Paris law should be re-written in terms of cyclic variation of the energy release rate ΔG ($\Delta G = G_{max} - G_{min}$):

$$\frac{\partial A}{\partial N} = C_T{}'(\Delta G)^{m'}\left\{\frac{1 - \left(\frac{\Delta G_{th}}{\Delta G}\right)^{n_1{}'}}{1 - \left(\frac{\Delta G}{G_C}\right)^{n_2{}'}}\right\} \tag{3.74}$$

where $C_T{}', m', n_1{}', n_2{}', \Delta G_{th}$ are the new fitting parameters (see Figure 3.15), which in a general case could be treated as functions of β, F and R (the definition of G_c does not change).

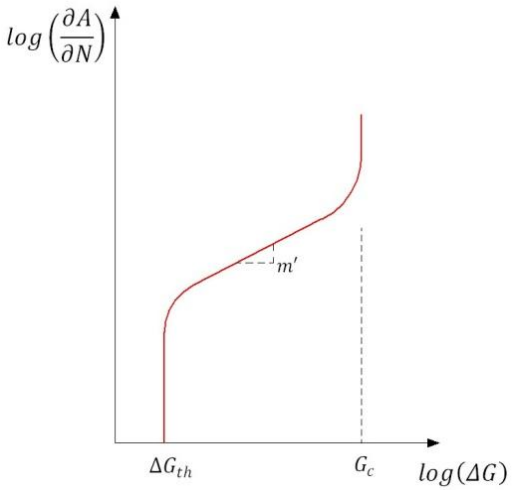

Figure 3.15. Typical shape of fatigue data as a function of ΔG

A suitable expression for ΔG should also be provided. In line with the assumptions made in (3.35), ΔG is assumed to remain constant in the interval $[t, t+\Delta t]$ and equal to the value corresponding to the instant t ($\Delta G(t)$).

$$\Delta G(t) = G_{max}(t) - G_{min}(t) = G_{max}(t)\left(1 - \frac{G_{min}(t)}{G_{max}(t)}\right) = G_{max}(t)\big(1 - g(\lambda_{max}, R)\big) \quad (3.75)$$

Both $G_{max}(t)$ and $G_{min}(t)$ would be calculated as the areas under the traction-separation curves up to $\lambda_{max}(t)$ by $\lambda_{min}(t)$ respectively (see Figure 3.16). Obviously (3.71) is still valid for the evaluation of $G_{max}(t)$, whereas the same equation could be adapted for the calculation of $G_{min}(t)$ by substituting $\lambda_{max}(t)$ by $\lambda_{min}(t)$. Taking into account the definition of R ($\lambda_{min}(t) = R \cdot \lambda_{max}(t)$), this would result in

$$G_{min}(t) = \begin{cases} \frac{1}{2}k\big(R \cdot \lambda_{max}(t)\big)^2 & R \cdot \lambda_{max}(t) \le \Delta^0 \\ \frac{1}{2}k(\Delta^0)^2 + S\big(R \cdot \lambda_{max}(t)\big) & \Delta^0 < R \cdot \lambda_{max}(t) \le \Delta^f \\ \frac{1}{2}k\Delta^0\Delta^f & R \cdot \lambda_{max}(t) > \Delta^f \end{cases} \quad (3.76)$$

As opposed to [304], where the load ratio was defined in energy instead of displacement terms, the function $g(\lambda_{max}, R)$ adopts here different expressions depending on the values of $\lambda_{max}(t)$ and R.

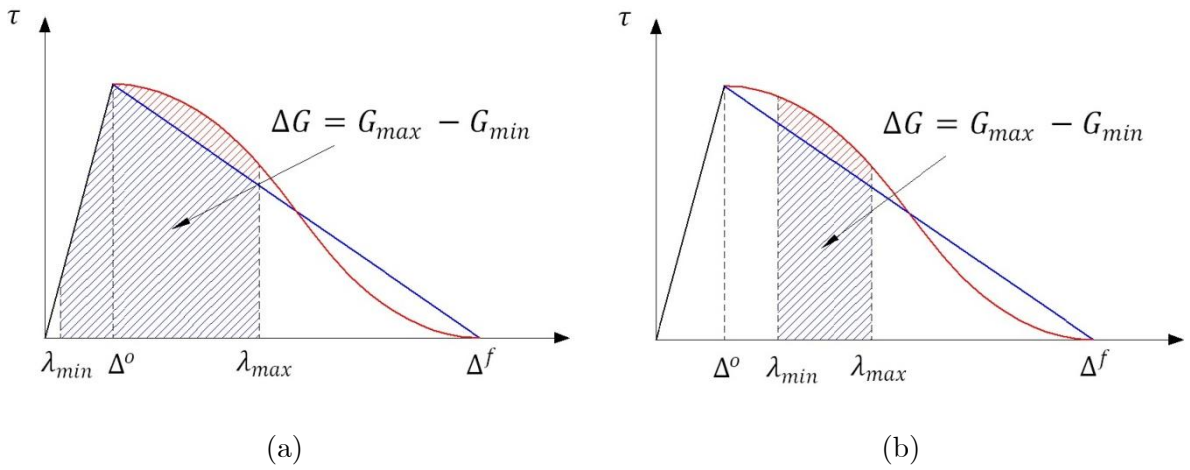

Figure 3.16. Definition of $\Delta G = G_{max} - G_{min}$ in a general case with $R = \lambda_{min}/\lambda_{max} \neq 0$ when (a) $\Delta^0 < \lambda_{max} \leq \Delta^f$ and $\lambda_{min} < \Delta^0$ and (b) $\Delta^0 < \lambda_{min} \leq \Delta^f$ for the bilinear (blue) and linear-cubic (red) cohesive laws.

3.3.4.4.3 Cohesive Zone Area

The damage evolution law proposed for fatigue simulation in the present work requires accurate predictions of the size of the cohesive zone in order to determine $\partial d/\partial N$. Previous formulations, including those by Turón et al. [304] and Pirondi and Moroni [305, 339], relied on some variation of Rice's analytical estimate (see equation (2.41)). However, as discussed in Chapter 2, the assumptions made to obtain these closed-form solutions (e.g. neglecting bondline thickness and substrate effects) make their applicability to adhesive joint problems questionable. Furthermore, equations (2.41) and (2.42) were derived for pure mode cases, which could lead to significant errors when modelling mixed mode problems.

In an attempt to overcome these limitations, the element formulation presented here incorporates an algorithm to compute the numerical cohesive zone length at the end of each time increment. Note that, in constant-width components with a crack covering the whole width B, the area of the cohesive zone A_{CZ} and the cohesive zone length l_{CZ} are related via equation (3.61). According to Harper and Hallet [240], the numerical cohesive zone length corresponds to distance ahead of the numerical crack tip over which the interface elements lie on the softening part of the traction-separation law.

Following this, the elements satisfying the condition $0< d <1$ demarcate the numerical cohesive length ($l_{CZ,numerical}$). To be more precise, since the damage variable is evaluated in every integration point, those elements in which at least one integration point fulfils the condition $0<d<1$ belong to the numerical cohesive zone. The numerical crack tip would then be within the only element which, being part of the numerical cohesive zone ($0<d<1$), were

adjacent to a fully cracked element (i.e. d=1 in every integration point) on one side and to either a partially damaged or an intact element on the other (the latter corresponds to the case where the numerical cohesive zone extends over a single element). If l_e^i is the length of the cohesive element "i" and N_{CZ} comprises all the elements satisfying the cohesive zone condition, the total cohesive length would then be given by:

$$l_{CZ,numerical} = \sum_{i \in N_{CZ}} l_e^i \tag{3.77}$$

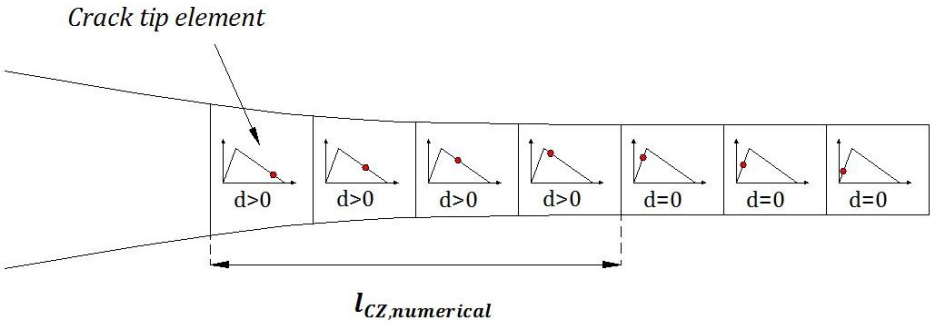

Figure 3.17. Schematic representation of the numerical cohesive zone length $l_{CZ,numerical}$ (defined by the cohesive elements satisfying the condition 0<d<1). The red dots represent the current cohesive strength of each element.

However, the previous method could be problematic or imprecise, especially for the models with very coarse meshes where the damage state can change notably within a given element. Thus, a modified version using the length associated with the integration points that experience irreversible damage is proposed here. Instead of considering whether a whole element is part of the cohesive zone, this approach evaluates the contribution of each integration point separately. As a result, sections of an element can be taken as part of the cohesive zone. The equivalent length associated with an integration point would be obtained from the total element length (length of the deformed mid-surface) and the corresponding Gauss weighting factor w_j used in the numerical integration (divided by two since Gauss-Legendre integrates in the interval [-1,1]).

$$l_{CZ,numerical} = \sum_{j}^{0<d<1} \frac{w_j}{2} l_e^i \tag{3.78}$$

Large displacements and rotations are taken into account to calculate the element length l_e^i, which is measured along the deformed mid-surface. For simplicity reasons, the parabola

defining the mid-surface in the quadratic element case is approximated by two straight lines. Defining A, B and C as the extreme and central points of the mid-surface, and using vector notation:

$$\begin{cases} \vec{x}_A = \frac{1}{2}(\vec{x}^1 + \vec{x}^4) = \frac{1}{2}(\vec{X}^1 + \vec{X}^4) + \frac{1}{2}(\vec{u}^1 + \vec{u}^4) \\ \vec{x}_B = \frac{1}{2}(\vec{x}^2 + \vec{x}^3) = \frac{1}{2}(\vec{X}^2 + \vec{X}^3) + \frac{1}{2}(\vec{u}^2 + \vec{u}^3) \\ \vec{x}_C = \frac{1}{2}(\vec{x}^5 + \vec{x}^6) = \frac{1}{2}(\vec{X}^5 + \vec{X}^6) + \frac{1}{2}(\vec{u}^5 + \vec{u}^6) \end{cases} \tag{3.79}$$

$$l_e^i \approx \begin{cases} |\vec{x}_B - \vec{x}_A| \ (linear\ element) \\ |\vec{x}_C - \vec{x}_A| + |\vec{x}_B - \vec{x}_C| \ \ (quadratic\ element) \end{cases} \tag{3.80}$$

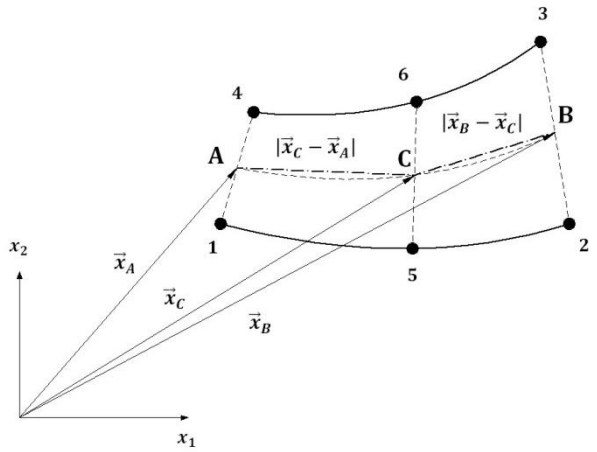

Figure 3.18. Schematic of the approximation made for measuring the element length l_e^i along the deformed mid-surface.

According to (3.60)/(3.62), only the area/length of the cohesive zone at the instant t ($A_{CZ}(t)/l_{CZ}(t)$) is required to calculate the damage increment due to the number of cycles at time $t + \Delta t$. As a result the application of (3.77) and (3.78) is straightforward, as all the damage information needed would be available at the end of previous time increment. Consequently both methodologies were implemented in the user subroutine and used to evaluate the numerical A_{CZ} (l_{CZ}). Additionally the closed-form solutions shown in (2.41) and (2.42) were implemented for comparison purposes.

Note that some difficulties may arise from the use of the definition when no damage has been accumulated yet in any element ahead of the crack tip and the applied displacement is such that $\lambda_{max} \leq \Delta^0$. In that case, (3.77) and (3.78) would result in $l_{CZ} = 0$, which would produce a singularity when introduced in (3.62). The problem would persist until some damage had been accumulated due to fatigue or the maximum displacement increased above Δ^0 (to

produce quasi-static damage). To circumvent the problem, the analytical estimate (2.42) is initially employed until some damage is accumulated and values of $l_{CZ} \neq 0$ are obtained with the definition. This is particularly important for the identification of the fatigue threshold as this would be below Δ^0.

3.3.5 Damage Evolution Law for Fatigue Threshold prediction

As mentioned before, the methodology proposed in section 3.2.2 to predict the fatigue threshold of adhesively-bonded joints might require the use of a special traction-separation law. This would be caused by the difficulties of the quasi-static bilinear and linear-cubic laws to model the material´s behaviour in the threshold region.

For an accurate reproduction of the physics of the problem no damage accumulation should occur below Δ^0, quasi-statically or in fatigue. At the same time the elastic response below the fatigue threshold (controlled solely by the penalty stiffness) should be independent of the loading conditions. Furthermore, these conditions define a critical value of the threshold fracture energy $(G_{th})_{crit}$ (see Figure 3.19):

$$(G_{th})_{crit} = \frac{1}{2} k (\Delta^0)^2 \tag{3.81}$$

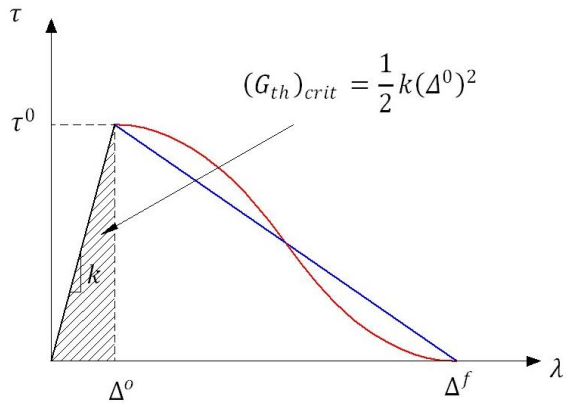

Figure 3.19. Definition of the critical value of the threshold fracture energy ($(G_{th})_{crit}$) defined by the cohesive parameters (Δ^0 and k) used in the quasi-static traction-separation bilinear (blue) and linear-cubic (red) laws.

Meeting these requirements while accommodating an area smaller than G_c could only be achieved by modifying the shape of the traction-separation law. A specific damage evolution law for the prediction of the fatigue threshold is therefore introduced. It shares the cohesive parameters with the quasi-static laws seen in section 3.3.3, but would be truncated at the

threshold displacement jump norm Δ^{th}, so the area under the curve is equal to the experimental threshold fracture energy $\left(G_{th}(\beta,F,R)\right)_{exp}$ (see Figure 3.20).

The parameter Δ^{th} is calculated by equating the area under the truncated traction-separation curve to $(G_{th})_{exp}$. Obviously, the resulting expression depend on the relative values of $(G_{th})_{exp}$ and $(G_{th})_{crit}$, and in some cases (if $(G_{th})_{exp} > (G_{th})_{crit}$) on the shape of the cohesive law taken for reference. In accordance with sections 3.3.3 and 3.3.4, where the cohesive parameters and G_{th} were defined as functions of the mixed mode ratio and potentially the frequency and the displacement ratio, in the most general case Δ^{th} would be a function of β, F and R.

Case I: $(G_{th})_{exp} \leq (G_{th})_{crit}$

In this case Δ^{th} is smaller than (or equal to) Δ^0 and its value is easy to calculate (see (3.82)). The shape of the new traction-separation law is reduced to a triangle (see Figure 3.20-a), with the corresponding damage evolution given in (3.83).

$$\Delta^{th}(\beta,F,R) = \sqrt{\frac{2\left(G_{th}(\beta,F,R)\right)_{exp}}{k(\beta)}} \tag{3.82}$$

$$d(\lambda) = \begin{cases} 0 & \lambda \leq \Delta^{th}(\beta,F,R) \\ 1 & \lambda > \Delta^{th}(\beta,F,R) \end{cases} \tag{3.83}$$

The behaviour of this cohesive element is similar to that of VCCT, with the bonding state changing from undamaged to completely failed when the critical strain energy release rate reaches critical value (G_{th} in this case). However it allows certain control over the stiffness of the bond.

Case II: $(G_{th})_{exp} > (G_{th})_{crit}$

Despite this situation not being physically as relevant as that posed in case I, it is included here to cover all possible experimental outcomes. Unfortunately the use of the adhesive's mechanical properties in the definition of Δ^0 and k (and hence $(G_{th})_{crit}$) does not guarantee meeting the condition $(G_{th})_{exp} \leq (G_{th})_{crit}$. Now Δ^{th} is larger than Δ^0 and its value obtained by solving the following equation:

$$\left(G_{th}(\beta,F,R)\right)_{exp} = \frac{1}{2}k(\Delta^0)^2 + S\left(\Delta^{th}(\beta,F,R)\right) \tag{3.84}$$

where the function $S(\Delta^{th})$ varies with the shape of the cohesive law used up to Δ^{th} and is defined in equations (3.72) for the bilinear case. While the bilinear shape allows an analytical solution (see (3.85)), solving a cubic equation is necessary in the linear-cubic case. Note that the bilinear and linear-cubic laws produce different values of Δ^{th} for the same $(G_{th})_{exp}$.

$$\Delta^{th}(\beta,F,R) = \Delta^{f}(\beta) - \sqrt{\left(\Delta^{f}(\beta) - \Delta^{o}(\beta)\right)\left(\Delta^{f}(\beta) - \frac{22\left(G_{th}(\beta,F,R)\right)_{exp}}{k(\beta)\Delta^{o}(\beta)}\right)} \tag{3.85}$$

The damage evolution follows (3.86) and the shapes of the resulting traction-separation laws can be seen in Figure 3.20-(b and c).

$$d(\lambda) = \begin{cases} 0 & \lambda \leq \Delta^{0} \\ Q(r^{t}) & \Delta^{0} < \lambda \leq \Delta^{th}(\beta,F,R) \\ 1 & \lambda > \Delta^{th}(\beta,F,R) \end{cases} \tag{3.86}$$

Suitable expressions for Q and r^{t} can be found in equations (3.18) and (3.20).

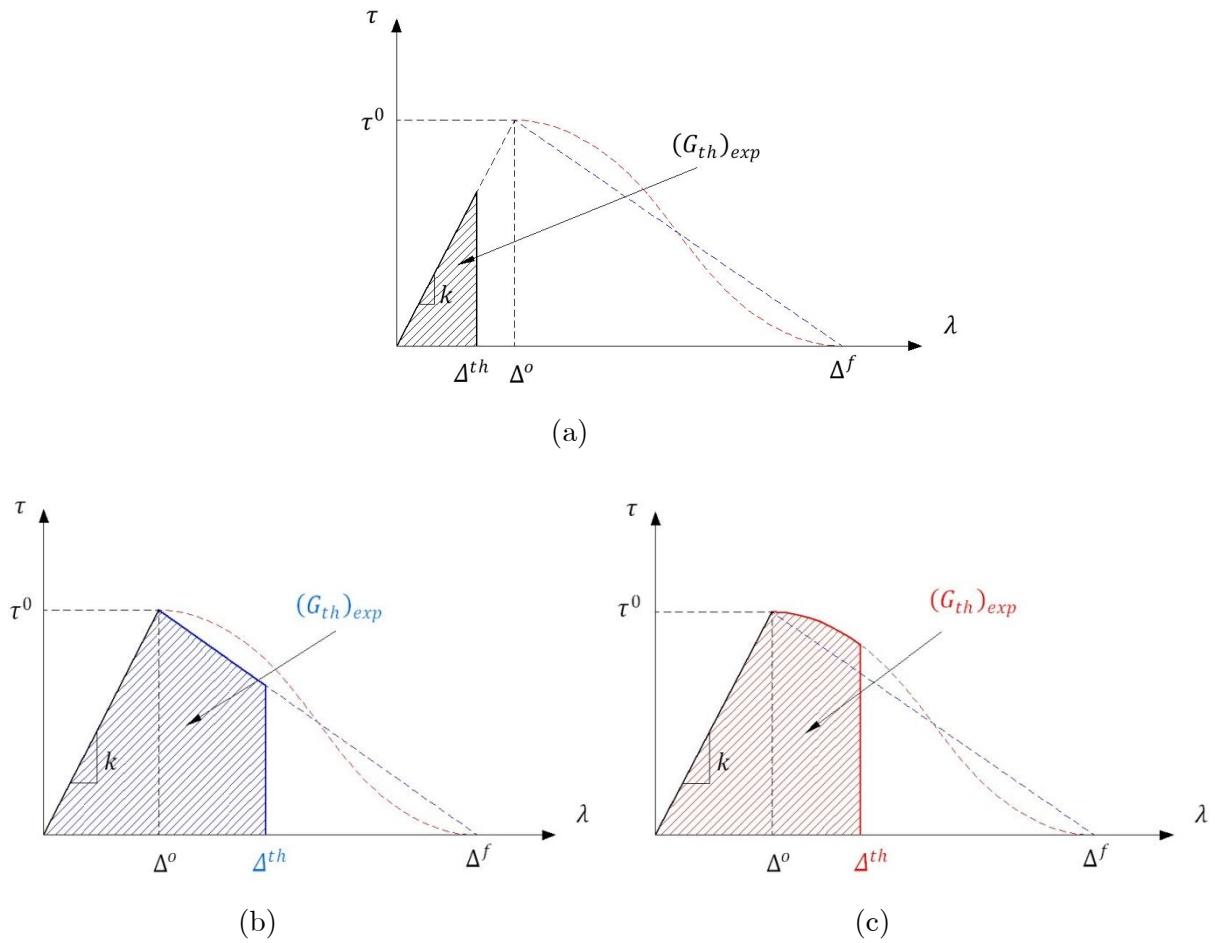

Figure 3.20. Definition of the threshold displacement jump norm Δ^{th} and the traction separation laws for the fatigue threshold prediction when (a) $(G_{th})_{exp} \leq (G_{th})_{crit}$ and (b, c) $(G_{th})_{exp} > (G_{th})_{crit}$ (b – bilinear law; c – linear-cubic law). The discontinuous lines represent the quasi-static cohesive laws taken as reference.

3.3.6 Tangent Stiffness Tensor

A consistent tangent stiffness tensor is required for the numerical implementation of the element. The components of this tensor D_{ij}^{TAN} can be obtained by deriving the cohesive tractions (τ_i) with respect to the interfacial relative displacements (Δ_j). So for a quasi-static problem

$$D_{ij}^{TAN} = \frac{\partial \tau_i}{\partial \Delta_j} = \frac{\partial \left(D_{ij} \cdot \Delta_j\right)}{\partial \Delta_j} = D_{ij} + \frac{\partial D_{ij}}{\partial \Delta_j}\Delta_j = D_{ij} + \frac{\partial D_{ij}}{\partial d}\frac{\partial d}{\partial \Delta_j}\Delta_j = D_{ij} + D_{ij}^{r} \tag{3.87}$$

According to van der Meer and Sluys [356], for the tangent stiffness matrix D_{ij}^{TAN} to be fully consistent not only has it to account for the variation of the damage variable with respect to

the displacement jump norm (λ), but it also has to consider the effects of the mixed mode ratio changes on the cohesive parameters ($\Delta^o$and Δ^f) and hence on the damage.

$$D_{ij}^r = \frac{\partial D_{ij}}{\partial \Delta_j}\Delta_j = \frac{\partial D_{ij}}{\partial d}\left[\frac{\partial d}{\partial \lambda}\frac{\partial \lambda}{\partial \Delta_j} + \frac{\partial d}{\partial\, \Delta^o}\frac{\partial\, \Delta^o}{\partial \beta}\frac{\partial \beta}{\partial \Delta_j} + \frac{\partial d}{\partial\, \Delta^f}\frac{\partial\, \Delta^f}{\partial \beta}\frac{\partial \beta}{\partial \Delta_j}\right]\Delta_j = D_{ij}^{ro} + D_{ij}^{rw} \tag{3.88}$$

$$\begin{cases} D_{ij}^{ro} = \dfrac{\partial D_{ij}}{\partial d}\dfrac{\partial d}{\partial \lambda}\dfrac{\partial \lambda}{\partial \Delta_j}\Delta_j \\ D_{ij}^{rw} = \dfrac{\partial D_{ij}}{\partial d}\left[\dfrac{\partial d}{\partial\, \Delta^o}\dfrac{\partial\, \Delta^o}{\partial \beta} + \dfrac{\partial d}{\partial\, \Delta^f}\dfrac{\partial\, \Delta^f}{\partial \beta}\right]\dfrac{\partial \beta}{\partial \Delta_j}\Delta_j \end{cases} \tag{3.89}$$

On the other hand, Turón et al. [294] obviate the latter contribution adducing that the variation of the cohesive parameters with the mixed mode ratio is negligible for small time increments. For simplicity reasons this assumption is also made in this work, although the use of the fully consistent tensor could be discussed in highly non-linear problems with important convergence issues.

$$D_{ij}^r = \frac{\partial D_{ij}}{\partial \Delta_j}\Delta_j = \frac{\partial D_{ij}}{\partial d}\left[\frac{\partial d}{\partial \lambda}\frac{\partial \lambda}{\partial \Delta_j} + \frac{\partial d}{\partial\, \Delta^o}\frac{\partial\, \Delta^o}{\partial \beta}\frac{\partial \beta}{\partial \Delta_j} + \frac{\partial d}{\partial\, \Delta^f}\frac{\partial\, \Delta^f}{\partial \beta}\frac{\partial \beta}{\partial \Delta_j}\right]\Delta_j \underset{\Delta t \ll 1}{\approx} \frac{\partial D_{ij}}{\partial d}\frac{\partial d}{\partial \lambda}\frac{\partial \lambda}{\partial \Delta_j}\Delta_j \tag{3.90}$$

Using equations (3.14), (3.17):

$$\frac{\partial D_{ij}}{\partial d} = -D_{ij}^0\left(1 + \bar{\delta}_{2j}\frac{\langle -\Delta_j\rangle}{\Delta_j}\right) \tag{3.91}$$

$$\frac{\partial \lambda}{\partial \Delta_j} = \frac{\Delta_j}{\lambda}\left(1 + \bar{\delta}_{2j}\frac{\langle -\Delta_j\rangle}{\Delta_j}\right) \tag{3.92}$$

$$D_{ij}^r = -D_{ij}^0\left(1 + \bar{\delta}_{2i}\frac{\langle -\Delta_i\rangle}{\Delta_i}\right)\left(1 + \bar{\delta}_{2j}\frac{\langle -\Delta_j\rangle}{\Delta_j}\right)\varphi(\lambda)\Delta_i\Delta_j \tag{3.93}$$

where $\varphi(\lambda)$ depends on the shape of the traction-separation law (see equations (3.39)) and is defined as

$$\varphi(\lambda) = \frac{1}{\lambda}\frac{\partial d}{\partial \lambda} \tag{3.94}$$

It is worth noting that damage variations with respect to λ will only occur under increasing loading conditions, thus resulting in the following tangent tensor:

$$D_{ij}^{TAN} = \begin{cases} D_{ij} & r > \lambda \; or \; \Delta^f < \lambda \\ D_{ij} + D_{ij}^{ro} & r < \lambda < \Delta^f \end{cases} \tag{3.95}$$

In principle, in fatigue problems the tangent stiffness tensor should also account for rate effects, or at least for the variation of damage with the number of cycles. Hence $\frac{\partial d}{\partial t}$ should be included in (3.88). However, like in [304], this contribution is omitted here as the equilibrium is always be obtained using the static model [357]. Note that the fatigue formulation employs the quasi-static constitutive equations given in (3.13), while only the damage evolution law is modified to include degradation due to cyclic load. Furthermore, the sinusoidal applied load does not appear in the simulations. As a result equations (3.87), (3.93) and (3.94) are valid for both quasi-static and fatigue problems.

3.4 Input data required for implementing the proposed methodologies

The formulation presented in section 3.3 has been implemented in Abaqus as a user-defined cohesive element using a UEL subroutine. However, its use for performance prediction of adhesively-bonded joints requires the definition of some parameters, which in most cases need to be determined experimentally. This section describes briefly the tests carried out in order to obtain these values as well as the various steps of the process followed for the validation of the proposed methodologies.

In the most general case, the following input data is required for the use of the subroutine:

- The cohesive parameters that define the quasi-static traction-separation law: k, Δ^0, Δ^f. According to section 3.3.3.3, in this work the value of these parameters is to be derived from the propagation criterion $G_c = G_c(\beta)$ and the mechanical properties of the adhesive $(E, G_{12}, \upsilon_{12}, \sigma_Y)$ corrected by the bondline thickness (t_a).
- Fatigue crack growth rate data, in the form of suitable functions (of β, F and R) for the characteristic parameters of the modified Paris law used to approximate the experimental points, namely: C_T, m, n_1, n_2, G_{th}. While G_{th} is necessary in both fatigue life-time prediction methodologies proposed, the other variables would be needed only if the full fatigue degradation strategy were employed.
- In addition to the material data, information on the type of analysis to be performed in each case needs to be provided. Firstly, the value of the frequency must be specified to differentiate between quasi-static $(F = 0)$ fatigue $(F \neq 0)$ problems. If

$F \neq 0$ the user would have to indicate the loading ratio R and also whether a full fatigue or only a threshold analysis were required. Information on the shape of the cohesive law (bi-linear or linear-cubic) is also necessary. Finally, in two dimensional problems the width of the cohesive elements (B) is also needed.

Part I of this thesis (chapters 4, 5, 6 and 7) describes the obtaining of these parameters via various tests, while the second part (chapters 8, 9 and 10) deals with the validation of the formulation and methodologies and their application to the performance prediction of a simple adhesively-bonded structure: a titanium-to-CFRP tapered double lap joint.

The experimental section comprises quasi-static (Chapter 6) and fatigue (Chapter 7) tests. A series of fracture mechanics specimens have been manufactured and tested under quasi-static loading conditions in order to obtain relevant values of the critical strain energy release rate. The results obtained for the different mixed mode ratios (i.e. different specimens: DCB, ELS, FRMM, AFRMM...) have been combined and fitted to a suitable function to define a propagation criterion of the form $G_c = G_c(\beta)$. The load-displacement traces have also been stored for their subsequent use in the validation process. Additionally quasi-static tests of the simplified structures (i.e. TDLJ) have been carried out for latter comparison with the numerical predictions. Note that since the elastic properties of the adhesive are provided by the manufacturer (see [358]), no mechanical tests on the bulk material have been completed.

Similarly, fracture mechanics specimens have been tested in fatigue to obtain crack growth rate data. The da/dN results have then been fitted to modified Paris laws and used to derive suitable expressions for C_T, m, n_1, n_2 and G_{th}. The original data from these tests, in the form of S-N curves and threshold loads T_{th}, has been stored for validation purposes. Fatigue tests have also been carried out with the TDLJ to obtain the S-N curve and the fatigue threshold of the structure in order to evaluate the accuracy of the fatigue life-time prediction methodologies.

Two dimensional FE models of the fracture mechanics specimens tested have been created in Abaqus using the user-defined cohesive element. Numerical load-displacement and S-N curves have been extracted from quasi-static and fatigue simulations and the results compared with those obtained in the corresponding experiments (Chapter 8). Obviously, these numerical results do not represent independent predictions, but they could assist in the validation of the methodologies as well as help highlighting potential limitations or problems with the element formulation. Finally, the quasi-static and fatigue response of the TDLJ have been modeled using the element and the results compared with the experimental values (Chapter 9). Note that, although an accurate reproduction of the quasi-static response does not assure the success of the fatigue prediction methodologies, it is essential to legitimate the method, as the

fatigue estimates are based on the quasi-static constitutive equations. Figure 3.21 summarizes the overall process.

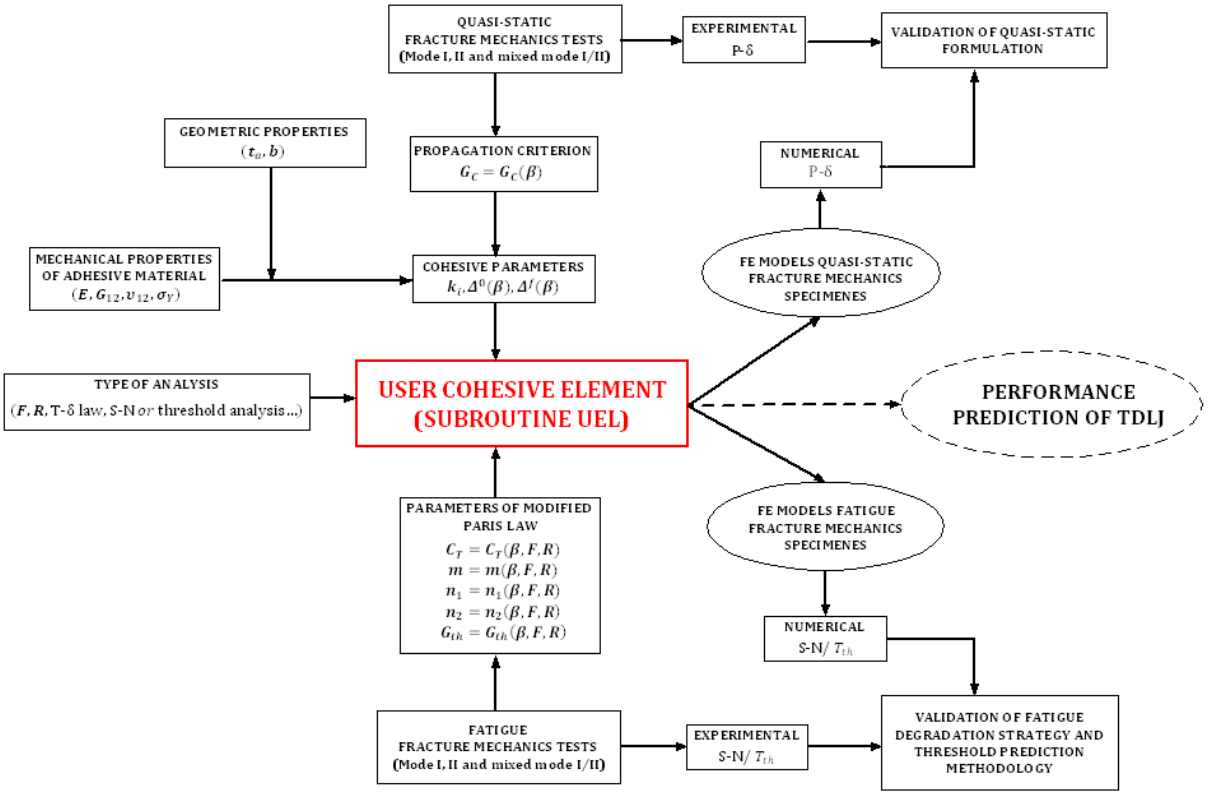

Figure 3.21. Diagram of the input data required by the cohesive element formulation described in section 3.3 to predict the performance of the TDLJ. The diagram also shows the tests to be carried out to obtain such data

It is worth pointing out that the validity of this process is subject to the applicability of the fracture mechanics data to the TDLJ problem. The type of failure observed in the TDLJ must be equivalent to that seen in the fracture mechanics specimens used to obtain the propagation criterion and the crack growth rate data. Otherwise the use of any data derived from those tests in the performance prediction of the TDLJ could not be justified and the results would be compromised.

3.5 Chapter Summary

Two complementary methodologies which combine experimental fracture mechanics data and FE techniques to predict the fatigue performance of adhesively-bonded joints have been proposed in this chapter. Whilst the first attempts to predict the S-N response of the bonded structure, the second only focuses on the fatigue threshold. Based on the concept of the CZM,

both employ a specialized, two-dimensional cohesive element formulation, the details of which were also presented in this chapter.

Derived from the work of Camanho and co-workers, the quasi-static formulation has been considerably revised to improve the mixed-mode behaviour and reduce the dependence on the calibration steps. Linear (4 nodes) and quadratic versions have been developed, allowing a user-defined number of integration points in both cases. Two damage evolution laws have been implemented: bilinear and linear-cubic. Following the fracture mechanics approach suggested by Turón et al., these have been enhanced to incorporate degradation due to cyclic loading. By using the modified Paris law rather than just the approximation to the linear region of the crack growth rate diagram, this new version is able to capture the threshold and rapid-growth fatigue regimes. In addition, an algorithm to compute the numerical cohesive zone length has been included in the element formulation. Finally, a simplified version of the evolution laws intended only for the prediction of the fatigue threshold has also been developed.

These prediction methodologies will be used to estimate the performance of a CFRP-to-Ti TDLJ, evaluating their accuracy by direct comparison with experimental results. Next, Chapter 4 describes the test program carried out to determine the various input parameters required for the FE models and the tests undertaken to obtain TDLJ data for validation purposes.

4. Materials, Surface Treatments and Experimental Procedures

4.1 Introduction

As stated in section 3.4, a significant amount of empirical data is required to implement and validate the prediction methodologies presented in Chapter 3. This chapter focuses on the experimental procedures followed to obtain such information. Details of the adhesives investigated and the substrate materials are presented first. The manufacturing processes and specific preparations for the different types of joints tested are described next, paying special attention to the surface treatments applied in each case prior to bonding. Finally, the methods for the quasi-static and fatigue testing of both the fracture mechanics specimens and the simplified structure (i.e. the TDLJ) are discussed.

4.2 Materials

Titanium and aluminium alloys as well as three types of unidirectional CFRP laminates have been employed as substrates in the present study. They were always bonded with a rubber-modified structural film adhesive (AF163-2), available with or without a supporting carrier mat (AF163-2OST and AF163-2U respectively). A second epoxy paste adhesive (Araldite® 2014-1) was used to attach aluminium end-blocks to the fracture mechanics specimens when necessary. The properties of these materials are briefly described in this section. Information on the composition is also provided when available (in the case of the adhesives, epoxy resins for the prepregs and primers these details are closely guarded by the manufacturers and

therefore very rarely published). Characterizing the elastic response of the individual materials was beyond the scope of this project and thus no specific tests for that purpose were carried out. Hence most data presented here have been primarily extracted from the relevant manufacturers' datasheets.

4.2.1 Adhesives

4.2.1.1 AF-163-2

A rubber-toughened epoxy film adhesive (AF-163-2) was investigated in this project. Produced by 3M Inc., this thermosetting resin is designed primarily for aerospace structural applications due to its high strength and fracture toughness values. It was tested here mainly in its supported form with a tacky side (AF-163-2OST, OST="one side tacky"), which uses a non-woven carrier matt on the low tack surface to ease handling and positioning of the adhesive. Two layers of this material (nominal thickness 0.24mm) were stacked together (with the tacky face of the first layer facing the non-tacky side of the second one) to manufacture all the joints. In addition, a reduced number of mode I tests were performed with the unsupported version (AF163-2U) to assess the influence of the carrier mat on the fracture toughness.

A thermocouple was inserted in the adhesive layer to monitor its temperature during the curing cycle. The oven was initially set to 155°C and was held at this temperature until the thermocouple reached 121°C. The temperature of the oven was then reduced to 121°C and maintained constant for 60 minutes, after which it was switched off and the specimens were left inside to cool down to room temperature until the following day (minimum 18 hours). Obviously, due to the different thermal conductivities and thicknesses of the substrates employed, the heating and cooling rates varied with the type of joint, even though they always remained within the manufacturer's recommended range [358].

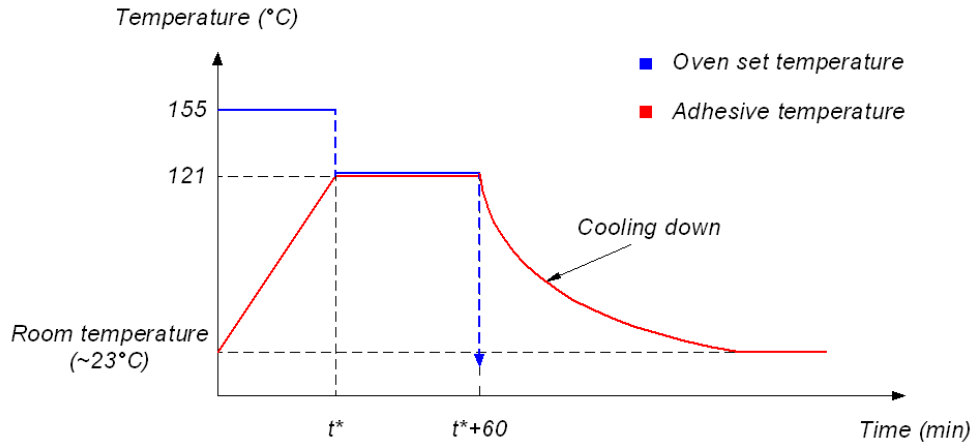

Figure 4.1. Schematic representation of the curing cycle (t^* varies with the material and thickness of the substrates).

A minimum pressure of 90kPa was applied during the entire process (using either weights or appropriate torque on the bolts depending on the jig design). This would minimize the air trapped within the bondline and between the adhesive and the substrates while not being sufficiently high to cause bond line starvation (i.e. when the adhesive is forced out of the joint due to excess pressure). Rubber pieces were always placed between the adherends and the jig in order to distribute the applied pressure homogenously.

The mechanical properties used in the FE models were directly extracted from the manufacturer's data sheet [358] (see Table 4.1):

Table 4.1. Properties of the AF-162-2 film adhesive [358].

Young's modulus, E (GPa)	1.110
Shear modulus, G_{12} (GPa)	0.414
Poisson's ratio, ν_{12}	0.34
Yield stress, σ_Y (MPa)	36.2
Thermal expansion coefficient (10^{-6}·°C^{-1})	90 (at -30 to 50°C)

The bulk of the film adhesive was stored in a freezer at -20°C in the container originally provided by the manufacturer. However several pieces of approximately 200x250mm were periodically cut from the main adhesive roll to facilitate handling during the bonding

operations. These smaller pieces, cut only after the film roll had warmed to room temperature as suggested in [358] (which usually took about 2.5 hours), were kept in polythene self-sealing bags also at -20°C.

4.2.1.2 Araldite® 2014-1

Most of the fracture mechanics specimens used in this work employed aluminium alloy end-blocks to apply the load during the test. These end-blocks were attached to the various substrate materials using Araldite® 2014-1 (by Huntsman Advanced Materials). This is a two-part epoxy paste adhesive designed for bonding a wide range of materials. According to the manufacturer [359], it exhibits high strength and good resistance to high temperatures and environmental attack while producing low out gassing. This makes it suitable for aerospace applications. Even though room temperature curing is possible with this adhesive, the cycle followed was 105 minutes at 40 °C to ensure sufficient bond strength.

4.2.1.3 BR® 127 Primer

When used to join titanium substrates, the structural film adhesive was combined with a corrosion inhibiting primer, BR®127 by CYTEC. Formulated to provide maximum environmental resistance and durability as well as to prevent corrosive undercutting, this primer was applied to the Ti alloy beams after the anodising step and then cured at 119°C during 30 minutes. As stated by the manufacturer, once cured the resulting protective layer would extend the shelf life of the treated surfaces virtually indefinitely [360] (provided they are wrapped in Kraft paper to prevent contamination by dust or dirt).

4.2.2 Substrate Materials

4.2.2.1 Al Alloy

The TDCB geometry described in section 4.4.2.2.1 was manufactured from aluminium alloy 2014-T6 (see composition in Table 4.2). Strengthened by precipitation-hardening and with good corrosion resistance, this Cu-Al alloy was selected to prevent plastic deformation in the substrates. A second aluminium alloy, 6082-T6 was employed in the end-blocks attached to the fracture mechanics specimens to apply the load. As this is much softer material than 2014A, it was also used in the end tabs of the TDLJ to protect the substrates while improving friction with the grips to prevent slippage. The mechanical properties of both alloys are shown in Table 4.3.

Table 4.2. Chemical composition (% weight) of Al 2014A-T6 [361] and Al 6082-T6 [362].

	Al	Cr	Cu	Fe	Mg	Mn	Si	Ti	Zn	Other
2014-T6	90.4-95.0	≤0.10	3.90-5.0	≤0.70	0.20-0.80	0.40-1.20	0.50-1.20	≤0.15	≤0.25	≤0.15
6082-T6	95.2-98.3	≤0.25	≤0.10	≤0.50	0.60-1.20	0.40-1.00	0.70-1.30	≤0.10	≤0.20	≤0.15

Table 4.3. Properties of the aluminium alloys 2014A-T6 [149, 361] and 6082-T6 [117, 362, 363].

	2014A-T6	6082-T6
Young's modulus, E (GPa)	72.4	70.0
Shear modulus, G_{12} (GPa)	28.0	26.4
Poisson's ratio, ν_{12}	0.33	0.35
Yield stress, σ_Y (MPa)	414	260
Tensile strain at yielding, ϵ_Y	0.0057	0.0037
Ultimate tensile strength, σ_U (MPa)	483	310
Tensile strain at break, ϵ_U	0.13	0.10
Hardness, H_V	155	95
Thermal expansion coefficient ($10^{-6} \cdot ℃^{-1}$)	22.5 (at 20 to 100°C)	23.4 (at 20°C)

4.2.2.2 Titanium Alloy Ti-6Al-4V Substrates

A titanium alloy Ti-6Al-4V (Grade 5) was employed in various fracture mechanics specimens as well as in the simplified structure used to validate the fatigue prediction methodologies (i.e. TDLJ). Probably the most widely used of the high strength Ti alloys in the aerospace industry, this alpha-beta alloy combines low density with good mechanical strength and excellent corrosion resistance in a wide range of environments. The composition and typical mechanical properties are shown in Table 4.4 and Table 4.5 respectively:

Table 4.4. Chemical composition (% weight) of Ti-6Al-4V (Grade 5) [364].

	Al	C	H	Fe	N	O	Ti	V	Other
Ti-6Al-4V	5.50-6.75	≤0.08	≤0.015	≤0.40	≤0.03	≤0.20	87.725-91.0	3.50-4.50	≤0.30

Table 4.5. Typical properties of alloy Ti-6Al-4V (Grade 5) [364].

Young's modulus, E (GPa)	114
Shear modulus, G_{12} (GPa)	44
Poisson's ratio, ν_{12}	0.33
Yield stress, σ_Y (MPa)	1100
Tensile strain at yielding, ϵ_Y	0.0903
Ultimate tensile strength, σ_U (MPa)	1170
Tensile strain at break, ϵ_U	0.10
Hardness, H_V	396
Thermal expansion coefficient (10^{-6}·°C^{-1})	9.20 (at 20 to 315°C)

The fracture mechanics specimens were manufactured employing 7, 8 and 11mm thick beams (received as panels from TIMET UK Ltd and Smith Metals Centres Ltd and then water-jet cut to the required dimensions). Super Alloys International Ltd (UK) supplied 2mm thick Ti sheets which were cut and machined to shape (7°, 30° or 45° taper) in house at Imperial College London for their subsequent use in the TDLJ.

4.2.2.3 Unidirectional (UD) CFRP

Various types of unidirectional CFRP substrates were tested. The main two, used in most fracture mechanics test specimens as well as in the composite substrate and spacer of the TDLJ, combined the same resin (CYCOM 977-2 by CYTEC Industries, USA) with two different carbon fibres (high strength 12k-HTS and intermediate modulus IM7 respectively).

A third laminate, using HexPly M21 (Hexcel Corporation, UK) and intermediate modulus T800S fibres, was employed for testing some particular mixed mode ratios. Plates with various thicknesses were manufactured at Imperial College London from unidirectional prepreg tape supplied by CYTEC Industries USA (CYCOM 977-2X1-34-12K-HTS-196-T1-150) and Hexcel Corporation UK (CYCOM 977-2X1-35-IM7-145-ALTL-152 and HexPly M21/34%/UD134/T800S) respectively, and then cut to shape in a wet saw fitted with a diamond blade.

The properties of the neat resins, both rubber-modified epoxies of which typical applications include aircraft primary and secondary structures and ballistics, are given in Table 4.6:

Table 4.6. Properties of the epoxy resin CYCOM 977-2 [365].

	CYCOM 977-2	**HexPly M21**
Density (g/cm^3)	1.31	1.28
Tensile Modulus (GPa)	3.52±0.14	-
Tensile Strength (MPa)	81.4±11	-
Flexural Modulus (GPa)	3.45±0.07	3.5
Flexural Strength (MPa)	197±7	147
G_{Ic} (J/m^2)	478±84	-

4.2.2.3.1 CFRP- 1: UD 977-2/HTS (CYCOM 977-2X1-34-12K HTS-196-T1-150)

Unidirectional CFRP plates with nominal thickness of 2 and 4mm were prepared using 11 and 22 plies of the prepreg tape supplied by CYTEC (CYCOM 977-2X1-34-12K HTS-196-T1-150) respectively. In the laying-up process, sets of four plies were stacked together and introduced in a vacuum bag which was then subjected to negative pressure for 5 minutes. Pairs of the resulting sets were then joined together and put under vacuum again. This process was repeated until the desired thickness was achieved in order to minimize the entrapped air bubbles. The panels were then cured in an autoclave according to the manufacturers' recommended cycle (see Figure 4.2). Typical values for the mechanical

properties of the resulting material, with an approximate fibre volume fraction of 60-65%, are given in Table 4.7 (see Figure 4.3 for the definition of the principal directions).

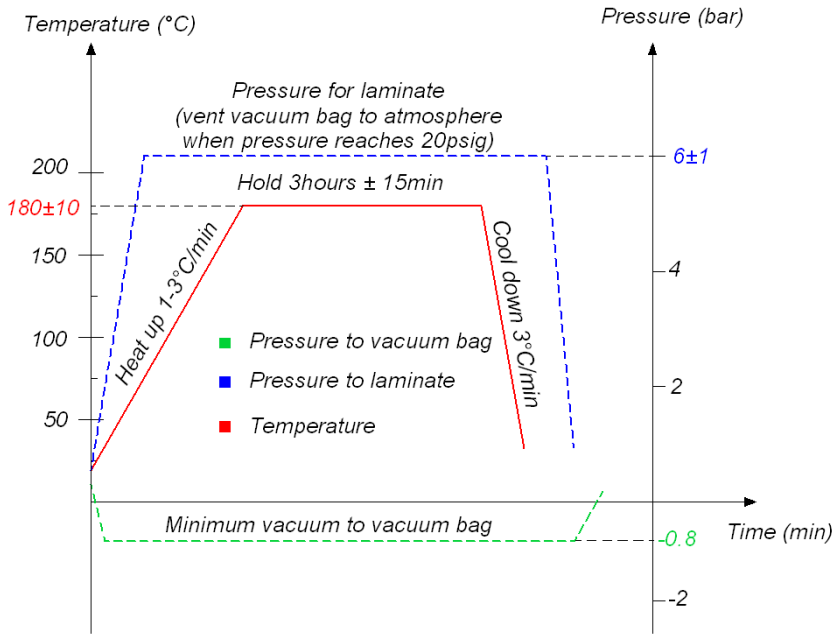

Figure 4.2. Curing cycle parameters for UD 977-2/HTS and UD 977-2/IM7 [365].

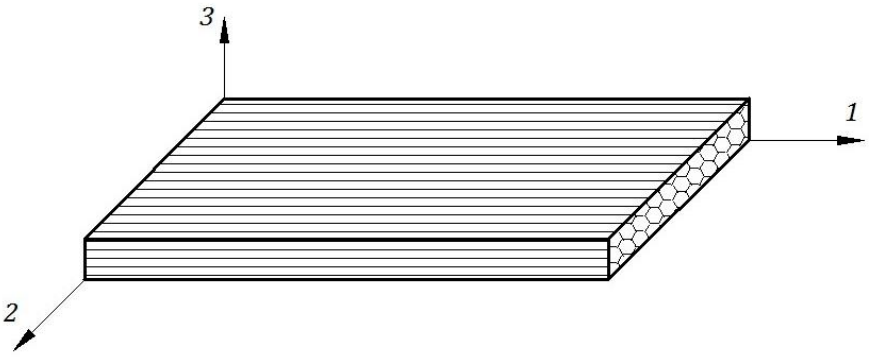

Figure 4.3. Directions considered for the mechanical properties of the CFRP laminates.

Table 4.7. Properties of the UD laminates made from CYCOM 977-2/HTS [366].

Tensile Modulus 0°, E_{11} (GPa)	142
Tensile Modulus 90°, E_{22} (GPa)	8.72
Tensile Strength 0° (MPa)	2305
Tensile Strength 90° (MPa)	83
Compression Modulus 0° (GPa)	125
Compression Modulus 90° (GPa)	9.69
Compression Strength 0° (MPa)	1650
Compression Strength 90° (MPa)	252
In Plane Shear Modulus, G_{12} (GPa)	4.63
In Plane Shear Strength (MPa)	117
Interlaminar Shear Strength 0° (MPa)	105
G_{Ic} (J/m^2)	371
G_{IIc} (J/m^2)	922

4.2.2.3.2 CFRP- 2: UD 977-2/IM7 (CYCOM 977-2X1-35-IM7-145-ALTL-152)

Thirty two plies of prepreg tape supplied by Hexcel Corporation UK (CYCOM 977-2X1-35-IM7-145-ALTL-152) were stacked together to produce 4mm thick unidirectional panels. The lay-up and cure procedures followed for this composite were equivalent to those described in section 4.2.2.3.1. Table 4.8 shows the typical properties for a 66% fibre volume content.

Table 4.8. Properties of the UD laminates made from CYCOM 977-2/IM7 [218, 367].

Tensile Modulus 0°, E_{11} (GPa)	174.44
Tensile Modulus 90°, E_{22} (GPa)	9.65
Tensile Strength 0° (MPa)	2861.3
Tensile Strength 90° (MPa)	75.8
Compression Modulus 0° (GPa)	155.13
Compression Strength 0° (MPa)	1551.32
In Plane Shear Modulus, G_{12} (GPa)	5.31
In Plane Shear Strength (MPa)	94.46
G_{23} (GPa)	2.87
Poisson's ratio, ν_{12}	0.272
Poisson's ratio, ν_{23}	0.415
Thermal expansion coefficient 1 (10^{-6}·°C^{-1})	2.47
Thermal expansion coefficient 2 (10^{-6}·°C^{-1})	27.5
G_{Ic} (J/m^2)	314
G_{IIc} (J/m^2)	1512

4.2.2.3.3 CFRP-3: UD M21/T800S (HexPly M21 / 34% / UD134 / T800S)

Fabricated from M21/34%/UD134/T8002 prepreg tape (Hexcel Corporation, UK) by M. Brett at Imperial College London, this material was available with nominal thicknesses of 3 and 4mm (corresponding to 24 and 32 plies respectively). Additionally, it incorporated a wet peel ply (Hysol EA 9895 by Henkel Corporation, USA) at the top face to improve surface bondability.

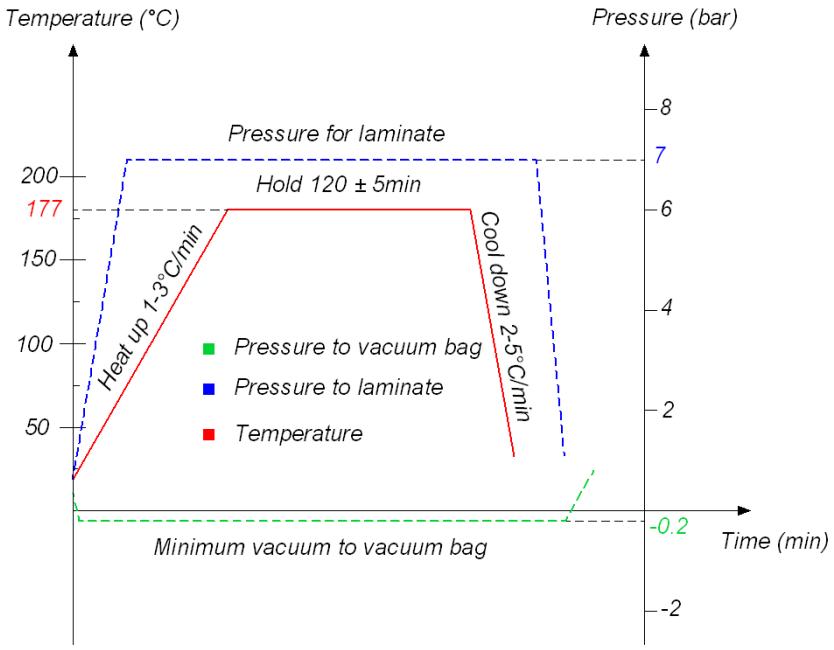

Figure 4.4. Curing cycle parameters for UD M21/T800S according to Hexcel Corporation [368].

The lay-up procedure was equivalent to that described for the other two laminates (i.e. sets of four plies were stacked together and subjected to vacuum before joining them in pairs and applying vacuum again repeatedly until the desired thickness was achieved), with Figure 4.4 illustrating the curing cycle for UD M21/T800S. The resulting material, the characteristic mechanical properties of which for a fibre volume content of 64% are shown in Table 4.9, was employed as substrate in some asymmetric fracture mechanics specimens for mixed mode testing (see section 4.4.2.2.3).

Table 4.9. Properties of the UD laminates made from Hexcel Hexply M21/T800S [266].

Tensile Modulus 0°, E_{11} (GPa)	170.00
Tensile Modulus 90°, E_{22} (Gpa)	8.10
In Plane Shear Modulus, G_{12} (Gpa)	4.80
Transverse Shear Modulus (Gpa)	4.80
Through-thickness Shear modulus (Gpa)	4.01
Poisson's ratio, ν_{12}	0.33
Poisson's ratio, ν_{13}	0.33
Poisson's ratio, ν_{23}	0.01

4.2.3 Surface Treatments and Substrate Preparation

The surfaces of the various substrate materials introduced above always received pre-treatments prior to bonding. Designed to increase the strength of the joints by promoting failure within the adhesive layer rather than in the adhesive-substrate interface, these preparation procedures were specific to each material regardless of the joint geometry. Ranging from simple mechanical abrasion to complex etching processes, these operations are detailed next. Note that, despite some of these surface pre-treatments involving several operations, the acronyms employed here to identify each of them often make reference to their most distinctive step. For example, SHA (Sodium Hydroxide Anodising) refers to the anodising treatment applied to the titanium substrates, even though it also comprises cleaning, degreasing, grit-blasting and primer stages.

4.2.3.1 Surface treatment for Al-alloy substrates and end-tabs: Chromic Acid Etching (CAE)

Chromic acid etching (CAE) is regarded as one of the best surface treatments for aluminium alloys, partly due to the good bond-durability it provides [55, 116, 119]. It was applied here to both the TDCB substrates and the end-tabs used in the TDLJ.

The samples were first cleaned in a two-stage (liquid and vapour, see Figure 4.5) solvent degreaser using Triklone 'N' (C_2HCl_3). The bonding surfaces were then "dry" grit-blasted

with 180/220 micron mesh alumina grit at 80psi to improve their roughness and cleanliness. After undergoing a second degreasing step, the substrates were placed in a chromium acid bath preheated up to 68°C for 30 minutes. With the composition shown in Table 4.10, this bath removes the superficial oxides and exposes a fresh and chemically active surface with enhanced micro-roughness [31, 149]. Once the etching had concluded, the specimens were rinsed with water and submerged in a tank with cold running water for 15 minutes in order to complete the growth of a stable hydration-resistant oxide layer. Due to its porosity, this layer increases the wetability by allowing the adhesive to penetrate deeper in the substrate material. The bonding surfaces were then given a final rinse with distilled water before drying them in hot circulating air (using a fan-oven at 60°C for 30 minutes). When the substrates were not to be bonded immediately, they were wrapped in aluminium foil to prevent contamination and bonded within the week.

(a) (b)

Figure 4.5. (a) Solvent degreaser and (b) its internal liquid and vapour compartments.

Table 4.10. Composition of the chromic acid etch bath [148].

Distilled Water	40 litres
Concentrated sulphuric acid (s.g. 1.84) [H_2SO_4]	7.2 litres
Sodium dichromate [$Na_2Cr_2O_72H_2O$]	3.87Kg
Copper sulphate [$CuSO_4$]	0.1kg
Powdered aluminium	<0.06kg

4.2.3.2 Surface treatment for Ti-alloy substrates: Sodium Hydroxide Anodising (SHA)

Sodium hydroxide anodising (SHA), although complex and hazardous to apply, is regarded as the benchmark treatment for long term durability of Ti-alloy joints [369, 370]. The substrates were subjected to a degreasing – grit-blasting – degreasing pre-treatment equivalent to that described in section 4.2.3.1 before being pickled in two acid solutions: after a first stage of 15 minutes in a nitric acid bath and the subsequent rinse in distilled water, they were submerged for 30 seconds in a hydrofluoric acid solution and then washed again (see compositions in Table 4.11). Next the titanium beams were anodised in a 5M NaOH solution at 20°C for 30 minutes with a constant applied voltage of 10V (see Figure 4.7). Following a final rinse of the bonding surfaces with distilled water to stop any superficial chemical reactions, the specimens were dried in a fan oven at 60°C for 10 minutes. The resulting SHA oxide films had a high surface roughness, medium thickness and porosity similar to those obtained with chromic acid anodising (see Figure 4.8, [59, 60]).

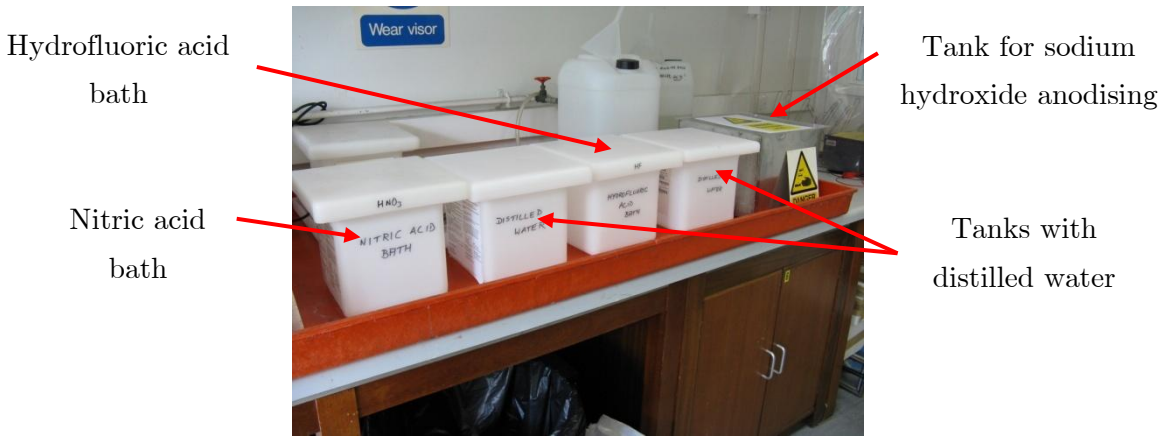

Figure 4.6. Set-up for sodium hydroxide anodising pre-treatment of Ti-alloys.

Figure 4.7. Ti-alloy plate in sodium hydroxide bath during anodising.

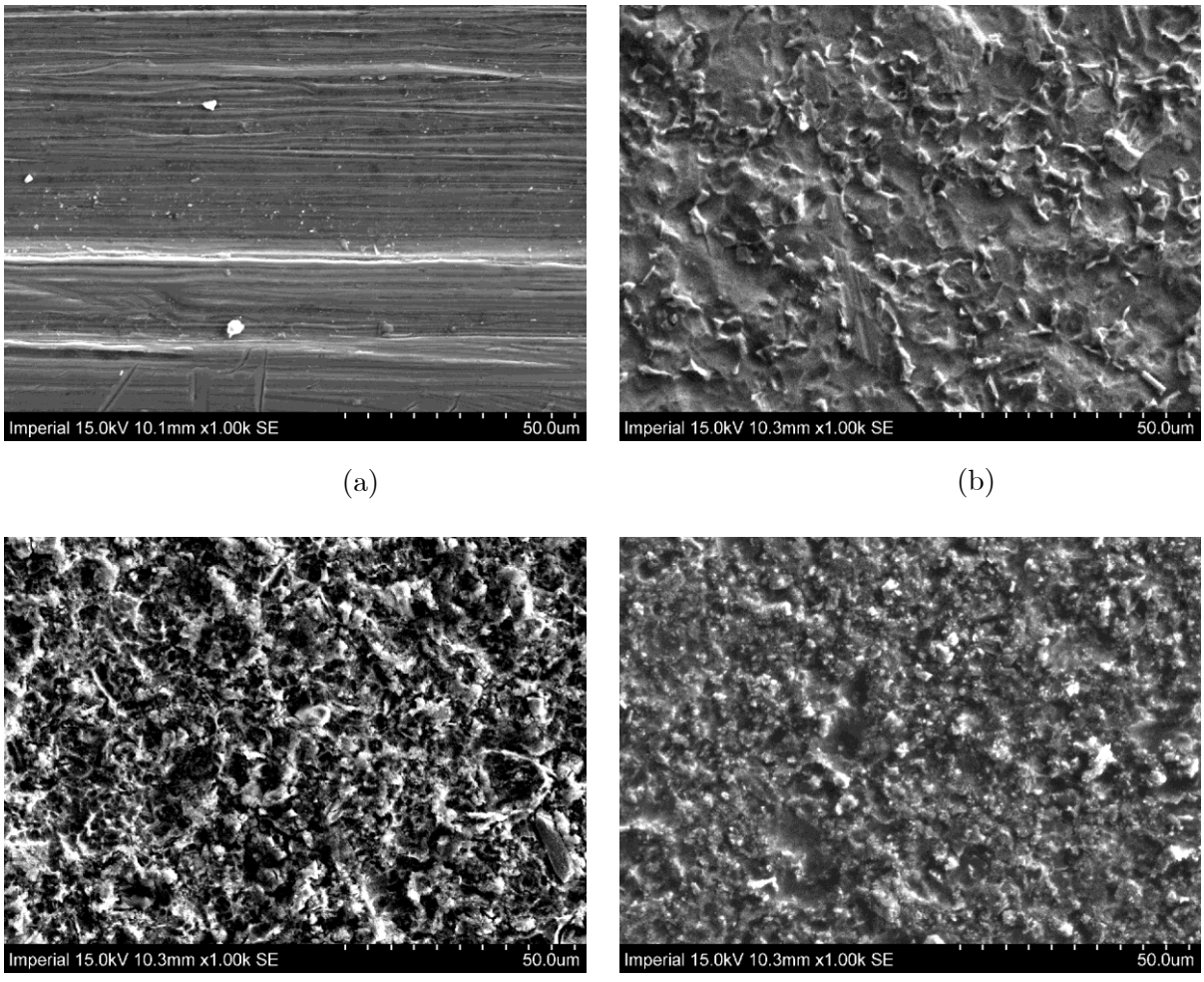

Figure 4.8. SEM images at a magnification of x1000 of the surface of the titanium substrates at various stages of the SHA treatment: (a) as-received (a) after grit-blasting and degreasing; (b) after anodising; and (c) after the application of the primer

Once the substrates had cooled down, they were brush-coated with a thin layer of primer (BR® 127 from Cytec Industries, UK) and subsequently dried at 119°C for 30 minutes. Although the cured primer layer should protect the treated surfaces virtually indefinitely [360], the anodised titanium samples were bonded within the week. In the meantime they were wrapped in kraft paper (i.e. produced by the kraft process and therefore stronger than regular paper) to prevent contamination by dust or dirt.

Table 4.11. Composition of the acid baths used in the SHA treatment [371, 372].

Nitric Acid Bath	
Distilled water	0.3 litre
Nitric acid at 70% (HNO_3)	1.7 litre
Hydrofluoric Acid Bath	
Distilled water	1.94 litre
Hydrofluoric acid 49% (HF)	0.06 litre
Sodium Hydroxide Bath (5M NaOH)	
Distilled water	14.0 litre
Sodium hydroxide (NaOH)	2.8 kg

4.2.3.3 Surface treatments for CFRP substrates: Grit-blasting and Drying (GBD) and Wet Peel Ply and Drying (WPPD)

Prior to bonding the CFRP substrates made from UD 977-2/HTS and UD 977-2/IM7 were "dry" grit-blasted with 180/220 micron mesh alumina grit. A lower pressure (40psi) and a 45° spray angle were used in this case to prevent damaging the material or exposing the carbon fibres. Following the abrasion process, the bonding surfaces were thoroughly wiped with acetone and clean paper towels to remove gross contamination (oils, excess of grit, etc) that could hinder subsequent adhesion. In contrast, these operations were not applied to the UD M21/T800S beams, since in that case the removal of the wet peel ply on the surface of the laminate is intended to produce a suitable surface finish for bonding.

It has been reported in the literature that moisture trapped in the composite substrates can negatively affect the curing process of the adhesive [133, 149, 373]. This humidity tends to be absorbed by the adhesive, modifying its T_g and creating holes in the bondline once it evaporates, which subsequently reduces the toughness of the joints. To mitigate the detrimental influence of this factor, all the CFRP substrates were dried in a fan-oven for 24 hours at 100°C. Obviously this process did not produce a "fully dried" material (achieving that state would take weeks, see [148]), but it did at least result in a reproducible set of curing conditions which allowed consistent toughness measurements.

Once the drying process was completed the specimens were taken out of the oven and left to cool. Those initially grit-blasted received a second acetone wiping to remove any potential contaminants deposited within the oven and then bonded immediately afterwards to avoid new humidity absorption. For UD M21/T800S laminates this cleaning step was unnecessary, as the peel ply protected the bonding surface during the drying cycle (note that the peel ply was on one surface only, so water could be removed in the oven). In that case the peel ply was removed at a 45° angle after the specimens had cooled down and just before bonding.

4.2.3.4 Surface treatment for Al-alloy end-blocks: Grit-blasting (GB)

The adhesive bond between the aluminium end-blocks and the substrates of the fracture mechanics specimens needed to be sufficiently strong to withstand the experimental loads. Following the manufacturer's recommendation to maximise the strength of the joints made with Araldite® 2014-1, the end-blocks were routinely grit-blasted with 180/220 micron mesh alumina grit at 80psi. The abraded surfaces were then cleaned with acetone. Similarly, the titanium or CFRP surfaces where the end-blocks were to be located received an equivalent treatment (grit-blasting with 180/220 micron mesh alumina grit at 80psi – 40psi in the case of the CFRP beams – followed by acetone wiping).

4.3 Adhesive Joint Manufacture

Cutting the adhesive to shape represented the first step of the bonding operation. Two strips per joint were cut to size with the aid of a template and these were then kept in polythene self-sealing bags at -20°C up the moment of use. The size of these pieces was marginally bigger than the area to be bonded to ease their positioning while assuring the coverage of the entire bonding surface.

With a substrate on a flat and clean surface, the first adhesive layer was placed on the bonding surface with its tacky side facing the pre-treated adherend. Gentle pressure was then manually applied to improve adhesion and remove major air-bubbles. Then, stainless steel wires with a diameter of 0.4mm were placed to control the bondline thickness. Their location, length and number were always carefully selected so that the interaction with the advancing crack in the subsequent test was minimal. A minimum of two spacers were used in all cases, positioned at each end of the specimen perpendicular to the longitudinal axis of the beams (i.e. the direction of crack propagation). Their diameter choice was based on previous studies in which the toughness of similar epoxy systems had been reported to reach a plateau for bondline thicknesses greater than 0.35mm [149].

In the fracture mechanics specimens, a 12.7μm thick PTFE film with the appropriate dimensions was then put at one end of the substrate. Designed to act as an initial crack, the PTFE section of the joint represented an ideal location for some of the steel wires, as wires placed in this region would not affect the measured toughness. The second strip of adhesive was then laid with its tacky side facing the first layer (i.e. "tacky"-"non-tacky" sequence), using manual pressure to eliminate trapped air bubbles before closing the joint.

The un-cured specimens were then transferred to the appropriate jig, coated beforehand with a high-temperature release agent (FREKOTE 700, Henkel Corporation). These purpose-built fixtures (see Figure 4.9) guarantee proper alignment of the substrates and apply pressure during the curing cycle. In each batch of three specimens the end of a thermocouple was inserted in the bondline of one of the joints. This made it possible to monitor the temperature of the adhesive during curing. Rubber sheets were placed between the jig plates and the joints to ensure a homogeneous distribution of the pressure. Given the different jig designs for the various specimens, the required pressure was applied either via a prescribed torque in the bolts (TDLJ and TDCB cases, with 5 and 20N·m respectively) or by the addition of weights to the top plate.

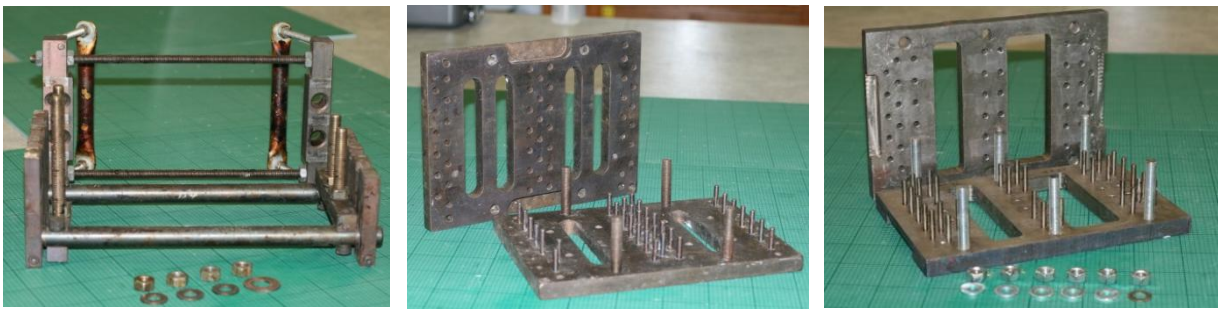

(a) (b) (c)

Figure 4.9. Purpose-built for bonding (a) TDCB specimens; (b) flat fracture mechanics specimens (i.e. ADCB, ELS, ENF and AFRMM); and (c) double lap joints

The jigs and samples were then transported to a pre-heated oven and cured according to the cycle shown in Figure 4.1 (taking the reading from the thermocouple as indicative of the temperature in the adhesive layer). In the case of the TDLJ the geometry of the spew fillets was controlled during the curing process so a reproducible shape was obtained. With that intention the door of the oven was opened periodically during the heating phase and the excess of adhesive removed using wooden rods with semicircular-shaped heads. This procedure was repeated every five minutes until the temperature had reached 100°C, the point at which the epoxy resin was considered to have gelled and the normal curing cycle was resumed. Note that, due to the thermal inertia of the metallic jig and the Ti-alloy substrates, the temperature of the bondline remained almost constant during the short time periods that the door remained open.

Once the curing cycle was completed and the oven cooled down (minimum 18 hours), the jig was taken out and the specimens were carefully extracted. The excess of adhesive was then cautiously removed using sand-paper, paying special attention so that neither the substrates nor the glue line were damaged in the process. The joints were then examined under an optical microscope incorporating a CCD camera with a calibrated measuring facility. Images of the bondline were taken at various locations (front, centre and back sections of each sample) with magnifications ranging between 50x and 100x. Primarily intended to evaluate the thickness of the cured adhesive layer, these pictures also served to identify potential defects such as voids or poorly bonded areas. Additionally, a second estimate of the bondline thickness was calculated as the difference between the thickness of the cured joint and those of the individual substrates, which were measured at three different locations with a micrometer.

Aluminium alloy end-blocks were then attached if required, following the surface treatment of the surfaces involved as described in section 4.2.3.4. A special jig was used to ensure proper alignment of the various parts during the curing process. Finally, in all the fracture mechanics specimens the bondline along the edge of the joint was covered with a thin layer of white paint or correcting fluid (i.e. tipp-ex) in order to facilitate the crack detection in the subsequent tests. Vertical lines were marked every 2.5mm starting 10mm ahead of the end of the PTFE insert to allow optical measurements of the crack length. Alternatively, a ruler grid was fixed onto one side of the specimen next to the bondline for the same purpose.

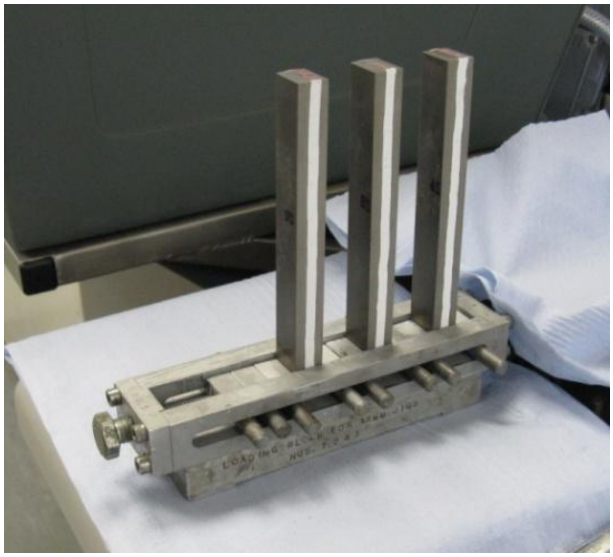

Figure 4.10. View of the jig used in to bond end-blocks to the relevant fracture mechanics specimens (titanium DCB joints in the picture).

4.4 Experimental Procedures

4.4.1 Introduction

Various types of fracture mechanics specimens (i.e. DCB, TDCB, ELS, AFRMM, etc) were manufactured and tested quasi-statically in order to characterize the fracture behavior of AF163-2. The critical strain-energy release rate results obtained for the different mixed mode ratios were combined and fitted to a suitable function to define the failure criterion $G_c = G_c(\beta)$ required for the cohesive element formulation. In addition, a limited number of joints were tested in fatigue to obtain crack growth rate data. Titanium alloy DCB and ENF specimens were employed in the mode I and in-plane shear investigations respectively, using the results to derive suitable expression for the parameters of the modified Paris law (i.e. C_T, m, n_1, n_2 and G_{th}). Finally, experimental data obtained for an independent geometry was needed to fully evaluate the accuracy of the performance prediction methodologies proposed in Chapter 3. Therefore a simplified adhesively-bonded structure (i.e. Ti-CFRP tapered double lap joint, TDLJ) was tested under quasi-static and fatigue loading conditions to determine both its ultimate strength and the corresponding S-N diagram.

This section describes the different tests carried out as well as the equipment used and the procedures followed in each case.

4.4.2 Monotonically-Loaded Tests

4.4.2.1 Details of the testing machines

Two different screw-driven tensile testing machines were used in the monotonically loaded tests: an INSTRON 5584 and an INSTRON 5585H (see Figure 4.11). Both incorporated electronic units responsible for the cross-head motion control, data acquisition and triggering of the safety limits, while computers running INSTRON's proprietary Bluehill application software acted as user interfaces and data storage mediums.

(a) (b)

Figure 4.11. Screw-driven tensile testing machines used in the monotonically loaded tests of the (a) fracture mechanics specimens and (b) the TDLJs.

The first machine, with a load cell of ±150kN capacity attached, was employed for the testing of all the fracture mechanics specimens. The load was applied to these samples using 8mm steel pins fitting in the holes of the Al-alloy end-blocks or in those drilled in the TDCB substrates. Extension rods, shackles and specific fixtures (see sections 4.4.2.2.2 and 4.4.2.2.3) were also required in some cases. Additionally, the crack length was monitored using a travelling microscope with 15 times magnification positioned perpendicularly to the edge of the specimens. The double lap joints tests were performed in an INSTRON model 5585H

with a 250kN load cell equipped with a set of heavy-duty pneumatic wedge action grips (300kN W-5180, INSTRON). The power of their pneumatic pistons combined with a wedge design that causes the gripping force to increase as the tension is applied made this the obvious choice for the TDLJ testing so as to help eliminate slippage.

All the monotonically-loaded tests were carried out in a controlled environment (temperature of 23±1°C and a relative humidity of approximately 55±10%) in displacement control.

4.4.2.2 Fracture Mechanics Test Specimens

4.4.2.2.1 Mode I: DCB and TDCB Test Specimens

Two different geometries were investigated to obtain the value of the mode I fracture energy G_{Ic}, namely: the TDCB and DCB specimens. While the former used Al-alloy substrates, 7, 8 and 11 mm thick, titanium alloy beams were employed in the DCBs. A minimum of three joints were tested in each case. Manufactured following the process described in section 4.3, their typical dimensions (in mm) can be seen in Figure 4.12. Even though the width of each type of joint was different (10 and 20mm respectively), it was selected in both cases to ensure plane-strain conditions in the majority of the crack front and hence the direct measurement of a material property (fracture toughness). However, some doubts still remain regarding the suitability of the narrower TDCB specimen. This aspect is discussed further in Chapter 6.

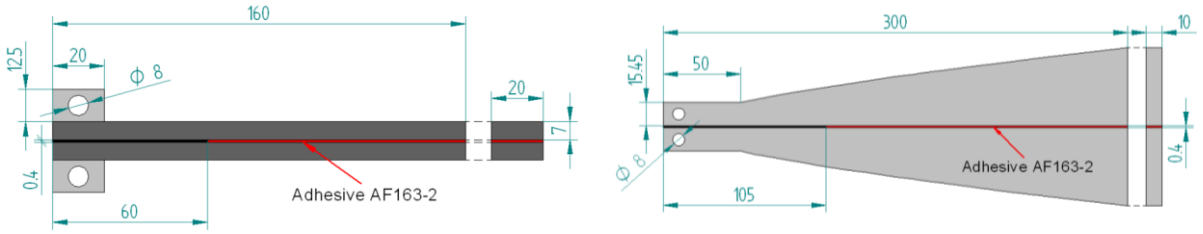

(a) (b)

Figure 4.12. Nominal dimensions (in mm) of the mode I test specimens: (a) DCB joint with end-blocks and; (b) TDCB specimen with drill holes in the substrates.

All the mode I tests were performed in accordance with the international standard ISO 25217 [165]. The specimens were mounted in the testing machine using 8mm diameter steel pins that fit in the holes of the end-blocks attached to the DCBs or in those drilled in the TDCB substrates. An additional support was used to level the samples and guarantee that the bondline remain orthogonal to the loading path at all times (see Figure 4.13-a). Once in place they were loaded at a constant rate (0.1mm/min for the metallic joints and 0.5mm/min if

CFRP beams were employed). The load (P) and displacement (δ) were recorded by the computer, while the corresponding crack lengths (defined here as the maximum visible length of continuous rupture of the adhesive layer) were monitored with the help of a travelling microscope with 15 times magnification (see Figure 4.13-c). After applying suitable corrections for system compliance and initial non-linearity to the experimental data, the resulting sets of P_i-δ_i-a_i values were used to calculate initiation and propagation values of G_{Ic} according to the various analysis methods discussed in Chapter 5 (see section 5.3).

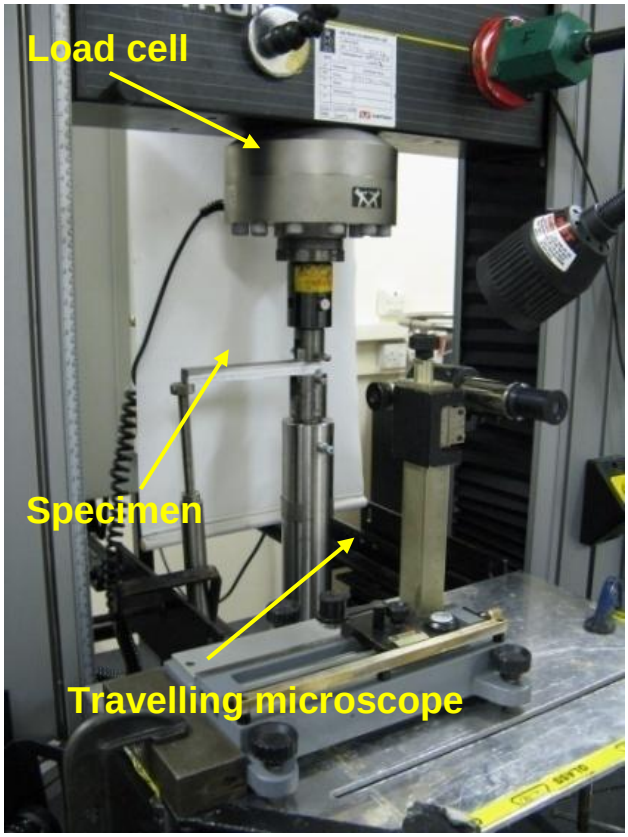

(a)

(b)

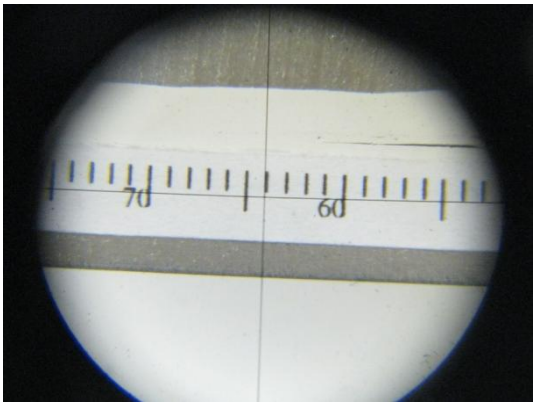

(c)

Figure 4.13. Examples of the set-up for mode I tests of (a) a DCB specimen and (b) a TDCB joint; (c) View of the crack tip through the optical microscope during a mode I test (propagating from the right to left).

Once the crack tip reached the 200mm mark in the TDCB or 110mm in the DCB, the test was stopped and the specimen manually unloaded at an approximate rate of 0.5mm/min. Load and displacement were recorded at intervals during this process, serving later as a plasticity check. Had the substrates experienced any permanent deformation, the unloading path would not return to the origin. Finally, the specimens were broken apart and the fracture surfaces carefully inspected in order to assess the type of failure (i.e. cohesive, interfacial, interlaminar or a mixture of these).

Several authors have highlighted the significant influence of the crack tip radius or crack "sharpness" in the fracture toughness determination of epoxy adhesives [64, 374]. With the intention of obtaining reproducible initial conditions and hence comparable fracture energy measurements, all the mode II and mixed mode specimens were pre-cracked in mode I. Following a process equivalent to that described above, the crack was propagated about 5mm from the end of the PTFE insert. Obviously in some cases this implied the attachment of additional end-blocks that were then removed prior to carrying out the actual tests to prevent unnecessary changes in the compliance of the joints. The same process was followed for the "asymmetric" mixed mode specimens.

4.4.2.2.2 Mode II: ELS and ENF Test Specimens

A number of mode II tests were carried out using both the ELS and ENF geometries. Manufactured in accordance with the process described in section 4.3 using 4mm thick CFRP (UD 977-2/HTS) and 8mm thick titanium substrates respectively, the dimensions of this specimens can be seen in Figure 4.14. The relevant ESIS TC4 protocol [164] was followed for the ELS tests in an attempt to obtain the entire mode II resistance curves, whereas only initiation G_{IIc} values were derived from the ENF joints to avoid any plastic deformation in the metallic beams.

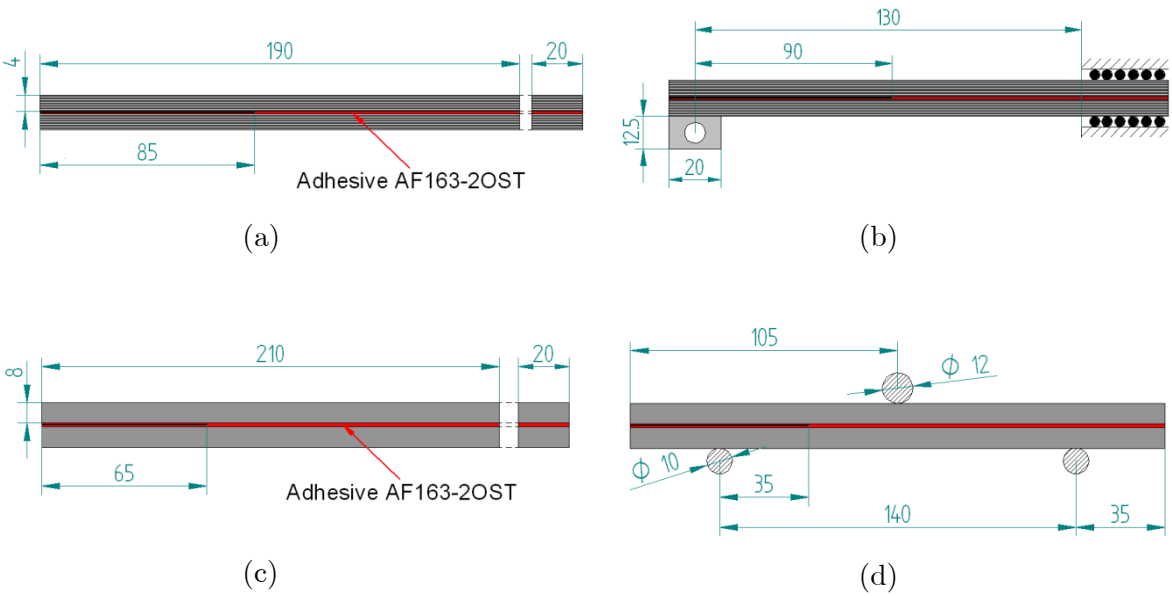

Figure 4.14. Nominal dimensions (in mm) of the mode II test specimens: (a) ELS joints as manufactured and (b) after mode I pre-cracking; (c) ENF specimens as manufactured and (d) after mode I pre-cracking.

The samples were initially pre-cracked in mode I as described in the previous section to propagate the crack approximately 5mm from the end of the PTFE insert. This operation

required the attachment of two end-blocks, which were then carefully removed (only one in the case of the ELS joints) before transferring the specimens to the mode II fixtures. Mounted on slide bearings, this ELS rig was designed to eliminate any horizontal loads. One end of the sample was clamped to the rig, while at the opposite end the load was applied vertically at a constant rate of 0.5mm/min through an 8mm pin fitting in the block (see Figure 4.14-a). As result the loading point was free to rotate and consequently pure shear conditions were achieved at the crack tip. To maintain repeatable clamping conditions, a constant torque of 8Nm was always used to tighten the clamping bolts. A free length of 130mm was selected to prevent instability and at the same time hold a substantial portion of the joint under the clamp. A three point bending rig was used for the ENF tests. The specimen rested on two round supports of diameter 10mm, while the load was applied downwards at the centre point (at a constant rate of 0.1mm/min) via a cylindrical indenter of diameter 12mm. The total span length ($2L$) was fixed to 140mm (see Figure 4.14-b).

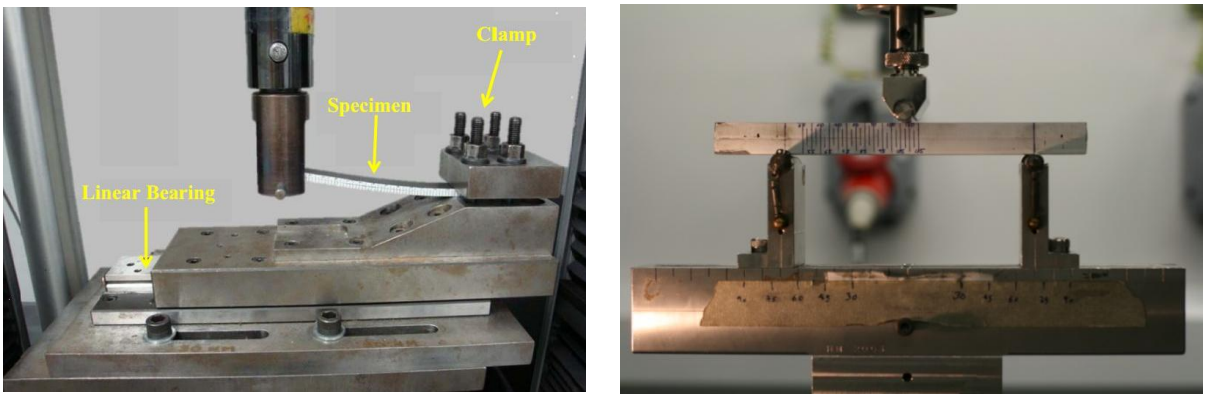

(a) (b)

Figure 4.15. Experimental set-up for mode II tests using (a) the CFRP-ELS specimens (b) titanium alloy ENF joints.

The load (P) and displacement (δ) together with the corresponding crack lengths were recorded during the test. Given the difficulties to distinguish between the end of the continuous crack and the damage ahead of the crack tip, both were monitored using a travelling microscope and were marked at intervals on the P-δ trace saved by the computer. For the ELS, once the continuous crack or the damage ahead of the tip had grown to approximately within 20mm from the clamping point the test was stopped. Conversely, the ENF tests were stopped before the applied displacement reached 2mm so as to prevent plastic yielding in the substrates. The joints were then manually unloaded at ~0.5mm/min. The unloading path was always recorded and would serve as plasticity check for both the ELS and ENF tests. Finally the samples were removed from the respective fixtures and, after

re-attaching the end-blocks previously detached, they were loaded in mode I to complete failure. The fracture surfaces were then carefully examined and the fracture path noted.

After applying suitable corrections for system compliance and initial non-linearity to the experimental data, the resulting sets of P_i-δ_i-a_i values were used to calculate initiation and propagation values of G_{IIc} according to the various analysis methods presented in Chapter 5 (see section 5.4). Note that, in the case of the ELS configuration, an additional clamp correction factor ΔL_{clamp} was required for the effective crack length reduction scheme. Dependent on the rig design, the clamping torque and the stiffness of the joints, this value was determined via the so-called "inverse ELS test". A specimen identical to those tested but absent of the PTFE insert was employed in the calibration of the fixture. The joint was clamped at various free lengths L_i (130, 120, 100, 90, 80, 70, 60 and 50mm) and loaded at 0.5mm/min up to a constant load of 300N so that it deformed elastically. The maximum applied displacement in each case was recorded and used to calculate a compliance value C_i for each free length. The results were then plotted on a graph of $(C_i)^{1/3}$ versus L_i and a linear regression performed on the data so that the length value corresponding to $C_i = 0$ was identified as ΔL_{clamp} [139].

4.4.2.2.3 Mixed Mode I/II: FRMM, AFRMM and ADCB Test Specimens

The symmetric (i.e. both substrates with the same thickness) and asymmetric versions of the fixed ratio mixed mode test geometry (FRMM and AFRMM respectively) were selected to characterize the mixed mode I/II fracture behaviour of the adhesive AF163-2. The same fixture described for the ELS was employed, although in this case the upper substrate rather than the lower arm was loaded vertically (Figure 4.16). These configurations produce nearly constant ratios of mode I to mode II for any given crack length. However, there is no clear consensus on what mixed mode ratio is obtained with the different specimens. While most partitioning methods agree on the value for the symmetric joints, the unbalanced case still remains an open question and attracts the attention of numerous researchers. According to the most established theories, the mode mix in problems where both substrates share the same material depends on the relative thickness of the loaded and unloaded arms, and in some cases on the particular conditions at the crack tip (specifically whether a singular or non-singular field exists at that point). Some of these decomposition schemes, as will be discussed in detail in Chapter 5, were used to analyse the experimental data acquired in the tests.

A number of mixed mode ratios were tested by combining CFRP beams of the various nominal thicknesses available: 2, 3 and 4mm (see section 4.2.2.3). For simplicity a single type of unidirectional laminate was used in each case (i.e. no dissimilar substrate materials were bonded together). After the appropriate surface treatment and drying cycle, the joints were manufactured as described in section 4.3. Note that, regardless of the partitioning theory considered, any AFRMM specimen would produce two different mixed mode ratios depending on whether the thicker or thinner arm was loaded. Each option is treated here as an independent specimen.

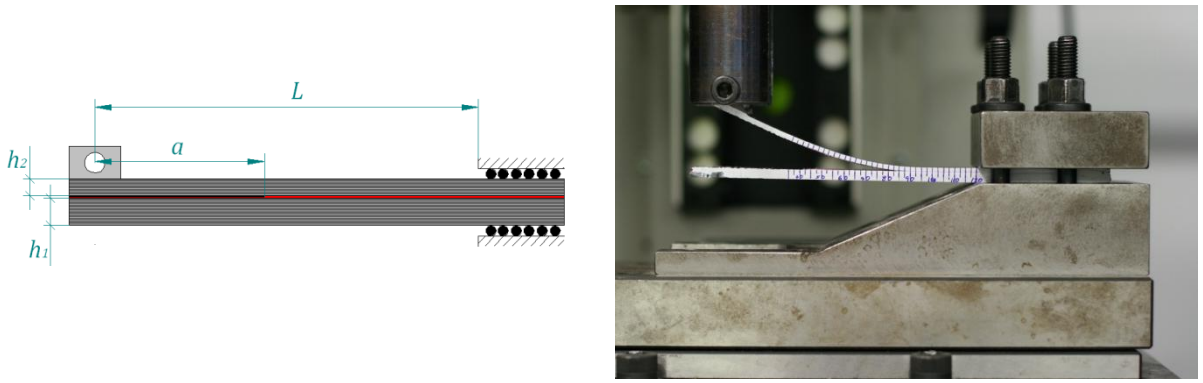

(a) (b)

Figure 4.16. Definition of the geometrical parameters in a AFRMM specimen and (b) experimental set-up for a quasi-static AFRMM test.

The ESIS TC4 test protocol [207] developed for the FRMM test was followed for both the FRMM and AFRMM tests. In accordance with [207] the samples were firstly pre-cracked in mode I to propagate the initial defect approximately 5mm from the end of the PTFE foil (at a constant rate of 0.5mm/min). This implied the attachment of two end-blocks prior to loading as described in section 4.4.2.2.1. The symmetric FRMM required standard DCB samples, whereas the AFRMM test required asymmetric DCB (ADCB) specimens (see Table 4.12). During pre-cracking the load, displacement and crack length were monitored and subsequently analysed using the theories described in Chapter 5.

Once the pre-cracking step was completed, the lower end-block was carefully removed and the specimen transferred to the rig. The un-cracked end of the joint was held under the clamp, which was free to slide horizontally, using a constant torque of 8Nm to tighten the bolts. As shown in Figure 4.16-b, loading was vertically applied at the opposite side at a constant rate of 0.5mm/min via an 8mm pin fitting the remaining end-block. The values of the free length and the initial crack length were carefully selected for each thickness ratio to promote stable propagation (see Table 4.13).

Table 4.12. Substrate material and nominal dimensions of the DCB and ADCB tests carried out (corresponding to the pre-cracking phase of the specimens subsequently tested in mode II and mixed mode).

	Substrate Material	Nominal thickness h_2 (mm)	Nominal thickness h_1 (mm)	Nominal initial crack length a_0 (mm)
CFRP-DCB*	UD 977-2/HTS	4	4	70
CFRP-ADCB1	UD 977-2/HTS	2	4	40-70
CFRP-ADCB2	UD M21/T800S	3	4	45

*Note: This type of specimen also corresponds to the joints pre-cracked for mode II testing (ELS)

Table 4.13. Substrate material and nominal dimensions of the FRMM and AFRMM specimens tested.

	Substrate Material	Nominal thickness h_2 (mm)	Nominal thickness h_1 (mm)	Free length L (mm)	Nominal initial crack length a_0 (mm)	Nominal crack length after pre-cracking a_P (mm)
FRMM	UD 977-2/HTS	4	4	130	70	75
AFRMM1	UD 977-2/HTS	2	4	120	40	45
AFRMM2	UD 977-2/HTS	4	2	110/120	70	75
AFRMM3	UD M21/T800S	4	3	100	45	50
AFRMM4	UD M21/T800S	3	4	100	45	50

The load (P) and displacement (δ) together with the corresponding crack lengths were recorded during the test. Given the difficulties to distinguish between the end of the continuous crack and the damage ahead of the crack tip, both were monitored with the aid of a travelling microscope and marked at intervals on the recorded P-δ trace. Once the continuous crack or the damage ahead of the tip had grown to within approximately 20mm from the clamping point the test was stopped and the joint manually unloaded at roughly

0.5mm/min. The unloading path was recorded and would serve as a plasticity check. Finally, after removing the specimen from the clamp and inspecting for any damage to the arms, the joint was broken apart in mode I. The fracture surfaces were carefully examined and the failure path noted.

Initiation and propagation values of $G_{I/IIc}$ and their respective pure mode components (G_I^{mixed} and G_{II}^{mixed} respectively) were derived from the experimental data P_i-δ_i-a_i, corrected for system compliance and initial non-linearity, using the different theories presented in Chapter 5 (see section 5.5). An additional clamp correction factor ΔL_{clamp} was needed in some of those methods as described previously.

It is worth noting that the true laminate thicknesses, measured at three locations along the beams with a micrometer, rather than the nominal values were employed in the analysis of the experimental data.

4.4.2.3 Simplified Structure: Quasi-Static TDLJ

Figure 4.17-a illustrates the geometry of the simplified structure used to assess the accuracy of the performance prediction methodologies presented in Chapter 3. This particular design, referred to here as tapered double lap joint (TDLJ), does not comply to any particular standard but was selected instead because of its resemblance to the real adhesively-bonded structure that motivated this project: the CFRP-Ti fan blade. Thus it has two Ti-alloy strips bonded to either side of a CFRP (UD 977-2/IM7) central part, simulating the metalwork protective layers covering both the leading and tailing edges of the composite airfoil.

In order to minimize the "peel" stresses at the ends of the overlap, the metallic substrates featured beveled edges. Three different chamfer angles (i.e. 7°, 30° and 45°) were tested quasi-statically. Machined in a conventional grinder before anodising, the titanium substrates did not exhibit sharp edges (see Figure 4.17-b). The vertical tip (of depth 0.1 to 0.4mm) depended on the taper angle. A CFRP spacer with appropriate dimensions was placed between the titanium strips to balance the joint. Al-alloy end-tabs were bonded at both ends. Given the softer nature of the aluminium, these increase the friction with the wedge grips and at the same time protect the substrates (specially the CFRP) from the compressive stresses imposed during loading.

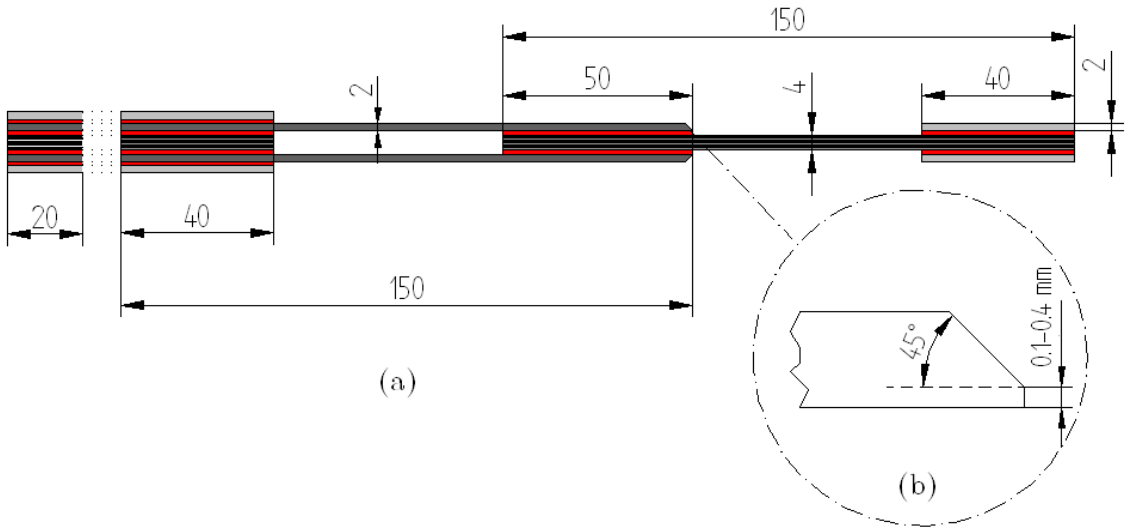

Figure 4.17. (a) Nominal dimensions (in mm) of the Ti-CFRP TDLJ tested quasi-statically (the thickness of the various bondlines – nominal value 0.4mm – has been exaggerated for illustration purposes; (b) Schematic representation of the tip at the tapered end of the Ti-alloy substrates.

After the appropriate surface treatments for the individual components, the joints were manufactured in accordance with the procedure described in section 4.3 in a single curing cycle. Note that two layers of AF-163-2OST and steel wires were used in every section to be bonded to give a nominal bondline thickness of 0.4mm. The excess of adhesive was removed only from the central overlap but it was left intact everywhere else to improve strength and prevent de-bonding of the end-tabs. One side of each sample was then coated with a thin layer of matte black paint. White speckles were then deposited on the fully-dry black background using a spray gun. These would serve as the high-contrast random pattern required for the Digital Image Correlation (DIC) system employed to monitor the strain field in the overlap region (Figure 4.18-a).

The samples were then inserted into the pneumatic wedge grips fitted to the INSTRON machine. Vertical alignment was ensured with a level and a set square, while the grips were set to the maximum available pressure (i.e. 6 bars). Loading was applied at a constant rate of 0.5mm/min until complete failure. Load and cross-head displacement were recorded by the computer running Bluehill application software, while a 3D DIC system was used to obtain full-field displacement plots of the lateral face of the joints. Equipped with two 5 Megapixel cameras sampling at 12 frames per minute, this apparatus traced the position of the high-contrast pattern covering the surface. The sequences of images acquired with each camera, the relative positions of which were known from a previous calibration step, were subsequently combined and processed with a dedicated software (ARAMIS by GOM mbH) to compute the displacement and strain fields of the deforming body. Estimates of the extension

along the overlap were derived from the displacement between various pairs of points at each side of the centre, and then combined with the measured load to obtained the P-δ curves.

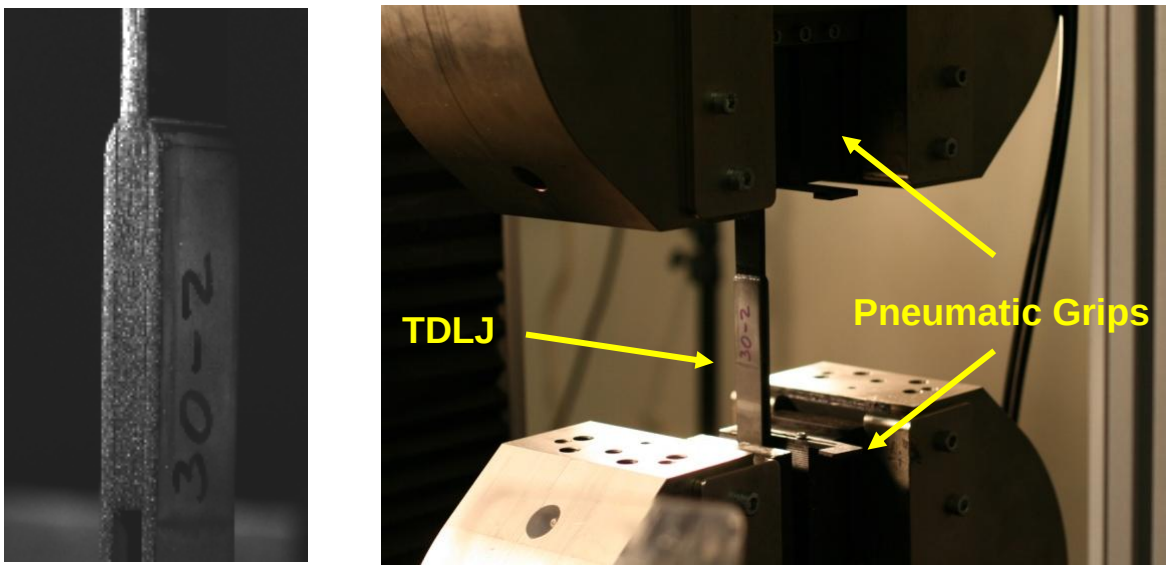

(a) (b)

Figure 4.18. (a) Detail of the high-contrast random pattern applied to the TDLJs for the use of the DIC system; (b) Set-up for the quasi-static tests of the TDLJs.

For the first two specimens the extension in the overlap was also obtained using a 50mm gauge length extensometer. However, the use of this device was discontinued because it obstructed the line-of-sight of the DIC cameras and hindered the capture of good quality pictures. Furthermore, the optical technique was considered more accurate given that the arms of the extensometer tended to slip on the surfaces of the substrates, particularly on the metallic side. Additionally, an attempt to video the instant of failure was made using a high-speed camera. The camera was connected to the data acquisition unit of the INSTRON machine and its trigger synchronized with the load readings so that it would capture the moments preceding a sudden drop in load. Unfortunately the light sources available were not powerful enough to capture high-quality images or to use sampling rates greater than 2000fps.

After the test the fracture surfaces were visually inspected and photographed, and the type of failure noted. The other bonded areas were also inspected for further damage that could have affected the results.

4.4.3 Cyclic Fatigue Tests

4.4.3.1 Details on the testing machines

Mode I cyclic fatigue tests were carried out using three different INSTRON machines (models 8878, 8501 and 8516 equipped with 25, 10 and 100kN load cells respectively) and a bespoke Phoenix Calibration & Services frame fitted with a 25kN load cell. All were connected to their own digital controllers and computers running proprietary software applications in each case (WaveMatrix™ for the INSTRONs and Alpha Digital Control in the Phoenix). The first INSTRON and the Phoenix system were used for the "dry" tests, whereas the other two machines incorporated Perspex water tanks for the "wet" tests.

(a) (b)

Figure 4.19. Servo-hydraulic testing systems employed in the fracture mechanics mode I fatigue tests: (a) INSTRON 8501 and (b) Phoenix.

A 30kN Dartec frame connected to a digital controller and computers running Phoenix proprietary software application (Alpha Digital Control) was used for the mode II tests. With the actuator conveniently located at the cross-head, it incorporated a T-slot base ideally suited for securing the three point flexure fixture required for the ENF configuration. Finally, another INSTRON (model 8032) located in the Aeronautics Department at Imperial College London and operated by J.P. Maggyesi was employed for testing the TDLJ in fatigue. With a 100kN dynamic load cell and connected to an electronic control unit, this machine was equipped with a set of flat-serrated hydraulic grips which provided the compressive forces necessary to minimize slippage at the aluminium end-tabs.

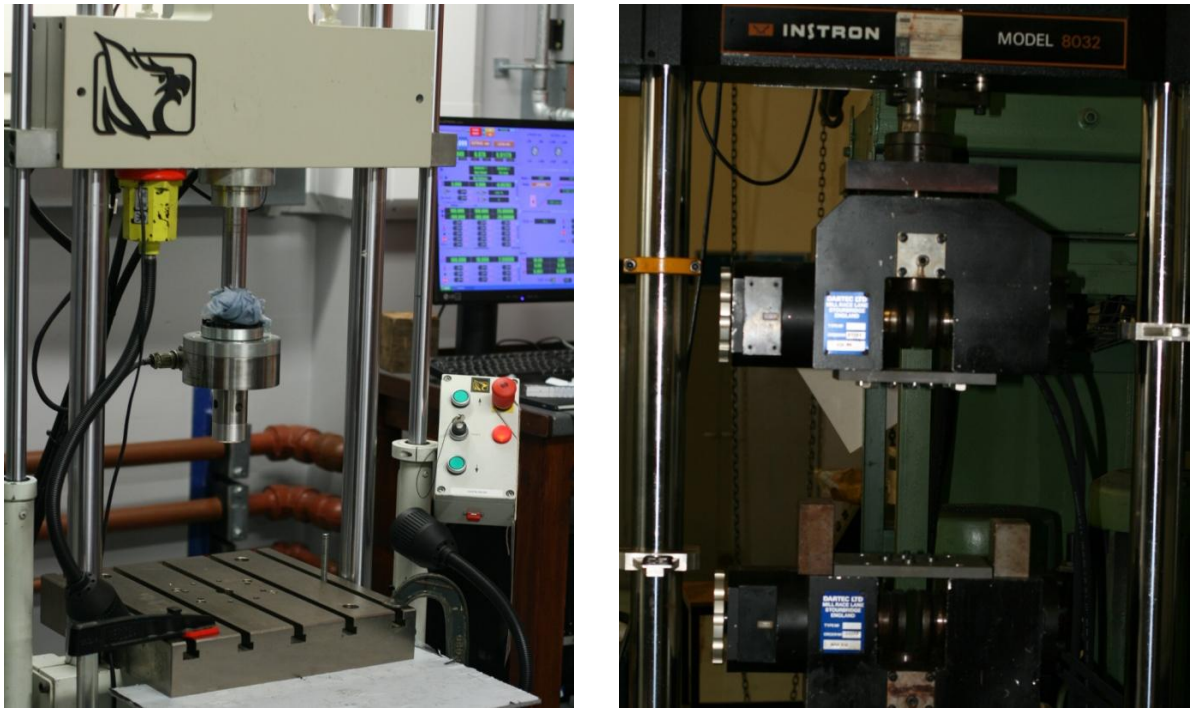

(a) (b)

Figure 4.20. (a) Dartec testing machine used in the mode II fatigue tests and (b) INSTRON 8032 system with hydraulic grips employed in the fatigue tests of the TDLJ.

4.4.3.2 Fracture Mechanics Test Specimens

4.4.3.2.1 Mode I: DCB Test Specimen

The work described in this section was carried out by Dr Sabine Frenz as part of a larger project sponsored by Rolls Royce Plc to study the susceptibility of different surface treatments for Ti-alloys to environmental attack. DCB specimens equivalent to those described in section 4.4.2.2.1 (i.e. using 7mm thick anodised Ti-alloy beams and a 60mm PTFE crack starter, i.e. 50mm initial crack measured from the loading point) were subjected to cyclic-loading in both "dry" and "wet" environments. “Dry” experiments were performed at ambient conditions (23±1°C, ≈55% R.H.), whereas coupons were submerged in a bath of distilled water at approximately 25±3°C for “wet” testing. Manufactured according to the procedure described in section 4.3, the joints were attached to the testing machine with 8mm pins fitting in the Al-alloy end-blocks bonded to the substrates. These pins, made from stainless steel for the wet samples, incorporated retainers to prevent them working free during the tests. A support was also placed to level the joints so that they remained orthogonal to the loading direction at all times.

(a) (b)

Figure 4.21. Set-up used in the mode I fatigue in (a) "dry" and (b) "wet" conditions (polypropylene spheres in the tank to minimize water evaporation).

Loading was then applied in cyclic displacement control using a sinusoidal function of frequency 5Hz varying between constant maximum and minimum displacements (δ_{max} and δ_{min} respectively). The value of δ_{max} was selected so that it would induce an initial G of approximately 75% of the experimental G_{Ic} ($\delta_{max} = 1.35$ mm), while the displacement ratio $R = \delta_{min}/\delta_{max}$ was fixed to 0.1.

During the test the crack length was monitored at intervals with the aid of a travelling microscope (magnification 15 times) and the grid marked on the side of the specimen. The corresponding number of cycles (N) and the maximum and minimum loads (P_{max} and P_{min} respectively) were also recorded, and the resulting sets of experimental data ($P^i_{max}, P^i_{min}, N_i, a_i$) were then analysed according to the methods described in Chapter 5 (section 5.6) to obtain da/dN versus G_{max} (or ΔG) plots. Once no further crack growth was observed, the test was stopped and the samples broken apart quasi-statically in mode I. The fracture surfaces were then visually inspected and the type of failure noted.

4.4.3.2.2 Mode II: 3ENF Test Specimen

The three point End Notched Flexure Test (ENF) geometry, was used to characterize the fatigue behaviour of AF163-2 in mode II. This configuration was chosen over the ELS for various reasons, despite the latter having proven less problematic in quasi-static tests. Firstly it would require smaller applied displacements, which not only makes the substrates less likely to yield or fail, but was also highly advantageous when using servo-hydraulic systems. Furthermore, it eliminates potential inertial effects associated with the movable fixture

Figure 4.22 shows the dimensions (in mm) of the specimens tested. Manufactured in accordance to the procedure described in section 4.3 using 8mm thick Ti-alloy beams

anodised beforehand, these joints incorporated Al-alloy end-blocks for an initial mode I pre-cracking stage. After propagating the crack approximately 5mm from the end of the PTFE insert the end-blocks were removed and the samples transferred to the ENF fixture. Based on a typical three point bending rig, the fatigue version was solidly attached to the base of the Dartec machine and incorporated a pair of dowel pins and adjustable bolts at each end for positioning purposes (see Figure 4.23). It featured two round supports of diameter 10mm on which the specimens rested, while the load was applied at the centre point with a 10mm diameter round indenter. The total span length ($2L$) was fixed to 140mm, whereas the specimen was positioned so that the initial crack (measured from the centre of the closest support) was approximately 30mm (see Figure 4.22-b).

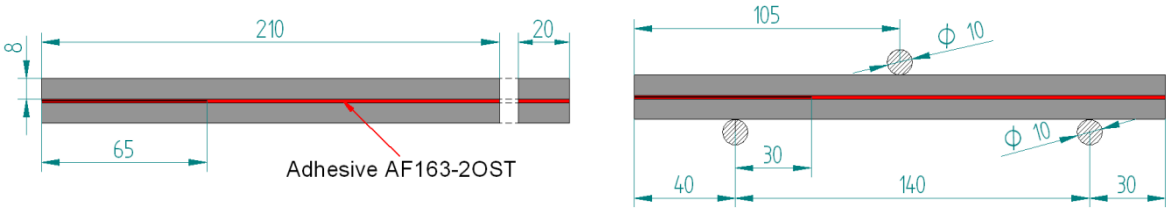

(a) (b)

Figure 4.22. Nominal dimensions (in mm) of the 3ENF fatigue test specimens (a) as manufactured and (b) after pre-cracking in mode I.

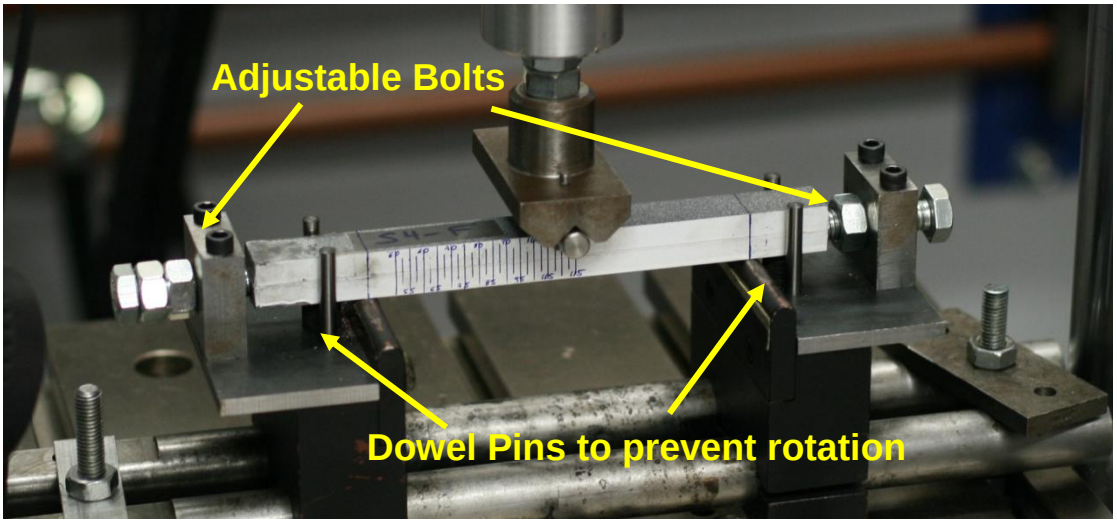

Figure 4.23. 3ENF fixture used in mode II fatigue tests.

Loading was applied in cyclic displacement control using a sinusoidal function with a frequency of 5Hz. The sample remained in compression during the entire fatigue cycle, hence the negative wave shown in Figure 4.24. As in mode I, the maximum and minimum displacements (δ_{max} and δ_{min} respectively) were maintained constant, with the ratio

$R = \delta_{min}/\delta_{max}$ being set to 0.1. Following an iterative process to ensure stable crack propagation, the value of δ_{max} was adjusted to 0.6mm (i.e. δ_{min}=-0.06mm in compression).

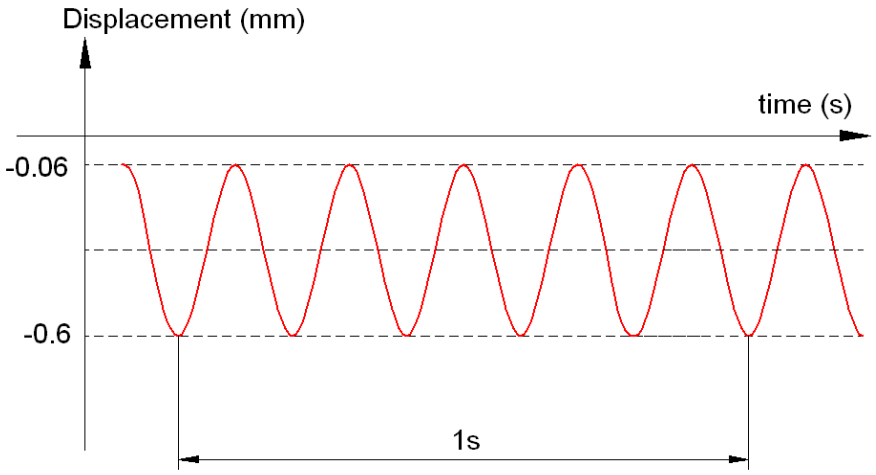

Figure 4.24. Schematic representation of the sinusoidal loading function used in the mode II fatigue tests (the negative displacement values represent compression).

For the duration of the test the maximum and minimum loads (P_{max} and P_{min}) were recorded at intervals together with the corresponding number of cycles (N) and crack length (a). Given the difficulties to distinguish between the end of the continuous crack and the damage ahead of its crack tip, both were monitored with the help of a travelling microscope. The cyclic loading was stopped once no further crack growth was observed and the adherends inspected for signs of plastic deformation. Next two aluminium end-blocks were re-attached and the joint loaded in mode I up to complete failure. The fracture surfaces were carefully examined and the type of failure noted. Plots of da/dN versus G_{max} (or ΔG) were obtained from the experimental data sets ($P^i_{max}, P^i_{min}, N_i, a_i$) using the analysis methods as will be described in Chapter 5.

4.4.3.3 Simplified Structure: Fatigue TDLJ

The accuracy assessment of the fatigue prediction methodologies presented in Chapter 3 was carried out by direct comparison with experimental data obtained for an independent geometry: the Ti-CFRP TDLJ. Consequently the structure described in section 4.4.2.3 was fatigued at different load levels and the resultant number of cycles to failure recorded to generate the required S-N curve. The characteristic threshold was also identified in this process.

Out of the three versions tested quasi-statically, only the configuration with a 45° chamfer angle was tested in fatigue. The predominantly cohesive failure obtained with this design in

the monotonically loaded experiments (as opposed to the combination of interlaminar, interfacial and cohesive fracture observed with 7° and 30° tapers) was the defining factor for this choice. The method employed to machine the tapers in the metallic substrates was improved to produce sharper ends, even though this resulted in slightly shorter lengths (134 instead of 150 mm). After the application of the surface treatment, the joints were manufactured according to the procedure described in section 4.3 in a single curing cycle. Figure 4.25 illustrates the final design, which was equivalent to that used in the quasi-static test except for the shorter length of the Ti arms. The excess adhesive was removed only from the central overlap, leaving it intact everywhere else to improve strength and prevent de-bonding of the end-tabs. The adhesive layer was examined under the optical microscope to measure the bondline thickness at various locations.

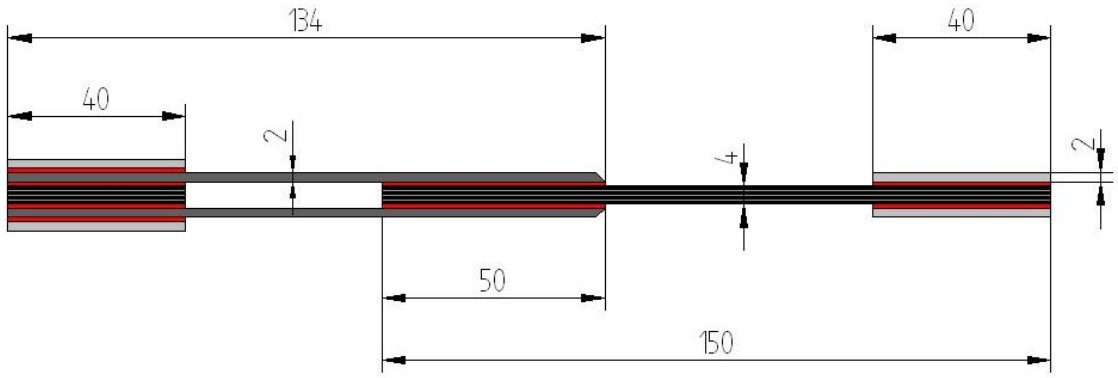

Figure 4.25. (a) Nominal dimensions (in mm) of the Ti-CFRP TDLJ tested in fatigue (the thickness of the various bond-lines – nominal value 0.4mm – has been exaggerated for illustration purposes.

The samples were then introduced into the servo-hydraulic grips fitted to the INSTRON machine used for these experiments. Their pressure was adjusted so that the compressive force exerted did not crush the CFRP substrate or spacer but at the same time provided enough friction to prevent slippage. Loading was applied in load-control employing a sinusoidal waveform with constant amplitude and a frequency of 5Hz. The ratio between the minimum and maximum stresses ($\sigma_{min}/\sigma_{max}$) was fixed at 0.1, while a number of maximum loads were investigated (50, 40, 30 and 20 kN). These conditions should make the crack growth rate data obtained with the fracture mechanics specimens directly applicable for the subsequent fatigue life-time predictions. The number of cycles to failure was recorded and the fracture surfaces carefully inspected for signs of interlaminar of interfacial crack growth. If no breakage or appreciable damage had occurred after 10 million cycles, the test was stopped and the load level assumed to be equal or below to the fatigue threshold. A minimum of three joints were tested for each load level.

4.5 Chapter Summary

This chapter has provided details of the adhesive and substrate materials employed in the present research. The different surface treatments applied prior to bonding have also been described. Finally, the experimental procedures followed to test the fracture mechanics specimens and the TDLJ both quasi-statically and in fatigue have been described.

The different data reduction schemes used to analyse the results of these experiments are discussed next, in Chapter 5.

5. Analysis Methods in Experimental Fracture Mechanics: Determination of the Adhesive Fracture Energy G_c

5.1 Introduction

The present chapter presents the data reduction schemes employed for the analysis of the results obtained with the various fracture mechanics specimens described in Chapter 4. Of those techniques introduced in the literature review for the determination of the critical strain-energy release rate, Berry's method [161] and three forms of the beam theory proposed by Williams [146] are applied to each type of joint. Three different decomposition strategies are considered for the study of mixed mode problems, namely: Williams' "global" approach and both the singular and non-singular versions of Davidson's technique. Finally, the secant and polynomial methods are presented as potential alternatives for the calculation of fatigue crack growth rates from the experimental data obtained in the cyclic tests.

5.2 Fracture Mechanics Specimens: Data Reduction Schemes

The load (P), displacement (δ) and corresponding crack length (a) were monitored during testing of the various fracture mechanics specimens described in Chapter 4. After applying suitable corrections for system compliance and initial non-linearity, the resulting sets of P_i-δ_i-a_i values were used to determine the relevant crack resistance curves (i.e. variation of G_c with the crack length).

As discussed in the literature review (section 2.3.2), it can be demonstrated that, if transverse shear effects were omitted, both the beam analysis proposed by Williams and Davidson's crack tip element would predict the same expressions for the total energy release rate when applied to the typical test geometries (see Appendix D). Considering this equivalence (i.e. $G_{Total}^{Williams} = G_{Total}^{Davidson}$) and bearing in mind that correction factors for large displacements, crack-tip rotations and the presence of end-blocks have already been derived for the former, Williams' has been the method of choice for the calculation of the total G_c in the various specimens investigated. Moreover, this option still offers the possibility to include shear effects, which could prove significant for certain joints depending on the crack-length-to-thickness ratios. Three different forms of this analysis were used, namely: simple beam theory (SBT), corrected beam theory (CBT) and corrected beam theory with effective crack length (CBTE). In addition, the experimental compliance method (ECM) was also implemented.

5.2.1 Initiation Criteria

Whenever possible, initiation values of the critical strain energy release rate ($(G_c)_{initiation}$) were determined and included in the resistance curves. Given the difficulties associated with its identification, several initiation criteria suggested in the relevant standards and protocols (see [164, 165, 190, 207]) were evaluated:

- **Deviation from linearity in the load-displacement trace (NL)**

  Often the load-displacement trace exhibits non-linear behaviour prior to the maximum load. In those cases the point of deviation from linearity (NL) can be used as an indication of crack initiation. Although such point would be typically determined by drawing a straight line from the origin (disregarding any initial deviations due to take-up or play in the loading system), it has been suggested that performing a linear regression of the P-δ trace starting at 5% of the maximum load may produce more consistent results [164, 165].

- **Visual Observation (VIS)**

  The point at which the crack tip is observed (through the travelling microscope) to move from its original position is marked in the P-δ trace and then employed to calculate $(G_c)_{initiation}$ using the various data reduction schemes mentioned above.

- **Maximum load point or 5% increase in compliance (MAX/5%)**

  Initiation is taken as whichever point occurs at a smaller displacement in the P-δ trace: the maximum load (MAX) or the load corresponding to a 5% increase in the initial compliance (5%). To determine the latter a best straight line is first drawn from the origin to calculate the initial compliance C_0 (ignoring any initial deviations), followed by a second line with compliance equal to $1.05 \cdot C_0$ whose intersection with the load-displacement curve defines the 5% point.

Note that except for the mode I tests, all the initiation values were determined using the crack lengths obtained after pre-cracking. Leaving aside any potential mixed mode effects in the asymmetric samples, all the pre-cracking procedures were equivalent and therefore the resulting tip conditions (i.e. sharpness) should be comparable.

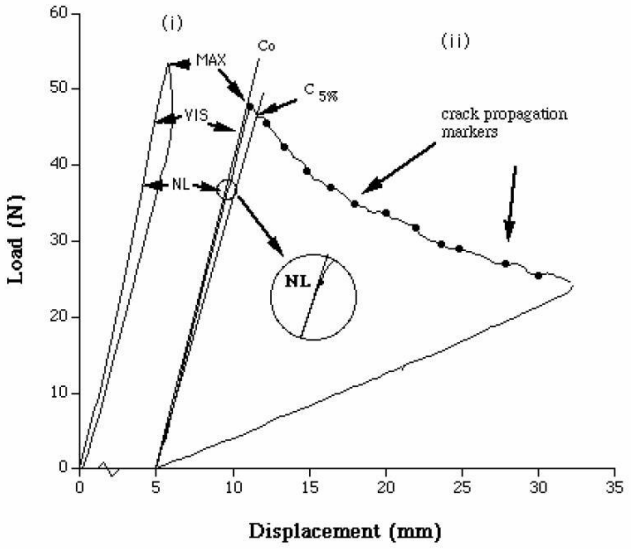

Figure 5.1. Schematic representation of the P-δ trace illustrating the three criteria for initiation (NL, VIS and MAX/5%) when (i) pre-cracking from the insert and (ii) testing from the pre-crack [164].

5.2.2 Mixed mode partitioning strategies: "Local" versus "Global" Approach

Despite the extensive literature devoted to the subject, which is the best mode decomposition strategy still remains an open question currently at the centre of a very intense debate among the fracture mechanics community. As highlighted in Chapter 2 (section 2.3.3), most experimental evidence to date seems to point to the ratio between the sizes of the singularity-dominated field and the damage zone ahead of the crack-tip as the parameter controlling the

range of applicability of the different partitioning strategies. Whilst local approaches (including FE techniques based on classical LEFM solutions such as the VCCT) tend to be more accurate for problems with small failure process zones, global methods have been proven more suitable when large scale plasticity or significant damage develops ahead of the crack tip. However, to the knowledge of the author no real attempt to establish the validity intervals of this parameter for the different methods has been carried out yet (apart from the preliminary work in [136]). This is partly because the size of these zones is very difficult to quantify both experimentally or analytically. Numerical simulations could undoubtedly help in this regard, but the assumptions made in the models (VCCT, shape of the traction-separation law for cohesive zone models, etc) could imply predisposition towards a specific partitioning scheme and hence compromise the results.

Nevertheless, it is extremely important to clarify this matter, especially taking into account the discrepancies between the existing approaches when any level of asymmetry (geometrical or in terms of material properties) is present in the problem. That is the nature of most real applications, particularly in the case of adhesively bonded joints, given their superiority over other mechanical techniques when it comes to joining dissimilar materials. The structure that motivated the present research project is just an example of this, but many other can be found in the literature. The same applies to debonding of protective layers or delamination in fibre composite materials, which typically have multidirectional configurations for optimal performance (i.e. the crack propagation path is hardly ever a symmetry plane).

Consequently, a number of methods have been evaluated here. Namely, Williams and Davidson's decomposition schemes (see [136, 137, 146, 147, 166] and [160, 162, 171, 172]) have been used to partition the critical strain energy release rates measured experimentally. Both singular and non-singular versions of Davidson's strategy (herein referred to as CTE/SF and CTE/NSF respectively) have been investigated. As a result the local approach proposed by Suo and Hutchinson [169, 170] has also been indirectly assessed, since its equivalence with CTE/SF has already been established in [172]. Even though some other theories have recently shown their potential (see Wang-Harvey [184-186]), these still remain as the most widespread methods. In addition, finite element models of the various fracture mechanics specimens tested have been created using the cohesive element described in Chapter 3. The mode mixity obtained in those simulations is compared with the analytical estimates in Chapter 8.

Finally, it is worth noting that both Davidson's and Williams' methods were originally conceived for delamination in fibre-reinforced composites. Thus the contribution of the bondline is neglected when these techniques are used in the study of adhesive joints. The

application of each data reduction scheme and partitioning strategy to the different test geometries employed in the present work is now described.

5.3 Determination of G_{Ic}: Analysis of the DCB and TDCB Test Specimens

The data reduction schemes for the mode I test geometries employed in this project are reviewed next. Probably the most popular fracture mechanics specimens for testing composite materials and adhesive joints, the DCB and TDCB have been among the first configurations to undergo standardization. The analysis methods described here are recommended in most standards [165, 190] and as a result are widely accepted.

Note that the analysis is restricted to the problems where the same material is used in both the upper and bottom substrates. Furthermore, given the disagreement between some of the main mode partitioning theories regarding the mode mix in the unbalanced case, only the symmetric configuration is considered at this point. The asymmetric specimen (ADCB) is discussed in more detail in section 5.5.2.

5.3.1 Double Cantilever Beam Test (DCB)

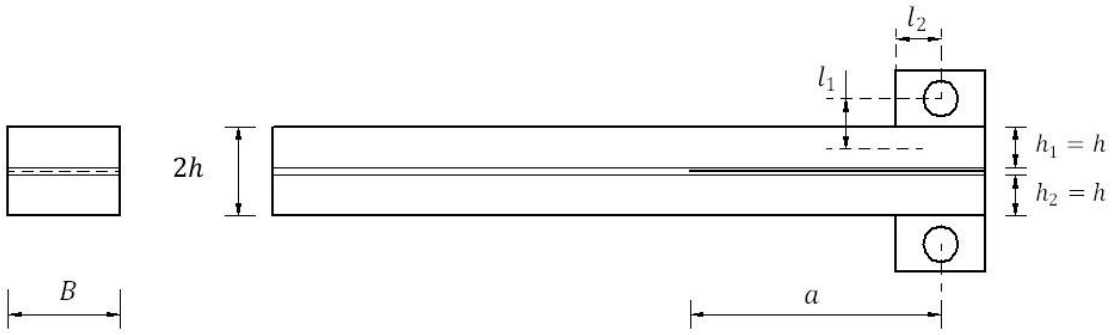

Figure 5.2. Schematic representation of the DCB test specimen (constant width, B).

5.3.1.1 Simple Beam Theory (SBT)

According to the shear corrected beam analysis proposed by Williams [146] (see section 2.3.3.1), the critical strain energy release rate for the DCB specimen illustrated in Figure 5.2 is given by:

$$G_{Ic} = \frac{12P^2a^2}{B^2E_sh^3}\left[1 + \left(\frac{1+\upsilon}{5}\right)\left(\frac{h}{a}\right)^2\right] \approx \frac{4P^2}{B^2E_s}\left[\frac{3a^2}{h^3} + \frac{1}{h}\right] \tag{5.1}$$

where B, h and E_s are the width, thickness and flexural modulus (in the longitudinal direction) of the substrates respectively, and the crack length a is measured from the loading point (see Figure 5.2). The compliance of the joint could then be determined by introducing the last result into the Irwin-Kies equation (2.11) and integrating with respect to the crack length (the integration constant C_{DCB}^0 would be obtained from beam analysis of a DCB specimen with no crack):

$$C_{DCB}^{SBT} = \int \frac{2B}{P^2} G_{Ic} da + C_{DCB}^0 = \frac{8\left(a^3 + 3\left(\frac{1+\upsilon}{5}\right)ah^2\right)}{BE_sh^3} \approx \frac{8(a^3 + ah^2)}{BE_sh^3} \tag{5.2}$$

5.3.1.2 Corrected Beam Theory (CBT)

Even though the SBT described above includes the deformation in the substrates due to shear stresses, it neglects deflections at the crack tip. As shown in [375, 376], extending the measured crack length by an amount Δ_I is a practical way to model both transverse shear and root rotation effects in DCB specimens:

$$C_{DCB}^{CBT} = \frac{8(a + \Delta_I)^3}{BE_sh^3} \cdot N_v \tag{5.3}$$

The correction factor N_v accounts for the influence of the loading end-blocks, which stiffen the substrates and induce reductions in the bending arms as they rotate. Δ_I can be estimated experimentally as the negative intercept of a plot of $(C/N_v)^{\frac{1}{3}}$ versus the measured crack length a. However, analytical approximations have been derived for isotropic and orthotropic materials using beam-on-elastic foundation models (see [375, 377]):

$$\Delta_{\mathrm{I}} \approx \chi h = \left(\frac{E_{11}}{11G_{12}}\right)^{\frac{1}{2}}\left[3 - 2\left(\frac{1.18\sqrt{E_{11}E_{22}}}{G_{12} + 1.18\sqrt{E_{11}E_{22}}}\right)^2\right]^{\frac{1}{2}} h \tag{5.4}$$

Differentiating (5.3) and substituting in the Irwin-Kies equation (2.11) would result in the CBT expression of G_{Ic}. Note that, if not known accurately, the flexural modulus could be eliminated using the compliance ($C = \delta/P$).

$$G_{Ic} = \frac{12P^2(a+\Delta_I)^2}{B^2E_sh^3}\cdot F_v = \frac{3P\delta}{2B(a+\Delta_I)}\cdot\frac{F_v}{N_v} \tag{5.5}$$

Further geometry changes (i.e. shortening of the bending arms) caused by large displacements are taken into account via the correction factor F_v. General expressions for F_v and N_v were derived by Williams [166, 378] using large deflection beam theory and can be found in Appendix E.

5.3.1.3 Corrected Beam Theory with Effective Crack Length (CBTE)

Initially proposed by Blackman et al. [139, 141] for the analysis of mode II fracture, this data reduction scheme is not included in the mode I standards [165, 190]. However, it has been applied to the study of DCB joints before [379, 380], and it is incorporated here for consistency. Taking equation (5.3) as a starting point, this method uses the experimental compliance values (corrected for end-block effects via N_v if necessary) to compute the effective crack length a_e:

$$a_e = a + \Delta_I = \frac{h}{2}\left(E_sB\frac{C}{N_v}\right)^{\frac{1}{3}} \tag{5.6}$$

Substituting into (5.5):

$$G_{Ic} = \frac{12P^2{a_e}^2}{B^2E_sh^3}\cdot F_v \tag{5.7}$$

Despite requiring previous knowledge of the flexural modulus, the last result is independent of the measured crack length. This could prove advantageous given the difficulty in identifying the true crack-tip position. Although the uncertainties in crack length measurements are typically associated with mode II and mixed mode problems, they could also lead to significant errors in mode I tests when a large damage zone develops ahead of the crack tip [380].

5.3.1.4 Experimental Compliance Method (ECM)

The results of the DCB tests have been also analysed using Berry's method, assuming a power-law compliance function of the form:

$$C = \mu a^n \tag{5.8}$$

where n and μ are empirically determined constants identified as the slope and origin ordinate of a plot of $log(C)$ versus $log\,(a)$ (excluding initiation data points from the regression analysis) respectively. Differentiating, eliminating μ and substituting into Irwin-Kies equation (2.11) leads to:

$$G_{Ic} = \frac{nP\delta}{2Ba} \cdot \frac{F_v}{N_v} \tag{5.9}$$

Contrasting with the CBTE, the experimental compliance method does not require information on the flexural modulus of the substrates but relies heavily on the crack length measurements, which could prove problematic when non self-similar or unstable crack propagation occurs.

5.3.1.5 Back-calculated Modulus

The flexural modulus of the substrates may be back-calculated from simple shear corrected beam theory and CBT equations, and the obtained value (E_e) used as a cross-check for the accuracy of the experimental results:

$$E_e = \frac{8(a^3 + ah^2)}{Bh^3(C/N_v)} \tag{5.10}$$

$$E_e = \frac{8(a + \Delta_I)^3}{Bh^3(C/N_v)} \tag{5.11}$$

According to [133], if the computed modulus varied significantly (>10%) with the crack length, the validity of the fracture energy estimates should be re-examined. Substantial discrepancies between the back-calculated and the independently measured values would also call for reassessment of the results.

5.3.2 Tapered Double Cantilever Beam Test (TDCB)

As initially suggested in [113], the profile of the tapered double cantilever beam (TDCB) substrates is selected so that the term in brackets in equation (5.1) (referred to as m_b)

remains constant for any crack length. A value of $m_b = 2\text{mm}^{-1}$ was chosen for the joints tested in the present work project.

$$m_b = \frac{3a^2}{h^3} + \frac{1}{h} = \text{constant} = 2\text{mm}^{-1} \tag{5.12}$$

Not only does the resulting shape produce a constant value of dC/da , but it also allows testing of tough adhesive systems employing substrate materials with relatively low yield stresses while fulfilling the LEFM requirements (i.e. without the arms deforming plastically).

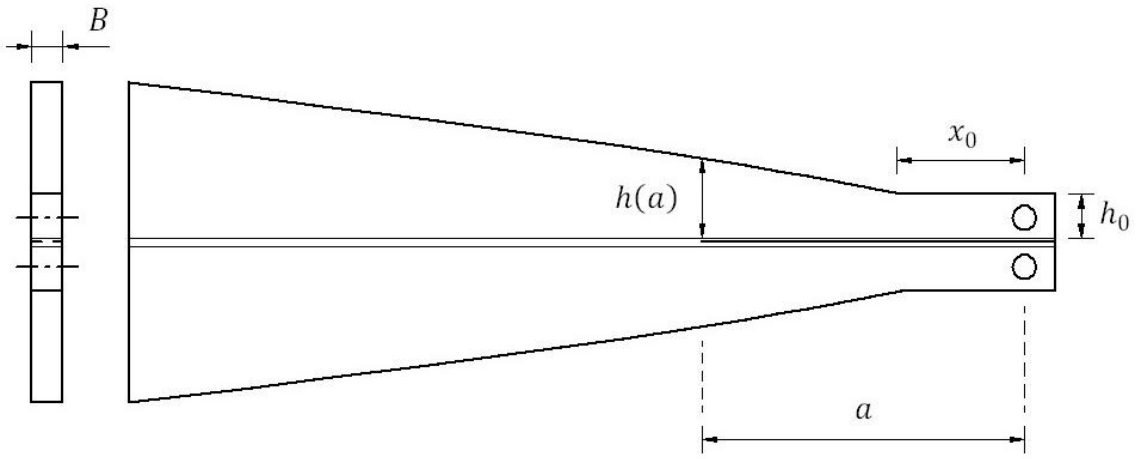

Figure 5.3. Schematic representation of the TDCB test specimen (constant width, B).

5.3.2.1 Simple Beam Theory (SBT)

Considering the profile of the metallic substrates, the mode I fracture energy could be easily determined from the loads measured during the test of the adhesive joint:

$$G_{Ic} = \frac{4P^2 m_b}{B^2 E_s} \tag{5.13}$$

The compliance would then vary linearly with the crack length:

$$C_{TDCB}^{SBT} = \frac{8 m_b a}{B E_s} \tag{5.14}$$

5.3.2.2 Corrected Beam Theory (CBT)

Despite allowing for the contribution of transverse shear stresses, the SBT assumes built-in conditions at the crack tip. Furthermore, it presumes profiled substrates (i.e. m_b=constant) from the loading point as opposed to the typical joint design illustrated in Figure 5.3, which exhibits an initial straight section of height h_o and length x_0. The corrected version of the beam analysis tries to resolve these shortcomings: while the influence of the real shape on the compliance is accounted for using the expression proposed by Blackman et al. [134], the effects of both shear deformation and beam root rotation are modelled as an extension Δ in the crack length (taken here as $\Delta \approx 0.64h$ following Kanninen´s work [377]). The resulting compliance would be given by:

$$C_{TDCB}^{CBT} = \frac{8m_b}{BE_s}\left[a + 0.64\left(\frac{3}{m_b}\right)^{1/3} a^{2/3} - \frac{2}{3}x_0\right] \tag{5.15}$$

Differentiating (5.15) and substituting into (2.11):

$$G_{Ic} = \frac{4P^2 m_b}{B^2 E_s}\left[1 + 0.43\left(\frac{3}{m_b a}\right)^{1/3}\right] \tag{5.16}$$

Note that, according to (5.15) the original shape of the TDCB substrates would not produce a constant value of dC/da. Evidently equation (5.12) could be modified to incorporate the contribution of root rotation as suggested in [134], although that option has not been explored in the present work.

5.3.2.3 Experimental Compliance Method (ECM)

Berry's method was implemented assuming a linear variation of the compliance with the crack length:

$$C = \mu a \tag{5.17}$$

where μ could be determined as the slope of the line of best fit to the experimental $C - a$ propagation data. Differentiating and introducing the result into the Irwin-Kies equation:

$$G_{Ic} = \frac{P\mu}{2B} \tag{5.18}$$

5.3.2.4 Back-calculated *dC/da*

In the same way that the back-calculated modulus served as a cross-check for the results obtained with the DCB specimens, the value of dC/da determined from the CBT equations could be used for validation purposes in the TDCB case:

$$\frac{dC}{da} = \frac{8m_b}{BE_s}\left[1 + 0.43\left(\frac{3}{m_b a}\right)^{1/3}\right] \tag{5.19}$$

5.4 Determination of G_{IIc}: Analysis of the ELS and 3ENF Test Specimens

In contrast to mode I problems, where the DCB (tapered or not) is widely accepted, there is no clear consensus yet on what is the best configuration for mode II testing of adhesive joints. As reviewed in Chapter 2 (section 2.3.4) a number of geometries have been proposed in the literature, two of which were considered for the present work: the end-loaded split (ELS) and the end-notched flexure (ENF) specimens. Fatigue characterization was carried with the latter using thick titanium substrates, whereas ELS specimens with CFRP substrates were preferred for the quasi-static tests due to their superior stability.

The same data reduction schemes introduced for mode I joints were applied to the in-plane shear specimens. However, in this case the effective crack length approach was openly favoured over the others given the significant difficulties in accurately measuring the crack length in these tests. Substantial damage often develops ahead of mode II cracks, making it very difficult to locate the position of the true crack tip [139]. As before, the analysis presented here is restricted to the symmetric case, in terms of both geometry and substrate material. Furthermore, any friction effects have been neglected, thus accepting the measured or "apparent" values as the mode II fracture energies.

5.4.1 End Loaded Split Test (ELS)

Figure 5.4 shows a schematic representation of the ELS geometry. One end of the specimen is constrained in the vertical direction but free to slide horizontally, while at the opposite side

the load is applied vertically (upwards) through an end-block. Since the loading point is free to rotate and both arms experience the same curvature, pure shear conditions are achieved at the crack tip.

The ESIS TC4 protocol for mode II delamination in fibre-composites [164] has been taken as reference for the analysis presented next. However, as stated in [141] those methods are applicable to adhesive joints under the assumption of thin bond-lines provided that the stiffness of the substrates is much greater than the elastic modulus of the adhesive.

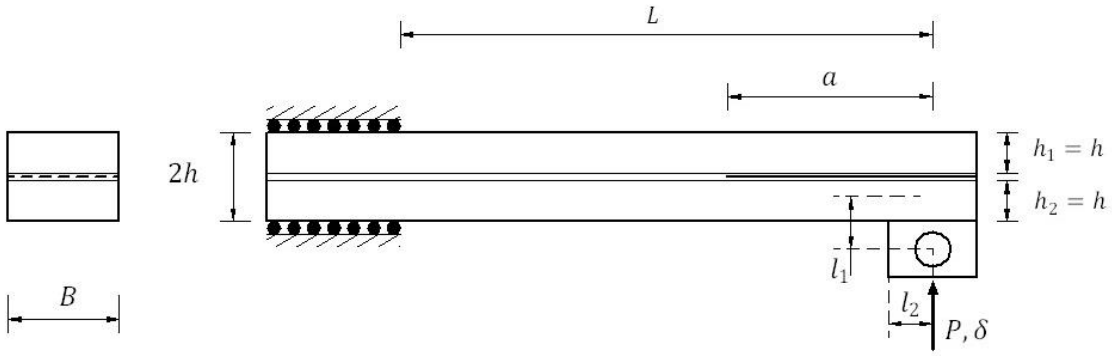

Figure 5.4. Schematic representation of the ELS test specimen and applied loading (width, *B*).

5.4.1.1 Simple Beam Theory (SBT)

A direct application of Williams´ beam analysis to the ELS geometry would yield the following mode II critical strain energy release rate:

$$G_{IIc} = \frac{9P^2a^2}{4B^2E_sh^3} \tag{5.20}$$

The compliance can then be easily obtained by introducing the last result into the Irwin-Kies equation (2.11) and integrating with respect to the crack length. Unlike the mode I cases, the integration constant for the ELS is not zero but instead depends on the free length L, and can be determined from the analysis of an ELS with no crack:

$$C_{ELS}^{SBT} = \int \frac{2B}{P^2} G_{IIc} da + C_{ELS}^0 = \frac{3a^3 + L^3}{2BE_sh^3} \tag{5.21}$$

5.4.1.2 Corrected Beam Theory (CBT)

Simple beam theory neglects the important contribution of transverse shear and beam root rotation at the crack tip. Furthermore, it assumes an infinitely stiff clamping arrangement when in reality small deflections occur at the clamping point. In line with the approach followed for the mode I tests, these factors are accounted for by increasing both the crack and free lengths. Initially Hashemi et al. [147] proposed a crack length extension equal to the theoretical mode I value (i.e. Δ_{II}=Δ_I=χh), whereas $2\Delta_I$was chosen for the free length:

$$C_{ELS}^{CBT} = \frac{3(a+\Delta_{II})^3 + (L+2\Delta_I)^3}{2BE_s h^3} \cdot N_v \tag{5.22}$$

where N_v allows for the contribution of the end-blocks [166] (see Appendix E). Subsequent refinements using finite element methods [381] suggested that, if the experimental mode I correction factor were available from a DCB test, a more appropriate value of Δ_{II} would be:

$$\Delta_{II} = 0.42\Delta_I \tag{5.23}$$

Blackman et al. [141] highlighted that the aforementioned correction for the free length could lead to important errors, suggesting its experimental determination via the "inverse ELS test" as a more suitable alternative. In the so-called clamp calibration process, a specimen is mounted in the ELS fixture so that its cracked section is fully held under the clamp. Using the same clamping conditions employed in the fracture tests, the joint is loaded elastically and the compliance recorded. The procedure is repeated for a number of free lengths and the results plotted on a graph of $(C/N_v)^{1/3}$ versus L. A linear regression is then performed and the clamp calibration factor Δ_{clamp} obtained as the intercept with the horizontal axis (see Figure 5.5).

$$\left(\frac{C_0}{N_v}\right)^{\frac{1}{3}} = \left(\frac{1}{2BE_s h^3}\right)^{\frac{1}{3}} L + \left(\frac{1}{2BE_s h^3}\right)^{\frac{1}{3}} \Delta_{clamp} \tag{5.24}$$

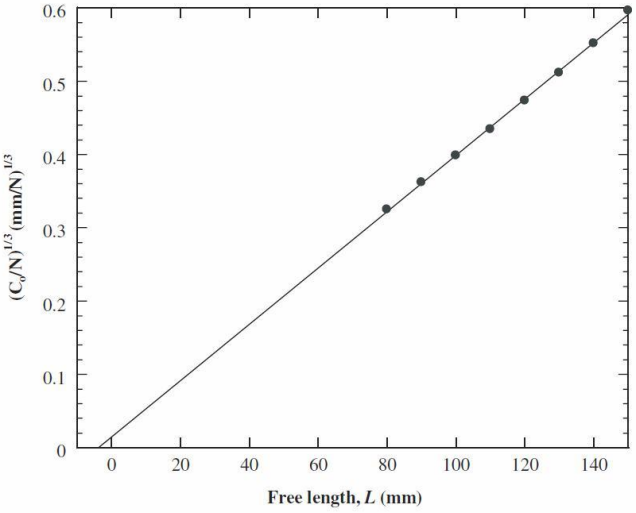

Figure 5.5. Typical clamp calibration data (values of $(C_0/N_v)^{1/3}$ versus L) [141].

If defined this way, not only would the clamp correction factor Δ_{clamp} take into account the finite stiffness of the specific rig, but it would also consider the severity of the clamping conditions (represented here by the applied torque) and the influence of the joint itself. Note that whether a clamp design is "stiff enough" for a particular test will very much depend on the thickness and elastic properties of the specimen to be tested. The compliance of the joint can then be written as:

$$C_{ELS}^{CBT} = \frac{3(a+\Delta_{II})^3 + \left(L+\Delta_{clamp}\right)^3}{2BE_s h^3} \cdot N_v \tag{5.25}$$

Equation (5.25) has been favoured throughout this work, reverting to the original expression (5.22) only when not enough experimental data were available. Differentiating and substituting into equation (2.11) leads to:

$$G_{IIc} = \frac{9P^2(a+\Delta_{II})^2}{4B^2E_s h^3} \cdot F_v \tag{5.26}$$

where the correction factor for large displacements F_v was derived in [166] and can be found in the Appendix E.

5.4.1.3 Corrected Beam Theory with Effective Crack Length (CBTE)

Taking equation (5.25) as a starting point, Blackman et al. [139, 141] proposed a data reduction scheme independent of the measured crack length. Instead, an "effective" value a_e

is computed from the experimental compliance data (corrected for the presence of the end-block if necessary) and introduced in (5.26) to determine the mode II fracture energy:

$$a_e = a + \Delta_{II} = \left(\frac{1}{3}\left[\left(2BE_s h^3 \frac{C}{N_v}\right) - \left(L + \Delta_{clamp}\right)^3\right]\right)^{\frac{1}{3}} \tag{5.27}$$

$$G_{IIc} = \frac{9P^2 {a_e}^2}{4B^2 E_s h^3} \cdot F_v \tag{5.28}$$

Even though it requires prior determination of the flexural modulus, this approach is often seen as the most accurate one of the four reviewed here. Hence it has been favoured over the others in the present work.

5.4.1.4 Experimental Compliance Method (ECM)

Despite the significant uncertainties associated with visual crack length measurements in mode II test, Berry´s method was also implemented for the analysis of the ELS specimens. Assuming a cubic relationship between the compliance and crack length,

$$C = C_0 + \mu a^n = C_0 + \mu a^3 \tag{5.29}$$

where the constants μ and C_0 are determined from a linear regression of the C versus a^3 data, the mode II fracture energy are then given by:

$$G_{IIc} = \frac{nP^2 a^2 \mu}{2B} \cdot F_v = \frac{3P^2 a^2 \mu}{2B} \cdot F_v \tag{5.30}$$

A Modified version of this technique using the effective crack lengths obtained from (5.27) instead of the experimental values has been proposed elsewhere (see [380]) in order to reduce its sensitivity to the crack length measurements. However, this option has not been pursued here.

5.4.1.5 Back-calculated Modulus

The flexural modulus of the specimen could be back-calculated from (5.25) and compared to an independently measured value (often determined from a three point bending test of the substrate material) as a cross-check for the soundness of the analysis.

$$E_e = \frac{3(a + \Delta_{II})^3 + \left(L + \Delta_{clamp}\right)^3}{2Bh^3(C/N_v)} \tag{5.31}$$

Additionally, a second value could be computed from the slope of the linear regression performed on the clamp calibration data (see equation (5.24)):

$$\left(\frac{C_0}{N_v}\right)^{\frac{1}{3}} = (slope)^{\frac{1}{3}}L + (slope)^{\frac{1}{3}}\Delta_{clamp} \;\longrightarrow\; E = \frac{1}{2Bh^3 \cdot slope^3} \tag{5.32}$$

In contrast to E_e, the modulus obtained from (5.32) does not serve as a cross-check but could be used in the determination of G_{IIc} if no other value were available.

5.4.1.6 Stability Criterion

For the simple case where the resistance curve is constant (i.e. does not vary with the crack length), Williams [146, 168] proposed the following stability criterion for systems under fixed displacement:

$$\left.\frac{dG}{da}\right|_{u\ constant} \leq 0 \;\longrightarrow\; \frac{1}{2}C\frac{d^2C}{da^2}\frac{1}{(dC/da)^2} \leq 1 \tag{5.33}$$

This condition, when applied to the ELS geometry, leads to:

$$a/L \geq 0.55 + 0.1(\chi h/L) \tag{5.34}$$

where χ depends on the elastic properties of the substrates and is defined in (5.4). This result played a major role in the selection of the initial crack and free lengths to ensure stable crack propagation.

5.4.2 End Notch Flexure Test (ENF)

A typical ENF specimen with a mid-plane crack is illustrated in Figure 5.6. Intrinsically prone to instability under quasi-static loading conditions [382, 383], the three point-bending version of the ENF test is often only useful for measuring mode II initiation values. However, it has been reported that this configuration could yield stable crack growth in fatigue if sufficiently small displacements are applied.

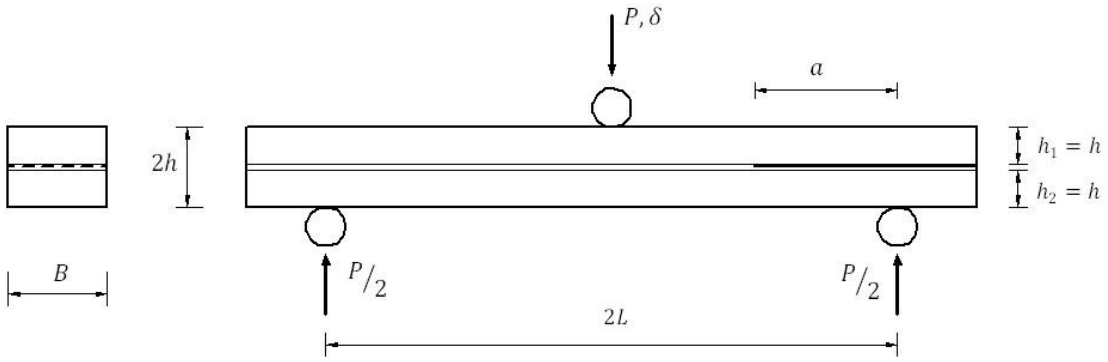

Figure 5.6. Schematic representation of the 3ENF test specimen and applied loading (width, *B*).

In the present work this geometry was mainly employed for in-plane shear fatigue characterization, although a reduced number of monotonically loaded tests were performed to measure the mode II initiation fracture energy. In any case G_{II} was computed according to the various data reduction schemes described next, even if the CBTE analysis was *a priori* considered the most accurate option.

5.4.2.1 Simple Beam Theory (SBT)

The beam theory method proposed by Williams predicts the following critical strain energy release rate for the loading configuration showed in Figure 5.6:

$$G_{IIc} = \frac{9P^2a^2}{16B^2E_sh^3} \tag{5.35}$$

Substituting this into (2.11) and integrating with respect to the crack length, the compliance of the joint becomes:

$$C_{3ENF}^{SBT} = \int \frac{2B}{P^2} G_{IIc} da + C_{3ENF}^{0} = \frac{3a^3 + 2L^3}{8BE_sh^3} \tag{5.36}$$

The term containing the half-span length (L) represents the compliance of an un-cracked joint and arises from the integration of the Irwin-Kies equation.

5.4.2.2 Corrected Beam Theory (CBT)

Following the same reasoning employed in the DCB and ELS cases, Hashemi et al. [147] corrected (5.36) for the effects of both shear and beam root rotation at the crack tip by

replacing the crack length for $a + \Delta_{II}$. Initially they proposed a crack extension equal to χh, but it was deemed unnecessary to modify the span length. Alternatively, Δ_{II} could be also determined from the mode I value as explained for the ELS geometry (see equation (5.23)).

$$C_{3ENF}^{CBT} = \frac{3(a + \Delta_{II})^3 + 2L^3}{8BE_s h^3} \cdot N_v \tag{5.37}$$

where N_v is a correction factor derived by Williams in [167] to account for the influence of large displacements on the compliance. Based on Timoshenko's beam theory Wang and Qiao [384] obtained a different expression for C which some authors have preferred (e.g. [380, 385]) over the Williams formulation as it incorporates higher order terms:

$$C_{3ENF}^{CBT} = \frac{3(a + \Delta_{II})^3 + 2L^3}{8BE_s h^3} + \frac{3L}{10G_{13}Bh} \tag{5.38}$$

Finally, differentiating (5.37) or (5.38) and substituting into (2.11) leads to:

$$G_{IIc} = \frac{9P^2(a + \Delta_{II})^2}{16B^2E_s h^3} \cdot F_v \tag{5.39}$$

5.4.2.3 Corrected Beam Theory with Effective Crack Length (CBTE)

To reduce the dependency on the measured crack length exhibited by the CBT analysis, an "effective" approach equivalent to that proposed by Blackman et al. [139, 141] for the ELS was also adopted for the ENF. In this scheme an "effective crack length" a_e is calculated from the experimental compliance and then used to determine G_{IIc}. Note that there are two possible definitions of a_e depending on the expression assumed for the compliance:

$$a_e = a + \Delta_{II} = \begin{cases} \left(\frac{1}{3}\left[\left(8BE_s h^3 \frac{C}{N_v}\right) - 2L^3\right]\right)^{\frac{1}{3}} & \text{or} \\ \left(\frac{1}{3}\left[\left(8BE_s h^3 \left(C - \frac{3L}{10G_{13}Bh}\right)\right) - 2L^3\right]\right)^{\frac{1}{3}} \end{cases} \tag{5.40}$$

Both expressions, the first one extracted from Williams beam theory and the second one corresponding to Timoshenko theory, lead to:

$$G_{IIc} = \frac{9P^2 {a_e}^2}{16B^2 E_s h^3} \cdot F_v \tag{5.41}$$

where F_v allows for large displacements (see [167]) and is given in Appendix E together with N_v.

5.4.2.4 Experimental Compliance Method (ECM)

A compliance calibration analysis method was also implemented for the ENF geometry presuming a cubic relationship between the compliance and measured crack length:

$$C = C_0 + \mu a^n = C_0 + \mu a^3 \tag{5.42}$$

where the constants μ and C_0 are the slope and origin ordinate resulting from a linear regression of C versus a^3 respectively. Differentiating and substituting into equation (2.11) gives:

$$G_{IIc} = \frac{nP^2 a^2 \mu}{2B} \cdot F_v = \frac{3P^2 a^2 \mu}{2B} \cdot F_v \tag{5.43}$$

5.4.2.5 Back-calculated Modulus

Using the CBT equations, it is possible to back-calculate the flexural modulus of the substrates:

$$E_e = \frac{3(a + \Delta_{II})^3 + 2(L + \Delta_l)^3}{8Bh^3(C/N_v)} \tag{5.44}$$

This value could serve as a cross check for the accuracy of the analysis, but unfortunately does not eliminate the need for an independent measurement (usually via a three point bending test of the substrates). In contrast, Moura and Morais [385] suggested the calculation of an apparent longitudinal modulus from the initial measured compliance and crack length which could actually be used leading to G_{IIc}. This technique was not used in the present work, as some uncertainty on the actual value of the initial crack length exists after pre-cracking in mode I.

5.4.2.6 Stability Criterion

Finally, according to (5.33), the condition for stable crack propagation in the ENF test could be expressed as (see [147]):

$$a/L \geq 0.69 - (\chi h/L) \tag{5.45}$$

5.5 Determination of $G_{I/IIc}$: Analysis of the AFRMM and ADCB Test Specimens

Very rarely does failure in bonded joints occur under pure mode loading conditions. Crack growth under a combination of opening and shear modes is more realistic, thus making it necessary to characterize the mixed mode behaviour of the adhesive. Even though several alternatives have been proposed over the years for mixed-mode I/II testing (see section 2.3.4.3), the fixed ratio mixed mode (FRMM) specimen is a convenient choice to complement the results obtained with the DCB and ELS geometries. However, extrapolating the entire failure envelope from only three data points (corresponding to pure modes I and II and a single mode-mix) may lead to significant errors. Consequently various ratios should be tested to improve the accuracy of any subsequent predictions. A range of mode mixities can be obtained with the asymmetric FRMM (AFRMM) by altering the relative thickness of the substrates, even if this brings up the question of which is the most appropriate partitioning theory. As mentioned in section 5.2.2, most decomposition schemes predict the same mode mix for the symmetric specimens, but often disagree on the unbalanced cases. Similarly, additional points of the curve $G_c = G_c(G_{II}/G)$ could be obtained from asymmetric DCB (ADCB) specimens. Yet again the mixed mode ratio of these joints is still an active research debate.

The application of the most common data reduction schemes to these geometries is presented next. The determination of the total energy release rate is based on three variations of the Williams beam analysis (i.e. SBT, CBT and CBTE) and a compliance calibration (ECM), whereas three different mode decompositions are investigated: the global method proposed by Williams and both singular and non-singular field versions of Davidson's partitioning scheme. As before the effective crack length approach is *a priori* favoured over the other techniques, especially as the mode II component increases.

5.5.1 Asymmetric Fixed Ratio Mixed Mode (AFRMM)

The AFRMM test uses the same loading fixture described for the ELS (clamping arrangement free to slide horizontally and fixed load-point) but, as Figure 5.7 illustrates, only one arm is loaded via an end-block. This results in specimens with virtually constant mixed mode ratios regardless of the crack length (although rigorous analysis [204] shows that small variations appear between very small and large cracks).

Given the lack of standards for this particular test configuration, the ESIS TC4 protocol for mixed mode [207] has been taken as a reference despite only covering the symmetric case. The extensive work published on the subject by Kinloch et al. [137] and Hashemi et al. [147, 175] has been also carefully considered. However these publications focus primarily on delamination in fibre-composites. Therefore the applicability of their results to adhesive bonded joints is restricted to problems with thin bond-lines where the modulus of the adhesive is negligible compared to the stiffness of the substrates.

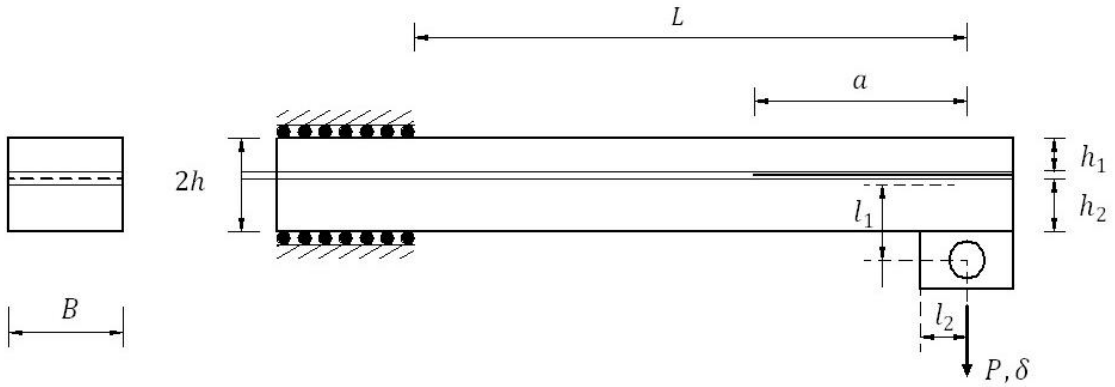

Figure 5.7. Schematic representation of the AFRMM test specimen (width, *B*) for the cases in which the the lower arm(thickness h_2) is loaded.

In the subsequent analysis, corresponding to the case where the thickness of the loaded beam is h_2, all the equations are written in terms of the thickness ratio α, defined as

$$\alpha = \frac{h_2}{h_1} = \frac{LOADED\ ARM}{UNLOADED\ ARM} \tag{5.46}$$

Nevertheless, exactly the same relationships would be obtained for the complementary case if α was interpreted as the quotient between the thickness of loaded and unloaded substrates (see Appendix D).

5.5.1.1 Simple Beam Theory (SBT)

Direct application of the beam analysis proposed by Williams [146] to the AFRMM geometry would yield the following expression of the total critical strain energy release rate:

$$G_{I/IIc} = \frac{3P^2a^2}{4E_sB^2h^3}\left[\left(\frac{(1+\alpha)^3-\alpha^3}{\alpha^3}\right)+\frac{4}{3}\frac{1}{\alpha}\left(\frac{h}{a}\right)^2\right] \approx \frac{3P^2a^2}{4E_sB^2h^3}\left[\frac{(1+\alpha)^3-\alpha^3}{\alpha^3}\right] \tag{5.47}$$

Note that the term arising from the transverse shear stresses is henceforth neglected since $(h/a) \ll 1$ for all the tests carried out. This is also necessary to perform a realistic comparison between the Davidson and Williams partitioning theories as the plate theory used in the former cannot account for this contribution. The corresponding mode I and II components (G_{Ic}^{mixed} and G_{IIc}^{mixed} respectively) would be expressed as:

$$\begin{cases} G_{Ic}^{mixed} = G_{I/IIc}\cdot\left(1-\Phi(\alpha)\right) \\ G_{IIc}^{mixed} = G_{I/IIc}\cdot\Phi(\alpha) \end{cases} \tag{5.48}$$

where $\Phi(\alpha)$ defines the mixed mode ratio (mode II component over total fracture energy, i.e. G_{II}/G) and depends on the thickness parameter α and the decomposition strategy considered. The expressions corresponding to the Williams and Davidson methods can be found in section 5.5.1.7.

The compliance for the AFRMM specimen can be obtained introducing (5.47) into the Irwin-Kies equation and integrating with respect to the crack length (once more the integration constant is determined from the analysis of an un-cracked joint and depends on the free length):

$$C_{AFRMM}^{SBT} = \int \frac{2B}{P^2}G_{I/IIc}da + C_{AFRMM}^{0} = \frac{1}{2BE_sh^3}\left[\left(\frac{(1+\alpha)^3-\alpha^3}{\alpha^3}\right)a^3+L^3\right] \tag{5.49}$$

5.5.1.2 Corrected Beam Theory (CBT)

As suggested in [207], in the corrected beam theory the crack length is extended by an amount Δ to rectify the built-in assumption made in the SBT. Different extensions are used to calculate the opening and shear components of the fracture energy though: while the mode I value Δ_I is preferably extracted from a DCB test, the shear term is taken as $\Delta_{II} = 0.42\Delta_I$. Additionally the free length is also increased to allow for any deflections and rotations at the clamping point.

$$C_{AFRMM}^{CBT} = \frac{1}{2BE_s h^3}\left[\left(\frac{(1+\alpha)^3-\alpha^3}{\alpha^3}\right)(a+\Delta)^3 + \left(L+\Delta_{clamp}\right)^3\right]\cdot N_v \tag{5.50}$$

where N_v takes into account the influence of the end-block on the compliance. Even though $2\Delta_{\mathrm{I}}$ could be employed as the free length correction factor [137, 147], a clamp calibration process equivalent to that proposed for the ELS configuration by Blackman et al. [141] is preferred here. As described in section 5.4.1.2, the experimental compliance measured for different free lengths with an un-cracked specimen would be used to plot a graph $(C_0/N_v)^{1/3}$ versus L, and Δ_{clamp} taken as the intercept with the L-axis after a linear regression:

$$\left(\frac{C_0}{N_v}\right)^{\frac{1}{3}} = \left(\frac{1}{2BE_s h^3}\right)^{\frac{1}{3}} L + \left(\frac{1}{2BE_s h^3}\right)^{\frac{1}{3}} \Delta_{clamp} \tag{5.51}$$

Despite differing just marginally from the mode II value (at least theoretically), Δ_{clamp} should be calculated for each thickness ratio tested. The total fracture energy is then computed as the sum of the mode I and II components rather than differentiating (5.50) directly as a consequence of employing different crack length extensions for opening and in-plane shear modes:

$$\left.\begin{array}{l} G_{Ic}^{mixed} = \dfrac{3P^2(a+\Delta_{\mathrm{I}})^2}{4E_s B^2 h^3}\left[\dfrac{(1+\alpha)^3-\alpha^3}{\alpha^3}\right]\left(1-\Phi(\alpha)\right)F_v \\ G_{IIc}^{mixed} = \dfrac{3P^2(a+\Delta_{\mathrm{II}})^2}{4E_s B^2 h^3}\left[\dfrac{(1+\alpha)^3-\alpha^3}{\alpha^3}\right]\Phi(\alpha)F_v \end{array}\right\} \longrightarrow G_{I/IIc} = G_{Ic}^{mixed} + G_{IIc}^{mixed} \tag{5.52}$$

As usual F_v takes into account the shortening of the bending arms and rotations of the end-blocks caused by large displacements. Suitable expressions for both F_v and N_v were derived in [166] and can be found in the Appendix E.

5.5.1.3 Corrected Beam Theory with Effective Crack Length (CBTE)

Even if the uncertainties in the crack length measurement are less important in mixed mode than in pure shear, the effective approach proposed in [139, 141] has been also applied to the AFRMM problem. Therefore the crack length would be computed from the experimental compliance (corrected for the presence of the end-block):

$$a_e = a + \Delta = \left[\left(\frac{\alpha^3}{(1+\alpha)^3-\alpha^3}\right)\left[2BE_s h^3\frac{C}{N_v} + \left(L+\Delta_{clamp}\right)^3\right]\right]^{\frac{1}{3}} \tag{5.53}$$

Since in this case there are no issues with different values of Δ for each mode, the total fracture energy can be obtained by simply substituting a_e into (5.47) and introducing the correction factor F_v for large displacements. The individual components are calculated according to the various methods considered as described in section 5.5.1.1 as

$$G_{I/IIc} = \frac{3P^2{a_e}^2}{4E_sB^2h^3}\left[\frac{(1+\alpha)^3-\alpha^3}{\alpha^3}\right]\cdot F_v \longrightarrow \begin{cases} G_{Ic}^{mixed} = G_{I/IIc}\cdot\left(1-\Phi(\alpha)\right) \\ G_{IIc}^{mixed} = G_{I/IIc}\cdot\Phi(\alpha) \end{cases} \tag{5.54}$$

5.5.1.4 Experimental Compliance Method (ECM)

Berry's method has been also implemented for the AFRMM specimen assuming a cubic variation of the compliance with the crack length:

$$C = C_0 + \mu a^n = C_0 + \mu a^3 \tag{5.55}$$

where the constants C_0 and μ are experimentally determined from the appropriate regression on the propagation data. Differentiating and substituting into equation (2.11) (corrected with F_v) yields the critical strain energy release rate, which can then be partitioned into its pure mode components using the mixed mode ratio $\Phi(\alpha)$ predicted by the decomposition scheme considered:

$$G_{I/IIc} = \frac{nP^2a^2\mu}{2B}\cdot F = \frac{3P^2a^2\mu}{2B}\cdot F_v \longrightarrow \begin{cases} G_{Ic}^{mixed} = G_{I/IIc}\cdot\left(1-\Phi(\alpha)\right) \\ G_{IIc}^{mixed} = G_{I/IIc}\cdot\Phi(\alpha) \end{cases} \tag{5.56}$$

5.5.1.5 Back-calculated Modulus

The flexural modulus of the substrates could be back-calculated from the experimental compliance using equation (5.50):

$$E_e = \frac{1}{2Bh^3(C/N_v)}\left[\left(\frac{(1+\alpha)^3-\alpha^3}{\alpha^3}\right)(a+\Delta)^3 + \left(L+\Delta_{clamp}\right)^3\right] \tag{5.57}$$

This result could then be compared with the independently measured modulus for verification purposes. Should the difference between these values be significant (usually >10%), the validity of the fracture energy estimates would need to be re-examined. Additionally, a second modulus could be computed from the slope of the linear regression performed to

determine the clamp calibration factor (see equation (5.51)), but unlike E_e this value could be used in the analysis if necessary:

$$\left(\frac{C_0}{N_v}\right)^{\frac{1}{3}} = (slope)^{\frac{1}{3}}L + (slope)^{\frac{1}{3}}\Delta_{clamp} \;\longrightarrow\; E = \frac{1}{2Bh^3 \cdot slope^3} \tag{5.58}$$

5.5.1.6 Stability Criterion

Finally, according to (5.33) the condition for stable crack propagation in the AFRMM test would adopt the form:

$$a/L \geq \frac{\alpha}{1+\alpha}\left[\frac{(1+\alpha)^2(1+\alpha^3)}{2((1+\alpha)^2+3\alpha^4)}\right]^{\frac{1}{3}} \tag{5.59}$$

5.5.1.7 Mixed Mode Partitioning

The total fracture energy calculated for the AFRMM geometry with the data reduction schemes described above has been partitioned into its pure mode components according to the Williams and Davidson methods, represented in each case by the appropriate expression of $\Phi(\alpha)$.

If the influence of the transverse shear stresses is neglected, the global approach proposed by Williams predicts a mixed mode ratio independent of the crack length (see equation (2.25)):

$$\left.\frac{G_{II}}{G_I}\right|_{\text{Williams}}^{\text{AFRMM}} = \frac{3\alpha^4}{(1+\alpha)^2} \longrightarrow \Phi(\alpha)|_{\text{Williams}}^{\text{AFRMM}} = \frac{3\alpha^4}{3\alpha^4+(1+\alpha)^2} \tag{5.60}$$

Similarly, particularizing equation (2.28) for the AFRMM geometry would render the mode mix estimated by the Davidson method:

$$\Phi(\alpha)|_{\text{Davidson}}^{\text{AFRMM}} = \frac{\alpha^3}{(1+\alpha)^2[(1+\alpha)^3-\alpha^3]}\left[2\sqrt{3\alpha}\cos\Omega + \sqrt{\frac{(1+\alpha^3)(1+3\alpha)^2}{\alpha^3(1+\alpha)}}\sin(\Gamma+\Omega)\right]^2 \tag{5.61}$$

where

$$\sin\Gamma = \frac{\sqrt{3}(1-\alpha^2)}{2\sqrt{(1+\alpha)(1+\alpha^3)}} \tag{5.62}$$

Valid for either the singular or non-singular field versions of the analysis, equation (5.61) would only require the appropriate definition of the mixed mode parameter Ω in each case (see section 2.3.3.2). Nevertheless, while both Ω_{SF} and Ω_{NSF} are functions of α, only the former depends on the nature of the substrate materials. Davidson et al. [172] proposed general solutions of Ω_{SF} for the isotropic problem and various orthotropic materials, which were briefly discussed in Chapter 2 together with the CTE/NSF case [160, 162] (see sections 2.3.3.2.1 and 2.3.3.2.2).

Figure 5.8 illustrates the mode mix predicted for the AFRMM test by each partitioning scheme as a function of the thickness parameter α. Four different CTE/SF curves have been included, corresponding to the various substrate materials employed in the present work (i.e. titanium alloy and unidirectional CFRP laminates). The discrepancies between the solutions are evident, affecting not only the specific values of G_{II}/G estimated for a particular α but also the mixed mode range covered by this test configuration. Virtually any ratio could be achieved according to the global decomposition, with the $\alpha = 0$ representing pure mode I and the shear component rising as α increases (pure mode II would occur for $\alpha \to \infty$). On the other hand Davidson´s method predicts a more restricted range, which is even more limited in the case of singular field solution. However, they all agree for the symmetric case ($\alpha=1$) as had been anticipated:

$$\Phi(\alpha = 1) = \frac{3}{7} \approx 0.42857 \tag{5.63}$$

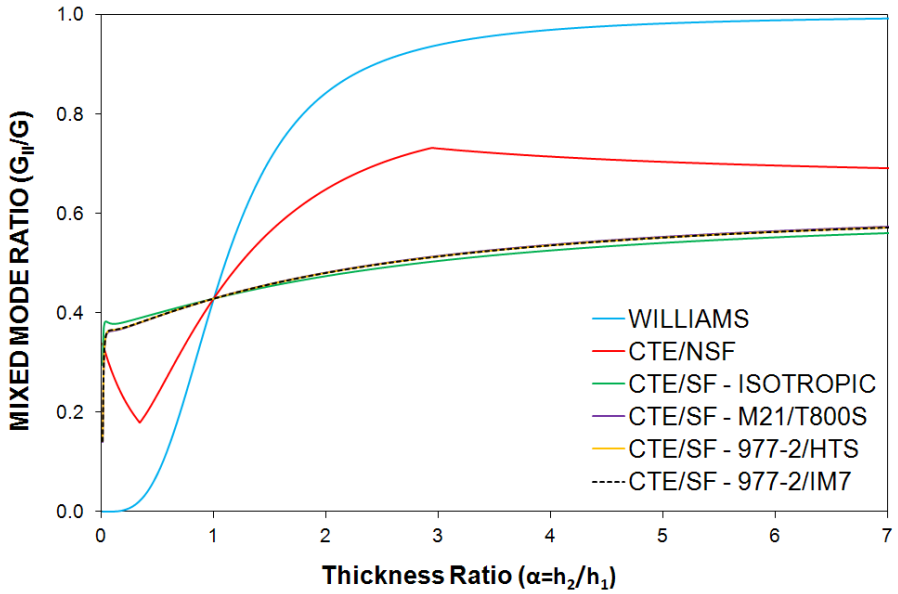

Figure 5.8. Mixed mode ratio predicted by the different partitioning methods for the AFRMM test specimen (load is applied to the substrate with thickness h_2).

5.5.2 Asymmetric Double Cantilever Beam Test (ADCB)

A schematic representation of the asymmetric double cantilever beam (ADCB) configuration is shown in Figure 5.9. This is a generalization of the conventional DCB test which uses substrates of different thicknesses (the case of dissimilar materials is not considered here). Hence it would render the same results presented in section 5.3.1 if $h_1 = h_2$. However, the mixed mode obtained with this specimen is still a matter of controversy: while both the LEFM solution containing a singularity at the crack tip and Davidson´s decomposition predict a mode mix which varies with $\alpha = h_2/h_1$ [203, 386], the global method always gives pure mode I [136, 175]. This issue has been investigated further using the experimental data obtained during the pre-cracking stage of the AFRMM joints. The usual reduction schemes (i.e. SBT, CBT, CBTE and ECM) and mode partitioning theories have been therefore implemented for this geometry.

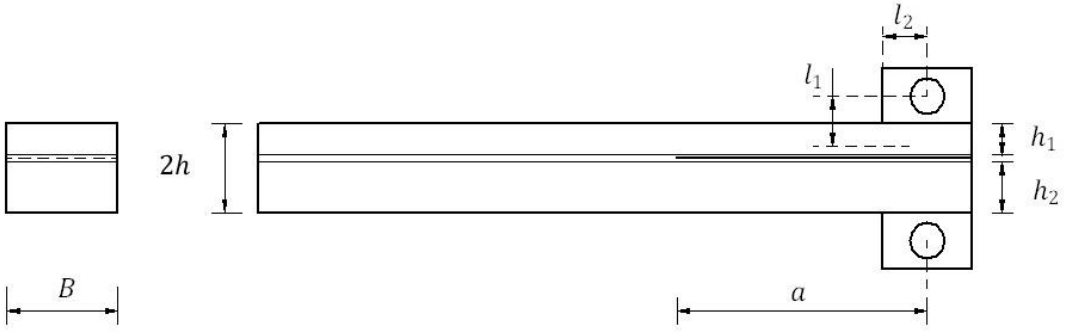

Figure 5.9. Schematic representation of the ADCB test specimen (width, B).

5.5.2.1 Simple Beam Theory (SBT)

The critical energy release rate for the ADCB configuration as predicted by Williams´ beam analysis [146] would be:

$$G_{I/IIc} = \frac{3P^2a^2}{4E_sB^2h^3}\left[\frac{(1+\alpha)^3(1+\alpha^3)}{\alpha^3} + \frac{4}{3}\frac{(1+\alpha)^2}{\alpha}\left(\frac{h}{a}\right)^2\right] \approx \frac{3P^2a^2}{4E_sB^2h^3}\left[\frac{(1+\alpha)^3(1+\alpha^3)}{\alpha^3}\right] \quad (5.64)$$

Bearing in mind that $(h/a) \ll 1$ in all the ADCB joints tested for the present project, the contribution of transverse shear stresses is neglected hereafter. The mode I and II components of the total fracture energy (G_{Ic}^{mixed} and G_{IIc}^{mixed} respectively) could be calculated using the mode mix $\Phi(\alpha) = G_{II}/G$ predicted by the different decomposition schemes (see section 5.5.2.6):

$$\begin{cases} G_{Ic}^{mixed} = G_{I/IIc} \cdot \left(1 - \Phi(\alpha)\right) \\ G_{IIc}^{mixed} = G_{I/IIc} \cdot \Phi(\alpha) \end{cases} \quad (5.65)$$

Introducing (5.64) into the Irwin-Kies equation (2.11) and integrating with respect to the crack length, the compliance of the ADCB specimen would result in:

$$C_{ADCB}^{SBT} = \int \frac{2B}{P^2} G_{I/IIc} da + C_{ADCB}^0 = \frac{1}{2BE_sh^3}\left[\frac{(1+\alpha)^3(1+\alpha^3)}{\alpha^3}\right]a^3 \quad (5.66)$$

5.5.2.2 Corrected Beam Theory (CBT)

Following the same approach described for the symmetric DCB configuration, both shear and beam root rotations at the crack tip in the ADCB specimen are modelled by increasing the measured crack length:

$$C_{AFRMM}^{CBT} = \frac{1}{2BE_sh^3}\left[\frac{(1+\alpha)^3(1+\alpha^3)}{\alpha^3}\right](a+\Delta)^3 \cdot N_v \quad (5.67)$$

where N_v accounts for the stiffening influence of the loading end-blocks, which also induce changes in the bending arms as they rotate. Instead of using different crack length extensions for each mode as suggested in section 5.5.1.2, a single value is estimated as the negative intercept of a plot of $(C/N_v)^{\frac{1}{3}}$ versus the measured crack length a.

$$G_{I/IIc} = \frac{3P\delta}{2B(a+\Delta)} \cdot \frac{F_v}{N_v} \rightarrow \begin{cases} G_{Ic}^{mixed} = G_{I/IIc} \cdot \left(1 - \Phi(\alpha)\right) \\ G_{IIc}^{mixed} = G_{I/IIc} \cdot \Phi(\alpha) \end{cases} \tag{5.68}$$

Once more F_v is a correction factor for large displacements. Note that due to the dissimilar bending stiffnesses, the entire joint tends to rotate towards the thinnest substrate. Consequently the bending arms shorten significantly, specially for the extremely unbalanced cases (i.e. $\alpha \gg 1$ or $\alpha \ll 1$). The use of suitable expressions for F_v and N_v is therefore essential to get accurate results (see Appendix E).

5.5.2.3 Corrected Beam Theory with Effective Crack Length (CBTE)

In order to minimize the uncertainties arising from the crack length measurements, equation (5.67) can be used to compute an effective value a_e from the experimental compliance:

$$a_e = a + \Delta = \left[\left(\frac{\alpha^3}{(1+\alpha)^3(1+\alpha^3)}\right) 2BE_s h^3 \frac{C}{N_v}\right]^{\frac{1}{3}} \tag{5.69}$$

The total fracture energy is obtained by simply substituting a_e into (5.64) (corrected for large displacements via F_v) and subsequently partitioned into its individual components:

$$G_{I/IIc} = \frac{3P^2 {a_e}^2}{4E_s B^2 h^3}\left[\frac{(1+\alpha)^3(1+\alpha^3)}{\alpha^3}\right] \cdot F_v \rightarrow \begin{cases} G_{Ic}^{mixed} = G_{I/IIc} \cdot \left(1 - \Phi(\alpha)\right) \\ G_{IIc}^{mixed} = G_{I/IIc} \cdot \Phi(\alpha) \end{cases} \tag{5.70}$$

5.5.2.4 Experimental Compliance Method (ECM)

Finally, Berry's method has been implemented assuming a power law relationship of the form:

$$C = \mu a^n \tag{5.71}$$

where n and μ are respectively the slope and origin ordinate of a logarithmic plot of the experimental compliance versus the crack length. Differentiating, eliminating μ and substituting into Irwin-Kies equation:

$$G_{I/IIc} = \frac{nP\delta}{2Ba} \cdot \frac{F_v}{N_v} \rightarrow \begin{cases} G_{Ic}^{mixed} = G_{I/IIc} \cdot \left(1 - \Phi(\alpha)\right) \\ G_{IIc}^{mixed} = G_{I/IIc} \cdot \Phi(\alpha) \end{cases} \tag{5.72}$$

5.5.2.5 Back-calculated Modulus

The flexural modulus of the specimen could be back-calculated from (5.67) and compared to the value obtained in a three point bending test as a cross-check for the soundness of the analysis.

$$E_e = \frac{(a+\Delta)^3}{2Bh^3(C/N_v)}\left[\frac{(1+\alpha)^3(1+\alpha^3)}{\alpha^3}\right] \tag{5.73}$$

5.5.2.6 Mixed Mode Partitioning

The total fracture energy obtained for the ADCB tests with the data reduction schemes described above has been partitioned into its mode I and II components according to the Williams and Davidson methods, represented in each case by the appropriate function $\Phi(\alpha)$.

Since in the ADCB configuration both arms are loaded with equal but opposite bending moments ($M_2 = -M_1 = Pa$), the global method proposed by Williams predicts pure mode I conditions regardless of the thickness ratio α [136].

$$\left.\frac{G_{II}}{G_I}\right|_{\text{Williams}}^{\text{ADCB}} = 0 \longrightarrow \Phi(\alpha)|_{\text{Williams}}^{\text{ADCB}} = 0 \tag{5.74}$$

Conversely, the application of equation (2.28) to this particular geometry results in a mixed mode ratio which varies with α:

$$\Phi(\alpha)|_{\text{Davidson}}^{\text{ADCB}} = \sin^2(\Gamma + \Omega) \tag{5.75}$$

where Γ is defined in (5.62) and the mixed mode parameter Ω depends not only on α but also on the conditions assumed at the crack tip. Whether the stresses in this region are dominated by a singularity or localized damage would determine the expression of $\Omega(\alpha)$, leading to the CTE/SF and CTE/NSF versions of the analysis respectively (see sections 2.3.3.2).

The variation of the mode mix with the thickness ratio α predicted for the ADCB geometry by each partitioning method considered is illustrated in Figure 5.10. Given that the solution of Davidson's CTE/SF partitioning depends on the nature of the substrate material, the curves corresponding to the titanium alloy and unidirectional CFRP laminates described in Chapter 4 have been included in the graph. Unsurprisingly all the partitioning schemes agree for the conventional DCB, whereas significant discrepancies arise for the unbalanced

problems. Moreover, the differences increase notably with the degree of the asymmetry. But even if Davidson's decomposition is accepted, the range of mixed mode ratios achievable with this type of specimen is much more limited than in the AFRMM case. For example, the maximum shear component estimated by the CTE/NSF is limited to a 34.5% of G as opposed to the 73.2% obtainable with the AFRMM. Furthermore, more extreme values of α are required to reach those values, making the ADCB test less attractive for mixed mode characterization. Nevertheless, it could potentially offer a very simple way to depict the near-mode I fracture behaviour of adhesive joints.

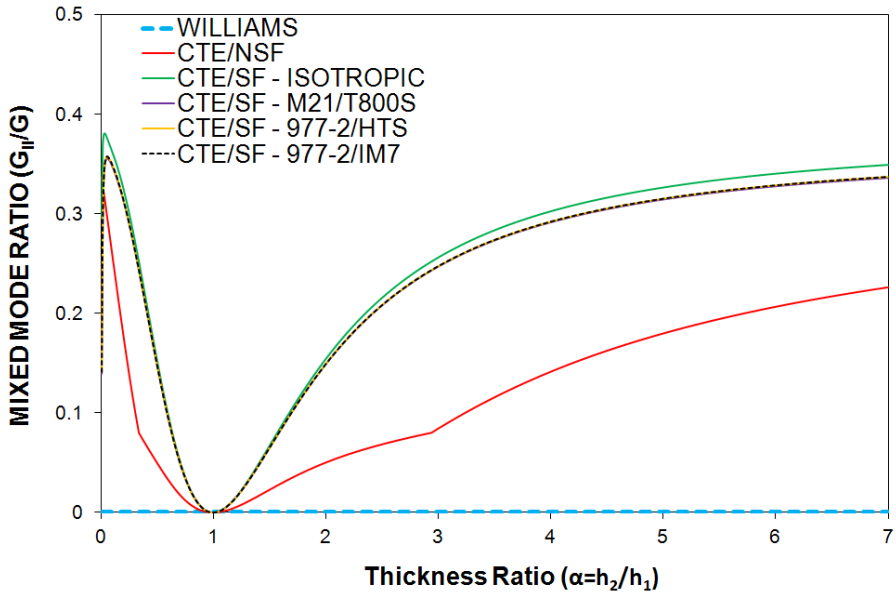

Figure 5.10. Mixed mode ratio predicted by the different partitioning methods for the ADCB test specimen.

5.6 Determination of *da/dN* vs. G_{max}: Analysis of the Fracture Mechanics Tests under Fatigue Loading Conditions

As described in Chapter 4 (section 4.4.3), the crack length (a), maximum load (P_{max}) and number of cycles (N) were recorded at intervals during the fatigue tests performed on fracture mechanics specimens. The resulting sets of data (P_{max_i}-a_i-N_i) would have to be subsequently converted into an expression relating the crack growth per cycle (da/dN) to the maximum applied strain energy release rate (G_{max}) in a fatigue cycle. Note that, since the displacement ratio $R = \delta_{min}/\delta_{max}$ remains constant, $\Delta G = G_{max} - G_{min}$ could be used instead of G_{max} to plot the crack growth rate data. Nevertheless, the original option is favoured here as facial interference could occur on crack closure during the unloading semi-cycle. Finally, the results are fitted to a modified Paris law and inputted into the cohesive element formulation detailed in Chapter 3 prior to carrying out any fatigue life-time predictions.

The values of G_{max_i} are calculated from the data sets P_{max_i}-δ_{max_i}-a_i using the various reductions schemes detailed in sections 5.3.1 and 5.4.1. However, the difficulties in measuring the crack length accurately in mode II left CBTE as the best analysis option for the ENF specimens. A number of techniques have been proposed to transform the a_i-N_i information into $(da/dN)_i$ points. Following the ASTM standard E647-08 [387], the most popular two are employed here: the secant and incremental polynomial methods.

5.6.1 The Secant Method

According to this technique the fatigue crack growth rate is calculated as the gradient of the straight line connecting two adjacent points in the $a - N$ curve:

$$\left.\frac{da}{dN}\right|_{\bar{a}_i} = \frac{a_{i+1} - a_i}{N_{i+1} - N_i} \tag{5.76}$$

Given that $(da/dN)_i$ is an average rate over the interval $[N_i, N_{i+1}]$, if this method is to be used the average crack length $\bar{a}_i$ and the corresponding maximum load $\overline{P_{max_i}}$ should be employed to compute G_{max_i}.

$$\bar{a}_i = \frac{a_{i+1} + a_i}{2} \tag{5.77}$$

5.6.2 The Incremental Polynomial Method

In this approach sets of $(2n+1)$ successive points of the $a-N$ curve (where n is typically equal to 1, 2, 3 or 4) are fitted to a second-order polynomial. The parabola for the local fit adopts the form:

$$\hat{a}_i = b_0 + b_1 \cdot \left(\frac{N_i - C_1}{C_2}\right) + b_2 \cdot \left(\frac{N_i - C_1}{C_2}\right)^2 \tag{5.78}$$

where

$$-1 \leq \left(\frac{N_i - C_1}{C_2}\right) \leq 1 \tag{5.79}$$

and b_0, b_1 and b_2 are the regression coefficients determined by the least square method over the range $a_{i-n} \leq a \leq a_{i+n}$. The parameters C_1 and C_2 are given by

$$C_1 = \frac{N_{i+\mathrm{n}} + N_{i-n}}{2} \tag{5.80}$$

$$C_2 = \frac{N_{i+\mathrm{n}} - N_{i-n}}{2} \tag{5.81}$$

The value of da/dN is calculated differentiating and particularizing at N_i, while the fitted crack size $\hat{a}_i$ is employed to compute the corresponding G_{max_i}.

$$\left.\frac{da}{dN}\right|_{\hat{a}_i} = \frac{b_1}{C_2} + 2 \cdot b_2 \cdot \frac{(N_i - C_1)}{(C_2)^2} \tag{5.82}$$

5.7 Chapter Summary

In this chapter, four different data reduction schemes to determine the adhesive fracture energy from the results obtained with the fracture mechanics specimens described in Chapter 4 have been discussed, namely: simple beam theory (SBT), corrected beam theory (CBT), corrected beam theory with effective crack length (CBTE) and the experimental compliance method (ECM). In addition, suitable expressions have been derived to partition the fracture energy measured with the AFRMM and ADCB test specimens into its individual components according to three widely-accepted mode decomposition strategies: Williams'

"global" approach and both the singular and non-singular versions of Davidson's technique (CTE/SF and CTE/NSF respectively). Finally, the secant and incremental polynomial methods have been proposed to compute the fatigue crack growth rate.

The results obtained after applying these techniques to the experimental data obtained in the test described in Chapter 4 are presented and discussed in Chapters 6 and 7.

6. Experimental Fracture Mechanics: Quasi-Static Test Results and Discussion

6.1 Introduction

For its use in the performance prediction of adhesively-bonded joints, the cohesive element formulation described in Chapter 3 requires a series of input parameters which must be determined experimentally. In particular, the present chapter focuses on the tests carried out to characterize the fracture behaviour of AF163-2 under quasi-static loading conditions. The results of the pure opening and in-plane shear tests are presented first, immediately followed by a discussion of those obtained with the AFRMM and ADCB specimens. In Chapter 7 these results will be employed to define a fracture criterion of the form $G_c = G_c(G_{II}/G)$, which will then be imported into the user element subroutine.

Figure 6.1 shows a summary of the various specimen types tested. Details on the substrate materials, manufacturing and testing procedures and analysis techniques can be found in Chapters 4 and 5 respectively.

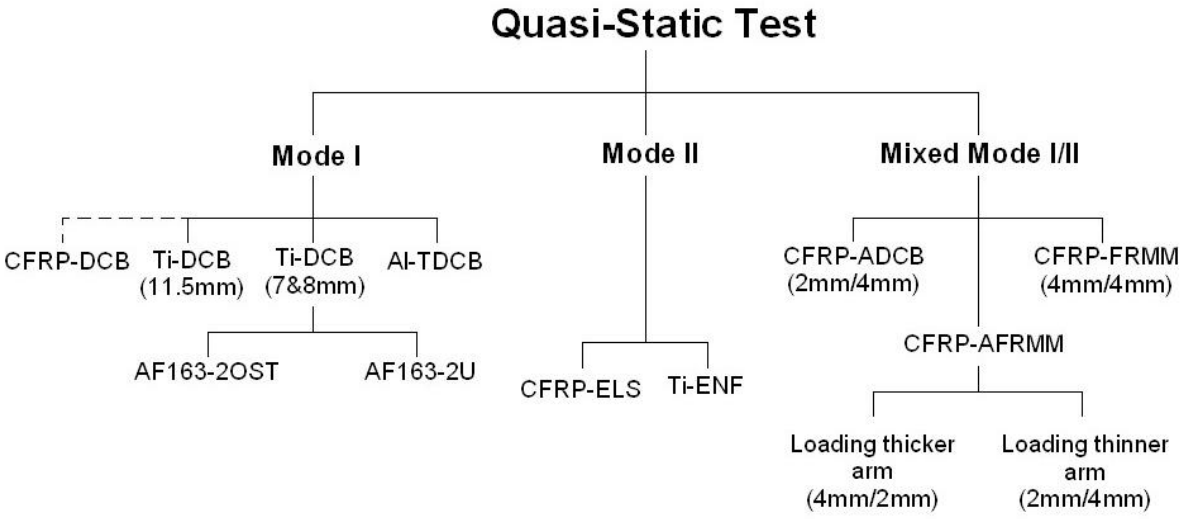

Figure 6.1. Schematic representation of the various types of specimens tested quasi-statically.

6.2 Mode I Fracture

6.2.1 Introduction

The importance of the mode I critical strain energy release rate, G_{Ic}, is more than justified from an engineering perspective. Associated with the most damaging type of loading for the interface, this value is used to characterize the performance of the entire adhesive system (i.e. adhesive + surface treatment) rather than just that of the adhesive. Bonded joints are typically designed to minimize the opening mode component and conservative predictions of their strength can be obtained using G_{Ic}. Furthermore, some authors [136, 137] maintain that crack propagation only occurs under pure mode I conditions (at least at the very local level), highlighting the significance of this property. The results obtained with the titanium DCB and aluminium TDCB specimens described in sections 4.4.2.2.1 (Chapter 4) are presented next. Additionally, these results are compared with the values of G_{Ic} previously measured within the group using DCB joints manufactured with unidirectional CFRP substrates (see [388]).

6.2.2 Titanium DCB Tests

Titanium DCB specimens were used to measure the mode I fracture toughness of both versions of AF163-2, namely the supported and unsupported film adhesives. In principle, only the value of G_{Ic} corresponding to the former (i.e. AF163-2OST) was required for the simulations. However, as discussed later in the chapter, questions regarding the potential

effects of the carrier mat arose after analysing the mixed mode data. In an attempt to clarify this issue further, a number of DCB tests were performed with AF163-2U towards the end of this project, the results of which are presented here alongside those obtained for AF163-2OST for comparison and clarity. Unfortunately, this study was limited to mode I due to time constraints, but the preliminary findings suggest the need for an in-depth investigation into this subject.

Manufactured according to the procedure described in section 4.3 after the substrates had undergone the relevant SHA surface treatment, the bondline thickness of all the joints was measured with the aid of an optical microscope and a micrometer prior to testing. Despite not appearing in the equations used to compute G_{Ic} (see Chapter 5), the bondline thickness had been previously shown to have a significant influence on the mode I fracture energy, particularly in rubber-toughened adhesives (e.g. [24, 129, 152], see section 2.3.1.4). Thus, maintaining a constant bondline thickness within the specimen itself and across the range of joints tested was essential to obtain consistent results. The average of the measured thickness was 0.44±0.09 mm for the samples employing the adhesive with the carrier mat and 0.39mm±0.15 for those bonded with the unsupported material. Whilst no detailed study was carried out, previous studies with similar systems would suggest that these values corresponded to the plateau region [149].

Figure 6.2 shows examples of typical P-δ curves obtained with the Ti-DCB joints bonded with both the supported and unsupported version of AF163-2. After an initial linear region, the graphs curved slightly before reaching a maximum. The load then decreased gradually as the crack propagated. Note that the two plots shown in the graph do not allow direct comparison because of the different substrate thickness and initial crack length used in each case (7 and 8 mm and 50 and 55mm respectively).

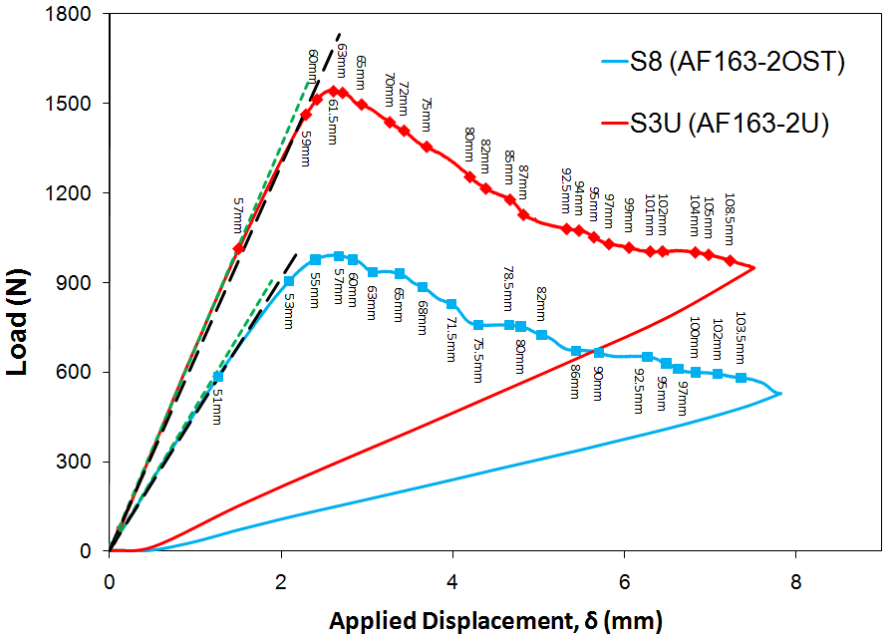

Figure 6.2. Typical load-displacement traces obtained with the Ti-DCB specimens bonded with both the supported and unsupported versions of the film adhesive AF-163-2. The dots correspond to the experimental crack lengths measured during the test, while the green and black lines indicate the initial value and a 5% increase over the initial compliance (C_0) respectively.

The unloading behaviour of all these specimens was equivalent to that illustrated in Figure 6.2. This type of response, with the unloading trace returning to the origin (or very close, as in some cases the roughness of the newly created fracture surfaces prevents the crack from closing completely), indicated that the metallic substrates had remained elastic during the test and therefore allowed the use of the LEFM methods in the analysis. In addition, the plots included two straight lines symbolizing the initial compliance (C_0) and a 5% increase over the original value (5% C_0). The points at which the P-δ curve deviated from the first line and crossed the second one were used to define the nonlinear (NL) and 5% (5%/MAX) criteria for initiation respectively.

The response during the propagation stage agreed well with the beam theory predictions. As shown in Figure 6.3, the linear regressions performed on the experimental compliance (corrected for the presence of the end-blocks) and crack length data to obtain the exponent subsequently used in Berry's method consistently produced slopes very close to the theoretical value (i.e. $n = 3$). Correspondingly, the same cubic relationship was confirmed by the plots of $(C/N_v)^{1/3}$ versus a, which showed that the data were linear and intersected the a-axis at negative values, implying Δ_I=10.1±0.9mm and Δ_I=7.4±1.2mm for the DCB joints manufactured with the AF163-2OST and AF163-2U respectively (see Figure 6.4).

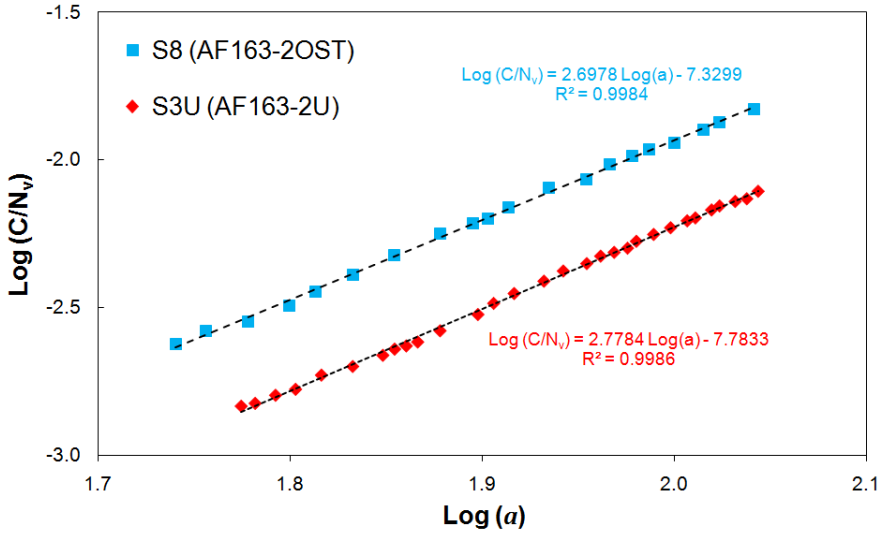

Figure 6.3. Values of $log(C/N_v)$ versus $log(a)$ for typical Ti-DCB joints bonded with the supported and unsupported versions of AF163-2. Linear regressions are performed over this data range to obtain the exponent n required in Berry's method (see Chapter 5).

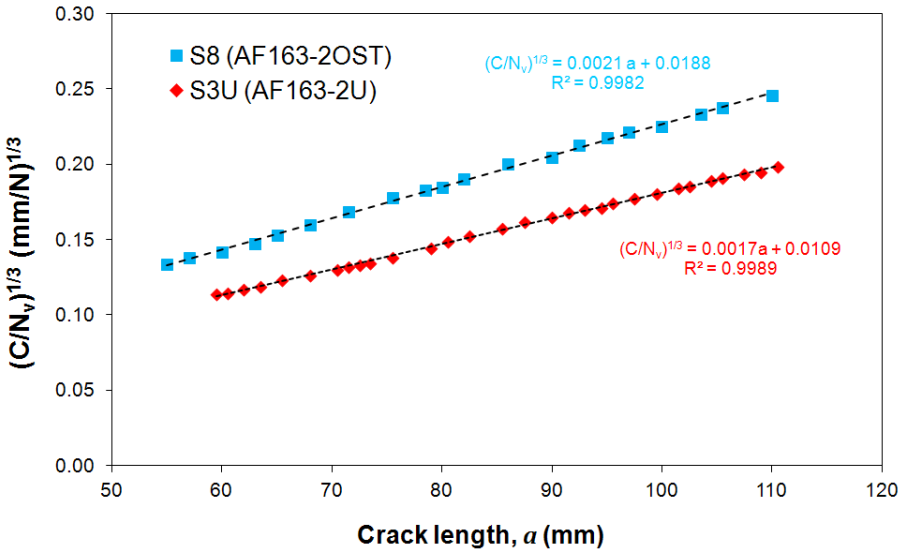

Figure 6.4. Values of $(C/N_v)^{1/3}$ versus crack length a for typical titanium DCB specimens bonded with the supported and unsupported versions of AF163-2.

Visual inspection of the fracture surfaces revealed cohesive failure with the crack propagating through the adhesive layer. Examples for the supported and unsupported versions of AF163-2 can be seen in Figure 6.5. Note that a certain amount of voids were observed in these specimens and, even though the failure can still be considered fully cohesive, the small differences in their number and size could explain some of the scatter in the results obtained.

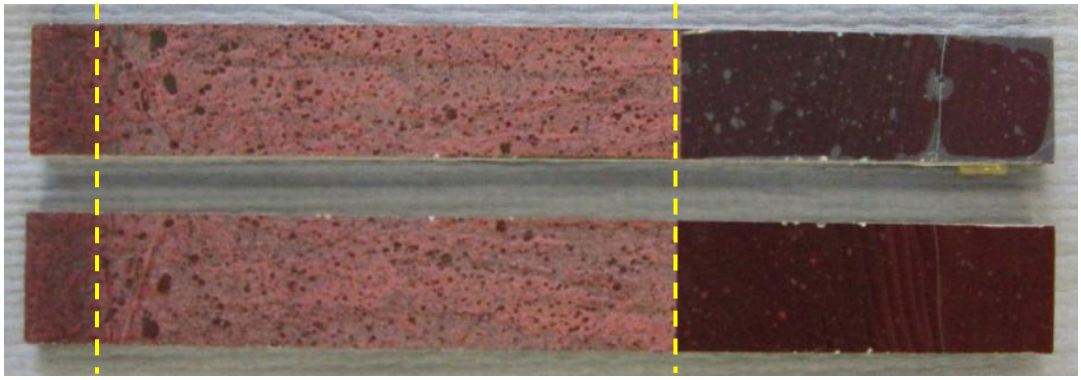

(a)

(b)

Figure 6.5. Examples of the fracture surfaces obtained after testing DCB specimen manufactured with titanium substrates bonded with the (a) supported and (b) unsupported versions of the film adhesive investigated

The sets of experimental $P_i - \delta_i - a_i$ data were analysed according to the methods described in Chapter 5 (see section 5.3.1) in order to determine the variation of the mode I critical strain-energy release rate G_{Ic} with the crack length. The resistance curves corresponding to the SBT, CBT, ECM and CBTE were plotted using the three initiation values previously mentioned and those obtained for the various crack lengths measured during the propagation stage. Figure 6.6 shows typical results for the titanium DCB joints bonded with (a) the supported and (b) unsupported versions of AF163-2.

The resulting R-curves exhibited the characteristic rising effect regardless of the analysis method considered: after a first stage where G_{Ic} increased with the crack length, the curves reached a relatively stable plateau. The rising section was particularly marked if the non-linear criterion was considered, as this criterion consistently yielded the lowest values of G_{Ic}. However, despite fairly consistent plateau values among joints bonded with the same type of adhesive, the severity of this rising effect varied moderately from sample to sample due to the scatter in the fracture energy measured at initiation. This variability could be partly

explained by the difficulties of accurately identifying the crack tip position, although the fact that initiation was measured from the PTFE insert rather than a pre-crack perhaps aggravated the problem.

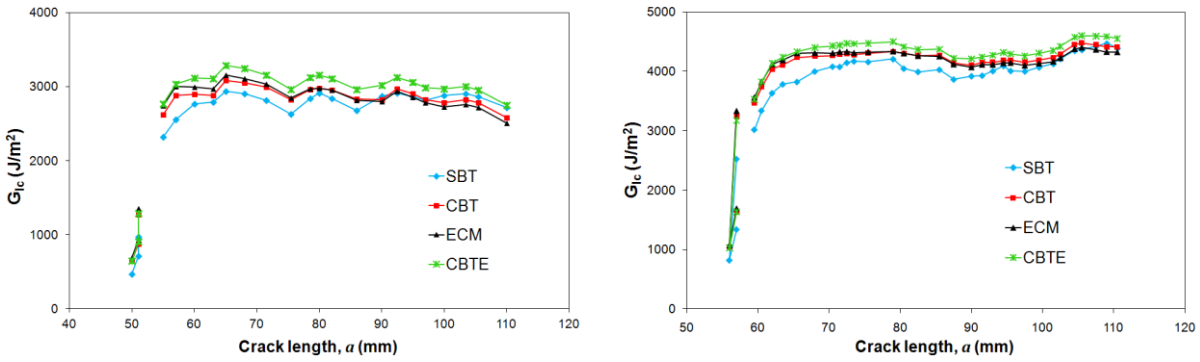

(a) (b)

Figure 6.6. Typical R-curves obtained for Ti-DCB specimens manufactured with (a) the supported and (b) the unsupported versions of AF162-2

In most cases, the fracture energies for propagation predicted by the simple beam theory were slightly lower than those obtained by both the corrected beam theory and experimental compliance methods. In fact, the agreement between the last two techniques was usually remarkably good, suggesting that the visual measurements of the crack length on which the ECM heavily relies were consistent and accurate. As a general rule, the CBTE returned the highest values of G_{Ic}. Associated with the limitations of using a constant correction factor for the crack length, the discrepancies between CBT and CBTE are discussed in more detail in section 6.2.4.2.

Figure 6.7 illustrates the initiation G_{Ic} values extracted from the DCB tests for the supported and unsupported versions of AF-163-2. The results obtained in [388] using unidirectional CFRP substrates have also been included for comparison. Only the MAX/5% points are given, as this was found to be the more consistent criterion. Unsurprisingly, the scatter in this data was considerable, reflecting the difficulty in detecting crack initiation for stiff substrates as previously reported in [133]. The average propagation fracture energies corresponding to the mean value in the plateau region for the same test are presented in Figure 6.8. Aside from the visual definition, the crack lengths taken into account for the calculation of the latter were selected so that the standard error of the final critical strain-energy release rate (as calculated with the CBTE) would be less than 6% (standard deviation/mean value<0.06).

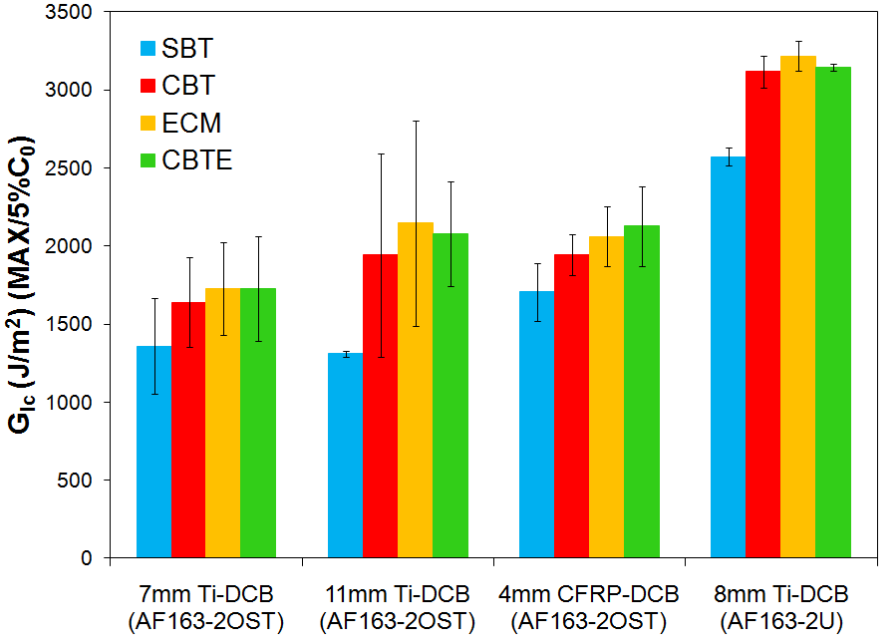

Figure 6.7. Average initiation values of G_{Ic} corresponding to the MAX/5% C_0 criterion obtained with the DCB specimens bonded with the supported and unsupported versions of AF163-2. The results obtained in [388] using CFRP substrates have been included for comparison.

Unlike initiation, the propagation results (Figure 6.8) were reasonably consistent and showed less scatter. As stated in Chapter 5, the CBT and CBTE were considered the most accurate methods, producing plateau values of 2832±143 and 3032±170 J/m^2 respectively for AF163-2OST. In contrast, the same analyses returned much higher values for the unsupported adhesive (4084±135 and 4214±145 J/m2). The potential effect of the substrate thickness and material are discussed in detail in section 6.2.4.1.

In view of the results showed in Figure 6.8, the detrimental effect of the carrier mat to the mode I toughness is evident. Furthermore, although not published, an equivalent conclusion had been reached with a similar adhesive system (AF-500, by 3M). Possible explanations for this phenomenon are examined in depth in section 6.2.4.3. However, the advantages in bondline control and ease of handling offered by the supported version seem difficult to justify against such a big reduction (approximately 28%) in the value of G_{Ic}.

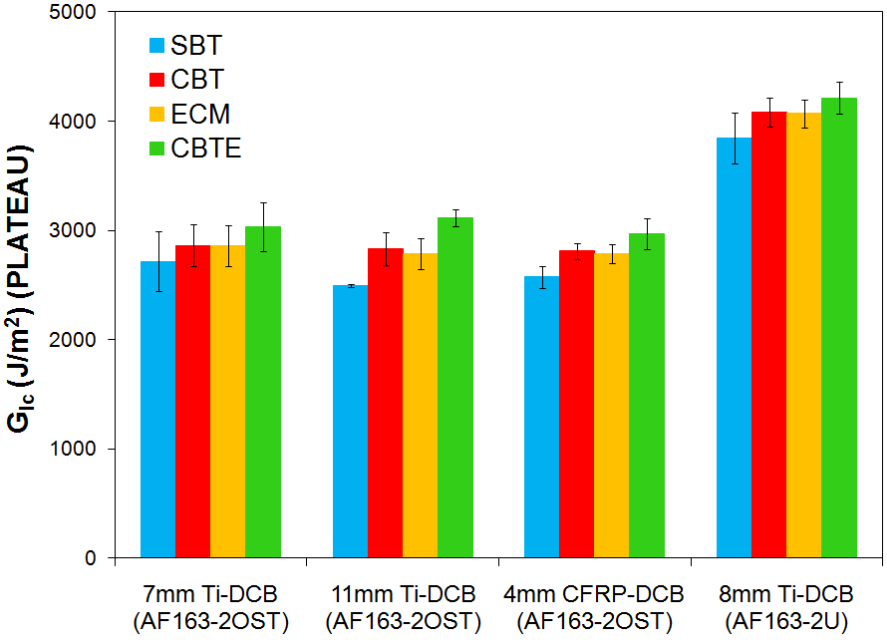

Figure 6.8. Average propagation values of G_{Ic} (corresponding to the "Plateau") obtained with the DCB specimens bonded with the supported and unsupported versions of AF163-2. The results obtained in [388] using CFRP substrates have been included for comparison.

Finally, the confidence in the results was supported by the back-calculated modulus obtained from equation (5.11). Although slightly higher than the expected value for the titanium alloy employed in the present work (i.e. E_s=114GPa), the computed modulus (i.e. E_e=127±7GPa) remained constant for the different crack lengths, see Figure 6.9. Similar discrepancies between E_e and the independently measured modulus have been reported elsewhere [133, 149] and fall within the accepted experimental error (approximately 11%).

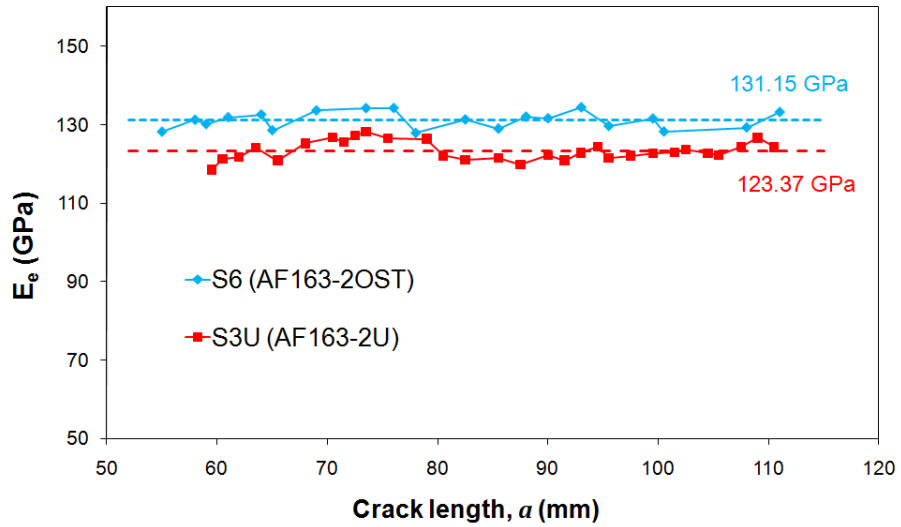

Figure 6.9. Typical plot of the back calculated modulus obtained for titanium DCB joints bonded with the supported and unsupported versions of AF-163-2.

6.2.3 Aluminium TDCB Tests

In addition to the DCB joints discussed above, the mode I fracture energy was also measured using TDCB specimens. These supplementary tests would serve to corroborate previous experimental G_{Ic} values and investigate any dependence on the joint geometry. Employing aluminium alloy substrates pretreated as described in section 4.2.3.1, the TDCB joints were manufactured with the supported version of AF-163-2 (AF-163-2OST). Inspection of the cured adhesive layer with the aid of an optical microscope revealed a bondline thickness of around 0.38±0.15mm.

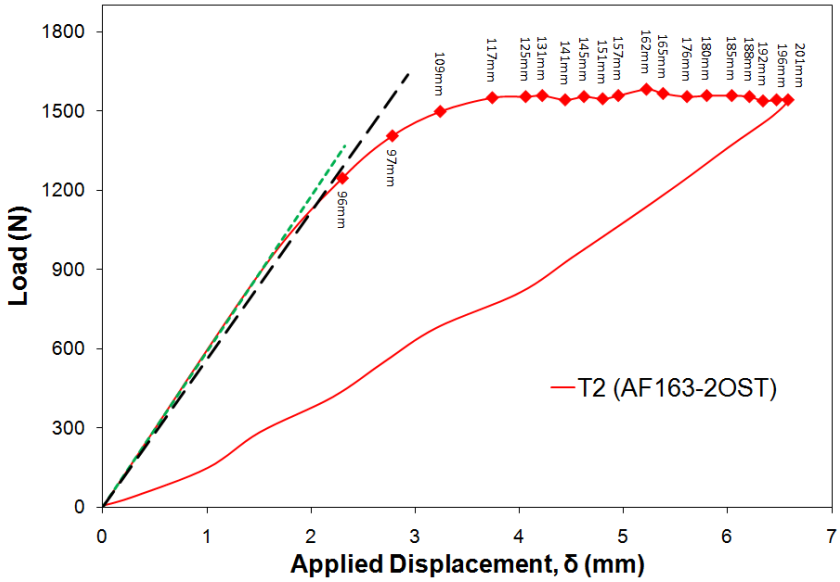

Figure 6.10. Example of load-displacement curve obtained for a TDCB specimen (AF163-2OST). The red dots correspond to the experimental crack lengths measured during the test, while the green and black lines indicate the initial value and a 5% increase over the initial compliance (C_0) respectively.

As shown in Figure 6.10, which illustrates the typical load-displacement curve obtained for a TDCB specimen corrected for the system compliance and initial non-linearity, the load increased linearly up to the initiation point and then remained approximately constant during the propagation phase. In all cases the unloading trace intercepted the horizontal axis at, or in very close proximity to, the origin, indicating that the metallic beams had not deformed plastically and confirming the validity of the LEFM analysis. This joint design results in a constant proportional relationship between the compliance of the specimen and the crack length as reflected in Figure 6.11:

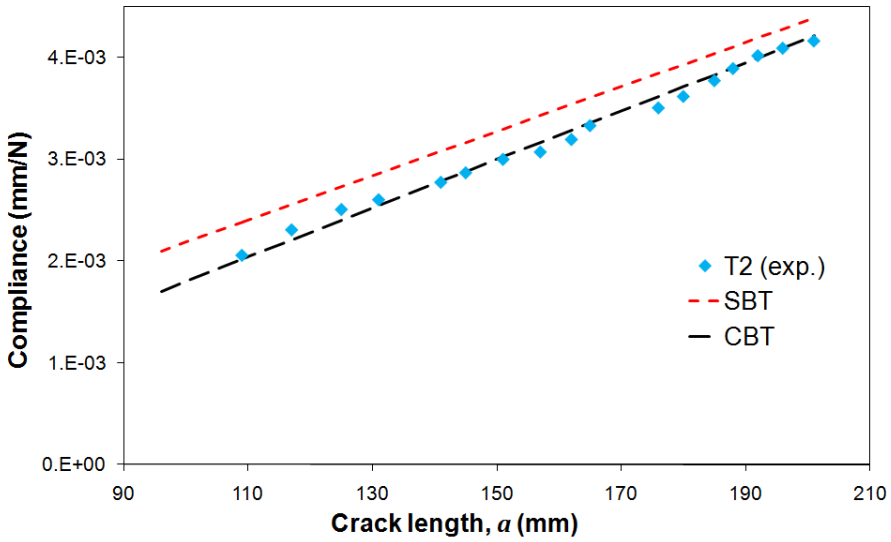

Figure 6.11. Variation of the compliance with the crack length in the propagation phase for an aluminium alloy TDCB specimen manufactured with AF-163-2OST. Experimental values are shown together with the SBT and CBT predictions (see Chapter 5).

The results of the linear regressions performed on the experimental C-a data yielded correlation coefficients very close to unity (between 0.993 and 0.998) in all cases. Furthermore, the agreement between the experimental values and the CBT predictions was excellent, confirming the accuracy of the corrected equations derived by Blackman et al. [134]. On the other hand, the slope estimated by the simple beam theory was usually smaller than that observed in the tests, ultimately producing lower values of G_{Ic}.

Careful post-test visual inspection of the fracture surfaces revealed failure by a crack propagating cohesively through the adhesive layer (see Figure 6.12).

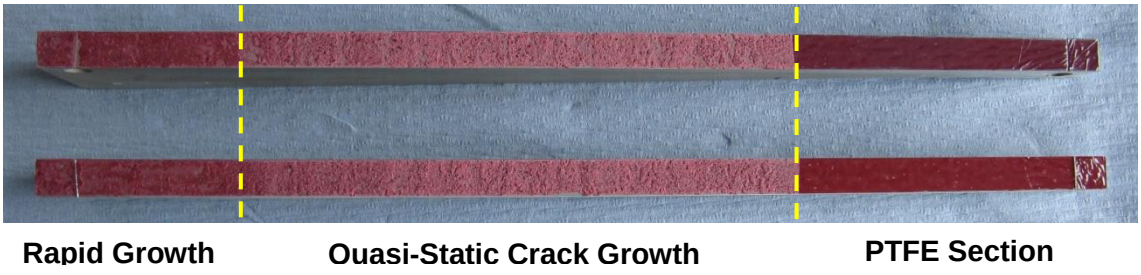

Figure 6.12. Example of the fracture surfaces obtained for TDCB specimens bonded with AF163-2OST.

The value of the mode I critical strain-energy release rate was calculated for every crack length measured during the tests using the various data reduction schemes described in Chapter 5 for this geometry (i.e. SBT, CBT and ECM, see section 5.3.2). The results were combined with the initiation values corresponding to the three usual criteria (NL, VIS and MAX/5%) to generate the resistance curves for each specimen. An example is shown in

Figure 6.13. As observed in the DCB cases, these R-curves exhibited the typical rising effect, with an initial rising section followed by a plateau region where G_{Ic} was independent of the crack length. Whilst the rising effect was particularly significant if the non-linear (NL) criterion was considered, it was also evident for the MAX/5% criterion, which yielded initiation values approximately 40% lower than the average plateau G_{Ic}.

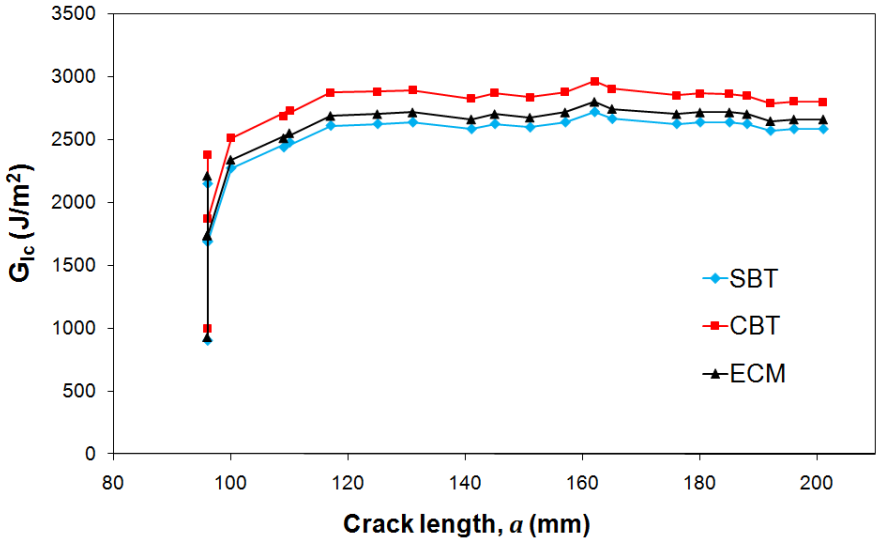

Figure 6.13. Typical resistance curve obtained for a TDCB specimen bonded with AF-163-2OST.

As expected from the trends shown in Figure 6.11, the simple beam theory produced the lowest curves, while the CBT yielded the highest G_{Ic} values. However, unlike in the DCB joints, the results obtained with the experimental compliance method were closer to those of SBT than to the predictions of the CBT. This could be linked to added difficulties in the visual determination of the crack length, perhaps associated with the smaller applied displacements involved with this test geometry (i.e. stiffer substrates) as suggested in [134].

Figure 6.14 illustrates the average initiation (MAX/5%) and propagation (plateau) values of G_{Ic} obtained with the TDCB specimens tested quasi-statically. The repeatability of the initiation values was acceptable, showing less scatter than in the titanium DCB joints. Similarly, the consistency of the propagation results was also very good. Furthermore, the agreement between the average plateau value corresponding to CBT obtained with this geometry (2847±91 J/m^2) and that measured with the metallic DCB joints was excellent. Note that it was not possible to compare the values calculated with the effective crack length approach, as this data reduction scheme is not readily applicable to the tapered specimen.

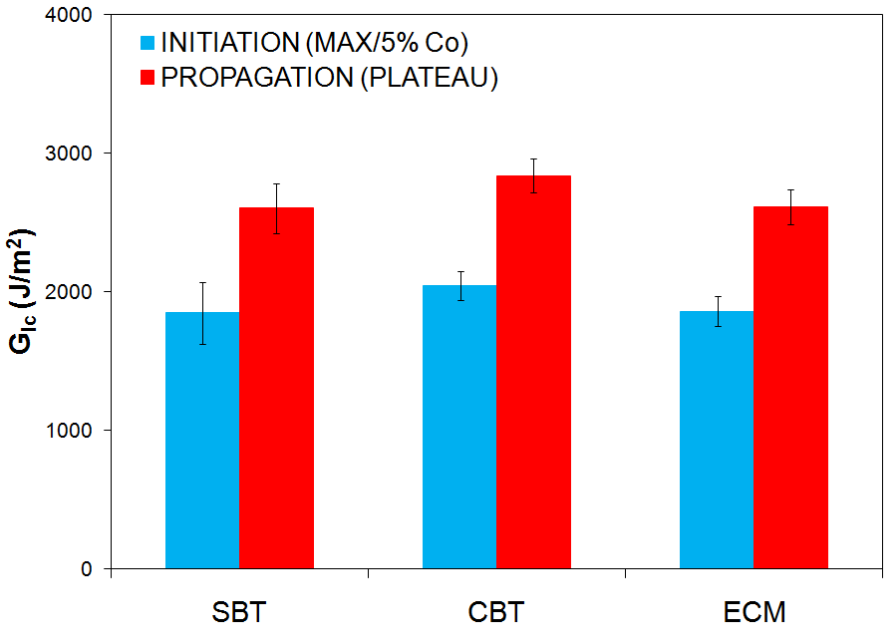

Figure 6.14. Average initiation (MAX/5% C_0) and propagation ("plateau") values of G_{Ic} obtained with the aluminium TDCB specimens bonded with AF163-2OST.

6.2.4 Discussion of Mode I Results

The results presented above are now compared to assess the influence of various aspects on the measured G_{Ic} values. Adhesive and substrate material, joint geometry or data reductions scheme are the parameters considered. Note that this comparison is possible as the type of failure was cohesive in the adhesive layer and the bondline thickness was similar (approximately 0.4mm) in all cases. CBT and CBTE (if available) are favoured over the other analysis methods, since they are believed to be the most accurate.

6.2.4.1 Effect of the Joint Geometry and Substrate Material

Table 6.1 presents a summary of the average fracture energies measured for AF163-2OST with the different types of mode I joints investigated. It can be seen from the results corresponding to the CFRP and metallic DCB specimens that the substrate material did not influence G_{Ic}. Similarly, comparing the values obtained with the joints manufactured with 8 and 11 mm thick titanium beams, no substrate thickness effect was evident. Moreover, despite the larger experimental scatter, this also appeared to hold true for the MAX/5% initiation values.

These observations seem to contradict [389], where the transverse modulus of the substrates rather than the axial modulus was highlighted as the controlling factor in influencing the form of the stress field ahead of the crack tip and thus the size of the process zone.

Furthermore, they would suggest that the local curing conditions of the epoxy resin were equivalent in all cases despite the different heat transfer properties of the various substrate materials employed. Hence, following the same reasoning used in [133, 373], it would appear that the drying cycle applied to the composite laminates prior to bonding was sufficient to ensure similar values of T_g for the adhesive in the CFRP and metallic joints.

Table 6.1. Average MAX/5% initiation and plateau values of G_{Ic} obtained for the different mode I specimens tested with AF163-2OST.

TYPE OF SPECIMEN	G_{Ic} (J/m^2)			
	Initiation MAX/5% C_0		Propagation Plateau	
	CBT	CBTE	CBT	CBTE
7mm Ti-DCB (±SDV)	1639±288	1724±335	2861±192	3033±223
11mm Ti-DCB (±SDV)	1942±652	2077±335	2830±151	3115±79
CFRP-DCB (±SDV)	1900±379	2127±254	2813±84	2969±167
Al-TDCB (±SDV)	2004±204	-	2847±91	-
AVERAGE (±SDV)	1903±385	1991±371	2837±133	3032±179

A comparison between the CBT results obtained for the DCB and TDCB specimens, which showed remarkably good agreement, revealed no significant geometry dependence upon the measured G_{Ic}. Equivalent findings were reported in [133, 149] when testing similar adhesive systems, and implies that the width of the tapered substrates was sufficiently large to guarantee plane strain conditions across the majority of the crack front.

6.2.4.2 Effect of the calculation method: CBT versus CBTE

The CBTE approach consistently yielded higher fracture energies than the traditional CBT for the DCB specimens. For example, the difference in the predictions for the titanium joints varied between 100 and 260 J/m^2, representing around a 5-8% increase in the final plateau value of G_{Ic}. Equivalent results were reported by de Morais and Pereira [380] when they used effective crack lengths rather than the measured values in the ECM.

After closer examination of the characteristics of these two reduction schemes, it appeared that the values of the crack length used in each case were in fact the source for this discrepancy. Errors in the visual measurement are presumed in both methods but, while CBT corrects them using a constant parameter Δ_I, CBTE relies entirely on the experimental compliance data to compute new lengths. Following [141], the back-calculated crack lengths could be interpreted as the sum of the measured values plus an implied correction factor $\Delta_{implied}$ (i.e. $a_e = a + \Delta_{implied}$). However, as illustrated in Figure 6.15, the implied values were in all cases lower than Δ_I and decreased with the measured crack length. This agreed well with the trends reported in [380]. Consequently, the longer cracks used in CBT produced smaller fracture energies (since the term $a + \Delta_I$ appears in the denominator of equation 5.5) than those estimated by CBTE. It is also worth noting that, if extrapolated linearly to a=0, the implied data yielded very similar values to Δ_I (typically less than 5% difference).

Various aspects could contribute to explain this behaviour and thus highlight the drawbacks of using a constant Δ. As previously mentioned, this parameter was originally introduced in [375, 376] to account for the beam root rotations and transverse shear stresses. However, the magnitude of these effects depends on the crack length, suggesting a variable correction factor would be more appropriate. In the original derivation of the critical strain energy release rate for a cracked laminates, Williams [146] presumed a parabolic distribution for the shear stresses proportional to the shear forces Q, which in a DCB specimen loaded with wedge forces would arise from the moment gradients (i.e. $Q = dM/da = P$). Since in the DCB geometry the load decreases with the crack length during stable propagation (see Figure 6.2), it is reasonable to assume that so would the shear stresses. The same could be concluded for the end rotation correction employing the beam on elastic foundation model described in [375].

Additionally, it has also been suggested before that the crack lengths computed from experimental compliance data (i.e. CBTE) include the size of the FPZ [379, 380, 385]. This effect, which in principle cannot be accounted for by the operator and therefore contributes to the error in the visual measurements, would be indirectly embedded in $\Delta_{implied}$. However, according to Suo et al. [298], a small decrease in the length of the process zone with the crack length is to be expected during the propagation phase in DCB joints loaded with shear forces. This variation, corroborated by the numerical results described in Chapter 8 and those in [390], would also imply a decrease in the value of Δ. In view of this evidence, it would appear clear that the CBTE is theoretically sounder than CBT.

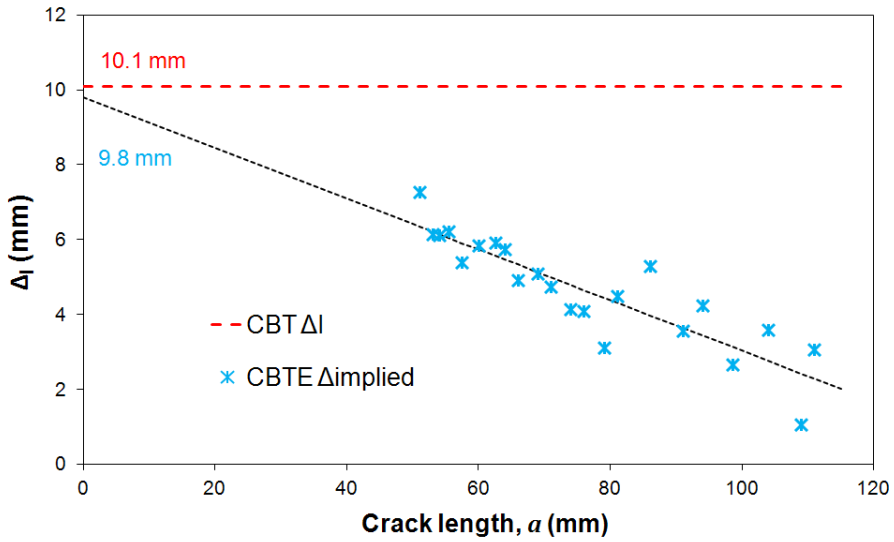

Figure 6.15. Typical plot of the constant correction factor Δ_I used in CBT and the implied values deduced from the effective crack length for a titanium DCB specimen. Linear extrapolation of $\Delta_{implied}$ data to $a = 0$ consistently results in values very similar to Δ_I.

6.2.4.3 Effect of the carrier mat

Although incorporating a woven or non-woven carrier mat is a very common practice to ease handling, facilitate positioning and control of the bondline thickness in film adhesives, no detailed study of their influence has been published thus far to the knowledge of the author. The presence of this scrim material would give the adhesive certain characteristics of a composite, and it would require a special treatment due to the low fibre volume involved. The works of Tolan et al. [391], Francis and Gutierrez-Lemini [392], Sancaktar et al. [393] and Aglan et al. [394] are some of the very few references on the subject.

Investigating this issue was not among the main objectives of the present work. However, the detrimental effect of the scrim material on the mode I fracture energy became evident after testing the titanium DCB joints manufactured with both the supported (AF163-2OST) and unsupported (AF163-2U) versions of the adhesive (see Figure 6.8). The non-woven carrier mat would appear to provide a weak path for crack propagation under opening mode, resulting in a 28% reduction in G_{Ic} with respect to the unsupported system. In particular, it is postulated here that local debonding between the adhesive and the polymer fibres of the carrier rather than fracture of the epoxy resin itself would be the main mechanism controlling crack growth/failure in the DCB joints bonded with AF163-2OST. That is, microscopically failure did not take place cohesively in the adhesive layer but it was "internally interfacial" instead.

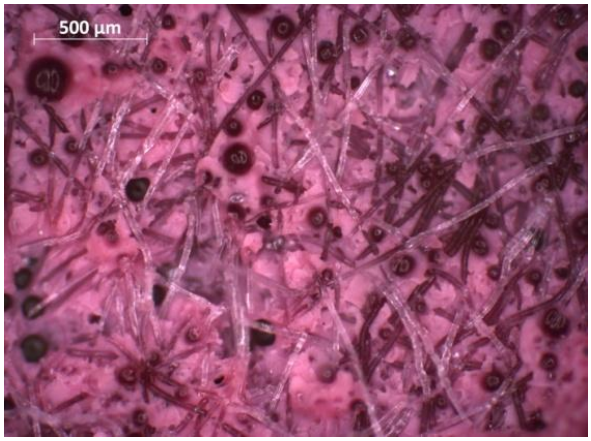

(a) Optical microscope (x5)

(d) Optical microscope (x5)

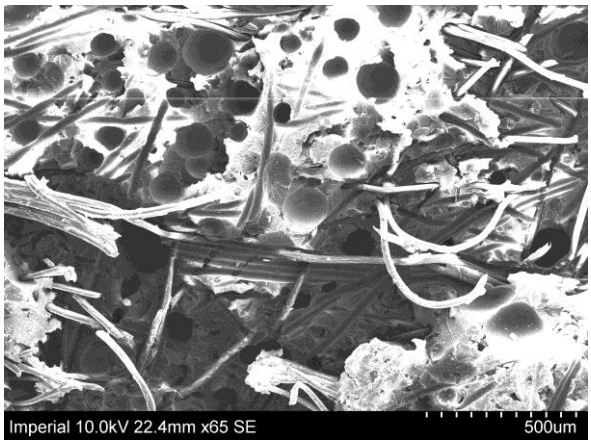

(b) SEM (x65)

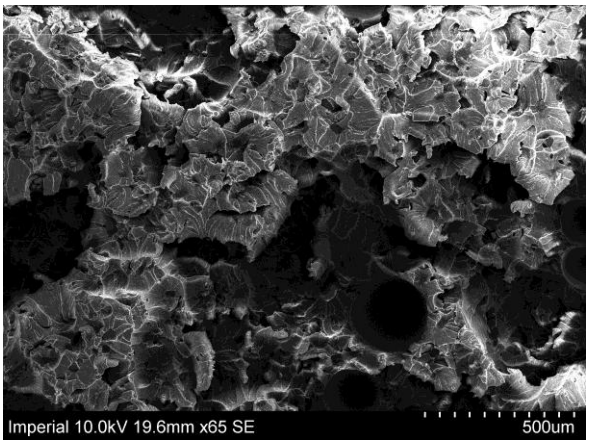

(e) SEM (x65)

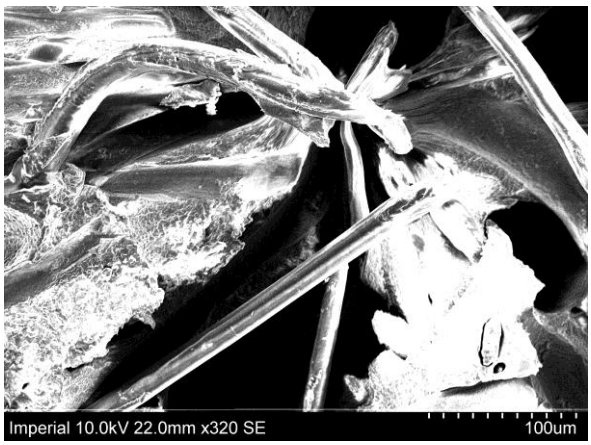

(c) SEM (x320)

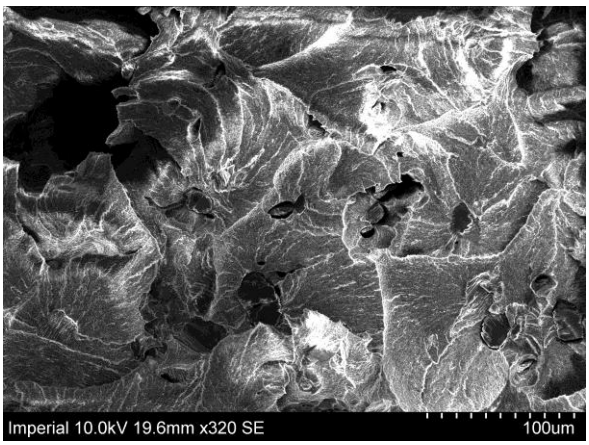

(f) SEM (x320)

Figure 6.16. Micrographs of the fracture surfaces obtained with the Ti-DCB specimens bonded with the supported (a-c) and unsupported (d-f) versions of the film adhesive (AF163-2OST and AF163-2U respectively).

This hypothesis was confirmed by the results of a microscopy analysis performed on the fracture surfaces obtained for the titanium DCB specimens bonded with both AF163-2OST

and AF163-2U. As illustrated in Figure 6.16-a/c, the fibres of carrier mat were easily identifiable. Many of them had debonded from the bulk adhesive, leaving very characteristic tracks on the surface of the epoxy. Both the lack of resin on the surface of the fibres and the smoothness of the aforementioned tracks suggest that this failure was mainly interfacial. In contrast, none of these formations were visible in the micrographs of AF163-2U, which exhibited a more conventional morphology. Therefore, there would appear to be a price to be paid for the use of the version of AF163-2 supported on the scrim carrier, this being the reduction in the mode I toughness by 28% over the unsupported version of the adhesive.

6.3 Mode II Fracture

6.3.1 Introduction

The next sections describe the results obtained in the mode II tests carried out with the ENF and ELS configurations. Whilst the former were manufactured using titanium alloy substrates, the ELS specimens employed CFRP beams. In all cases the joints were pre-cracked in mode I prior to mode II testing. Details of the manufacturing and testing processes can be found in Chapter 4, whereas the analysis methods were discussed in Chapter 5. It should be noted that the analysis used here does not take friction into account, hence yielding apparent values of the mode II fracture energy.

6.3.2 Titanium ENF Tests

Several ENF specimens manufactured using titanium alloy substrates were tested quasi-statically to determine the mode II fracture energy of joints bonded with AF-163-2OST. Visual inspection of the cured adhesive layer using an optical microscope revealed a repeatable bondline thickness of 0.42±0.09 mm.

Even though some preliminary tests had not exhibited the unstable behaviour typically associated with this configuration, the metallic arms had deformed plastically during the propagation stage. Consequently the loading was stopped at around 12kN in subsequent tests to ensure the validity of the LEFM methods, and therefore only initiation values of G_{IIc} were extracted. In those cases the unloading trace went back to the origin, confirming that the substrates had remained in the elastic regime.

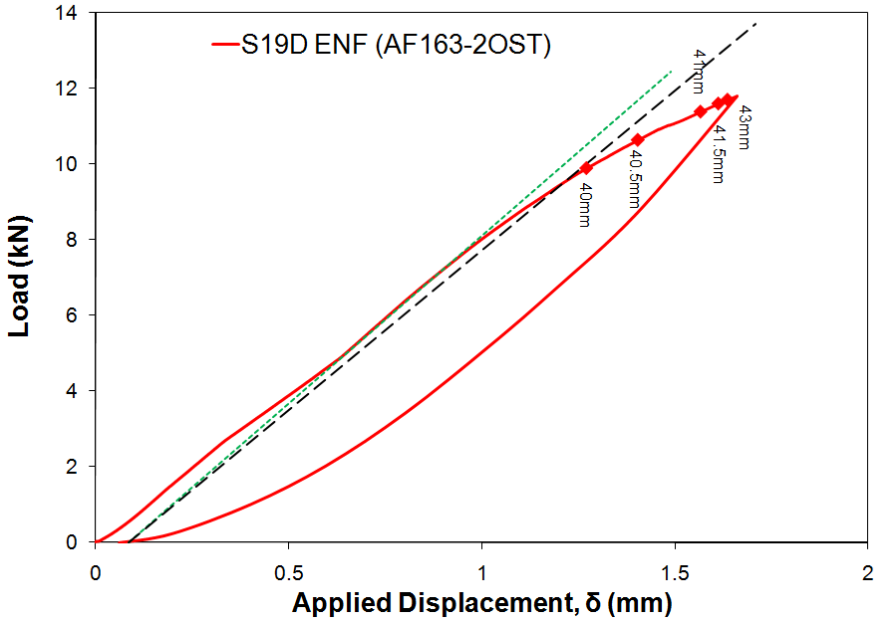

Figure 6.17. Typical load-displacement curve obtained for a 3ENF specimen. The red dots correspond to the experimental crack lengths measured during the test, while the green and black lines indicate the initial value and a 5% increase over the initial compliance (C_0) respectively.

As shown in Figure 6.17, the P-δ curves for the ENF tests exhibited some significant non-linearity in the early part of the loading trace. Since this phenomenon was not visible when only the metallic beams (unbonded) were loaded in the same three point bending rig, it would appear that the non-linearity was associated with the presence of the adhesive layer. Visual examination of the fracture surfaces revealed that the failure had been fully cohesive, with the crack propagating through the adhesive layer.

Despite the non-linearity, the SBT, CBT and CBTE analysis schemes described in Chapter 5 were used to determine the initiation values of G_{IIc}. The application of Berry's method was not possible due to the very few data points acquired. The fracture energies obtained (see Table 6.2) were considerably higher than those corresponding to mode I. Whilst the simple beam theory repeatedly produced the lowest results, the predictions of CBT were usually slightly higher than those obtained with the effective crack length approaches. As expected, the effective crack lengths computed from Williams beam theory were marginally longer than those derived using Timoshenko theory, hence resulting in greater values of G_{IIc}.

Table 6.2. Initiation G_{IIc} values corresponding to the MAX/5% C_0 criterion obtained for the titanium alloy ENF specimens bonded with AF163-2OST.

SPECIMEN	INITIATION G_{IIc} (J/m^2)			
	MAX/5% C_0			
	SBT	CBT	CBTE (Williams)	CBTE (Timoshenko)
ENF-1	4921	6275	6504	6158
ENF-2	4893	6296	8517	8180
ENF-3	3993	5106	4977	4676
ENF-4	4904	6105	5644	5378
ENF-5	4106	5283	4916	4573
Average	4563±471	5813±573	6111±1490	5793±1478

6.3.3 CFRP ELS Tests

The ELS configuration was also used in an attempt to measure the mode II critical strain-energy release rate G_{IIc}. CFRP substrates were employed in this case, since the metallic arms tended to deform plastically at the clamping point. Before pre-cracking the specimens under mode I conditions, the bondline thickness was inspected under an optical microscope and measurements were made at various points along the length of the specimen, obtaining an average value of 0.41±0.14mm.

Before fracture testing, the calibration of the clamping fixture was performed using the inverse ELS (IELS) test. As explained in Chapters 4 and 5, a joint specifically manufactured without the PTFE insert was employed in this process to determine the clamp correction factor, Δ_{clamp}. Figure 6.18 shows a typical plot of $(C_0/N)^{1/3}$ versus the free length (obtained for a constant torque of 8Nm). The negative intercept of the line of best fit with the horizontal axis was taken as the value of Δ_{clamp} (approximately 17.8mm), whereas an estimate of the flexural modulus was deduced from its slope (see equation 5.32). The latter value (approximately 138GPa) was relatively larger than that derived from three point bending tests carried out on various CFRP beams (119±2 GPa).

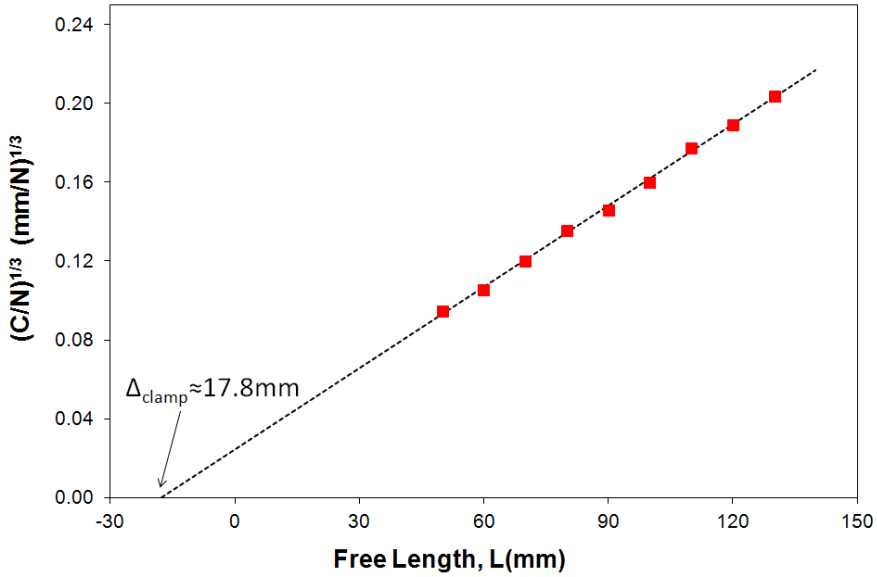

Figure 6.18. Graph of $(C_0/N)^{1/3}$ versus the free length L obtained during the calibration of the ELS fixture (for a constant torque of 8 Nm). The clamp correction factor Δ_{clamp} was determined as the intercept of the best fit line with the horizontal axis.

As illustrated in Figure 6.19, the characteristic load-displacement trace for an ELS joint bonded with AF-163-2OST deviated from linearity at approximately the visual crack initiation point. After visual initiation the load continued rising despite the crack growth and extensive damage accumulated along the adhesive layer. A possible explanation for the continuous increase in the load despite the visible damage accumulated can be found in [395]. The slope of the curve decreased progressively, but the tests were stopped before the maximum was reached because the damage zone ahead of the crack reached to within 10mm of the clamp point. Ending the tests when the applied displacement exceeded approximately 32mm was also necessary to prevent transverse fracture of the CFRP laminates due to excessive bending. Moreover, larger displacements could call into question the validity of the subsequent analysis since the value of the correction factors F_v and N_v could fall below the minimum recommended values of around 0.9 (see [165]). In all cases the unloading trace returned to the origin, revealing no permanent deformation of the substrates had occurred.

The formation of numerous micro-cracks and the extensive damage accumulated ahead of the continuous crack tip significantly hindered the definition of the true crack lengths. This made the identification of the initiation point particularly difficult, given that the assumed crack growth could have been easily mistaken for damage. Consequently, the very few data points available and their uncertainties impeded the application of Berry's method and highlighted, yet again, the advantages of the effective crack length approach.

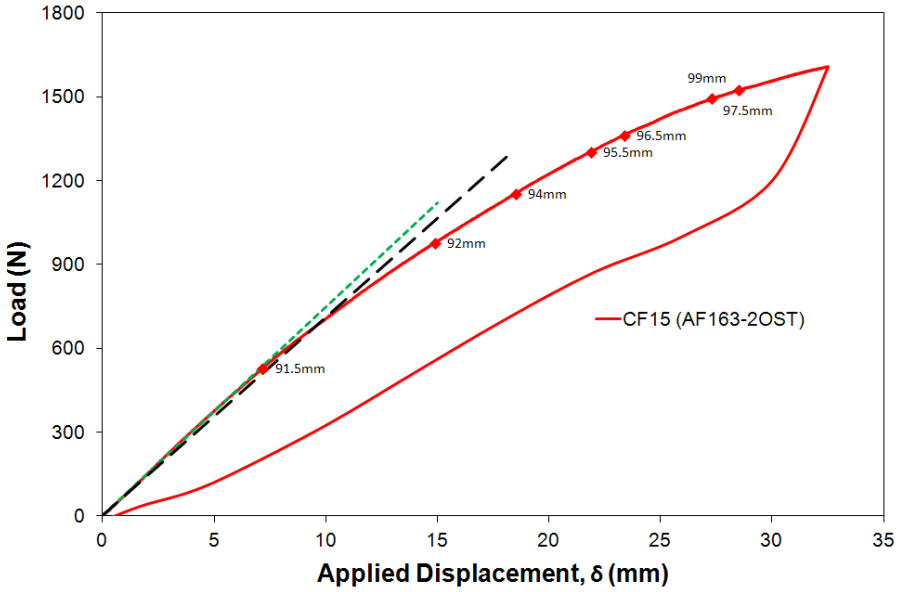

Figure 6.19. Typical load-displacement trace for a CFRP-ELS specimen bonded with AF163 OST. The red dots represent experimental crack lengths, while the straight lines indicate the initial value and a 5% increase of the compliance.

After unloading, the specimens were broken apart in mode I to expose the fracture surfaces. Visual inspection confirmed that the failure had been cohesive, in the adhesive layer (see Figure 6.20). The mode II region exhibited a characteristic roughness (i.e. "hackle" marks) very different from that observed in mode I tests. This was most likely associated with the approximately 45° inclination of micro-cracks.

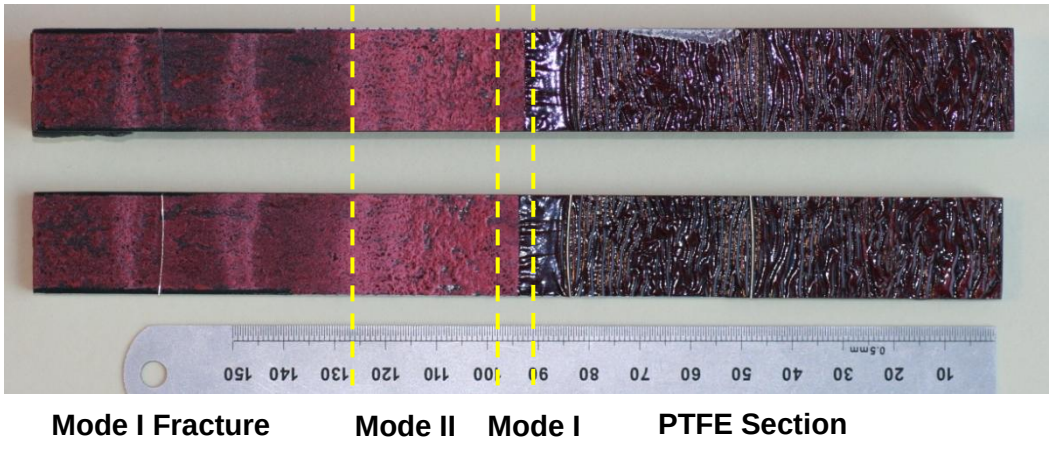

Figure 6.20. Example of the fracture surfaces obtained for a CFRP-ELS specimen bonded with AF-163-2OST.

Values of G_{IIc} were computed for all the measured crack lengths using the analysis methods described in Chapter 5. These results were combined with those obtained for the three usual initiation criteria to generate the corresponding resistance curves. An example is illustrated in

Figure 6.21. Given the shape of the P-δ trace, it was to be expected that the mode II fracture energy would increase progressively with the crack length without reaching a stable value or plateau, which held true regardless of the reduction scheme. The effective crack length approach consistently yielded the highest values of G_{IIc}, while the lowest predictions typically corresponded to CBT. The difference between these two methods also increased gradually, suggesting that the errors in the crack length determination became more important for larger displacements. Equivalent conclusions, consistent with the phenomenon of micro-cracking noted above, were also reported in [141, 149] when testing a similar film adhesive (AF-126 by 3M).

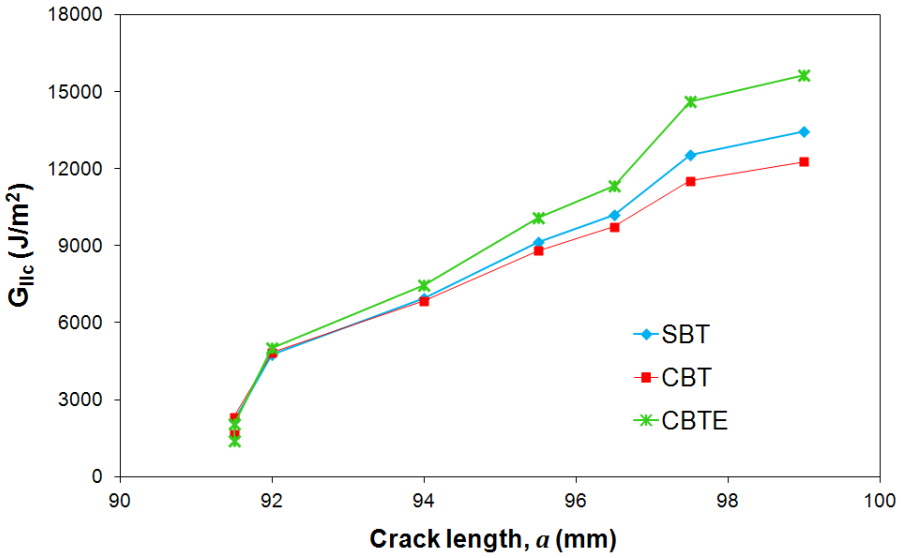

Figure 6.21. Typical rising R-curves obtained for a CFRP-ELS specimen bonded with AF-163-2OST (corresponding to the joint shown in the Figure 6.20).

Table 6.3 contains the values of G_{IIc} for initiation (MAX/5% criterion) and propagation (average). Considering the rising nature of the R-curves, the latter are not very representative for mode II fracture, but are included here to emphasize the large values relative to the mode I results. As in the ENF tests, the very few experimental crack lengths available for propagation and the significant uncertainties associated with their measurement advised against the use of ECM for the analysis of these tests. The values of the back-calculated modulus computed were in good agreement with the results from the independent three-point bending tests.

Table 6.3. G_{IIc} values for initiation (MAX/5%) and propagation (average) obtained for CFRP-ELS specimens bonded with AF-163-2OST.

SPECIMEN	INITIATION G_{IIc} (kJ/m²)			PROPAGATION G_{IIc} (kJ/m²)		
	MAX/5% C_0			AVERAGE		
	SBT	CBT	CBTE	SBT	CBT	CBTE
CF15	2.21	2.31	2.06	10.45±2.34	9.83±1.93	11.82±2.98
CF16	3.75	3.80	4.42	10.06±1.36	9.31±1.08	12.61±1.64

6.3.4 Discussion of Mode II Results

Regardless of the test geometry considered, mode II testing was influenced by the difficulties in distinguishing between true crack growth and the damage accumulated ahead of the tip. This problem, exacerbated in case of the ELS by the considerable bending of the substrates, led to significant scatter in the G_{IIc} results. At the same time, it highlighted the advantages of the effective crack length approach, as the CBTE analysis method is less dependent on the visual estimates of a.

The values obtained for initiation were also severely affected by the uncertainties in the crack length measurements, particularly for the visual criterion. The results corresponding to MAX/5%, approximately 46% higher than for the NL criterion, were more consistent in the ELS joints. However, these also led to substantial scatter in the ENF tests due to the initial non-linear response observed for these specimens and the subsequent difficulty in defining the initial compliance. Together with the absence of stable crack propagation, this non-linear behaviour severely impeded the use of the ENF geometry. Overall, the ELS configuration proved a more suitable mode II configuration to characterize the fracture behaviour of AF163-2. Nonetheless, it did not allow the determination of a plateau value of G_{IIc}.

Despite all this, there was clear evidence to suggest that the mode II fracture energy of AF163-2OST, for both initiation and propagation, is higher than the corresponding mode I values. Taking into account the resistance curves obtained with the ELS specimens (see Figure 6.21), had the fracture energy reached a plateau then the G_{IIc} plateau value would have been above 15000 J/m^2, which represents a minimum of a five-fold increase with respect to G_{Ic}. This difference could be partly explained by the different failure mechanisms involved in each case. Specifically, the formation of multiple micro-cracks ahead of the continuous tip

and their subsequent coalescence and friction between the fracture surfaces would account for the additional energy absorption as well as the rising P-δ traces obtained in these tests [149, 395].

6.4 Mixed Mode I/II Fracture

6.4.1 Introduction

The various nominal thicknesses of CFRP available (i.e. 2, 3 and 4mm) were combined to produce three different types of joints to study the mixed mode fracture behaviour of AF163-2OST: (a) Symmetric specimens were manufactured using 4mm thick CFRP beams (UD 977 2/HTS); (b) unbalanced joints resulted from bonding together 2mm and 4mm thick CFRP substrates (UD 977-2/HTS); and (c) CFRP beams (UD M21/T800S) of thickness 3mm and 4mm respectively were employed to create a second type of asymmetric specimen (see Figure 6.22).

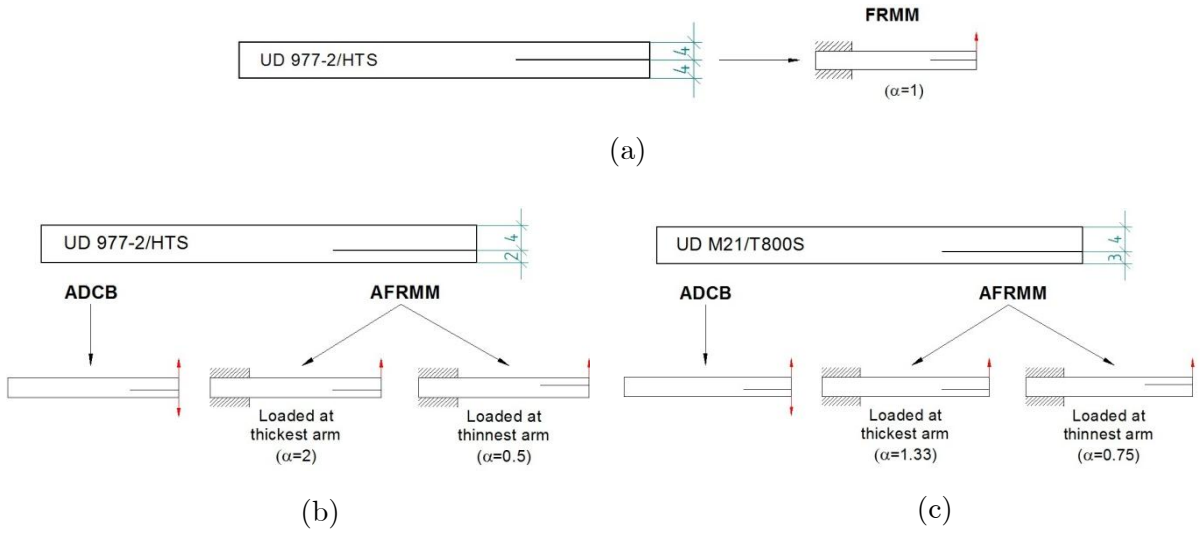

Figure 6.22. Types of joints manufactured for mixed mode I/II testing (the thickness of the substrates shown corresponds to the nominal values of the CFRP beams employed).

When tested as ADCB specimens (i.e. loaded as mode I), each asymmetric configuration yields a single mixed mode ratio. In contrast, when tested as AFRMM (i.e. one arm loaded) each specimen produced two different ratios, depending upon whether the thickest or the thinnest arm was loaded. Finally, the symmetric FRMM specimen provided an additional mixed mode ratio. It should be noted that according to the partitioning methods described in Chapter 5, the mode mix ratio for these test geometries depends only on the parameter α. Furthermore, the measured thickness of the substrates (determined with a micrometer at various points along the length of each beam and then averaged) rather than the nominal

values was employed in the analysis of the experimental results. Consequently, given the variability in these measurements, each specimen had a specific value of α and therefore produced a unique mixed mode ratio.

The results obtained in these tests are presented and discussed in the next sections. Whilst the total fracture energy was calculated using various analysis techniques (i.e. SBT, CBT, ECM and CBTE), the mode decomposition was performed according to three different schemes: the Williams global approach and both the singular and non-singular field versions of Davidson's partitioning method (CTE/SF and CTE/NSF respectively). Prior to testing, the bondline thickness was measured using an optical microscope equipped with a camera, yielding an average of 0.38±0.07mm.

6.4.2 CFRP ADCB Tests

In most cases the ADCB tests described here represented the pre-cracking stage for the AFRMM joints. The initial crack was propagated for between 5 and 10mm, and the results were analysed according to the methods presented in section 5.5.2.

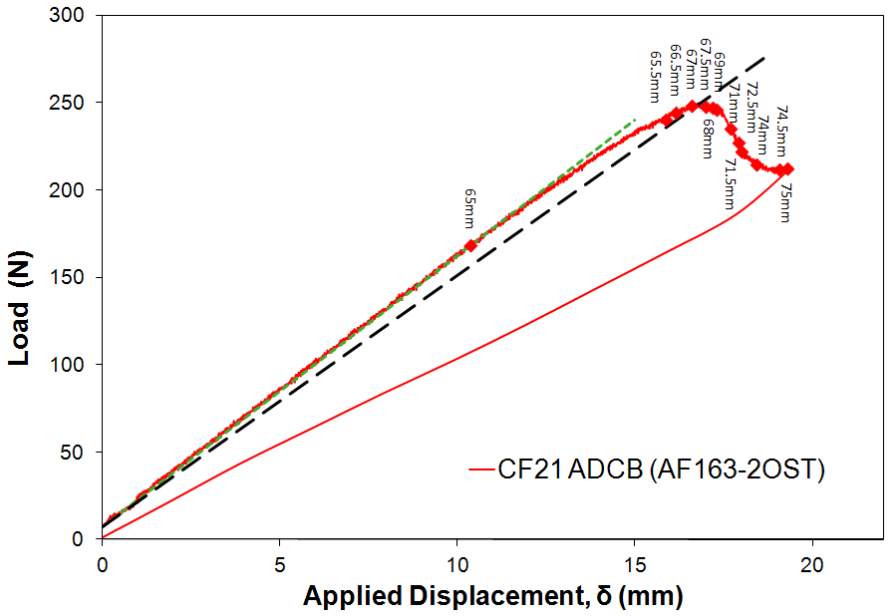

Figure 6.23. Typical load-displacement trace for a CFRP-ADCB specimen bonded with AF163-2OST. The red dots represent experimental crack lengths, while the straight lines indicate the initial value (green) and a 5% increase (black) of the compliance.

Figure 6.23 shows the typical load-displacement response obtained for an ADCB specimen. The shape of the curve was similar in all cases: after an initial proportional section, the traces became non-linear before reaching the maximum point. Then the load decreased progressively

as the crack propagated. Stable crack growth was observed for all the samples. The initial compliance and the peak load varied with the type of specimen (i.e. the thickness of the arms). The unloading traces always returned to the origin, indicating that the substrates had not experienced permanent deformation and supporting the validity of LEFM.

Visual inspection of the fracture surfaces, which took place after the AFRMM tests, revealed that the failure was mainly cohesive. Examples of this can be seen in Figure 6.30, where the pre-cracking region is easily identifiable by a lighter colour of the adhesive. Very small regions of interlaminar failure in the CFRP substrates were observed in some specimens, probably caused by excessive damage to the outer composite plies during the surface pre-treatment of the beams. Data from these sections were excluded from the fracture $G_{I/IIc}$ calculations.

The change in compliance with the crack length during the propagation stage agreed well with the theoretical predictions, as demonstrated by the linear trend observed in the plots of $(C/N_v)^{1/3}$ versus a (see Figure 6.24). The line of best fit to the experimental data did not intercept the origin but intersected at a negative value on the horizontal axis. This negative intercept Δ, typically between 9 and 12 mm, was used in the corrected beam theory analysis as proposed by Williams and co-workers [166, 376] for the symmetric case.

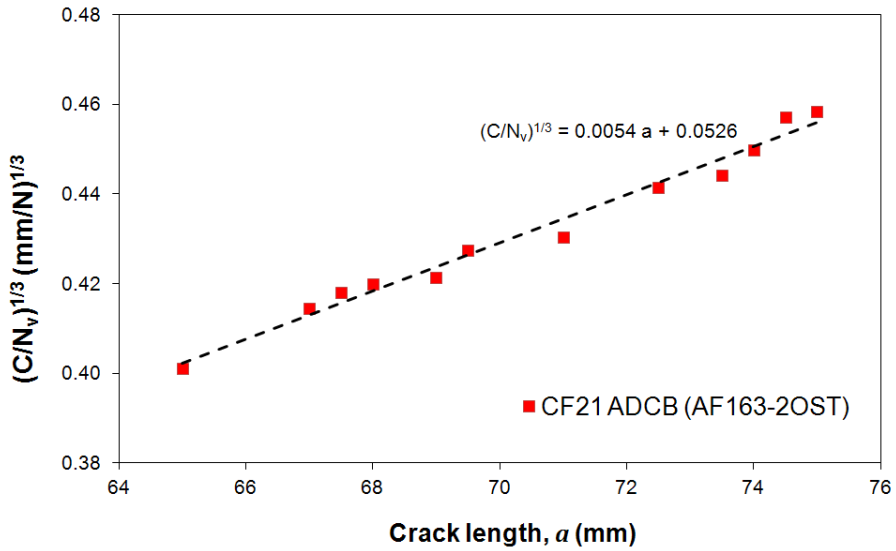

Figure 6.24. Values of the $(C/N_v)^{1/3}$ versus the crack length for a typical ADCB joint manufactured with 2mm and 4mm CFRP substrates. The correction factor Δ is taken as the negative intercept of the line of best fit to the experimental data with the horizontal axis rather than Δ_I, Δ_{II} or a combination.

The sets of P_i-δ_i-a_i were analysed using the methods described in Chapter 5 (i.e. SBT, CBT, ECM and CBTE) to determine the value of the total mixed mode facture energy for each crack length. The results were then combined with those deduced for the various initiation

criteria (i.e. NL, VIS and MAX/5%) to generate resistance curves. These typically showed a first part in which G_c increased with the crack length before reaching a stable value or plateau (see Figure 6.25). Whilst the upper bound consistently corresponded to the effective crack length approach, Berry's method produced the lowest values in most cases. Both the SBT and CBT yielded intermediate results, although typically closer to the CBTE.

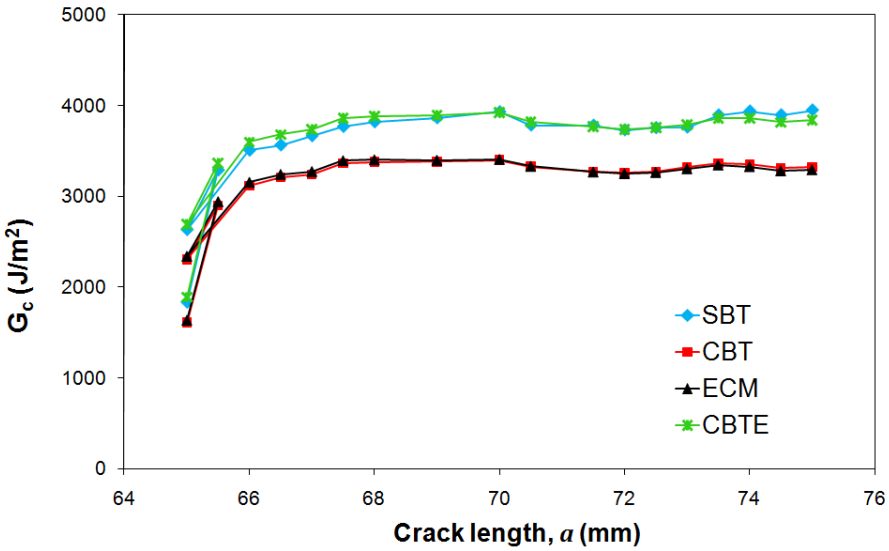

Figure 6.25. Typical resistance curves obtained for a ADCB specimen bonded with AF163-2OST. The total fracture energy, rather than its individual components, is plotted.

As discussed for the symmetric case in section 6.2.4.2, the reasons for the discrepancies between CBT and CBTE appear to be related to the use of a constant correction factor Δ in the former. As shown in Figure 6.26, the implied value of Δ ($\Delta_{implied}$) deduced from CBTE decreased gradually with the crack length. This variation was consistent with a reduction in both the transverse shear stresses and the correction for beam root rotation with the crack length, which is also predicted by beam theory (see models of beam on elastic foundation, [375, 377]). Moreover, it could also imply lower uncertainties in the identification of the crack tip position for longer cracks, which agree well with the progressive decrease in the size of the failure process zone predicted by Suo et al. [298] and the reduction of the cohesive length observed in the numerical simulations (see Chapter 8). Furthermore, if extrapolated linearly to a=0, the implied data tended to the same value obtained from the plot of $(C/N)^{1/3}$ versus a and used in the CBT.

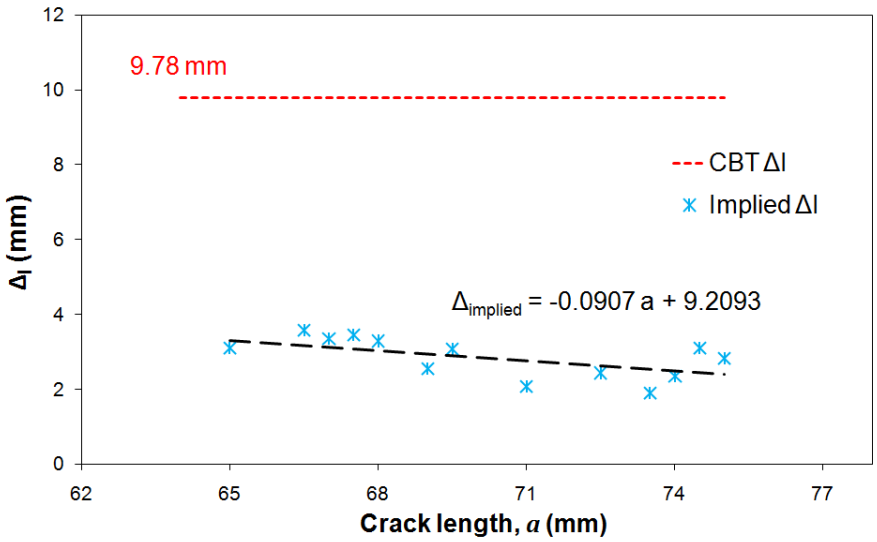

Figure 6.26. Values of the implied Δ versus the crack length for a typical ADCB specimen. If extrapolated to $a = 0$, the line of best fit for those values tends to the same value used in the CBT method (obtained as the negative intercept with the horizontal axis in a plot of $(C/N)^{1/3}$ versus the crack length).

Decomposition of the total fracture energy into the pure mode I components was carried out according to the Williams method, and both CTE/SF and CTE/NSF versions of Davidson's partitioning scheme. The results were, nevertheless, surprising regardless of the decomposition strategy considered. For the asymmetric joints, the mode I component of the fracture energy determined was consistently higher than the G_{Ic} values measured in the pure mode I tests for AF163-2OST. This was applicable to both initiation and propagation. It is proposed that this phenomenon (i.e. $G_{Ic}^{mixed} > G_{Ic}$ for the supported adhesive) is due to the presence of the carrier mat. The damaging effect of the carrier affects the mode I toughness disproportionately, and decreases significantly in intensity (or even vanishes entirely) when the shear component is very small.

Also, the results obtained for the ADCB specimens seem to question the soundness of the Williams partitioning method. As stated in Chapter 5, this theory predicts pure opening mode (i.e. $G_{II}/G = \Phi = 0$) for any ADCB joint irrespective of the thickness parameter α. However, the tests carried out here did not seem to yield a unique value of the critical strain energy release rate for mode I. That is, the adhesive fracture energies measured for the unbalanced specimens were notably higher than the value obtained from the symmetric DCB tests. This limitation has been reported elsewhere (e.g. [179]), suggesting that the Williams solution represents an upper bound [396].

Figure 6.27 shows the $G_{I/IIc}$ values for initiation (MAX/5%) and propagation (average plateau) obtained for the various ADCB specimens tested using CBTE. These results,

including the individual thickness parameters (α) and the mixed mode ratios predicted by the three partitioning methods considered are also tabulated in Appendix F.

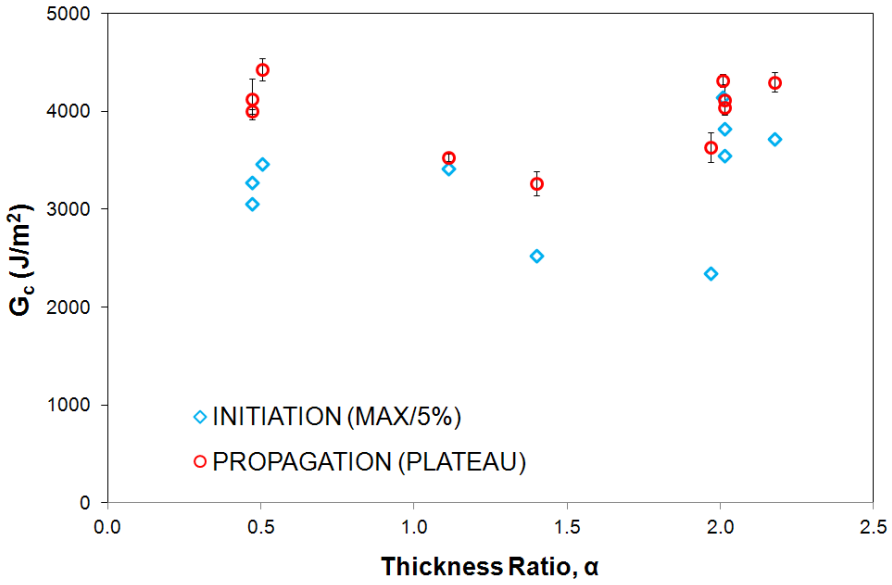

Figure 6.27. Initiation (MAX/5%) and propagation (plateau) values of $G_{I/IIc}$ obtained for various CFRP-ADCB specimens bonded with AF-163-2OST (corresponding to CBTE).

Finally, the accuracy of the analysis was assessed by inspection of the flexural modulus computed from the compliance data. The variation of the back-calculated modulus with the crack length was typically less than 5%, and the average values (approximately 123±7GPa) were very close to the independently measured value.

6.4.3 CFRP AFRMM Tests

Prior to transferring the specimens to the AFRMM fixture after the pre-cracking step, the calibration of the clamp was performed. Conducted using joints specifically manufactured for the inverse tests without any PTFE insert, this procedure was intended to determine the value of Δ_{clamp} for each type of specimen. Figure 6.28 illustrates the plots of $(C_0/N)^{1/3}$ versus free length L obtained during the calibration of the symmetric and unbalanced configurations.

In all cases the data exhibited the linear trend predicted by beam theory (see equation (5.51)), but the slopes were different due to the various joint thicknesses and laminates (i.e. compliances). Moreover, each configuration produced a different clamp correction factor. The negative intercept of the lines of best fit with the L-axis was inversely proportional to the slope. That is, the value of Δ_{clamp} decreased with decreasing compliance of the joints, showing evidence of a relationship between the stiffness of the clamping arrangement and that of the specimen clamped. This appeared a reasonable conclusion in view of the fixture

design (see Figure 4.15): for a given applied force, the displacements at the clamping point would depend on the span of the bolts used to apply the clamping force, which would increase for thicker joints.

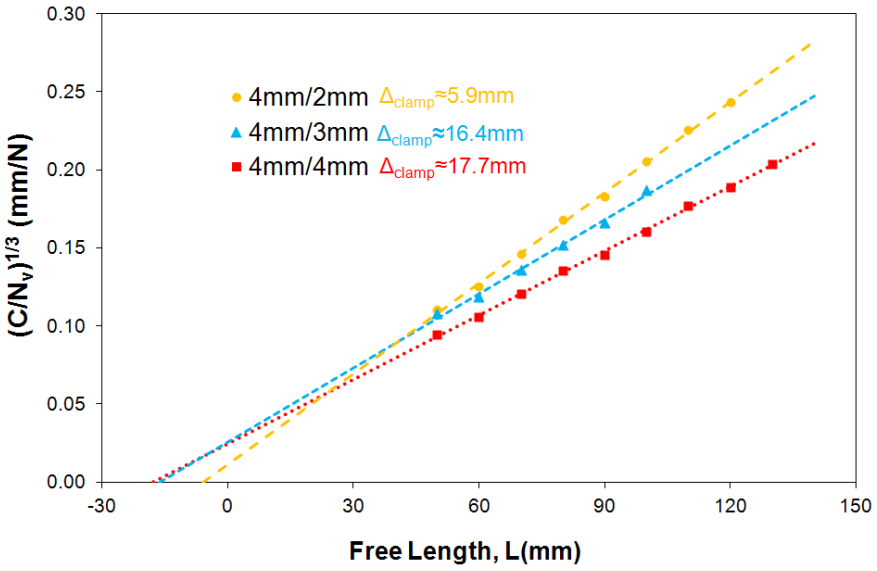

Figure 6.28. Graph of $(C_0/N)^{1/3}$ versus the free length L measured during the clamp calibration with both symmetric and asymmetric joints.

Figure 6.29 shows the characteristic load-displacement curves obtained for the FRMM and AFRMM joints. The initial response was always linear, deviating from this trend before reaching a maximum load. Two different types of behaviour were then observed: In the symmetric FRMM specimens and the AFRMM joints where the thinnest arm was loaded, the load decreased progressively as the crack grew. In those cases, the corresponding unloading traces returned to the origin indicating that the substrates had not experienced significant permanent deformation. In contrast, in the asymmetric joints loaded with the thickest arm the response became unstable soon after the inflexion point, with the crack propagating rapidly to the clamping point and the load dropping abruptly.

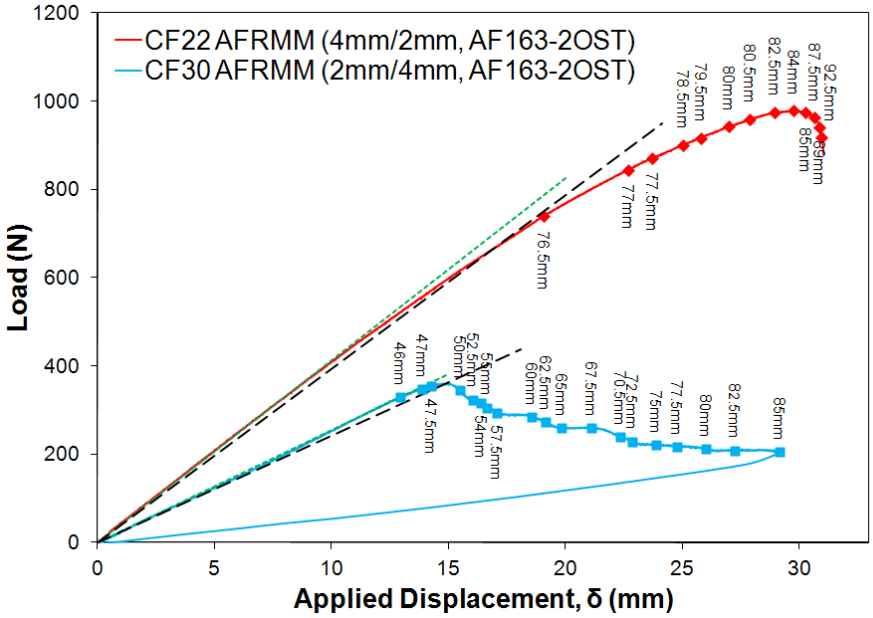

Figure 6.29. Typical load-displacement curves obtained for the AFRMM joint loaded at the thicker (4mm/2mm) and thinner (2mm/4mm) arms. The dots represent experimental crack lengths, while the straight lines indicate the initial value (green) and a 5% increase (black) of the compliance.

Subsequent inspection of the fracture surfaces revealed that those P-δ curves with a stable crack propagation region corresponded to joints that had failed cohesively. Conversely, sudden failure was often associated with a change in the type of failure from cohesive in the adhesive layer to interlaminar in the CFRP substrates. Typically occurring in the specimens subjected to greater mode II components, this change in the locus of failure could be partially explained by the particularly damaging effect of shear micro-cracks forming in the adhesive. It has been previously reported [148, 149] that their inclination tends to shift the failure path towards one of the arms, making its interface more prone to failure. Furthermore, in a recent study Blackman et al. [125] concluded that the propensity of this type of joints to fail in the composite depends on the transverse tensile stresses exerted on the CFRP substrates as compared to the transverse strength of the laminates. In addition, the response also proved to be very sensitive to the grit-blasting step of the surface pre-treatment. If overdone, this process could easily damage the outer layers of the laminate and increase the likelihood of interlaminar failure.

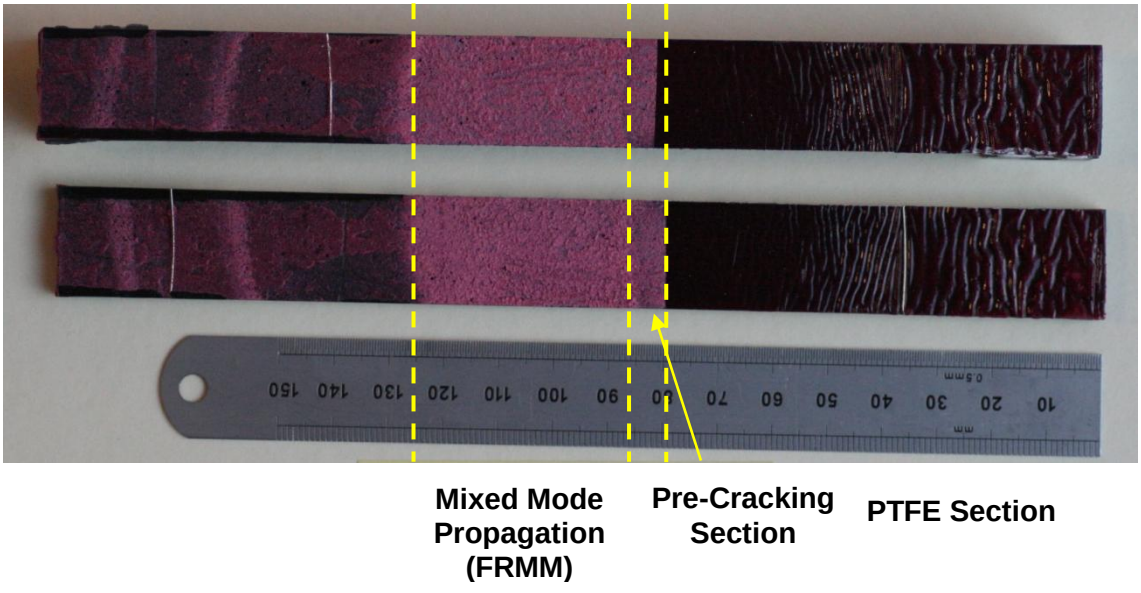

(a)

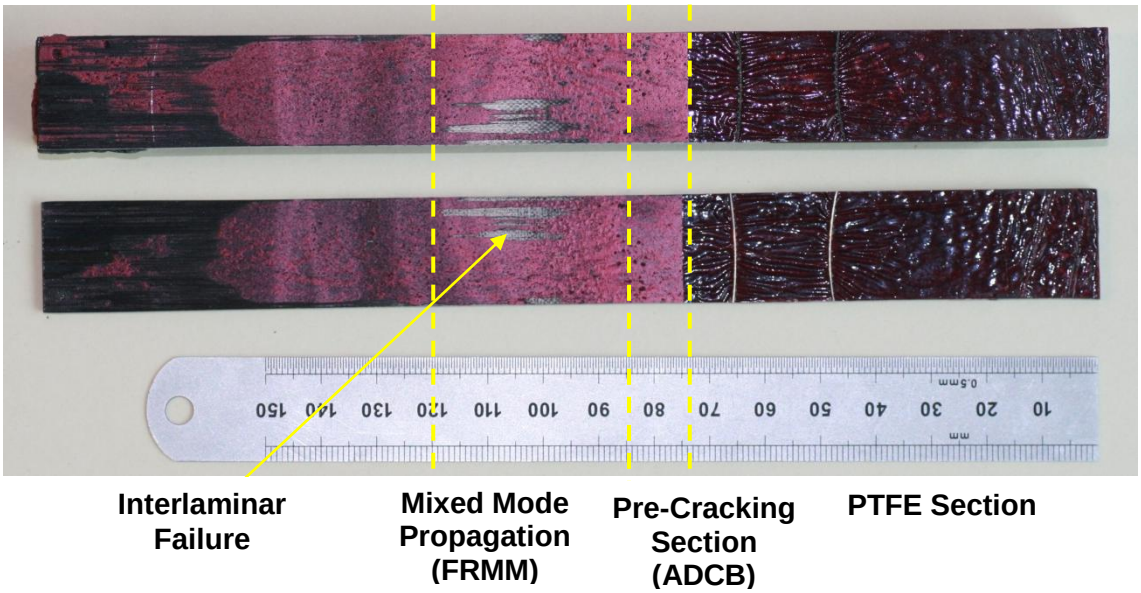

(b)

Figure 6.30. Typical examples of (a) fully cohesive and (b) partially interlaminar failure observed with AFRMM joints. The first image corresponds to a FRMM specimen, whereas the second one was obtained with an asymmetric joint loaded at the thickest arm. The pre-cracking section, analysed as an ADCB specimen, is easily identifiable.

The various analysis schemes described in Chapter 5 were used to determine the values of $G_{I/IIc}$ for each crack length, and the results were then combined with those of the typical initiation criteria to generate the relevant resistance curves. Very pronounced rising R-curves were always observed, especially if the non-linear criterion for initiation was considered as this often produced the lowest values. The curves reached a stable region where $G_{I/IIc}$ was fairly constant. This plateau was attained approximately after 5mm of crack growth in the

those specimens with smaller mode II components, whereas it required further growth in those with larger mixed mode ratios (≈10-15mm in the symmetric joints and even more when the thickest arm of the AFRMM was loaded).

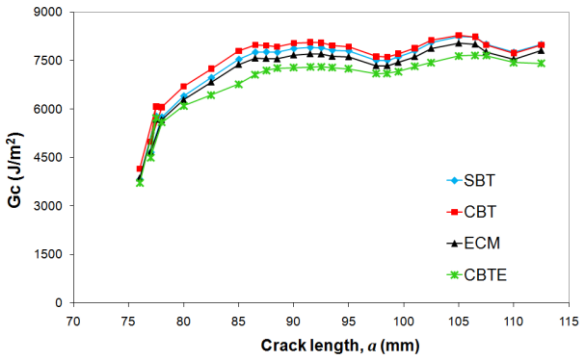

(a) FRMM Specimen (4mm/4mm)

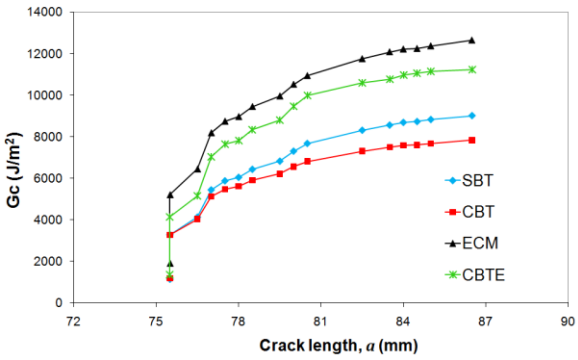

(b) Asymmetric joint (4mm/2mm) loaded at the thickest arm

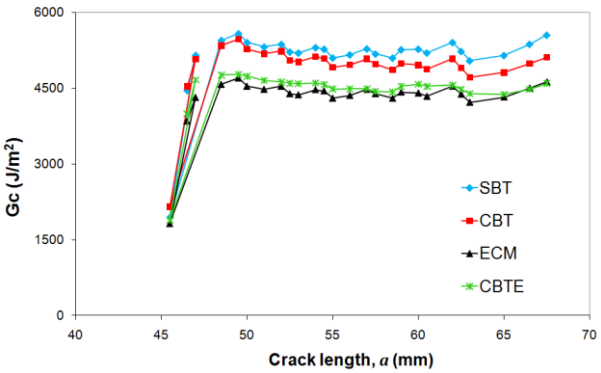

(c) AFRMM joint (2mm/4mm) loaded at the thinnest arm

Figure 6.31. Typical resistance curves for various types of AFRMM specimens bonded with AF163-2OST.

As shown in Figure 6.31-a, for the "quasi-symmetric" specimens the curves obtained with the four analysis techniques were very similar. The CBT consistently returned the highest G_c values, whereas the lower bound corresponded to the effective crack length approach. For the unbalanced joints in which the thickest arm was loaded (Figure 6.31-b) these methods swapped positions, while the SBT remained in between. However the ECM predictions became irregular and inaccurate due to the greater uncertainties in the crack length measurements. As in the mode II tests, the extensive damage developed ahead of the continuous crack tip in the form of micro-cracks complicated noticeably the visual measurement of the crack length. The severity of this problem increased with the shear component and led to a reliance on the CBTE values. This was also supported by the results obtained when the thinnest arm was loaded (Figure 6.31-c). In those cases, where the mixed

mode ratio was much closer to pure mode I, the ECM and CBTE curves were very similar, with the former usually slightly lower. On the other hand the simple beam theory yielded the highest values closely followed by CBT. The implied values of Δ ($\Delta_{implied}$) were relatively small for the symmetric configurations and those unbalanced joints where the thinnest arm was loaded. However, they rose dramatically as the proportion of mode II increased, due to (a) larger uncertainties in the visual crack length measurements and (b) the longer failure process zones. This agreed well with the extent of the micro-cracks and accumulated damage observed in these cases.

Figure 6.32 illustrates the initiation (MAX/5%) and propagation values of $G_{I/IIc}$ obtained for the various AFRMM specimens tested using the CBTE data reduction scheme. These results, including the individual thickness parameters (α) and the mixed mode ratios predicted by the three partitioning methods considered are also tabulated in Appendix F. Note that no averages have been included due to the inter-specimen variability of the mixed mode ratios obtained. For the same reason assessing the scatter was also difficult, although in general it appeared larger than in the mode I tests, especially as the shear component increased.

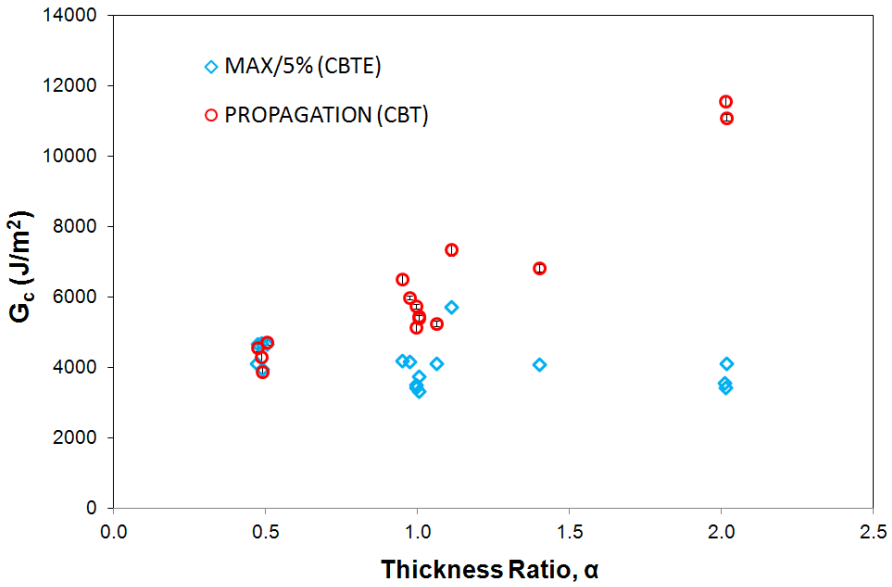

Figure 6.32. Initiation(MAX/5%) and propagation (average plateau) values of $G_{I/IIc}$ obtained for the CFRP-AFRMM specimens bonded with AF163-2OST (corresponding to CBTE).

As reported for the ADCB tests, some of the specimens yielded G_{Ic}^{mixed} values higher than the measured G_{Ic} (see section 6.2,G_{Ic}≈3032±170 J/m^2 for CBTE). This was the case for most joints with α<1 or α=1 regardless of the decomposition technique, whereas it only held true for those with α≈2 if Davidson's decomposition strategies were considered. Following the same reasoning employed in section 6.4.2, this behaviour could be linked to the damaging

effect of the carrier mat on the fracture energy of the film adhesive, which would be particularly damaging under pure mode I conditions.

Finally, the flexural modulus was back-calculated at each crack length for all the joints using equation (5.57). In general these resulted in fairly constant values very similar to those measured independently in three point bending tests (see Figure 6.33). However, sudden changes were observed in some specimens coinciding with regions of interlaminar failure. Obviously the data corresponding to those sections was excluded from the fracture energy calculations.

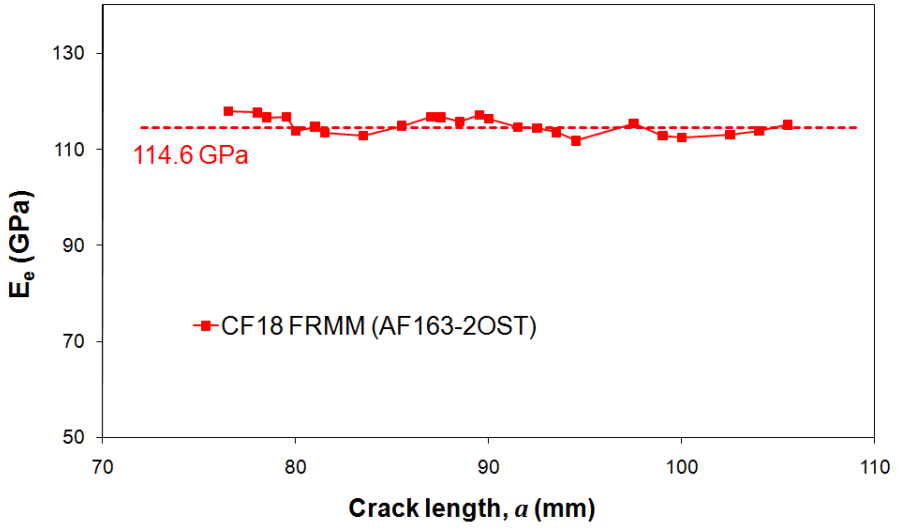

Figure 6.33. Example of back-calculated modulus for a FRMM specimen.

6.4.4 Discussion of Mixed Mode Results

It was clear that the total critical strain-energy release rate measure in the mixed mode tests (i.e. $G_{I/IIc}$) increased with the mode II component (see Figure 6.27 and Figure 6.32). This was typically accompanied by a change in the failure mechanism, which moved progressively towards that observed in pure mode II. That is, the number and size of the micro-cracks formed ahead of the continuous crack tip, as well as the area they covered, increased with the value of G_{II}/G. Even though it was not possible to identify the G_{IIc} plateau, this would seem to confirm that $G_{Ic}<G_{I/IIc}<G_{IIc}$.

In addition to an increment in the total fracture energy, the increase in the shear contribution induced by the geometrical asymmetry had important consequences concerning the locus of failure. The formation of micro-cracks and their subsequent coalescence gradually drove the crack propagation path closer to the interface, increasing the likelihood of interlaminar failure. Particularly evident in the AFRMM joints where the load was applied at

the thickest substrate, this problem appeared to be more severe in mixed mode than under pure shear because only one arm is loaded in the mixed mode specimens (see [148, 149]).

It was also observed that, regardless of the decomposition strategy considered, the mode I component measured with many of the configurations tested (i.e. G_{Ic}^{mixed}) was higher than G_{Ic}. Similar behaviour had been reported previously for delamination in carbon and glass-fibre composites, but often only for small mixed mode ratios [174, 213, 217, 224]. Associated in the past with experimental errors or the artificial effect of the partitioning method, this did not appear to be the case with the present adhesive system (especially where Davidson approaches were used). It was postulated here that this was due to the damaging effect of the carrier mat on the mode I toughness. The weaker path provided by the woven mat for mode I crack propagation would not be as well-defined, or exist at all, under mixed mode conditions, resulting in higher total fracture energies even if the shear contribution were very small, as in the ADCB specimens.

The effects of the partitioning method are discussed in depth in the next chapter, but a preliminary examination of the ADCB results identified certain inconsistencies with the Williams analysis. According to this method, these specimens should produce pure opening mode and therefore yield total fracture energies equal to G_{Ic} irrespective of α. However, the increasing $G_{I/IIc}$ values obtained seemed to suggest otherwise. One could argue that this is yet another by-product of the carrier mat but, even if this were exclusively restricted to pure mode I, it would hint at the existence of a mode II component.

With regard to the influence of the data reduction scheme, the effective crack length approach was considered the most accurate technique in all cases. Unsurprisingly, the discrepancies between these results and those obtained with the other methods increased with the mixed mode ratio, due to the additional uncertainties in the visual crack length measurements. The implied values of Δ bore witness to this: whilst small and fairly constant (≈3mm) for the symmetric configurations and those unbalanced joints where the thinnest arm was loaded, they increased dramatically (up to 21mm) for those cases with a larger shear component.

6.5 Chapter Summary

The results obtained for the different fracture specimens tested quasi-statically have been presented and discussed in this chapter. Initiation and propagation values of the adhesive fracture energy were calculated from the sets of load-displacement-crack length data recorded using the SBT, CBT, CBTE and ECM analysis methods.

Failure was generally cohesive, with the crack propagating through the adhesive layer in a stable manner. However, extensive damage in the form of micro-crack development ahead of the crack tip was observed as the proportion of mode II in the test was increased. These micro-cracks gradually directed the propagation path towards the adhesive/substrate interface, leading to interlaminar, unstable fracture in AFRMM joints loaded via the thickest arm.

The resistance curves exhibited the typical rising effect, the magnitude of which increased with the mixed mode ratio. With the exception of pure shear, G_c reached a relatively stable plateau, which increased with the mode II component. This would suggest that, for AF163-2OST, $G_{Ic}<G_{I/IIc}<G_{IIc}$. Further, neither the substrate material nor the geometry of the joint appeared to influence the initiation or plateau values of G_{Ic}.

The mode I component measured with many of the mixed mode configurations tested (i.e. G_{Ic}^{mixed}), particularly with the ADCB joints, was higher than G_{Ic}. In view of the G_{Ic} difference observed between the supported and unsupported version of the adhesive ($(G_{Ic})_{CBTE}$=3032±170 J/m^2 and $(G_{Ic})_{CBTE}$=4214±145 J/m^2 respectively), this behaviour was explained by the damaging effect of the carrier mat on the mode I toughness. Fractographic evidence has revealed that, in the DCB specimens bonded with AF163-2OST, failure occurred in the adhesive/scrim mat interface. The weaker path provided by the woven mat for mode I crack propagation would not be as well-defined, or exist at all, under mixed mode conditions, resulting in higher total fracture energies.

Uncertainties arose in the visual crack length measurements due to the extensive damage accumulated ahead of the crack tip. As a result, the effective crack length approach was considered the most accurate data reduction scheme, particularly as the mode II component increased.

Next, in Chapter 7, the results obtained for the different mixed mode ratios, are combined and fitted with a suitable function to define a propagation criterion of the form $G_c = G_c(\beta)$.

7. Quasi-Static Failure Criterion and Fatigue Experimental Results

7.1 Introduction

The first part of this chapter considers the definition of an appropriate fracture criterion for AF163-2OST. The fracture energies measured for the various mixed mode ratios tested were combined to generate plots of the form $G_c = G_c(G_{II}/G)$, fitting the experimental data points to suitable functions which could be then imported into the element user subroutine. In line with the results presented in Chapter 6, different solutions were obtained for each of the decomposition methods investigated (i.e. Williams, CTE/SF and CTE/NSF). The outcomes of the fracture mechanics fatigue test are discussed at the end of the chapter. Crack growth rates were computed from the experimental raw data obtained with the fracture specimens using the secant and polynomial methods. The resulting $da/dN = da/dN\,(G_{max})$ diagrams were then approximated by modified Paris laws, identifying the coefficients required by the cohesive formulation presented in Chapter 3 (i.e. $C_T, m, n_1, n_2,$ and G_{th}).

7.2 Quasi-Static Locus of Failure: Propagation Fracture Criterion

Originally proposed by O'Brien [397] for delamination in fibre-composite materials, a typical procedure to predict failure in bonded structures involves comparing the strain energy release rate applied to the joint with the critical value for the adhesive system considered. Most crack prediction methodologies are based on this idea, including those using common

numerical techniques such as VCCT or CZM [398, 399]. Measuring G_c for the material of interest is therefore necessary to implement this type of approach.

Failure in real bonded components often occurs under mixed mode conditions. Further, as demonstrated by the results presented in Chapter 6, the value of G_c generally depends on the mode mix. This dependence has also been frequently reported in the literature (e.g. [137, 162, 175, 213, 214]). Given that it is impractical to test all possible ratios, the fracture behaviour is typically extrapolated from the values measured for a small number of cases, requiring an appropriate function to fit the experimental data. The accuracy of any subsequent predictions depends on that of the individual measurements as well as on the suitability of the function chosen to approximate them. The element formulation presented in Chapter 3, which uses the function $G_c = G_c(G_{II}/G)$ to define the area under the traction-separation law (i.e. the cohesive parameter $\Delta^f(\beta)$), represents a good example of this approach.

Taking into account the considerations discussed in Chapter 2 (see section 2.3.5), three different functions have been employed in the present work to approximate the G_c results obtained with the various fracture specimens tested quasi-statically: a fourth or fifth order polynomial [223], the modified B-K criterion proposed in [217] and the bilinear law suggested in [213] (equations (7.1), (7.2) and (7.3) respectively). A least squares analysis was performed in each case to obtain the optimum values of the fitting parameters α_i.

$$G_c = \sum_{i=0}^{i=3,4,5} \alpha_i \left(\frac{G_{II}}{G}\right)^i \tag{7.1}$$

$$G_c = \frac{\mathrm{A} \cdot B}{B\left(1-\frac{G_{II}}{G}\right) + A\left(\frac{G_{II}}{G}\right)} \begin{cases} A = G_{IIc} + (G_{Ic} - G_{IIc})\left(1-\frac{G_{II}}{G}\right)^{\alpha_1} \\ B = G_{Ic} + (G_{IIc} - G_{Ic})\left(\frac{G_{II}}{G}\right)^{\alpha_2} \end{cases} \tag{7.2}$$

$$G_{Ic}^{mixed} = \begin{cases} \alpha_1 G_{IIc}^{mixed} + G_{Ic} & G_{IIc}^{mixed} \leq G_{IIc}^0 = (G_{Ic} + \alpha_2 G_{IIc})/(\alpha_2 - \alpha_1) \\ \alpha_2 G_{IIc}^{mixed} - \alpha_2 G_{IIc} & G_{IIc}^{mixed} > G_{IIc}^0 = (G_{Ic} + \alpha_2 G_{IIc})/(\alpha_2 - \alpha_1) \end{cases} \tag{7.3}$$

In addition to a suitable fracture criterion, the implementation of a prediction methodology such as that suggested by O'Brien requires a mode decomposition strategy for two reasons. Firstly, this strategy is needed to partition the total fracture energy measured with the test specimens into its individual components in order to define a suitable function $G_c = G_c(G_{II}/G)$. Secondly, a method to calculate the characteristic mixed mode ratio in the structure of interest is also essential to ensure that the applied strain energy release rate is compared to the correct critical value.

With regard to the first aspect, three different techniques have been evaluated for the analysis of the fracture mechanics joints, namely: Williams' global approach and both the CTE/SF and CTE/NSF decompositions proposed by Davidson. Consequently, different solutions were anticipated depending on the partitioning method considered. The most appropriate option for the adhesive investigated had to be indentified and then imported into the user subroutine for the accurate simulation of the TDLJ. On the other hand, the mode mix in the real component was computed at each individual integration point within the cohesive elements from the relative opening and sliding displacements (see Chapter 3, equations (3.26)). Obviously, consistency between both methods (that is, agreement in the mode mix predicted for any given geometry) would be crucial to ensure the theoretical soundness of the predictions, as discussed in Chapter 8.

The fracture criteria obtained using Williams and Davidson's theories are presented in the next sections. The plateau values of G_c measured with the fracture mechanics specimens tested quasi-statically were combined and approximated by equations (7.1)-(7.3). The corresponding initiation criterion, not required for the subsequent simulations, is included in Appendix G. Considered the most accurate data reduction scheme of those investigated, only the effective crack length results were employed, hence excluding the data gathered with the TDCB specimens (CBTE was not available for this test configuration).

7.2.1 Williams Mode Decomposition

The results obtained for Williams' global partitioning scheme are shown in Figure 7.1. The plot of G_{Ic}^{mixed} versus G_{IIc}^{mixed} (Figure 7.1-a) exhibited two distinct regions: an initial section where the mode I component rose very rapidly from G_{Ic} to a maximum of approximately 4300 J/m^2 was followed by a progressive decrease of G_{Ic}^{mixed} with the mode II component, G_{IIc}^{mixed}. Even though similar but less marked responses have been reported elsewhere (e.g. [174, 224, 293]), this behaviour appeared a by-product of the woven carrier mat, which provided a weak path for crack propagation under mode I conditions and therefore induced an artificially low value of G_{Ic}. The higher mode I fracture energy measured for the unsupported adhesive supports this theory. Additionally, the difficulties of this decomposition method to deal with the ADCB configuration became evident yet again in Figure 7.1-a, since the critical strain-energy release rates obtained with these joints were higher than those yielded by the symmetric specimens.

Unlike many well-established criteria such as the power law, the three functions used here to approximate the experimental data were all able to capture the overall fracture response of AF163-2OST. Both the fourth order polynomial and the modified B-K criterion provided excellent fits, whereas the agreement attained with the bilinear function was poorer due to

the limitations of its mathematical formulation. Table 7.1 presents the values of the fitting parameters obtained after a non-linear least square analysis in each case. Although included in the plots, the data points corresponding to the ADCB joints were not taken into account in the calculation of the fitting parameters.

Despite the scatter in the AFRMM results and not having been able to reach a stable crack propagation stage or plateau in any of the mode II tests, the trend observed in Figure 7.1-b indicates that $G_{Ic}<G_{I/IIc}<G_{IIc}$, which facilitates the extrapolation of G_{IIc}. The inferred value of G_{IIc} was almost identical for the three functions: approximately 17800 J/m^2. Similarly, the mode I fracture energies estimated by both the polynomial and the modified B-K criterion were remarkably close to the average of the DCB results (i.e. 3032 J/m^2).

The extrapolated values of G_{IIc} (≈17800 J/m^2) agreed well with the information extracted from the ELS tests, as the partial resistance curves obtained for those specimens (see Figure 6.21) suggest that $G_{IIc}>16000$ J/m^2. Should this value be correct, it would represent approximately a 6 times increment over the mode I fracture energy, which is slightly larger but still similar to the proportions observed for other rubber-toughened epoxy adhesives [141, 149]. Of course, the G_{IIc}/G_{Ic} ratio would be smaller if the results obtained with the unsupported material were considered, given that the damaging influence of the carrier mat is thought to affect almost exclusively the mode I toughness.

Table 7.1. Least square curve fit parameters for the propagation criterion corresponding to Williams' global approach.

PROPAGATION CRITERION: Williams (No ADCB Specimens)							
Fracture Criterion	**Least Square Fitting Parameters**					G_{Ic} (J/m^2)	G_{IIc} (J/m^2)
	α_0	α_1	α_2	α_3	α_4		
Polynomial	3049	25108	-72944	76881	-14274	3049	17820
Modified B-K	-	1.68	4.05	-	-	3039	17975
Bi-Linear	-	1.76	-0.22	-	-	3169	17926

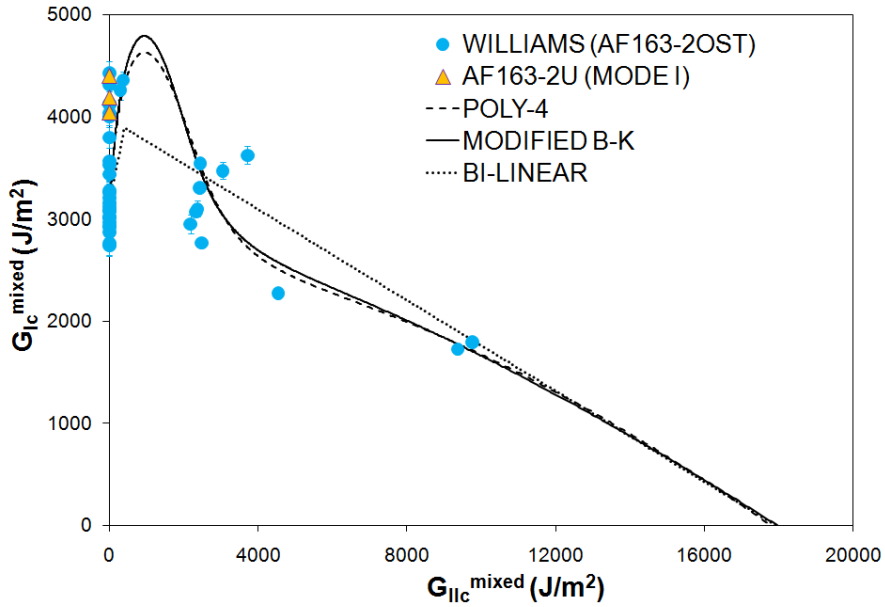

(a)

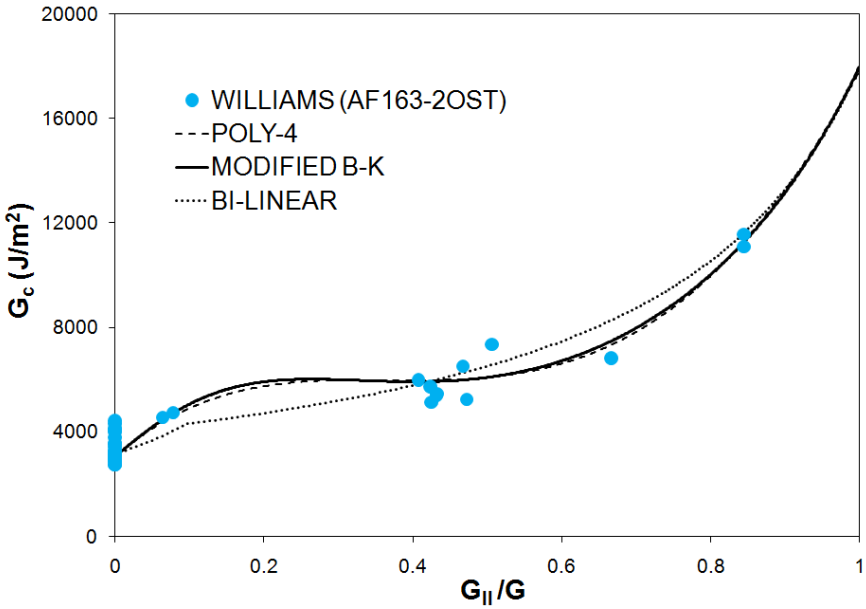

(b)

Figure 7.1. "Plateau" fracture energies obtained with Williams' decomposition scheme. The experimental data points have been approximated by three criteria: a 4th order polynomial, the modified B-K criterion and a bilinear law. The G_{Ic} values measured for the unsupported adhesive have also been included.

7.2.2 CTE/NSF Mode Decomposition

In contrast to the propagation locus obtained with Williams' global approach, the plot of G_{Ic}^{mixed} versus G_{IIc}^{mixed} corresponding to the CTE/NSF mode decomposition did not decrease with G_{IIc}^{mixed} after the initial rising section (see Figure 7.2-a). Instead, the mode I component

of the fracture energy appeared to stabilize somewhere between 3500 and 4500 J/m^2. The damaging effect of the carrier mat was still noticeable (i.e. $G_{Ic}^{mixed} > G_{Ic}$), while the resulting shape made the extrapolation of a G_{IIc} value much more difficult. In fact, each of the functions used to approximate the experimental data provided very different estimates, which in all cases were considerably larger than those obtained from Williams' partitioning (see Table 7.2).

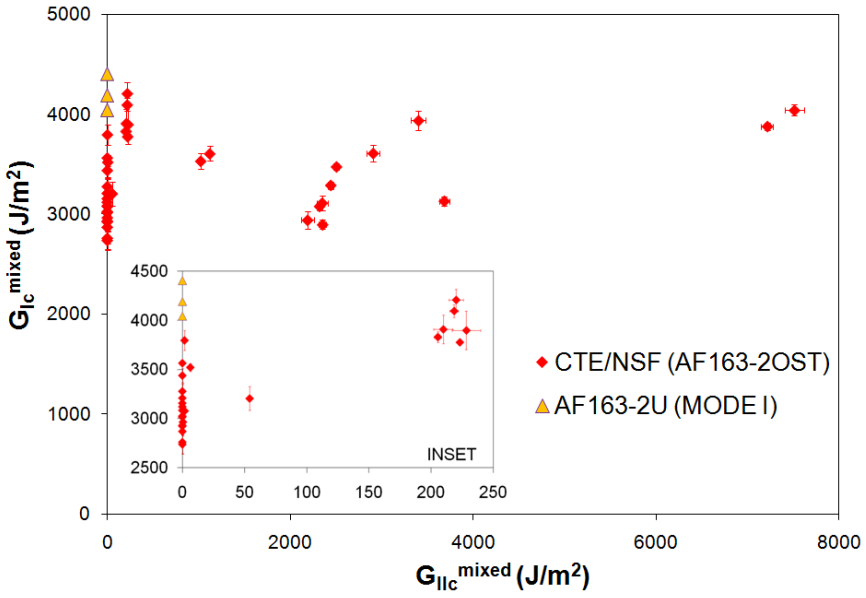

(a)

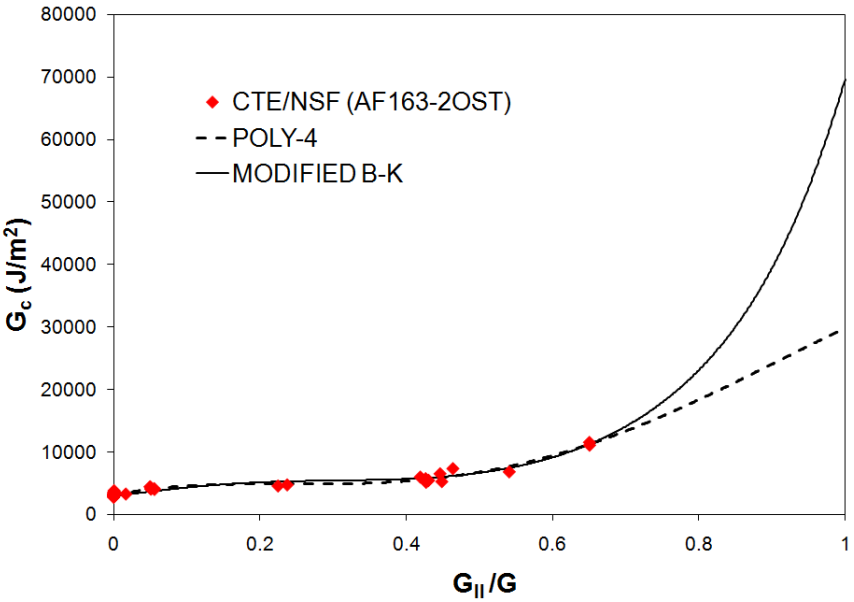

(b)

Figure 7.2. "Plateau" fracture energies obtained with Davidson's non-singular field decomposition. The experimental data points have been approximated by a 4th order polynomial and the modified B-K criterion. The G_{Ic} values measured for the unsupported adhesive have also been included in (a).

Table 7.2. Least squares curve fit parameters for the propagation criterion corresponding to CTE/NSF decomposition.

PROPAGATION CRITERION: CTE/NSF							
Fracture Criterion	**Least Square Fitting Parameters**					G_{Ic} $(\mathrm{J/m^2})$	G_{IIc} $(\mathrm{J/m^2})$
	α_0	α_1	α_2	α_3	α_4		
Polynomial	3055	24975	-119740	221783	-103039	3055	27035
Modified B-K	-	0.24	5.41	-	-	2889	69598
Bi-Linear	-	2.86	-0.0024	-	-	2902	1531572

These extremely high values of the mode II fracture energy would suggest a very tough adhesive in shear. However, they seem unrealistic and physically not very relevant. Furthermore, G_{IIc} would be expected to be independent of the mode partitioning method. As discussed in Chapter 2 (section 2.3.3), the three decomposition strategies used in the present work would agree in the mode mix for any symmetric configuration, including the ELS joints [136, 137, 160, 175]. Moreover, experimental evidence suggests that the significant discrepancies in the mixed mode response obtained with different partitioning methods are compatible with the same values of the fracture toughness for the pure modes (e.g. [162, 178], see Figure 7.3).

Bearing this in mind, even if the mixed mode behaviour predicted by Williams and Davidson methods could be completely different (except for the data points corresponding to the symmetric FRMM joints), both approaches should yield the same values of G_{Ic} and G_{IIc}. Since the shape of Williams' locus was much better suited for the extrapolation than that of the non-singular field version of Davidson's analysis, the mode II fracture energy determined from the former was adopted hereafter. Consequently, new least squares fitting analyses had to be performed for CTE/NSF to take into account the additional constraint G_{IIc}≈17800 $\mathrm{J/m^2}$. Table 7.3 contains the resulting values for the fitting parameters, and the corresponding criteria are illustrated in Figure 7.4.

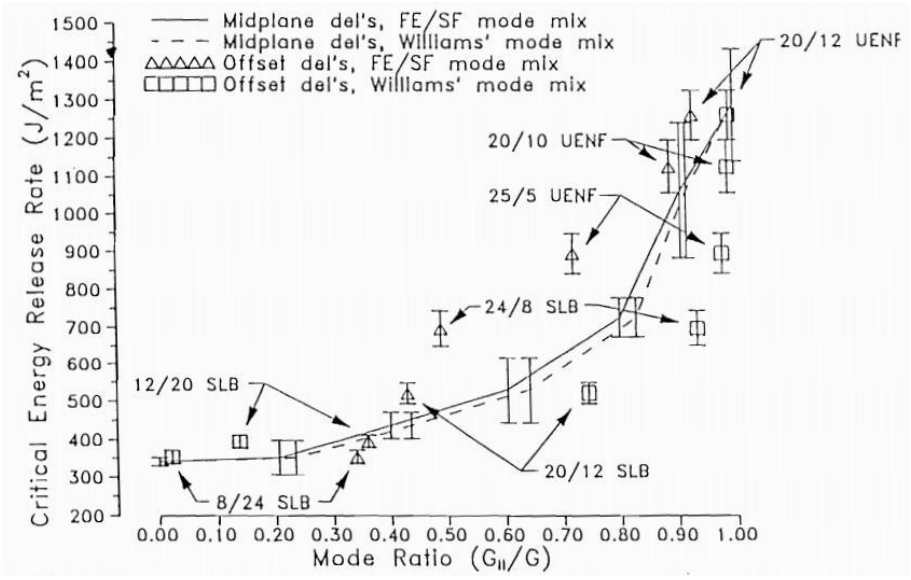

Figure 7.3. Comparison of the delamination results in CFRP laminates obtained for various mode decomposition strategies [162]

Table 7.3. Least squares curve fit parameters for the propagation criterion corresponding to CTE/NSF decomposition after imposing the additional constraint G_{IIc}≈17800 J/m^2.

PROPOAGATION CRITERION: CTE/NSF (Constrained G_{IIc}≈17800 J/m^2)							
Fracture Criterion	**Least Square Fitting Parameters**					G_{Ic} (J/m^2)	G_{IIc} (J/m^2)
	α_0	α_1	α_2	α_3	α_4		
Polynomial	3038	27177	142538	285655	155526	3038	17806
Modified B-K	-	0.43	1.51	-	-	3185	17845
Bi-Linear	-	0.46	-0.32	-	-	3192	15985

Even though there was no certainty that this value (i.e. G_{IIc}≈17800 J/m^2) corresponded to the actual in-plane shear fracture energy, it was deemed a plausible estimate in view of the experimental information available (i.e. the partial ELS resistance curves and the William's extrapolations). In addition, it would appear to represent a lower bound which, in the worst case scenario, should provide conservative predictions.

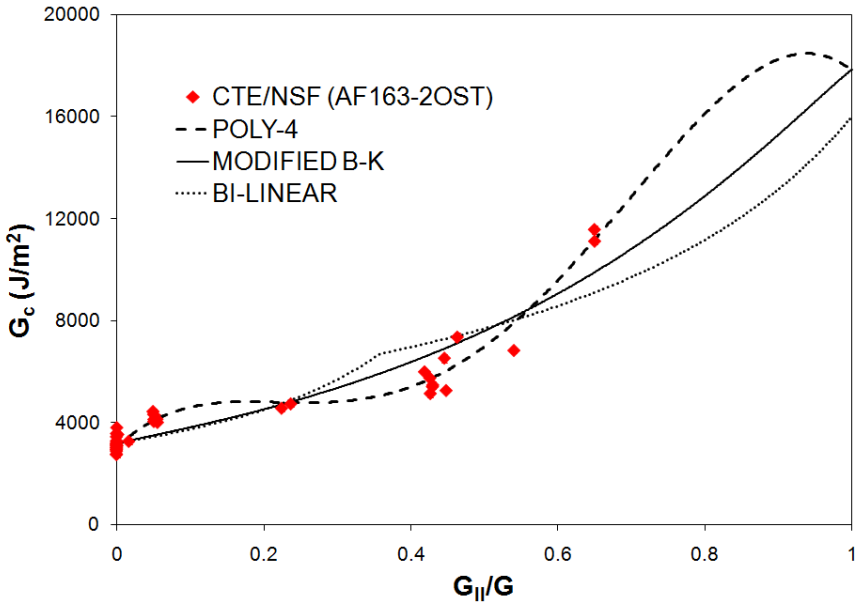

Figure 7.4. Functions used to approximate the CTE/NSF "plateau" fracture energies. The least square fitting parameters were chosen so that G_{IIc}≈17800 J/m².

The 4th order polynomial clearly stood out as the most suitable criterion of those considered for the CTE/NSF decomposition. A 5th order version was also studied, but the results were almost identical. Finally, it should be noted that if this function was accepted, the relationship $G_{Ic}<G_{I/IIc}<G_{IIc}$ would no longer hold true for very large mixed mode ratios.

7.2.3 CTE/SF Mode Decomposition

The propagation locus corresponding to the singular field version of Davidson's analysis was very different to those obtained for the CTE/NSF or the global approach. As illustrated in Figure 7.5-a, rather than decreasing with G_{IIc}^{mixed} or remaining fairly constant, the mode I component of the fracture energy measured for the AFRMM specimens rose linearly with the shear contribution. Hashemi et al. [175] and Davidson et al. [178] reported similar trends for this type of joint when using the local decomposition for the study of delamination in carbon-fibre composites. Albeit not as abruptly as in the other cases, the damaging effect of the carrier mat manifested itself as an initial increase in G_{Ic}^{mixed}.

Equations (7.2) and (7.3) were unable to describe this shape, whereas the approximation with the 4th order polynomial seemed unrealistic given the extremely large mode II toughness predicted. Higher order functions were considered, but they often led to important undulations which lacked physical relevance. Therefore, following the same reasoning introduced in section 7.2.2, it was decided to accept the value of G_{II} extrapolated from Williams' locus and repeat the least squares analysis to compute new "constrained" coefficients for the polynomial (see Table 7.4).

It was evident from Figure 7.5-b that some of the intermediate critical strain energies predicted by this "constrained" criterion were still extremely high. Consequently, the relationship $G_{Ic}<G_{I/IIc}<G_{IIc}$ did not appear to hold true for the plateau values in this case.

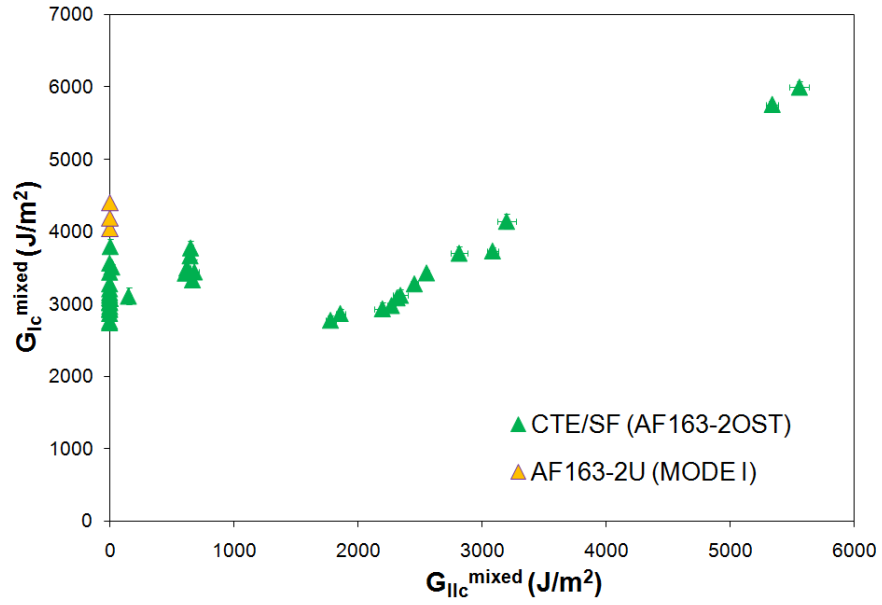

(a)

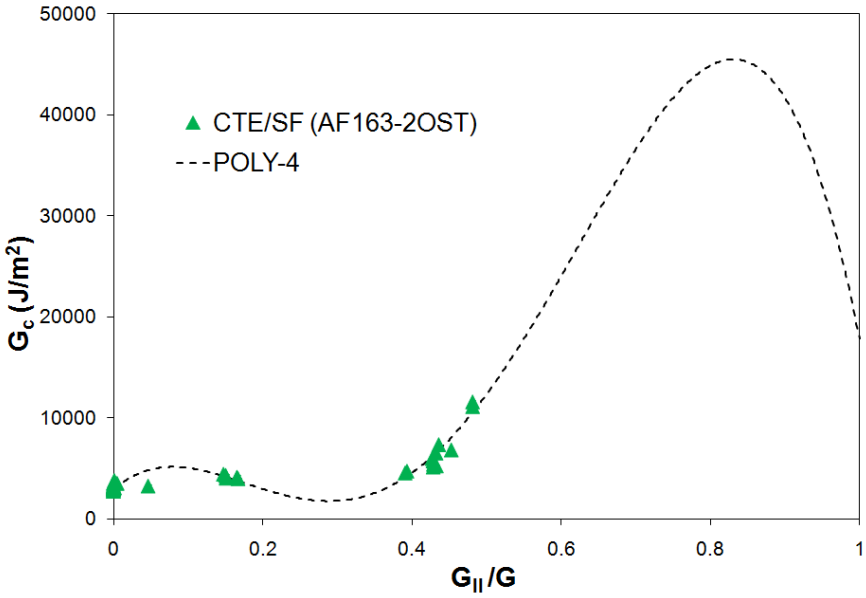

(b)

Figure 7.5. "Plateau" fracture energies obtained with Davidson's singular field mode decomposition. The additional condition G_{IIc}≈17800 J/m^2 was imposed to calculate the coefficients of the 4th order polynomial fit. The G_{Ic} values measured for the unsupported adhesive have also been included in (a).

Table 7.4. Coefficients of the 4th order polynomial used to approximate the propagation fracture criterion corresponding to the CTE/SF decomposition. The values obtained after imposing the additional constraint G_{IIc}≈17800 J/m^2 have also been included.

PROPAGATION CRITERION: CTE/SF DECOMPOSITION							
Fracture Criterion	**Least Square Fitting Parameters**					G_{Ic} (J/m^2)	G_{IIc} (J/m^2)
	α_0	α_1	α_2	α_3	α_4		
Polynomial	2975	-3658	209062	-1113010	1594420	2975	689789
Polynomial (Constrained G_{IIc}≈17800 J/m^2)	2897	65082	-565226	1376752	-861698	2897	17807

7.2.4 Further Comments: Effect of the Mode Decomposition Strategy

The propagation failure loci obtained with the three mode decompositions investigated in the present work are illustrated in Figure 7.6. However, the plots of G_c versus the mixed mode G_{II}/G shown in Figure 7.7 are better suited than the traditional loci to carry out a comparison because they employ two independent variables. As seen in Chapter 5, the mode mix for the fracture mechanics specimens is controlled by the joint geometry and the substrate materials and, since the same values of G_c were used in all cases (corresponding to CBTE), any discrepancies observed between the three $G_c = G_c(G_{II}/G)$ solutions would be solely attributable to the different partitioning strategies employed. In addition, this representation of the fracture criterion is easier to implement in the UEL subroutine. Considered the most suitable functions of those studied, the 4th order polynomials used to approximate the experimental data (with the supplementary constraint G_{IIc}≈17800 J/m^2) have also been included in Figure 7.7.

Despite being forced to agree at the pure mode values, the relative position of the three curves varied for the mixed mode cases. The singular field solution predicted higher fracture energies than both the non-singular and Williams' approaches for any ratio above that of the symmetric FRMM configuration (i.e. $G_c^{SF} < G_c^{NSF} < G_c^W$ for $G_{II}/G > 0.429$). For the interval $0.15 < G_{II}/G < 0.429$, the global and CTE/SF curves exchanged positions, while the non-singular field values remained somewhere in between the two (i.e. $G_c^W < G_c^{NSF} < G_c^{SF}$ for $0.15 < G_{II}/G < 0.429$). Finally, influenced by the ADCB results, the CTE/SF curve was again above that of the NSF method in the near pure mode I region (i.e. $G_c^{NSF} < G_c^W < G_c^{SF}$ for $G_{II}/G < 0.15$). Equivalent responses can be found elsewhere (e.g. [162]).

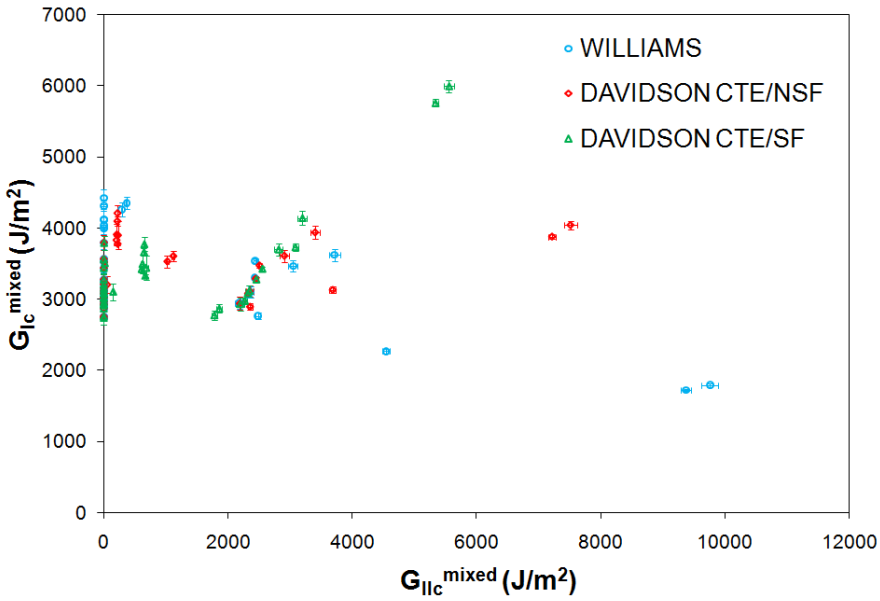

Figure 7.6. Propagation loci obtained for AF163-2OST for the various partitioning schemes investigated.

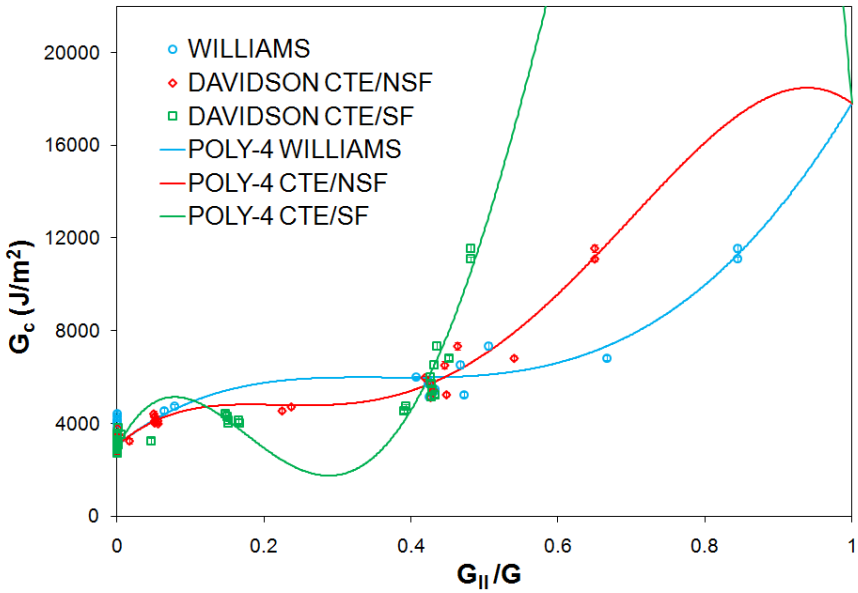

Figure 7.7. Plots of G_c (AF163-2OST) versus the mixed mode ratio G_{II}/G for the three mode decompositions investigated. The fourth order polynomial used to approximate the experimental data have also been included (the coefficients in the CTE/SF and CTE/NSF were chosen so that G_{IIc}≈17800 J/m^2).

Despite the substantial differences, there was not sufficient experimental evidence to identify the correct partitioning strategy. The fracture criterion should be independent of the test geometry, thus for any decomposition to be fully consistent, it would have to produce the same $G_c = G_c(G_{II}/G)$ function irrespective of whether it was derived using symmetric or asymmetric specimens (or a combination of both). Bearing in mind that all the methods

agree in the mode mix for the symmetric cases, additional tests would have to be performed using a symmetric configuration (for example the MMB) in order to determine which one of these partitioning theories, if any, was correct. Note that a similar approach was followed in [160, 162] to derive the expression for Ω_{NSF}.

Nevertheless, even though no final decision could be made without those complementary tests, the extensive damage observed ahead of the crack tip in the mixed mode and in-plane shear tests would suggest that the local solution is not the most appropriate one for this particular adhesive. Whilst not directly applicable to adhesive problems due to ply thickness effects, similar conclusions (i.e. large process zones and therefore invalidity of the CTE/SF for epoxy resins) have been reported by other authors when investigating delamination in carbon-epoxy composites (e.g. [136, 137, 162, 175]). Some of those studies also highlighted the shortcomings of Williams' global approach [160, 162, 179], the theoretical soundness of which should be examined in depth due to the inconsistencies observed for the ADCB joints. Of course, this does not mean that the CTE/NSF provided the correct results, but it has certain advantages over the others.

Finally, to ensure the consistency of the prediction methodology, it is essential that the technique (numerical or analytical) used to compute the mode mix in the structure investigated were in accordance with that employed in the derivation of the fracture criterion. That is, they both should predict the same mixed mode ratio for any given geometry. Although this equivalence alone would not be sufficient to circumvent the disagreement between the various partitioning strategies, it is a requirement for the consistency of the methodology. This aspect is discussed in more detail in Chapter 8.

7.3 Fracture Mechanics Fatigue Results

Two different methodologies are proposed in the present work for the prediction of the fatigue life-time in adhesively-bonded joints. Based on the cohesive element formulation introduced in Chapter 3, their implementation requires fatigue crack growth rate data in addition to the quasi-static fracture criterion discussed above. Whilst the first technique designed to model the full S-N response of the structure under consideration requires the whole $da/dN = da/dN\,(G_{max})$ curve as input data, only the fracture energy corresponding to the threshold is required in the second technique in order to estimate the fatigue limit.

There is good evidence to suggest that the fatigue response (i.e. the crack growth rate data) generally depends on the mode mix (e.g. [204, 206, 228, 400]). Following an equivalent approach to that adopted for the quasi-static problems, the entire behaviour could be

extrapolated from the experimental results obtained for a reduced number of ratios. As described in Chapter 3, plots of da/dN versus G_{max} would be derived from these tests and the then fitted to individual modified Paris laws. The values of the fitting parameters (i.e. C_T, m, n_1, n_2, G_{th} and G_c) obtained for each ratio tested would be then combined and used to generate functions that describe their variation with the mode mix (see equations (3.65)-(3.69)). Obviously, G_c would be set equal to one of the "plateau" fracture criteria discussed in the previous section.

Due to time constraints, only tests under pure modes I and II were performed in the present work. Furthermore, the latter, carried out using ENF specimens manufactured with titanium substrates, were unsuccessful. The following sections detail the results obtained in these experiments.

7.3.1 Mode I Fatigue: Results and Discussion

7.3.1.1 Introduction

Mode I fatigue testing is often the method of choice to assess the durability of adhesive joints [11]. This is because mode I loading is thought to represent the severest test of the interface. Furthermore, when carried out under the appropriate temperature, humidity and atmospheric conditions, this type of test can be used to evaluate the susceptibility of diverse surface treatments to environmental attack or to simulate accelerated degradation [21, 23].

The results obtained with titanium DCB specimens tested in fatigue under both "dry" and "wet" conditions are discussed next. "Dry" experiments were performed at ambient conditions (approximately 23±1°C and 55%RH), whereas coupons were submerged in a bath of distilled water roughly at 25±3°C for "wet" tests. Only the "dry" data has subsequently been used in this thesis to validate the fatigue prediction methodologies proposed in Chapter 3. However, the "wet" results provide valuable information for the design phase regarding the performance of the adhesive system under investigation.

7.3.1.2 DCB Fatigue Results

A minimum of three DCB specimens were employed to characterize the mode I fatigue behaviour of AF163-2OST (i.e. supported material) under both "dry" and "wet" conditions. Manufactured according to the procedure described in section 4.3 using 7mm thick titanium beams previously anodised, the joints were pre-cracked quasi-statically prior to applying the cyclic loading. Previous measurements using an optical microscope and a micrometer had

revealed that the average bondline thickness values were very close to the nominal value (i.e. 0.4mm).

As explained in Chapter 4, the crack length (a), maximum load (P_{max}) and number of cycles (N) were recorded at intervals during these tests. Figure 7.8 illustrates examples of the typical curves obtained for "dry" and "wet" specimens. The crack length increased with time, while the growth rate rapidly decreased with time until propagation eventually ceased. When da/dN <10^{-7} mm/cycle the test was stopped and the specimen assumed to have reached the threshold. Crack growth led to an increase in the compliance of the joint and thus to a drop in P_{max} given that the maximum displacement remained unchanged for the duration of the experiment (δ_{max}=1.35mm).

Even though these trends were observed for both the "dry" and "wet" tests, the relative position of the resulting curves was unexpected. Instead of damaging the interface, the wet environment appeared to somehow slow down the crack growth. It was also noticed that the scatter was greater in the "wet" experiments.

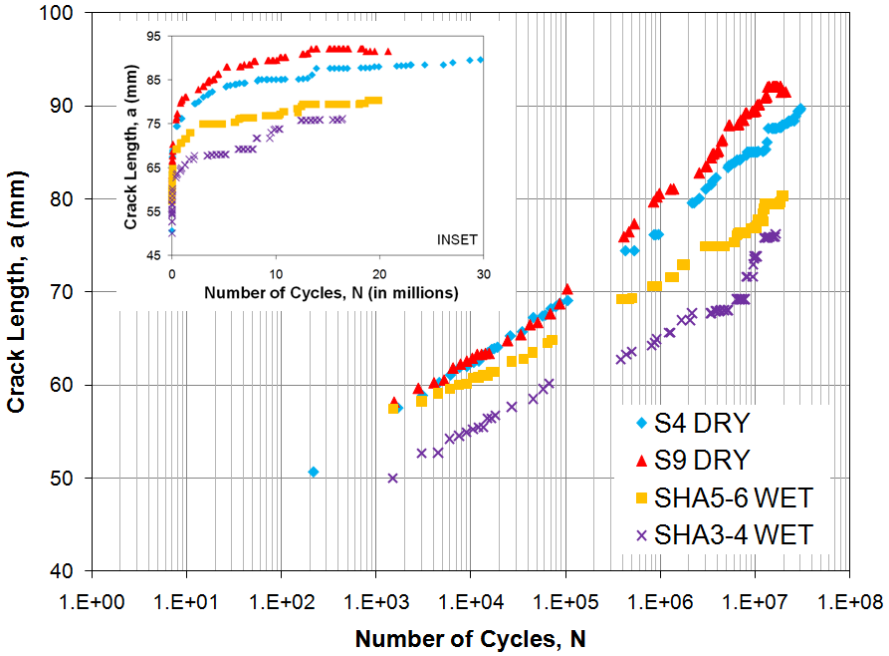

(a)

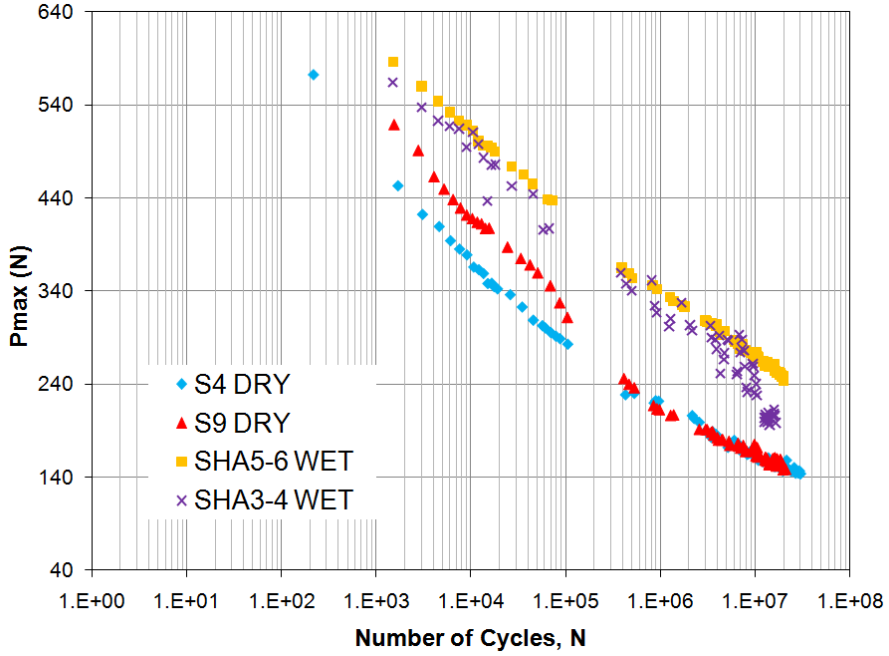

(b)

Figure 7.8. Typical plots of (a) the crack length a and (b) the maximum load P_{max} versus the number of cycles N obtained for the Ti-DCB specimens tested in cyclic fatigue under both "dry" and "wet" conditions.

The change in compliance with the crack length was in good agreement with the theoretical predictions, as demonstrated by the linear trend observed in the plots of $(C/N)^{1/3}$ versus a

(see Figure 7.9). In line with the quasi-static results, the lines of best fit did not intercept the origin of the graph but a negative value approximately between 10 and 12mm.

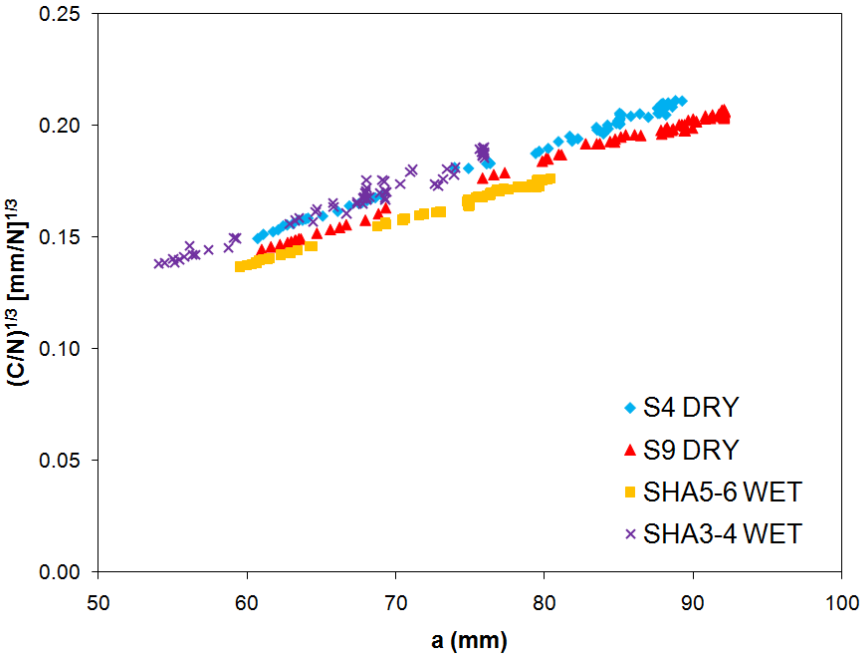

Figure 7.9. Values of $(C/N)^{1/3}$ versus crack length a for typical titanium DCB specimens tested in fatigue.

After the tests, the specimens were loaded monotonically and broken apart. Visual inspection of the fracture surfaces revealed that the failure had been mainly cohesive in the adhesive layer in all cases (see Figure 7.10). Not only did this confirm that the water had not weakened the interface, but it would also suggest that some alteration had occurred within the epoxy resin to justify the consistently slower crack growth and apparent higher toughness obtained in the "wet" specimens.

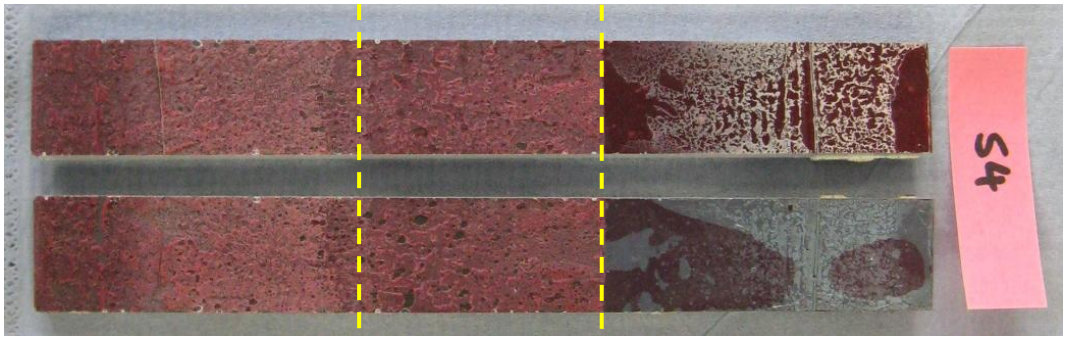

(a)

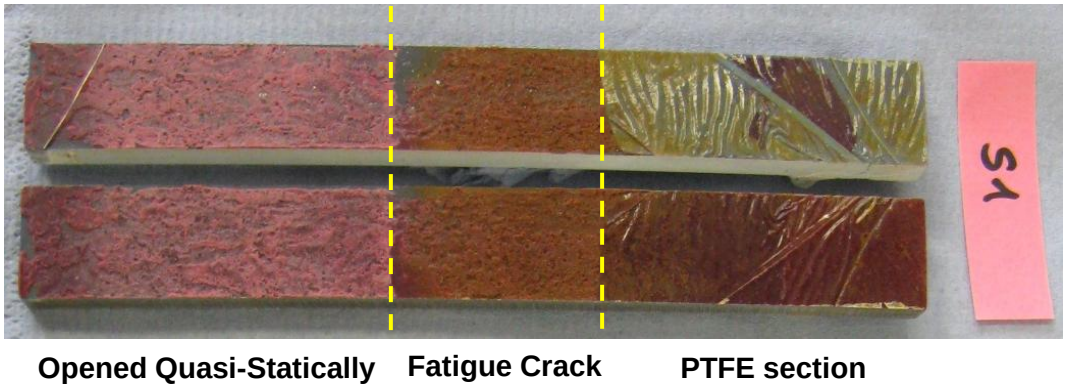

(b)

Figure 7.10. Examples of the fracture surfaces obtained after testing DCB specimen in fatigue under (a) "dry" and (b) "wet" conditions.

The sets of experimental data ($N_i - P_{max_i} - a_i$) were then analysed to generate plots of da/dN versus G_{max}. Although the usual data reduction schemes (i.e. SBT, CBT, ECM and CBTE) were employed to calculate the values of G_{max}, the results of the effective crack length approach were typically favoured since this was considered the most accurate technique. The corresponding fatigue crack growth rates were computed according to both the secant and incremental polynomial methods (see Chapter 5).

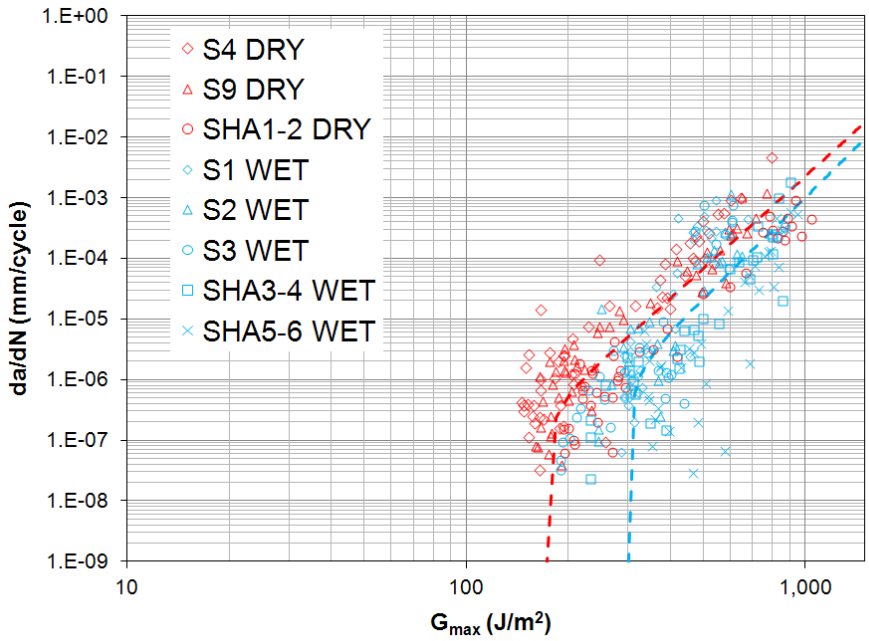

Figure 7.11. Typical $da/dN = da/dN\,(G_{max})$ curves obtained for Ti-DCB specimens fatigued under both "dry" and "wet" conditions using the secant method to determine the crack growth rates.

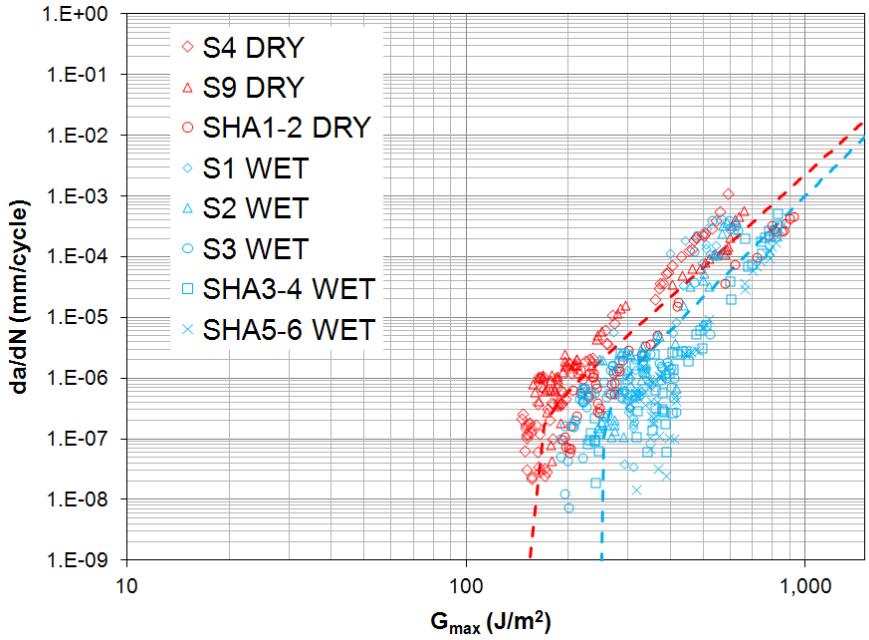

Figure 7.12. Typical $da/dN = da/dN\,(G_{max})$ curves obtained for Ti-DCB specimens fatigued under both "dry" and "wet" conditions using the incremental polynomial method ($n = 3$) to determine the crack growth rates.

As illustrated in Figure 7.11 and Figure 7.12, the resulting $da/dN = da/dN\,(G_{max})$ curves exhibited the characteristic sigmoidal shape, displaying well-defined linear regimen and threshold regions. It was not possible to obtain reliable information from the rapid growth

section due to the difficulties to measure the crack length accurately in the initial stages of the tests. In accordance with previous studies (e.g. [401, 402]), the incremental polynomial method appeared to reduce the scatter and produced smoother results. Albeit appreciable in both the "wet" and "dry" cases, the improvement was particularly significant in the former as a consequence of the larger scatter in the original data points.

Independent of the analysis technique considered, the relative position of the "dry" and "wet" curves confirmed the apparent higher toughness of the specimens tested in water. These exhibited larger threshold fracture energies (250J/m^2 versus 155J/m^2) and steeper linear regions than the joints fatigued at ambient conditions. Bearing in mind that in all cases the failure was mainly cohesive, this would suggest that the saturated environment somehow modified the properties of the epoxy resin, probably via plasticisation (e.g. [403]).

Despite requiring long periods of exposure, the tensile properties of bulk structural adhesives have been found to change upon ingress of water (e.g. [18, 20, 404]). In "wet" fatigue tests this effect often goes unnoticed because the moisture attacks primarily the adhesive-substrate interface and the joint tends to fail interfacially (i.e. the toughness drops notably). However, when both the "dry" and "wet" specimens fail cohesively, this phenomenon becomes evident. Obviously, the susceptibility of the adhesive to water absorption would determine the outcome of the tests in those situations. For example, for cases of low propensity to water absorption, virtually the same fatigue response has been obtained under both "dry" and "wet" conditions [23], whereas bigger differences can be seen for other materials such as those under investigation in the present work (e.g. [405, 406]).

Finally, the results corresponding to the "dry" specimens were approximated by a modified Paris law. The values of the fitting parameters, the meaning and determination of which have discussed in depth in [119, 234, 407], were calculated using the least squares method. Despite not being able to obtain information on the rapid growth region, the value of G_c was set equal to the mode I fracture energy measured quasi-statically (i.e. $G_{Ic} \approx 3030\ \text{J/m}^2$). Following references [23, 408], the values of the transition coefficients (i.e. n_{1_I} and n_{2_I}) were held constant during the regression process to avoid undesired changes in m and C_T. Furthermore, given the lack of data in close proximity to G_{Ic}, the calculations were simplified by letting $n_{1_I} = n_{2_I}$ (see Table 7.5).

Finally, it should be noted that the ratio $G_{Ith}/G_{Ic} \approx 0.05$, was much smaller than that of many typical commercial systems (see [409]). This could be yet another negative consequence of the carrier mat. If the weak interface existing between the adhesive and the woven mat was an issue in the quasi-static tests, it is likely that it also offered a weak path for crack propagation under fatigue loading.

Table 7.5. Fitting coefficients of the modified Paris law for pure mode I tests carried out under "dry" conditions. The least square fit has been applied using the results obtained with the incremental polynomial method.

	m_I	$C_{T_I}(mm/cycle)$	n_{1_I}	n_{2_I}	$G_{th_I}\,(J/m^2)$	$G_{Ic}(J/m^2)$
Pure mode I "Dry"	5.065	$1.421 \cdot 10^{-18}$	10	10	155	3030

7.3.2 Mode II Fatigue

Titanium ENF specimens were employed to characterize the mode II fatigue behaviour of AF163-2OST. Manufactured using 8mm thick substrates, these joints were pre-cracked in mode I and then tested at ambient conditions (approximately 23±1°C and 55%RH) according to the procedure described in section 4.4.3.2.2.

The maximum load (P_{max}), crack length (a) and number of cycles (N) were monitored during these experiments. Unfortunately, the precision of the cyclic load applied to the specimens was limited by that of the control unit in the test machine. Increasing the maximum applied displacements minimized the extent of this problem and improved the overall accuracy of the system, but it led to rapid crack propagation and plastic deformation in the metallic arms. Similarly, considerable uncertainties surrounded the determination of the crack lengths due the damage accumulated in the adhesive layer.

As illustrated in Figure 7.13, the ENF joints failed mainly at the adhesive-substrate interface. The tests parameters were modified in an attempt to promote cohesive failure. Different combinations of half-span length, initial crack length and maximum applied displacement were investigated. However, interfacial fracture always resulted. Hence, any fatigue crack growth rate derived from these tests should not be used in the FE simulations.

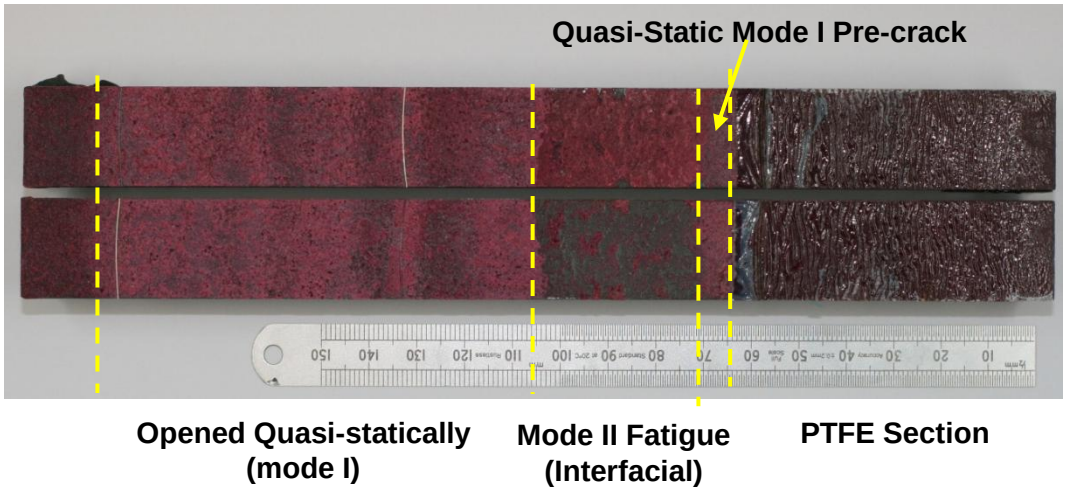

Figure 7.13. Examples of the fracture surfaces obtained after testing TI-ENF specimen in fatigue

Taking into account the inability to determine the coefficients of the Paris law for mode II, it has been necessary to make additional assumptions in the subsequent FE models. As for the mode II fatigue tests, a more detailed study, possibly considering alternative configurations or specimen designs, is required.

7.4 Chapter Summary

The adhesive fracture energies obtained for the various mixed mode ratios tested have been combined to generate a propagation criterion of the form $G_c = G_c(G_{II}/G)$, fitting the experimental data points to suitable functions: a fourth order polynomial, a modified B-K criterion and a bilinear law. Different solutions have been obtained for each of the decomposition methods investigated (i.e. Williams, CTE/SF and CTE/NSF). Only the effective crack length results were employed as this was considered the most accurate data reduction scheme.

The shape of the plot of G_{Ic}^{mixed} versus G_{IIc}^{mixed} obtained for Williams global partitioning allowed an extrapolation to be made to estimate the value of G_{IIc}, which was approximately independent of the function used to fit the data. This approach suggested a value of $G_{IIc} \approx 17800$ J/m^2. This value was consistent with the measured section of the R-curve obtained in the ELS tests. Given that the results attained with Davidson's theories made extrapolation very difficult, the value of G_{IIc} derived from Williams' decomposition (i.e. 17800 J/m^2) was employed in the definition of the fracture criteria for CTE/SF and CTE/NSF. In those cases, the polynomial function stood out as the most suitable criterion.

However, despite the apparent inconsistencies observed for some partitioning theories, there was not sufficient experimental evidence to identify the correct one.

The results obtained with the titanium DCB and ENF specimens tested in fatigue have been discussed in the final part of the chapter. Stable, cohesive fracture was observed in the mode I tests performed in both "dry" and "wet" conditions. In contrast, the crack propagated along the adhesive/substrate interface in the ENF joints. Consequently, only the mode I results were analysed to generate plots of da/dN versus G_{max}, and these results were fitted to a modified Paris law.

8. Modelling Fracture Mechanics Test Specimens

8.1 Introduction

The previous four chapters (4-7) focused on the determination of the experimental inputs required to implement the performance prediction methodology proposed in the present work. Nonetheless, prior to using this data to simulate the response of an independent adhesively-bonded structure, the cohesive element formulation on which this approach relies had to be validated.

Two-dimensional models of the fracture mechanics specimens discussed in the experimental part were created using Abaqus v6.9. A brief summary of their main characteristics, including details of the materials, mesh designs and boundary conditions is described first. The outcomes of a parametric study conducted to evaluate the effects of the elastic properties of the adhesive on the mode mix predicted by the cohesive elements are presented next. After selecting the most appropriate fracture criterion for the case under consideration, the response of the joints tested under both quasi-static and fatigue loading conditions was simulated, and the accuracy of the numerical estimates assessed by direct comparison with the experimental results (using the P-δ and P_{max}-N curves respectively). The length of the numerical cohesive zone for each configuration and the influence of the shape of the traction-separation law were also examined, while special attention was paid to assess the robustness of the cycle-jump strategy used. Even though a mesh convergence analysis has not been included here, an in-depth investigation on the effects of the element size, order and number of integration points is presented in Chapter 10.

8.2 Model Details

This section describes the fundamental aspects of the finite element models employed in the present chapter. Figure 8.1 shows the geometry and dimensions of the various fracture mechanics test specimens modelled (i.e. Ti-DCB, Al-TDCB, CFRP-ADCB, CFRP-AFRMM and CFRP-ELS joints). The 3ENF configuration was not considered since it was only loaded quasi-statically up to initiation and the mode II fatigue experiments were deemed unsuccessful. Rather than using the nominal values, the thicknesses of the substrates were selected to reproduce the specimens actually tested as closely as possible.

Whilst the mode I joints were manufactured using titanium and aluminium alloys, the mode II and mixed mode specimens employed unidirectional CFRP laminates (UD 977-2/HTS) as substrates. In order to account for their stiffening effect, the aluminium end-blocks were also included in the models when they had been employed in the experimental test specimen. The specifications for these materials were reviewed in Chapter 4 (see Table 4.3, Table 4.5 and Table 4.7). Only the joints bonded with the supported version of AF163-2 were modelled, and, based on the experimental measurements, the bondline thickness was assumed to be constant and equal to the nominal value (i.e. 0.4mm).

Two-dimensional models of these joints were built using Abaqus/CAE v.6.9. The metallic substrates and end-blocks were modelled as isotropic, bilinear, elastic-plastic materials. In contrast, the CFRP beams were modelled as orthotropic, homogeneous laminates, using the "engineering constants" (expressed in the appropriate coordinate system) to define their elastic response. Moreover, given that they did not exhibit any visible signs of permanent deformation after the tests, no damage or failure criterion was specified for the composite arms. These material models were combined with *Generalized Plane Strain* conditions to fully define the behaviour of the substrates and end-blocks. The substrates were considered to be initially bonded along the length of the symmetry plane excluding the initial pre-crack. The loading holes in the end-blocks and those through the TDCB profiles were not represented in the models, as their influence on the overall response of the joints was found to be negligible.

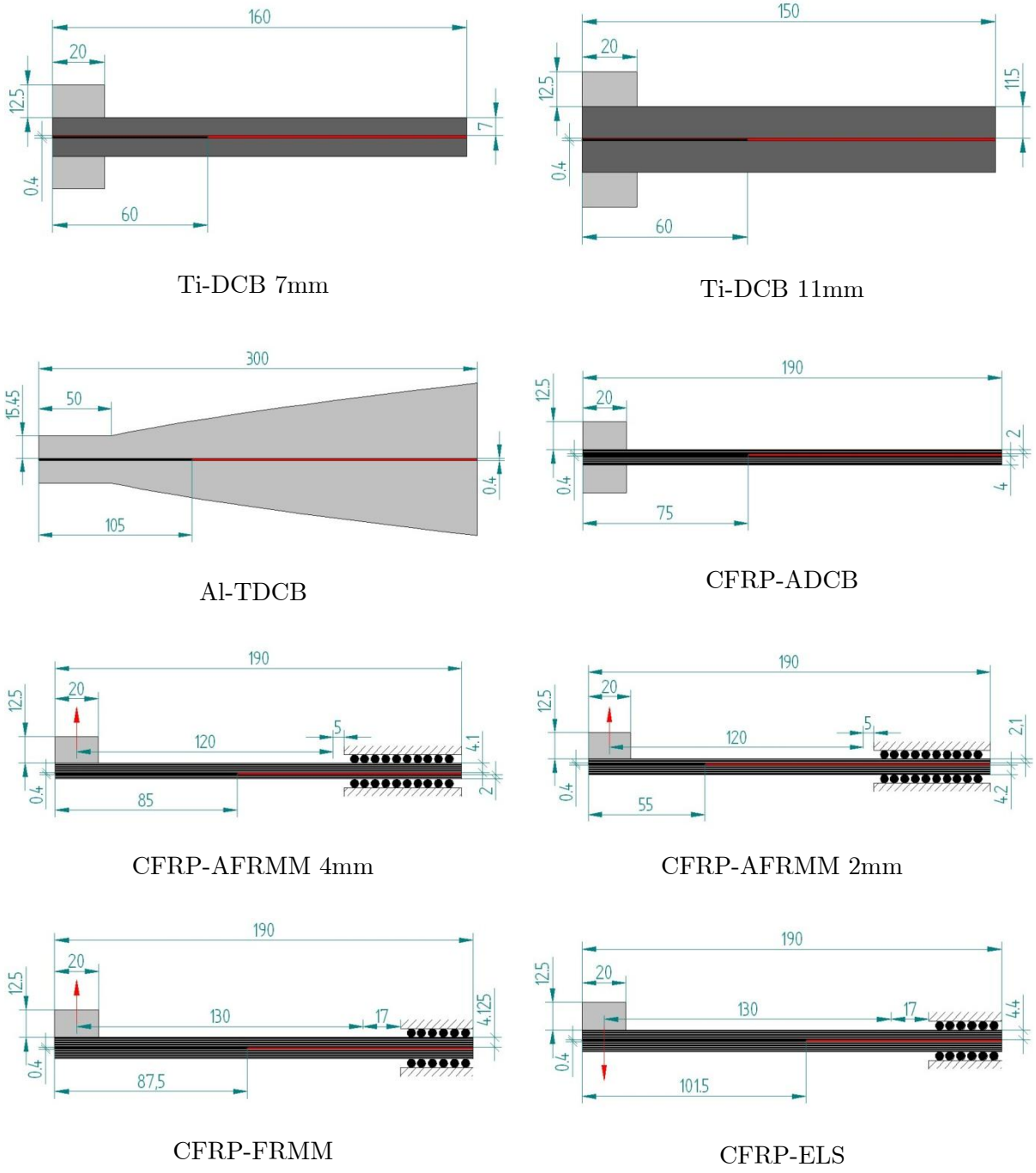

Figure 8.1. Dimensions (in mm) of the models built in Abaqus to simulate the response of the fracture mechanics specimens previously tested.

Since the experimental locus of failure was cohesive, with a crack propagating cohesively through the epoxy layer, a single layer of finite-thickness cohesive elements was used to model the bondline. Had the failure been interfacial, the combination of continuum elements for the adhesive and zero-thickness cohesive elements placed along the interface to simulate fracture would have been more appropriate and physically more relevant. The effects of the shape of the traction-separation law were evaluated using the bi-linear and linear-cubic laws

described in Chapter 3 and Appendix A. Bearing in mind that these elements were responsible for simulating both the elastic response prior to the onset of damage and the fracture process, the cohesive parameters needed to be chosen accordingly. Hence, the penalty stiffness and the displacement at damage initiation were derived from the macroscopic elastic properties of the epoxy resin using equations (3.31) and (3.32) (see Table 8.1), while the area under the traction-separation law (i.e. the displacement at complete failure, Δ^f) would be equated to one of the experimental criteria for propagation reviewed in Chapter 7. This last aspect is discussed in more detail in the next section. Bulk material properties were considered here, thus neglecting any potential constraint effects or property changes due the particular curing conditions.

Table 8.1. Elastic properties and corresponding cohesive parameters for AF-162-2OST (E, σ_Y, υ obtained from [358]).

$E\ (GPa)$	$\sigma_y\ (MPa)$	υ	$t_a\ (mm)$	$\Delta_I^0\ (m)$	$\Delta_{II}^0\ (m)$	$k_I\ (Pa/m)$	$k_{II}\ (Pa/m)$
1.11	36	0.34	0.4	1.297E-5	3.478E-5	2.775E12	1.035E12

Due to the lack of experimental fatigue data (the 3ENF tests were unsuccessful and no additional information was available in the literature for AF163-2), the fatigue behaviour of the cohesive elements was simplified. Specifically, the functions defining the crack growth rate for any mode mix (see section 3.3.4.4.1, equations (3.65)-(3.69)) were assumed to be constant and equal to the fitting coefficients of the modified Paris law for pure mode I (see section 7.3.1.2, Table 7.5).

A unified, structured mesh design was employed for all the models discussed in this chapter. The adhesive was discretized using 0.5mm long quadratic elements, with the number of integration points fixed to 30 in all cases. Fully integrated, quadrilateral elements matching the size (0.5mm x 0.5mm) and order (CPEG8) of those used in the bondline were mainly employed in the end-blocks and substrates, although a small number of triangular elements were required to mesh the arms of the TDCB joint. It has been reported by several authors that the mesh density along the crack propagation path can have a significant influence on the overall response of the structure in this type of problems [239, 240, 242, 244]. This issue is analysed in depth in Chapter 10 using the same geometries illustrated in Figure 8.1 and a series of meshes created by progressively increasing the length of the interface elements.

Nevertheless, as concluded in that study, the combination of element size, order and number of integration points chosen here should guarantee convergence to the right solution.

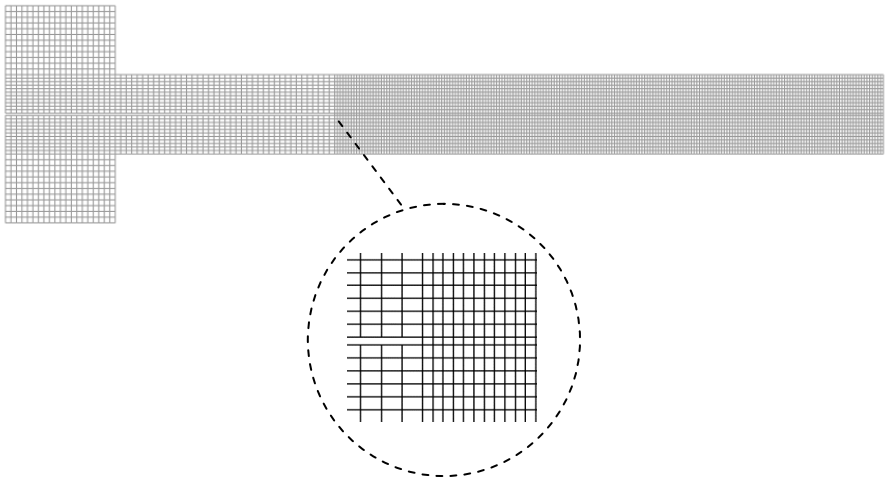

Figure 8.2. Example of the mesh employed in the Ti-DCB joint with 11mm thick substrates.

The loading conditions were prescribed at the nodes located where the centre of the holes in the end-blocks would have been. The horizontal displacement at both those points was constrained in the mode I and ADCB specimens, with the vertical movement only restricted at the lower point. On the other hand, in the AFRMM and ELS joints both degrees of freedom were constrained in those nodes in contact with the clamping arrangement, while horizontal translation at the centre of the end block was allowed to simulate the bearing trolley (see Figure 8.3). Additionally, a frictionless "hard" contact was defined between the upper and bottom crack faces in the ELS to avoid interpenetration. Finally, a suitable vertical displacement was applied to the centre point of the top end-block. Static analyses were then carried out using Abaqus/Standard.

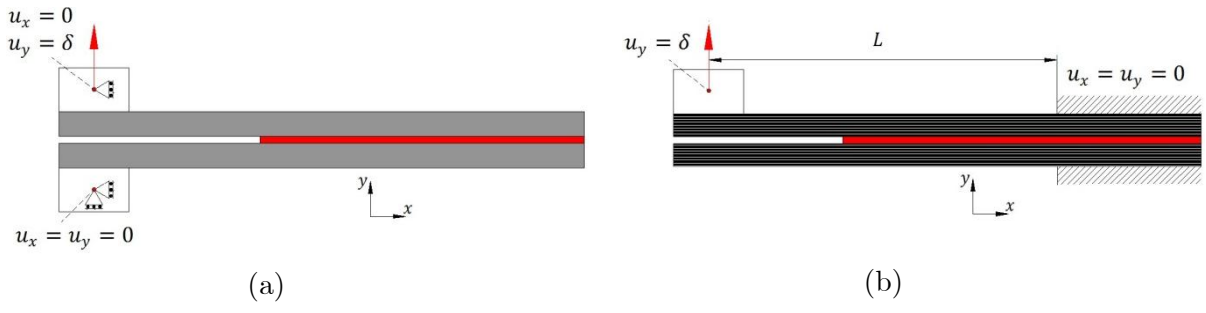

Figure 8.3. Schematic representation of the boundary conditions for (a) the mode I and ADCB joints and (b) the specimens using the clamping fixture (i.e. AFRMM and ELS configurations).

It is important to note that, although they remained elastic, the substrates underwent substantial deformation during some tests. The resulting geometrical nonlinearities had to be considered in the numerical analysis if errors were to be minimized. For that purpose the

"NLGEOM" feature available in Abaqus, which accounts for large deformations, was activated in all the numerical analyses. Non-linear geometry was also taken into account in the cohesive element formulation via a suitable definition of the Jacobian matrix.

8.3 Mixed Mode Response of Cohesive Elements: Selection of a Quasi-Static Fracture Criterion

8.3.1 Introduction

The discrepancies between the different mode decomposition strategies were clearly highlighted in previous chapters of this thesis. Even though most of these predict the same mode mix for symmetric cases, they differ when it comes to the analysis of unbalanced test configurations. The extent of the problem, seemingly associated with the nature of the material under investigation and in particular with the relative sizes of the 'damaged' and 'singularity dominated' zones in the near-tip region, was discussed in Chapters 6 and 7. Each one of the partitioning theories considered (i.e. Williams, CTE/NSF and CTE/SF) resulted in a different fracture criterion. Furthermore, aside from certain inconsistencies noticed for some methods, there was not sufficient experimental information to identify the right solution.

As stated in section 7.2, for the performance prediction methodology proposed here to be fully consistent, it was vital to ensure the equivalence between the numerical and analytical techniques used to compute the mode mix. That is, both the scheme employed to determine the function $G_c = G_c(G_{II}/G)$ (i.e. to partition the fracture energy measured with the test specimens) and the FE technique used in the analysis of the real component had to give the same mixed mode ratio for any given geometry. However, as important as it is, fulfilment of this condition would not necessarily guarantee the soundness of any subsequent predictions given that, at best, only one of the fracture criteria would concur with the solution obtained entirely with symmetric joints.

A better understanding of the mixed mode behaviour of the cohesive elements was therefore required. Since a single layer of elements was used to model the entire bondline thickness, the evolution law had to contain enough information to capture the elastic response of the adhesive. Hence, the penalty stiffness for mode I was derived from the Young's modulus, whereas the mode II value was related to the shear modulus (i.e. E and υ in an elastic material). The potential effect of the triaxial stress state in the near tip region was neglected,

so the uniaxial properties were used instead. Taking this into account, according to Chapter 3, the mixed mode seen by the interface elements could be expressed as:

$$\frac{G_{II}}{G} = \frac{k_{II}\beta^2}{k_I - 2k_I\beta + (k_I + k_{II})\beta^2} \tag{3.26}$$

where β is the ratio written in terms of the local opening and sliding relative displacements (Δ_I and Δ_{II} respectively, see equation (3.15)). Bearing this in mind, a parametric study was carried out to assess the influence of the elastic properties of the adhesive (E and υ) on the value of G_{II}/G seen by the elements. The values of the penalty stiffness for pure modes I and II were derived from the modulus of elasticity in tension and shear (assuming isotropic behaviour, i.e. $G_{12} = \frac{E}{2(1+\upsilon)}$), corrected with the thickness of the unstrained configuration, t_a:

$$k_I = \frac{E}{t_a};\ \ k_{II} = \frac{E}{2(1+\upsilon)t_a} \tag{8.1}$$

Using the models of the mixed mode configurations tested (i.e. FRMM, AFRMM and ADCB), the ratio at the crack tip element was evaluated for a range of different E and υ values. Neither the DCB or ELS geometries were taken into account for this study, as it is widely accepted that they produce pure mode conditions and so it was reflected by the numerical solutions. Only the results corresponding to the closest integration point to the tip were considered. It soon became evident that the mode mix at that point changed with the local damage state. Since such variation would depend on the fracture criterion, the analysis was restricted to the results obtained prior to any damage accumulation had occurred (i.e. $\lambda < \Delta^o(\beta)$). Hence any conclusions derived from this investigation would be applicable to both the bi-linear and linear-polynomial traction-separation laws, because they share the same initial response.

Five different values of E and υ were evaluated, including those quoted by the manufacturer for the bulk film adhesive AF163-2 (E=1.11 GPa, and υ=0.34). The ranges were chosen to cover most structural epoxies. In all cases the finite element estimates were compared with the theoretical predictions yielded by Williams and Davidson's techniques, albeit those methods neglect the presence of the adhesive.

The analysis of the ADCB geometry is discussed first, followed by the results obtained for both the symmetric and asymmetric versions of the FRMM configuration. The variation of the mode mix with the damage state was studied once the most appropriate fracture criterion was selected (see section 8.4.3).

The finite element models clearly did not include a detailed representation of the crack tip geometry, hence neglecting any local sharpness or constraint. Nonetheless, even though this could limit the physical relevance of the numerical ratios, the results of this analysis would allow an assessment of the versatility of the CZM as well as confirming whether the cohesive elements could be combined with any of the analytical mode decomposition theories to carry out performance predictions.

8.3.2 Asymmetric DCB Configuration

Despite the similarities with the symmetric DCB specimen, the asymmetric DCB (ADCB) configuration remains contentious in the debate surrounding the mode partitioning strategies. Rather than just differing on the amount of mode II present, the different theories have fundamental discrepancies over the nature of the test: Whilst both the singular and non-singular versions of Davidson's analysis see this as a mixed mode problem, the Williams global approach maintains that it corresponds to pure mode conditions irrespective of the level of asymmetry. However, given that the total fracture energy obtained with this type of joint was notably greater than the value of G_{Ic} measured with the symmetric DCB tests, the latter assumption would seem to pose serious doubts about the consistency of Williams' method (see Chapters 6 and 7).

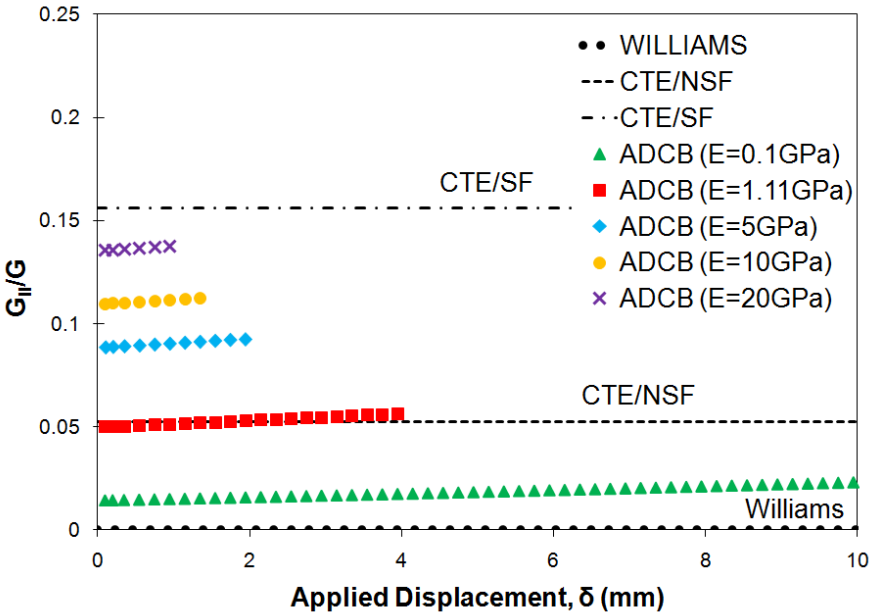

Figure 8.4. Variation with the applied displacement of the mixed mode ratio seen by the integration point located at the crack tip in the ADCB model (α=2.05) for different values of the elastic modulus E and ν=0.34. The analytical solutions corresponding to Williams, CTE/SF and CTE/NSF decomposition methods have been included for comparison.

As shown in Figure 8.4, the mode mix seen by the cohesive element located at the crack tip (i.e. at the closest integration point to the tip) was strongly dependent on the elastic modulus of the adhesive. Although a further study is needed to confirm whether the trends observed can be extrapolated to other values of the thickness parameter, α, it would appear that the numerical solution approached that of the singular field theory as the adhesive became stiffer. However, for very compliant materials the shear component decreased and the conditions in the near-tip region tended to pure opening mode. For intermediate values of the modulus, and in particular for the case of AF163-2, the mixed mode ratio computed by the cohesive element was in excellent agreement with the result obtained with CTE/NSF.

Even though the simplified crack geometry impeded an accurate reproduction of the tip singularity, the steep gradients in the stress field predicted by the CTE/SF immediately ahead of the crack tip could be partially modelled by employing large values of the penalty stiffness (i.e. very stiff adhesives or small bondline thicknesses). Whilst the limiting case (i.e. $k_{I,II} \to \infty$) would be of course unattainable with traditional FE methods, various authors have managed to combine an infinite penalty stiffness with a Dugdale model using the superior capabilities of finite volume techniques (e.g. [267, 268]). Obviously, in any case the stress in the FPZ would be limited to a finite value equal to, or smaller than, the maximum defined in the pure mode traction-separation laws.

In contrast with the constant mode mix predicted by the theoretical decompositions, the numerical ratios increased slightly with the applied displacement. This behaviour was almost certainly caused by the influence of large deformations and axial forces, which are typically ignored in the analytical models due to the considerable complexities they introduce. A good example of these difficulties can be found in [203], where the application of non-linear plate theory to the ADCB test configuration led to a set of highly-coupled integral equations which were virtually impossible to solve analytically. Nevertheless, the expression for the mixed mode presented in [203] was combined with a simple FE model of the ADCB joint in order to confirm the reasons for the rising values. The variations of θ_0 and $\bar{x}$ (see Figure 8.5-a) with the applied displacement δ were directly extracted from a linear elastic simulation and subsequently used to calculate the concentrated crack tip force and moment (N_c and M_c respectively) according to equation (8.2) (see [203]). The resulting functions were then introduced in equation (2.28) to determine the changes in G_{II}/G (corresponding to CTE/NSF) with δ, which, as shown in Figure 8.5-b, exhibited the same rising trends observed with the cohesive elements.

$$\begin{cases} N_c = P \sin\theta_0 \\ M_c = P\left(\bar{x}_1 + \dfrac{t_1}{2}\sin\theta_0\right) = P\bar{x} \end{cases} \tag{8.2}$$

Taking this into account, only the initial mixed mode ratios computed with the elements were considered for the parametric study. Moreover, the small displacements and rotations at that instant agreed well with the hypothesis made in the theoretical decompositions, hence facilitating direct comparisons between the different methods.

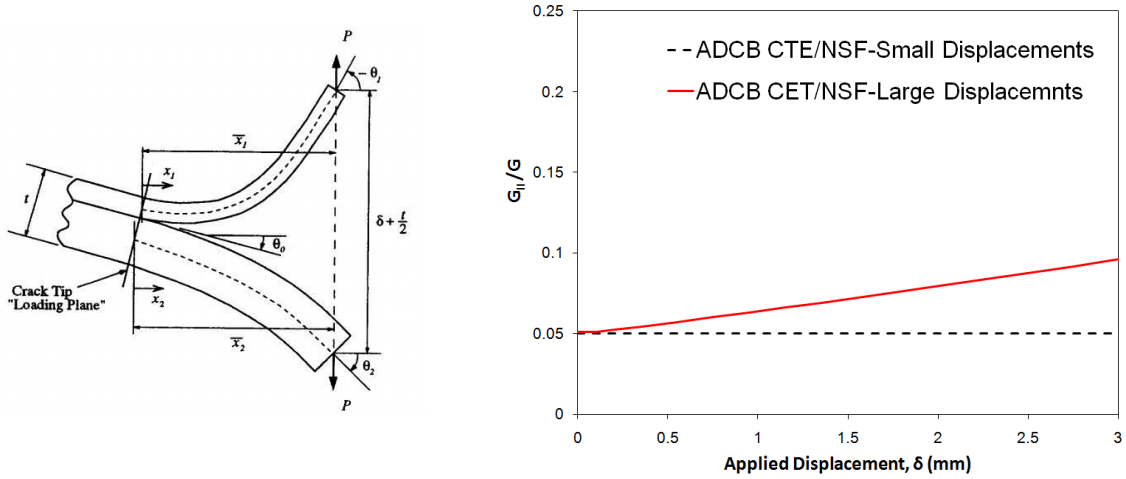

(a) (b)

Figure 8.5. (a) Deformed configuration of the ADCB joint [203]; (b) Comparison between the constant theoretical mixed mode ratio obtained with the simple CTE/NSF (small displacements) theory and that using the non-linear plate theory (large displacements).

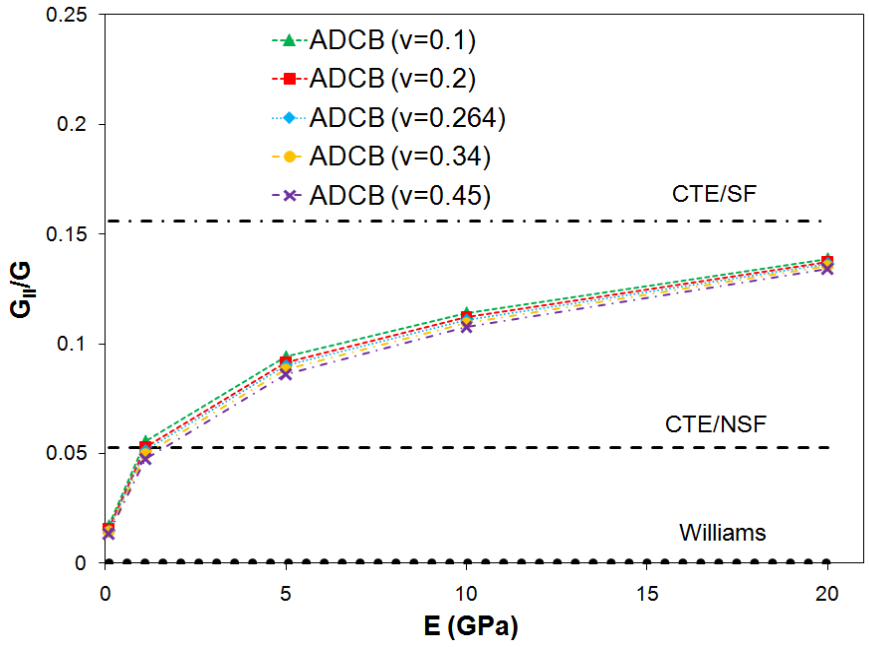

Figure 8.6. Variation of the mixed mode ratio computed at the crack-tip cohesive element of an ADCB model with the modulus of the adhesive for several values of the Poisson's ratio. Applied displacement, δ=0.125mm in all cases.

As illustrated in Figure 8.6, the ratios computed with the cohesive elements followed the same general trends described above regardless of the value of Poisson's ratio. The influence of υ was found to be minimal, with higher values of υ typically resulting in marginally smaller shear components.

Finally, for the case investigated (α=2.05), the results obtained with the cohesive element were in excellent agreement with the analytical partitioning proposed for bonded joints by Alfredsson and Hogberg [188]. This was to be expected however, since the so-called 'b/a model' simulates the flexible adhesive layer using springs, the behaviour of which are equivalent to the elastic region of the evolution law (k_I, k_{II}) employed in the CZM.

8.3.3 Symmetric FRMM Test Configuration

Given its symmetric nature, most partitioning strategies (including the three schemes considered in the present work) concur on the mode mix for this type of test specimen: $G_{II}/G = 3/7$. Consequently, one would expect the cohesive elements to yield a mixed mode ratio independent of the elastic properties of the adhesive. The results obtained with medium and large values of the elastic modulus supported this idea, as the numerical predictions were extremely close to the analytical estimate. Furthermore, no significant variations with υ were noticed. However, the behaviour of the element deviated from the theoretical solution for very compliant adhesive layers ($E \ll 1$GPa), leading to high shear components (see Figure 8.7).

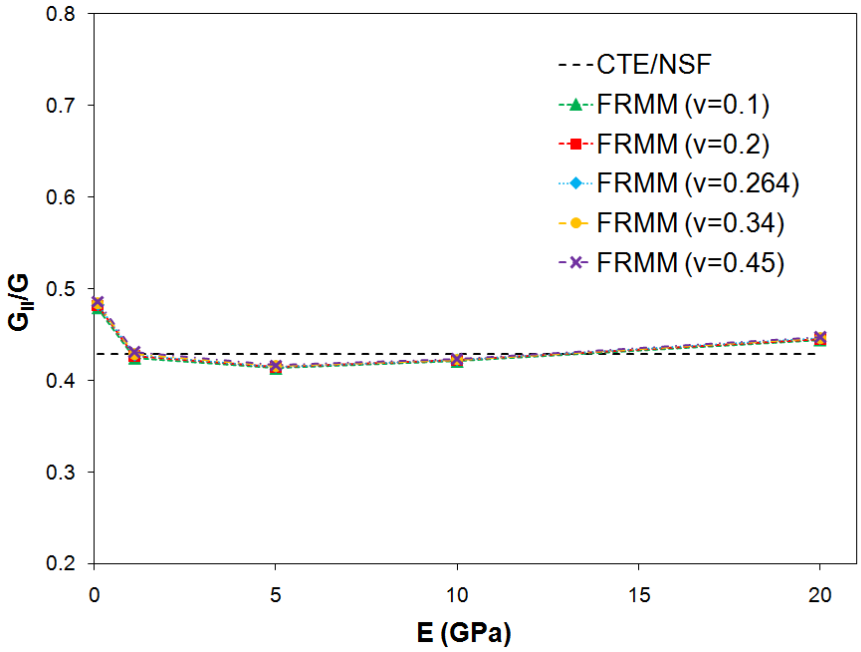

Figure 8.7. Mixed mode ratio predicted by the crack-tip cohesive element (at the closest integration point to the geometrical tip) in a FRMM specimen for different values of the elastic modulus and Poisson's ratio of the adhesive. Applied displacement, δ=0.375mm in all cases.

The small changes in G_{II}/G with υ predicted by the FE models were ignored, and only the initial values were considered to generate Figure 8.7. As discussed in section 8.3.2, such variations were caused by non-linear geometric effects, which are typically neglected by the analytical partitioning theories.

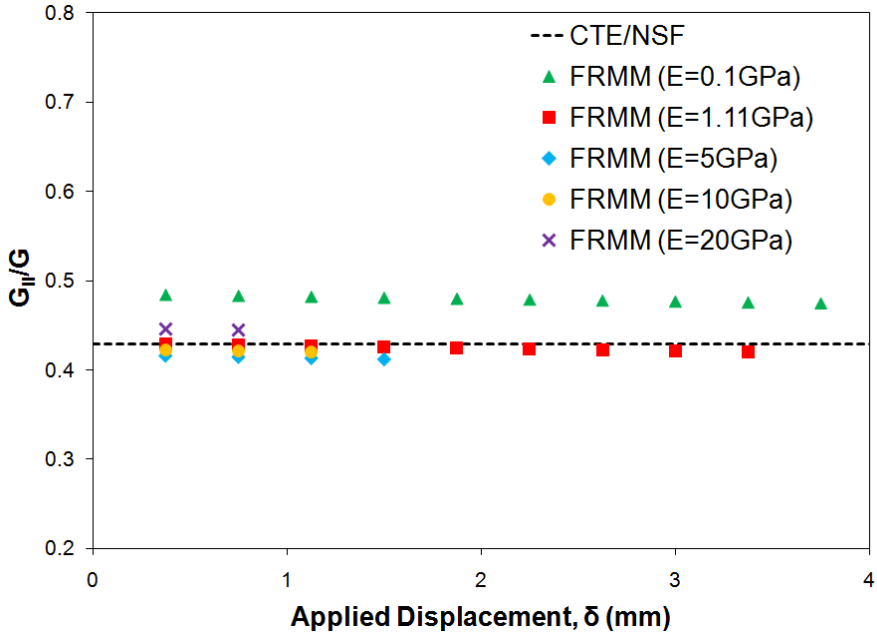

Figure 8.8. Variation with the applied displacement of the mixed mode ratio seen by the integration point located at the crack tip in the FRMM model (α=1) for different values of the elastic modulus E and υ=0.34.

8.3.4 Asymmetric AFRMM Test Configuration

The analysis performed on the two different types of asymmetric fixed-ratio mixed mode (AFRMM) joints tested revealed equivalent trends to those observed for the ADCB and symmetric FRMM configurations. Namely, the mode mix seen by the cohesive elements located at the crack tip were found to be markedly dependent upon the elastic modulus of the adhesive. Very stiff bondlines produced numerical mixed mode ratios very similar to those predicted by the singular field decomposition, especially when the load was applied to the thinnest arm. On the other hand, the solutions obtained with extremely compliant adhesives approached the Williams' theory. Finally, for intermediate moduli, and in particular for the value corresponding to AF163-2, the FE results were in excellent agreement with the non-singular version of Davidson´s theory (see Figure 8.9).

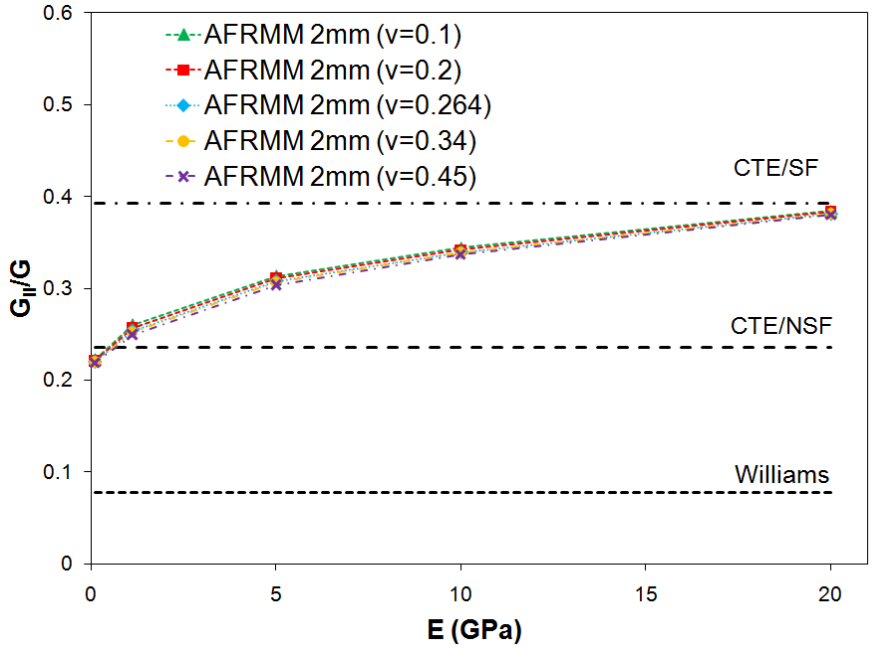

(a)

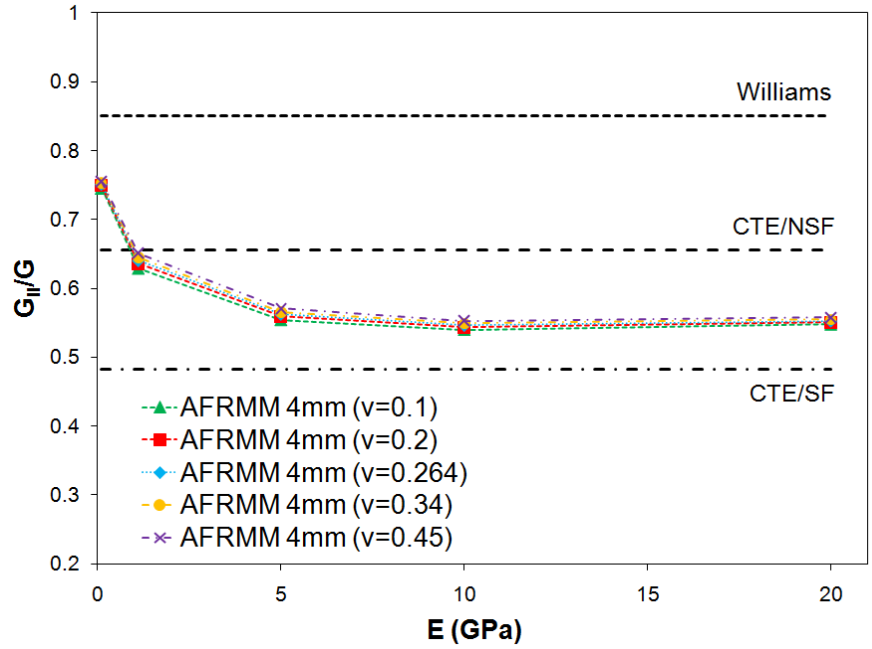

(b)

Figure 8.9. Variation of the numerical mixed mode ratio with the modulus of the adhesive for the AFRMM joint models when (a) the thinner and (b) thickest arm are loaded (2 and 4 mm respectively). Applied displacement, δ=0.175mm in all cases.

The relatively minor influence of the Poisson's ratio was found to have opposite effects depending upon whether the thinnest or thickest arm was loaded. Higher values of υ led to marginally larger mode II components when the thickest substrate was loaded, which seems reasonable since a lower shear modulus would favour greater sliding relative displacements

(i.e. Δ_{II}). Conversely, in line with the results obtained with the ADCB models, the opposite held true if the load was applied to the thinnest beam.

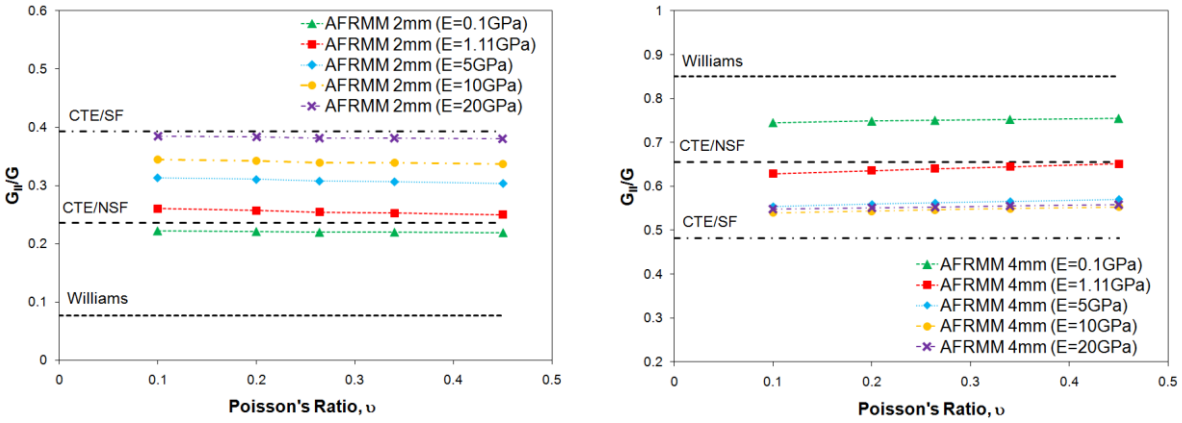

(a) (b)

Figure 8.10. Effect of the Poisson's ratio on the mode mix seen by the cohesive element at the crack tip in the models of the AFRMM joints when load is applied to (a) the thinner and (b) the thicker substrates (2 and 4 mm respectively). Applied displacement, δ=0.175mm.

Again, given that the mixed mode ratio seen by the tip element decreased slightly with the applied displacement, only the initial mixed mode ratios obtained in each case were employed to generate Figure 8.9 and Figure 8.10. Linked to large deformations and non-linear geometries, these effects were more significant for the joint loaded via the thinnest arm due to the additional compliance of this substrate.

8.3.5 Final Remarks: Selection of a Quasi-Static Fracture Criterion

The preceding sections highlighted the close relationship existing between the elastic properties of the adhesive layer (i.e. E and υ) and the mixed mode ratio predicted by the cohesive elements used to model various fracture mechanics specimens. It would appear that the tensile modulus plays a major role in the mode mix experienced by the crack tip element. On the other hand, the influence of Poisson's ratio was found to be only minor, but exhibiting opposite effects depending on whether the geometry of the joint intrinsically promoted opening or shear modes.

High values of E produced mixed mode ratios approaching those predicted by the singular field theory, whereas when the adhesive became very compliant the numerical results tended to the Williams solution. For the particular case of AF163-2 (E=1.11GPa), the mode mixities computed with the cohesive elements were in very good agreement with the non-singular version of Davidson's analysis for the various geometries examined. The close connection

between E and the near-tip stress distribution could partly explain this behaviour. The mode I penalty stiffness (k_I) also considerably affects the magnitude of the compressive stresses ahead of the crack tip, which contribute to define the mode mix. In addition, taking into account the relationship between k_I and k_{II} and both the bondline thickness and the modulus (i.e. $k_I = \frac{E}{t_a}$ and $k_{II} = \frac{E}{2(1+\upsilon)t_a}$), it would seem reasonable to assume that t_a and E have opposite effects on the value of G_{II}/G. That is, for a given modulus, thinner adhesive layers would produce steeper stress gradients, hence leading to numerical mixed mode ratios closer to those obtained by the singular field theory.

Most mixed mode theories neglect the presence of the bondline by assuming that its thickness is very small and therefore not contributing substantially to the overall compliance. However, in the light of the previous results, and as stated by Alfredsson and Hogberg [188], the properties of the bondline could continue to influence the mode mix even when t_a is small.

It is evident that, for the case under consideration (i.e. E=1.11GPa, υ=0.34), the mixed mode ratio seen by the cohesive elements corresponded to the CTE/NSF solution. The propagation criterion obtained with the CTE/NSF was therefore selected to guarantee the equivalence between the partitioning methods used in the analysis of the fracture mechanics experiments and the double lap joint. Consequently, all the simulations described hereafter used the propagation criterion obtained with the non-singular field version of Davidson's analysis. In particular, the 4th order polynomial approximation discussed in Chapter 7 (see section 7.2.2) was included in the UEL subroutine due to its ability to fit the experimental data and ease of implementation:

$$G_c = 3038 + 27177\left(\frac{G_{II}}{G}\right) + 14258\left(\frac{G_{II}}{G}\right)^2 + 285655\left(\frac{G_{II}}{G}\right)^3 + 155526\left(\frac{G_{II}}{G}\right)^4 \qquad (8.3)$$

8.4 Modelling the Quasi-Static Fracture Mechanics Tests

8.4.1 Introduction

Having identified the most appropriate propagation criterion, it was possible to completely define the quasi-static behaviour of the cohesive elements. This information was then used to simulate the failure of the various fracture mechanics specimens. Whilst the main purpose of this exercise was to evaluate the ability of the models to describe the overall fracture response of the joints bonded with AF163-2 for a range of mixed mode ratios, it would also improve the confidence in the use of both the formulation and the cohesive parameters chosen.

The accuracy of the simulations was evaluated by direct comparison with the experimental results and the analytical solutions (in the form of load-deflection curves). The variability in substrate thickness and initial crack lengths observed for the real joints was not accounted for in the FE analysis. This aspect must be therefore taken into account when considering the level of agreement between the numerical and experimental curves, especially with regards to the initial compliance.

In addition to the P-δ traces, the length of the numerical process zone was determined for the different joint designs using the method described in Chapter 3 and then compared to analytical estimates. The normal and shear stress distributions along the bondline were also examined. Finally, in order to complement the results of the parametric study presented in the previous section, the variation of the mode mix at the crack tip with the accumulated damage was also investigated for the mixed mode cases.

Both the bilinear and linear-cubic cohesive laws were employed in the analysis. Whilst it is generally accepted that under pure mode I the shape of the traction-separation law is of secondary importance when only the global quasi-static response is required, the mixed mode problems have not received the same level of attention. The two laws employed here, which shared exactly the same cohesive parameters, allow further investigation of this issue.

Of course, the results of these simulations do not represent independent predictions. However, they have been pursued in order to gain a better understanding of some experimental observations and test results as discussed in the next sections.

8.4.2 Mode I Test Specimens

Figure 8.11 shows the numerical load-displacement curves obtained with the Ti-DCB and Al-TDCB models described above. As expected for mode I, the differences between the bi-linear and linear-cubic laws were minimal, with the latter typically producing slightly higher loads.

Despite matching the initial slope predicted by the corrected beam theory, the FE models appeared to overestimate the initial stiffness of the joints. The origin of this problem, which has been reported elsewhere (e.g. [266]) even when using other FE techniques such as the VCCT, is not fully understood. A reduction in the modulus of the adhesive used in the model could reduce the mismatch, but it would be difficult to justify this physically. Constraint imposed on the bondline by the adjacent substrates would, if anything, justify a value greater than that used (see [24, 188]). Another possible explanation could be related to the inability of the models to simulate properly the beam root rotation at the crack tip, perhaps caused by an excessive compressive stiffness of the cohesive elements. For simplicity, the same penalty

stiffness was assumed for both tension and compression (under pure mode I) in the present work. An excessively large value of E or k_I would result in substantial compressive stresses ahead of the crack front and hence would reduce the rotation of the substrates at the tip. This would also help to explain the good agreement with the analytical solution for the DCB, since the crack correction factor used in that case was derived from equation (5.4) rather than from the tests. However, small changes in the values of E and k_I did not yield any improvement but modified the displacements at which the maximum or plateau loads were reached instead.

As observed in the tests, whilst matching the slope of the CBT response at first, the simulations deviated from the linear trend before reaching the maximum or plateau loads. This phenomenon was associated with damage accumulation in the elements located near the tip, and would support the chosen damage initiation criterion. The initial extra stiffness yielded by the DCB models led to slightly high peak loads (approximately 8% greater than in the tests). In contrast, their agreement with experimental P-δ curves in the propagation section was excellent. Equivalent results were obtained in the simulations of the TDCB joints which, despite correctly describing the overall response, overestimated the load during crack growth by approximately 5%.

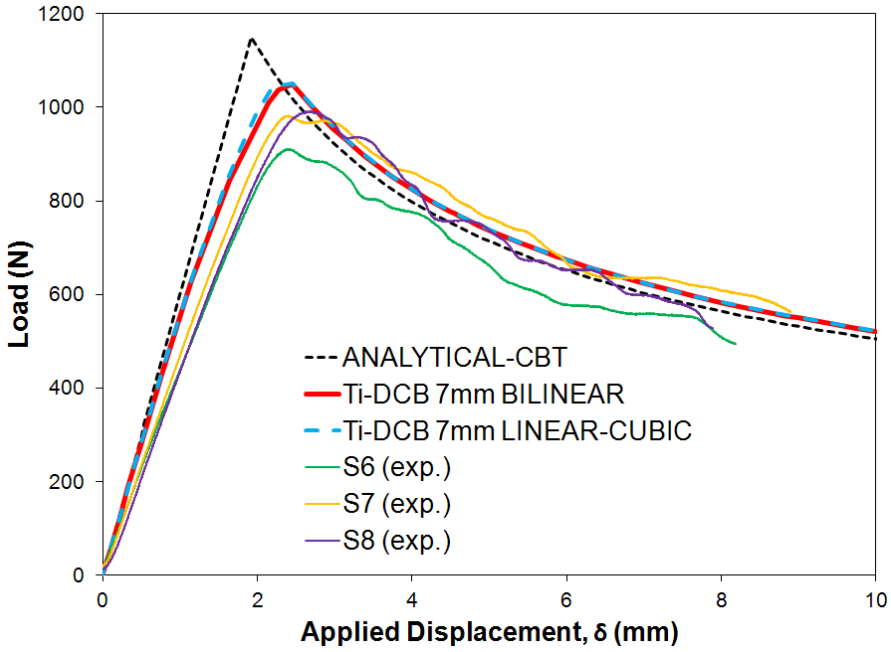

(a)

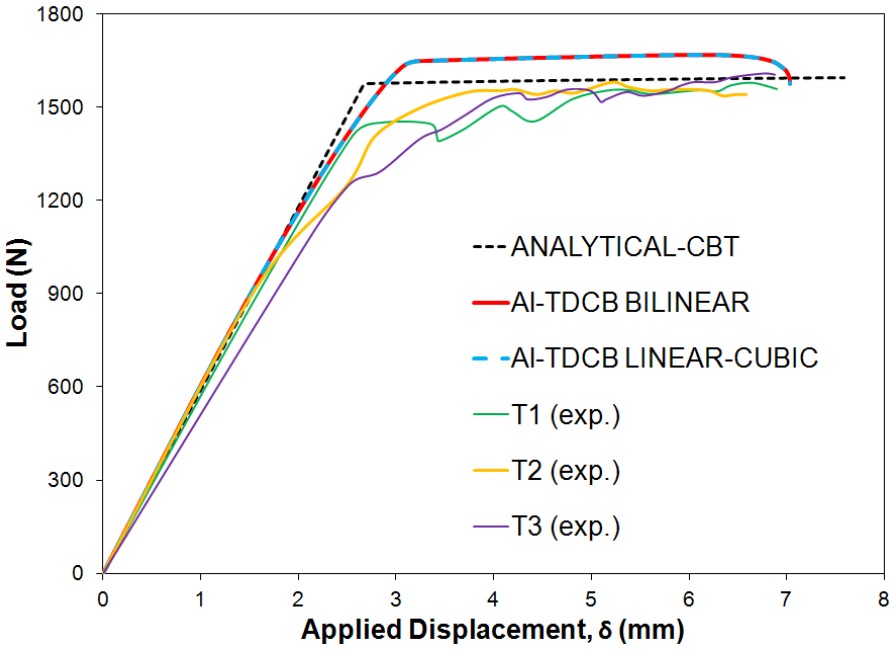

(b)

Figure 8.11. Comparison between the numerical, experimental and analytical (CBT) load-displacement curves for the 7mm Ti-DCB and Al-TDCB specimens.

The fatigue degradation strategy proposed in Chapter 3 (section 3.3.4) requires the accurate prediction of the size of the process zone. Furthermore, the traditional approach to cope with the mesh-dependency of the cohesive elements also relies heavily on these estimates [240, 242, 310], see Chapter 10. In addition, as discussed in previous sections (see chapters 2, 5, 6

and 7), the cohesive zone length (l_{CZ}) appears to have important implications for the selection of the most appropriate mode partitioning strategy.

Since it is extremely difficult to measure the lengths of the cohesive zones experimentally, the values of l_{CZ} are typically computed using one of the analytical solutions presented in section 2.5.3.6 (equations (2.41) and (2.42)). It is noteworthy that these solutions employ very basic assumptions (such as constant stress within the FPZ) and therefore only produce approximations to the true values.

Equation (2.41) predicts a cohesive zone length of the order 0.8-2.5mm for AF163-2OST bonded joints (the exact size depends on the parameter M and hence on the model employed, but it would be the same for both the Ti-DCB and Al-TDCB specimens as this formula neglects the influence of the substrates). However, this value was greater than the bondline thickness (i.e. 0.4mm). As discussed in Chapter 2, in those cases where the adhesive layer is constrained between much stiffer substrates, the shape and size of the process zone can be severely affected ([24, 374]). It seems therefore likely that these estimates are not realistic here and that (2.42) would be more appropriate for the present problem.

Figure 8.12 shows the estimates of the fully developed cohesive zone length obtained with (2.42) for the Ti-DCB (manufactured with 7 and 11.5mm substrates) and the Al-TDCB joints. According to this analytical solution, l_{CZ} increased with the crack length in the TDCB specimen due to the profile of the substrates. However, equation (2.42) predicted a constant fully developed cohesive length for the DCB with uniform substrates. This last result does not concur with that presented by Suo et al. [298], who working with the J-integral concluded that only DCB test specimens loaded with bending moments reach a steady state. Conversely, no self-similar propagation of the damage strip (i.e. no steady state) is expected in the wedge force loading case, where the fully developed cohesive length reaches a maximum value and then decreases as the crack grows. However, Suo et al. concluded that the variation of l_{CZ} with the crack length was negligible if the ratio a/h was sufficiently large.

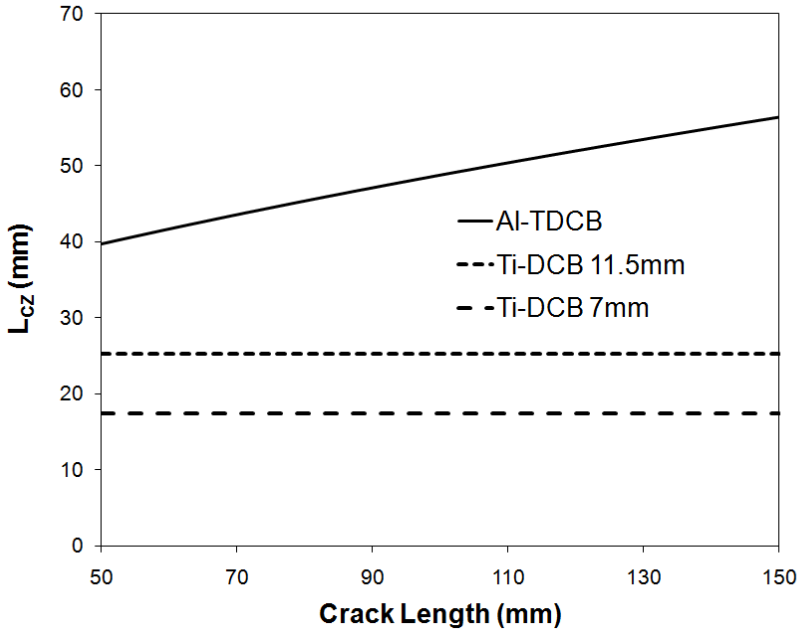

Figure 8.12. Analytical estimate of the fully developed cohesive zone length for the titanium DCB and Al-TDCB specimens as a function of the position of the crack tip (equation (2.42)).

A comparison between the previous closed form solutions and the results obtained from simulations using interface elements was also carried out. Of course, both methods produce mere estimates. However, whilst the shape of the evolution laws had no physical basis as nor did they reflect the local damage micro-mechanisms occurring ahead of the crack tip, the assumptions made by the CZM appeared closer to reality than those made in the analytical solutions discussed above (i.e. constant stress equal to the interfacial strength within the PFZ).

Figure 8.13 illustrates the variation of the numerical cohesive zone length with the applied displacement for the Ti-DCB and Al-TDCB joints. This is conceptually equivalent to the variation of l_{CZ} with the crack length, as the applied displacement and crack tip position are linked via G_{Ic} in the fracture specimens. Only the results obtained with the second method described in section 3.3.4.4.3 (i.e. which takes into account the damage state at each integration point and its individual contribution to the cohesive length) were included in the graphs as this was found to produce smoother results.

The numerical cohesive zone lengths initially increased with the applied displacement until the critical strain-energy release rate was reached. At that point, the FPZ was fully developed and the crack and damage zone propagated together. In the TDCB simulations, l_{CZ} continued increasing with the applied displacement. Conversely, the DCB models predicted a small reduction in the cohesive zone length as the crack propagated. This result

was in accordance with the findings of Suo et al. [298]. As observed with the P-δ curves, the differences between the bi-linear and linear cubic laws were again minimal, with the latter predicting marginally shorter cohesive zone lengths.

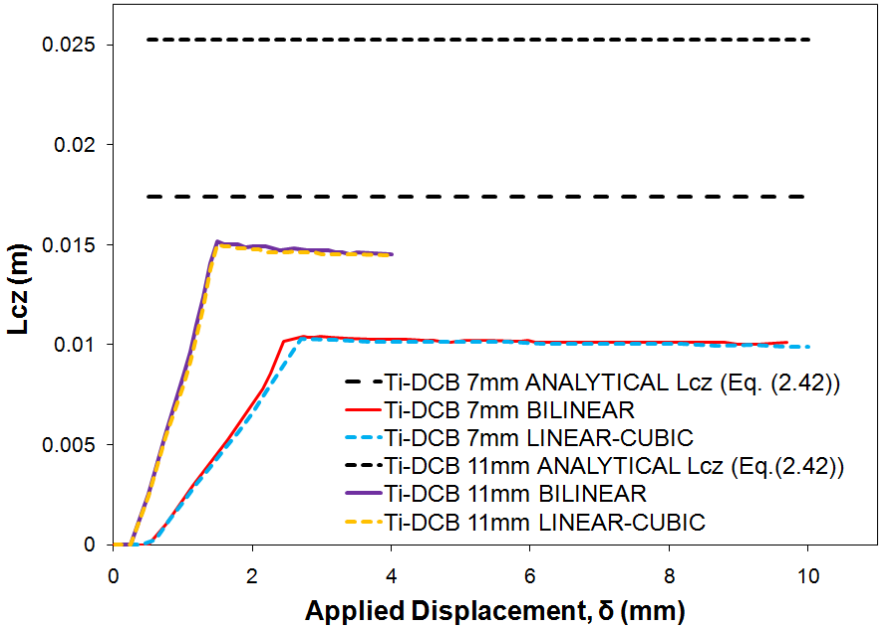

(a)

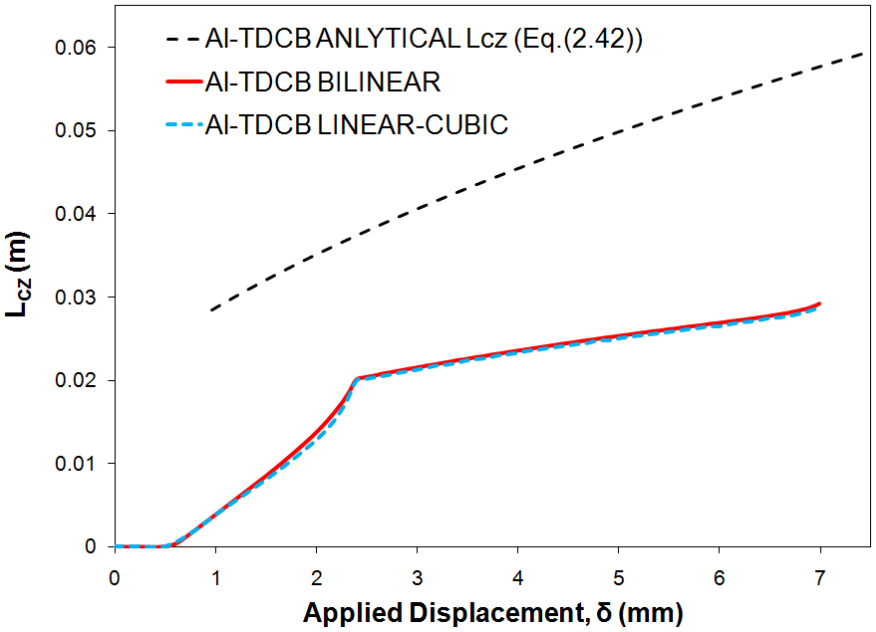

(b)

Figure 8.13. Numerical cohesive zone length (method II) as a function of the applied displacement estimated from (a) the Ti-DCB and (b) the Al-TDCB models using 0.5mm quadratic cohesive elements with 30 integration points. The analytical solutions corresponding to (2.42) have been included for comparison.

The numerical values of l_{CZ} were notably smaller than those derived from (2.42). Harper and Hallett [240] also pointed out the apparent over-predictions obtained with this formula, suggesting a correction factor (M=0.5) in order to ensure a conservative estimate for mesh design purposes.

Regardless of whether the analytical or FE method is used, the thickness of the substrates (h) plays a major role in determining the length in the cohesive zone. The local curvature of the substrates in the near tip region, which is a function of h, influences the stresses imposed on the adhesive layer and hence affects the size of the FPZ. For example, the higher bending stiffness of the thicker metallic beams implies a lower curvature and therefore a longer distance between the points where the local opening displacements are equal to Δ_I^f and Δ_I^0 (i.e. the points that delimit l_{CZ}, see Figure 8.14).

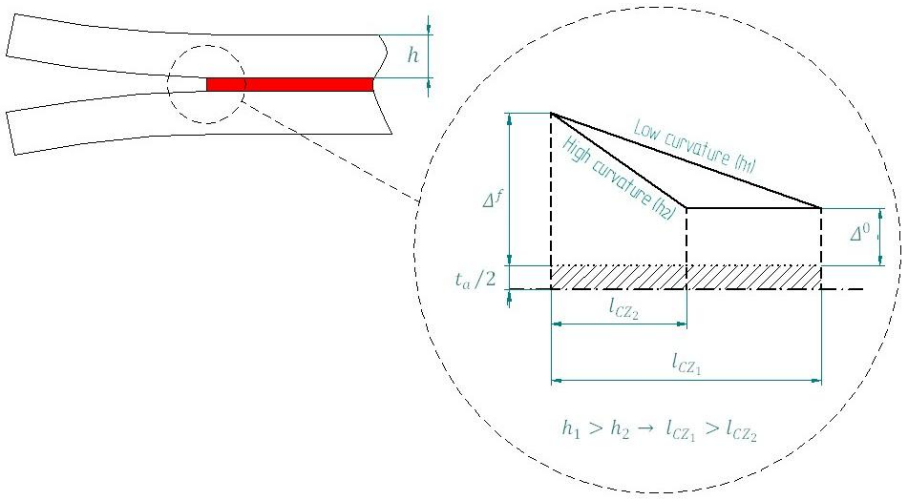

Figure 8.14. Schematic representation of the effect of the substrate thickness on the length of the cohesive zone.

To fully understand the variation of the numerical cohesive length with the applied displacement it is necessary to analyse in more detail the stress distribution along the bondline. As illustrated in Figure 8.15, for a given initial crack length the normal stresses immediately ahead of the crack tip rose gradually with the applied displacements until $\tau^0 = \sigma_Y$ (i.e. Δ_I^0) was reached. At that point, when the first signs of irreversible damage emerged, the stress at the tip decreased and the position of the maximum moved forward. This coincided with the instant when the numerical cohesive zone started developing. The process progressed as the applied displacement increased, with more material undergoing irreversible deformation and the process zone constantly growing. In parallel, the stress at the crack tip decreased until it vanished completely. The FPZ was then fully developed, and both the crack and damage zone advanced. This instant corresponded to the peak (DCB) or plateau (TDCB) load of the numerical P-δ traces.

Along the bondline, the cohesive zone was followed by an elastic region featuring a sudden drop in the normal stresses. The stress gradient in this region was directly controlled by the penalty stiffness. By increasing the modulus of the adhesive (i.e. increasing k_I), that drop would become more abrupt and the local state would approach that of a singularity as discussed in section 8.3. Further ahead, the stresses became negative (i.e. compressive) due to bending in the substrates, reaching a maximum and then becoming negligible far from the tip. The magnitude of the compression and the length of the process zone developed simultaneously, with both reaching their peaks at the same time.

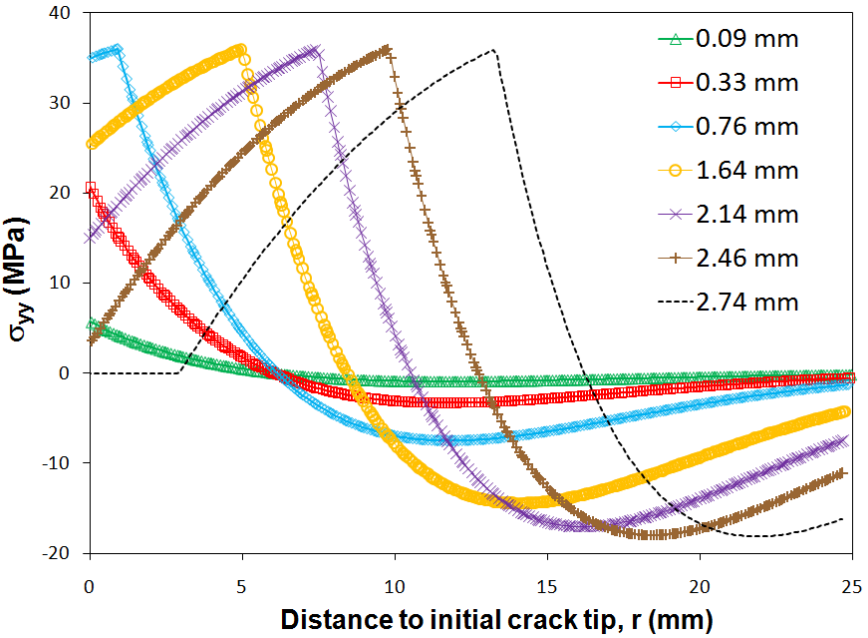

Figure 8.15. Distribution of normal stresses ahead of the crack tip in a Ti-DCB specimen manufactured with 7mm thick substrates for different applied displacements. The bi-linear traction-separation law was used to illustrate the development of the numerical cohesive zone.

The process described above was similar in the three types of mode I joints modelled. Furthermore, it was equivalent for both the bilinear and linear-cubic damage evolution laws. Figure 8.16 shows a comparison of the normal stresses ahead of the crack tip (corresponding to a fully developed l_{CZ}) obtained in each case for the 7mm Ti-DCB. Unsurprisingly, since both laws shared the same linear section and cohesive parameters, the solutions only differed in the distribution of stresses within the process zone, exhibiting identical behaviour over the elastic and compressive regions.

The stress fields obtained for different crack lengths (i.e. applied displacements) confirmed that crack propagation was not a self-similar process in the Ti-DCB or in the Al-TDCB specimens. As may be seen in Figure 8.17, the stress distribution "contracted" for DCB case, whereas it "expanded" for the tapered model. This behaviour was consistent with the

variations of the process zone length shown in Figure 8.13. The curvature of the DCB substrates at the crack tip increased as the crack grew, leading to higher compressive stresses and to a small reduction in l_{CZ}. In contrast, the curvature of the TDCB arms decreased with the crack length due to their profile, causing a mild reduction in the compressive stresses and a progressive increase of the cohesive zone length.

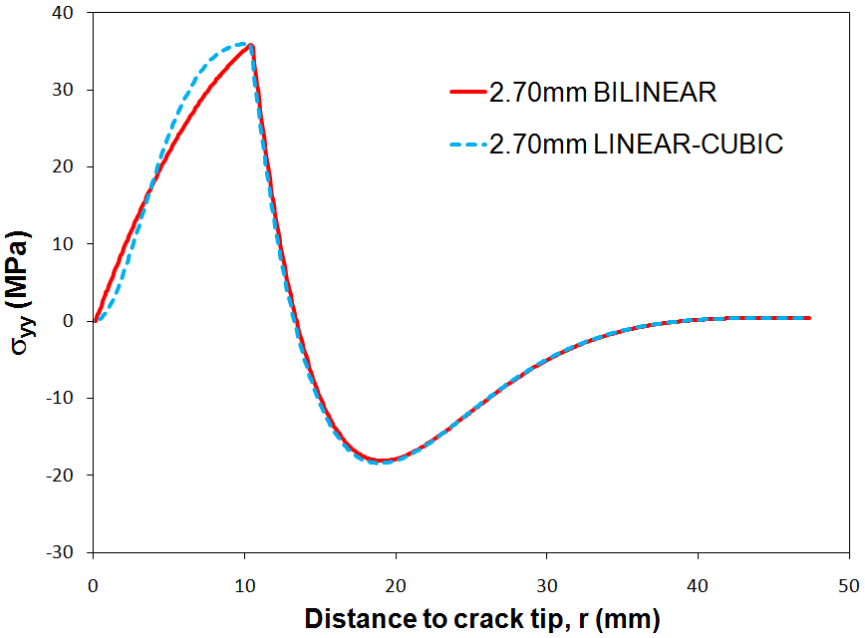

Figure 8.16. Normal stress distributions ahead of the crack tip in a Ti-DCB specimen manufactured with 7mm thick substrates obtained with the bilinear and linear-cubic traction-separation laws corresponding to a fully developed cohesive zone.

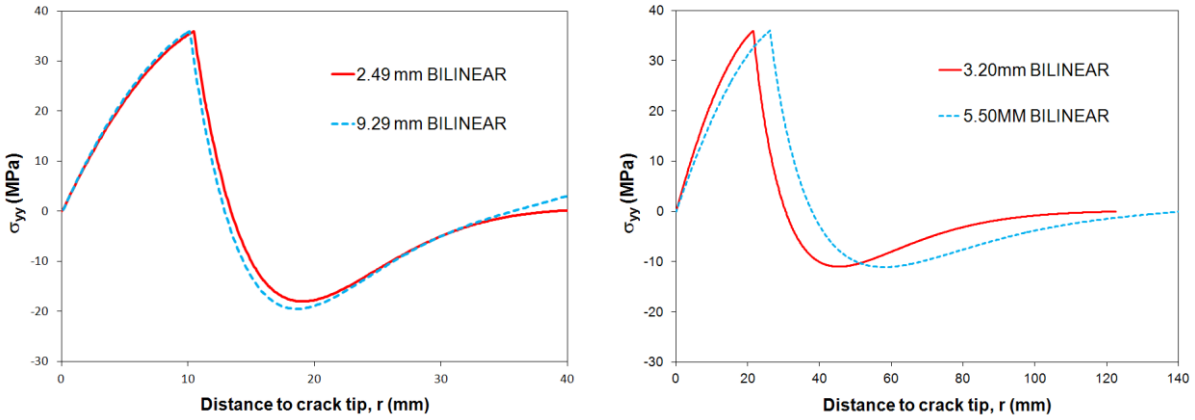

(a) (b)

Figure 8.17. Normal stress distributions ahead of the crack tip in (a) the 7mm Ti-DCB specimen and (b) the Al-TDCB joint obtained with the bilinear law for two different applied displacements. In each case the distributions have been plotted using the same origin of coordinates to highlight their differences.

8.4.3 Mixed Mode I/II Test Specimens

8.4.3.1 Modelling the CFRP ADCB Specimens

The ADCB models yielded equivalent results (qualitatively at least) to those obtained with the symmetric specimens. As illustrated in Figure 8.18, the agreement between the numerical and experimental load-displacement curves was good. Even though the scatter in the initial stiffness was larger than for the metallic joints, probably due to the variability in the thickness and elastic properties of the CFRP substrates, the linear response of the models compared well with that of the test specimens. In contrast to the DCB joints, the simulations predicted a slightly higher initial slope than the corrected beam theory. However, this mismatch could be easily attributed to deficiencies in the analytical model, which used the pure mode I correction factor for the crack length (Δ_I) and neglected any potential mixed mode contributions.

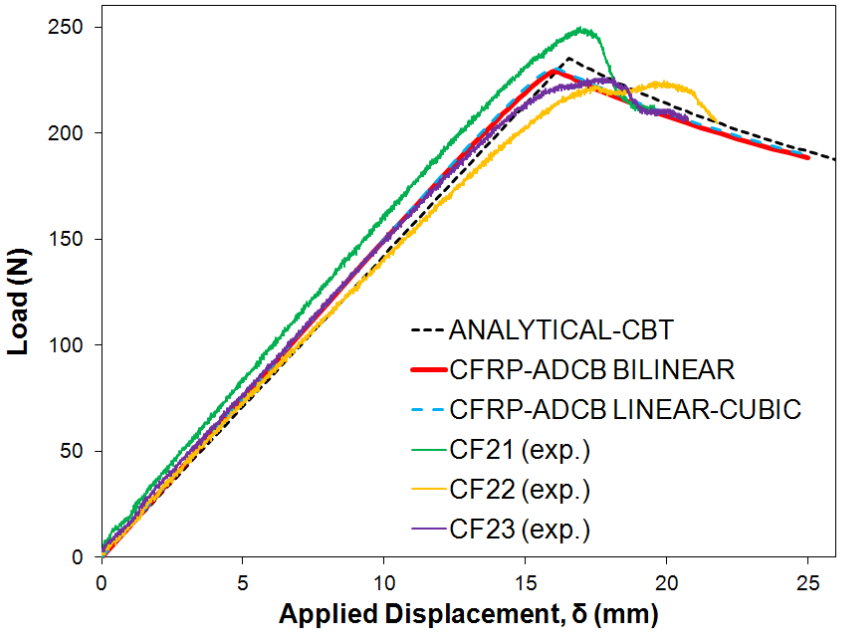

Figure 8.18. Comparison between the numerical, experimental and analytical (CBT) load-displacement curves for the CFRP-ADCB specimens.

For crack propagation, the FE simulations were also in good agreement with the experimental results but differed slightly from the analytical solution. An interesting phenomenon was observed: whilst in the DCB specimen the distance between the theoretical and FE curves remained constant during propagation, this was not the case for the asymmetric specimen. Even though this might seem a trivial issue given the negligible magnitude of the mismatch, it has been previously reported for different mixed mode configurations (e.g. [410]).

To explain the reasons for this behaviour it is necessary to revisit the issue of the accurate determination of the mode mix seen by the cohesive elements. Section 8.3 examined the influence of the elastic properties of the adhesive on the mode mix, but it considered only the elastic response at the crack tip. Under those conditions, the value of G_{II}/G was found to vary slightly with the applied displacement due to geometrical non-linearity. However, as shown in Figure 8.19, the mode mix seen by the crack tip element also varied significantly with the damage state. Furthermore, the elements ahead of the tip were subjected to a range of ratios, all of which depended on the local damage state, see Figure 8.20. Consequently, in contrast with the analytical models, in the simulations the crack did not propagate under constant mixed mode conditions.

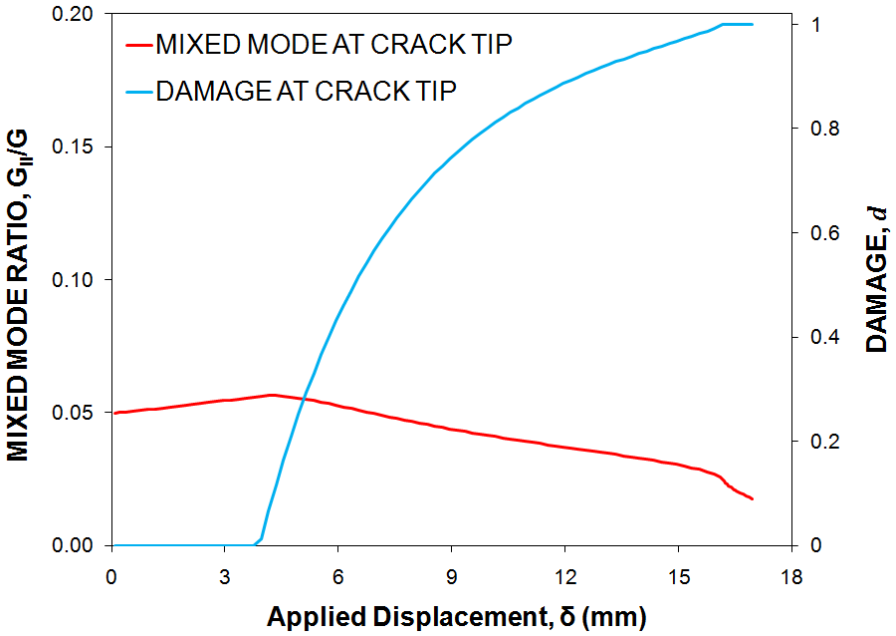

Figure 8.19. Variation of the mixed mode ratio and damage state with the applied displacement at the crack tip element (i.e. tip integration point) in the CFRP-ADCB model (using the bilinear traction-separation law).

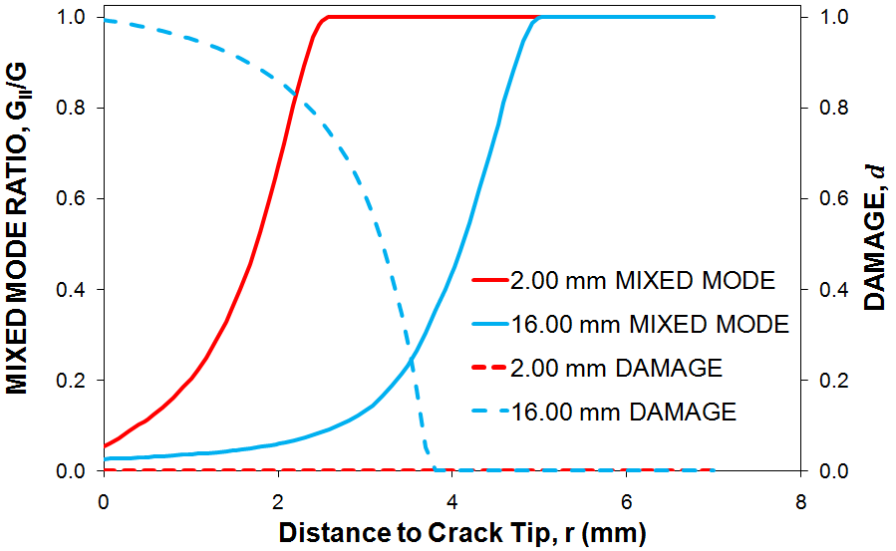

Figure 8.20. Mixed mode ratio and damage state of the cohesive elements immediately ahead of the crack tip for two different applied displacements in a ADCB model (bilinear traction-separation law).

This phenomena would have major implications for the overall load-displacement response during propagation, given that, for a fixed fracture criterion, the value of G_c changes with the ratio G_{II}/G. In this particular case, the mode mix appeared to increase slightly and, although the FE model yielded a lower peak than the corrected beam theory, the numerical load soon exceeded the analytical predictions.

It should be noted that, due to implementation reasons, the cohesive formulation assumed pure mode II when the relative opening displacement was equal to, or smaller than, zero. Therefore, as may be seen in Figure 8.20, the numerical mode mix in the undamaged elements located far from the crack tip tended towards pure shear (i.e. $G_{II}/G \rightarrow 1$).

The variation of the numerical cohesive zone length with the applied displacement was similar to that obtained for the DCB models. After an initial phase with no damage, there followed a rising period and the size of the FPZ appeared to reach a maximum coinciding with the peak load. However, instead of decreasing slightly with the crack length as in the DCB specimens, the raise in G_c induced by the variations in the mode mix counteracted the changes in the curvature of the substrates to produce a small but continuous increase in l_{CZ}. Together with the different mixed mode ratios ahead of the tip, this lengthening of the numerical cohesive zone length implies that the crack propagation is not a self similar process.

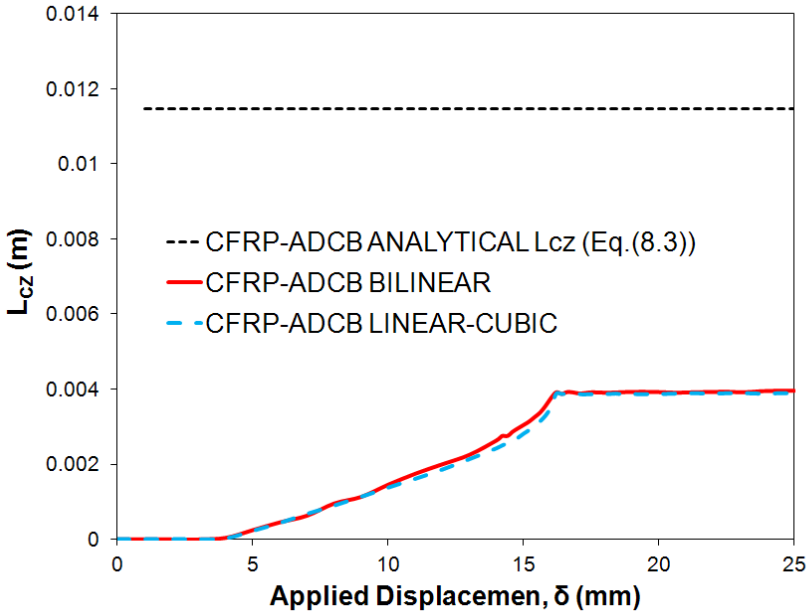

Figure 8.21. Variation of the numerical cohesive zone length with the applied displacement in CFRP-ADCB model using bilinear and linear-cubic traction-separation laws.

Comparison between the theoretical and numerical predictions for l_{CZ} was difficult in the mixed mode case because equations (2.41) and (2.42) were originally derived for the pure modes. Although it lacked theoretical soundness, an analytical estimate was calculated by adding the contributions of the pure mode components of $G_{I/IIc}$ (namely G_{Ic}^{mixed} and G_{IIc}^{mixed}):

$$l_{CZ}^{mixed} = l_{CZ,I}\left(G_{Ic}^{mixed}\right) + l_{CZ,II}\left(G_{IIc}^{mixed}\right) \tag{8.3}$$

In line with the simulations for mode I, the resulting value was larger than the numerical prediction by approximately a factor of 3, which would suggest that a different correction factor to that proposed by Harped and Hallett [240] for mode I is required: M=1/3.

Regarding the influence of the shape of the traction-separation law, both the bilinear and linear-cubic laws produced virtually the same overall P-δ responses. In contrast, small discrepancies became visible in the l_{CZ}-δ graphs, especially during the rising period. These could be explained by the different damage evolutions within the FPZ predicted in each case, as they would lead to different mixed mode ratios ahead of the crack tip.

Finally, as expected from mixed mode loading, failure in the ADCB model took place under a combination of tensile and shear stresses. Figure 8.22 illustrates the distributions corresponding to each component for a fully developed cohesive zone length. For this low mixed mode ratio ($G_{II}/G \approx 0.05$), fracture was dominated by the normal stresses (σ_{yy}).

However, the presence of σ_{xx} meant that the peak value of σ_{yy} within the FPZ was below the yield stress for the bulk adhesive (i.e. σ_y). Both fields, which changed signs ahead of the FPZ, reached their respective maximum points simultaneously, hence facilitating the identification of l_{CZ}.

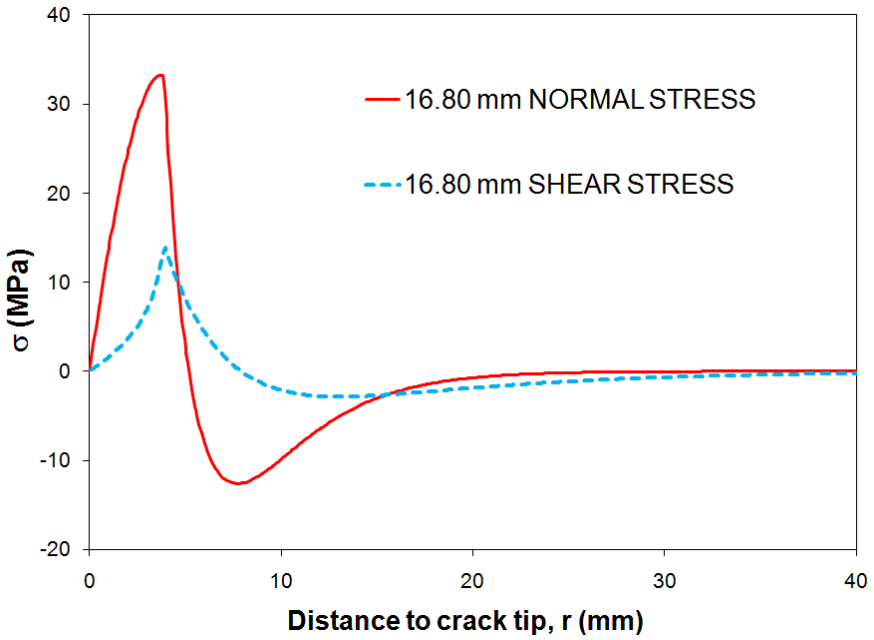

Figure 8.22. Tensile and shear stress distributions ahead of the crack tip in an ADCB model obtained with the bilinear traction-separation law for an applied displacement δ=16.80mm.

8.4.3.2 Modelling the CFRP FRMM and AFRMM Specimens

8.4.3.2.1 Clamp modelling

As explained in sections 4.4.2.2 and 5.4.1.2, the fixture employed in the FRMM, AFRMM and ELS tests was not infinitely stiff. That is, the section of the specimens held under the clamp experienced small rotations and displacements. This behaviour needed to be included in the simulations if the response of these joints was to be predicted accurately.

Experimentally, this effect was accounted for via the correction factor Δ_{clamp}. Determined from the relevant inverse test performed on un-cracked samples (see section 5.5.1.2), this parameter was used to extend the free length (L) and imitate a more compliant rig. In the present work an equivalent approach was followed in the FE models. Instead of explicitly modelling the clamp, its effects were simulated by applying suitable boundary conditions. The same "perfect" boundary conditions described in section 8.2 were prescribed for the clamped region but were offset in each case by a distance equal to the experimental value of Δ_{clamp}.

To assess the validity of this method, the inverse tests were also simulated in Abaqus and the numerical results (in the form of P-δ traces) were compared to the experimental calibration data. Figure 8.23 shows the curves obtained with both the original and the corrected values of the free length in the inverse FRMM test. The use of the corrected free length (including Δ_{clamp}) is seen to give much better agreement with the experiments.

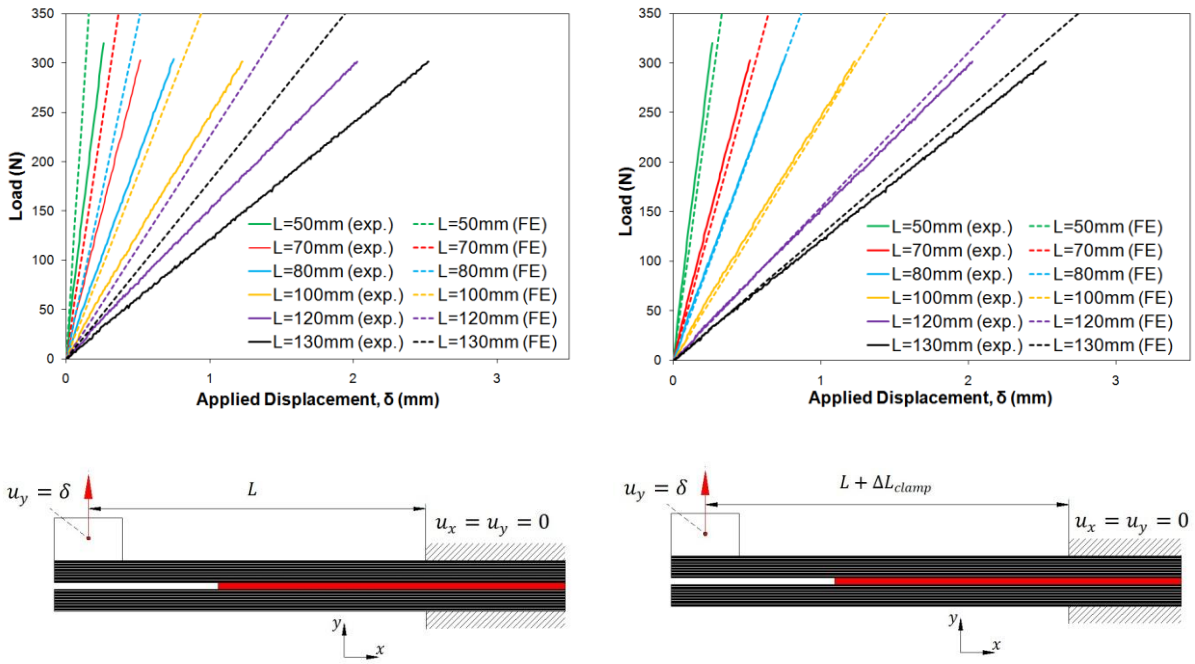

Figure 8.23. Comparison of the FRMM clamp calibration data and the load-displacement responses obtained in the simulations of the inverse test for various free lengths using (a) the original free length and (b) the Δ_{clamp} extension.

The relationship between the stiffness of the clamp and the free length was in reality non-linear. Despite the obvious improvements illustrated in Figure 8.23-b, a simple free length extension would not be capable of fully describing a non-linear response. More sophisticated modelling alternatives based on elastic foundations and springs were investigated but finally discarded because the gains they offered were relatively small in comparison to the additional complexity they introduced. Consequently, increasing the nominal free length by a suitable value of Δ_{clamp} was the option chosen in this work to model the finite stiffness of the clamping arrangement.

8.4.3.2.2 Simulation Results

Figure 8.24 illustrates the load-displacement responses obtained with the FE models featuring the free length correction. Despite the scatter observed in the tests, the numerical results corresponding to the symmetric configuration and the AFRMM joint loaded at the thinnest arm compared very well with the experimental curves, especially with regard to the slope of the linear section. Reasonable agreement was also attained in the initial section for the AFRMM specimens loaded at the thickest arm. However, in this case the models could not reproduce the failure path or the unstable behaviour often observed in the tests. They predicted stable growth instead, leading to considerable differences with the experimental traces during the propagation phase.

The numerical response obtained for the AFRMM joint loaded at the thinnest arm compared very well with the corrected beam theory. Good agreement was also achieved for the symmetric configuration, although in this case the simulations slightly under-predicted the initial slope and consequently the peak load. In contrast, substantial discrepancies with the analytical solution may be seen in Figure 8.24-c, particularly during propagation. The use of the crack length correction factor for mode I (Δ_I) rather than a specific mixed mode value in the CBT equations could explain the initial stiffness mismatch (note that Δ_{clamp} was also included in the theoretical solution).

The agreement between the numerical and analytical results during crack propagation was again a function of the applied displacement. Also, in contrast to the constant value of G_{II}/G assumed by the CBT, the mode mix seen by the cohesive elements (i.e. integration points) placed along the bondline was a function of both the local damage state and its distance to the numerical crack tip (see Figure 8.25). Since any variation in G_{II}/G affects the value of the cohesive parameters (including G_c), this has an important influence on the total energy dissipation and therefore on the overall response.

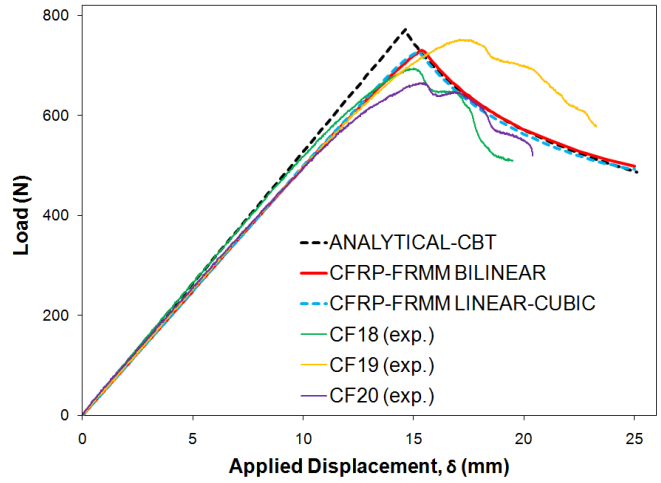

(a)

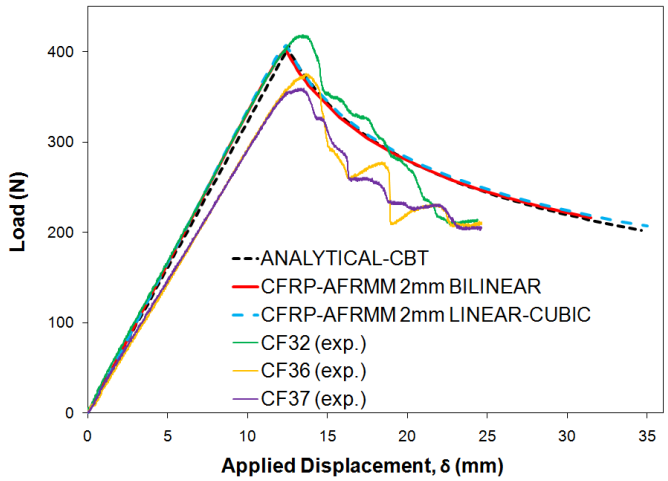

(b)

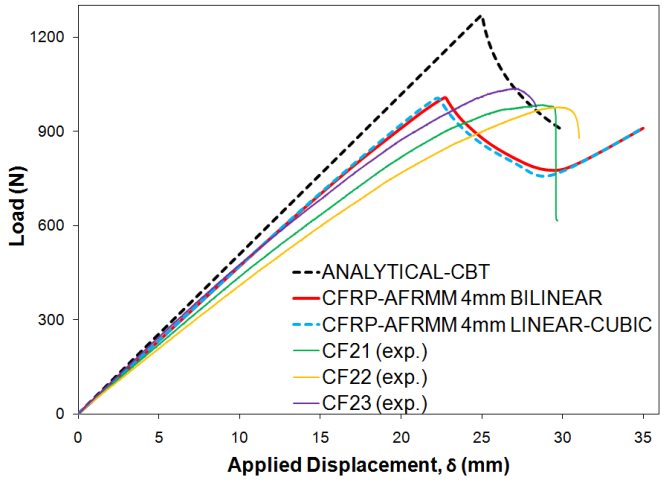

(c)

Figure 8.24. Comparison between the numerical, experimental and analytical (CBT) load-displacement curves for the (a) the CFRP-FRMM specimen, (b) the CFRP-AFRMM joint loaded at the thinnest arm and (c) the CFRP joint loaded at the thickest arm.

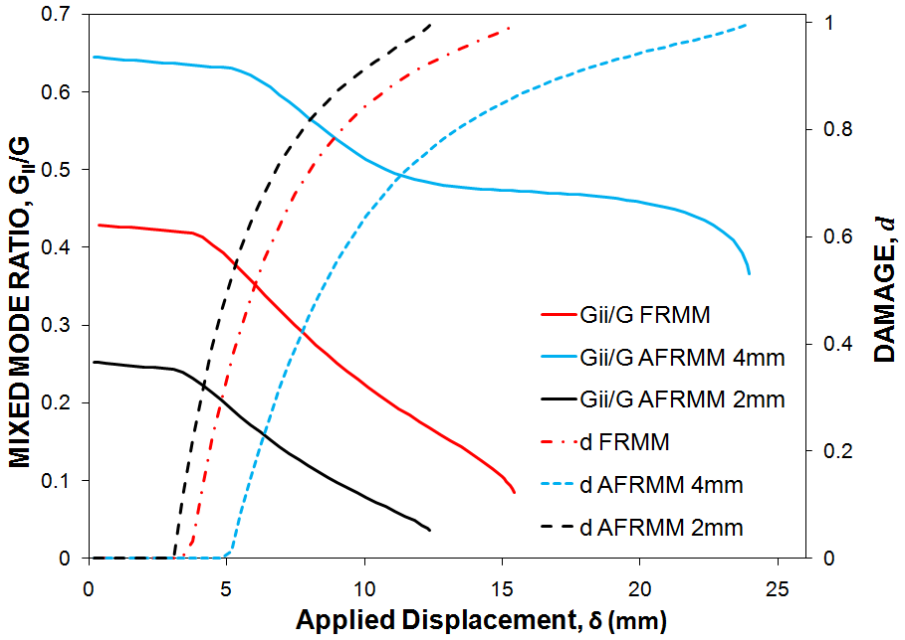

(a)

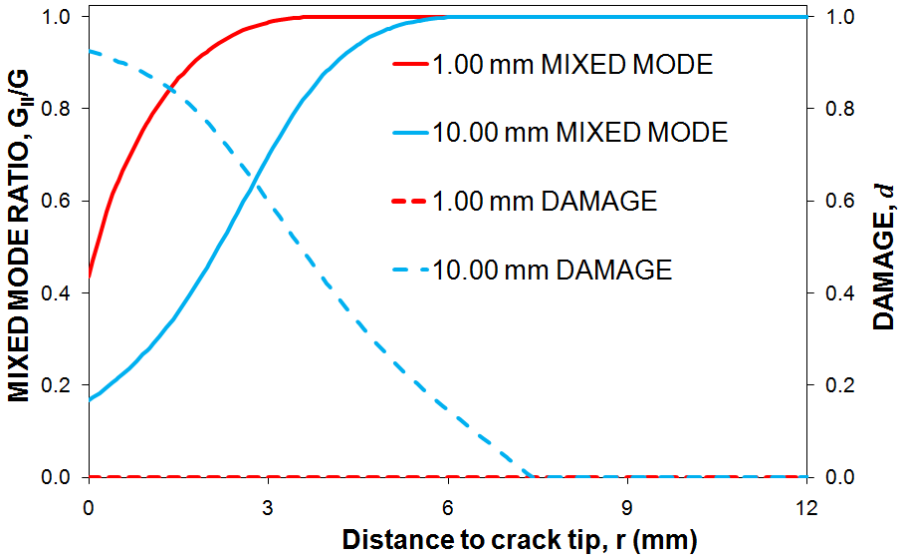

(b)

Figure 8.25. (a) Variation of the mixed mode ratio and damage state with the applied displacement at the crack tip element (integration point) in the FRMM and AFRMM models; (b) Mixed mode ratio and damage state of the cohesive elements immediately ahead of the crack tip for two different applied displacements in a FRMM model. In both cases the results correspond to the bilinear traction-separation law.

Even though the total change in G_{II}/G was similar in all the FRMM and AFRMM models, a much bigger drop in G_c was seen for the AFRMM joint loaded at the thickest arm due to the high shear component involved and the particular shape of the fracture criterion. Figure 8.26 illustrates the variation of the mode mix ratio with the damage at the crack tip and the

corresponding changes in G_c for the various mixed mode specimens investigated. These results partly explain the discrepancies between the numerical and analytical P-δ curves observed in Figure 8.24-c.

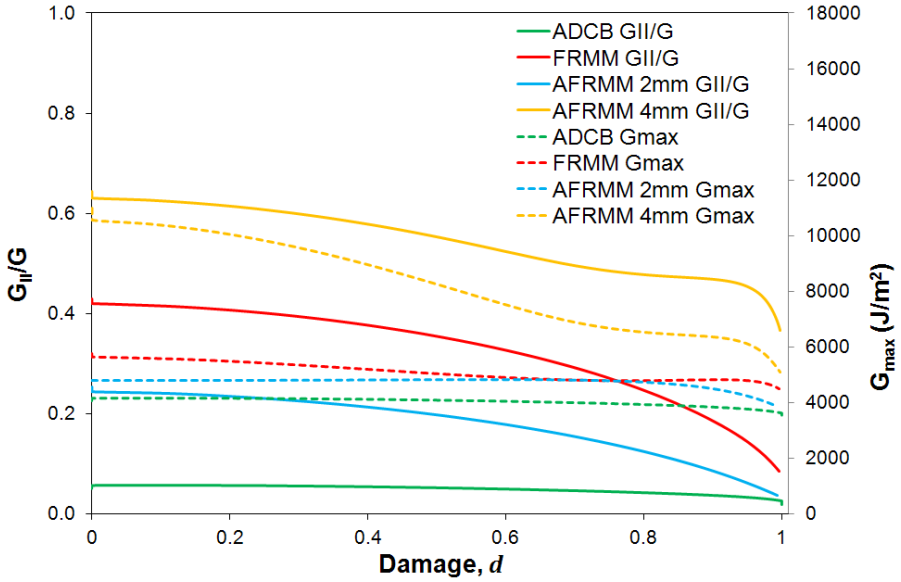

Figure 8.26. Variation of the mixed mode ratio and the value of G_c with the damage at the crack tip of the various mixed mode configurations studied (corresponding to the bilinear traction-separation law).

A comparison between the numerical cohesive zone lengths and the analytical estimate calculated using the procedure described for the ADCB joint (i.e. by adding the contributions of the individual components of G_c, see equation (8.3)) is shown in Figure 8.27. For the symmetric configuration and the AFRMM joint loaded at the thinnest arm, the variation of the numerical l_{CZ} with the applied displacement followed the same trend described for the DCB specimens. After an initial rising period where l_{CZ} gradually increased, it reached a maximum, coinciding with the peak load, and then decreased as the crack grew. Due to an increase in the local curvature of the loaded substrate at the tip, the magnitude of this reduction was significantly more important in the FRMM models. These results contrasted with the constant analytical estimates (between 30% and 60% higher than the corresponding maximum numerical lengths) and again challenged the idea of a self-similar propagation process.

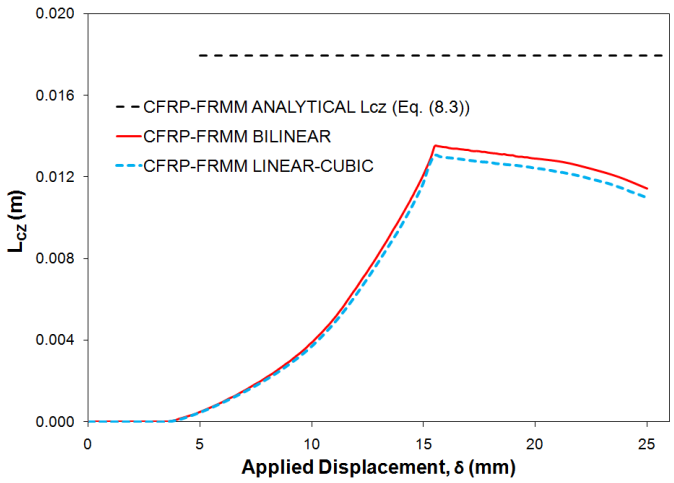

(a)

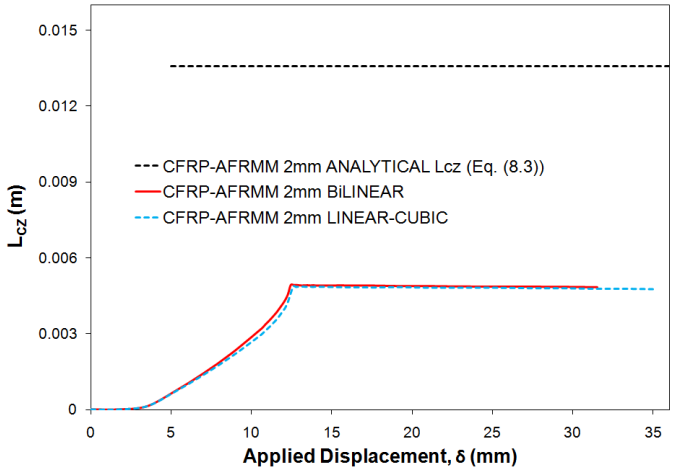

(b)

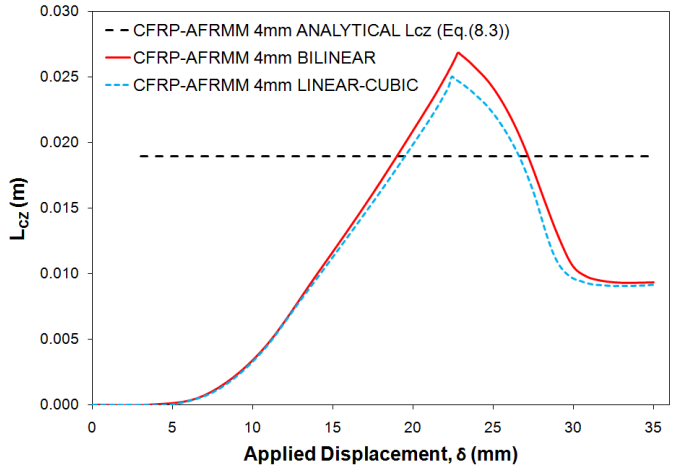

(c)

Figure 8.27. Variation of the numerical cohesive zone length with the applied displacement in (a) the FRMM model, and the AFRMM joint loaded at (b) the thinnest and (c) the thickest arms obtained using the bilinear and linear-cubic traction-separation laws.

In line with the extensive damage accumulated ahead of the crack tip in the tests, considerably longer cohesive zones were obtained in the simulations of the AFRMM specimen loaded via the thicker arm. Such a large FPZ could induce important changes in the overall compliance of the joint, partly accounting for the non-linear behaviour observed in the experimental P-δ curves before the peak load, but at the same time calling into question the applicability of LEFM (which assumes that any increase in compliance is due to crack growth). In addition to its exceptionally large size, in this case l_{CZ} very quickly decreased after reaching its maximum value. This abrupt reduction, being much more significant than in the symmetric configuration, could explain the unstable nature of these tests.

The stress distributions along the bondline provide a better understanding of the reasons behind the shape of the l_{CZ}-δ curves. Although the relative importance of the normal and shear stresses depended on the mixed mode ratio, the latter was always dominant in these joints. In contrast to the ADCB case, in the AFRMM models the normal and shear fields did not reach their respective peak values nor did they change sign at the same points. Furthermore, they changed signs again in the vicinity of the clamp. The magnitude of the maximum compressive stress intensified with the crack length as a consequence of the increasing curvature of the loaded substrate. As seen in Figure 8.28, almost the entire adhesive layer was subjected to shear from the beginning of the simulation. Particularly, the models of the AFRMM specimen loaded via the thicker arm revealed that a very large portion of the bondline had been already damaged (mostly) in shear when the peak load was reached (see Figure 8.28-b). Very soon after the crack started propagating, the edge of the cohesive zone reached the clamping point and could not move any further. However, as the applied displacement kept raising the continuous advance of the crack front forced a rapid reduction in the length of the FPZ which, eventually, led to catastrophic failure (i.e. the crack running into the clamped section of the joint).

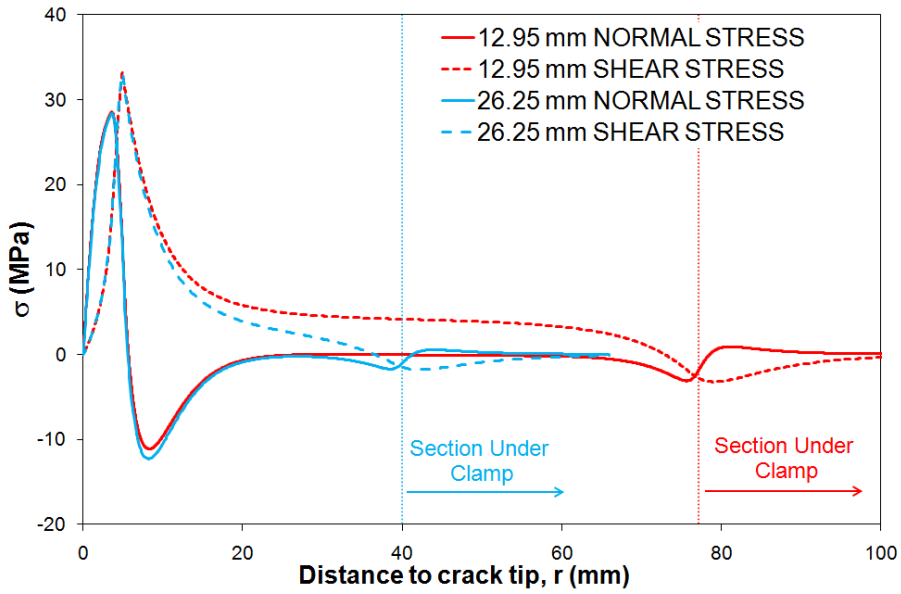

(a)

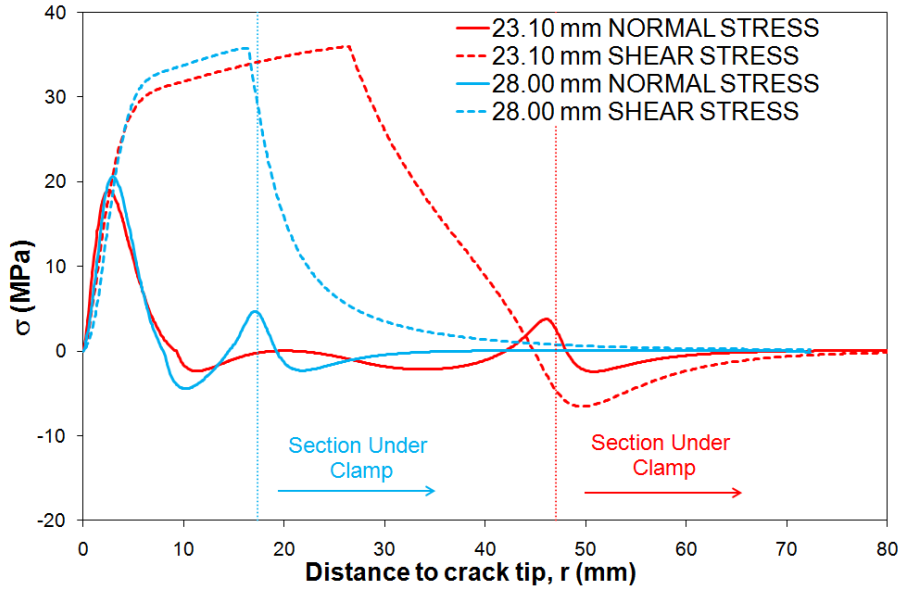

(b)

Figure 8.28. Normal and shear stress distributions along the adhesive layer obtained in the models of the AFRMM joints loaded at (a) the thinner and (b) the thicker arms for different applied displacements using the bilinear traction-separation law.

The dependence of the mode mix on the damage state mentioned above induced small discrepancies between the responses obtained with the bilinear and linear-cubic laws. Each law would predict a distinctive damage distribution and therefore different mixed mode ratios within the FPZ (see Figure 8.29-a), affecting the local cohesive parameters. As seen with the value of G_c at the crack tip (see Figure 8.26), this effect was more noticeable for the AFRMM joint loaded via the thickest arm because of the larger mode II component involved and the

specific shape of the fracture criterion. Nevertheless, these differences were minor, with the bilinear law yielding longer estimates of l_{CZ} and slightly lower loads during propagation for the symmetric configuration and the AFRMM specimen loaded at the thicker substrate. Similarly, this issue had repercussions on the stress state ahead of the crack tip, typically exhibiting lower normal stresses for the triangular traction-separation law.

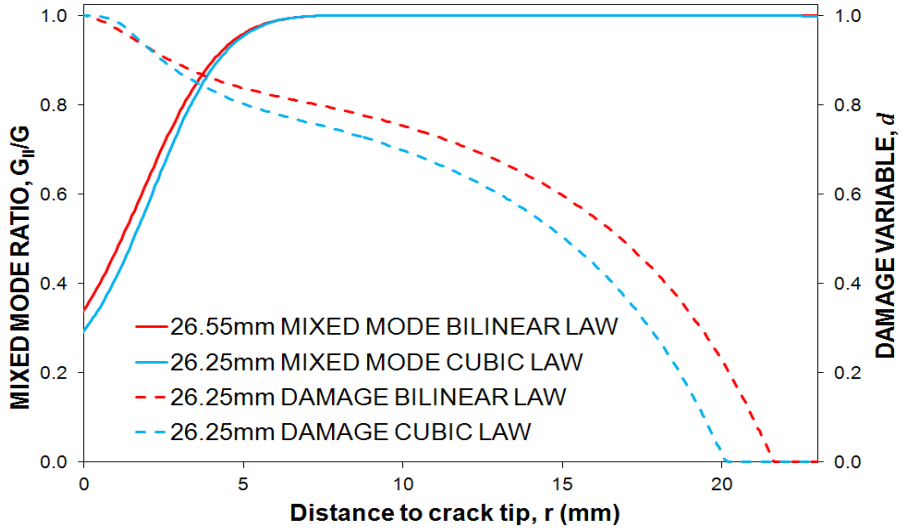

(a)

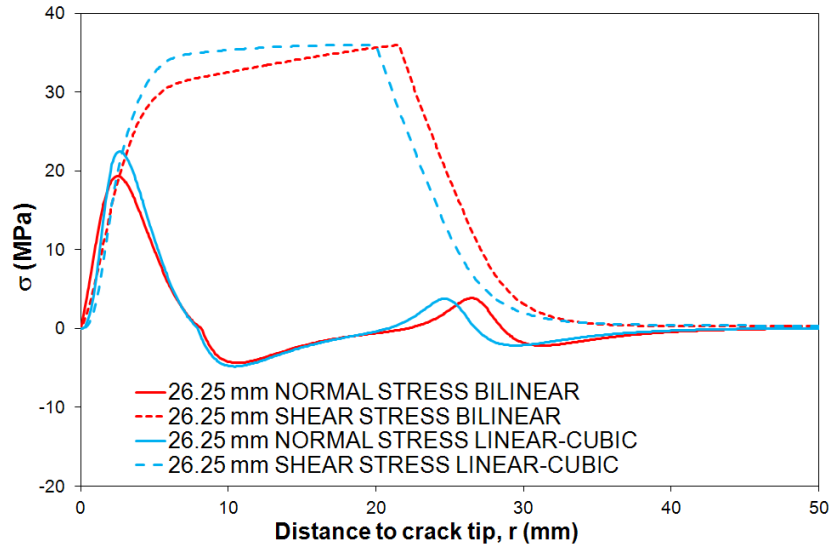

(b)

Figure 8.29. (a) Mixed mode ratios and damage state ahead of the crack tip obtained with the bilinear and linear-cubic evolution laws in the FRMM models for δ=26.25mm.

Whether the variations in the local mixed mode are physically relevant or just a consequence of the element formulation remains unclear. However, the axial forces and geometrical non-linearity typically neglected by the theoretical models but inevitably present in the FE, could

play an important role, especially in cases with large applied displacements and considerable bending. Leaving aside the physical meaning of the shape of the traction-separation law and taking into account the relationship between local damage and mode mix, the type of cohesive law would be expected to affect the overall response in mixed mode problems. In contrast, this was not an issue in pure mode I problems as local mixed mode did not occur, explaining why the form of the traction-separation law is often considered of secondary importance in those cases [134, 241, 269, 277].

8.4.4 Mode II Test Specimens

8.4.4.1 Modelling the CFRP ELS

In order to avoid permanent damage to the CFRP substrates and to prevent sudden failure, the mode II tests were stopped prior to the maximum load. Thus, no stable crack propagation region could be clearly identified nor did the fracture energy reach a plateau. Since the value of G_{IIc} employed to define the failure criterion had been obtained from extrapolating the mixed mode data, it was essential to check its suitability to reproduce the know-section of the experimental P-δ traces.

As may be seen from Figure 8.30, the load-deflection curves obtained in the simulations were in excellent agreement with the test results, especially those corresponding to the bilinear evolution law. On the other hand, agreement with the analytical solution was poor. The FE models successfully captured the marked non-linear behaviour exhibited by the real joints, whereas the CBT response remained linear up to the peak load.

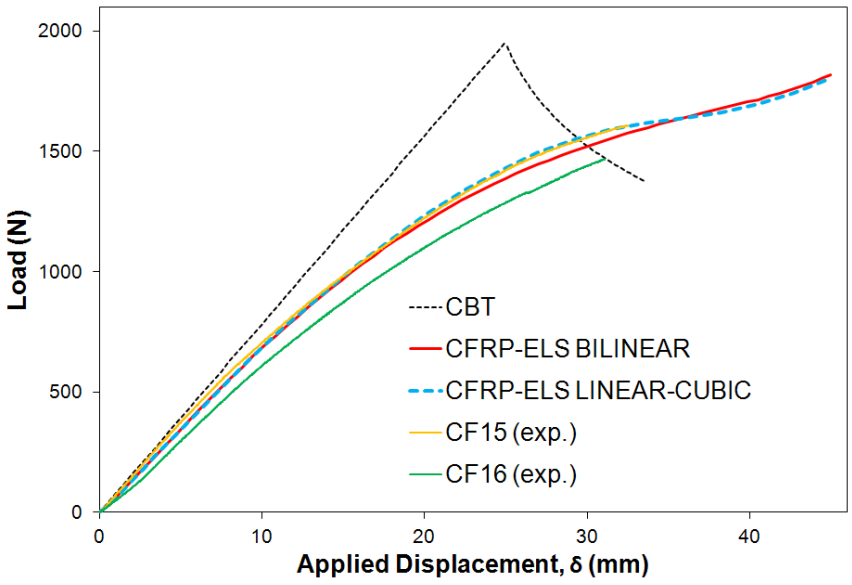

Figure 8.30. Comparison between the numerical, experimental and analytical load-displacement curves for the CFRP-ELS specimens.

The extent of the non-linearity was much greater in the mode II tests than in any other configuration. This phenomenon has been experimentally justified by the large amount of damage accumulated ahead of the crack tip. The size of the numerical cohesive zone (l_{CZ}) would appear to support this hypothesis (see Figure 8.31). According to the simulations, virtually the entire adhesive layer between the initial tip and the clamping point would have become part of the FPZ before crack initiation. Whilst the fracture surfaces presented in Figure 6.20 indicated otherwise, Figure 8.31 would suggest that the extensive damage observed in the experiments had been mistaken for crack growth. Furthermore, it would call into question the applicability of the LEFM methods for the analysis of the mode II specimens, as inelastic deformation was partly responsible for the changes in compliance measured in the ELS tests.

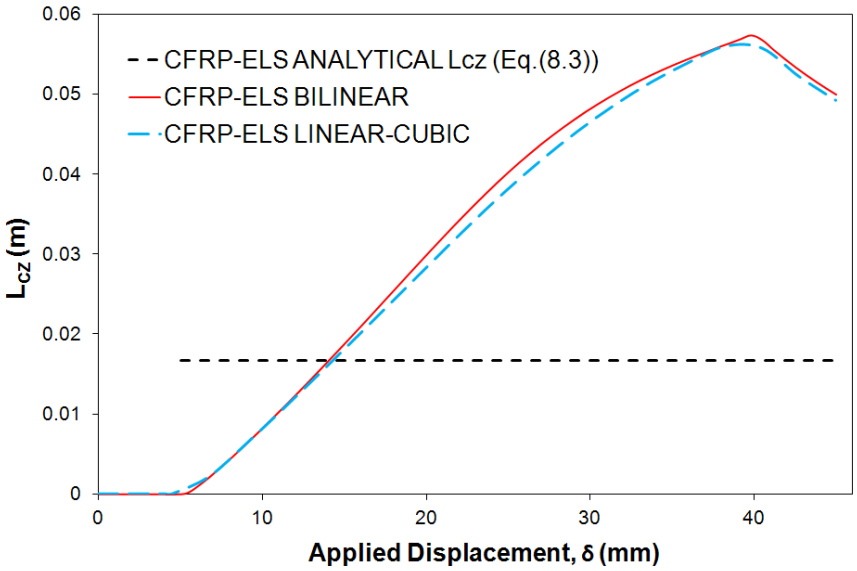

Figure 8.31. Variation of the numerical cohesive zone length with the applied displacement in the ELS model using the bilinear and linear-cubic traction-separation laws (the analytical estimate has been included for comparison).

Even if the principles of LEFM were violated, the cohesive elements may still be used to model the ELS test. However, little can be said about the extrapolated value of G_{IIc} except that it appeared sufficiently high to reproduce the experimental result accurately. The overall response of the ELS models would not change considerably if higher G_{IIc} values were used because the numerical cohesive zone length could not increase further, as its size was already limited by the position of the clamp.

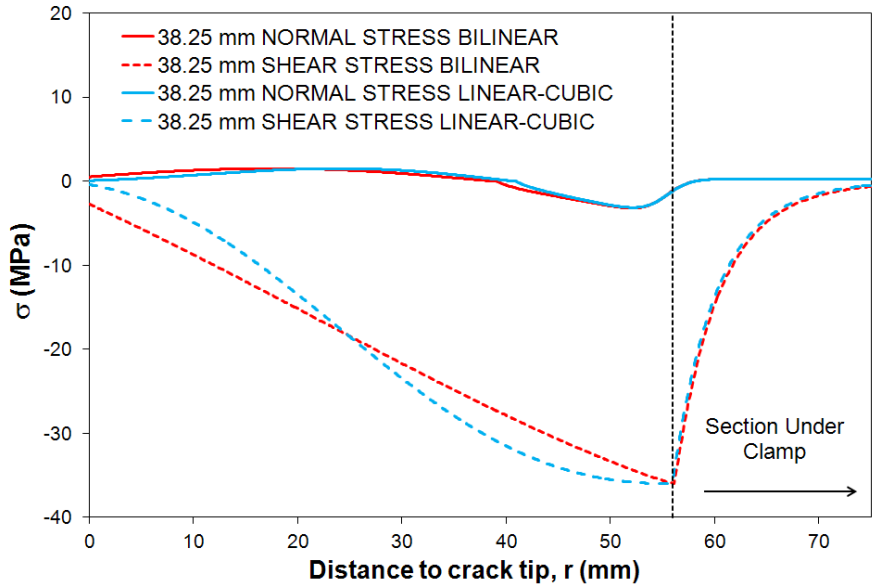

Figure 8.32. Normal and shear stress distributions along the bondline of the ELS model obtained with the bilinear and linear-cubic traction-separation laws.

The stress distributions illustrated in Figure 8.32 would indicate the conditions at the numerical crack tip did not correspond to pure in-plane shear. Although very modest, the opening mode contribution would transform this into a mixed mode problem, bringing up once more the dependence of the mode mix on both the local damage state and the distance to the crack tip. Taking this into account, the different damage distributions within the cohesive zone predicted by the bilinear and linear-cubic laws (see Figure 8.33) would be enough to explain the discrepancies between the P-δ and l_{CZ}-δ responses obtained in each case (especially considering the large size of the FPZ).

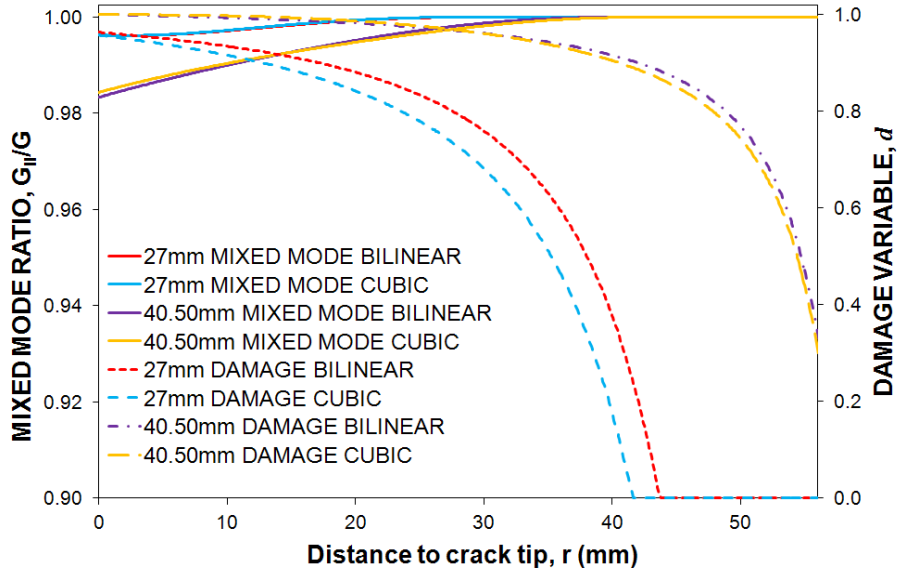

Figure 8.33. Mixed mode ratio and damage state of the cohesive elements immediately ahead of the crack tip for two different applied displacements in the ELS model.

8.4.5 Final Remarks

In addition to providing specific information concerning the ability of the cohesive element formulation to describe the fracture behaviour of AF163-2OST, this study has shed some light on certain aspects of fracture testing of adhesively-bonded joints. The additional information concerning the stress and mode mix distributions ahead of the crack tip has been particularly enlightening.

According to the FE simulations, fracture in the mixed mode specimens did not take place under a constant mixed mode ratio. Instead, the mode mix within the FPZ depends on both the distance to the crack tip and the local material state. Moreover, in contrast with the general belief, not even in the pure mode cases is crack propagation a self-similar process, as the size of the FPZ and the mode mix within this region changes with the applied displacement and crack length. Further, when the adhesive layer is constrained between much stiffer substrates, the stress field ahead of the tip and therefore the size of the process zone is considerably influenced by the bending stiffness of the arms and the loading conditions (i.e. the mixed mode ratio).

The models also revealed the potential effect of the substrate thickness on the mixed mode tests. Thicker arms typically yield larger FPZ (assuming a constant bondline thickness) which, due to the variation of the mode mix with the local damage state within the cohesive zone, could lead to changes in the global mode mix and consequently to different measured G_c values. Additionally, this could hinder reaching a stable propagation phase (for example if the clamping point in the AFRMM test were too close to the initial crack tip) or even compromise the validity of LEFM if extremely large FPZ are produced.

These observations highlight even further the need for an accurate and complete failure criterion in order to carry out performance predictions of real structures. However, at the same time they hint at potential limitations with the reduction schemes used to analyse the experimental data. Particularly, the mode decomposition theories could be too "simplistic" for cases with long process zones. In these cases, the concept of "effective mixed mode ratio" proposed by Davidson becomes very useful.

Selecting configurations that minimize the size of the FPZ could be a possible solution to circumvent these problems, although this could produce unrealistic fracture results (i.e. excessively conservative values of G_c). Furthermore, it could lead to geometrical issues and the potential violation of the principles of LEFM by subjecting the substrates to permanent deformation. Finally, the size of the cohesive zone could not be known "a priori".

Therefore, the design of a testing programme to determine a suitable fracture criterion would have to find an equilibrium point between various competing aspects, including stability, validity of the LEFM, avoidance of excessive geometrical non-linearity, practicality and physical relevance.

8.5 Modelling the Fatigue Fracture Mechanics Tests

The two prediction methodologies proposed in Chapter 3 were applied to the study the titanium DCB joints tested under "dry" fatigue conditions. The results of these simulations do not represent independent predictions, but they allow an assessment of the potential of the techniques and have identified possible limitations. A simple model with a single cohesive element had been previously used to verify the cycle-jump degradation strategy described in section 3.3.4 (see Appendix H).

8.5.1 Simulation of the Fatigue Response of Ti DCB joints

The cohesive elements, incorporating degradation due to cyclic loading, were used to simulate the P_{max}-N-a response of the titanium DCB joints previously tested in "dry" fatigue. In addition, the experimental value of G_{th} was combined with the simplified formulation described in section 3.3.5 in an attempt to estimate both the threshold load and final crack length (P_{th} and a_{th} respectively) obtained in the experiments.

8.5.1.1 Model Details

Equivalent 2D models to those described for the quasi-static case (see section 8.2) were used in the fatigue analysis but now with the specific fatigue damage formulation. These employed second-order cohesive elements featuring 30 integration points. Only the bilinear evolution law was considered in this study.

Figure 8.34 shows the displacement applied at the centre of the top end-block (the motion of the centre point of the bottom one was fully constrained). Designed for high cycle fatigue, the real sinusoidal function was replaced in the model by the envelope of its cyclic variation. The maximum displacement matched that of the experiments (i.e. δ_{max}=1.35mm), while the frequency (5Hz) and ratio R (R=0.1) were defined as internal parameters. In order to simulate the effect of 25 million cycles, δ_{max} was held constant for $7.5 \cdot 10^6$ seconds (i.e. the approximate duration of the experiments). Note that only the initial ramp (i.e. $t \leq t_0$=1s) was considered in those models used to predict the threshold.

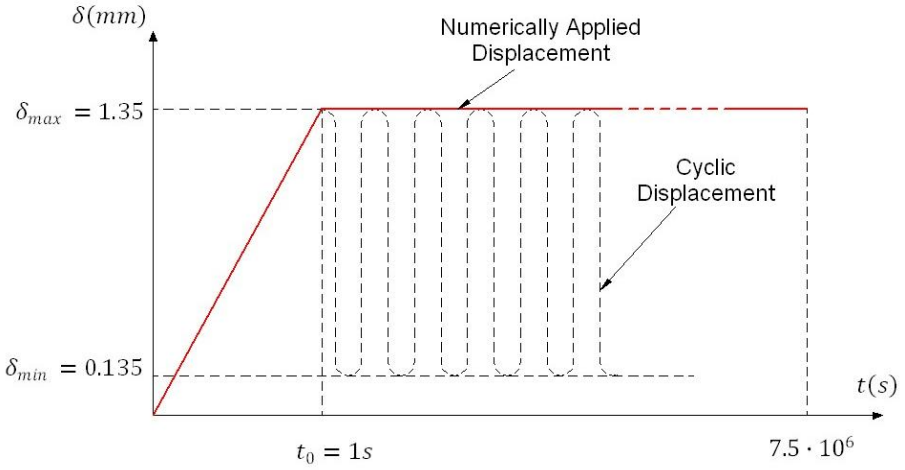

Figure 8.34. Schematic representation of the cyclic displacement applied to the structure and the displacement function for which it was substituted in the numerical model.

As indicated in [304, 324, 348], the use of excessively large time increments could lead to instabilities or to poor accuracy when using a jump-cycle strategy. In addition, the size of the cohesive elements could aggravate the problem. On the other hand, large values of Δt_{max} during the integration would be desirable to minimize the computing time. While the first aspect was analysed here, a detailed investigation of the influence of the mesh density can be found in Chapter 10.

To reduce the influence of the mesh density, the numerical crack length (a_{num}) was determined following a similar approach to that used for l_{CZ} (see section 3.3.4.4.3). The total value of a_{num} was calculated as the sum of the initial crack length (a_0) and the lengths associated with the integration points that had been completely damaged (i.e. d=1). By evaluating the contribution of each integration point separately (via the corresponding Gauss weighting factor w_j used in the numerical integration), the crack growth increments could be smaller than the element size (l_e), producing smoother responses. Thus:

$$a_{num} = a_0 + \sum_{j}^{d=1} \frac{w_j}{2} l_e^i \tag{8.3}$$

8.5.1.2 Prediction of the P_{max}-N-a response

Figure 8.35 shows the maximum load (P_{max}) versus the number of cycles (N) obtained in the simulations, which were in excellent agreement with the experimental curves regardless of the value of Δt_{max}. In order to model the initial rising phase accurately and avoid instabilities, the time increment was always gradually increased from 0.05 seconds to the corresponding

value of Δt_{max}. As a result, the early response (N<30000 cycles) was virtually identical in all cases. Thereafter the solution exhibited a mild dependence on Δt_{max}, with the larger time increments producing slightly faster reductions in P_{max}. However, despite the significant convergence issues encountered for the larger values of Δt_{max}, all the simulations approached the same final load (for N>$15{\cdot}10^6$ cycles). Finally, the importance of the quasi-static cohesive parameters was noteworthy, as they controlled the initial response and the peak value of P_{max}.

Similar conclusions could be drawn for the numerical crack lengths and growth rates, as these also compared very well with the experiments (see Figure 8.36). While the variation of a_{num} with N in the early stages was identical for all cases, the models with larger time increments predicted faster crack propagation in the intermediate region. However, the final crack length was approximately independent of Δt_{max}. Overall, Δt_{max}=5000s offered the best compromise between accuracy and computing time.

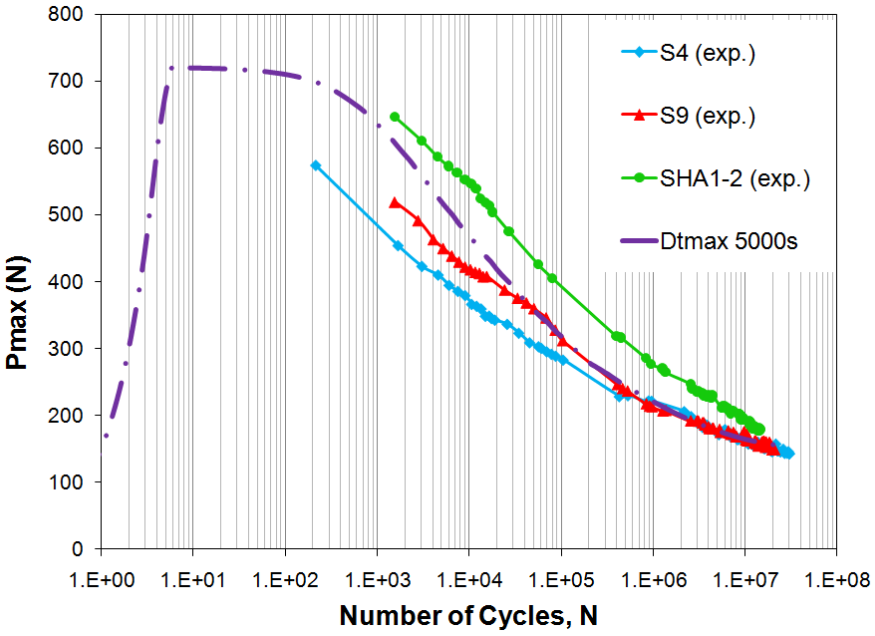

(a)

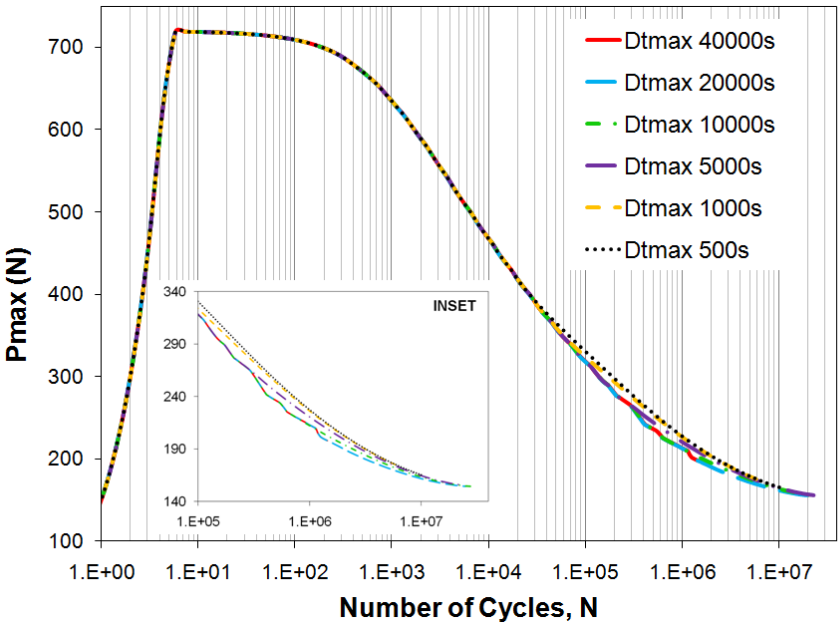

(b)

Figure 8.35. (a) Comparison between the experimental results and the numerical P_{max}-N curves obtained for Δt_{max}=5000s; (b) Comparison between the numerical P_{max}-N curves obtained for various values of Δt_{max}.

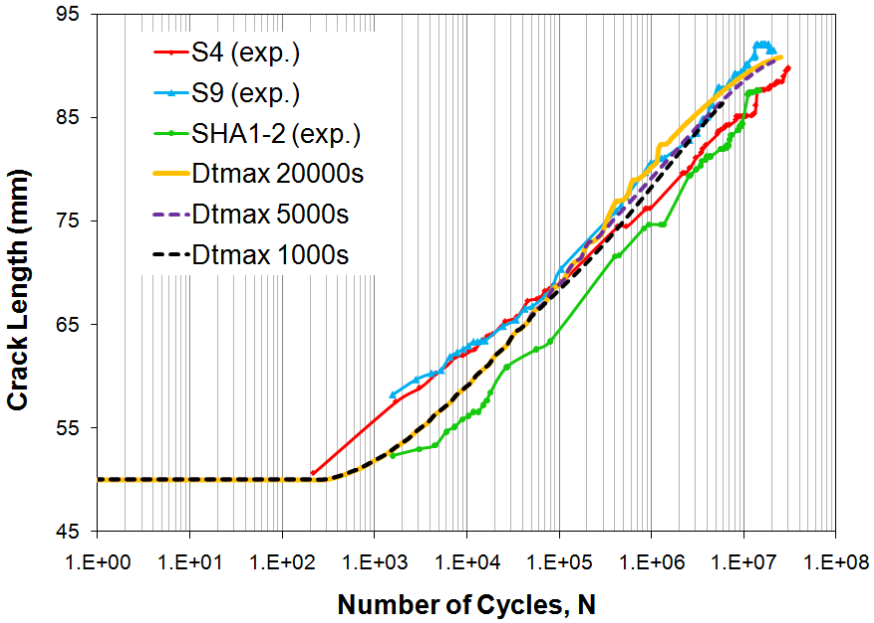

Figure 8.36. Comparison between the numerical and experimental *a-N* curves.

Bearing in mind the success in the simulation of the P_{max}-N-a response, it was unsurprising that the fatigue diagram derived from the FE results (using the polynomial method) matched the modified Paris law inputted into the cohesive elements, see Figure 8.37. This agreement emphasized further the soundness of the damage degradation strategy implemented for cyclic loading.

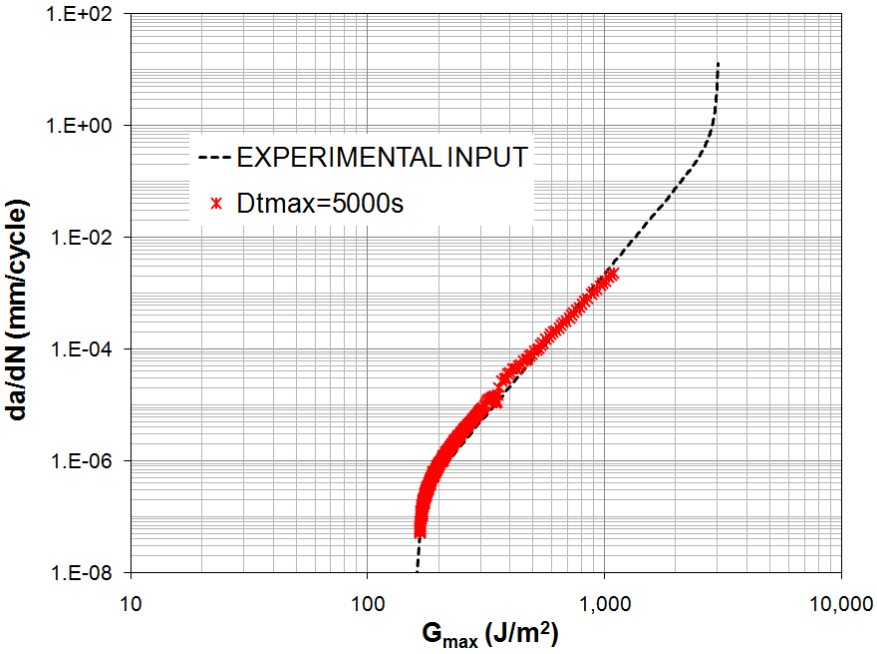

Figure 8.37. Comparison between the fatigue crack growth rate estimated from the DCB model, the experimental results and the modified Paris law used as input for the UEL subroutine.

The advantages of using the definition of l_{CZ} proposed in Chapter 3 (see equation (3.78)) rather than the theoretical estimate obtained from (2.42) (used by Turón et al. [304] and Pirondi ad Moroni [305]) are highlighted in Figure 8.38. Despite yielding reasonable final values of P_{max} and a_{num}, the models employing the analytical estimate predicted much faster degradation in the early and intermediate stages of the simulations. Moreover, as discussed in Chapter 10, the definition of l_{CZ} based on the damage state of the individual integration points combined with the use of quadratic elements minimized the drawback of coarse meshes reported elsewhere [323, 324, 348]. The application of equation (2.42) required the determination of G_{max}, the value of which would be highly dependent on the element size in problems with significant bending if first-order kinematics were adopted.

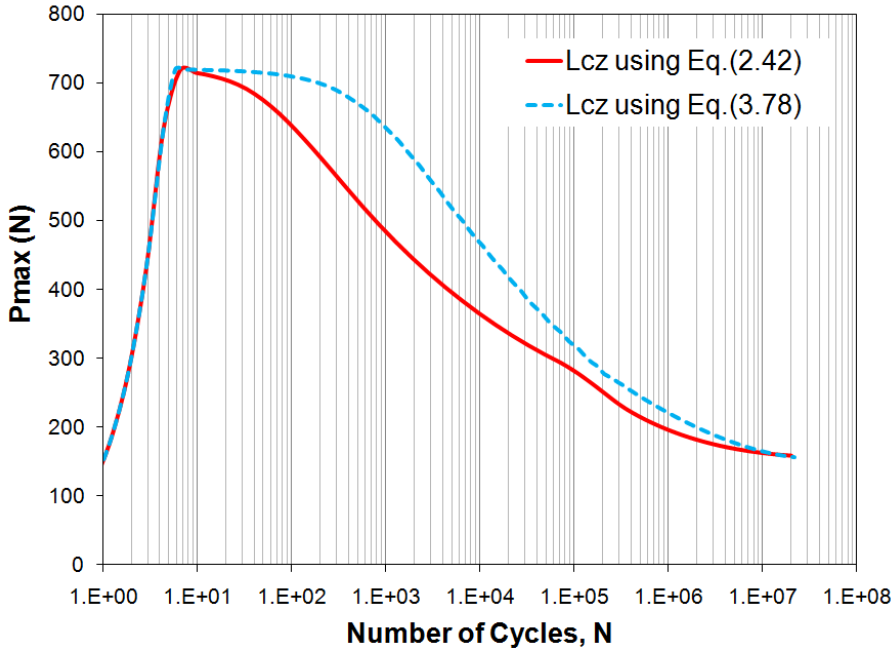

Figure 8.38. P_{max}-N response obtained using the theoretical estimate of the FPZ (2.42) and the definition based on the damage state of the individual integration points (3.78) for Δt_{max}=5000s.

8.5.1.3 Prediction of the Fatigue Threshold

As discussed in Chapter 3, this methodology does not aim to predict the entire P_{max}-N-a response but aims only to predict the threshold load below which fatigue does not occur. It is based on the damage formulation descried in section 3.3.5, which uses a special evolution law to accommodate an area equal to the experimental value of G_{th} while complying with the physics of the problem. The behaviour of these elements is very similar to that of VCCT. However the latter technique was not applied here for various reasons, namely: (i) It would not be adequate to simulate the response of the TDLJ, as it requires a pre-existing defect;

(ii) The mixed mode ratios predicted by the VCCT would be very similar to those obtained with CTE/SF, which would not appear to be appropriate for the long FPZ expected for the adhesive under consideration

For this simulation, the applied displacement was a simple ramp function, with the final value set equal to the maximum displacements (i.e. 1.35mm). Even though shape-wise the resulting load-deflection curves were equivalent to those obtained for the quasi-static models (i.e. linear raising section up to a peak value followed by crack propagation and gradual decrease in the load), they lacked any physical meaning. Only the last point (corresponding to δ_{max}=1.35mm) had some validity, as it represented the estimate for the threshold load.

Despite not accounting directly for the influence of the R ratio, the results of the threshold simulations were always in very good agreement with those obtained with the damage degradation strategy due to cyclic fatigue (see Figure 8.39). This equivalence supported the idea that these are complementary rather than incompatible methodologies.

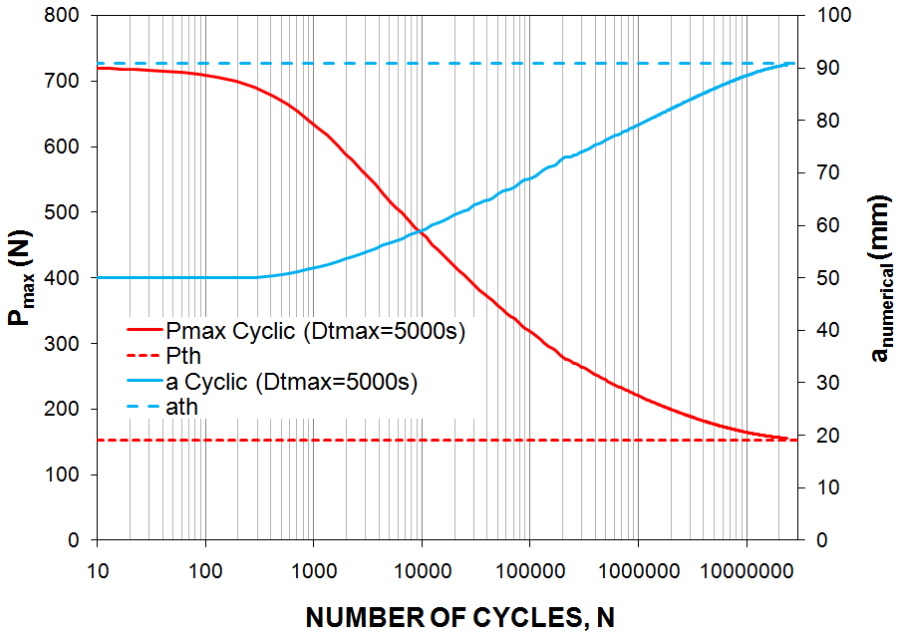

Figure 8.39. Numerical results obtained with both fatigue prediction methodologies (i.e. cyclic damage accumulation and threshold) for the titanium DCB joint.

8.6 Chapter Summary

In this chapter, two-dimensional, finite element models of the fracture specimens discussed in the experimental part have been created in Abaqus. A single layer of finite-thickness cohesive elements has been used to model the bondline in all cases, deriving the penalty stiffness and the condition for damage initiation from the elastic properties of the adhesive.

A parametric study has been carried out using the mixed mode test geometries to evaluate the influence of the elastic properties of the adhesive layer on the mode mix seen by the cohesive element located at the crack tip prior to the onset of damage. The mode mix seen by the elements has been found to depend significantly of the elastic modulus of the adhesive, being in excellent agreement with the results obtained with CTE/NSF for the case of AF163-2. Based on these findings, the non-singular field fracture criterion was adopted for all the FE models to guarantee the consistency of the subsequent predictions. Then, the fracture behaviour of the joints tested under both quasi-static and fatigue loading conditions has been simulated, comparing the numerical load-displacement and S-N curves with those obtained in the corresponding experiments

Quasi-statically, the models successfully reproduced the overall response in all cases except for the asymmetric FRMM joints loaded via the thickest substrate. The influence of the shape of the traction-separation law was minimal in the pure mode cases. In contrast, the bilinear and linear-cubic laws produced slightly different solution in the mixed mode cases because: (i) the mixed mode ratio seen by the cohesive elements varied with the distance to the crack tip; (ii) the mode mix seen by the cohesive elements varied significantly with the local damage state. The numerical cohesive zone length, typically considerably smaller than the analytical estimates, was found to vary with the applied displacement.

The two prediction methods proposed in this work have been applied to the titanium DCB joints tested under "dry" fatigue conditions, using the experimentally determined coefficients of the Paris law as inputs to the models. The FE simulations successfully reproduced the P_{max}-N-a response. In this respect, the use of the numerical cohesive zone length has proven to be more accurate than the analytical estimates given by equation (2.42). Both methodologies predicted virtually the same threshold load.

In the next chapter, to validate the procedures developed above, the model is used to predict the failure of the tapered double lap joint.

9. Predicting the Performance of a Simplified Adhesively-Bonded Structure: Ti-to-CFRP Tapered Double Lap Joint

9.1 Introduction

Whilst the potential of the cohesive formulation to model the quasi-static and fatigue responses of various fracture mechanics specimens was evaluated in the previous chapter, its predictive capability had yet to be put to the test with an independent geometry. Thus, this chapter focuses on the application of the prediction methodologies proposed in Chapter 3 to a simple adhesively-bonded structure: a Ti-CFRP tapered double lap joint (TDLJ). So as to assess their accuracy, the simulations are compared with experimental results. The quasi-static behaviour is investigated first, followed by a discussion of the response to cyclic loading.

9.2 Quasi-Static Response

9.2.1 Experimental Results

Three double lap joints were tested for each taper angle (7°, 30° and 45°) quasi-statically to failure. The test rate employed was 0.5mm/min. Manufactured in accordance with the procedure described in Chapter 4 (section 4.3), their final geometry differed slightly from the

nominal design shown in Figure 4.17. There was some variability in the thickness of the substrates: the thickness of the titanium and CFRP beams were 1.97±0.04mm and 4.19±0.05mm respectively. Also, some variability in the bondline thickness was noted, with the nominal value of 0.4 mm reduced to 0.24±0.07mm at the ends of the overlap.

A direct consequence of the grinding process used to produce the bevelled edges, the size of the tip of the tapered-end varied approximately between 0.1 and 0.4mm (see Figure 9.1). This feature appeared to influence the effectiveness of the tapers to reduce the peel stresses at the end of the overlap. As a result, the ultimate strengths of the joints were very similar in all cases (see Table 9.1).

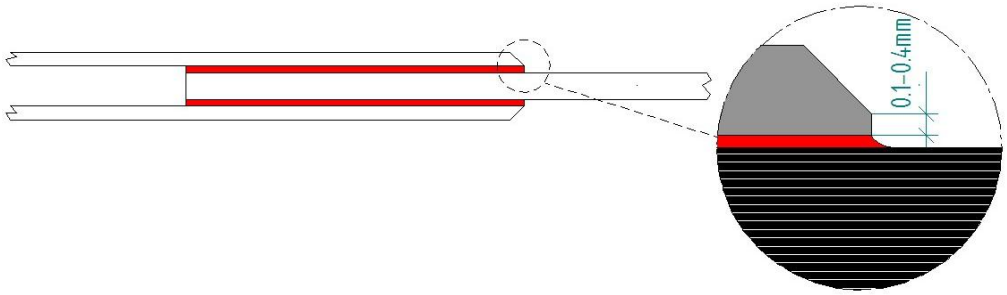

Figure 9.1. Schematic representation of the tapered end-tip observed in the titanium substrates.

Rather than employing the cross-head displacement, the DIC method was used to generate the load-extension curves for the joints. Several pairs of points (one at either side of the overlap initially 10mm from the corresponding edge, see Figure 9.2) were selected and their relative distance monitored during the tests. The average separation was then calculated and combined with the readings from the load cell to create the load-extension plots. The optical technique was favoured over the traditional extensometer, the arms of which often slipped, causing an unsmooth response, see Figure 9.3.

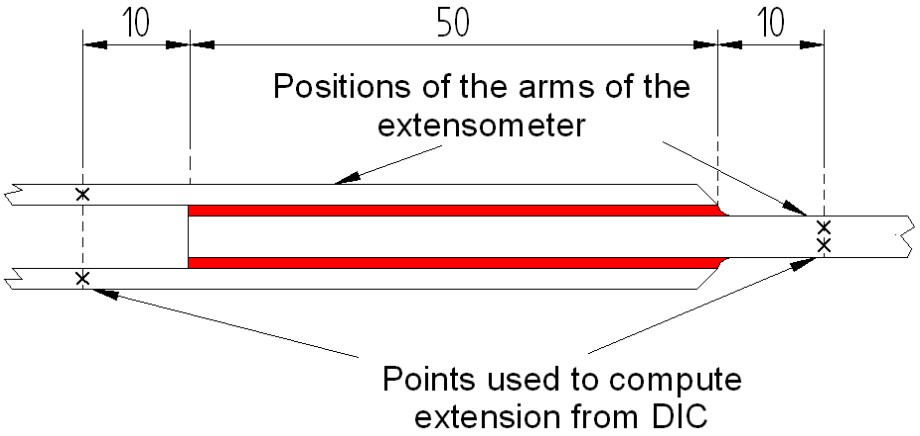

Figure 9.2. Schematic representation of the initial positions of the arms of the extensometer and the points used to compute the extension from the DIC data (dimension in mm).

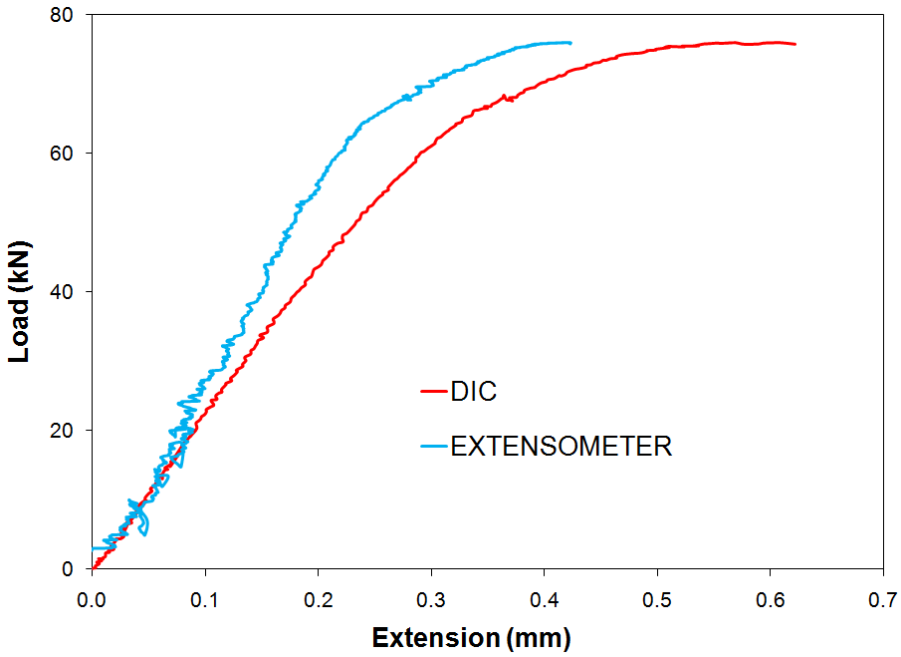

Figure 9.3. Comparison of the load-extension traces obtained for a TDLJ with 30° taper using the DIC and the extensometer data.

As illustrated in Figure 9.4, very similar load-extension responses were obtained for the three different taper angles tested. All the traces exhibited three well-defined regions. An initial linear section was followed by a region of gradual reduction in slope starting between 40 and 50kN. Then the gradient stabilized and the load increased more or less linearly up to the point of catastrophic failure. Whilst the initial stiffness and the curved section were comparable for all the specimens, the final segment was longer for the sharper tapers.

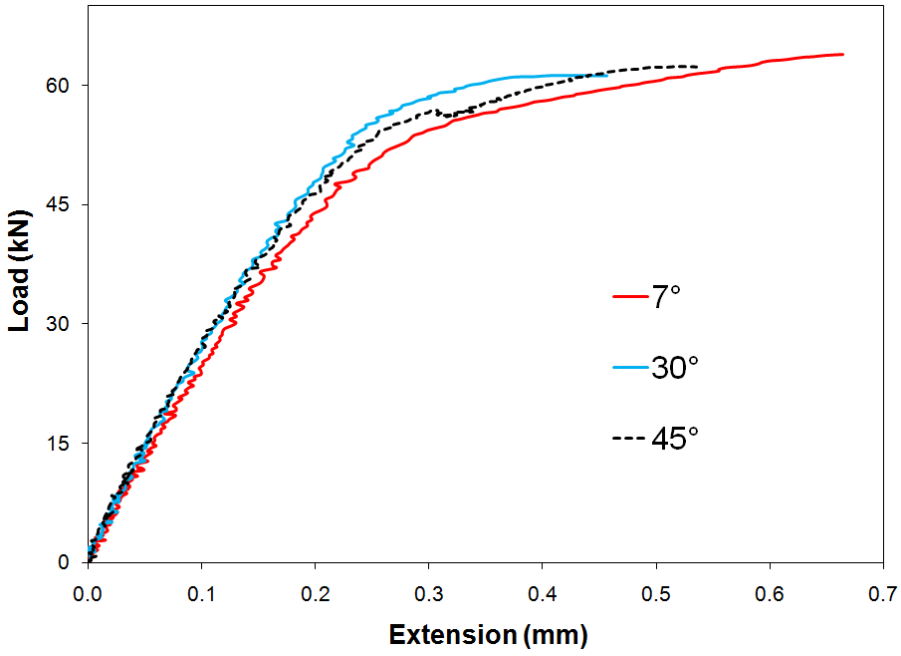

Figure 9.4. Typical load-extension curves obtained for the TDLJ with different taper angles.

Table 9.1. Maximum load and strength obtained for the CFRP-Ti double lap joints tested quasi-statically

Taper Angle (°)	Maximum Load (kN)	Average Cross Sectional Area CFRP Substrate (mm^2)	Ultimate Strength (MPa)
7-1	63.58	83.29	763.32
7-2	64.43	84.22	765.04
7-3	62.82	83.54	751.91
30-1	75.97	83.99	904.54
30-2	68.23	84.03	812.04
30-3	60.84	83.33	730.09
45-1	70.81	82.65	856.70
45-2	65.91	80.48	819.02
45-3	62.42	84.02	742.93

The DIC results suggest that the response was related to the behaviour of the adhesive layer. However, neither the DIC nor the high speed video provided a sufficient level of detail to clarify whether this behaviour was caused by plastic yielding or crack propagation. As seen in Figure 9.5, the maximum strain gradually built-up in the adhesive layer at both ends of the overlap. Both the magnitude and the area affected increased with the increasing load until almost the entire bondlines were highly deformed. As the strain developed in the adhesive layer, its load-transferring capability was reduced. The simultaneous variations in the strain field within the CFRP and Ti-alloy substrates would indicate degradation of the mechanical properties of the epoxy resin. For example, the damage accumulated in the adhesive layer near the taper led to strain relaxation in the corresponding section of the metallic strip. The same occurred in the CFRP substrate on the opposite side of the overlap. Unfortunately, the resolution of the pictures was not sufficient to distinguish clearly between simple damage or complete failure of the adhesive (i.e. crack growth).

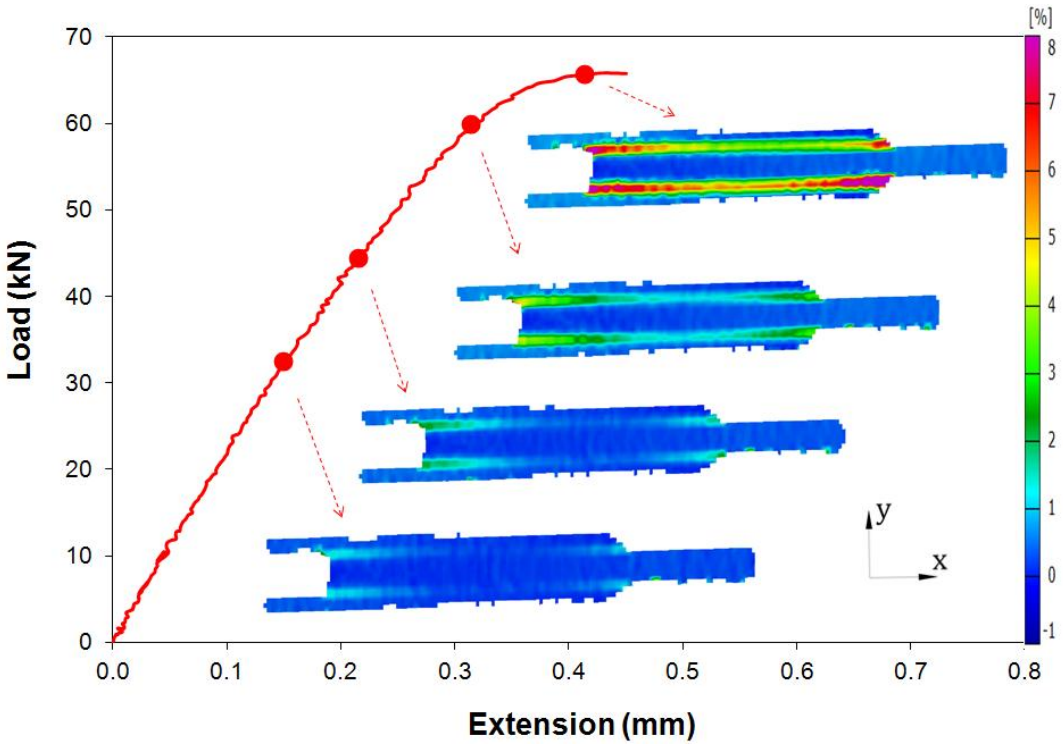

Figure 9.5. DIC images (major principal strain) obtained for a TDLJ with a 45° taper at different stages during the test.

The visual inspection of the fracture surfaces, examples of which are shown in Figure 9.6, revealed that crack propagation had been mainly cohesive in the joints with 45° tapers. In contrast, a combination of cohesive, interfacial and even interlaminar failure was observed in the specimens with 30° and 7° tapers. In those cases, the interlaminar and interfacial failure only affected one side of the joints, with the former type primarily coming into sight near the tapered end of the overlap.

In addition, despite measuring strain values considerably below nominal yield for the titanium alloy with the DIC equipment, the metallic substrates exhibited permanent deformation outside the bonded section. Careful study of the high speed films revealed that this had taken place after the joint had failed due to asymmetric deformation. Rather than debonding simultaneously, one side of the overlap failed marginally earlier, unbalancing the specimen for a short period of time and inducing bending in the titanium arms at the moment of fracture. Furthermore, this transient asymmetry could partly explain the different types of failure observed at each side of the overlap for some joints.

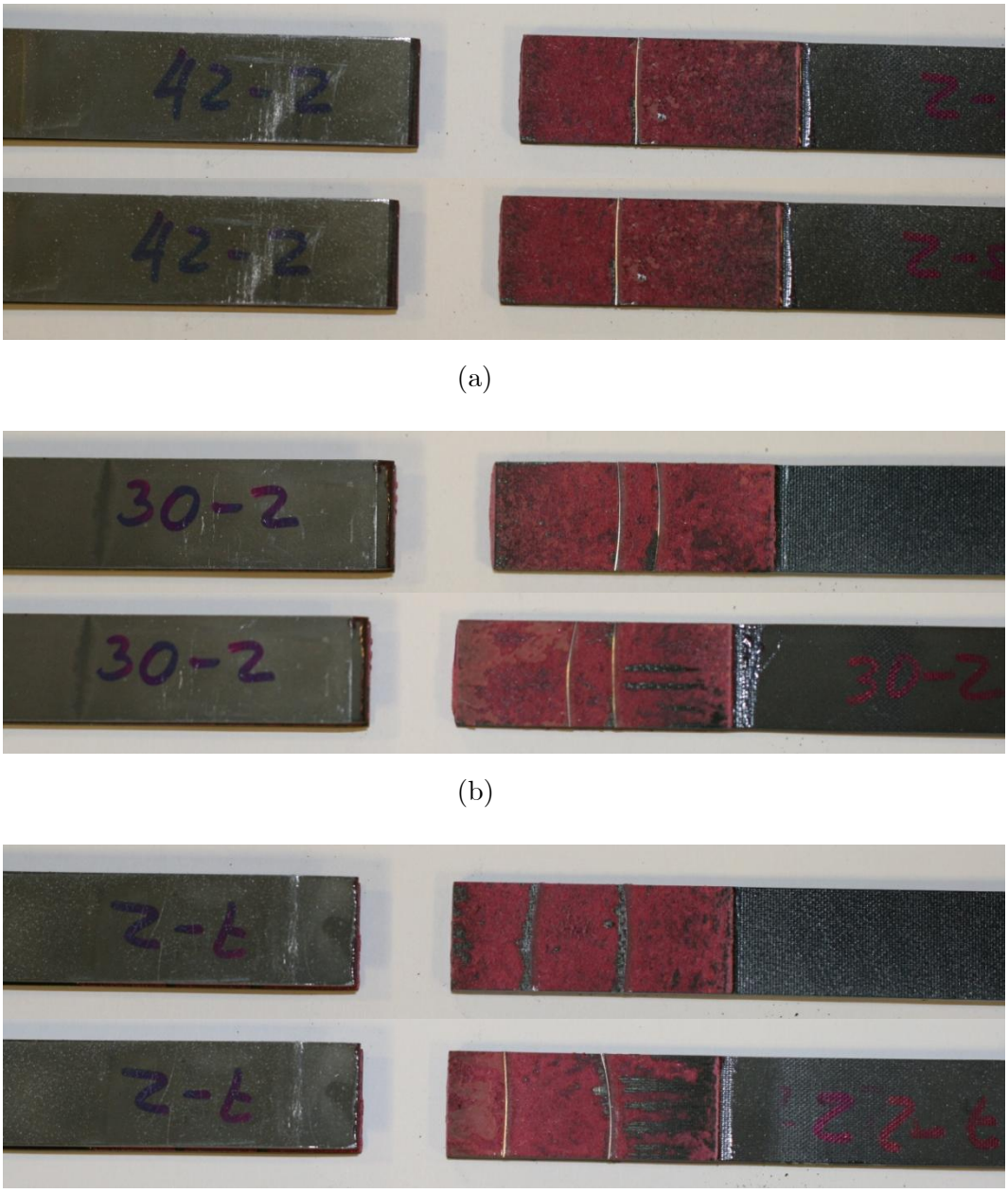

Figure 9.6. Examples of the fracture surfaces obtained for the Ti-CFRP double lap joints with (a) 45°, (b) 30° and (c) 7° taper angles tested quasi-statically.

9.2.2 Numerical Simulations

The quasi-static response of the tapered double lap joints was modelled in Abaqus v.6.9 using the cohesive formulation described in Chapter 3. Only the 45° case was considered, given that the traces of interlaminar and interfacial failure observed for sharper angles would not follow the fracture criterion proposed in Chapter 7. The accuracy of these simulations, which was

later evaluated by direct comparison with the experimental results, is important for the validation of the subsequent fatigue predictions, which are based on the static solutions.

A brief description of the main characteristics of the models, including details on the materials, mesh design and boundary conditions is given first. The FE predictions are discussed next, paying special attention to the mixed mode ratios seen by the cohesive elements and their potential variation with the local damage state.

9.2.2.1 Model Details

Figure 9.7-a illustrates the original joint design used for the test specimens, whereas the simplified geometry modelled is represented in Figure 9.7-b. Instead of considering the entire length of the substrates (and the end-tabs), only the central section (i.e. the overlap plus 10mm at either side) was included in the models. The analysis of this region, equivalent to the area monitored by the DIC cameras, would facilitate the comparison with the experimental results. In addition, taking advantage of the symmetry with respect to the horizontal plane, only half of the joint was modelled. Not only did this reduce the computing time, but it also allowed the focus to be on a single layer of adhesive.

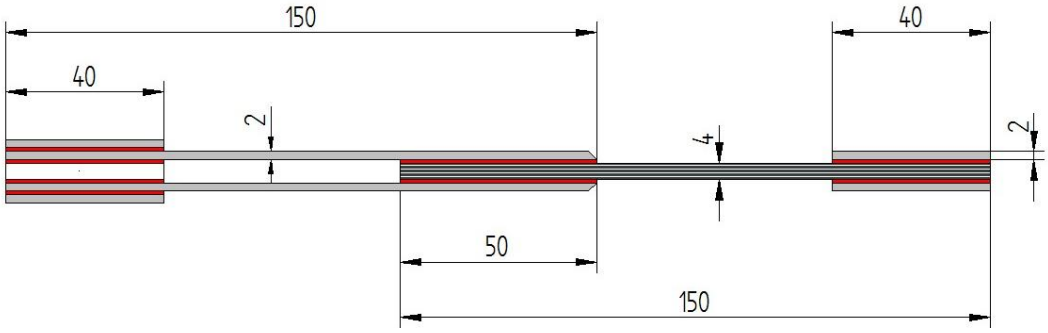

(a)

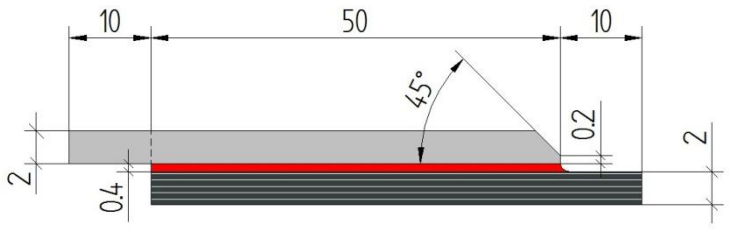

(b)

Figure 9.7. Dimensions (in mm) of (a) the original TDLJ design and (b) the simplified geometry used in the FE models built in Abaqus to simulate their quasi-static response.

The tip length of the taper was assumed to be 0.2mm, although a simple parametric study revealed no significant effects on the quasi-static response of tip lengths between 0.05 and 0.4mm. The bondline thickness was considered uniform and equal to the nominal value (i.e. 0.4mm), while any residual stresses arising during curing, due to the different coefficients of thermal expansion of the substrates were neglected.

A two-dimensional model of this simplified geometry was built using Abaqus/CAE v.6.9. The titanium-alloy strip was modelled as an isotropic, bilinear, elastic-plastic material. In contrast, the CFRP (UD 977-2/IM7) beam was treated as an orthotropic, homogeneous laminate, using the "engineering constants" to define its elastic response. The mechanical properties of both materials were tabulated in Chapter 4, see Table 4.5 and Table 4.8. Given that the CFRP laminates did not exhibit any visible signs of permanent deformation or damage after the tests, the incorporation of a composite failure criterion was deemed unnecessary. These material models were combined with *Generalized Plane Strain* conditions to fully define the behaviour of the substrates, which were considered to be initially bonded with AF163-2OST along the length of the overlap.

Since the experimental locus of failure in the joints with a 45° taper was cohesive with a crack propagating through the adhesive layer, a single layer of finite-thickness cohesive elements was used to model the bondline. Both the bi-linear and liner-cubic evolution laws described in Chapter 3 were evaluated. The penalty stiffness and the displacement at damage initiation were derived from the macroscopic elastic properties of the bulk adhesive (see Table 8.1). The 4^{th} order polynomial fracture criterion corresponding to CTE/NSF (see Chapter 7, section 7.2.2) was used to define the area under the traction-separation law.

The single layer of cohesive elements used to simulate the bondline hindered an accurate representation of the "circular" spew fillet. Two different structured mesh designs were investigated (see Figure 9.8). Whilst the first (Figure 9.8-a) neglected the presence of the fillet altogether, in the second (Figure 9.8-b) trapezoidal cohesive elements were placed at either side of the overlap in an attempt to simply replicate the effects of the meniscus. In both cases the central section of the bondline was discretized using 0.2mm long six-noded elements, with the number of integration points fixed to 30. Fully integrated, quadrilateral elements matching the size and order of those used in the adhesive layer were employed in the substrates (i.e. 0.2 mm x 0.3 mm, CPEG8). The influence of the mesh density along the crack propagation path is discussed in Chapter 10. Nevertheless, as concluded in that study, the combination of element size, order and number of integration points chosen here guaranteed convergence to the right solution.

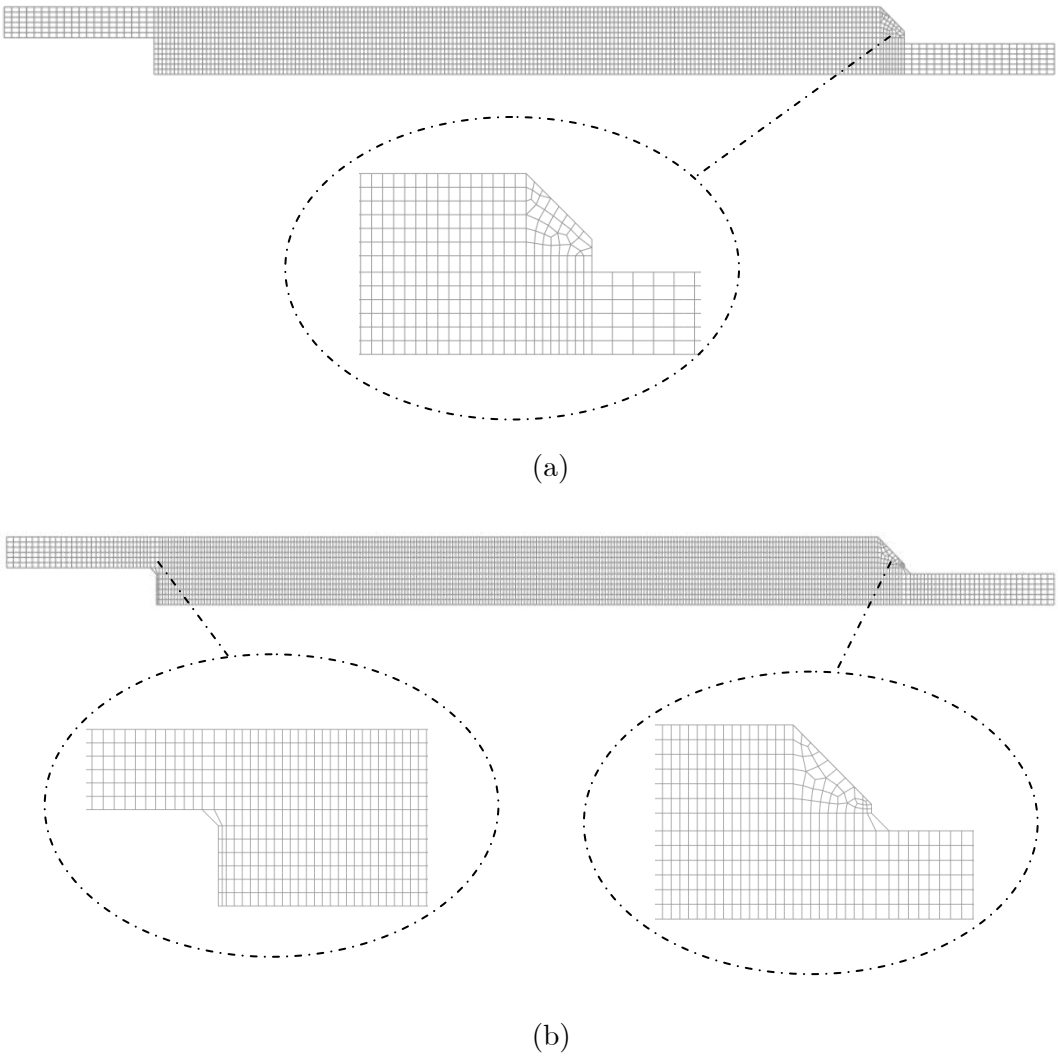

Figure 9.8. Examples of the two meshes using for the quasi-static simulation of TDLJ: (a) neglecting the presence of the fillet and (b) with trapezoidal cohesive elements placed at either side of the overlap to replicate the effects of the fillet.

The vertical edge of the metallic strip was fully constrained (i.e. u_x=u_y=0), while symmetric conditions (u_y=0) were prescribed along the bottom face of the CFRP substrate (see Figure 8.3). So as to replicate the movement of the cross-head of the test machine, suitable horizontal displacements were applied at the nodes on the right hand side of the model. Even though neither the titanium nor the composite beams bend significantly prior to failure, the "NLGEOM" feature available in Abaqus to account for large displacements was activated in all the numerical analyses. Non-linear geometry was also taken into account in the cohesive element formulation via a suitable definition of the Jacobian matrix. Static analyses were then carried out using Abaqus/Standard.

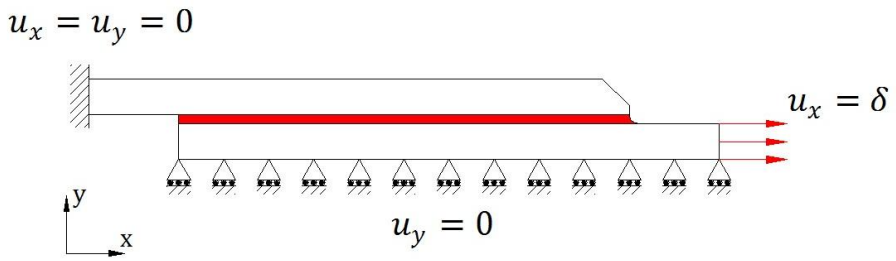

Figure 9.9. Schematic representation of the boundary conditions used in the TDLJ.

9.2.2.2 Finite Element Results

As illustrated in Figure 9.10, the response obtained by the FE models described above was in fairly good agreement with the test results. The experimental and numerical stress-extension responses were compared, rather than the load-extension curves, as this comparison was not affected by the dimensional variability of the substrates.

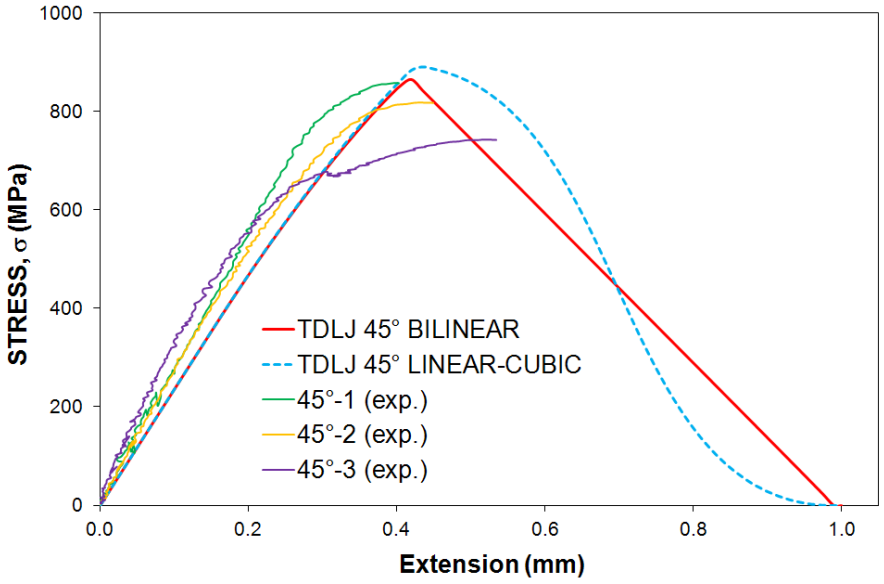

Figure 9.10. Comparison between the stress-extension response obtained in a typical test and that predicted by the FE models.

In the initial region, the numerical solutions were more compliant than the experimental curves. However, despite giving close estimates of the ultimate strength, the FE models did not capture accurately the subsequent non-linear behaviour nor did they predict the sudden failure. Instead, after reaching a peak value, the numerical stress decreased progressively in what appeared to be a phase of stable crack growth.

Table 9.2. Experimental and numerical values of the ultimate strength for the 45° TDLJ.

	Ultimate Strength (MPa)
Experimental (Average ± SDV)	806.4±58.0
FE Model: Bilinear Law	864.9
FE Model: Linear-Cubic Law	889.7

Predictably, those models incorporating the basic representations of the spew fillets were marginally stiffer and stronger. In addition, whilst the form of the evolution law did not influence the early response, the linear-cubic option produced higher strengths (approximately 3%). Nevertheless, the differences between the bilinear and linear-polynomial laws became more evident during the propagation stage, where the shape effect was apparent.

As shown in Figure 9.11, almost the entire adhesive layer was loaded in shear. Ranging between 0.85 (at the tapered end) and 1, the numerical mixed mode ratios barely changed with the local damage state, as bending in the substrates was negligible. To assess the potential influence of the mode II fracture energy on the numerical solution, a number of simulations were run using modified fracture criteria. These adopted different values of G_{IIc}, while maintaining the near-mode I region relatively unchanged. However, despite the substantial increase in toughness, neither the initial stiffness nor the ultimate strength varied significantly. On the other hand, important reductions in the slope of the stress-extension plots during propagation were observed as G_{IIc} increased. The overall numerical σ–δ response appeared to mirror the shape of the mode II traction-separation law, with the maximum stress of the evolution law controlling the strength of the joints (see Figure 9.12).

These results illustrate the intrinsic limitations of the bilinear and linear-cubic laws to describe the behaviour of AF163-2OST. Moreover, this highlights even further the importance of the selection of the cohesive parameters, bringing up once more the subject of their physical meaning and potential relationship with various aspects of the fracture process, for example the damage mechanisms involved, plasticity, level of constraint and stress triaxiality.

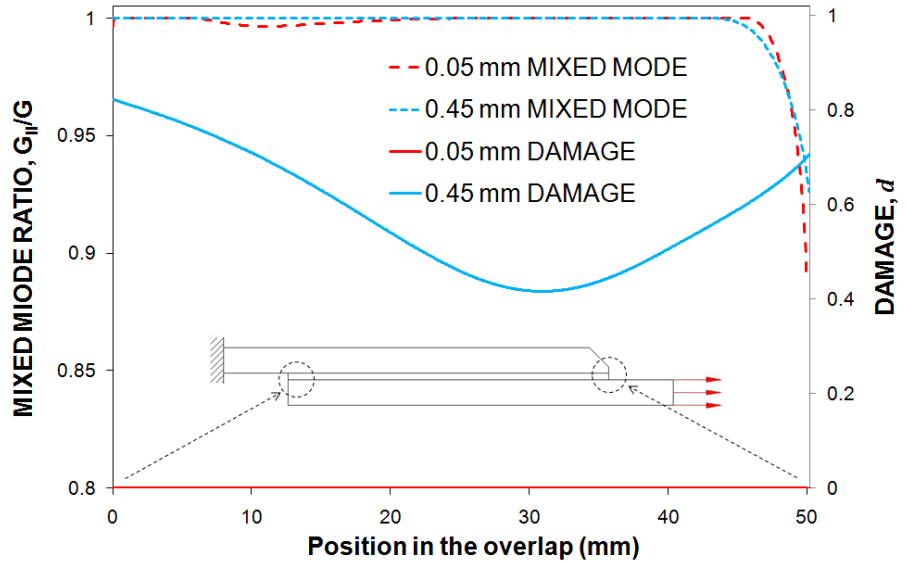

Figure 9.11. Mixed mode ratio (dashed lines) and damage state (continuous lines) along the overlap corresponding to various applied displacements (obtained with the linear-cubic traction-separation law).

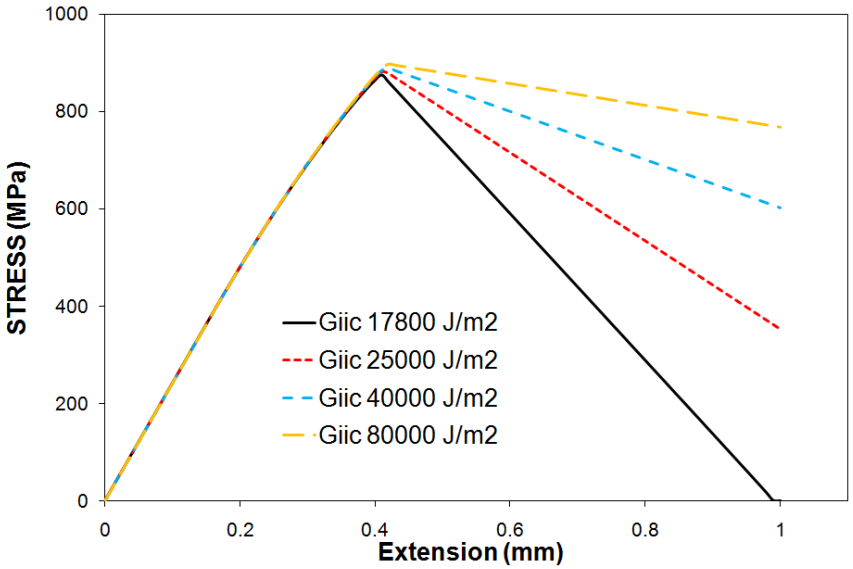

Figure 9.12. Numerical stress-extension response obtained with the bilinear law for different values of the mode II fracture energy, G_{IIc}.

Despite their apparent limitations, not only did the FE models yield reasonable estimates of the strength, but they also predicted sensible stress distributions both along the overlaps and within the substrates. The load was transferred between the CFRP laminate and the titanium substrates mainly though shear stresses in the adhesive layer. These were initially highest at the ends of the overlap (particularly at the non-tapered end, see Figure 9.13), gradually increasing with the applied displacement up to the point of damage initiation. Peel

stresses also developed at either end of the overlap, but were negligible in the central section. Positive under the taper (although some compression appeared ahead of the tip due to bending of the metallic strip) and compressive on the opposite side, their magnitude was significantly smaller than σ_{xx}. It should be noted that, within the linear-elastic regime, the shape of these distributions agreed well with various analytical models (see section 2.2.4, e.g. [411-413]).

The onset of damage took place at the ends of the overlap, subsequently spreading towards the centre and leading to a reduction of both the maximum shear and tensile stresses. Since the adhesive layer degraded faster at the non-tapered end, a crack nucleated first on that side and eventually led to failure. Another crack propagated from the opposite edge. Even though this seemed a plausible failure mode, it could not be confirmed experimentally. Furthermore, the assumptions made in the fracture criterion and interfacial strength could have induced this result. That is, much tougher adhesives under shear could have led to different solutions.

Qualitatively at least, these observations were applicable to both the bilinear and linear-cubic evolution laws. However, minor differences in the local damage state and hence the numerical mode mix seen by the cohesive elements in each case caused small discrepancies in the overall response and stress distributions.

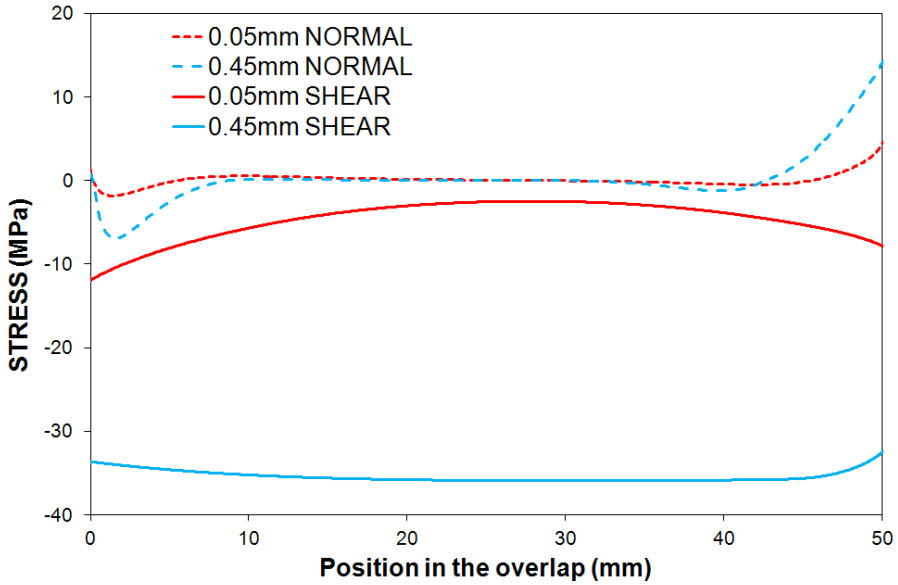

Figure 9.13. Normal and shear stress distributions along the overlap of the TDLJ for different applied displacements (obtained with the linear-cubic traction-separation law).

9.3 Cyclic Fatigue Response

9.3.1 Experimental Results: S-N Curve

Based on the type of failure obtained under monotonic loading, only the TDLJ configuration with 45° tapers was tested in fatigue. In contrast with the smaller taper angles, which displayed a combination of interlaminar, interfacial and cohesive fracture, this geometry always failed cohesively in the adhesive layer.

Due to the observation that the length of the taper end-tips affected the quasi-static results, an improved technique was used to give smaller and mode reproducible values. On the other hand, it resulted in slightly shorter metallic arms (see Figure 4.25).

The joints were tested in load control using a sinusoidal waveform with constant amplitude and a frequency of 5Hz. Whilst various maximum loads were considered (20, 30, 40 and 50 kN), the ratio $R = \sigma_{min}/\sigma_{max}$ remained unchanged and equal to 0.1. A minimum of three repetitions were performed for each load level, and the corresponding number of cycles to failure was measured. If no damage was detected after 10 million cycles, the test was stopped and the load level assumed to be equal or below the threshold.

The results of these experiments together with the quasi-static strength results were combined to generate the S-N diagram shown in Figure 9.14. The maximum stresses were computed using the maximum applied load and the cross-sectional area of the CFRP laminates. Since the shear and peel stresses were not constant along the overlap, this plot was characteristic of the joint design studied rather than specific to the adhesive material. Moreover, in some cases the metallic substrates failed before the adhesive. Any combination of stress and cycles to the right of the line in Figure 9.14 would produce failure of the coupon in fatigue, either in the bondline or in one of the titanium substrates. Conversely, joints subjected to loading combinations to the left of the line would still retain load carrying capability (although they could have been partially damaged). For maximum applied stresses below approximately 250 MPa, the joint strength would remain intact regardless of the number of cycles. Because only a small number of load levels were tested, the fatigue threshold could be anywhere between 250 and 350 MPa, corresponding to 32% and 45% of the quasi-static strength respectively.

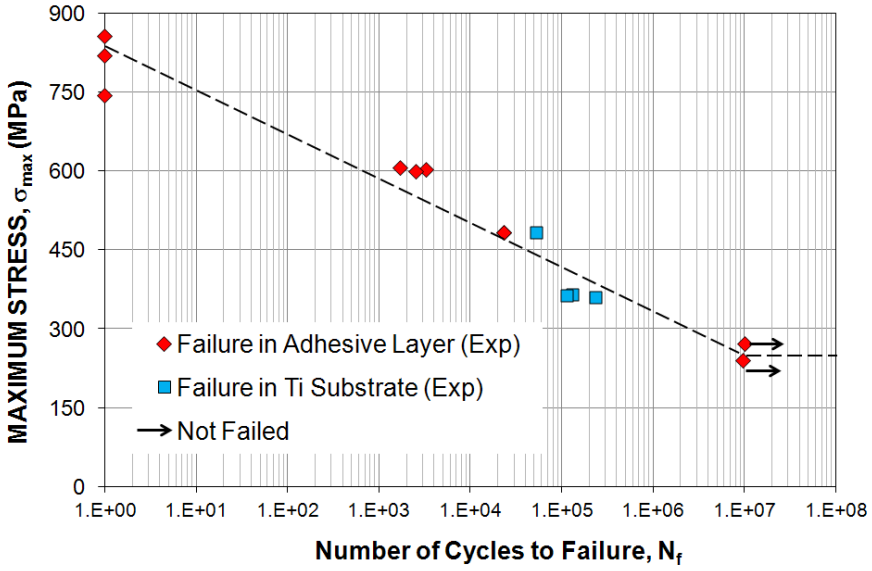

Figure 9.14. Experimental S-N response for the TDLJ.

Excluding some preliminary specimens which developed longitudinal cracks in the composite due to excessive pressure exerted by the hydraulic grips, most joints failed at the central overlap. As shown in Figure 9.15-a, visual inspection of the resulting fracture surfaces revealed that in those cases failure had been mainly cohesive in the adhesive layer. However, in some cases (particularly when P_{max}=30kN) the metallic substrates failed first, see Figure 9.15-b.

(a)

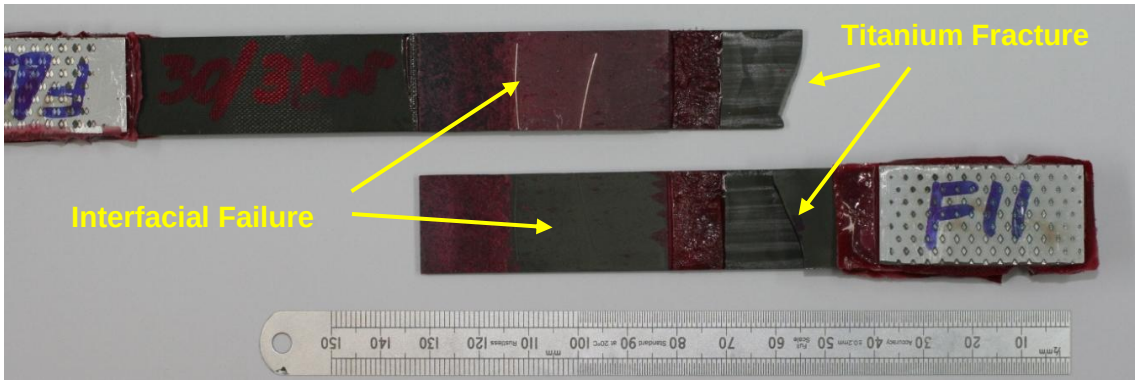

(b)

Figure 9.15. Typical examples of failure in the CFRP-Ti TDLJ tested in fatigue: (a) debonding in the overlap and (b) fracture in the titanium arms.

9.3.2 Numerical Simulations

The two fatigue prediction methodologies proposed in Chapter 3 were applied to the tapered double lap joints with 45° taper angles, comparing the numerical estimates with the experimental results presented in the previous section.

As a result of the different types of failure observed in the tests, the possibility of either fracture in the adhesive layer or in the metallic substrates was considered. This would provide a more comprehensive understanding of the fatigue lifetime for the TDLJ, considering its performance as an integral structural component rather than just focusing on the adhesive bond. Instead of analysing both failure modes at the same time, they were considered separately. Similar models to those described in section 9.2.2 were employed to study debonding in the central overlap. On the other hand, rupture in the titanium adherends was simulated using simple 2D models of the metallic strips which incorporated a single layer of cohesive elements. The quasi-static and fatigue behaviour of the latter were defined with mode I experimental fracture mechanics data for Ti-6Al-4V extracted directly

from the literature. The main characteristics of these models are now reviewed, followed by a discussion of the results obtained in each case.

9.3.2.1 Model Details

9.3.2.1.1 Models for Prediction of Debonding in the Overlap

The modelling details of the TDLJ were discussed in section 9.2.2.1. However, it is also noted here that, since calculating the extension along the overlap was not a priority in this case (DIC data was not available), the entire length of the substrates was now considered (excluding the end-tab section held under the grips). Had this extra material not been included, part of the energy dissipated during deformation would have been transferred directly into the adhesive, altering the results. Also, to account for sharper tapers, the end-tip length was reduced to 0.1 mm.

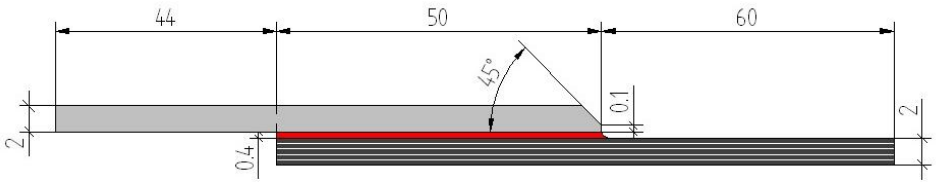

(a)

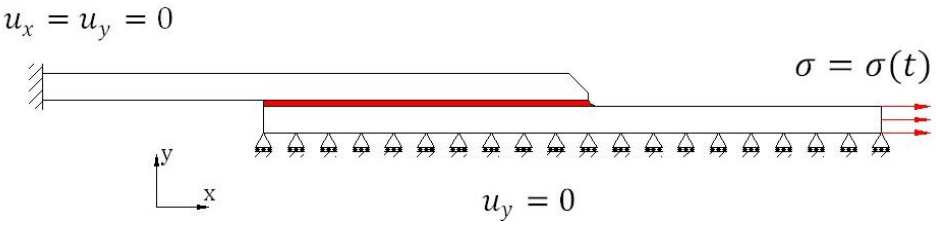

(b)

Figure 9.16. (a) Dimensions (in mm) of the TDLJ modelled in fatigue and (b) schematic representation of the boundary conditions.

Only the mesh design incorporating a simplified representation of the spew fillet was investigated. Most characteristics of the discretization remained unchanged, including element size, type, order, and number of integration points. The material models and mechanical properties also remained the same, although the fatigue degradation feature was now activated. As explained in Chapters 7 and 8, due to the lack of mode II fatigue data, all the parameters of the modified Paris law except G_c were considered mode independent and equal to the fitting coefficients obtained for mode I.

The symmetric boundary conditions prescribed along the lower face of the composite laminate and the fully constrained vertical edge of the titanium substrate were maintained. However, the loading defined at the nodes on the opposite side (i.e. the vertical edge of the CFRP beam) depended on the prediction methodology. While they were subjected to a displacement ramp to determine the threshold, a stress function equivalent to that shown in Figure 9.17 was applied when damage accumulation due to cyclic loading was considered. A number of maximum stress values were specified for this function, which replaced the sinusoidal waveform applied to the real joint (the frequency F=5Hz and ratio R=0.1 were defined as material parameters in the input file). In either case simulations were run in Abaqus/Standard with then Non-linear Geometry feature activated. The maximum time increment was limited to Δt_{max}=5000s (i.e. 25000 cycles) when necessary.

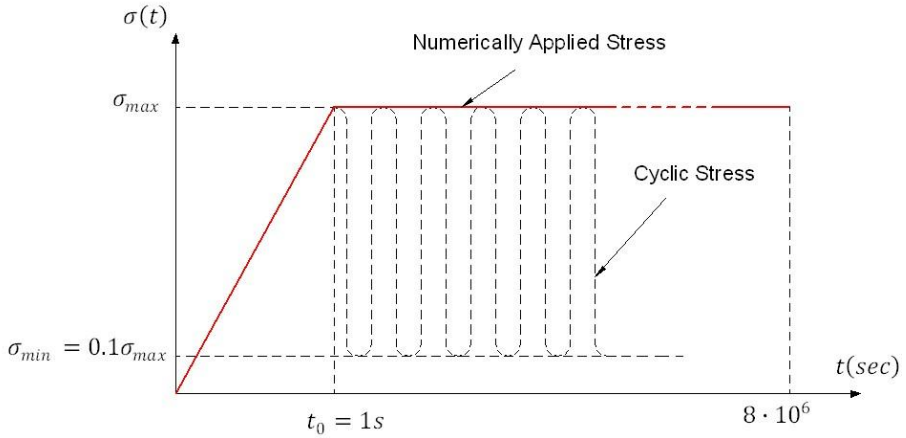

Figure 9.17. Schematic representation of the stress function applied to the TDLJ to predict its fatigue lifetime.

The fatigue threshold was identified by a sudden drop in the horizontal reaction force at any of the loaded nodes. Conversely, a very steep increase in their horizontal displacement would precede complete fracture and would allow the determination of the number of cycles to failure for a given stress level (see Figure 9.21).

9.3.2.1.2 Models for Predicting Fracture in the Titanium Substrates

Experimentally, the fatigue cracks leading to rupture of the metallic substrates nucleated somewhere between the central overlap and the end-tabs. This section of the titanium strips, illustrated in Figure 9.18, was modelled in Abaqus as a 2D plate and used to predict the S-N diagram corresponding to this failure mode.

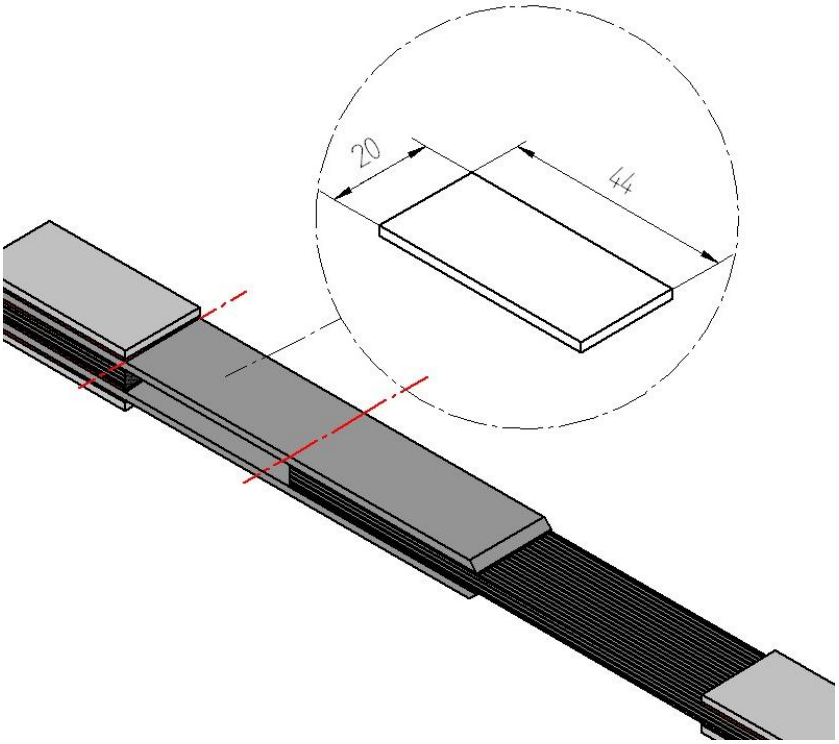

Figure 9.18. Section of the metallic strips modelled in fatigue.

The titanium plate consisted of two continuum sections connected by a layer of finite thickness (1mm) cohesive elements which would allow for fatigue damage accumulation. Isotropic, bilinear, elastic-plastic material behaviour was combined with Generalized Plane Strain conditions to define the response of the continuum regions. In contrast, the formulation presented in Chapter 3 was employed for the interface elements.

While the quasi-static cohesive parameters were derived from the macroscopic elastic properties of Ti-6Al-4V alloy corrected by the element thickness (1 mm), G_c and the coefficients of the modified Paris law were extracted from experimental fracture mechanics data available in the literature [414-416] (see Table 9.3). It should be noted that, fatigue data is typically expressed in terms of the stress intensity factor for metals, hence requiring a suitable transformation prior to its use in the models here. As a consequence of the discrepancies between different publications, two different values of G_{th} were considered.

Table 9.3. Elastic properties, cohesive parameters and mode I coefficients of the modified Paris law for Ti-6Al-4V (obtained from [364, 414-416]).

$E\ (GPa)$	$\sigma_y\ (MPa)$	υ	$\Delta_I^0\ (m)$	$\Delta_{II}^0\ (m)$	$k_I\ (Pa/m)$	$k_{II}\ (Pa/m)$
114	1100	0.33	$9.65{\cdot}10^{-6}$	$3.627{\cdot}10^{-6}$	$1.14{\cdot}10^{14}$	$4.29{\cdot}10^{13}$
m_I	$C_{T_I}(mm/cycle)$	n_{1_I}	n_{2_I}	$G_{th_I}\ (J/m^2)$		$G_{Ic}(J/m^2)$
1.935	$2.662{\cdot}10^{-11}$	5	5	334 [415]	232 [416]	19609

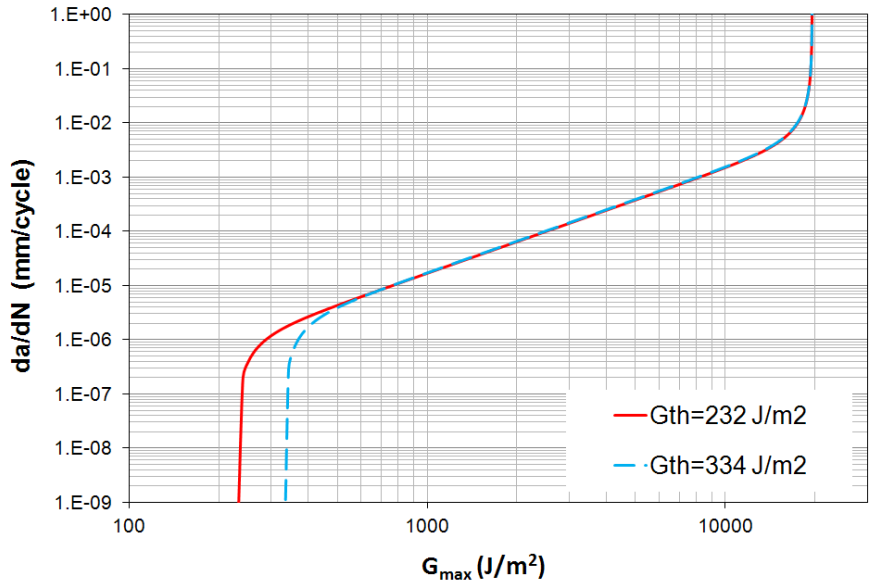

Figure 9.19. Mode I fatigue diagram for Ti-6Al-4V (see [414-416]).

A structured mesh was created using second order quadrilateral elements (0.5 x 1.0 mm). Full integration was employed in the continuum regions (i.e. element type CPER8), while the number of integration points was fixed at 30 in the cohesive elements. Both degrees of freedom were constrained at the left edge of the strip, and a stress function equivalent to that shown in Figure 9.17 was prescribed at the opposite boundary to replace the sinusoidal wave form (F=5Hz, R=0.1) applied to the real joints. Various values of the maximum stress σ_{max} were considered, identifying the number of cycles to failure N_f in each case to generate the corresponding S-N diagram.

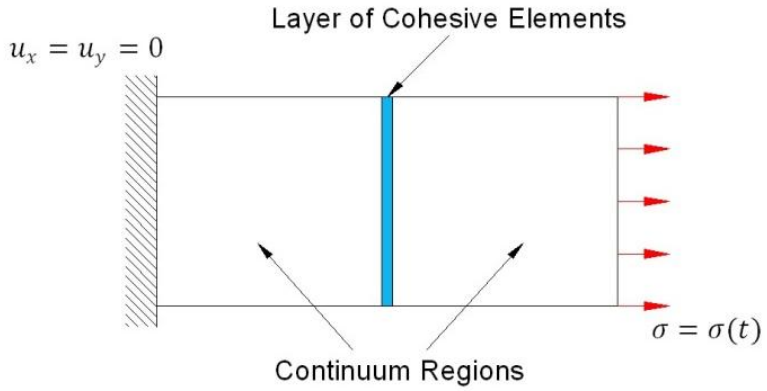

Figure 9.20. Boundary conditions used in the FE models of the metallic substrates.

9.3.2.2 Finite Element Results: TDLJ Fatigue

9.3.2.2.1 Failure by Debonding in the Central Overlap

Figure 9.21 shows the horizontal displacement obtained at the loaded nodes for different values of the maximum applied stress, σ_{max}. As a consequence of the initial ramp of the loading trace (see Figure 9.17), the magnitude of the displacement increased rapidly in the first five cycles (t≤1s). For values of σ_{max} below the threshold (i.e. the lower curve) it then remained constant. In contrast, for σ_{max}>183MPa the displacement continued increasing due to fatigue damage accumulation, rising abruptly just before debonding. This final steep increase coincided with the sudden crack propagation from both sides of the overlap (especially from the non-tapered end), suggesting that for intermediate or small applied stresses a large portion of the fatigue lifetime was spent in the crack nucleation phase.

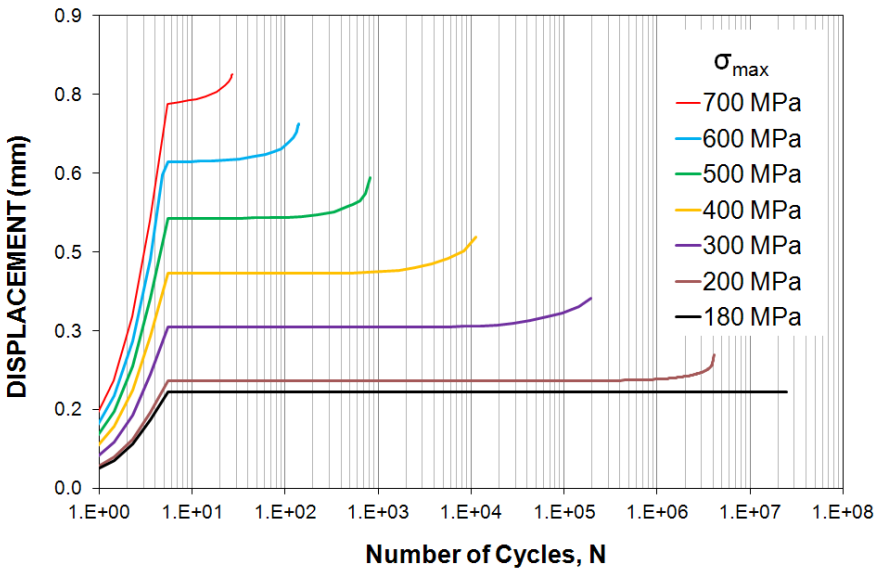

Figure 9.21. Horizontal displacement at the loaded nodes for different values of the maximum applied displacement, σ_{max}.

The number of cycles to failure obtained in the simulations for each stress level were subsequently employed to generate the S-N curve. A comparison between the numerical fatigue lifetime predictions for the TDLJ assuming debonding in the central overlap and the experimental results is presented in Figure 9.22. The threshold estimate corresponding to the same type of failure has been also included (dashed line).

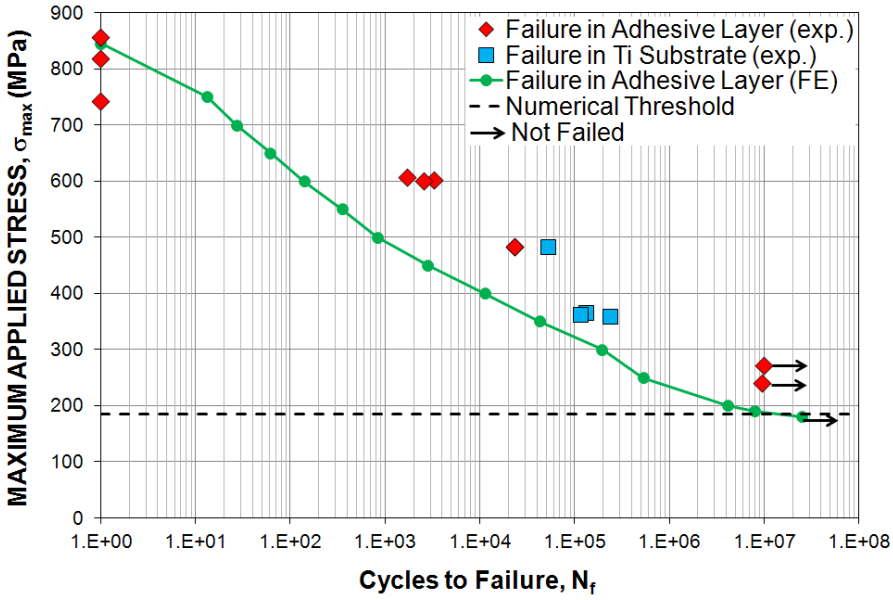

Figure 9.22. Comparison between the numerical fatigue lifetime predictions for the TDLJ assuming debonding in the central overlap and the experimental results. The horizontal arrows indicate no failure, while the dotted line represent the numerical estimate for the threshold.

The models generally underestimated the fatigue lifetime of the real bonded joints. Good results were only obtained for the static case ($N \rightarrow 0$), where failure was controlled by the static component of the damage, particularly by the interfacial strength (i.e. maximum stress of the traction-separation law). With respect to the threshold, even though the numerical estimates were low, the agreement between the two predictive methodologies proposed in Chapter 3 was excellent. They predicted almost identical values of the fatigue limit.

The differences between the experimental results and the numerical predictions was probably due to the absence of experimental fatigue data in mode II. As shown in section 9.2.2.2, almost the entire adhesive layer was loaded in pure shear in the TDLJ. Moreover, bearing in mind the shape of the quasi-static fracture criterion (highly mode dependent and exhibiting a significant increase in toughness with the mode II component), one would expect the adhesive to be more resistant to cyclic loading in shear than in tension. Specifically, lower crack growth rates and higher threshold fracture energies than in mode I (i.e. $G_{th_{II}} > G_{th_I}$) would be

expected. Therefore, conservative predictions would be anticipated in mixed mode problems when mode I values are used for the coefficients in the modified Paris law.

To explore the implications of the above simplification further, additional simulations were run to assess the influence of the mode II parameters $C_{T_{II}}, m_{II}$ and $G_{th_{II}}$ (see Figure 9.23) on the overall fatigue response of the TDLJ. Figure 9.24 highlights the effects of either reducing or increasing their values with respect to the mode I coefficients, which remained unchanged. Clearly, small variations in these parameters (and hence mode dependent fatigue behaviour) would have a considerable impact on the accuracy of the numerical predictions.

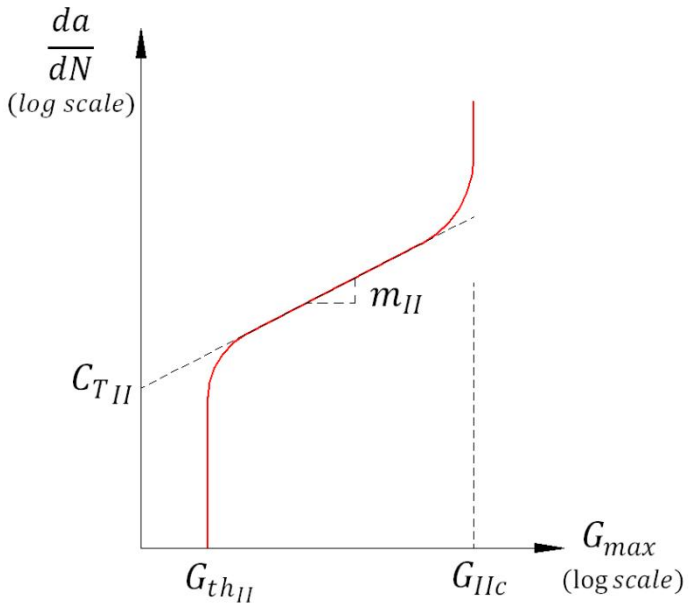

Figure 9.23. Schematic representation of the modified Paris law for mode II, illustrating the meaning of the parameters $C_{T_{II}}, m_{II}$ and $G_{th_{II}}$.

Based on the results shown in Figure 9.24-a, the predictions are particularly sensitive to the value of m_{II}. Changing this parameter by $\pm 5\%$ has a very significant effect on the fatigue lifetime of the TDLJ, and a 3% reduction in this coefficient would bring the response of the models into close agreement with the experiments for intermediate applied stresses. The numerical results were also considerably influenced by $C_{T_{II}}$ (i.e. coefficient controlling the slope of the linear region in the mode II Paris law). A comparison between Figure 9.22 and Figure 9.24-b indicates that the predictions would improve for smaller values of this coefficient. However, neither m_{II} nor $C_{T_{II}}$ appear to have any repercussion on the fatigue limit predicted by the models. In this respect, only doubling the mode I value of G_{th_I} (i.e. $G_{th_{II}} \approx 310$ J/m^2) would yield good estimates of the threshold load. Conversely, changes in $G_{th_{II}}$ had no visible effects on the slope of the S-N diagram.

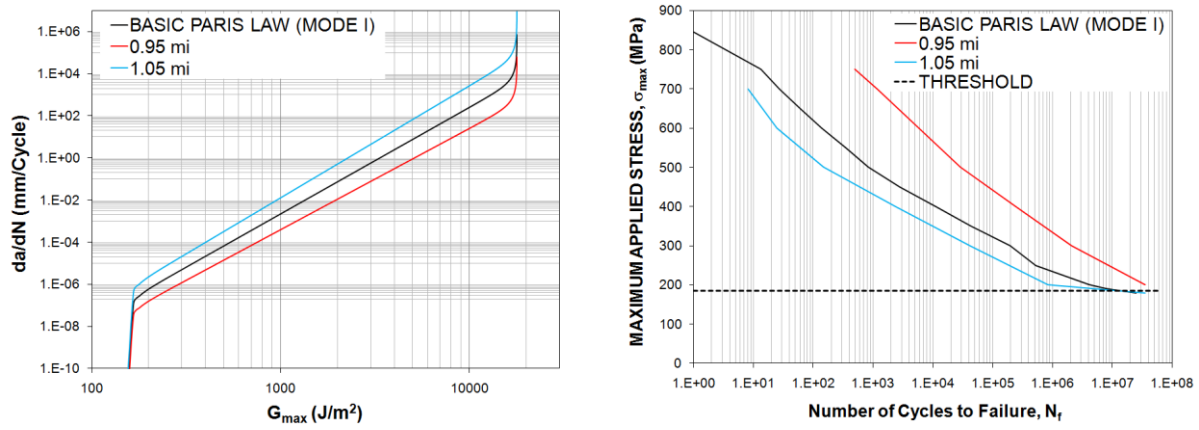

(a)

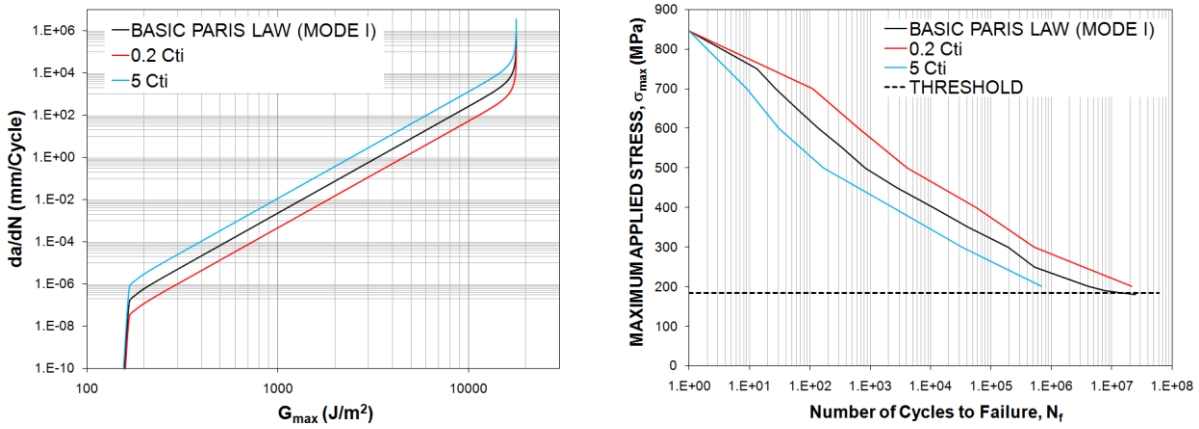

(b)

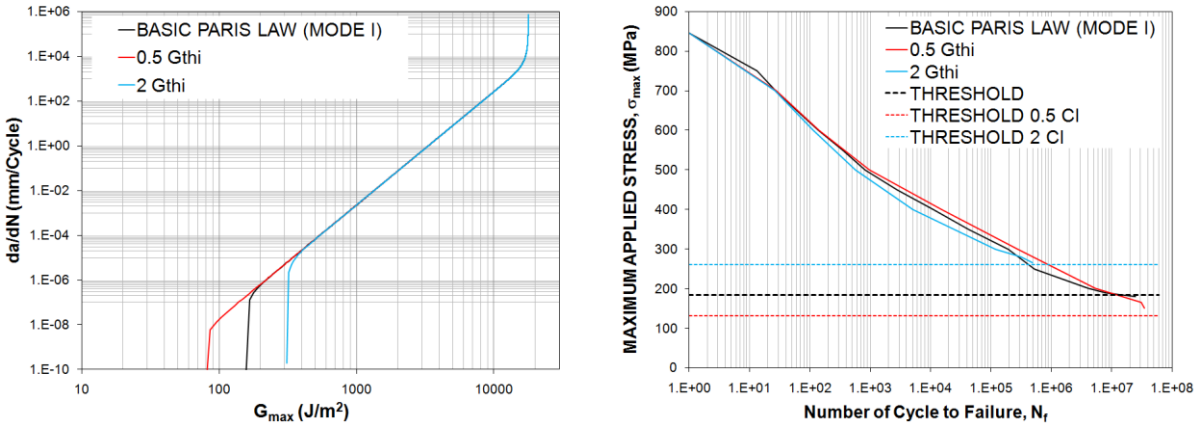

(c)

Figure 9.24. Effects of varying the value of (a) m_{II}, (b) $C_{T_{II}}$ and (c) $G_{th_{II}}$ on the fatigue lifetime predictions for the TDLJ.

9.3.2.2.2 Failure in the Metallic Substrates

Identified as a possible failure mode when the TDLJ is subjected to cyclic loading, fracture in the metallic substrates was simulated using a single layer of cohesive elements. The enhanced damage formulation presented in Chapter 3 was employed to predict the corresponding S-N diagram, which would complement the results discussed in the previous section to give a more complete view of the fatigue response of the joint. Crack growth was assumed to occur under mode I conditions.

As illustrated in Figure 9.25, despite the geometrical simplicity of the models, the fatigue lifetime estimates were extremely close to those obtained in the tests. In this case the relevant fracture mechanics data was available (see [414-416]), possibly explaining the remarkably good agreement with the experiments. Only small discrepancies were found in the literature with regard to the threshold stress intensity factor (K_{th}), which were resolved by considering two different values (hence the two S-N curves). Furthermore, these results reinforce the hypothesis that the discrepancies observed in Figure 9.22 between the numerical and experimental curves were caused by the lack of experimental mode II fatigue data. The predicted S-N curve complemented very well those obtained for debonding in the central overlap, and together they captured the overall fatigue response of the adhesively-bonded structure investigated.

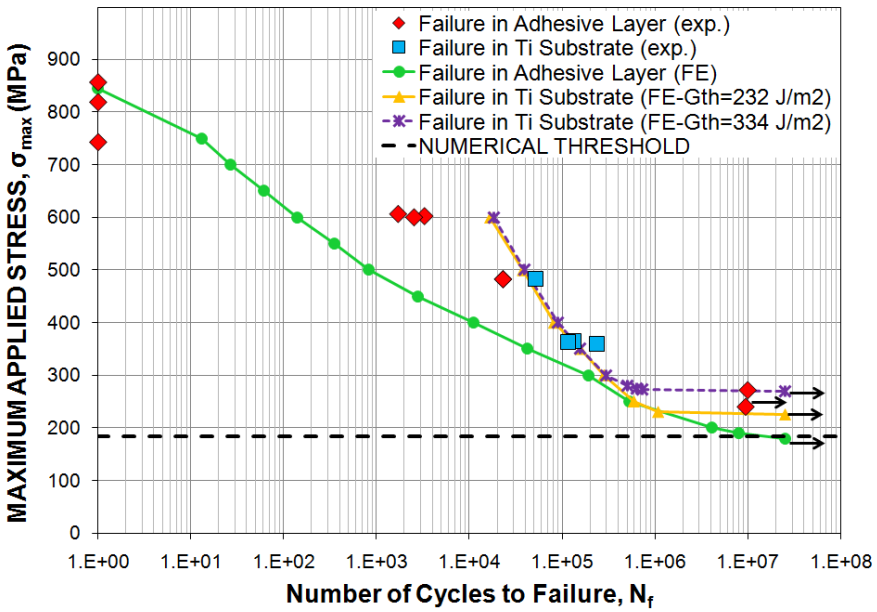

Figure 9.25. Numerical S-N curves for the TDLJ assuming failure in the metallic substrates or debonding at the central overlap. The experimental results have been also included for comparison. The horizontal arrows indicate no failure.

Finally, the abovementioned equivalence with the experimental results also highlighted the versatility of the cohesive element formulation proposed in Chapter 3. Even though it had been originally devised for adhesive layers, it could be potentially applied to the study of fracture in other types of materials if correctly modified. Nonetheless, its suitability for those problems should be assessed on a case-by-case basis.

9.4 Chapter Summary

In this chapter, the prediction methodologies proposed in Chapter 3 have been applied to a Ti-to-CFRP TDLJ. Their accuracy has been evaluated by direct comparison with the experimental results obtained for this joint, which were also described here.

Double lap joints with three different taper angles (7°, 30° and 45°) were tested quasi-statically, monitoring the strains along the overlap with a DIC system. Whilst crack propagation was mainly cohesive in the joints with 45° tapers, a combination of cohesive, interfacial and interlaminar failure was observed for the 30° and 7° cases. The configuration with a 45° taper has been also tested in fatigue, using a sinusoidal waveform with constant amplitude, frequency and load ratio and various maximum loads. The number of cycles to failure was noted in each case, combining the results to generate the S-N diagram for the joint. Fracture was typically cohesive, but a number of these specimens failed in the metallic substrates.

The quasi-static and fatigue responses of the TDLJ with a 45° tapers have been simulated, representing the bondline with a single layer of cohesive elements. The static models successfully predicted the initial stiffness and ultimate strength of the joints. In contrast, due to the unavailability of mode II data, the simulations underestimated the fatigue life of the joints. However, a parametric study has revealed that small changes in the coefficients of the mode II Paris law would bring the numerical solution into close agreement with the experimental results.

Finally, models of the titanium substrates incorporating a layer of cohesive elements have been created to simulate failure in the metallic arms. Using fatigue data extracted from the literature, these agreed very well with the test results. In the next chapter, the findings of a mesh-sensitivity analysis are presented and discussed.

10. Mesh Sensitivity Analysis

10.1 Introduction

As discussed in chapters 8 and 9, cohesive elements represent an effective technique for the simulation of adhesively-bonded joints. However, despite their current popularity, the use of the CZM is not without difficulties. In addition to the controversy surrounding the shape of the traction separation law and the selection of suitable cohesive parameters [239, 241, 242], the requirement for extremely fine meshes along the crack propagation path represents a significant impediment to their industrial application for the analysis of large and complex structures [242, 244]. The CFRP-Ti fan blade would be an example of such a structure. This aspect is studied in more detail in the present chapter.

The effects of size, order (i.e. linear or quadratic) and the number of integration points in the cohesive elements were investigated. Their influence on the global response, the numerical cohesive zone length and the mode mix at the crack tip was evaluated using the various test configurations previously discussed. Additionally, the potential interactions between the mesh density and the maximum time increment employed in the cyclic fatigue simulations were also assessed. Some specific details of the models are discussed next, followed by a review of both the quasi-static and fatigue results obtained for the fracture mechanics specimens and then finally for the double lap joint.

10.2 Model Details

The finite element models described in sections 8.2, 8.5.1.1 and 9.2.2.1 were taken as the starting point for those used in the mesh sensitivity study. Most of their fundamental

characteristics, including geometry, boundary conditions and material properties remained unchanged, whereas the discretizations were modified.

A series of meshes were created for each type of specimen by progressively increasing the length of the cohesive elements. The lower bound was 0.5mm in all cases, but the maximum size depended on the configuration studied (7.5, 15, 20 and 45 mm were considered). Examples of the resulting meshes are given at the beginning of the relevant sections. Linear or quadratic cohesive elements were used for the adhesive layer, with the number of integration points varying between two and thirty in both cases. The mesh density employed in the substrates and end-blocks was adapted in each case to ensure a proper representation of bending (i.e. with a minimum of three elements through thickness) while maintaining suitable aspect ratios if possible. However, since the element length in the substrates matched the element length for the cohesive elements, the mesh density in the substrates was relatively sparse for the longer cohesive elements. Fully integrated, quadrilateral elements were generally used, although a small number of triangular elements were required to mesh the TDCB. The integration time step was maintained constant at Δt=0.01s in the quasi-static simulations. On the other hand, various values of this parameter were considered in the fatigue cases to evaluate potential interactions with the element size when using the jump cycle strategy.

10.3 Mesh Sensitivity in Quasi-Static Fracture Mechanics Tests

10.3.1 Mode I: Metallic DCB and TDCB Test Specimens

Examples of the meshes employed in the mode I test specimens are illustrated in Figure 10.1.

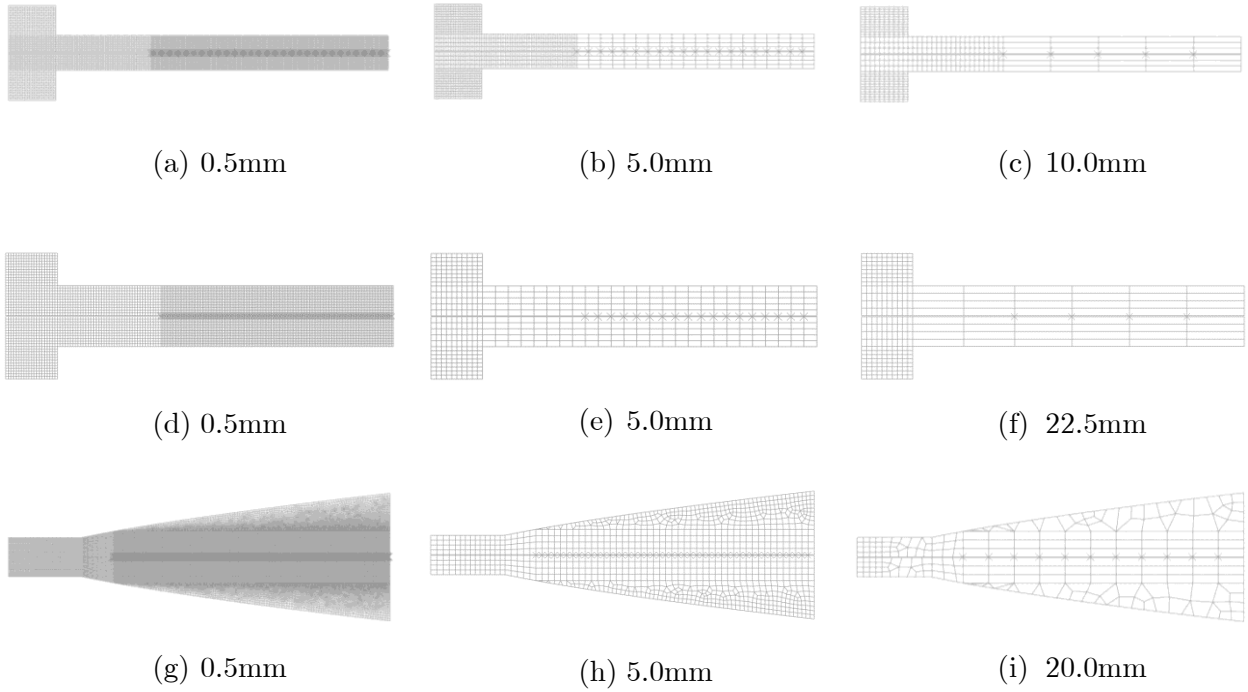

(a) 0.5mm (b) 5.0mm (c) 10.0mm

(d) 0.5mm (e) 5.0mm (f) 22.5mm

(g) 0.5mm (h) 5.0mm (i) 20.0mm

Figure 10.1. Examples of the different meshes employed in (a-c) the 7mm Ti-DCB, (d-f) the 11mm Ti-DCB and (g-i) the Al-TDCB. The numbers under the figures indicate the length of the cohesive elements.

10.3.1.1 Linear cohesive elements: Effects of the element size and the number of integration points on the P-δ response

Figure 10.2 shows the load-displacement traces obtained in (a) the Ti-DCB with 7mm thick substrates, (b) the Ti-DCB with 11mm thick substrates and (c) the TDCB simulations, using linear cohesive elements with two integration points, for different mesh densities. The finer meshes (0.5 or 2mm in the thinner DCB, 0.5 to 5mm in the 11mm Ti-DCB and 0.5 to 10mm in the TDCB) provided excellent agreement with the theoretical results. However, the numerical response progressively deviated from the analytical solution as the length of the cohesive elements increased. Not only did the mesh density influence the initial linear-elastic response, but it also affected the maximum load and the propagation stage. Furthermore, it

was found that relatively long cohesive elements hindered convergence. This behaviour, previously reported by numerous researchers, clearly demonstrates the mesh-dependency issue when using linear cohesive elements. With only two integration points, these elements are equivalent to those available within many commercial packages, including Abaqus.

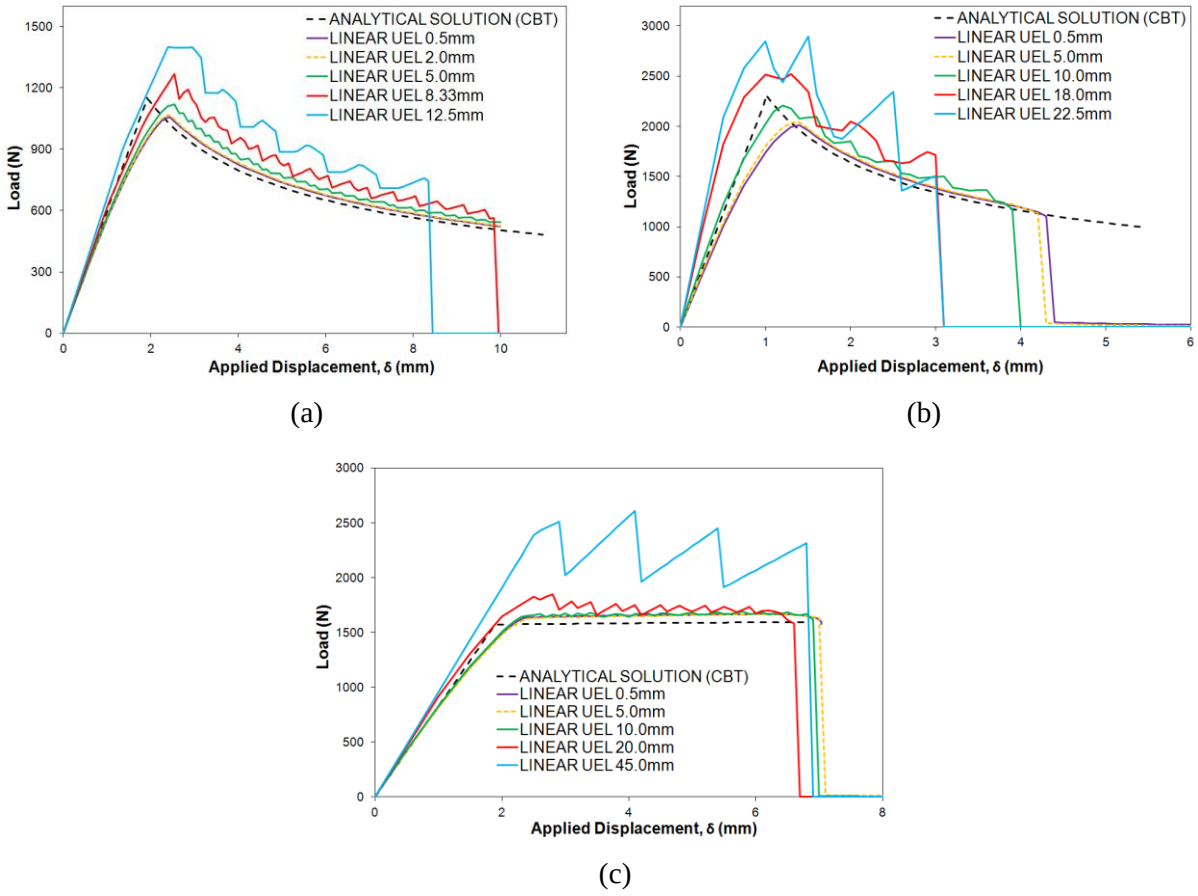

Figure 10.2. Load-displacement traces obtained for (a) the 7mm Ti-DCB, (b) the 11mm Ti-DCB and (c) the Al-TDCB adhesive joints using linear cohesive elements with two integration points and different mesh densities.

The cohesive elements developed as part of this work allow a user-defined number of integration points. The consequences of varying the number of integration points for a given mesh density are highlighted in Figure 10.3. Increasing their number resulted in relatively smoother responses and at the same time improved convergence. However, despite improving the numerical performance, it was not a substitute for mesh refinement (i.e. the ultimate solution remained unaffected and the mesh-dependency persisted). Similar conclusions were reached by Alfano and Crisfield [239] and Feih [417].

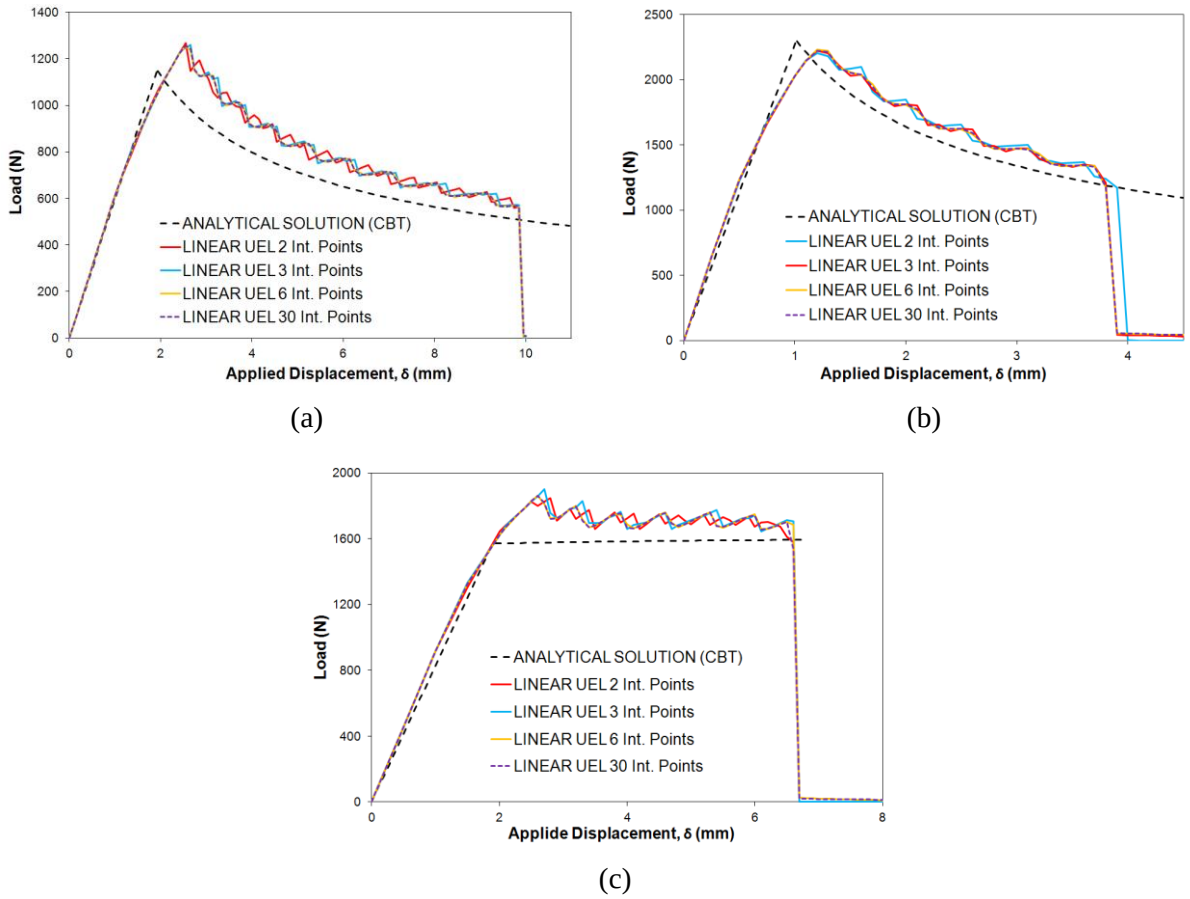

Figure 10.3. Load-displacement traces obtained for (a) the 7mm Ti-DCB, (b) the 11mm Ti-DCB and (c) the Al-TDCB adhesive joint using linear cohesive elements with constant mesh density (8.33, 10 and 20mm long respectively) and varying the number of integration points.

As illustrated in Figure 10.4, important undulations appeared in the propagation section of the load-displacement traces for the coarser meshes. These can be primarily attributed to abrupt changes in the system compliance induced by damage and the subsequent failure of the long cohesive elements. The thickness of the substrates (h) also appeared to influence the magnitude of these fluctuations, as they were more severe and became evident earlier (i.e. for finer meshes) in the thinner specimens. In fact, not only does h affect the rate of change in compliance with the crack length (dC/da, see Chapter 5), but it also dictates the aspect ratio and therefore the bending properties of the continuum elements used to mesh the adherends. Consequently, given that the metallic arms were thicker and less compliant in the TDCB joint than in the DCB specimens, coarser meshes could be used in the former before these oscillations became apparent.

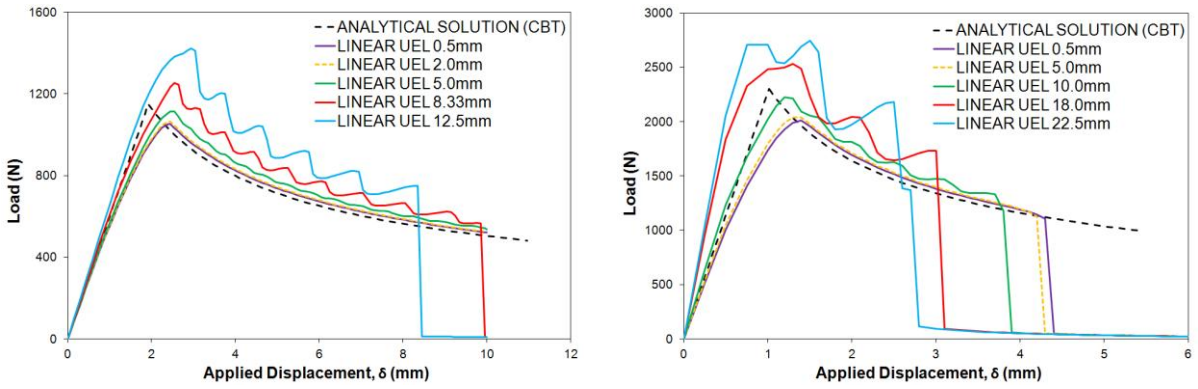

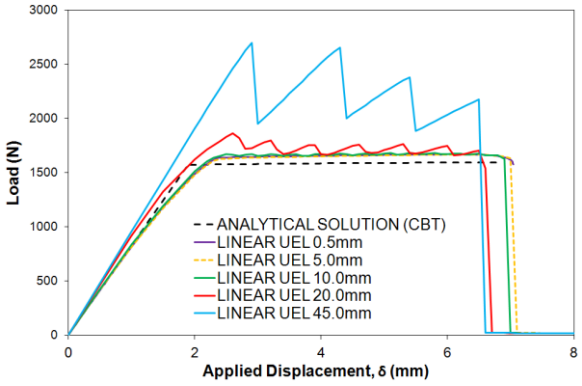

(c)

Figure 10.4. Load-displacement traces obtained for (a) the 7mm Ti-DCB, (b) the 11mm Ti-DCB and (c) the Al-TDCB adhesive joints using linear cohesive elements with thirty integration points and different mesh densities.

It is noteworthy that the mesh-dependency problem was less severe in the bonded TDCB specimen when compared to the titanium DCB joints. That is, larger cohesive elements could be used to mesh the TDCB joint before the simulation converged to an incorrect solution. For example, while 8.33mm elements were clearly too long in the 7mm Ti-DCB case (i.e. the model converged to a completely different solution than that obtained with 0.5mm elements), reasonable agreement was achieved in the TDCB joint with elements as long as 10mm. This behaviour was related to the limited ability of linear elements to reproduce the profile of the deformed substrates. Thicker and more compliant than in the DCB cases, the arms of the TDCB specimen exhibited a lower curvature and therefore could be accurately modelled using coarser meshes. The same rationale would explain why slightly coarser meshes could be employed successfully in the thicker DCB specimen: 5mm elements were suitable in that case, but produced poor results when used in the thinner Ti-DCB joint.

10.3.1.2 Quadratic cohesive elements: Effects of the element size and the number of integration points on the P-δ response

Equivalent simulations to those described in section 10.3.1.1 were run using second-order elements. Figure 10.5, corresponding to thirty integration points, shows that the various mesh densities tested using the quadratic elements always converged to the same solution. Even the load-displacement traces obtained with extremely long elements (10-20mm in the DCB cases or 20-45mm in the TDCB models) were in excellent agreement with the theoretical results. These element sizes are very much larger than those previously reported in the literature. Although the relatively small interfacial strength used in the present work (i.e. 36MPa) could have somewhat alleviated the mesh-dependency [239, 242], the improvement over the linear formulation was remarkable.

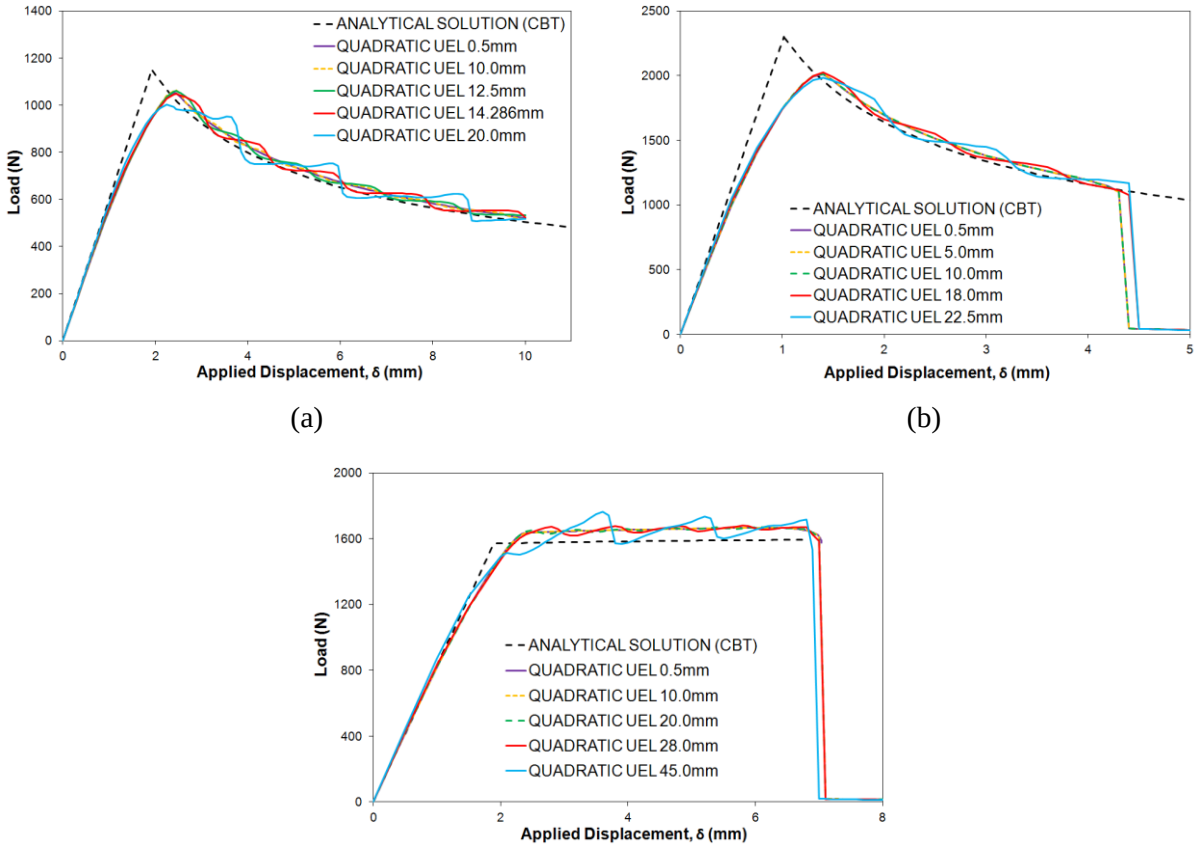

Figure 10.5. Load-displacement traces obtained for (a) the 7mm Ti-DCB, (b) the 11mm Ti-DCB and (c) the Al-TDCB adhesive joints using quadratic cohesive elements with thirty integration points and different mesh densities.

It is clear that the mesh-independent response obtained with the quadratic formulation was not a result of the number of integration points used. This is illustrated in Figure 10.6 where,

as may be seen, increasing the number of integration points smoothed the response and improved the numerical efficiency but without changing the nature of the ultimate solution.

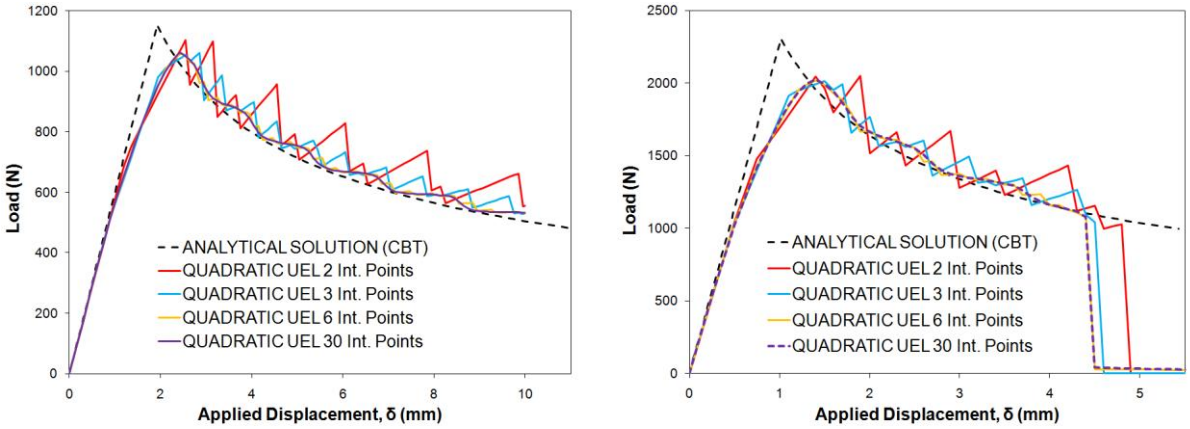

(a) (b)

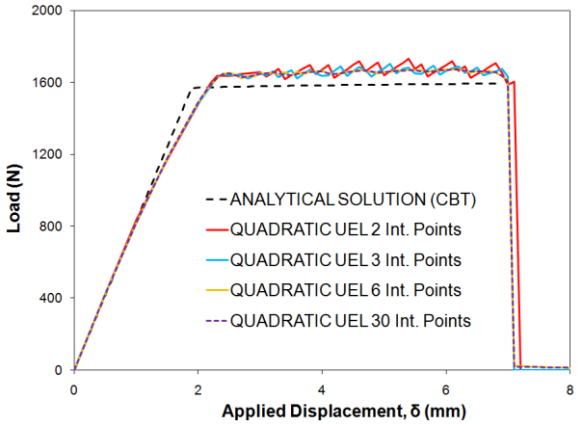

(c)

Figure 10.6. Load-displacement traces obtained for (a) the 7mm Ti-DCB, (b) the 11mm Ti-DCB and (c) the Al-TDCB adhesive joints using quadratic cohesive elements with constant mesh density (12.5, 18 and 20mm long respectively) and different numbers of integration points.

Nevertheless, despite the clearly improved performance of the second order formulation, spurious oscillations appeared in the P-δ traces for extremely coarse meshes. This was probably due to the resulting poor mesh quality used for the substrates. Furthermore, these numerical instabilities were more serious in the DCB cases (particularly for the thinner specimen), which given the larger compliance of their substrates when compared with those in the TDCB joint, reinforces this hypothesis. The severity of these undulations could be partially mitigated by increasing the number of integration points, with the resulting curves still tending to the correct solution.

10.3.1.3 Further Comments: Cohesive zone length analysis

The mesh-dependency exhibited by cohesive elements has been traditionally attributed to their inability to reproduce the steep gradients of the stress and displacement fields in the region immediately ahead of the crack tip. Many researchers agree that this issue can be easily overcome by ensuring a minimum number of cohesive elements within the process zone. Despite the minimum number of elements necessary not being well-established yet, the general consensus is that between two to five elements should be sufficient to guarantee convergence to the correct solution [242, 310]. This section critically examines this notion in the light of the results obtained with the CZM employed in the present work.

Mesh design techniques based on the traditional understanding of size effects rely heavily on accurate estimations of the cohesive zone length (l_{CZ}). Since it is extremely difficult to determine this experimentally, the l_{CZ} is often calculated using one of the analytical expressions presented in section 2.5.3.6. The limitations of these equations have already been discussed in Chapter 8, where the closed-form solutions were compared to the numerical cohesive zone lengths obtained with the method proposed in Chapter 3. The results of the simulations were notably smaller than the values obtained from Equation (2.42), with the analytical estimates being almost twice as large as the corresponding numerical values for the mode I specimens.

Figure 10.7 shows the variation of the numerical cohesive zone length with the applied displacement for different mesh densities in both the thin Ti-DCB and TDCB specimens. The analytical solutions obtained with Equation (2.42) have been included for comparison. As observed with the load-displacement traces, the estimates of the cohesive zone length obtained with the linear formulation varied with the mesh density, see Figure 10.7a and b. In contrast, the quadratic element again produced a solution which appeared to be mesh-size independent, as may be seen from Figure 10.7c and d. With respect to the number of integration points, the trends were similar to those observed on the overall response: larger numbers of integration points resulted in smoother $l_{CZ} - \delta$ curves (and improved convergence) but did not alter the solution to which the model converged.

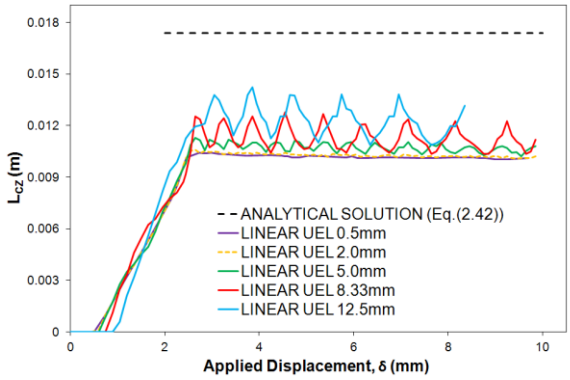

(a) Ti-DCB Linear Cohesive Element

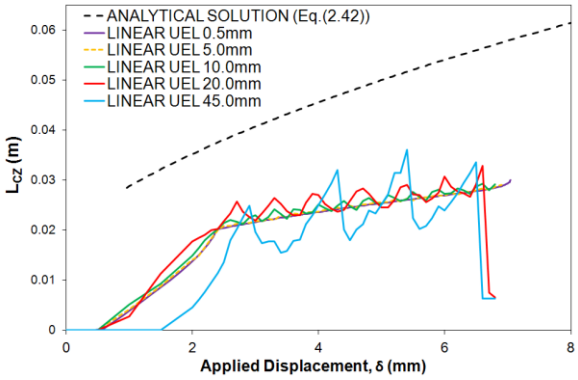

(b) Al-TDCB Linear Cohesive Element

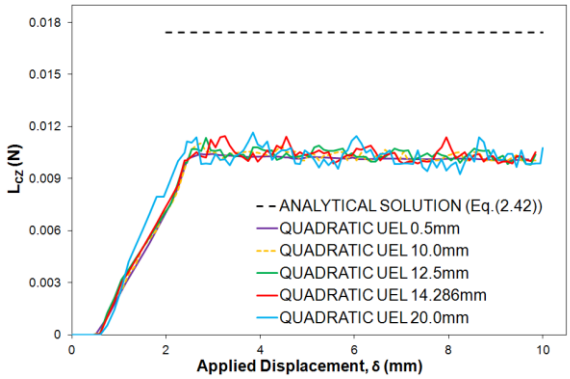

(c) Ti-DCB Quadratic Cohesive Element

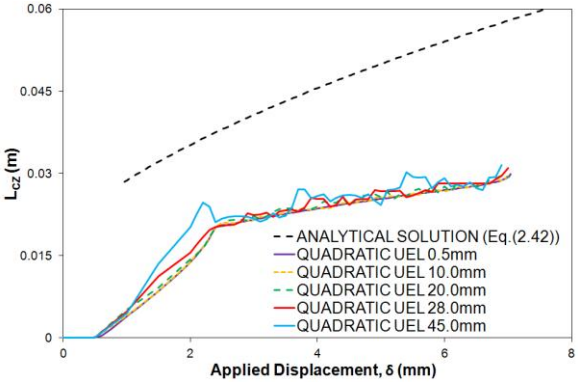

(d) Al-TDCB Quadratic Cohesive Element

Figure 10.7. Analytical (Equation (2.42)) and numerical cohesive zone length as a function of the applied displacement for thin Ti-DCB and TDCB adhesive joints using linear and quadratic cohesive elements with thirty integration points for various mesh densities.

Taking into account the previous results and values of l_{CZ} presented in section 8.4.2 (see Figure 8.13), it is evident that convergence to the correct solution could be achieved with quadratic cohesive elements longer than the corresponding cohesive zone lengths. For example, as shown in Figure 10.5a, an accurate load-deflection response was obtained for the thinner DCB joint using 20.0mm long elements when l_{CZ} was around 10mm. Similarly, the TDCB model employing 45.0mm quadratic elements yielded a satisfactory solution despite the cohesive zone length varying between 20 and 28 mm in that case. Overall, these results call into question the traditional view of mesh dependency. The requirement of a minimum number of cohesive elements within the FPZ becomes unnecessary when using the second-order formulation proposed in this work.

Finally, the superiority of the quadratic cohesive elements when it comes to reproduce the normal stresses along the bondline is noteworthy. As demonstrated in Figure 10.8a for the thinnest Ti-DCB, small and intermediate linear cohesive elements captured the stress distribution within the numerical cohesive zone reasonably well. However, they had difficulties with the subsequent abrupt drop and compressive region, with the longer elements

resulting in more moderate reduction gradients and higher peak compressive stresses. In contrast, the quadratic elements captured this gradient accurately and, despite predicting abnormally high compression for the coarser meshes, they always converged to the same solution far from the crack tip.

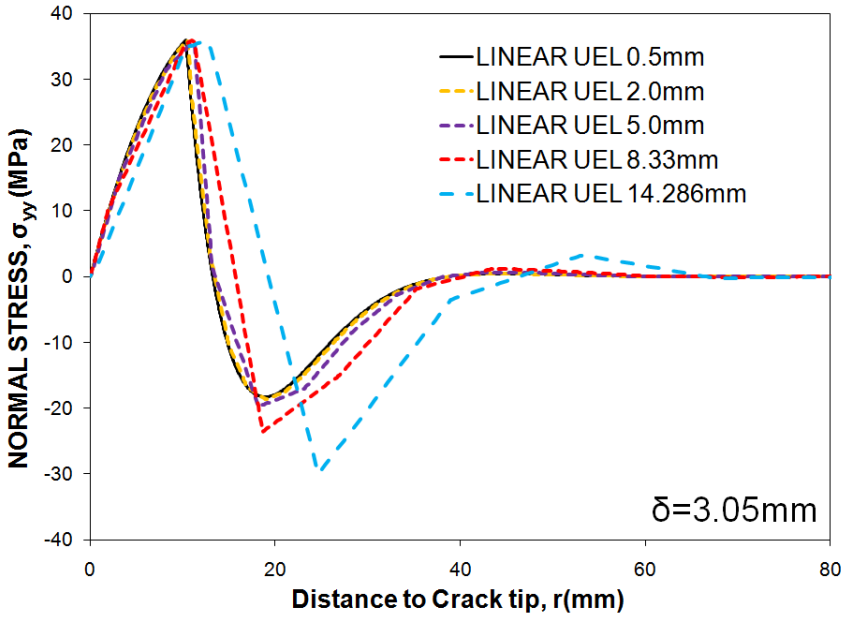

(a)

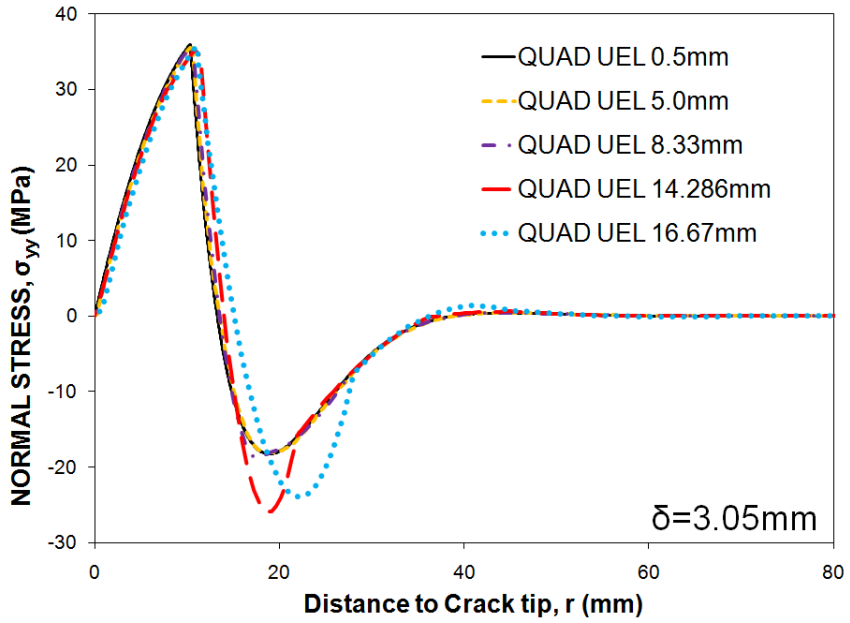

(b)

Figure 10.8. Distribution of normal stresses along the bondline in the 7mm Ti-DCB joint obtained using (a) linear and (b) quadratic cohesive elements with thirty integration points for various mesh densities (applied displacement, δ=3.05mm).

10.3.2 Mixed Mode I/II: ADCB and FRMM and AFRMM Test Specimens

Figure 10.9 shows examples of the meshes used in the models of the ADCB and FRMM specimens.

(a) 5mm

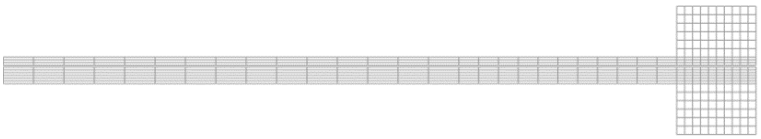

(b) 7.67mm

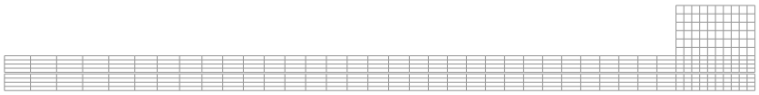

(c) 5mm

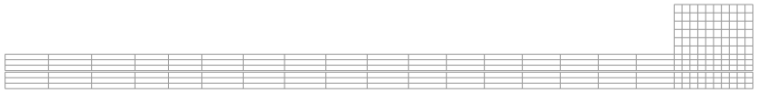

(d) 10.5mm

Figure 10.9. Examples of the different meshes employed in (a, b) the CFRP ADCB and (c, d) the FRMM joints. The numbers under the figures indicate the length of the cohesive elements.

The results obtained for the mixed mode test specimens were basically equivalent to those reported for the mode I joints. As seen in Figure 10.10-a and Figure 10.11, the linear cohesive elements exhibited the typical mesh-dependent behaviour regardless of the number of integration points. This problem, which affected the initial linear response and the propagation section, manifested itself earlier (i.e. for shorter elements) in the unbalanced cases, particularly in the models of the ADCB and the AFRMM configuration loaded via the thinner substrate because of their higher compliance. In contrast, the models employing quadratic elements converged to the right solution irrespective of the mesh density. The improvements with respect to the linear case were especially evident in the initial stiffness, see Figure 10.10-b and Figure 10.12.

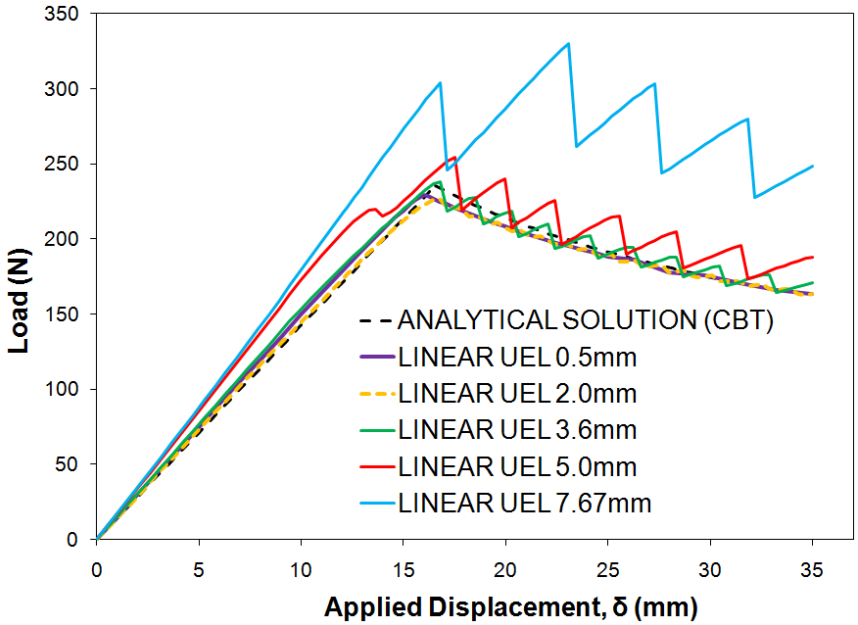

(a)

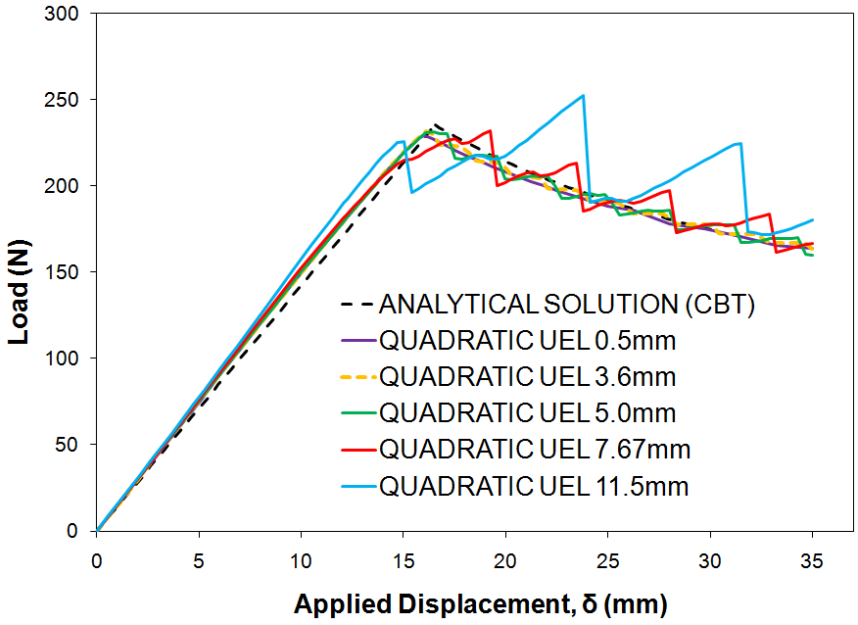

(b)

Figure 10.10. Load-displacement traces obtained for the CFRP-ADCB joints using (a) linear and (b) quadratic cohesive elements with thirty integration points and different mesh densities.

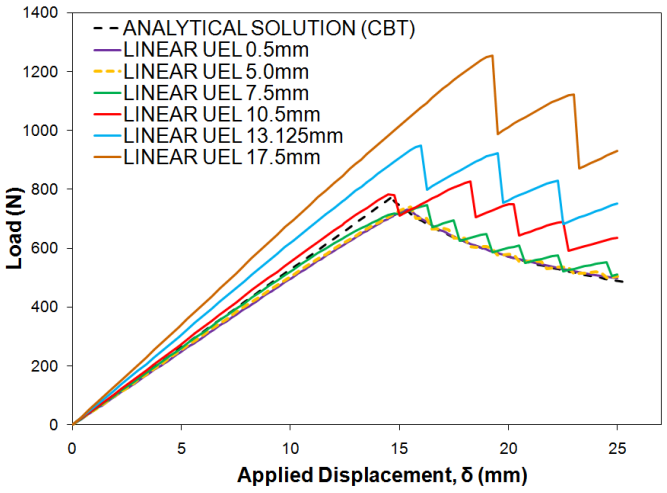

(a)

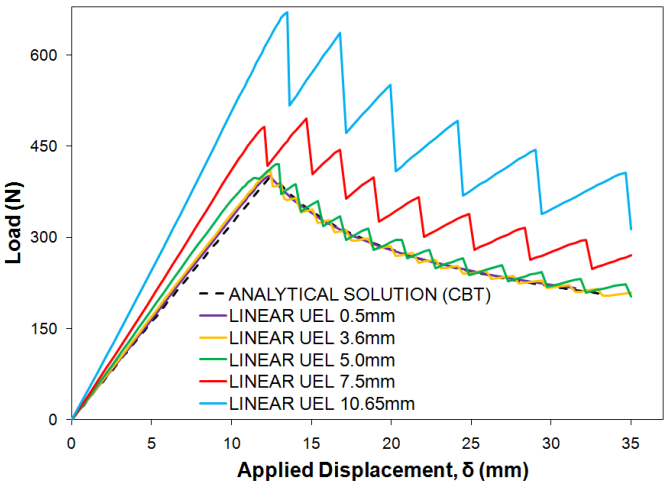

(b)

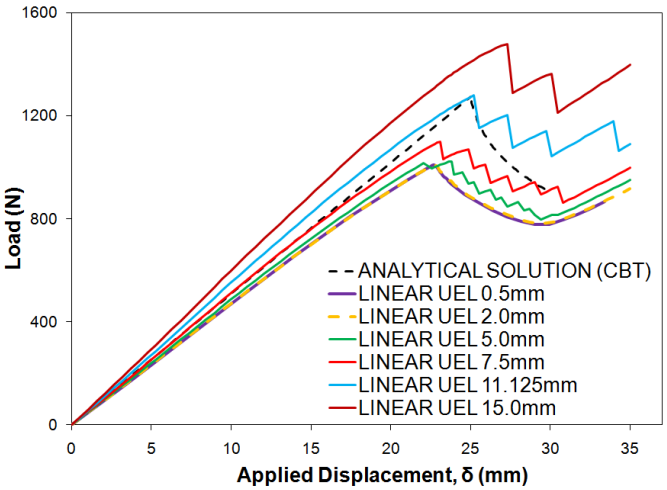

(c)

Figure 10.11. Load-displacement traces obtained for (a) the CFRP-FRMM specimen and the CFRP-AFRMM joints loaded at (b) the thinnest (2mm) and (c) at the thickest (4mm) arms using linear cohesive elements with thirty integration points and different mesh densities.

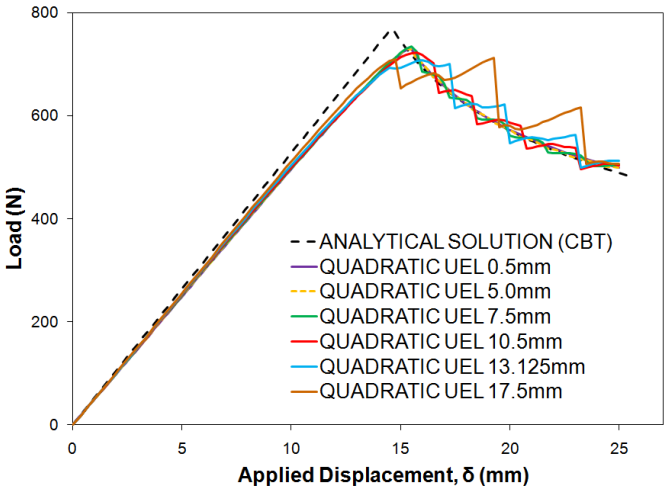

(a)

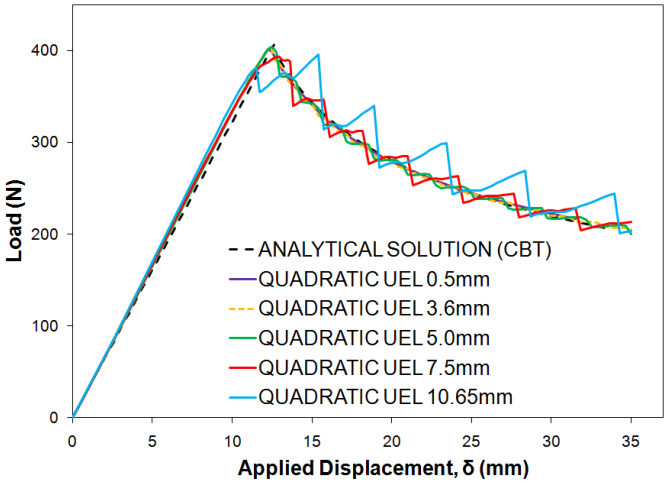

(b)

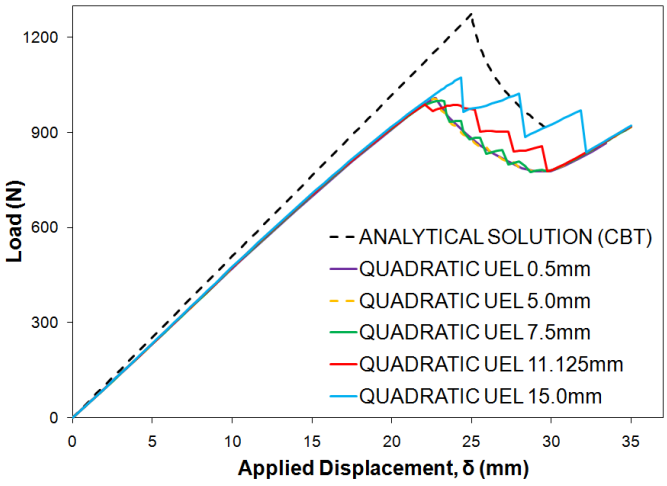

(c)

Figure 10.12. Load-displacement traces obtained for (a) the CFRP-FRMM specimen and the CFRP-AFRMM joints loaded at (b) the thinnest (2mm) and (c) at the thickest (4mm) arms using quadratic cohesive elements with thirty integration points and different mesh densities.

No changes were observed with regard to the effects of integration points, as increasing their number improved the convergence, stability and smoothness of the solutions. However, it would seem that a minimum of three integration points were required for the coarser meshes in order to extract the full potential from the second-order formulation. Take for instance Figure 10.13, where quadratic elements with two integration points yielded reasonably good estimates of the initial stiffness but did capture the propagation stage properly.

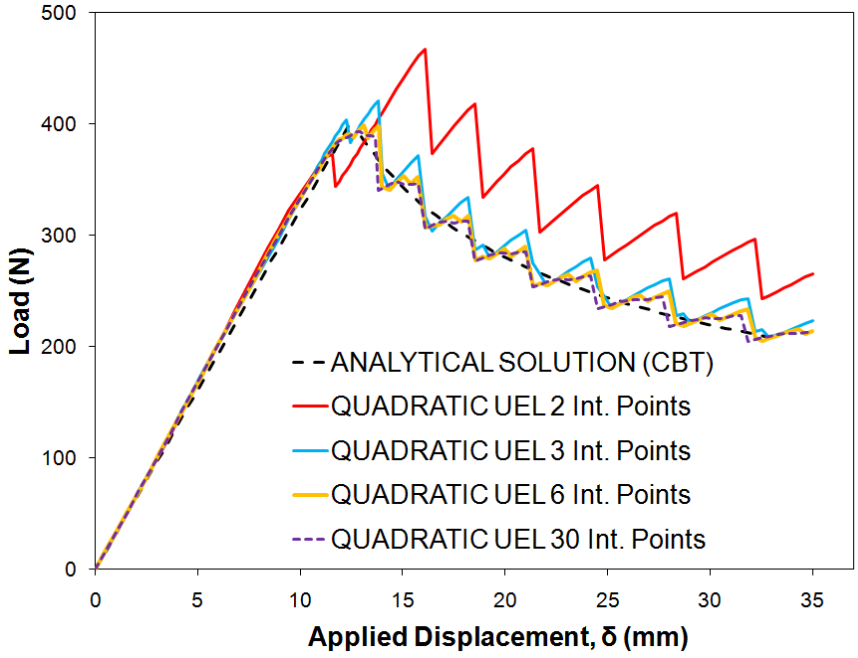

(a)

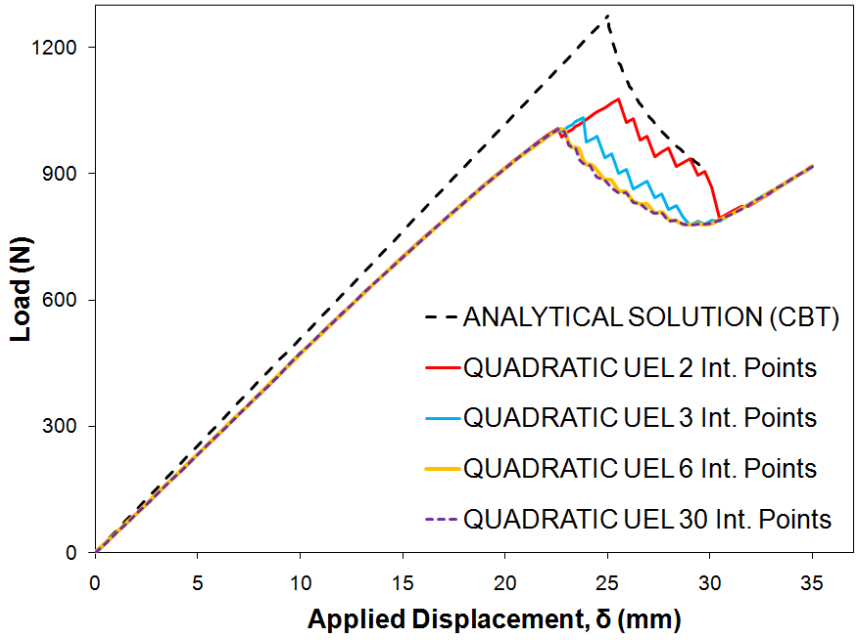

(b)

Figure 10.13. Load-displacement traces obtained for the CFRP-AFRMM joints loaded at (a) the thinnest and (b) the thickest arm using quadratic cohesive elements (7.5 and 5mm long respectively) with different numbers of integration points.

The characteristic undulations observed in the propagation section for the coarser meshes were more severe and became visible for shorter elements than in the pure mode I specimens. The thinner CFRP substrates were more compliant and therefore deformed more than the metallic arms. In addition, the smaller thickness led to poorer aspect ratios in the continuum

elements used to mesh the composite beams, hindering even further the accurate modelling of the additional curvature.

The numerical cohesive zone lengths obtained for the fixed ratio specimens using quadratic cohesive elements with thirty integration points are illustrated in Figure 10.14. Excluding the undulations observed during propagation for the coarser meshes, the second-order formulation yet again produced mesh-independent estimates of l_{CZ}. Analogous trends were observed for the ADCB specimen. The relationship between these predictions and the analytical estimates obtained with equation (8.3) (modified version of (2.42) accounting for the individual contribution of modes I and II) were discussed in detail in section 8.4.3. Bearing in mind the numerical results, the response obtained with the linear elements for the ADCB joint, the FRMM joints and the asymmetric specimen loaded at the thinnest substrate were in accordance with the well-established mesh design criterion. Namely, a minimum of three linear elements within the process zone would be enough to ensure convergence to the correct solution. Conversely, quadratic elements almost twice the size of the numerical cohesive zone length resulted in satisfactory load-deflection responses in those cases. Once more, this demonstrates that the long-established mesh design criterion for cohesive elements is not applicable to the second-order formulation.

For the AFRMM specimen loaded at the thickest arm, as for the mode II joints (see section 10.3.3), the numerical cohesive zone length was considerably longer than the analytical estimate. However, even though the quadratic formulation still produced relatively mesh-independent estimates for l_e<15mm , the abrupt drop in l_{CZ} together with the short propagation region impeded confirming the critical element sizes for that configuration. Nonetheless, a simple comparison between Figure 10.11c and Figure 10.12c highlights the clear superiority of the quadratic formulation.

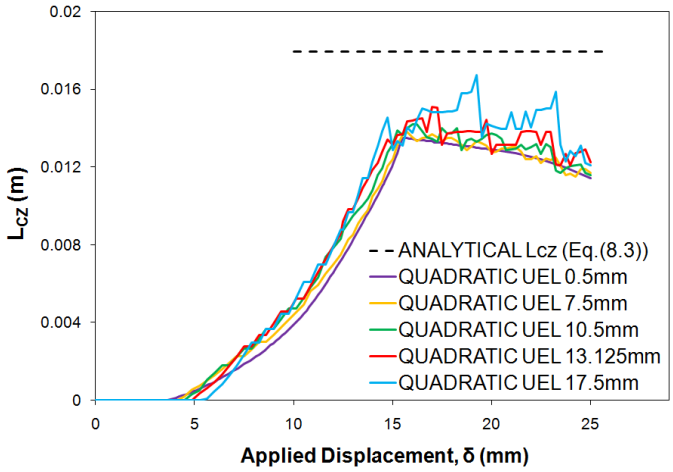

(a)

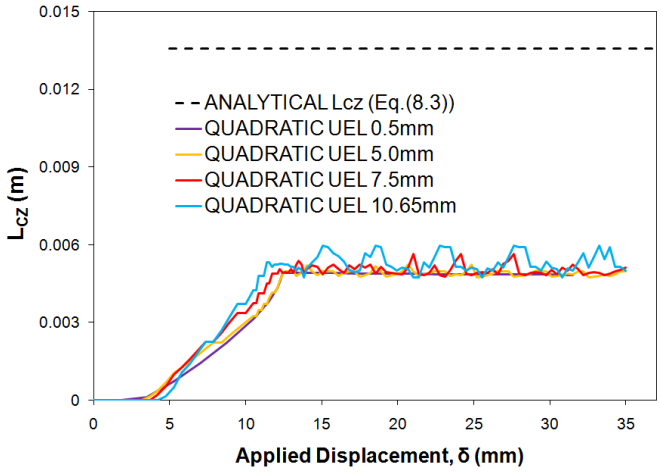

(b)

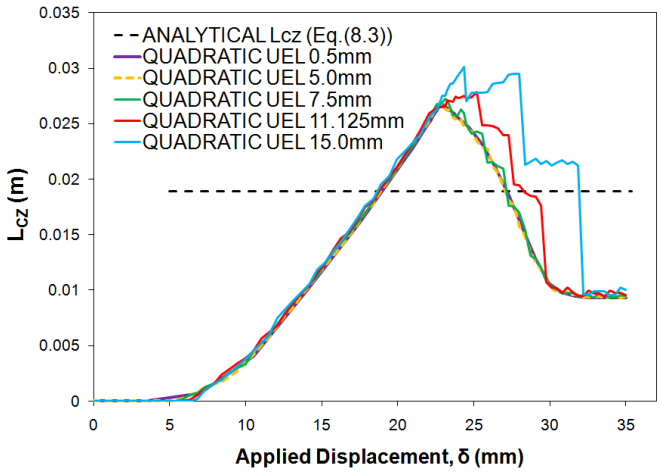

(c)

Figure 10.14. Numerical cohesive zone lengths as a function of the applied displacement for (a) the CFRP-FRMM specimen and the CFRP-AFRMM joints loaded at (b) the thinnest and (c) the thickest arms using quadratic cohesive elements with thirty integration points and various mesh densities.

Surprisingly, the global mesh-independent response reported for the quadratic elements contrasted with their local behaviour. As seen in Figure 10.15, the initial mode mix seen by the cohesive element located at the crack tip (i.e. evaluated at the closest integration point to the geometrical tip) was a function of the element length. The numerical mixed mode ratios obtained with both the linear and quadratic elements were in excellent agreement with the analytical estimates corresponding to CTE/NSF for fine meshes. However, the values of G_{II}/G increased and the results of the simulations deviated from the theoretical solutions as the elements became longer. Even though the use of the second-order formulation substantially reduced the magnitude of these variations, the dependence on the level of refinement could not be completely eliminated and the discrepancies with CTE/NSF became significant for very coarse meshes.

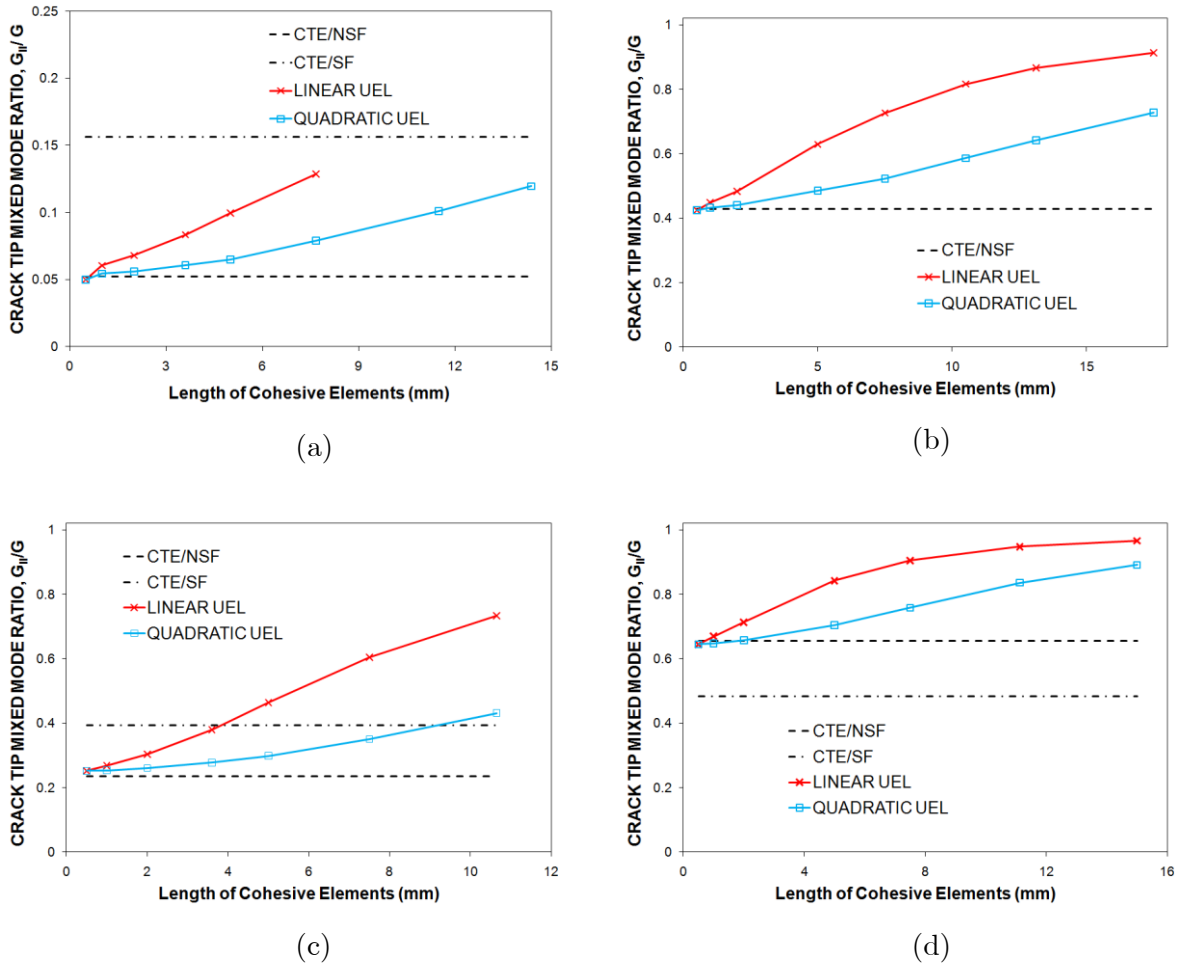

Figure 10.15. Initial mixed mode ratio at the closest integration point to the crack tip obtained for (a) the CFRP-ADCB joint, (b) the CFRP-FRMM specimen and the CFRP-AFRMM joints loaded at (c) the thinner and (d) the thinner arm using linear and quadratic cohesive elements with thirty integration points and different mesh densities.

10.3.3 Mode II: CFRP ELS Test Specimens

Examples of the meshes employed in the mode II test specimens are shown in Figure 10.16.

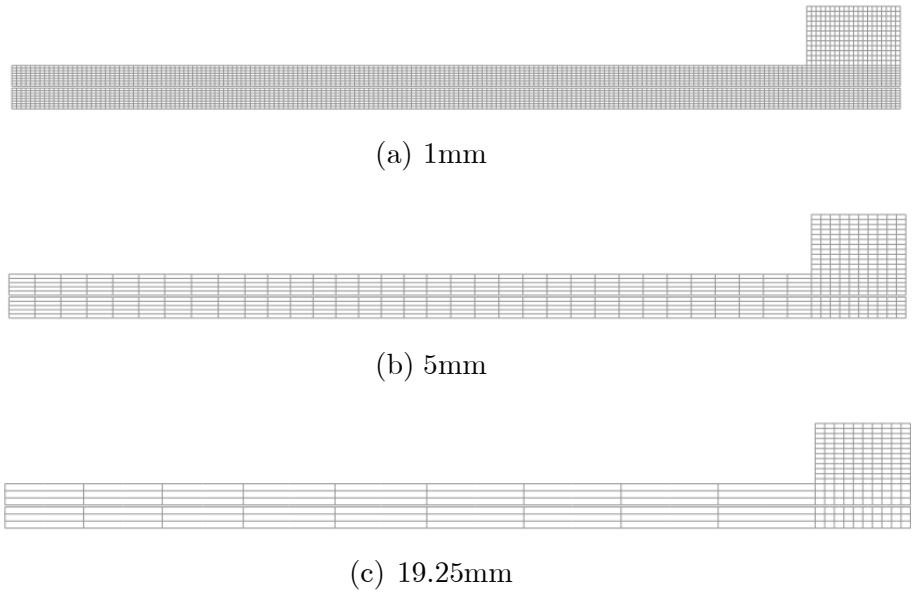

(a) 1mm

(b) 5mm

(c) 19.25mm

Figure 10.16. Examples of the different meshes employed in the CFRP ELS joints. The numbers under the figures indicate the length of the cohesive elements.

Despite not featuring substantial crack propagation (i.e. the non-linear response was mainly caused by extensive damage in the adhesive layer), the conclusions extracted from the mesh sensitivity analysis carried out for the ELS joint were similar to those presented for the other fracture mechanics specimens. That is, the different solutions obtained with the linear elements for the various levels of mesh refinement investigated contrasted with the apparently size-independent behaviour of the quadratic formulation (see Figure 10.17). However, in this case the number of integration points did not appear to have a major influence on the numerical response.

As illustrated in Figure 10.18, these observations applied not only to the load-deflection curves, but also to the numerical cohesive zone length. In addition, this being a pure mode configuration, the numerical mixed mode ratio at the crack tip remained unchanged and equal to G_{II}/G =1 for all the mesh densities considered.

Unfortunately, the nature of the test as well as the variation of l_{CZ} with the applied displacement made it very difficult to identify the minimum number of cohesive elements required in the FPZ to ensure convergence to the correct solution. Whilst six or seven linear elements should be enough, quadratic elements at least half the length of the maximum value of l_{CZ} could be employed successfully in this case. Once more, the advantages of the six-noded elements are clear.

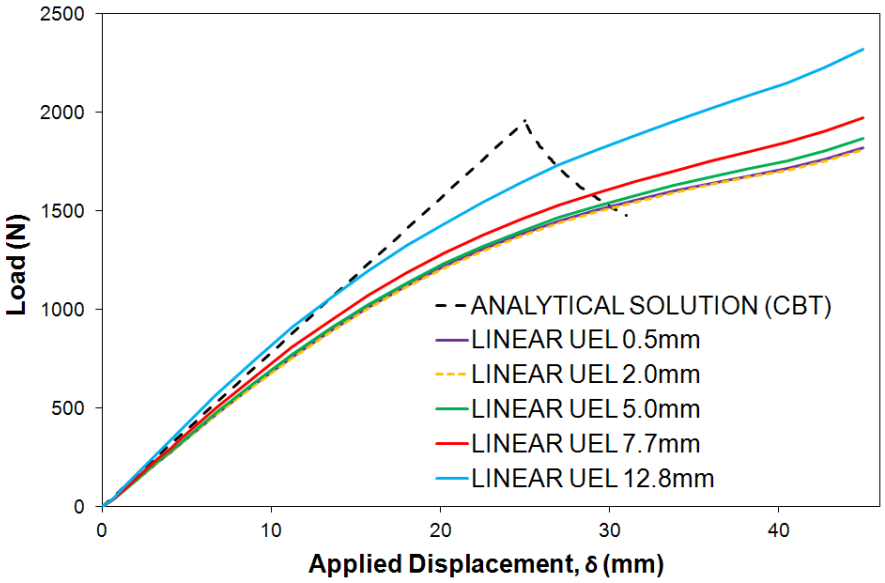

(a)

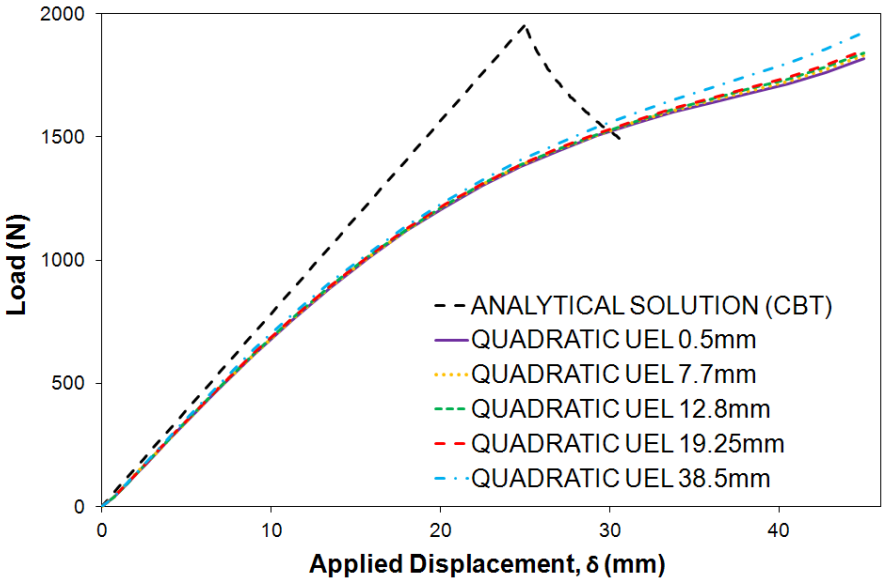

(b)

Figure 10.17. Load-displacement traces obtained for the CFRP-ELS joints using (a) linear and (b) quadratic cohesive elements with thirty integration points and different mesh densities.

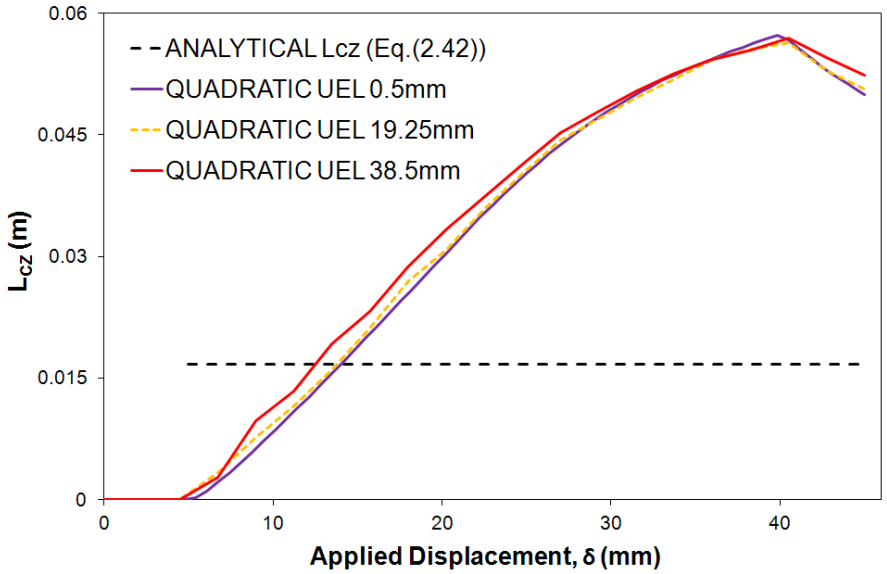

Figure 10.18. Analytical (Equation (2.42)) and numerical cohesive zone lengths as a function of the applied displacement for the CFRP-ADCB model using quadratic cohesive elements with thirty integration points and various mesh densities.

10.4 Mesh Sensitivity in Fatigue Fracture Mechanics Tests

The mesh-dependent behaviour reported for cohesive elements is not necessarily restricted to their monotonic response. Instead, it can also arise in the fatigue simulations. Furthermore, as indicated in [132, 324, 348], certain combinations of element size and time increments could interact negatively with the degradation strategy for cyclic loading, hindering convergence or leading to inaccurate results. These and other potential effects were investigated here using the titanium DCB joint tested experimentally. The same meshes described for the quasi-static case were employed to assess the influence of the element size on the response of this specimen. While four different values of Δt_{max} were considered (i.e. 1000, 5000, 10000 and 20000s), thirty integration points were defined for both the linear and quadratic cohesive elements.

In line with the outcomes of the quasi-static study (see section 10.3.1.1), the linear cohesive elements exhibited a pronounced size-dependent behaviour. As illustrated in Figure 10.19, whilst very fine meshes (i.e. 0.5 to 2.0mm) converged to virtually the same solution, the $P_{max} - N$ response progressively deviated from that result as the length of the elements increased. In addition, the smooth solutions yielded by the finer meshes contrasted with the stepped curve obtained with the longer elements, which also tended to hamper convergence and stability.

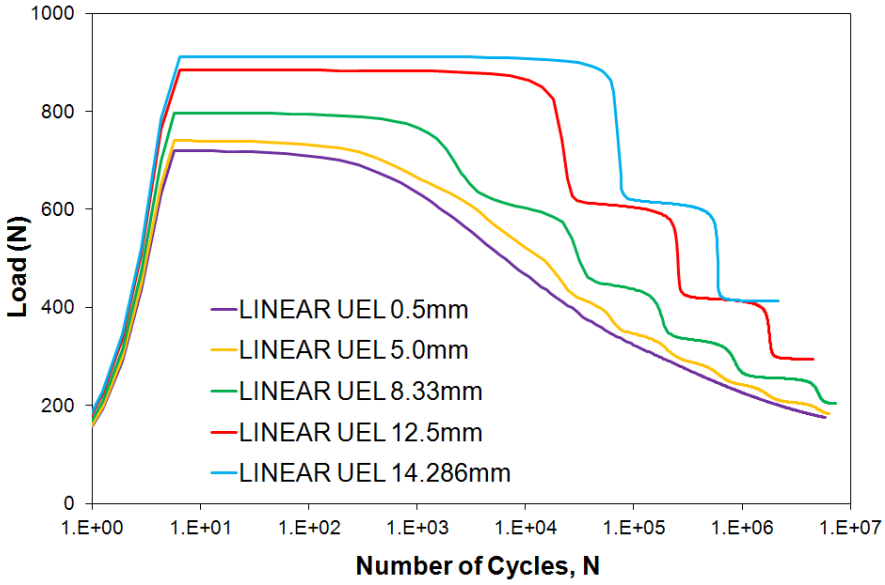

Figure 10.19. P_{max}-N traces obtained for the Ti-DCB joint using linear cohesive elements with thirty integration points and different mesh densities (Δt_{max}=1000s).

The mesh-dependency was visible for the linear cohesive elements regardless of the maximum time increment employed. In fact, aside from the convergence difficulties encountered with the larger values, Δt_{max} did not have a significant influence on the response of the models. While the larger Δt_{max} values caused slightly faster reduction in P_{max} for the finer meshes, they tended to smooth the steps in the solutions obtained for the longer elements. Nevertheless, these variations were limited to intermediate cycles, as the ultimate threshold load barely changed with Δt_{max}.

It should be noted that, in contrast to the static case, the source for this mesh dependency was not only related to the limitations of the linear kinematics to describe the profile of the curved substrates. The fatigue damage degradation strategy makes use of the numerical cohesive zone length, which, as seen in section 10.3.1.3, was also a function of the mesh density.

Figure 10.21 shows the $P_{max} - N$ curves obtained with the quadratic elements for different mesh densities and Δt_{max}=5000s. Once more, excluding the undulations observed for very coarse meshes, the response of the second-order formulation was effectively mesh-independent. This result came as no surprise, given the superior ability of second-order kinematics to reproduce bending. Moreover, as seen in Figure 10.7, the numerical cohesive zone length does not vary with the element size when using the quadratic formulation.

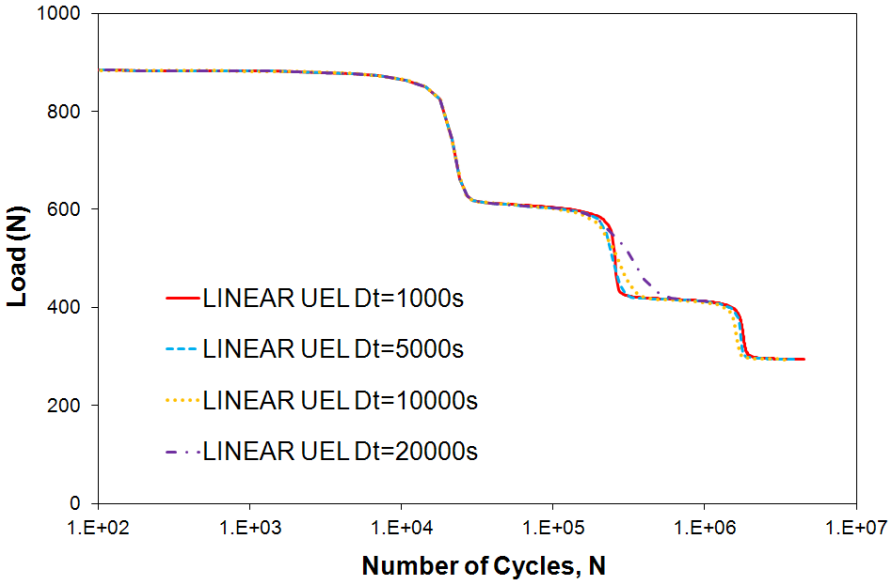

Figure 10.20. P_{max}-N traces obtained for the Ti-DCB joint using 12.5mm long linear cohesive elements with thirty integration points and different values of Δt_{max}

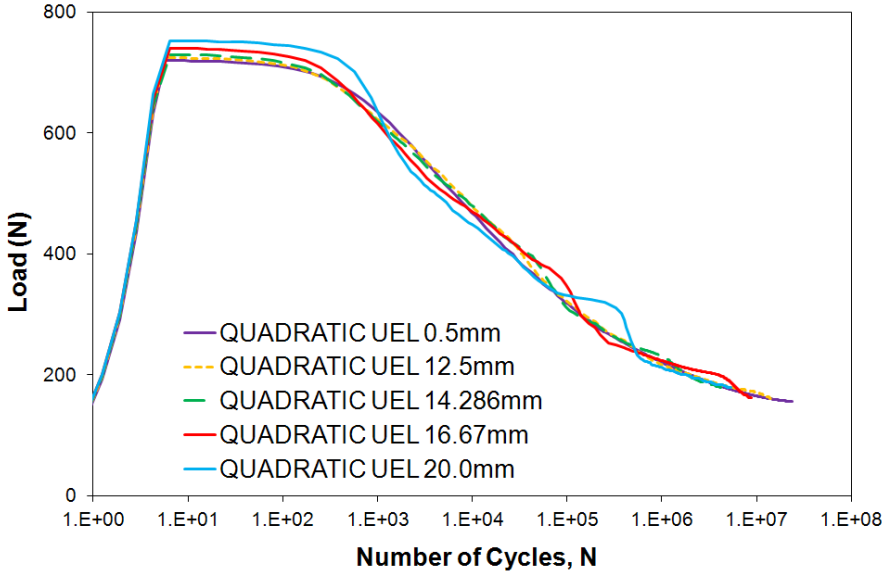

Figure 10.21. P_{max}-N traces obtained for the Ti-DCB joint using quadratic cohesive elements with thirty integration points and different mesh densities (Δt_{max}=5000s).

The effects of the maximum time increment were equivalent to those described for the linear case: the solution exhibited a mild dependence on Δt_{max} in the intermediate stages of the simulations, without noticeably influencing the ultimate solution or the threshold load. Also, even though large values of Δt_{max} would be highly desirable from the computational cost standpoint, they compromised convergence and stability.

10.5 Mesh Sensitivity in the TDLJ

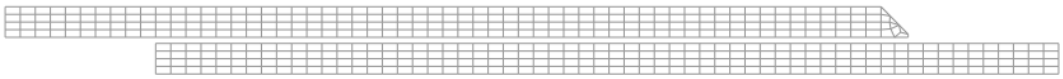

(a) 1mm

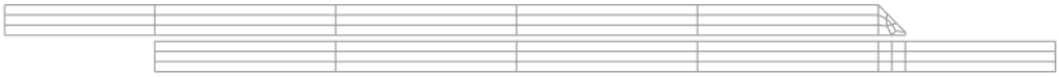

(b) 12.5mm

Figure 10.22. Examples of the different meshes employed in the Ti-CFRP double lap joints. The numbers under the figures indicate the length of the cohesive elements

Two examples of the meshes employed for the TDLJ are shown in Figure 10.22. In contrast to the models of the fracture mechanics specimens, the linear cohesive elements exhibited very little mesh dependency in the TDLJ simulations. As illustrated in Figure 10.23, the solutions corresponding to 10 or 12mm long elements were almost identical to those obtained for 0.2mm. Predictably, the results yielded by the quadratic formulation were also size-insensitive. Furthermore, the influence of the number of integration points was almost imperceptible in both cases.

This behaviour could be explained using an equivalent rationale to that employed to explain the mesh-dependency observed in the previous sections. The CFRP and Ti adherends of the TDLJ remained almost undeformed during the simulations. As a result, the linear elements were able to accurately describe their deformed profiles even if the aspect ratios of the continuous elements were very poor.

Finally, it should be noted that, in order to properly reproduce the taper while maintaining mesh continuity, a minimum of two cohesive elements (approximately 1mm long) were used to mesh the section of the adhesive layer in this region. Nevertheless, their effect on the overall response was of secondary importance since failure initiated at the opposite end of the overlap.

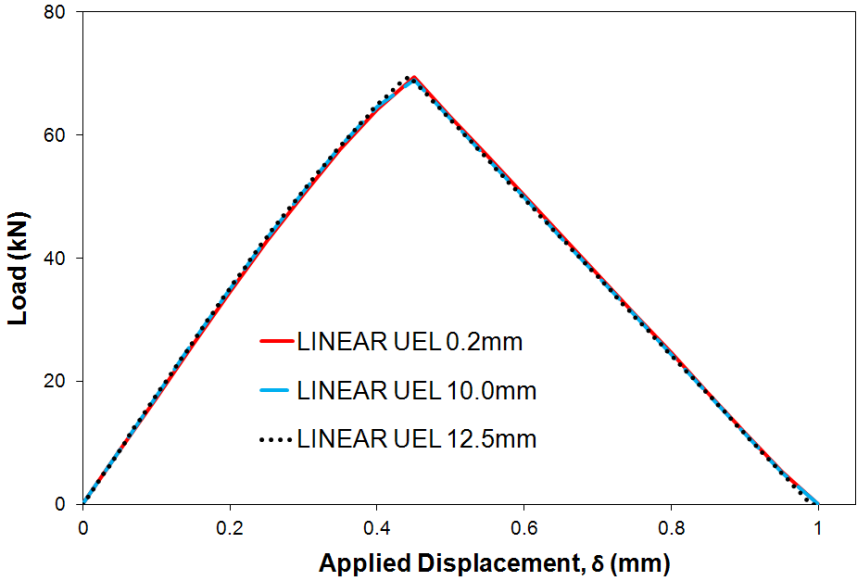

Figure 10.23. Load-displacement traces obtained for the Ti-CFRP double lap joints using 0.2, 10 and 12mm long linear cohesive elements with thirty integration points.

10.6 Discussion of Mesh Sensitivity

The reasons for the apparent mesh-independent behaviour are not fully understood. However, it appears that the superior ability of the quadratic elements to reproduce bending could explain their advantage over the traditional linear formulation. The change in the shape of the profile of the top and bottom surfaces of the cohesive elements (from straight to quadratic shape) would have dramatic effects on the relative displacements and damage state, thus affecting the energy dissipation within the elements. It is postulated that the aspect ratio of the continuum elements employed in the substrates may be the new limiting factor for mesh design when these new cohesive elements are used.

In contrast with the size-independent results obtained for the load-displacement and l_{CZ}-δ traces with the second order formulation, the mode mix seen by both the linear and quadratic elements located at the crack tip was a function of the level of mesh-refinement in the mixed mode problems investigated. In this respect, whilst the six-noded element represents a considerable improvement over linear kinematics, it does not eliminate the local size-effects entirely. However, despite the potential influence that changes in G_{II}/G would have on the values of the cohesive parameters and therefore on the energy dissipation within the elements, this issue did not affect the overall response obtained with the quadratic elements. The origin of the apparent mode dependence is worthy of further, more detailed, study.

10.7 Concluding Remarks

The outcomes of a mesh-sensitivity analysis performed for the various test geometries employed in the present work have been discussed in this chapter. The linear cohesive elements exhibited typical size-dependent behaviour and, in line with the usual mesh-design criterion, a minimum of three elements within the numerical FPZ were typically required to ensure convergence to the right solution. In contrast, the results obtained with the quadratic formulation have been found to be independent of the length of the cohesive elements, at least with respect to the global response. Furthermore, it has been shown that, if the number of integration points employed is sufficiently high, the solution is smooth and stable.

Consequently the potential of the second-order element would appear to be great. Due to their mesh-independent formulation, cohesive elements would no longer dictate the minimum element size when analysing real components, opening the door to a dramatic increase in the industrial applications of CZM.

11. Conclusions and Future Work

11.1 Introduction

Due to the ever-increasing fuel prices and a growing environmental awareness, recent years have seen an increase in the attention paid to energy efficiency in transportation. Consequently, weight saving has become a major concern and a very significant effort has been made to develop lighter materials. In this respect, carbon fibre-reinforced composites and titanium alloys are nowadays widely used in both the aerospace and automotive sectors because of their high values of stiffness-to-weight and strength-to-weight ratios.

Adhesive bonding has facilitated the incorporation of such materials into the different vehicles. The advances in the polymer science have led to the development of tougher adhesives, opening the door for structural applications. Not only does adhesive bonding offer additional weight savings, but it also has been shown to improve the fatigue performance compared to mechanically fastened assemblies. However their use imposes a number of challenges, including uncertainty about the durability of the joints and lack of methodologies to accurately predict their service life. These aspects, which must be fully addressed if designers are to rely on adhesives for the integrity of large and complex primary structures, represent the focus of the present thesis.

11.2 Prediction Methodology

Research has shown the advantages of using the methods of fracture mechanics to study the behaviour of adhesive joints. The combination of experimental fracture mechanics data and finite element methods, particularly those based on the concept of a cohesive zone, has

emerged as a powerful tool to simulate the response and to predict failure of bonded components.

Following this approach, a two-dimensional cohesive element formulation to model crack initiation and growth in adhesive joints under monotonic and cyclic fatigue mixed-mode loading conditions has been proposed. Its quasi-static definition, derived from the work of Camanho and co-workers, has been considerably revised to improve the mixed-mode behaviour and reduce the dependence on the calibration steps. First of all, the original linear element (4 nodes) has been supplemented with a quadratic version (6 nodes), while the topology has been modified to allow a user-defined number of integration points (between 2 and 30 Gauss-Legendre points). Optimized for a finite thickness unstrained configuration, the constitutive equations now tolerate a dissimilar penalty stiffness in tension and shear. Furthermore, a linear cubic damage evolution law similar to that proposed by Pinho et al. has been added to the typical bilinear traction-separation law.

The basic damage evolution law has also been extended to simulate fatigue problems. Following the fracture mechanics approach suggested by Turón et al., both the bilinear and linear-cubic laws have been enhanced to incorporate degradation due to cyclic loading. By using the modified Paris law rather than just the approximation to the linear region of the crack growth rate diagram ($dA/dN = dA/dN\,(G_{max})$), this new version is able to capture the threshold and rapid-growth fatigue regimes. The displacement ratio (R) and frequency have been defined as element properties. In addition, an algorithm developed to compute the numerical cohesive zone length has eliminated the dependence of earlier formulations on analytical estimates of the size of the failure process zone (FPZ). Finally, a simplified version of the evolution laws intended only for the prediction of the fatigue threshold has also been developed.

The resulting formulation has been implemented in Abaqus via a user element subroutine UEL. However, its use for performance prediction of adhesively-bonded joints relied heavily on experimental fracture mechanics data. The first part of this thesis (Chapters 4, 5, 6 and 7) describes the various fracture mechanics tests carried out to obtain the input parameters required for the models. The response of the test specimens was then simulated to gain a better understanding of the potential limitations of the formulation (Chapters 8 and 10). Finally, the proposed prediction methodologies were applied to a simple adhesively-bonded structure (a titanium-to-CFRP tapered double lap joint, TDLJ), evaluating their accuracy by direct comparison with experimental results. The main findings obtained in each part are briefly summarized in the next sections.

11.3 Experimental Studies

11.3.1 Fracture Mechanics Test: Determining the Input Parameters for the FE models

A series of fracture mechanics specimens were manufactured and tested under quasi-static loading conditions in order to obtain relevant values of the critical strain energy release rate. The results obtained for the different mixed mode ratios, which varied from pure mode I to in-plane shear (i.e. different specimens: symmetric and asymmetric double cantilever beam – DCB and ADCB; tapered double cantilever beam – TDCB; end-loaded split – ELS; end-notched flexure – ENF; and symmetric and asymmetric fixed ratio mixed mode – FRMM and AFRMM), were combined and fitted to a suitable function to define a propagation criterion of the form $G_c = G_c(\beta)$. Similarly, fracture mechanics specimens were tested in fatigue to obtain crack growth rate data. The da/dN results were then fitted to modified Paris laws and used to derive suitable expressions for the various parameters (C_T, m, n_1, n_2 and G_{th}).

The load, displacement, crack length and corresponding number of cycles of fatigue were recorded during the tests. After demonstrating the equivalence between the beam analysis proposed by Williams and Davidson's crack tip element (CTE) for the total energy release rate when applied to the typical test geometries, the sets of P_i-δ_i-a_i values were used to calculate initiation and propagation values of G_c according to four different data reduction schemes: simple beam theory (SBT), corrected beam theory (CBT), experimental compliance method (ECM) and corrected beam theory with effective crack length (CBTE). For the mixed mode cases, Williams' and Davidson's decomposition schemes were used to partition the measured G_c into its individual components. Both singular and non-singular versions of Davidson's strategy (CTE/SF and CTE/NSF respectively) were investigated. Finally, the secant and polynomial methods were employed to compute the fatigue crack growth rates from the experimental data obtained in the cyclic tests.

11.3.1.1 Quasi-Static Results

11.3.1.1.1 Mode I Tests: Conclusions

Titanium DCB specimens of various thickness and aluminium TDCB joints were manufactured with AF163-2OST and then tested quasi-statically. The results of these tests were complemented with those previously obtained in the group using CFRP substrates. In addition, a reduced number of Ti-DCB joints were bonded with the unsupported version of

the adhesive (i.e. AF163-2U) and then tested quasi-statically in order to investigate the potential effects of the carrier mat.

Failure was cohesive in all cases, with the crack propagating through the adhesive layer in a stable manner. The resulting resistance curves exhibited a small rising effect regardless of the data reduction scheme considered: after a first stage where the strain-energy release rate increased with the crack length, the curves reached a relatively stable plateau. Neither the substrate material nor the geometry of the joint influenced the initiation or plateau values of G_{Ic}. The effective crack length approach consistently yielded higher fracture energies than the traditional CBT for the DCB specimens. The implied values of the beam root rotation correction (Δ) were in all cases lower than the value obtained from CBT (Δ_I), and decreased with the measured crack length. This variation of Δ was consistent with a reduction in the size of the FPZ, the shear stresses and the beam root rotation with the crack length. The results suggest that CBTE is theoretically sounder than CBT.

The average mode I fracture energy of the unsupported adhesive was noticeably higher than that of the supported system for propagation ($(G_{Ic})_{CBTE}$=4214±145 J/m^2 and $(G_{Ic})_{CBTE}$=3032±170 J/m^2 respectively). The origin of this difference has been found to be associated with the effect of the carrier mat on the failure mechanisms. The non-woven mat appears to provide a weak path for crack propagation under opening mode, so debonding between the adhesive and the polymer fibres of the carrier rather than fracture of the epoxy resin itself would be a contributing failure mechanism in the DCB joints bonded with AF163-2OST. This hypothesis was supported by the results of microscopy analysis. Furthermore, bearing in mind the reduction in performance, it calls into question the benefits of the use of the mat carrier.

11.3.1.1.2 Mode II Tests: Conclusions

CFRP-ELS and Ti-ENF specimens were employed to test the supported adhesive in pure mode II. Due to its inherent unstable nature, the latter configuration was only used to derive initiation values. However, the initial non-linear response caused significant scatter in the measured values of $(G_{IIc})_{\text{initiation}}$.

No inflexion point was observed in the P-δ curves obtained in the ELS tests, resulting in rising R-curves which did not reach a plateau value. The formation of numerous micro-cracks and the extensive damage accumulated ahead of the continuous crack tip significantly hindered the definition of the true crack lengths in this case. Therefore CBTE, which consistently yielded the highest values of G_{IIc}, was the most appropriate data reduction scheme for the analysis of these tests.

Inspection of the fracture surfaces revealed that the failure had been cohesive in the adhesive layer. Despite the limited data available, the experimental results indicate that the mode II fracture energy of AF163-2OST, for both initiation and propagation, is considerably higher than the corresponding mode I values (i.e. $G_{IIc} \gg G_{Ic}$). A plateau value of G_{IIc} greater than 15000 J/m^2 was suggested by the results.

11.3.1.1.3 Mixed Mode I/II Tests: Conclusions

The mixed mode behaviour of AF163-2OST was investigated using symmetric and asymmetric FRMM specimens and unbalanced DCB joints manufactured with CFRP substrates of various thicknesses (2, 3 and 4mm). Whilst the total fracture energy was calculated using the usual analysis techniques (i.e. SBT, CBT, ECM and CBTE), the mode decomposition was performed according to three different schemes: the Williams global approach, and both the singular and non-singular field versions of Davidson's partitioning method.

Cohesive failure was obtained with the ADCB specimens, with the crack propagating in a stable manner. The composite arms remained elastic. The rising effect in the resulting $G_c = G_c(a)$ curves was more marked than in pure mode I, but they always reached a plateau region.

In the AFRMM cases, the behaviour varied with the mode mix. Stable, cohesive crack propagation was observed for the mixed mode ratio $G_{II}/G < 3/7$. On the other hand, when the thickest arm was loaded (i.e. $G_{II}/G > 3/7$), the response became unstable soon after the load reached a maximum, with the crack propagating rapidly to the clamping point. Traces of interlaminar failure were observed in those specimens that exhibited this type of catastrophic failure.

Regardless of the decomposition theory considered, it was clear that the total critical strain-energy release rate measured in the mixed mode tests (i.e. $G_{I/IIc}$) increased with the mode II component. Even though it was not possible to identify the G_{IIc} plateau, this would suggest that $G_{Ic} < G_{I/IIc} < G_{IIc}$. This increase in $G_{I/IIc}$ was typically accompanied by a change in the failure mechanism, which moved progressively towards that observed in pure mode II. That is, the number and size of the micro-cracks formed ahead of the continuous crack tip, as well as the area they covered, increased with the value of G_{II}/G. The increase in the shear contribution induced by the geometrical asymmetry had important consequences in the crack propagation path. The formation of micro-cracks and their subsequent coalescence gradually drove the crack closer to the interface, increasing the likelihood of interlaminar failure. Particularly evident in the AFRMM joints loaded at the thicker substrate, this problem

appeared to be more severe in mixed mode than under pure shear because only one arm is loaded in the mixed mode specimens.

The effective crack length approach was considered the most accurate technique in all cases, mainly due to the extensive damage accumulated ahead of the crack tip for large shear components. The discrepancies between CBTE and the results obtained with the other data reduction schemes increased with the mixed mode ratio, due to the additional uncertainties in the visual crack length measurements.

The mode I component measured with many of the configurations tested (i.e. G_{Ic}^{mixed}), particularly with the ADCB joints, was higher than G_{Ic}. This behaviour could be explained by the damaging effect of the carrier mat on the mode I toughness. The weaker path provided by the woven mat for mode I crack propagation would not be as well-defined, or exist at all, under mixed mode conditions, resulting in higher total fracture energies.

The ADCB results also indicated certain inconsistencies with the Williams mode decomposition theory. According to this method, these specimens should produce pure opening mode and therefore yield total fracture energies equal to G_{Ic} irrespective of the level of asymmetry. However, the values of $G_{I/IIc}$ obtained in the tests (i.e. $G_{I/IIc} > G_{Ic}$) suggest otherwise.

11.3.1.1.4 Fracture Criterion

The fracture energies measured for the various mixed mode ratios tested were combined to generate plots of the form $G_c = G_c(G_{II}/G)$, fitting the experimental data points to suitable functions: a fourth order polynomial, a modified B-K criterion and a bilinear law. Different solutions were obtained for each of the decomposition methods investigated (i.e. Williams, CTE/SF and CTE/NSF). Only the effective crack length results were employed as this was considered the most accurate data reduction scheme.

For Williams global partitioning, the plot of G_{Ic}^{mixed} versus G_{IIc}^{mixed} exhibited two distinctive regions: initially the mode I component rose rapidly and, after reaching a very early maximum, appeared to decrease progressively with G_{IIc}^{mixed}. This shape allowed an extrapolation to the value of G_{IIc}, which was roughly independent of the function used to approximate the data: G_{IIc}≈17800 J/m^2. This value was consistent with the measured section of the R-curve obtained in the ELS tests.

In contrast with the results obtained with the Williams method, the plot of G_{Ic}^{mixed} versus G_{IIc}^{mixed} corresponding to the CTE/SF and CTE/NSF did not decrease with G_{IIc}^{mixed}

after the initial rising section. Instead, the mode I component stabilized or increased. This made the extrapolation of a G_{IIc} value much more difficult. Therefore, the value of G_{IIc}≈17800 J/m^2 extrapolated from the Williams decomposition method was employed in the definition of the fracture criteria for CTE/SF and CTE/NSF. In those cases, the polynomial function stood out as the most suitable criterion.

Despite the substantial differences between the results obtained with the different partitioning strategies, there was not sufficient experimental evidence to identify the right one. However, although additional tests would have to be performed to determine which one of these methods, if any, was correct, the extensive damage developed ahead of the crack tip in the mixed mode and in-plane shear tests would suggest that the local solution is not the most appropriate one for this particular adhesive. The apparent theoretical inconsistencies in the Williams method with the asymmetric DCB joints also question its validity. This is a continuing area of research in the fracture community.

11.3.1.2 Fatigue Results

Titanium DCB specimens were tested in fatigue (displacement control, R=0.1, F=5Hz) under both "dry" and "wet" conditions. "Dry" experiments were performed at ambient conditions (approximately 23±1°C and 55%RH), whereas coupons were submerged in a bath of distilled water roughly at 25±3°C for "wet" tests. Additionally, a number of Ti-ENF specimens were subjected to cyclic loading in an attempt to characterize the fatigue response of AF163-2OST in shear.

In the mode I tests, failure was mainly cohesive in the adhesive layer, with the crack always propagating in a stable manner. Conversely, unstable crack propagation or near-interfacial failure was obtained for the ENF specimens.

The mode I results were analysed to generate plots of da/dN versus G_{max}. The effective crack length approach was favoured to compute G_{max}, whereas both the secant and incremental polynomial methods were used to compute the corresponding fatigue crack growth rates. The fatigue diagrams exhibited the characteristic sigmoidal shape, displaying well-defined linear regimen and threshold regions. The incremental polynomial method appeared to reduce the scatter and produced smoother results.

The relative position of the "dry" and "wet" curves indicated that the specimens tested under water were apparently tougher. These exhibited larger threshold fracture energies (250 J/m^2 versus 155 J/m^2) and steeper linear regions than the joints tested in ambient conditions, suggesting that the saturated environment modified the properties of the epoxy resin. This 'plasticisation effect' has been previously reported in the literature.

Finally, the results corresponding to the "dry" specimens were approximated by a modified Paris law, using the least squares method to determine the value of the fitting coefficients required for the FE models.

11.3.2 TDLJ Tests: Data for Validation

Quasi-static and fatigue tests were carried out on the simplified structure (i.e. CFRP-to-Ti TDLJ) for later comparison with the numerical predictions. Particularly, double lap joints with three different taper angles (7°, 30° and 45°) were tested quasi-statically to failure, monitoring the strains along the overlap with a DIC system.

The load-extension traces exhibited three well-defined regions: An initial linear section was followed by a curved part with a gradual reduction of the slope, and finally a second linear region where the load continued to increase to the point of catastrophic failure. The ultimate strengths of the joints were very similar in all cases. This result was associated with the vertical tip at the end of the tapers, which affected their effectiveness to reduce the peel stresses at the end of the overlap.

Crack propagation was mainly cohesive in the joints with 45° tapers. In contrast, a combination of cohesive, interfacial and interlaminar failure was observed for the specimens with 30° and 7° tapers.

Based on the type of failure obtained under monotonically loading, only the TDLJ configuration with 45° tapers was tested in fatigue. These joints were fatigued in load control using a sinusoidal waveform with constant amplitude, frequency and load ratio, whilst various maximum loads were considered. The number of cycles to failure was noted in each case. If no damage had been detected after 10 million cycles, the test was stopped and the load level assumed to be equal or below the threshold.

The results of these experiments together with the quasi-static strength were combined to generate the S-N diagram for the TDLJ. In some cases the metallic substrates failed before the bond. For the joints that failed in the overlap, fracture was mainly cohesive in the adhesive layer. The fatigue threshold was between 250 and 350 MPa, corresponding to 32% and 45% of the quasi-static strength respectively.

11.4 Finite Element Studies

Two dimensional FE models of the fracture mechanics specimens tested were created employing the user-defined cohesive elements. Numerical load-displacement and S-N curves were extracted from quasi-static and fatigue simulations and the results compared with those obtained in the corresponding experiments. Finally, the quasi-static and fatigue response of the double lap joints were modeled and the results compared with the experimental values to assess the accuracy of the proposed prediction methodology.

11.4.1 Models of the Fracture Mechanics Specimens tested Quasi-Statically

A single layer of finite-thickness cohesive elements was used to model the bondline in all cases. The penalty stiffness and the displacement at damage initiation were derived from the macroscopic elastic properties of the epoxy resin, while the area under the traction-separation law was equated to one of the experimental criteria for propagation.

Initially, a parametric study was carried out using the mixed mode test geometries in order to study the influence of the elastic properties of the adhesive layer (E, ν) on the mode mix seen by the cohesive element located at the crack tip prior to the onset of damage. The mode mix seen by the cohesive element located at the crack tip was strongly dependent on the elastic modulus of the adhesive. Conversely, the influence of the Poisson's ratio was found to be less significant. The numerical results approached that of the singular field theory as the adhesive became stiffer. On the other hand, for very compliant materials the shear component decreased and the conditions in the near-tip region tended to the Williams solution. For intermediate values of the modulus, and in particular for the case of AF163-2 (E=1.11GPa), the mixed mode ratio computed by the tip element was in excellent agreement with the results obtained with the CTE/NSF theory. These observations were in good agreement with the "b/a" model presented by Alfredsson and Hogberg.

In the light of the outcomes of this study, the applicability of the traditional mode partitioning theories (e.g. Williams, Hutchinson and Davidson) to the analysis of adhesively-bonded joints should be re-examined. Most of these decomposition schemes, which were originally developed for delamination in composites, neglect the presence of the bondline thickness by assuming that its contribution to the overall compliance is small. However, the FE results indicate that the properties of the adhesive should be taken into account when partitioning the total fracture energy into its individual components, even if the bondline thickness is small.

Based on the agreement between the CTE/NSF decomposition theory and the numerical results, the non-singular field fracture criterion was adopted in all the FE models. This was the only viable option to guarantee the equivalence between the partitioning methods used in the analysis of both the fracture mechanics experiments and the simplified structure investigated.

The FE models successfully reproduced the overall load-displacement response in all cases except for the asymmetric FRMM joints loaded via the thick substrate. The influence of the shape of the traction-separation law was minimal in the pure mode cases. On the other hand, the bilinear and linear-cubic laws produced slightly different solution in the mixed mode cases because: (i) the mixed mode ratio seen by the cohesive elements varied with the distance to the crack tip; (ii) the mode mix seen by the cohesive elements varied significantly with the local damage state. As a result, in the FE models of AFRMM and ADCB specimens the crack does not propagate under constant mixed mode conditions. These phenomena have major implications on the overall load-displacement response and the size of the numerical cohesive zone length during propagation, since the values of G_c and the other cohesive parameters changes with the ratio G_{II}/G.

The size of the numerical cohesive zone length varied with the applied displacement or the crack length in all cases. Furthermore, the numerical values were often significantly smaller than the analytical estimates. In line with the extensive damage ahead of the crack tip observed experimentally, long cohesive zones were obtained for the specimens with large shear components. This made it very difficult to attain a state of stable crack propagation, calling into question the applicability of linear elastic fracture mechanics (LEFM) for the study of some of those problems.

These findings must be taken into consideration in the design of a testing programme to determine a suitable fracture criterion. In order to achieve stable crack growth, the test configurations and the parameters of the fracture specimens should be selected so that they minimize the size of the process zone. Special care must be taken in the choice of the thickness of the substrates. Whilst thick arms may be desirable to avoid excessive geometrical non-linearity, they could lead to long process zones due to the imposed constraints on the adhesive layer, inducing unstable behaviour or compromising the validity of LEFM. It should also be noted that these aspects are not contemplated in the traditional stability criteria presented in Chapter 5, the applicability of which should be re-examined, at least when very tough systems are involved.

11.4.2 Models of the Fracture Mechanics Specimens tested in Fatigue

The two prediction methodologies proposed in this work (i.e. damage accumulation due to cyclic loading and prediction of the threshold) were applied to the study the titanium DCB joints tested under "dry" fatigue conditions. The models employed the coefficients of the Paris law determined experimentally.

The FE simulations successfully reproduced the P_{max}-N-a response, including the near-threshold behaviour. The solution exhibited a mild dependence on Δt_{max}, with the larger time increments producing slightly faster reduction in P_{max}. However, despite the significant convergence issues encountered for the larger values of Δt_{max}, all the simulations approached the same final load. Moreover, both methodologies predicted virtually the same threshold load, proving that they are consistent with each other and complementary.

The use of the numerical cohesive zone length rather than the analytical estimates (as in previous formulations) yielded greater accuracy, particularly for intermediate numbers of cycles. Furthermore, the definition of l_{CZ} based on the damage state of the individual integration points combined with the use of quadratic elements minimized the negative influence of coarse meshes reported elsewhere.

11.4.3 Validation of the Methodology: Models of the TDLJ

The quasi-static and fatigue responses of the TDLJ with a 45° tapers were simulated using the cohesive element formulation. A single layer of elements was used to model the bondline. The accuracy of these simulations was evaluated by direct comparison with the experimental results.

The models successfully predicted the initial stiffness and ultimate strength of the joints. However, the results highlighted the limitations of the bilinear and linear-cubic evolution laws to capture the load-extension behaviour after the onset of damage. Despite the large mixed mode ratios present in the overlap ($G_{II}/G \geq\geq 0.85$), a parametric study revealed that the strength of the joint was not significantly influenced by G_{IIc}. Instead, it was the maximum stress in the traction-separation law that controlled the static failure load.

The fatigue models incorporating degradation due to cyclic loading successfully capture the S-N response of the TDLJ. However, since they were based on the mode I coefficients of the modified Paris law, they yielded conservative estimates of the fatigue lifetime. Both prediction methodologies yielded virtually identical estimates of the fatigue threshold (approximately 200MPa versus the 250MPa value measured experimentally), reinforcing the conviction that they are complementary rather than mutually exclusive approaches.

Finally, given that fracture of the metallic substrates was identified as a potential mode of failure of the TDLJ in fatigue, models of the titanium strips with a single layer of cohesive elements were created to predict the corresponding S-N diagram. Crack growth was assumed to occur under mode I, obtaining the quasi-static cohesive parameters and the coefficients of the modified Paris law directly from the literature. Despite the geometrical simplicity of the models, the fatigue lifetime estimates obtained for this failure mode agreed extremely well with the test results.

11.4.4 Mesh Dependency Analysis

A mesh-sensitivity analysis was performed for the various test geometries modelled in the present work. The linear cohesive elements exhibited the typical size-dependent behaviour and, in line with the usual mesh-design criterion, a minimum of three elements within the numerical FPZ were typically required to ensure convergence to the right solution. In contrast, the results obtained with the quadratic formulation have been found to be independent of the length of the cohesive elements, at least with respect to the global response. Furthermore, it has been shown that, if the number of integration points employed is sufficiently high, the solution is smooth and stable.

The reasons for this apparently mesh-independent behaviour have not been yet fully clarified. However, it appears that the superior ability of the quadratic elements to reproduce bending could explain their advantage over the traditional linear formulation. The change in the shape of the profile of the top and bottom surfaces of the cohesive elements (from straight to quadratic shape) would have dramatic effects on the relative displacements and damage state, thus affecting the energy dissipation within the elements.

Consequently the potential of the second-order elements is great. Due to their mesh-independent formulation, cohesive elements will no longer dictate the minimum element size when analysing real components, opening the door to a dramatic increase in the industrial applications of CZM. It is postulated that the aspect ratio of the continuum elements employed in the substrates may be the new limiting factor for mesh design when these new cohesive elements are used.

Overall, this research has demonstrated the potential of fracture mechanics to study adhesively-bonded joints and to successfully predict their performance and durability. The results presented in this thesis represent significant progress towards the industrial implementation of cohesive zone models. However, the measurement of the required input data for the fracture mechanics models remains a significant challenge, particularly in mode II.

11.5 Future Work

A number of potential areas for further investigation have been identified in the course of this research. Some of them are briefly discussed below.

11.5.1 Mode II and Mixed Mode I/II Testing

The mode II tests carried out for this research did not allow a steady state crack propagation phase to be reached and therefore it was not possible determine the value of G_{IIc}. The same occurred in fatigue, where the ENF specimens often failed interfacially and no Paris diagram was obtained. As discussed in Chapters 8 and 9, these input parameters have a considerable influence in the response of the models even if fracture does not takes place under pure shear conditions. Further, this information is essential if the prediction methodologies proposed here are to be validated for their industrial use.

The various tests parameters (e.g. substrate thickness, initial crack length, free length or span length) should be optimized in order to achieve stable, cohesive fracture. Additional test configurations, including the four-point-bending ENF (i.e. 4ENF), could be also investigated. Similarly, different mixed mode rations could be tested in fatigue in order to extrapolate the mode II behavior.

11.5.2 Mode Decomposition Scheme

The non-singular field version of Davidson's theory (CTE/NSF) was selected as the most appropriate mode decomposition scheme here on the basis of its equivalence with the numerical results. However, there was not sufficient experimental information to guarantee that this was physically the correct choice. To be fully consistent, any partitioning method must yield the same fracture criterion regardless of the test configurations employed in its derivation. Bearing this in mind, the mixed mode results obtained with symmetric specimens (for example MMB joints tested for various mixed mode ratios), could be used to determine which one of the decomposition theories considered, if any, was correct. Additionally, more recent schemes, particularly those proposed by Wang and Harvey and Williams need further consideration.

Despite their popularity, many of the mode decomposition methods proposed to date neglect the presence of the adhesive layer. However, in the light of the numerical results discussed in Chapter 8, their applicability to the analysis of bonded joints should be re-examined. Specific schemes such as that presented by Alfredson and Hogberg which account for both the

thickness and properties of the adhesive bondline must be developed. Furthermore, given that most of the few alternatives are restricted the linear-elastic behaviour of the adhesive, they must be extended to allow for irreversible deformation or damage ahead of the crack tip.

11.5.3 Failure Process Zone

The size of the FPZ has been identified as a crucial parameter in the fracture process. Not only does it significantly affect the value of G_c, but it also appears to have considerable influence on both the mode mix and the stability of the fracture tests. However, in spite of its importance, the analytical solutions currently available to estimate its size are not very accurate nor do they appear well suited for adhesive joints (i.e. they ignore the influence of the bondline thickness and the constraints imposed by substrates). FE methods offer a simple way to predict the size of the FPZ, but the numerical results are very much dependent on the material models and the mechanical properties employed in the simulations (or the shape and characteristic values of the traction separation law if cohesive elements are used).

The strain field in the vicinity of the crack tip could be monitored using optical techniques, particularly DIC, in order to measure the FPZ experimentally. By studying its size and evolution for different test geometries, bondline thicknesses and substrate materials, the role of the FPZ on the fracture process could be clarified. Moreover, the results of such study could prove invaluable to understand the significance of both the shape of the traction-separation law and the cohesive parameters. Additionally, they would serve to validate the numerical predictions.

11.5.4 Effect of the Carrier Mat

The mode I tests carried out with the supported and unsupported version of AF163-2OST have revealed the detrimental effect of the carrier mat on the fracture toughness of the adhesive. It has been proposed here that, under pure opening mode conditions, the adhesive-carrier interface provides a weak path for crack propagation. However, whether this failure mechanism remains active under mixed mode conditions remains an open question. Bearing in mind the magnitude of reduction observed for G_{Ic}, a detailed investigation of the mixed mode behaviour of AF163-2U is required in order to gain a better understanding of the origins and extent of this effect.

11.5.5 Level of Constraint and Transferability

Whilst the level of constraint has been partially embedded into the FE models by using the experimental value of G_c, the potential influence of the triaxial stress state near the crack tip on the yield stress and elastic moduli has been neglected. As discussed in Chapter 3, this simplification could compromise the transferability of the results to other geometries. The cohesive element formulation developed in this research could be extended to allow for these effects. In that case, the bulk adhesive would have to be tested for different levels of triaxiality and the results used to derive suitable damage initiation criteria which could then be imported into the user-element subroutine.

11.5.6 Thermal Residual Stresses

Even though the bonded structure that inspired this research project is hybrid in nature (i.e. it uses dissimilar substrate materials), any residual stresses arising during the curing process due to the different coefficients of thermal expansion have been neglected in both the analysis of the experimental results and in the FE models. However, these are worthy of further study, as they could distort the geometry of the joints and lower their strength. In addition, an initial thermal analysis (carried out at the curing temperature minus the service temperature) could be added to the simulations in order to quantify the magnitude of these residual stresses and account for their influence on the service life predictions.

References

1. SWEDENBORG, E., *A Machine to Fly in the Air.* Daedalus Hyperboreus 1716.

2. NASA. *Kitty Hawk History.* 2012 Feb 26 2010 [cited 11/08/2012]; Available from: http://www.grc.nasa.gov/WWW/k-12/aerosim/LessonHS97/KittyHawk.html

3. AIRBUS. *A380 Family.* 2012 [cited 11/08/2012]; Available from: http://www.airbus.com/aircraftfamilies/passengeraircraft/a380family/

4. *FAA Regulations: Airworthiness Standards - Aircraft Engines.* FAA Regulations 2012 27 September 2012 [cited 30/09/2012]; Available from: http://ecfr.gpoaccess.gov/cgi/t/text/text-idx?sid=eaba20bfabdfe7be8599ac289e3d09c0&c=ecfr&tpl=/ecfrbrowse/Title14/14cfrv1_02.tpl

5. *Rolls Royce -Trent Newsletter Update: Key tests keep the Trent 1000 ahead.* 2007 June 2007 [cited 10/08/2012]; 6]. Available from: http://www.rolls-royce.com/trent_1000/documents/Trent1000_Iss6.pdf.

6. ZAREI, H., M. KRÖGER, and H. ALBERTSEN, *An experimental and numerical crashworthiness investigation of thermoplastic composite crash boxes.* Composite Structures, 2008. 85(3): p. 245-257.

7. CALISKAN, A.G., *Design and analysis of Composite Impact Structures for Formula One Using Explicit FEA Techniques*, in *2002 SAE Motorsports Engineering Conference and Exhibition* 2002, Society of Automotive Engineers, U.S.

8. BISAGNI, C., G. DI PIETRO, L. FRASCHINI, and D. TERLETTI, *Progressive crushing of fiber-reinforced composite structural components of a Formula One racing car.* Composite Structures, 2005. 68(4): p. 491-503.

9. JACOB, G.C., J.F. FELLERS, S. SIMUNOVIC, and J.M. STARBUCK, *Energy Absorption in Polymer Composites for Automotive Crashworthiness.* Journal of Composite Materials, 2002. 36(7): p. 813-850.

10. ROBINSON, T. *Blades of glory.* 2012 03/02/2012 [cited 11/08/2012]; Available from: http://media.aerosociety.com/aerospace-insight/2012/02/03/blades-of-glory/6204/.

11. KINLOCH, A.J., *Adhesives in engineering.* Proceedings of the Institution of Mechanical Engineers Part G - Journal of Aerospace Engineering, 1997. 211: p. 307 - 335.

12. KINLOCH, A.J., M.L. YUEN, and S.D. JENKINS, *Thermoplastic-toughened epoxy polymers.* Journal of Materials Science, 1994. 29(14): p. 3781-3790.

13. BUCKNALL, C.B., *Toughened plastics*. 1977, London: Applied Science Publishers Ltd.

14. RIEW, C.K. and A.J. KINLOCH, *Toughened Plastics I: Science and Engineering, Advances in Chemistry Series*. 1993, Washington, D.C.: American Chemical Society.

15. JEANDRAU, J.P., *Intrinsic mechanical characterization of structural adhesives.* International Journal of Adhesion and Adhesives, 1986. 6(4): p. 229-231.

16. BANEA, M.D. and L.F.M.d. SILVA, *Mechanical Characterization of Flexible Adhesives.* The Journal of Adhesion, 2009. 85(4-5): p. 261-285.

17. SILVA, L.F.M.d. and R.D. ADAMS, *Measurement of the mechanical properties of structural adhesives in tension and shear over a wide range of temperatures.* Journal of Adhesion Science and Technology, 2005. 19(2): p. 109-141.

18. LOH, W.K., A.D. CROCOMBE, M.M.A. WAHAB, and I.A. ASHCROFT, *Environmental degradation of the interfacial fracture energy in an adhesively bonded joint.* Engineering Fracture Mechanics, 2002. 69: p. 2113–2128.

19. CROCOMBE, A.D., Y.X. HUA, W.K. LOH, M.M.A. WAHAB, and I.A. ASHCROFT, *Predicting the residual strength for environmentally degraded adhesive lap joints.* International Journal of Adhesion & Adhesives, 2006. 26: p. 325–336.

20. LILJEDAHL, C.D.M., A.D. CROCOMBE, M.M.A. WAHAB, and I.A. ASHCROFT, *Modelling the environmental degradation of adhesively bonded aluminium and composite joints using a CZM approach.* International Journal of Adhesion & Adhesives, 2007. 27: p. 505–518.

21. HADAVINIA, H., A.J. KINLOCH, M.S.G. LITTLE, and A.C. TAYLOR, *The prediction of crack growth in bonded joints under cyclic-fatigue loading II. Analytical and finite element studies.* International Journal of Adhesion and Adhesives, 2003. 23: p. 463-471.

22. FERNLUND, G., M. PAPINI, D. McCAMMOND, and J.K. SPELT, *Fracture load predictions for adhesive joints.* Composites Science and Technology, 1994. 51: p. 587-600.

23. HADAVINIA, H., A.J. KINLOCH, M.S.G. LITTLE, and A.C. TAYLOR, *The prediction of crack growth in bonded joints under cyclic-fatigue loading I. Experimental studies.* International Journal of Adhesion & Adhesives, 2003. 23: p. 449-461.

24. KINLOCH, A.J., *Adhesion and Adhesives: Science and Technology* 1987, London: Chapman & Hall. 441.

25. BALDAN, A., *Adhesively-bonded joints and repairs in metallic alloys, polymers and composite materials: Adhesives, adhesion theories and surface pretreatment.* Journal of Materials Science, 2004. 39: p. 1-49.

26. LISTON, E.M., L. MARTINU, and M.R. WERTHEIMER, *Plasma surface modification of polymers for improved adhesion: a critical review.* Journal of Adhesion Science and Technology, 1993. 7(10): p. 1091-1127.

27. VAN DER LEEDEN, M.C. and G. FRENS, *Surface Properties of Plastic Materials in relation to their Adhering Performance* Advanced Engineering Materials, 2002. 4(5): p. 281-289.

28. ANDREWS, E.H. and A.J. KINLOCH, *Mechanics of Adhesive Failure I.* Proceedings of the Royal Society of London. Series A, Mathematical and Physical Sciences, 1973. 332: p. 385-399.

29. ANDREWS, E.H. and A.J. KINLOCH, *Mechanics of Adhesive Failure II.* Proceedings of the Royal Society of London. Series A, Mathematical and Physical Sciences, 1973. 332: p. 410-414.

30. BABURAJ, E.G., D. STARIKOV, J. EVANS, G.A. SHAFEEV, and A. BENSAOULA, *Enhancement of adhesive joint strength by laser surface modification.* International Journal of Adhesion & Adhesives, 2007. 27: p. 268-276.

31. DAVIES, M. and D. BOND, *Principles and practices of adhesive bonded structural joints and repairs.* International Journal of Adhesion & Adhesives, 1999. 16(2-3): p. 91-105.

32. HARRIS, A.F. and A. BEEVERS, *The effects of grit-blasting on surface properties for adhesion.* International Journal of Adhesion & Adhesives, 1999. 19: p. 445-452.

33. VENABLES, J.D., *Review: Adhesion and durability of metal-polymer bonds.* Journal of Materials Science, 1984. 19: p. 2431-2453.

34. McGAREL, W., H.A. FARNHAM, and R. McGUKIN, *Influence of pretreatment rinse waters on the durability of adhesive-bonded aluminium alloys.* International Journal of Adhesion & Adhesives, 1986. 6(2): p. 89-92.

35. DA SILVA, L.F.M., A. OCHSNER, and R.D. ADAMS, *Handbook of Adhesion Technology.* 2011, Berlin: Springer.

36. *Handbook of Adhesives and Surface Preparation*, ed. S. EBNESAJJAD. 2011, Oxford: Elsevier Inc.

37. BJORGUM, A., F. LAPIQUE, J. WALMSLEY, and K. REDFORD, *Anodising as pre-treatment for structural bonding.* International Journal of Adhesion & Adhesives, 2003. 23(5): p. 401-412.

38. RIDER, A., *Bond Durability of Grit-blast and Silane treated Metallic Adherends Bonded with Room Temperature Curing Adhesives*. 2001, Defence Science & Technology Organisation (Australia): Victoria. p. 61.

39. MAZZA, J.J., J.B. AVRAM, and R.J. KUHBANDER, *Grit-Blast/Silane (GBS) Aluminium Surface Preparation For Structural Adhesive Bonding*. 2003, Air Force Research Laboratory (US): Wright-Patterson Air Force Base.

40. FLINN, B. and M. PHARISS, *The Effect of Peel-Ply Surface Preparation Variables on Bond Quality*. 2006, U.S. Department of Transportation, Federal Aviation Administration: Washington.

41. HART-SMITH, L.J., G. REDMOND, and M.J. DAVIES, *The curse of the nylon peel ply*. 1996, McDonnell Douglas: California.

42. BENARD, Q., M. FOIS, and M. GRISEL, *Peel ply surface treatment for composite assemblies: Chemistry and morphology effects.* Composites Part A: Applied Science and Manufacturing, 2005. 36(11): p. 1562-1568.

43. BENARD, Q., M. FOIS, and M. GRISEL, *Influence of fibre reinforcement and peel ply surface treatment towards adhesion of composite surfaces.* International Journal of Adhesion & Adhesives, 2005. 25(5): p. 404-409.

44. BLAIS, P., D.J. CARLSSON, G.W. CSULLOG, and D.M. WILES, *The chromic acid etching of polyolefin surfaces, and adhesive bonding* Journal of Colloid and Interface Science, 1974. 47(3): p. 636-649.

45. ARROWSMITH, D.J. and A.W. CLIFFORD, *A new pretreatment for the adhesive bonding of aluminium.* International Journal of Adhesion & Adhesives, 1985. 5(1): p. 40-42.

46. KENNEDY, A.C., R. KOHLER, and P. POOLE, *A sodium hydroxide anodize surface pretreatment for the adhesive bonding of titanium alloys.* International Journal of Adhesion & Adhesives, 1983. 3(2): p. 133-139.

47. VENABLES, J.D., D.K. McNAMARA, J.M. CHEN, and T.S. SUN, *Oxide morphologies on aluminium prepared for adhesive bonding.* Applications of Surface Science, 1979. 3(1): p. 88-98.

48. LUNDER, O., B. OLSEN, and K. NISANCIOGLU, *Pre-treatment of AA6060 aluminium alloy for adhesivebonding.* International Journal of Adhesion & Adhesives, 2002. 22(2): p. 143-150.

49. CHU, C., H. ZHENG, C. YANG, and M. DAMRON, *Sol-Gel Coating as a Surface Pretreatment Process for Adhesive Bonding of Aluminum Alloys*, in *International Congress & Exposition: Aluminium Applications*. 1997: Detroit (USA).

50. LIU, J., M.K. CHAUDHURY, D.H. BERRY, J.E. SEEBERGH, J.H. OSBORNE, and K.Y. BLOHOWIAK, *Effect of Surface Morphology on Crack Growth at a Sol-Gel Reinforced Epoxy/Aluminium Interface.* The Journal of Adhesion, 2006. 20(4): p. 277-305.

51. HALL, J.R., A.L. WESTERDAHL, A.T. DEVINE, and M.J. BODNAR, *Activated Gas Plasma Surface Treatment of Polymers for Adhesive Bonding.* Journal of Applied Polymer Science, 1969. 13: p. 2085-2096.

52. BLACKMAN, B.R.K. and A.J. KINLOCH, *The plasma treatment of thermoplastic fibre composites for adhesive bonding.* Composites, 1994. 25(5): p. 332-341.

53. BLAIS, P., D.J. CARLSSON, and D.M. WILES, *Effects of corona treatment on composite formation. Adhesion between incompatible polymers.* Journal of Applied Polymer Science, 1971. 15(1): p. 129-143.

54. COMYN, J., L. MASCIA, and G. XIAO, *Corona-discharge treatment of polyetheretherketone (PEEK) for adhesive bonding.* International Journal of Adhesion and Adhesives, 1996. 16(4): p. 301-304.

55. ABEL, M.L., A.N.N. ADAMS, A.J. KINLOCH, S.J. SHAW, and J.F. WATTS, *The effects of surface pretreatment on the cyclic-fatigue characteristics of bonded aluminium-alloy joints.* International Journal of Adhesion & Adhesives, 2006. 26: p. 50–61.

56. ADAMS, A.N.N., *The durability of organosilane pretreated adhesive joints*, in *Department of Mechanical Engineering*. 2001, Imperial College: London.

57. GETTINGS, M. and A.J. KINLOCH, *Surface Analysis of polysiloxane/metal oxide interfaces.* Journal of Materials Science, 1977. 12: p. 2511-2518.

58. SENNETT, M.S., S.E. WENTWORTH, and A.J. KINLOCH, *Investigation of the interactions of silane-based adhesive primers with metal oxide surfaces using molecular dynamics simulations.* The Journal of Adhesion, 1995. 54(1): p. 23-31.

59. MOLITOR, P., V. BARRON, and T. YOUNG, *Surface treatment of titanium for adhesive bonding to polymer composites: a review.* international Journal of Adhesion & Adhesives, 2001. 21: p. 129-136.

60. CRITCHLOW, G.W. and D.M. BREWIS, *Review of surface pretreatments for titanium alloys.* International Journal of Adhesion & Adhesives, 1995. 15: p. 161-172.

61. MERTENS, T., F.J. GAMMEL, M. KOLB, L. KOTTE, S. TSCHOCKE, S. KASKEL, and U. KRUPP, *Investigation of surface pre-treatments for the structural bonding of titanium.* international Journal of Adhesion & Adhesives, 2012. 34: p. 46-54.

62. WINGFIELD, J.R.J., *Treatment of composite surfaces for adhesive bonding.* International Journal of Adhesion & Adhesives, 1993. 13(3): p. 151-156.

63. BRUNSELL, A.R. and J. RENARD, *Fundamentals of Fibre Reinforced Composite Materials.* Materials Science and Engineering, ed. B. Cantor, M.J. Goringe, and E.Ma. 2005, Bristol (UK): Institute of Physics Publishing.

64. KINLOCH, A.J. and R.J. YOUNG, *Fracture Behaviour of Polymers.* 1983, London: Applied Science Publishers.

65. KINLOCH, A.J., S.J. SHAW, D.A. TOD, and D.L. HUNSTON, *Deformation and fracture behaviour of a rubber-toughened epoxy: I. Microstructure and fracture studies.* Polymer, 1983. 24: p. 1341-1354.

66. YEE, A.F. and R.A. PEARSON, *Toughening mechanisms in elastomer-modified epoxies.* Journal of Materials Science, 1986. 21: p. 2462-2474.

67. HUANG, Y. and A.J. KINLOCH, *The role of plastic void growth in the fracture of rubber-toughened epoxy polymers.* Journal of Materials Science Letters, 1992. 11: p. 484-487.

68. GARG, A.C. and Y.W. MAI, *Failure mechanisms in toughened epoxy resins - A review.* Composite Science and Technology, 1988. 31: p. 179-223.

69. GUILD, F.J., A.J. KINLOCH, and A.C. TAYLOR, *Particle cavitation in rubber toughened epoxies: the role of particle size.* Journal of Materials Science, 2010. 45: p. 3882-3894.

70. NG, D.K.T., *The design and durability of adhesively-bonded joints* in *Department of Materials.* 2003, Imperial College London: London.

71. SHIGLEY, J.E., C.R. MISCHKE, and R.G. BUDYNAS, *Mechanical Engineering Design.* 7th ed. 2004, New York: McGraw-Hill.

72. VOLKERSEN, O., *Die nietkraftverteilung in zungbeansprunchten nietverbindunger mit konstanten laschenquerschnitten.* Luftfahrtforsch, 1938. 15: p. 4-47.

73. VOLKERSEN, O., *Neuere Untersuchungen zur Theorie der Klebverbindungen.* Wissenschaftliche Gesellschaft fur Luft - und Raumfahrt, Colone, 1963: p. 1-28.

74. GOLAND, M. and E. REISSNER, *The stresses in cemented joints.* Journal of Applied Mechanics, 1944. 11: p. A17-A27.

75. HART-SMITH, L.J., *The strength of adhesive-bonded single-lap joints.* 1970, Douglas Aircraft Company.

76. HART-SMITH, L.J., *Designing to minimize peel stresses in adhesive-bonded joints* Delamination and Debonding of Materials-ASTM STP.876, ed. W.S. Johnson. 1985: ASTM. 238-266.

77. HART-SMITH, L.J., *Stress Analysis: A continuum mechanics approach.* Developments in Adhesives - 2, ed. A.J. Kinloch. 1981, London: Applied Science Publishers.

78. HART-SMITH, L.J., *Design of adhesively-bonded joints.* Joining Fibre-Reinforced Plastics, ed. F.L. Mathews. 1987: Elsevier Applied Science Publishers Ltd.

79. TSAI, M.Y., *Improved theoretical solutions for adhesive lap joints.* International Journal of Solids and Structures, 1998. 35(12): p. 1163-1185.

80. VOLKERSEN, O., *Recherches sur la theorie des assemblages colles.* Construction Metallique, 1965. 4: p. 3-13.

81. ADAMS, R.D. and N.A. PEPPIATT, *Stress analysis of adhesive-bonded lap joints.* Journal of Strain Analysis for Engineering Design, 1974. 9(3): p. 185-196.

82. HART-SMITH, L.J., *Design and analysis of adhesive-bonded joints.* 1972, Douglas Aircraft Company: Long Beach, CA, USA.

83. HER, S.C., *Stress analysis of adhesively-bonded lap joints.* Composite Structures, 1999. 47: p. 673-678.

84. XIAO, X., P.H. FOSS, and J.A. SCHROEDER, *Stiffness prediction of the double lap shear joint. Part1: Analytical solution.* International Journal of Adhesion & Adhesives, 2004. 24: p. 229-237.

85. OSNES, H. and D. McGEORGE, *Analysis of overlaminated double-lap joints.* Composites: Part B, 2005. 36: p. 544-558.

86. ADAMS, R.D., R.W. ATKINS, J.A. HARRIS, and A.J. KINLOCH, *Stress Analysis and Failure Properties of Carbon-Fibre-Reinforced-Plastic/Steel Double-Lap Joints.* The Journal of Adhesion, 1986. 20(1): p. 29-53.

87. SANCAKTAR, E. and P. SANCAKTAR, *Increasing strength of single lap joints of metal adherends by taper minimization.* Journal of Adhesion Science and Technology, 2003. 17(5): p. 655-675.

88. OTERKUS, E., A. BARUT, E. MADENCI, S.S. SMELTZER III, and D.R. AMBUR, *Bonded lap joints of composite laminates with tapered edges.* International Journal of Solids and Structures, 2006. 43: p. 1459-1489.

89. DA SILVA, L.F.M. and R.D. ADAMS, *Techniques to reduce the peel stresses in adhesive joints with composites.* International Journal of Adhesion & Adhesives, 2007. 27: p. 227-235.

90. APALAK, M.K. and A. ENGIN, *Effect of adhesive free-end geometry on the initiation and propagation of damaged zones in adhesively bonded lap joints.* Journal of Adhesion Science and Technology, 2004. 18(5): p. 529-559.

91. TAIB, A.A., R. BOUKHILI, S. ACHIOU, S. GORDON, and H. BOUKEHILI, *Bonded joints with composite adherends. Part I. Effect of specimen configuration, adhesive thickness, spew fillet and adherend stiffness on fracture.* International Journal of Adhesion and Adhesives, 2006. 26(4): p. 226-236.

92. LANG, T.P. and P.K. MALLICK, *Effect of spew geometry on stresses in single lap adhesive joints.* International Journal of Adhesion & Adhesives, 1998. 18(3): p. 167-177.

93. RISPLER, A.R., L. TONG, G.P. STEVEN, and M.R. WISNOM, *Shape optimisation of adhesive fillets.* International Journal of Adhesion & Adhesives, 2000. 20: p. 221-231.

94. KILIC, B., E. MADENCI, and D.R. AMBUR, *Influence of adhesive spew in bonded single-lap joints.* Engineering Fracture Mechanics, 2006. 73(11): p. 1472-1490.

95. BELIINGARDI, G., L. GOGLIO, and A. TARDITI, *Investigating the effect of spew and chamfer size on the stresses in metal/plastics adhesive joints.* International Journal of Adhesion & Adhesives, 2002. 22: p. 273-282.

96. STRATFORD, T.J. and J.F. CHEN. *Designing for tapers and defects in FRP-strengthened metallic structures.* in *Proceedings of the International Symposium on Bond Behaviour of FRP in Structures (BBFS 2005).* 2005. Hong Kong: IIFC Secretariat.

97. VALLEE, T. and T. KELLER, *Adhesively bonded lap joints from pultruded GFRP profiles. Part III: Effects of chamfers.* Composites Part B: Engineering, 2006. 37(4-5): p. 328-336.

98. SRIVASTAVA, V.K., *Characterization of adhesive bonded lap joints of C/C-SiC composite and Ti-6Al-4V alloy under varying conditions.* International Journal of Adhesion & Adhesives, 2003. 23(1): p. 59-67.

99. DA SILVA, L.F.M., T.N.S.S. RODRIGUES, M.A.V. FIGUEIREDO, M.F.S.F. MOURA, and J.A.G. CHOUSAL, *Effect of Adhesive Type and Thickness on the Lap Shear Strength.* The Journal of Adhesion, 2006. 82(11): p. 1091-1115.

100. CROCOMBE, A.D. and D.A. BIGWOOD, *Development of a full elasto-plastic adhesive joint design.* Journal of Strain Analysis for Engineering Design, 1992. 27: p. 211-218.

101. HARRIS, J.A. and R.D. ADAMS, *Strength prediction of bonded single lap joints by non-linear finite element methods.* International Journal of Adhesion & Adhesives, 1984. 4: p. 65-78.

102. BIGWOOD, D.A. and A.D. CROCOMBE, *Non-linear adhesive bonded joint design analyses.* International Journal of Adhesion & Adhesives, 1990. 10: p. 31-41.

103. CHOUPANI, N., *Mixed-mode cohesive fracture of adhesive joints: Experimental and numerical studies.* Engineering Fracture Mechanics, 2008. 75: p. 4363-4382.

104. MOSTOVOY, S. and E.J. RIPLING, *Fracture Toughness of an Epoxy System.* JOURNAL OF APPLIED POLYMER SCIENCE 1966. 10: p. 1351-1371.

105. ANDERSON, G.P., S.H. BRINTON, K.J. NINOW, and K.L. DE VIRES. *A fracture mechanics approach to predicting bond strength* in *Advances in adhesively bonded joints; Proceedings of the Symposium, ASME Winter Annual Meeting*. 1988. Chicago, Illinois.

106. GRIFFITH, A.A., *The phenomena of rupture and flow in solids.* Philosophical Transactions of the Royal Society of London. Series A, Containing Papers of a Mathematical or Physical Character, 1921. 221: p. 163-198.

107. OROWAN, E., *Fracture and Notch Brittleness in Ductile Materials*, in *Brittle Fracture in Mild Steel Plates*. 1945, British Iron and Steel Research Association p. 69-78.

108. OROWAN, E., *Notch Brittleness and the Strength of Metals.* Trans. Inst. Eng. and Shipbuilders in Scotland, 1945. 89: p. 165-215.

109. IRWIN, G.R. *Fracture dynamics*. in *Proceedings of the ASM Symposium on Fracturing of Metals*. 1948. Cleveland (Ohio): American Society of Metals.

110. IRWIN, G.R., *Analysis of stresses and strain near the end of a crack traversing a plate.* Journal of Applied Mechanics, 1957. 24(3): p. 361-364.

111. IRWIN, G.R., *Discussion.* Journal of Applied Mechanics, 1957. 25(2): p. 299-303.

112. RIPLING, E.J., S. MOSTOVOY, and R.L. PATRICK, *Measuring fracture toughness of adhesive joints.* Materials Research and Standards (ASTM Bulletin), 1964. 4: p. 129-134.

113. MOSTOVOY, S., P.B. CROSLEY, and E.J. RIPLING, *Use of crack-line loaded specimens for measuring plane-strain fracture toughness.* Journal of Materials, 1967. 2(3): p. 661-681.

114. CHAI, H. and M.Y.M. CHIANG, *A crack propagation criterion based on local shear in adhesive bonds subjected to shear.* Journal of Mechanics and Physics of Solids, 1996. 44: p. 1669-1689.

115. PAPINI, M., G. FERNLUND, and J.K. SPELT, *The effect of geometry on the fracture of adhesive joints.* International Journal of Adhesion & Adhesives, 1994. 14: p. 5-13.

116. JETHWA, J.K. and A.J. KINLOCH, *The Fatigue and Durability Behaviour of Automotive Adhesives. Part I: Fracture Mechanics Tests* The Journal of Adhesion, 1997. 61(1-4): p. 71-95.

117. PEREIRA, A.M., J.M. FERREIRA, F.V.ANTUNES, and P.J. BARTOLO, *Study on the fatigue strength of AA 6082-T6 adhesive lap joints.* International Journal of Adhesion & Adhesives, 2009. 29: p. 633-638.

118. AL-GHAMDI, A.H., I.A. ASHCROFT, A.D. CROCOMBE, and M.M.A. WAHAB, *Crack growth in adhesively bonded joints subjected to variable frequency fatigue loading.* The Journal of Adhesion, 2003. 79: p. 1161–1182.

119. CURLEY, A.J., J.K. JETHWA, A.J. KINLOCH, and A.C. TAYLOR, *The Fatigue and Durability Behaviour of Automotive Adhesives. Part III: Predicting the Service Life* The Journal of Adhesion, 1998. 66(1-4): p. 39-59.

120. WESTERGAARD, H.M., *Bearing Pressures and Cracks.* Journal of Applied Mechanics, 1939. 6: p. 49-53.

121. INGLIS, C.E., *Stresses in a plate due to the presence of cracks and sharp corners.* Transactions of the Institute of Naval Architects. Vol. 55. 1913. 219-241.

122. ANDERSON, T.L., *Fracture Mechanics: Fundamentals and Applications.* 3rd Edition ed. 2005, London: Taylor & Francis. 621.

123. XU, C., T. SIEGMUND, and K. RAMANI, *Rate-dependent crack growth in adhesives I. Modelling approach.* International Journal of Adhesion & Adhesives, 2003. 23: p. 9-13.

124. XU, C., T. SIEGMUND, and K. RAMANI, *Rate-dependent crack growth in adhesives II. Experiments and analysis.* International Journal of Adhesion & Adhesives, 2003. 23: p. 15-22.

125. BLACKMAN, B.R.K., A.J. KINLOCH, F.S. RODRIGUEZ-SANCHEZ, and W.S. TEO, *The fracture behaviour of adhesively-bonded composite joints: effects of rate of test and mode of loading.* International Journal of Solids and Structures, 2012. 49(13): p. 1434-1452.

126. BLACKMAN, B.R.K., A.J. KINLOCH, A.C. TAYLOR, and Y. WANG, *The impact wedge-peel performance of structural adhesives.* Journal of Materials Science, 2000. 35(8): p. 1867-1884.

127. READ, B.E., G.D. DEAN, and B.C. DUNCAN, *Project PAJ2. Report No 11. Strain rate and temperature dependence of the properties of adhesives. Prediction of high-rate data*. 1999, National Physical Laboratory: Teddington, Middlesex, UK.

128. BASCOM, W.D. and R.L. COTTINGTON, *Effect of Temperature on the Adhesive Fracture Behaviour of an Elastomer-Epoxy Resin.* The Journal of Adhesion, 1976. 7(4): p. 333-346.

129. KINLOCH, A.J. and S.J. SHAW, *The Fracture Resistance of a Toughened Epoxy Adhesive.* The Journal of Adhesion, 1981. 12(1): p. 59-77.

130. COMYN, J., *Kinetics and mechanics of environmental attack*, in *Durability of Structural Adhesives*, A.J. Kinloch, Editor. 1983, Applied Science London: London.

131. HUA, Y., A.D. CROCOMBE, M.M.A. WAHAB, and I.A. ASHCROFT, *Continuum damage modelling of environmental degradation in joints bonded with EA9321 epoxy adhesive.* International Journal of Adhesion & Adhesives, 2008. 28: p. 302–313.

132. TURON, A., *Simulation of delamination in composites under quasi-static and fatigue loading using cohesive zone models*, in *Dept. de Ingenieria Mecanica y de la Construccion Industrial*. 2007, Universidad de Girona: Girona.

133. BLACKMAN, B.R.K., A.J. KINLOCH, M. PARASCHI, and W.S. TEO, *Measuring the mode I adhesive fracture energy, GIC, of structural adhesive joints: the results of an international round-robin.* International Journal of Adhesion & Adhesives, 2003. 23: p. 293–305.

134. BLACKMAN, B.R.K., H. HADAVINIA, A.J. KINLOCH, M. PARASCHI, and J.G. WILLIAMS, *The calculation of adhesive fracture energies in mode I: revisiting the tapered double cantilever beam (TDCB) test.* Engineering Fracture Mechanics, 2003. 70: p. 233–248.

135. BRUNNER, A.J., B.R.K. BLACKMAN, and J.G. WILLIAMS, *Calculating a damage parameter and bridging stress from Gic delamination tests on fibre composites.* Composites Science and Technology, 2006. 66: p. 785-795.

136. CHARALAMBIDES, M., A.J. KINLOCH., Y. WANG, and J.G. WILLIAMS, *On the analysis of mixed-mode failure.* International Journal of Fracture, 1992. 54: p. 269-291.

137. KINLOCH, A.J., Y. WANG, J.G. WILLIAMS, and P. YAYLA, *The Mixed Mode Delamination of Fibre Composite Materials.* Composite Science and Technology, 1993. 47: p. 225-237.

138. O'BRIEN, T.K., *Composite Interlaminar Shear Fracture Toughness, Giic: Shear Measurement of Sheer Myth?* . 1997, NASA, Langley Research Center: Hampton, VA.

139. BLACKMAN, B.R.K., A.J. BRUNNER, and J.G. WILLIAMS, *Mode II fracture testing of composites: a new look at an old problem.* Engineering Fracture Mechanics, 2006. 73: p. 2443-2455.

140. SCHUECKER, C. and B.D. DAVIDSON, *Effect of Friction on the Perceived Mode II Delamination Toughness from Three- and Four-Point Bend End-Notched Flexure Tests*, in *Composite Structures: Theory and Practice, ASTM STP 1383*, P. Grant and C.Q. Rousseau, Editors. 2000, American Society for Testing and Metals: West Conshhocken, PA.

141. BLACKMAN, B.R.K., A.J. KINLOCH, and M. PARASCHI, *The determination of the mode II adhesive fracture resistance, GIIC, of structural adhesive joints: an effective crack length approach.* Engineering Fracture Mechanics, 2005. 72: p. 877-897.

142. MOURA, M.F.S.F., R.D.S.G. CAMPILHO, and J.P.M. GONCALVES, *Pure mode II fracture characterization of composite bonded joints.* International Journal of Solids and Structures, 2009. 46: p. 1589-1595.

143. VINTILESCU, I. and J.K. SPELT, *Mixed Mode I, II, and III Fracture Characterization of Adhesive Joints.* Journal of Composites Technology and Research, 1998. 20(2): p. 11.

144. CHEN, Z., R.D. ADAMS, and L.F.M.d. SILVA, *Fracture toughness of bulk adhesives in mode I and mode III and curing effect.* International Journal of Fracture, 2011. 167(2): p. 221-234.

145. MORAIS, A.B.d. and A.B. PEREIRA, *Mixed mode II+III interlamninar fracture of carbon/epoxy laminates.* Composites Science and Technology, 2008. 68: p. 2022-2027.

146. WILLIAMS, J.G., *On the calculation of energy release rates for cracked laminates.* International Journal of Fracture, 1988. 36: p. 101-119.

147. HASHEMI, S., A.J. KINLOCH, and J.G. WILLIAMS, *The Analysis of interlaminar fracture in uniaxial fibre-polymer composites.* Proceedings of the Royal Society of London. Series A, Mathematical and Physical Sciences, 1990. 427: p. 173-199.

148. RODRIGUEZ SANCHEZ, F.S., *Fracture Behaviour of Automotive Adhesive Joints*, in *Mechanical Engineering Department*. 2008, Imperial College London: London.

149. PARASCHI, M., *A Fracture Mechanics approach to the failure of adhesive joints* in *Department of Mechanical Engineering*. 2001, Imperial College of Science, Technology and Medicine.

150. IRWIN, G.R. *Plastic zone near a crack and fracture toughness.* in *Proceedings of the Seventh Sagamore Ordnance Materials Conference*. 1960. New York: Syracuse University.

151. IRWIN, G.R., *Structural aspects of brittle fracture.* Applied Materials Research, 1963. 3(2): p. 65-81.

152. BASCOM, W.D., R.L. COTTINGTON, R.L. JONES, and P. PEYSER, *The fracture of epoxy- and elastomer-modified epoxy polymers in bulk and as adhesives.* Journal of Applied Polymer Science, 1975. 19(9): p. 2545-2562.

153. NARASIMHAN, R. and A.J. ROSAKIS, *Three Dimensional Effects Near a Crack Tip in a Ductile Three Point Bend Specimen - Part I: A Numerical Investigation.* 1988, California Institute of Technology, Division of Engineering and Applied Science: Pasadena, CA, USA.

154. WANG, R.X., A.N. SINCLAIR, and J.K. SPELT, *Strength of adhesive joints with adherend yielding: II. Peel experiments and failure criteria.* The Journal of Adhesion, 2003. 79(1): p. 49-66.

155. PARDOEN, T., T. FERRACIN, C.M. LANDIS, and F. DELANNAY, *Constraint effects in adhesive joint fracture.* Journal of Mechanics and Physics of Solids, 2005. 53: p. 1951-1983.

156. IMANAKA, M., A. FUJINAMI, and Y. SUZUKI, *Fracture and yield behaviour of adhesively bonded joints under triaxial stress conditions.* Journal of Materials Science, 2000. 35: p. 2481-2491.

157. RUGGIERI, C. and R.H. DODDS, *A transferability model for brittle fracture including constraint and ductile tearing effects: a probabilistic approach.* International Journal of Fracture, 1996. 79: p. 309-340.

158. McAULIFFE, D., A. KARAC, N. MURPHY, and A. IVANKOVIC, *Transferability of Fracture Properties between Peel and TDCB Tests for a Nano-Toughened Epoxy Adhesive*, in *Proceedings of the 10th International Conference on Fracture and Damage Mechanics.* 2011: Dubrovnik, Croatia.

159. IRWIN, G.R. *Onset of fast crack propagation in high strength steel and aluminium alloys.* in *Sagamore Research Conference Proceedings.* 1956.

160. DAVIDSON, B.D., S.J. GHARIBIAN, and L. YU, *Evaluation of energy release rate-based approaches for predicting delamination growth in laminated composites.* International Journal of Fracture, 2000. 105: p. 343-365.

161. BERRY, J.P., *Determination of Fracture Surface Energies by the Cleavage Technique.* Journal of Applied Physics, 1963. 34: p. 62-68.

162. DAVIDSON, B.D., P.L. FARIELLO, R.C. HUDSON, and V. SUNDARARAMAN, *Accuracy Assessment of the Singular-Field-Based Mode-Mix Decomposition Procedure for the*

Prediction of Delamination, in *Composite Materials: Testing and Design, Thirteenth Volume*, S.J. Hooper, Editor. 1997, American Society for Testing and Materials. p. 109-128.

163. DAVIDSON, B.D. and S.S. TELLER, *Recommendations for an ASTM Standardized Test for Determining GIIc of Unidirectional Laminated Polymeric Matrix Composites.* Journal of ASTM International, 2010. 7(2).

164. ESIS TC4, *An ESIS TC4 Protocol: Fibre-composites- The determination of the mode II fracture resistance (GIIc) of unidirectional fibre-composites using the calibrated end loaded split (C-ELS) tests and the effective crack length approach.* 2008, European Structural Integrity Society - Technical Committee 4 on Polymers, Composites and Adhesives.

165. ISO 25217, *Determination of the mode I adhesive fracture energy of structural adhesive joints using double cantilever beam and tapered double cantilever beam specimens.* 2009..

166. WILLIAMS, J.G., *The Fracture Mechanics of Delamination Tests.* Journal of Strain Analysis for Engineering Design, 1989. 24(4): p. 207-214.

167. WILLIAMS, J.G., *A Note of Finite Displacement Correction Factors for the End Notch Flexure (ENF) Test* Composite Science and Technology, 1990. 39: p. 279-282.

168. WILLIAMS, J.G., *Fracture Mechanics of Anisotropic Materials*, in *Applications of Fracture Mechanics to Composite Materials* K. Friedrich, Editor. 1989, Elsevier Science Publishers B.V.

169. SUO, Z. and J.W. HUTCHINSON, *Steady-State Cracking in Brittle Substrates Beneath Adherent Films.* International Journal of Solids and Structures, 1989. 25(11): p. 1337-1353.

170. SUO, Z. and J.W. HUTCHINSON, *Interface crack between two elastic layers.* International Journal of Fracture, 1990. 43: p. 1-18.

171. SCHAPERY, R.A. and B.D. DAVIDSON, *Prediction of energy release rate for mixed-mode delamination using classical plate theory.* Applied Mechanical Review, 1990. 43(5).

172. DAVIDSON, B.D., H. HU, and R.A. SCHAPERY, *An Analytical Crack-Tip Element for Layered Elastic Structures.* Journal of Applied Mechanics, 1995. 62: p. 294-305.

173. O'BRIEN, T.K., N.J. JOHNSTON, D.H. MORRIS, and R.A. SIMONDS, *Determination of interlaminar fracture toughness and fracture mode dependence of composites using the edge delamination test* in *Proceedings of the International Conference on*

Testing, Evaluation and Quality Control of Composites 1983: Guildford, Surrey, England. p. 223-232.

174. REEDER, J.R., *3-D Mixed Mode Delamination Fracture Criteria - An Experimentalist's Perspective.* NASA Langley Research Centre, 2006: p. 19.

175. HASHEMI, S., A.J. KINLOCH, and J.G. WILLIAMS, *Mixed-Mode Fracture in Fibre-Polymer Composite Laminates*, in *Composite Materials: Fatigue and fracture.* 1991, American Society for Testing and Materials: Philadelphia. p. 143-168.

176. RYBICKI, E.F. and M.F. KANNINEN, *A Finite Element Calculation of Stress Intensity Factors by a Modified Crack Closure Integral.* Engineering Fracture Mechanics, 1977. 9: p. 931-938.

177. BEUTH, J.L., *Separation of crack extension modes in orthotropic delamination modes.* International Journal of Fracture, 1996. 77: p. 305-321.

178. DAVIDSON, B.D., R.D. BIALASZEWSKI, and S.S. SAINATH, *A non-classical, energy release rate based approach for predicting delamination growth in graphite reinforced laminated polymeric composites.* Composite Science and Technology, 2006. 66: p. 1479-1496.

179. DUCEPT, F., D. GAMBY, and P. DAVIES, *A mixed-mode failure criterion derived from tests on symmetric and asymmetric specimens.* Composite Science and Technology, 1999. 59: p. 609-619.

180. XU, L. and H.V. TIPPUR, *Fracture parameters for interfacial cracks: an experimental-finite element study of crack tip fields and crack initiation toughness* International Journal of Fracture, 1995. 71: p. 345-363.

181. TVERGAARD, V. and J.W. HUTCHINSON, *The influence of plasticity on mixed mode interface toughness.* Journal of Mechanics and Physics of Solids, 1993. 41(6): p. 1119-1135.

182. LI, S., J. WANG, and M.D. THOULESS, *The effects of shear on delamination in layered materials.* Journal of Mechanics and Physics of Solids, 2004. 52(1): p. 193-214.

183. POINT, N. and E. SACCO, *Delamination of beams: an application to the DCB specimen.* International Journal of Fracture, 1996. 79: p. 225-247.

184. WANG, S. and C.M. HARVEY, *Mixed mode partitioning theories for one dimensional fracture.* Engineering Fracture Mechanics, 2012. 79: p. 329-352.

185. WANG, S. and C.M. HARVEY, *A theory of one-dimension fracture.* Composite Structures, 2012. 94: p. 758-767.

186. HARVEY, C.M. and S. WANG, *Experimental assessment of mixed-mode partitioning theories.* Composite Structures, 2012. Under Review.

187. ALFREDSSON, K.S., *Constitutive behaviour and fracture of adhesive layers.* 2004, Chalmers University of Technology: Goteborg, Sweden.

188. ALFREDSSON, K.S. and J.L. HOGBERG, *Energy release rate and mode-mixity of adhesive joint specimens.* International Journal of Fracture, 2007. 144: p. 267-283.

189. D3433, A., in *Annual Book of ASTM standards. Adhesives section 15.* 1990, ASTM: Philadelphia, PA.

190. BSI, *Determination of the mode I adhesive fracture energy, Gic, of structural adhesives using the double cantilever beam (DCB) and tapered double cantilever beam (TDCB) specimens.* 2001. BS 7991.

191. *ISO 11343 Adhesives - Determination of dynamic resistance to cleavage of high-strength adhesive bonds under impact conditions - Wedge impact method.* 2003, International Organization for Standardization.

192. KINLOCH, A.J., C.C. LAU, and J.G. WILLIAMS, *The peeling of flexible laminates.* International Journal of Fracture, 1994. 66(1): p. 45-70.

193. GENT, A.N. and S.Y. KAANG, *Effect of Peel Angle Upon Peel Force.* The Journal of Adhesion, 1987. 24: p. 173-181.

194. DAVIES, P., B.R.K. BLACKMAN, and A.J. BRUNNER, *Standard Test Methods for Delamination Resistance of Composite Materials: Current Status.* Applied Composite Materials, 1998. 5: p. 345-364.

195. BRUNNER, A.J., B.R.K. BLACKMAN, and P. DAVIES, *A status report on delamination resistance testing of polymer–matrix composites.* Engineering Fracture Mechanics, 2008. 75: p. 2779–2794.

196. RUSELL, A.J. and K.N. STREET. *Factors affecting the interlaminar fracture energy of graphite/epoxy laminates.* in *Progress in science and engineering of composites; Fourth International Conference on Composite Materials (ICCM-IV).* 1982. Tokyo.

197. KAGAYAMA, K., M. KIKUCHI, and N. YANAGISAWA, *Stabilized end-notched flexure test: characterization of mode II interlaminar crack growth*, in *Composite Materials: Fatigue and Fracture (Third Volume), ASTM STP*, T.K. O'BRIEN, Editor. 1991, American Society for Testing and Materials: Philadelphia.

198. KAGEYAMA, K., I. KIMPARA, I. OHSAWA, M. HOJO, and S. KABASHIMA, *Mode I and Mode II Delamination Growth of Interlayer Toughened Carbon/Epoxy*

(T800H/3900-2) Composite System, in *Composite Materials: Fatigue and Fracture (Fifth Volume), ASTM STP 1230*, R.H. MARTIN, Editor. 1995, Composite Materials: Fatigue and Fracture (Fifth Volume), ASTM STP 1230: Philadelphia. p. 19-37.

199. MARTIN, R.H. and B.S. DAVIDSON. *Mode II Fracture Toughness Evaluation Using a Four Point Bend End Notched Flexure Test*. in *Proceedings of 4th International Conference on Deformation and Fracture of Composites*. 1997. Manchester: IoM Communications Ltd.

200. SUN, X. and B.D. DAVIDSON, *Numerical evaluation of the effects of friction and geometric nonlinearities on the energy release rate in three- and four-point bend end-notched flexure tests.* Engineering Fracture Mechanics, 2006. 73(10): p. 1343-1361.

201. CREWS, J.H. and J.R. REEDER, *A mixed-mode bending apparatus for delamination testing* 1988, NASA TM 100662: Hampton, Virginia, USA.

202. REEDER, J.R. and J.H. CREWS, *Nonlinear Analysis and Redesign of the Mixed-Mode Bending Delamination Test*. 1991, NASA TM 102777: Hampton, Virginia, USA.

203. SUNDARARAMAN, V. and B.D. DAVIDSON, *An unsymmetric double contilever beam test for interfacial fracture toughness determination.* International Journal of Solids and Structures, 1997. 7: p. 799-817.

204. BLANCO, N., *Variable mixed-mode delamination in composite laminates under fatigue conditions: testing & analysis*, in *Dpt. d'Enginyeria Mecanics i de la Construccio Industrial*. 2004, Universitat de Girona: Girona. p. 314.

205. HASHEMI, S., A.J. KINLOCH, and J.G. WILLIAMS, *The Effects of Geometry, Rate and Temperature on the Mode I, Mode II and Mixed-Mode I/II Interlaminar Fracture of Carbon-Fibre/Poly(ether-ether ketone) Composites.* Journal of Composite Materials, 1990. 24.

206. BLANCO, N., E.K. GAMSTEDT, L.E. ASP, and J. COSTA, *Mixed-mode delamination growth in carbon–fibre composite laminates under cyclic loading.* International Journal of Solids and Structures, 2004. 41(15): p. 4219-4235.

207. ESIS TC4, *An ESIS TC4 Protocol: Determination of the Mixed Mode I/II Delamination Resistance of Unidirectional Fibre-Reinforced Polymer Laminates Using the Asymmetric Double Cantilever Beam Specimen (ADCB)*. 2003, European Structural Integrity Society - Technical Committee 4 on Polymers, Composites and Adhesives.

208. DAVIDSON, B.D. and V. SUNDARARAMAN, *A single leg bending test for interfacial fracture toughness determination.* International Journal of Fracture, 1996. 78: p. 193-210.

209. PARVATAREDDY, H. and D.A. DILLARD, *Effect of mode-mixity on the fracture toughness of Ti-6Al-4V/FM-5 adhesive joints.* International Journal of Fracture, 1999. 96: p. 215-228.

210. FERNLUND, G., H. LANTING, and J.K. SPELT, *Mixed Mode II-Mode III Fracture of Adhesive Joints.* Journal of Composites Technology and Research, 1995. 17(4).

211. DONALDSON, S.L., *Mode III interlaminar fracture characterization of composite materials.* Composites Science and Technology, 1988. 32(3): p. 225-249.

212. LEE, S.M., *An edge crack torsion method for mode III delamination fracture toughness.* Journal of Composites Technology and Research, 1993. 15(3): p. 193-201.

213. REEDER, J.R., *A Bilinear Failure Criterion for Mixed-Mode Delamination*, in *Composite Materials: Testing and Design (Eleventh Volume)*, E.T.C. Jr., Editor. 1993, American Society for Testing and Materials: Philadelphia. p. 303-322.

214. DUCEPT, F., P. DAVIES, and D. GAMBY, *Mixed mode failure criteria for a glass/epoxy composite and an adhesively bonded composite/composite joint.* International Journal of Adhesion & Adhesives, 2000. 20(3): p. 233-244.

215. DONALDSON, S.L., *Fracture toughness testing of graphite/epoxy and graphite/PEEK composites.* Composites, 1985. 16(2): p. 103-112.

216. HAHN, H.T. and T. JOHANNESSON. *A correlation between fracture energy and fracture morphology in mixed-mode fracture of composites* in *Proceedings of the Fourth International Conference on Composite Materials*. 1983. Stockholm, Sweden.

217. BUI, Q.V., *A Modified Benzeggagh-Kenane Fracture Criterion for Mixed-Mode Delamination.* Journal of Composite Materials, 2011. 45: p. 389-413.

218. REEDER, J.R., *An Evaluation of Mixed-Mode Delamination Failure Criteria*. 1992, NASA Technical Memorandum 104210: Hampton, Virginia. p. 49.

219. WHITCOMB, J.D., *Analysis of Instability-Related Growth of a through-Width Delamination*. 1984, NASA TM-86301.

220. GILLESPIE, J.W., L.A. CARLSSON, R.B. PIPES, R. ROTHSCHILDS, and B. TRETHEWEY, *Delamination Growth in Composite Materials* 1986, NASA CR-176416.

221. JOHNSON, W.S. and P.D. MANGALGIRI, *Influence of the Resin on the Interlaminar Mixed-Mode Fracture* in *Toughened Composites*, N.J. Johnston, Editor. 1987, Americal Society for Testing and Materials: Philadelphia. p. 295-315.

222. HASHEMI, S., A.J. KINLOCH, and J.G. WILLIAMS, *Mechanics and mechanisms of delamination in a poly(ether sulphone)—Fibre composite.* Composites Science and Technology, 1990. 37(4): p. 429-462.

223. YAN, X.Q., S.Y. DU, and W. DUO, *An engineering method of determining the delamination fracture toughness of composite laminates.* Engineering Fracture Mechanics, 1991. 39(4): p. 623-627.

224. BENZEGGAGH, M.L. and M. KENANE, *Measurement of mixed-mode delamination fracture toughness of unidirectional glass/epoxy composites with mixed-mode bending apparatus* Composites Science and Technology, 1996. 56(4): p. 439-449

225. KENANE, M. and M.L. BENZEGGAGH, *Mixed-mode delamination fracture toughness of unidirectional glass/epoxy composites under fatigue loading.* Composite Science and Technology, 1997. 57(5): p. 597-605.

226. GOYAL, V.K., E.R. JOHNSON, and C.G. DAVILA, *Irreversible Constitutive Law for Modeling the Delamination Process Using Interfacial Surface Discontinuities.* Composite Structures, 2004. 65(3-4): p. 289-305.

227. XU, X.X., A.D. CROCOMBE, and P.A. SMITH, *Mixed-mode fatigue and fracture behaviour of joints bonded with either filled or filled and toughened adhesive.* International Journal of Fatigue, 1995. 17(4): p. 279-286.

228. PIRONDI, A. and F. MORONI, *Mixed Mode I/II fatigue crack growth in adhesive joints.* Engineering Fracture Mechanics, 2006. 73(16): p. 2557-2568.

229. VEER, F., J. ZUIDEMA, T. RIEMSLAG, and K. van KRANENBURG, *Mode II Fatigue Failure in Transparent Adhesive Joints.* Materials Science, 2002. 38(6): p. 773-779.

230. AZARI, S., M. PAPINI, J.A. SCHROEDER, and J.K. SPELT, *The effect of mode ratio and bond interface on the fatigue behaviour of a highly-toughened epoxy.* Engineering Fracture Mechanics, 2010. 77(3): p. 395-414.

231. PIRONDI, A. and G. NICOLETTO, *Fatigue crack growth in bonded DCB specimens.* Engineering Fracture Mechanics, 2004. 71(4-6): p. 859-871.

232. XU, X.X., A.D. CROCOMBE, and P.A. SMITH, *Fatigue Crack Growth Rates in Adhesive Joints Tested at Different Frequencies.* The Journal of Adhesion, 1996. 58(3-4): p. 191-204.

233. AZARI, S., M. PAPINI, J.A. SCHROEDER, and J.K. SPELT, *Fatigue threshold behaviour of adhesive joints.* International Journal of Adhesion and Adhesives, 2010. 30(3): p. 145-159.

234. CURLEY, A.J., H. HADAVINIA, A.J. KINLOCH, and A.C. TAYLOR, *Predicting the service-life of adhesively-bonded joints.* International Journal of Fracture, 2000. 103: p. 41-69.

235. BEDEN, S.M., S. ABDULLAH, and A.K. ARIFFIN, *Review of Fatigue Crack Propagation Models for Metallic Components.* European Journal of Scientific Research, 2009. 28(3): p. 364-397.

236. PARIS, P., M. GOMEZ, and W. ANDERSON, *A rational analytical theory of fatigue.* The Trend in Engineering, 1961. 13: p. 9-14.

237. PARIS, P. and F. ERDOGAN, *Critical analysis of propagation laws.* Journal of Basic Engineering, 1963. 85: p. 528-534.

238. FORMAN, R.G. and S.R. METTU, *Behaviour of Surface and Corner Cracks Subjected to Tensile and Bending Loads in Ti-6A1-4V Alloy.* 1990, NASA TM 102165.

239. ALFANO, G. and M.A. CRISFIELD, *Finite element interface models for the delamination analysis of laminated composites: mechanical and computational issues.* International Journal for Numerical Methods in Engineering, 2001. 50: p. 1701-1736.

240. HARPER, P.W. and S.R. HALLETT, *Cohesive zone length in numerical simulations of composite delamination.* Engineering Fracture Mechanics, 2008. 75: p. 4774–4792.

241. KAFKALIDIS, M.S. and M.D. THOULESS, *The effects of geometry and material properties on the fracture of single lap-shear joints.* International Journal of Solids and Structures, 2002. 39: p. 4367-4383.

242. TURON, A., C.G. DAVILA, P.P. CAMANHO, and J. COSTA, *An engineering solution for mesh size effects in the simulation of delamination using cohesive zone models.* Engineering Fracture Mechanics, 2007. 74: p. 1665–1682.

243. GAO, Y.F. and A.F. BOWER, *A simple technique for avoiding convergence problems in finite element simulations of crack nucleation and growth on cohesive interfaces.* Modelling and Simulation in Materials Science and Engineering, 2004. 12: p. 453–463.

244. GUIAMATSIA, I., J.K. ANKERSEN, G.A.O. DAVIES, and L. IANNUCCI, *Decohesion finite element with enriched basis functions for delamination.* Composites Science and Technology, 2009. 69: p. 2616–2624.

245. IRWIN, G.R., *Fracture I*, in *Handbuch der Physik VI*, Flügge, Editor. 1958, Springer Verlag: Berlin. p. 558–590.

246. KRUEGER, R., *Virtual crack closure technique: History, approach and applications, Technical report.* 2002, NASA/CR-2002-211628.

247. BARSOUM, R.S., *On the use of isoparametric finite elements in linear fracture mechanics.* International Journal of Numerical Methods in Engineering, 1976. 10: p. 23-37.

248. BARSOUM, R.S., *Triangular quarter-point elements as elastic and perfectly-plastic crack tip elements.* International Journal of Numerical Methods in Engineering, 1977. 11: p. 85-98.

249. RAJU, I.S., *Calculation of Strain-energy release rates with higher order and singular finite elements.* Engineering Fracture Mechanics, 1987. 28: p. 251-274.

250. BONHOMME, J., A. A., J. VIÑA, and V. I., *Numerical and experimental validation of computational models for mode I composite failure fracture.* Computational Materials Science, 2009. 45: p. 993–998.

251. MARANNANO, G.V., L. MISTRETTA, A. CIRELLO, and S. PASTA, *Crack growth analysis at adhesive–adherent interface in bonded joints under mixed mode I/II.* Engineering Fracture Mechanics, 2008. 75: p. 5122–5133.

252. YANG, C., A. CHADEGANI, and J.S. TOMBLIN, *Strain energy release rate determination of prescribed cracks in adhesively-bonded single-lap composite joints with thick bondlines.* Composites: Part B, 2008. 39: p. 863–873.

253. ALDERLIESTEN, R.C., *On the available relevant approaches for fatigue crack propagation prediction in Glare.* International Journal of Fatigue, 2007. 29: p. 289–304.

254. JOHNSON, W.S., L.M. BUTKUS, and R.V. VALENTIN, *Application of Fracture Mechanics to the durability of bonded composite joints.* 1998, US Department of Transportation, Federal Aviation Administration.

255. RICE, J.R., *A Path Independent Integral and the Approximate Analysis of Strain Concentration by Notches and Cracks.* Journal of Applied Mechanics, 1968. 35: p. 379-386.

256. RICE, J.R. and G.F. ROSENGREN, *Plane Strain Deformation near a Crack Tip in a Power-law Hardening material.* Journal of the Mechanics and Physics of Solids, 1968. 16: p. 1-12.

257. HUTCHINSON, J.W., *Singular Behaviour at the end of a tensile Crack tip in a hardening material* Journal of the Mechanics and Physics of Solids, 1968. 16: p. 13-31.

258. *ABAQUS/CAE USER'S MANUAL VERSION 6.8.* 2008.

259. MARTINY, P.H., F. LANI, A.J. KINLOCH, and T. PARDOEN, *Numerical analysis of the energy contributions in peel tests: A steady-state multilevel finite element approach.* International Journal of Adhesion & Adhesives, 2008. 28: p. 222–236.

260. DUGDALE, D.S., *Yielding of Steel sheets containing slits.* Journal of Applied Mechanics, 1960. 8: p. 100-104.

261. HILLERBORG, A., M. MODEER, and P.E. PETERSON, *Analysis of crack formation and growth in concrete by means of fracture mechanics and finite elements.* Cement and Concrete Research, 1976. 6: p. 773-782.

262. HILLERBORG, A., *Application of fictitious crack model to different types of materials* International Journal of Fracture, 1991. 51: p. 95-102.

263. TVERGAARD, V. and J.W. HUTCHINSON, *The relation between crack growth and resistance and fracture process parameters in elastic-plastic solids.* Journal of Mechanics and Physics of Solids, 1992. 40: p. 1377-1397.

264. KAFKALIDIS, M.S., M.D. THOULESS, Q.D. YANG, and S.M. WARD, *Deformation and fracture of adhesive layers constrained by plastically-deforming adherends.* Journal of Adhesion Science and Technology, 2000. 14(13): p. 1593-1607.

265. MARTINY, P.H., F. LANI, A.J. KINLOCH, and T. PARDOEN, *A multiscale parametric study of mode I fracture in metal-to-metal low-toughness adhesive joints.* International Journal of Fracture, 2012. 173: p. 105-133.

266. BRETT, M., *Prediction of the Performance of Adhesively-Bonded Composite Joints*, in *Mechanical Engineering Department*. 2011, Imperial College London: London.

267. KARAC, A., B.R.K. BLACKMAN, V. COOPER, A.J. KINLOCH, F.S. RODRIGUEZ-SANCHEZ, W.S. TEO, and A. IVANKOVIC, *Modelling the fracture behaviour of adhesively-bonded joints as a function of test rate.* Engineering Fracture Mechanics, 2011. 78(6): p. 973-989.

268. TABAKOVIC, A., A. KARAC, A. IVANKOVIC, A. GIBNEY, C. MCNALLY, and M.D. GILCHRIST, *Modelling the quasi-static behaviour of bituminous material using a cohesive zone model.* Engineering Fracture Mechanics, 2010. 77(13): p. 2403-2418.

269. BLACKMAN, B.R.K., H. HADAVINIA, A.J. KINLOCH, and J.G. WILLIAMS, *The use of a cohesive zone model to study the fracture of fibre composites and adhesively-bonded joints.* International Journal of Fracture, 2003. 119: p. 25-46.

270. WIMMER, G., C. SCHUECKER, and H.E. PETTERMANN, *Numerical simulation of delamination in laminated composite components – A combination of a strength criterion and fracture mechanics.* Composites: Part B, 2009. 40: p. 158-165.

271. MOURA, M.F.S.F., M.V.C. FERNANDEZ, A.B.d. MORAIS, and R.D.S.G. CAMPILHO, *Numerical analysis of the Edge Crack Torsion test for mode III interlaminar fracture of composite laminates.* Engineering Fracture Mechanics, 2008.

272. HÖGBERG, J.L., *Mixed mode cohesive law* International Journal of Fracture, 2006. 141: p. 549-559.

273. LI, S., M.D. THOULESS, A.M. WAAS, J.A. SCHROEDER, and P.D. ZAVATTIERI, *Mixed-mode cohesive-zone models for fracture of an adhesively bonded polymer–matrix composite.* Engineering Fracture Mechanics, 2006. 73: p. 64–78.

274. MOURA, M.F.S.F., R.D.S.G. CAMPILHO, and J.P.M. GONCALVES, *Mixed-Mode Cohesive Damage Model Applied to the Simulation of the Mechanical Behaviour of Laminated Composite Adhesive Joints.* Journal of Adhesion Science and Technology, 2009. 23: p. 1477-1491.

275. BOSCH, M.J., P.J.G. SCHREURS, and M.G.D. GEERS, *An improved description of the exponential Xu and Needleman cohesive zone law for mixed-mode decohesion.* Engineering Fracture Mechanics, 2006. 73: p. 1220-1234.

276. PINHO, S.T., L. IANNUCCI, and P. ROBINSON, *Formulation and implementation of decohesion elements in an explicit finite element code.* Composites Part A: Applied Science and Manufacturing, 2006. 37(5): p. 778-789.

277. WILLIAMS, J.G. and H. HADAVINIA, *Analytical solutions of cohesive zone models.* Journal of Mechanics and Physics of Solids, 2002. 50: p. 809-825.

278. MURPHY, N. and A. IVANKOVIC, *The prediction of dynamic fracture evolution in PMMA using a cohesive zone model.* Engineering Fracture Mechanics, 2005. 72: p. 861-875.

279. SCHEIDER, I., *Micromechanical based derivation of traction-separation laws for cohesive model simulations.* Procedia Engineering, 2009. 1: p. 17-21.

280. SMITH, E., *The effect of the stress-relative displacement law on failure predictions using the cohesive zone model.* International Journal of Fracture, 1999. 99(1-2): p. 41-51.

281. SHET, C. and N. CHANDRA, *Effect of the Shape of T-δ Cohesive Zone Curves on the Fracture Response.* Mechanics of Advanced Materials and Structures, 2004. 11: p. 249-275.

282. HADAVINIA, H., L. KAWASHITA, A.J. KINLOCH, D.R. MOORE, and J.G. WILLIAMS, *A numerical analysis of the elastic-plastic peel test.* Engineering Fracture Mechanics, 2006. 73: p. 2324–2335.

283. YANG, Q.D., M.D. THOULESS, and S.M. WARD, *Numerical Simulations of Adhesively-Bonded Beams Failing with Extensive Plastic Deformation.* Journal of the Mechanics and Physics of Solids, 1999. 47: p. 1337-1353.

284. ANVARI, M., I. SCHEIDER, and C. THAULOW, *Simulation of dynamic ductile crack growth using strain-rate and triaxiality-dependent cohesive elements.* Engineering fracture Mechanics, 2006. 73: p. 2210-2228.

285. CHEN, C.R., O. KOLEDNIK, J. HEERENS, and F.D. FISCHER, *Three-dimensional modelling of ductile crack growth: Cohesive zone parameters and crack tip triaxiality.* Engineering Fracture Mechanics, 2005. 72: p. 2072-2094.

286. SCHEIDER, I., M. RAJENDRAN, and A. BANERJEE, *Comparison of different stress-state dependent cohesive zone models applied to thin-walled structures.* Engineering Fracture Mechanics, 2011. 78(3): p. 534-543.

287. KREGTING, R., *Cohesive zone models: towards a robust implementation of irreversible behaviour (Internal report).* 2005, Eindhoven University of Technology.

288. FOULK, J.W., D.H. ALLEN, and K.L.E. HELMS, *Formulation of a three-dimensional cohesive zone model for application to a finite element algorithm.* Computer Methods in Applied Mechanics and Engineering 2000. 183: p. 51-66.

289. HÖGBERG, J.L. and U. STIGH, *Specimen proposals for mixed mode testing of adhesive layer.* Engineering Fracture Mechanics, 2006. 73: p. 2541-2587.

290. ROY, Y.A., R. NARASIMHAN, and P.R. ARORA, *An experimental investigation of constraint effects on mixed mode fracture initiation in a ductile aluminium alloy.* Acta Materialia, 1999. 47(5): p. 1587-1596.

291. SØRENSEN, B.F. and P. KIRKEGAARD, *Determination of mixed mode cohesive laws.* Engineering Fracture Mechanics, 2006. 73: p. 2642-2661.

292. HÖGBERG, J.L., B.F. SØRENSEN, and U. STIGH, *Constitutive behaviour of mixed mode loaded adhesive layer.* International Journal of Solids and Structures, 2007. 44: p. 8335-8354.

293. CAMANHO, P.P., C.G. DAVILA, and M.F.S.F. MOURA, *Numerical Simulation of Mixed-mode Progressive Delamination in Composite Materials.* Journal of Composite Materials, 2003. 37(16).

294. TURON, A., P.P. CAMANHO, J. COSTA, and C.G. DAVILA, *A damage model for the simulation of delamination in advanced composites under variable-mode loading.* Mechanics of Materials, 2006. 38: p. 1072-1089.

295. SALOMONSSON, K. and U. STIGH, *An adhesive interphase element for structural analyses.* International Journal for Numerical Methods in Engineering, 2008. 76: p. 482-500.

296. LI, V.C., C.M. CHAN, and C.K.Y. LEUNG, *Experimental determination of the tension-softening relations for cementitious composites.* Cement and Concrete Research, 1987. 17: p. 441-452.

297. OLSSON, P. and U. STIGH, *On determination of the constitutive properties of thin interphase layers – an exact solution.* International Journal of Fracture, 1989. 41(71-76).

298. SUO, Z., G. BAO, and B. FAN, *Delamination R-Curve phenomena due to damage.* Journal of Mechanics and Physics of Solids, 1992. 40: p. 1-16.

299. LI, V.C., M. MAALEJ, and T. HASHIDA, *Experimental determination of the stress-crack opening relation in fibre cementitious composites with a crack-tip singularity.* Journal of Materials Science, 1994. 39: p. 2719-2724.

300. SØRENSEN, B.F. and T.K. JACOBSEN, *Determination of cohesive laws by the J integral approach.* Engineering Fracture Mechanics, 2003. 70: p. 1841-1858.

301. GOUTIANOS, S. and J. DREWS. *Estimation of interface cohesive laws by digital image correlation.* in *28th Risø International Symposium on Materials Science: Interface Design of Polymer Matrix Composites – Mechanics, Chemistry, Modelling and Manufacturing*. 2007. Roskilde, Denmark.

302. FERREIRA, M.C.D., W.S. VENTURINI, and F. HILD, *On the analysis of notched concrete beams: From measurement with digital image correlation to identification with boundary element method of a cohesive model.* Engineering Fracture Mechanics, 2011. 78(1): p. 71-84.

303. FEDELE, R., B. RAKA, F. HILD, and S. ROUX, *Identification of adhesive properties in GLARE assemblies using digital image correlation.* Journal of the Mechanics and Physics of Solids, 2009. 57(7): p. 1003-1016.

304. TURON, A., J. COSTA, P.P. CAMANHO, and C.G. DAVILA, *Simulation of delamination in composites under high-cycle fatigue.* Composites: Part A, 2007. 38: p. 2270-2282.

305. PIRONDI, A. and F. MORONI, *A Progressive Damage Model for the Prediction of Fatigue Crack Growth in Bonded Joints.* The Journal of Adhesion, 2010. 86: p. 501-521.

306. RICE, J.R. *The mechanics of earthquake rupture.* in *Physics of the earth's interior. Proceedings of the international school of physics "Enrico Fermi", Course 78.* 1980. Amsterdam: Italian Physical Society/North-Holland.

307. COX, B. and Q.D. YANG, *Cohesive models for damage evolution in laminated composites.* International Journal of Fracture, 2005. 133: p. 107-37.

308. YANG, Q.D., B. COX, R.K. NALLA, and R.O. RITCHIE, *Fracture Length scales in human cortical bone: the necessity of nonlinear fracture models.* Biomaterials, 2006. 27: p. 2095-113.

309. GUIAMATSIA, I., G.A.O. DAVIES, J.K. ANKERSEN, and L. IANNUCCI, *A framework for cohesive element enrichment.* Composite Structures, 2010. 92: p. 454–459.

310. FALK, F.L., A. NEEDLEMAN, and J.R. RICE, *A critical evaluation of cohesive zone models of dynamic fracture.* Journal de Physique IV, 2001: p. 543-550.

311. MOES, N. and T. BELYTSCHKO, *Extended finite element method for cohesive crack growth.* Engineering Fracture Mechanics, 2002. 69: p. 813-833

312. CARPINTERI, A., P. CORNETTI, F. BARPI, and F. VALENTE, *Cohesive crack model description of ductile to brittle size-scale transition: dimensional analysis vs. renormalization group theory.* Engineering Fracture Mechanics, 2003. 70: p. 1809–1839.

313. MI, Y., M.A. CRISFIELD, and G.A.O. DAVIES, *Progressive delamination using interface elements.* Journal of Composite Materials, 1998. 32: p. 1246-1272.

314. GONCALVES, J.P.M., M.F.S.F. MOURA, P.M.S.T. CASTRO, and A.T. MARQUES, *Interface element including point-to-surface constraints for three-dimensional problems with damage propagation.* Engineering Computations, 2000. 17: p. 28-47.

315. ELMARAKBI, A.M. and H. FUKUNAGA, *Finite element simulation of delamination growth in composite materials using LS-DYNA.* Composite Science and Technology, 2009. 69(14): p. 2383-2391.

316. HU, N., Y. ZEMBA, H. FUKUNAGA, H.H. Wang, and A.M. ELMARAKBI, *Stable numerical simulations of propagations of complex damages in composite structures under transverse loads.* Composite Science and Technology, 2007. 67: p. 752-765.

317. SAMIMI, M., J.A.W. van DOMMELEN, and M.G.D. GEERS, *An enriched cohesive zone model for delamination in brittle interfaces.* International Journal for Numerical Methods in Engineering, 2009. 80: p. 609-630.

318. HU, N., Y. ZEMBA, T. OKABE, C. YAN, H. FUKUNAGA, and A.M. ELMARAKBI, *A new cohesive model for simulating delamination propagation in composite laminates under transverse loads.* Mechanics of Materials, 2008. 40: p. 920-935.

319. BORG, R., L. NILSSON, and K. SIMONSSON, *Modelling of delamination using a discretized cohesive zone and damage formulation.* Composites Science and Technology, 2002. 62: p. 1299–1314.

320. DIEHL, T., *On using a penalty-based cohesive-zone finite element approach, Part I: Elastic solution benchmarks.* International Journal of Adhesion & Adhesives, 2008. 28: p. 237–255.

321. BORG, R., L. NILSSON, and K. SIMONSSON, *Simulating DCB, ENF and MMB experiments using shell elements and a cohesive zone model.* Composites Science and Technology, 2004. 64: p. 269–278.

322. ATTIA, O., A.J. KINLOCH, and F.L. MATTHEWS, *The prediction of fatigue damage growth in impact-damaged composite skin/stringer structures. Part I: theoretical modelling studies.* Composites Science and Technology, 2003. 63: p. 1463-1472.

323. ROBINSON, P., U. GALVANETTO, D. TUMINO, G. BELLUCCI, and D. VIOLEAU, *Numerical simulation of fatigue-driven delamination using interface elements.* International Journal for Numerical Methods in Engineering, 2005. 63: p. 1824-1848.

324. MUÑOZ, J.J., U. GALVANETTO, and P. ROBINSON, *On the numerical simulation of fatigue driven delamination with interface elements.* International Journal of Fatigue, 2006. 28: p. 1136–1146.

325. KINLOCH, A.J. and S.O. OSIYEMI, *Predicting the fatigue life of adhesively-bonded joints.* The Journal of Adhesion, 1993. 43: p. 79-90.

326. KRENK, S., *Energy release rate of symmetric adhesive joints.* Engineering Fracture Mechanics, 1992. 43(4): p. 549-559.

327. WAHAB, M.M.A., I.A. ASHCROFT, A.D. CROCOMBE, and P.A. SMITH, *Numerical prediction of fatigue crack propagation lifetime in adhesively bonded structures.* International Journal of Fatigue, 2002. 24: p. 705-709.

328. SHENOY, V., I.A. ASHCROFT, G.W. CRITCHLOW, A.D. CROCOMBE, and M.M.A. WAHAB, *An investigation into the crack initiation and propagation behaviour of bonded single-lap joints using back face strain.* International Journal of Adhesion & Adhesives, 2009. 45(4): p. 361-371.

329. NGUYEN, O., E.A. REPETTO, M. ORTIZ, and R.A. RADOVITZKY, *A cohesive model of fatigue crack growth.* International Journal of Fracture, 2001. 110: p. 351-369.

330. ROE, K.L. and T. SIEGMUND, *An irreversible cohesive zone model for interface fatigue crack growth simulation.* Engineering Fracture Mechanics, 2003. 70: p. 209–232.

331. SIEGMUND, T., *A numerical study of transient fatigue crack growth by use of an irreversible cohesive zone model.* International Journal of Fatigue, 2004. 26: p. 929-939.

332. JIANG, H., G. X., and T.S. SRIVATSAN, *Predicting the influence of overload and loading mode on fatigue crack growth: A numerical approach using irreversible cohesive elements.* Finite Elements in Analysis and Design, 2009. 45(10): p. 675-685.

333. WANG, B. and T. SIEGMUND, *Numerical simulation of constraint effects in fatigue crack growth.* International Journal of Fatigue, 2005. 27: p. 1328-1334.

334. MAITI, S. and P.H. GEUBELLE, *A cohesive mode for fatigue failure of polymers.* Engineering Fracture Mechanics, 2005. 72: p. 691-708.

335. MAITI, S. and P.H. GEUBELLE, *Cohesive modelling of fatigue crack retardation in polymers: Crack closure effect.* Engineering Fracture Mechanics, 2006. 73: p. 22-41.

336. URAL, A., V.R. KRISHNAN, and K.D. PAPOULIA, *A cohesive zone model for fatigue crack growth allowing for crack retardation.* International Journal of Solids and Structures, 2009. 46: p. 2453-2462.

337. PEERLINGS, R.H.J., W.A.M. BREKELMANS, R. de BROST, and M.G.D. GEERS, *Gradient-enhanced damage modelling of high-cycle fatigue.* International Journal for Numerical Methods in Engineering, 2000. 49(1547-1569).

338. KOUTSOURELAKIS, P.S., K. KUNTIYAWICHAI, and G.I. SCHUELLER, *Effect of material uncertainties on fatigue life calculations of aircraft fuselages: A cohesive element model.* Engineering Fracture Mechanics, 2006. 73: p. 1202-1219.

339. PIRONDI, A. and F. MORONI, *Simulation of Mixed-Mode I/II Fatigue Crack Propagation in Adhesive Joints with a Modified Cohesive Zone Model.* Journal of Adhesion Science and Technology, 2011. 25(18): p. 2483-2499.

340. RICE, J.R., *Mathematical analysis in the mechanics of fracture* in *Fracture*, H. Liebowitz, Editor. 1968, Academic Press: New York. p. 191-311.

341. HARPER, P.W. and S.R. HALLET, *A fatigue degradation law for cohesive interface elements – Development and application to composite materials.* International Journal of Fatigue, 2010. 32(11): p. 1774–1787.

342. ELMARAKBI, A.M., N. HU, and H. FUKUNAGA, *A new rate-dependent cohesive model for simulating dynamic composite delamination*, in *16TH INTERNATIONAL CONFERENCE ON COMPOSITE MATERIALS*. 2007: Kyoto.

343. ZHOU, F., J.F. MOLINARI, and T. SHIOYA, *A rate-dependent cohesive model for simulating dynamic crack propagation in brittle materials.* Engineering Fracture Mechanics, 2005. 72: p. 1383-1410.

344. BELYTSCHKO, T., R. GRACIE, and G. VENTURA, *A review of extended/generalized finite element methods for material modelling.* Modelling and Simulation in Materials Science and Engineering, 2009. 17(4): p. 1-24.

345. YAZID, A., N. ABDELKADER, and H. ABDELMADJID, *A state-of-the-art review of the X-FEM for computational fracture mechanics.* Applied Mathematical Modelling, 2009. 33: p. 4269-4282.

346. CAMPILHO, R.D.S.G., M.D. BANEA, F.J.P. CHAVES, and L.F.M. DA SILVA, *eXtended Finite Element Method for fracture characterization of adhesive joints in pure mode I.* Computational Materials Science, 2011. 50: p. 1543-1549.

347. PEERLINGS, R.H.J., W.A.M. BREKELMANS, R. DE BORST, and M.G.D. GEERS, *Gradient-enhanced damage modelling of high-cycle fatigue.* International Journal for Numerical Methods in Engineering, 2000. 49: p. 1547-1569.

348. LOPEZ ARMAS, C.A., *Evaluation of Constitutive Laws for the Computer Simulation of Fatigue-Driven Delamination in Composite Materials*, in *Department of Aeronautics*. 2008, Imperial College: London.

349. ELICES, M., G.V. GUINEA, J. GOMEZ, and J. PLANAS, *The Cohesive Zone Model: advantages, limitations and challenges.* Engineering Fracture Mechanics, 2002. 69: p. 137-163.

350. SCHEIDER, I., *Derivation of separation laws for cohesive models in the course of ductile fracture.* Engineering Fracture Mechanics, 2009. 76: p. 1450-1459.

351. ROY, Y.A. and R.H. DODDS, *Simulation of ductile crack growth in thin aluminium panels using 3-D surface cohesive elements.* International Journal of Fracture, 2001. 110: p. 21-45.

352. Van PAEPEGEM, W. and J. DEGRIECK, *A new coupled approach of residual stiffness and strength for fatigue of fibre-reinforced composites.* International Journal of Fatigue, 2002. 24: p. 747-762.

353. Van PAEPEGEM, W., J. DEGRIECK, and P. DE BAETS, *Finite element approach for modelling fatigue damage in fibre-reinforced composite materials.* Composites Part B, 2001. 32: p. 575-588.

354. van PAEPEGEM, W. and J. DEGRIECK, *Fatigue degradation modelling of plain woven glass/epoxy composites.* Composites Part A: Applied Science and Manufacturing, 2001. 32(10): p. 1433-1441.

355. MOSKALA, E.J., *Effects of Mean Stress and Frequency on Fatigue Crack Propagation in Rubber-Toughened Polycarbonate/Copolyester Blends.* JOURNAL OF APPLIED POLYMER SCIENCE, 2003. 49(1): p. 53-64.

356. van der MEER, F.P. and L.J. SLUYS, *Mesh-Independent modelling of both distributed and discrete matrix cracking in interaction with delamination in composites.* Engineering fracture Mechanics, 2010(77): p. 719-735.

357. TURON, A., *Personal Communication.* 2009.

358. *3M™ Scotch-Weld™ Structural Adhesive Film AF163-2.* 2009 [cited November 2009]; Available from: http://multimedia.3m.com.

359. *Araldite® 2014-1.* 2007 [cited 2012 January 2012]; Available from: http://www.intertronics.co.uk/data/ara2014-1.pdf.

360. *BR® 127 Corrosion Inhibiting Primer.* 2008 [cited January 2012]; Available from: https://www.cytec.com/engineered-materials/products/Datasheets/BR%20127%20Primer.pdf.

361. Blackman, B.R.K., H. HADAVINIA, A.J. Kinloch, and J.G. Williams, *The use of a cohesive zone model to study the fracture of fibre composites and adhesively-bonded joints.* International Journal of Fracture, 2003. 119(1): p. 25-46.

362. OSNES, H. and A. ANDERSEN, *Computational analysis of geometric nonlinear effects in adhesively bonded single lap composite joints.* Composites Part B: Engineering, 2003. 34(5): p. 417-427.

363. *ALLOY DATA SHEET EN AW 6082.* 2008 [cited January 2012]; Available from: http://www.cosmosaluminium.gr/pdf/alloy_data_sheet_6082.pdf.

364. Bell, A. and A. Kinloch, *The effect of the substrate material on the value of the adhesive fracture energy, Gc.* Journal of Materials Science Letters, 1997. 16(17): p. 1450-1453.

365. *CYCOM® 977-2 Toughened Epoxy Resin.* 2008 [cited January 2010]; Available from: http://www.cytec.com/engineered-materials/products/Cycom977-2.htm.

366. BAIDAK, A., *(CYTEC Industries Inc.), Personal Communication to B.R.K. Blackman.* 2010.

367. WELSH, J.S., J.S. MAYES, and A.C. BISKNER, *Experimental and Numerical Failure Predictions of Biaxially-loaded Quasi-Isotropic Carbon Composites*, in *16th International Conference on Composite Materials*. 2007: Kyoto, Japan. p. 10.

368. *HexPly® M21 Epoxy Matrix*. 2008 [cited January 2012]; Available from: http://www.hexcel.com/Resources/DataSheets/Prepreg-Data-Sheets/M21_global.pdf.

369. MAHOON, A., *Titanium Adherends*, in *Durability of Structural Adhesives*, A.J. KINLOCH, Editor. 1983, Elsevier Science Publishers: London.

370. *British Aerospace Aircraft Group Weybridge-Bristol Division.* Report No. AL/MAT/3864, 1984.

371. MOLITOR, P. and T. YOUNG, *Adhesives bonding of a titanium alloy to a glass fibre reinforced composite material.* International Journal of Adhesion and Adhesives, 2002. 22(2): p. 101-107.

372. LEAHY, W., T. YOUNG, M. BUGGY, and V. BARRON, *A Study of Environmentally Friendly Titanium Pretreatments for Adhesive Bonding to a Thermoplastic Composite.* Materialwissenschaft und Werkstofftechnik, 2003. 34(4): p. 415-420.

373. BLACKMAN, B.R.K., A.J. KINLOCH, and M. PARASCHI, *The effect of the substrate material on the value of the adhesive fracture energy, Gc: Further considerations.* Journal of Materials Science Letters, 2001. 20: p. 265-267.

374. KINLOCH, A.J. and S.J. SHAW, *The Fracture-Resistance of a toughened epoxy adhesive.* The Journal of Adhesion, 1981. 12: p. 59-77.

375. WILLIAMS, J.G., *End Corrections for Orthotropic DCB Specimens.* Composite Science and Technology, 1989. 35: p. 367-376.

376. HASHEMI, S., A.J. KINLOCH, and J.G. WILLIAMS, *Corrections needed in double-cantilever beam tests for assessing the interlaminar failure of fibre-composites.* Journal of Materials Science Letters, 1989. 8: p. 125-129.

377. KANNINEN, M.F., *A dynamic analysis of unstable crack propagation and arrest in the DCB test specimen.* International Journal of Fracture, 1974. 10(3): p. 415-430.

378. WILLIAMS, J.G., *Large Displacement and End Block Effects in the 'DCB' Interlaminar Test in Modes I and II.* Journal of Composite Materials, 1987. 21: p. 330-348.

379. BRUNNER, A.J., B.R.K. Blackman, and J.G. WILLIAMS, *Calculating a damage parameter and bridging stress from Gic delamination test on fibre composites.* Composite Science and Technology, 2006. 66: p. 785-795.

380. MORAIS, A.B.d. and A.B. PEREIRA, *Application of the effective crack method to mode I and mode II interlaminar fracture of carbon/epoxy unidirectional laminates.* Composites: Part A, 2007. 38: p. 785-794.

381. WANG, Y. and J.G. WILLIAMS, *Corrections for Mode II fracture toughness specimens of composite materials.* Composite Science and Technology, 1992. 43: p. 251-256.

382. ARRESE, A., N. CARBAJAL, G. VARGAS, and F. MUJIKA, *A new method for determining mode II R-curve by the End-Notched Flexure test.* Engineering Fracture Mechanics, 2010. 77: p. 51-70.

383. CARLSSON, L.A., J.W. GILLESPIE, and R.B. PIPES, *On the analysis and design of the end notched flexure (ENF) specimen for mode II testing.* Journal of Composite Materials, 1986. 20: p. 594-604.

384. WANG, J. and P. QIAO, *Novel beam analysis of end notched flexure specimen for mode-II fracture.* Engineering fracture Mechanics, 2004. 71: p. 219-231.

385. MOURA, M.F.S.F. and A.B.d. MORAIS, *Equivalent crack based analysis of ENF and ELS tests.* Engineering fracture Mechanics, 2008. 75: p. 2584-2596.

386. DAVIDSON, B.D., L. YU, and H. HU, *Determination of energy release rate and mode mix in three-dimensional layered structures using plate theory.* International Journal of Fracture, 2000. 105: p. 81-104.

387. *ASTM E647-08 Standard Test Method for Measurement of Fatigue Crack Growth Rates* ASTM International, 2008. E647-08.

388. SHADBOLT, W., *An investigation into the adhesive bonding of composites and titanium alloys.* 2009, Imperial College London: London.

389. BELL, A.J. and A.J. KINLOCH, *The effect of the substrate material on the value of the adhesive fracture energy, Gc.* Journal of MAterials Science Letters, 1997. 16: p. 1450-1453.

390. HERMES, F.H., *Process zone and cohesive element size in numerical simulations of delamination in bi-layers*, in *Department of Mechanical Engineering.* 2010, Eindhoven University of Technology: Eindhoven. p. 86.

391. TOLAN, F.C., S.A. MESTAN, and C.E.M. MORRIS, *Fiber orientation effects in supported adhesives.* Journal of Applied Polymer Science, 1984. 29(12): p. 4415-4420.

392. FRANCIS, E.C. and D. GUTIERREZ-LEMINI, *Effect of scrim cloth on adhesively bonded joints* in *Adhesive joints: Formation, characteristics, and testing.* 1984, Plenum Press: New York. p. 679-685.

393. SANCAKTAR, E., H. JOZAVI, J. BALDWIN, and J. TANG, *Elastoplastic Fracture Behavior of Structural Adhesives Under Monotonic Loading.* The Journal of Adhesion, 1987. 23(4): p. 233-262.

394. AGLAN, H., Z. ABDO, and S. SHROFF, *Fracture and fatigue behavior of scrim cloth adhesively bonded joints with and without rivet holes.* Journal of Adhesion Science and Technology, 1995. 9(2): p. 177-197.

395. LEE, S.M., *Mode II delamination failure mechanisms of polymer matrix composites.* Journal of Materials Science, 1997. 32: p. 1287-1295.

396. BLACKMAN, B.R.K., M. CONROY, A. IVANKOVIC, A. KARAC, A.J. KINLOCH, and J.G. WILLIAMS. *Mode-mixity in beam-like geometries: Linear elastic cases and local partitioning.* in *ECCM15 - 15th European Conference on Composite Materials.* 2012. Venice, Italy.

397. OBRIEN, T.K., *Towards a Damage Tolerance Philosophy for Composite Materials and Structures*, in *NASA Technical Memorandum 100548* 1988, NASA, Langley Research Centre: Hampton (VA).

398. *ABAQUS THEORY MANUAL VERSION 6.8.* 2008.

399. MABSON, G., B. DOPER, and L. DEOBALD, *User Manual for Fracture and Traction Interface Elements - Version 1.3.* 2004, The Boeing Company.

400. ASP, L.E., A. SJOGREN, and E. GREENHALGH, *Delamination growth and thresholds in carbon/epoxy composite under fatigue loading.* Journal of Composites Technology and Research, 2001. 23(2): p. 55-68.

401. YODER, G.R., L.A. COOLEY, and T.W. CROOKER, *Procedures for Precision Measurement of Fatigue Crack Growth Rate Using Crack-Opening Displacement Techniques*, in *Fatigue Crack Growth Measurement And Data Analysis*, S.J. HUDAK and R.J. BUCCI, Editors. 1981, ASTM International: Baltimore, USA.

402. O'BRIEN, T.K., W.M. JOHNSON, and G.J. TOLAN, *Mode II Interlaminar Fracture Toughness and Fatigue Characterization of a Graphite Epoxy Composite Material.* 2010, NASA/TM-2010-216838: Langley Research Center, Hampton, Virginia, USA.

403. BUTKUS, L.M., *Environmental Durability of Adhesively Bonded Joints.* 1997, The Georgia Institute of Technology. p. 343.

404. LOH, W.K., A.D. CROCOMBE, M.M.A. WAHAB, and I.A. ASHCROFT, *Modelling interfacial degradation using interfacial rupture elements.* The Journal of Adhesion, 2003. 79: p. 1135-1160.

405. TAYLOR, A.C., *Durability and Lifetime Predictions of Adhesive Joints*. 1996, AEA Technology: Didcot.

406. FERNANDO, M., W.W. HARJOPRAYITO, and A.J. KINLOCH, *A fracture mechanics study of the influence of moisture on the fatigue behaviour of adhesively bonded aluminium-alloy joints.* International Journal of Adhesion and Adhesives, 1996. 16(2): p. 113-119.

407. LITTLE, M.S.G., *The durability of structural adhesive joints*, in *Mechanical Engineering Department*. 1999, Imperial College London: London.

408. TAYLOR, A.C., *The impact and durability performance of adhesively bonded metal joints*, in *Mechanical Engineering Department*. 1997, Imperial College London: London.

409. LEE, S.H., *The Fatigue and Fracture Properties of Nano-modified Epoxy Polymers*, in *Mechanical Engineering Department*. 2012 (*Expected*), Imperial College London: London.

410. XIE, D. and A.M. WAAS, *Discrete cohesive zone model for mixed-mode fracture using finite element analysis.* Engineering Fracture Mechanics, 2006. 73(13): p. 1783-1796.

411. VOLKERSEN, O., *Recent research on the theory of bonded joints*. 1964, NASA: Washington. p. 27.

412. TSAI, M.Y. and J. MORTON, *An investigation into the stresses in double-lap adhesive joints with laminated composite adherends.* International Journal of Solids and Structures, 2010. 47: p. 3317-3325.

413. GOGLIO, L. and M. ROSSETTO, *Precision of the one-dimensional solutions for bonded double lap joints.* International Journal of Adhesion & Adhesives, 2011. 31: p. 301-314.

414. KORSUNSKY, A.M., X. SONG, J. BELNOUE, T. JUN, F. HOFMANN, P.F.P. DE MATOS, D. NOWELL, D. DINI, O. APARICIO-BLANCO, and M.J. WALSH, *Crack tip deformation fields and fatigue crack growth rates in Ti–6Al–4V.* International Journal of Fatigue, 2009. 31: p. 1771-1779.

415. YURI, T., Y. ONO, and T. OGATA, *Effect of Test Frequency on Fatigue Crack Growth Rates of Ti6Al4V ELI Alloy at Cryogenic Temperature*, in *Advances in Cryogenic Engineering: Transactions of the International Cryogenic Materials Conference - ICMC*, U. BALACHANDRAN, Editor. 2006, American Institute of Physics.

416. RITCHIE, R.O., D.L. DAVIDSON, B.L. BOYCE, J.P. CAMPBELL, and O. RODER, *High-cycle fatigue of Ti–6Al–4V.* Fatigue & Fracture of Engineering Materials & Structures, 1999. 22: p. 621-631.

417. FEIH, S., *Development of a user element in ABAQUS for modelling of cohesive laws in composite structures*. 2005, Risø National Laboratory: Roskilde (Denmark). p. 52.

Appendix A: Linear-Cubic Evolution Law

A.1 Linear-Cubic Evolution Law for Static Problems (F=0)

The monotonic scalar function $Q(\lambda)$ defining the shape of the traction-separation curve adopts the following expression for the linear-cubic law:

$$Q_{Linear-cubic}(\lambda) = 1 - \frac{\Delta^0}{\lambda}\left(1 + \left(\frac{\lambda - \Delta^0}{\Delta^f - \Delta^0}\right)^2 \cdot \left(2\frac{\lambda - \Delta^0}{\Delta^f - \Delta^0} - 3\right)\right) \tag{A.1}$$

The onset of damage occurs at Δ^0, while Δ^f represents a fully damaged interface ($d = 1$). The damage variable at the time t is given by $d(t) = Q(r^t)$.

A.2 Linear-Cubic Evolution Law for Fatigue Problems (F≠0)

A.2.1 Damage increment due to changes in the applied displacement

The derivative of the damage with respect to the displacement jump norm ($\frac{\partial d}{\partial \lambda}$) written in terms of λ for the linear-cubic evolution law is given by:

$$d_s(t) = Q(r^t) = 1 - \frac{\Delta^0}{r^t}\left(1 + \left(\frac{r^t - \Delta^0}{\Delta^f - \Delta^0}\right)^2 \cdot \left(2\frac{r^t - \Delta^0}{\Delta^f - \Delta^0} - 3\right)\right) \longrightarrow$$
$$\longrightarrow \frac{\partial d_s}{\partial \lambda} = \frac{\Delta^0}{\lambda^2(\Delta^f - \Delta^0)^2}\left[\left(\Delta^f - \Delta^0\right)^3 - 2(2\lambda^3 - 3\Delta^0\lambda^2 + (\Delta^0)^3) + 3\left(\Delta^f - \Delta^0\right)(\lambda^2 - (\Delta^0)^2\right. \tag{A.2}$$

$$\Delta d_s(t, t+\Delta t) = \int_{r^t}^{r^{t+\Delta t}} \frac{\Delta^0}{\lambda^2(\Delta^f - \Delta^0)^2}\left[\left(\Delta^f - \Delta^0\right)^3 - 2(2\lambda^3 - 3\Delta^0\lambda^2 + (\Delta^0)^3)\right.$$
$$\left. + 3\left(\Delta^f - \Delta^0\right)(\lambda^2 - (\Delta^0)^2)\right] d\lambda \tag{A.3}$$

$$\Delta d_s(t, t+\Delta t) = \frac{\Delta^0}{(\Delta^f - \Delta^0)^3}\left[\left(\Delta^f\right)^2(\Delta^f - 3\Delta^0)\left(\frac{1}{r^t} - \frac{1}{r^{t+\Delta t}}\right) + 3\left(\Delta^f + \Delta^0\right)\left(r^{t+\Delta t} - r^t\right)\right.$$
$$\left. - 2\left(\left(r^{t+\Delta t}\right)^2 - (r^t)^2\right)\right] \tag{A.4}$$

Unlike for the bilinear law, equation (3.42) is not enough to ensure that $\Delta d_s(t, t+\Delta t) \geq 0$ in the linear-cubic case. Additional precautions must be taken in the linear-cubic case to guarantee that no material healing occurs (i.e. avoid any damage decrease). As a result (A.4) should be re-written as:

$$\Delta d_s(t, t+\Delta t) =$$

$$= \begin{cases} \dfrac{\Delta^0\left[(\Delta^f)^2(\Delta^f - 3\Delta^0)\left(\frac{1}{r^t} - \frac{1}{r^{t+\Delta t}}\right) + 3(\Delta^f + \Delta^0)(r^{t+\Delta t} - r^t) - 2((r^{t+\Delta t})^2 - (r^t)^2)\right]}{(\Delta^f - \Delta^0)^3} & \Delta d_s \geq 0 \\ 0 & \Delta d_s < 0 \end{cases} \quad \text{(A.5)}$$

The same expression given in (A.4) (obtained by integration) would be obtained by direct application of the quasi-static evolution laws $Q(\lambda)$ assuming that $\Delta d_s(t, t+\Delta t)$ is the increment in quasi-static damage:

$$\Delta d_s = d_s(t+\Delta t) - d_s(t) = Q\left(r^{t+\Delta t}\right) - Q(r^t) =$$

$$= -\frac{\Delta^0}{r^{t+\Delta t}}\left(1 + \left(\frac{r^{t+\Delta t} - \Delta^0}{\Delta^f - \Delta^0}\right)^2 \cdot \left(2\frac{r^{t+\Delta t} - \Delta^0}{\Delta^f - \Delta^0} - 3\right)\right) + \frac{\Delta^0}{r^t}\left(1 + \left(\frac{r^t - \Delta^0}{\Delta^f - \Delta^0}\right)^2 \cdot \left(2\frac{r^t - \Delta^0}{\Delta^f - \Delta^0} - 3\right)\right) \quad \text{(A.6)}$$

$$= \frac{\Delta^0}{(\Delta^f - \Delta^0)^3}\left[\left(\Delta^f\right)^2\left(\Delta^f - 3\Delta^0\right)\left(\frac{1}{r^t} - \frac{1}{r^{t+\Delta t}}\right) + 3\left(\Delta^f + \Delta^0\right)\left(r^{t+\Delta t} - r^t\right) - 2\left(\left(r^{t+\Delta t}\right)^2 - (r^t)^2\right)\right]$$

A.2.2 Damage accumulation due to the number of cycles

For the linear-cubic law, the ratio between A_d (the damaged area of the element or integration point) and the area of the element (A_e) can be expressed as:

$$\frac{A_d}{A_e} = f(\lambda) = \frac{\Delta^0\Delta^f\left(3\Delta^f\Delta^0 - (\Delta^0)^2 - \left(\Delta^f\right)^2\right) - \lambda^4 + \left(\Delta^0 + \Delta^f\right)\lambda^3 + \left(\left(\Delta^f\right)^3 - \Delta^0\left(\Delta^f\right)^2\right)\lambda}{\Delta^f(\Delta^f - \Delta^0)^3} \quad \text{(A.7)}$$

Taking into account this result, the function $H(\lambda)$ defined in equation (3.52) would be given by:

$$H(\lambda) = \frac{\Delta^0\Delta^f\left[\left(\Delta^f - \Delta^0\right)^3 - 2(2\lambda^3 - 3\Delta^0\lambda^2 + (\Delta^0)^3) + 3(\lambda^2 - (\Delta^0)^2)\left(\Delta^f - \Delta^0\right)\right]}{\lambda^2[-4\lambda^3 + 3(\Delta^0 + \Delta^f)\lambda^2 + ((\Delta^f)^3 - 3\Delta^0(\Delta^f)^2)]} \tag{A.8}$$

A.2.3 Maximum applied G_{max}

The value of G_{max} required to evaluate the modified Paris law can be seen as the area under the cohesive law up to λ_{max} (the maximum displacement jump norm applied to the element). As shown in equation (3.71), the dependence of G_{max} on the shape of the traction-separation law is taken into account through $S\left(\lambda_{max}(t)\right)$, which adopts the following expression for the linear-cubic law:

$$\begin{cases} S_{Linear-Cubic}\left(\lambda_{max}(t)\right) = \dfrac{k\Delta^0(\lambda_{max} - \Delta^0)}{2(\Delta^f - \Delta^0)^3}\left[\lambda_{max}^3 + A_1\lambda_{max}^2 + A_2\lambda_{max} + A_3\right] \\ A_1 = -(\Delta^0 + 2\Delta^f) \\ A_2 = \Delta^0(4\Delta^f - \Delta^0) \\ A_3 = (2(\Delta^f)^3 - 6\Delta^0(\Delta^f)^2 + \Delta^f(\Delta^0)^2 - (\Delta^0)^3) \end{cases} \tag{A.9}$$

Appendix B: Summary of Classical Plate Theory for 2D problems

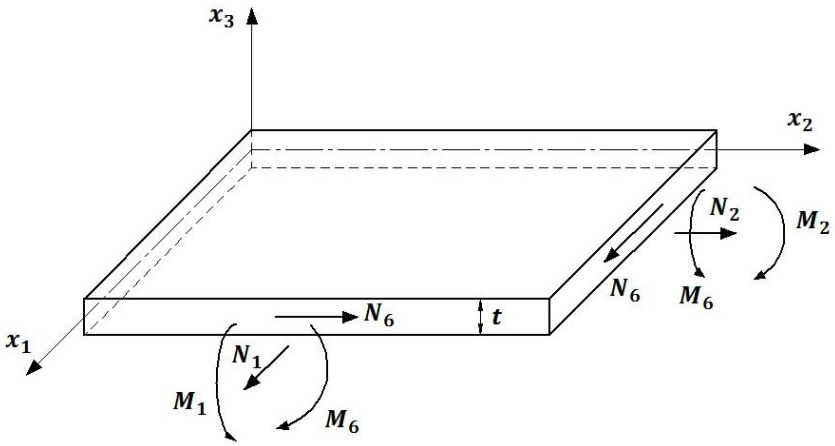

Figure B.1. Load and moment resultants per unit length in a thin laminate according to classical plate theory.

Displacement field:

$$\begin{cases} u_1 = u_1^0(x_1, x_2) - x_3 \dfrac{\partial w}{\partial x_1} \\ u_2 = u_2^0(x_1, x_2) - x_3 \dfrac{\partial w}{\partial x_2} \\ u_3 = w(x_1, x_2) \end{cases} \tag{B.1}$$

where u_1^0, u_2^0 and w are the mid-surface displacements.

Strain field:

$$\begin{bmatrix} \varepsilon_1 \\ \varepsilon_2 \\ \varepsilon_6 \end{bmatrix} = \begin{bmatrix} \dfrac{\partial u_1}{\partial x_1} \\ \dfrac{\partial u_2}{\partial x_2} \\ \dfrac{\partial u_1}{\partial x_2} + \dfrac{\partial u_2}{\partial x_1} \end{bmatrix} = \begin{bmatrix} \dfrac{\partial u_1^0}{\partial x_1} \\ \dfrac{\partial u_2^0}{\partial x_2} \\ \dfrac{\partial u_1^0}{\partial x_2} + \dfrac{\partial u_2^0}{\partial x_1} \end{bmatrix} + x_3 \begin{bmatrix} \dfrac{\partial^2 w}{\partial {x_1}^2} \\ \dfrac{\partial^2 w}{\partial {x_2}^2} \\ \dfrac{\partial^2 w}{\partial x_1 \partial x_2} \end{bmatrix} \longrightarrow \bar{\varepsilon} = \overline{\varepsilon^0} + x_3 \bar{\kappa} \tag{B.2}$$

where $\overline{\varepsilon^0}$ and $\bar{\kappa}$ are the mid-surface strains and curvatures respectively.

Constitutive behaviour:

$$\begin{bmatrix}\sigma_1\\ \sigma_2\\ \sigma_6\end{bmatrix}=\begin{bmatrix}Q_{11} & Q_{12} & Q_{16}\\ Q_{12} & Q_{22} & Q_{26}\\ Q_{16} & Q_{26} & Q_{66}\end{bmatrix}\begin{bmatrix}\varepsilon_1\\ \varepsilon_2\\ \varepsilon_6\end{bmatrix}\longrightarrow \bar{\sigma}=\bar{\bar{Q}}\bar{\varepsilon}=\bar{\bar{Q}}\overline{\varepsilon^0}+x_3\bar{\bar{Q}}\bar{\kappa} \tag{B.3}$$

Resultants per unit length in the x_2-direction:

$$\begin{bmatrix}N_1\\ N_2\\ N_6\end{bmatrix}=\bar{N}=\int_{-\frac{t}{2}}^{\frac{t}{2}}\bar{\sigma}\,dx_3=\int_{-\frac{t}{2}}^{\frac{t}{2}}\left(\bar{\bar{Q}}\overline{\varepsilon^0}+x_3\bar{\bar{Q}}\bar{\kappa}\right)dx_3=\bar{\bar{A}}\overline{\varepsilon^0}+\bar{\bar{B}}\bar{\kappa} \tag{B.4}$$

$$\begin{bmatrix}M_1\\ M_2\\ M_6\end{bmatrix}=\bar{M}=\int_{-\frac{t}{2}}^{\frac{t}{2}}x_3\bar{\sigma}\,dx_3=\int_{-\frac{t}{2}}^{\frac{t}{2}}x_3\left(\bar{\bar{Q}}\overline{\varepsilon^0}+x_3\bar{\bar{Q}}\bar{\kappa}\right)dx_3=\bar{\bar{B}}\overline{\varepsilon^0}+\bar{\bar{D}}\bar{\kappa} \tag{B.5}$$

where $\bar{N}$ and $\bar{M}$ are the load and moment resultants per unit length in the x_2-direction, and $\bar{\bar{A}}$, $\bar{\bar{B}}$ and $\bar{\bar{D}}$ are the extensional, coupling and bending stiffness matrixes.

Extensional ($\bar{\bar{A}}$), coupling ($\bar{\bar{B}}$) and bending ($\bar{\bar{D}}$) stiffness sub-matrixes:

$$\begin{cases}\bar{\bar{A}}=\int_{-\frac{t}{2}}^{\frac{t}{2}}\bar{\bar{Q}}\,dx_3\\ \bar{\bar{B}}=\int_{-\frac{t}{2}}^{\frac{t}{2}}x_3\bar{\bar{Q}}\,dx_3\\ \bar{\bar{D}}=\int_{-\frac{t}{2}}^{\frac{t}{2}}x_3^2\bar{\bar{Q}}\,dx_3\end{cases} \tag{B.6}$$

$$\begin{bmatrix}\bar{N}\\ \bar{M}\end{bmatrix}=\begin{bmatrix}\bar{\bar{A}} & \bar{\bar{B}}\\ \bar{\bar{B}} & \bar{\bar{D}}\end{bmatrix}\begin{bmatrix}\overline{\varepsilon^0}\\ \bar{\kappa}\end{bmatrix}\longrightarrow\begin{bmatrix}\overline{\varepsilon^0}\\ \bar{\kappa}\end{bmatrix}=\begin{bmatrix}\bar{\bar{A}}' & \bar{\bar{B}}'\\ \bar{\bar{B}}' & \bar{\bar{D}}'\end{bmatrix}\begin{bmatrix}\bar{N}\\ \bar{M}\end{bmatrix} \tag{B.7}$$

Simplification problems where only $N_1$and M_1 exist:

$$\begin{cases}N_1=A\varepsilon^0+B\kappa\\ M_1=B\varepsilon^0+D\kappa\end{cases}\longrightarrow\begin{matrix}\varepsilon^0=A'N_1+B'M_1\\ \kappa=B'N_1+D'M_1\end{matrix} \tag{B.8}$$

Simplification for homogeneous orthotropic material

$$\begin{cases}A=E_1't\\ B=0\\ D=\dfrac{E_1't^3}{12}\end{cases}\longrightarrow\begin{matrix}A'=\dfrac{1}{E_1't}\\ B'=0\\ D'=\dfrac{12}{E_1't^3}\end{matrix} \tag{B.9}$$

Appendix C: Geometrical and material constants derived from Davidson´s Crack Tip Element (CTE) analysis

The various constants derived in the analysis of the Crack tip Element (CTE, see Figure 2.9) proposed by Schapery and Davidson are presented in this section. These quantities depend only on the material properties and geometry (thickness) of the cracked and un-cracked sections of that CTE.

According to classical plate theory, the equations relating the resultants per unit width in the un-cracked portions of the CTE (N_3 and M_3) to the corresponding mid-surface strain (ε^0) and curvature (κ) are given by (see Appendix B):

$$\begin{cases} N_3 = A\varepsilon^0 + B\kappa \\ M_3 = B\varepsilon^0 + D\kappa \end{cases} \longrightarrow \begin{matrix} \varepsilon^0 = A'N_3 + B'M_3 \\ \kappa = B'N_3 + D'M_3 \end{matrix} \tag{C.1}$$

where A, B and D are the extensional, coupling and bending stiffness matrixes and A', B' and D' their respective inverses. Similarly, for the sub-laminate i in the cracked region:

$$\begin{cases} N_i = A_i\varepsilon_i^0 + B_i\kappa_i \\ M_i = B_i\varepsilon_i^0 + D_i\kappa_i \end{cases} \longrightarrow \begin{matrix} \varepsilon_i^0 = A_i'N + B_i'M \\ \kappa_i = B_i'N + D_i'M \end{matrix} \tag{C.2}$$

Adapting the results shown in references [171, 172] to the nomenclature used defined in Figure 2.9:

$$\begin{cases} a_{11} = A_1A' + \left(B_1 - A_1\dfrac{h_2}{2}\right)B' \\ a_{12} = A_1B' + \left(B_1 - A_1\dfrac{h_2}{2}\right)D' \\ a_{21} = B_1A' + \left(D_1 - B_1\dfrac{h_2}{2}\right)B' \\ a_{22} = B_1B' + \left(D_1 - B_1\dfrac{h_2}{2}\right)D' \end{cases} \tag{C.3}$$

$$\begin{cases} c_1 = A_1' + A_2' + B_1' h_1 - B_2' h_2 + D_1' \dfrac{{h_1}^2}{4} + D_2' \dfrac{{h_2}^2}{4} \\ c_2 = D_1' + D_2' \\ c_{12} = D_2' \dfrac{h_2}{2} - D_1' \dfrac{h_1}{2} - B_1' - B_2' \end{cases} \tag{C.4}$$

$$\sin \Gamma = \frac{c_{12}}{\sqrt{c_1 c_2}} \tag{C.5}$$

For orthotropic materials and taking into account that $2h = h_1 + h_2$ (see Figure 2.9):

$$\text{Un-cracked section } \begin{cases} A = E_1'(h_1 + h_2) & B = 0 & D = \dfrac{E_1'(h_1 + h_2)^3}{12} \\ A' = \dfrac{1}{E_1'(h_1 + h_2)} & B' = 0 & D' = \dfrac{12}{E_1'(h_1 + h_2)^3} \end{cases} \tag{C.6}$$

$$\text{Cracked sub-laminate "}i\text{" } \begin{cases} A_i = E_{1i}' h_i & B_i = 0 & D_i = \dfrac{E_{1i}' {h_i}^3}{12} \\ A_i' = \dfrac{1}{E_{1i}' h_i} & B_i' = 0 & D_i' = \dfrac{12}{E_{1i}' {h_i}^3} \end{cases} \tag{C.7}$$

For the case in which the both cracked sections are made from the same homogenous orthotropic material ($E_{1i}' = E_1'$), and defining $\alpha = h_2/h_1$

$$\begin{cases} a_{11} = \cdots = \dfrac{h_1}{h_1 + h_2} = \dfrac{1}{1 + \alpha} \\ a_{12} = \cdots = -\dfrac{6 h_1 h_2}{(h_1 + h_2)^3} = -\dfrac{6\alpha}{(1 + \alpha)^3} \dfrac{1}{h_1} \\ a_{21} = \cdots = 0 \\ a_{22} = \cdots = \dfrac{h_1^3}{(h_1 + h_2)^3} = \dfrac{1}{(1 + \alpha)^3} \end{cases} \tag{C.8}$$

$$\begin{cases} c_1 = \cdots = \dfrac{4}{E_1'} \left(\dfrac{1}{h_1} + \dfrac{1}{h_2} \right) = \dfrac{4}{E_1'} \dfrac{1}{h_1} \left(\dfrac{1 + \alpha}{\alpha} \right) \\ c_2 = \cdots = \dfrac{12}{E_1'} \left(\dfrac{1}{h_1^3} + \dfrac{1}{h_2^3} \right) = \dfrac{12}{E_1'} \dfrac{1}{h_1^3} \left(\dfrac{1 + \alpha^3}{\alpha^3} \right) \\ c_{12} = \cdots = \dfrac{6}{E_1'} \left(\dfrac{1}{h_2^2} - \dfrac{1}{h_1^2} \right) = \dfrac{6}{E_1'} \dfrac{1}{h_1^2} \left(\dfrac{1 - \alpha^2}{\alpha^2} \right) \end{cases} \tag{C.9}$$

Note that the last expressions are valid for both unidirectional composite laminates and isotropic materials ($E_1' = E$). Furthermore, they could be applied to plane stress ($E_1' = E_1$) or plane strain ($E_1' = E_1/(1 - \upsilon_{12}\upsilon_{21})$) conditions.

Appendix D: Equivalence in the total energy release rate obtained using beam and plate theories

The equivalence between the total energy release rates obtained with the methods proposed by Williams and Davidson when transverse shear effects are neglected in the former is established here for the specimen geometries discussed in this thesis. For simplicity these demonstrations are restricted here to the case of the same homogeneous orthotropic material being used for both arms.

D.1 The ADCB test specimen

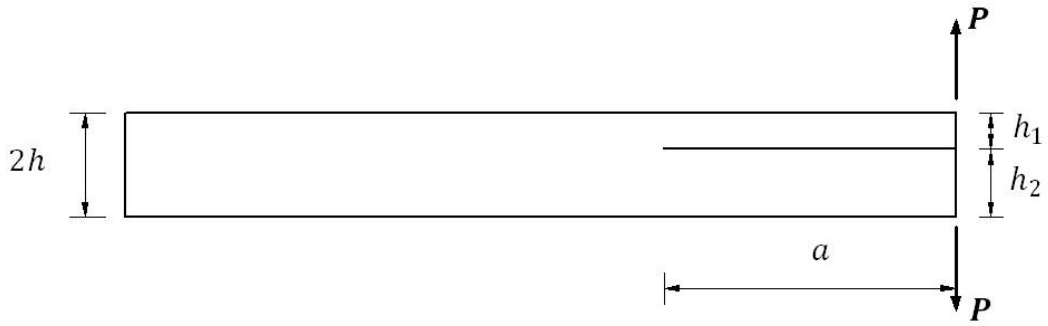

Figure D.1. Schematic representation of the ADCB test specimen (width, *B*).

This demonstration is also valid for the DCB test specimen (symmetric case, i.e. $h_1 = h_2 = h$)

Williams method (beam analysis)

Taking into account the sign criteria shown in Figure 2.8-b:

$$\begin{cases} N_1 = N_2 = 0 \\ M_1 = -Pa \\ M_2 = Pa \end{cases} \quad \text{(D.1)}$$

Using equation (2.13) and omitting the contribution of transverse shear stresses:

$$G_{ADCB}^{William} = \frac{1}{16E_1'IB}\left[\frac{P^2a^2}{\xi^3} + \frac{P^2a^2}{(1-\xi)^3}\right] = \frac{3P^2a^2}{4E_1'B^2h^3}\left[\frac{(1-\xi)^3+\xi^3}{(1-\xi)^3\xi^3}\right]$$
$$= \frac{3P^2a^2}{4E_1'B^2h^3}\left[\frac{1-3\xi+3\xi^2}{(1-\xi)^3\xi^3}\right] \tag{D.2}$$

where ξ is the thickness parameter defined in (2.14)

Davidson method (classical plate theory)

Taking the forces and moments as positive in the directions shown in Figure 2.9, and using the equilibrium equations (2.18) and (2.19):

$$\begin{cases} N_1 = N_2 = 0 \\ M_1 = \dfrac{Pa}{B} \\ M_2 = \dfrac{-Pa}{B} \end{cases} \longrightarrow \begin{cases} N_3 = M_3 = 0 \\ N_c = 0 \\ M_c = \dfrac{Pa}{B} \end{cases} \tag{D.3}$$

Using equation (2.17) and the definitions of the quantities c_1, c_2, c_{12} and a_{ij} given in Appendix C (expressed in terms of the thickness ration $\alpha = h_2/h_1$):

$$G_{ADCB}^{Davidson} = \frac{1}{2}\left[c_2\frac{P^2a^2}{B^2}\right] = \frac{6P^2a^2}{E_1'B^2h_1^3}\left(\frac{1+\alpha^3}{\alpha^3}\right) \overset{h_1=\frac{2h}{1+\alpha}}{=\!=} \frac{3P^2a^2}{4E_1'B^2h^3}\left[\frac{(1+\alpha^3)(1+\alpha)^3}{\alpha^3}\right] \tag{D.4}$$

Substituting $\alpha = (1-\xi)/\xi$ in the last expression and operating:

$$G_{ADCB}^{Davidson} = \frac{3P^2a^2}{4E_1'B^2h^3}\left[\frac{\left(1+\left(\frac{1-\xi}{\xi}\right)^3\right)\left(1+\left(\frac{1-\xi}{\xi}\right)\right)^3}{\left(\frac{1-\xi}{\xi}\right)^3}\right] = \frac{3P^2a^2}{4E_1'B^2h^3}\left[\frac{(1-\xi)^3+\xi^3}{(1-\xi)^3\xi^3}\right] \tag{D.5}$$
$$= G_{ADCB}^{William}$$

D.2 The ELS test specimen

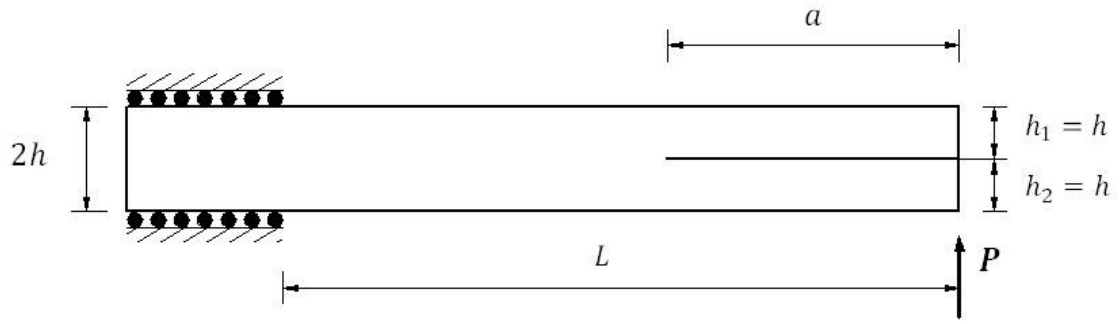

Figure D. 2. Schematic representation of the ELS test specimen (width, *B*).

The demonstration of the equivalence between expressions of the total energy release rate for the ELS geometry is restricted here to the symmetric case, since this was the only configuration used in this project. Note that for that that case ($h_1 = h_2 = h$), $\xi = 1/2$ and $\alpha = 1$.

Williams method (beam analysis)

Taking into account the sign criteria shown in Figure 2.8-b:

$$\begin{cases} N_1 = N_2 = 0 \\ M_1 = M_2 = -\dfrac{P}{2}a \end{cases} \tag{D.6}$$

Using equation (2.13) and omitting transverse shear effects:

$$G_{ELS}^{William} = \frac{1}{16E_1'IB}\left[\frac{\frac{P^2}{4}a^2}{\left(\frac{1}{2}\right)^3} + \frac{\frac{P^2}{4}a^2}{\left(\frac{1}{2}\right)^3} - P^2a^2\right] = \frac{3P^2a^2}{16E_1'IB} = \frac{9P^2a^2}{4E_1'B^2h^3} \tag{D.7}$$

Davidson method (classical plate theory)

Taking the forces and moments as positive in the directions shown in Figure 2.9, and using the equilibrium equations (2.18) and (2.19):

$$\begin{cases} N_1 = N_2 = 0 \\ M_1 = M_2 = \dfrac{Pa}{2B} \end{cases} \rightarrow \begin{cases} N_3 = 0 \\ M_3 = \dfrac{Pa}{B} \end{cases} \rightarrow \begin{cases} N_c = \dfrac{-3Pa}{4Bh} \\ M_c = 0 \end{cases} \tag{D.8}$$

Using equation (2.17) and the definitions of the quantities c_1, c_2, c_{12} and a_{ij} given in Appendix C:

$$G_{ELS}^{Davidson} = \frac{1}{2}\left[c_1 \frac{9P^2a^2}{16B^2h^2}\right] \overset{c_1=\frac{8}{h_1E_1'}}{\triangleq} \frac{9P^2a^2}{4E_1'B^2h^3} = G_{ELS}^{William} \tag{D.9}$$

D.3 The ENF test specimen

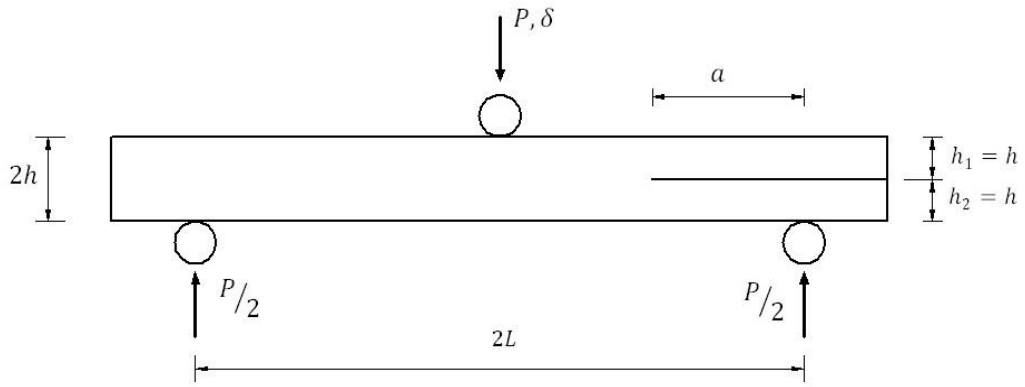

Figure D. 3. Schematic representation of the 3ENF test specimen (width, *B*).

The demonstration of the equivalence between expressions of the total energy release rate for the 3ENF geometry is restricted here to the symmetric case, since this was the only configuration used in this project. Note that for that that case ($h_1 = h_2 = h$), $\xi = 1/2$ and $\alpha = 1$.

Williams method (beam analysis)

Taking into account the sign criteria shown in Figure 2.8-b:

$$\begin{cases} N_1 = N_2 = 0 \\ M_1 = M_2 = -\dfrac{P}{4}a \end{cases} \tag{D.10}$$

Using equation (2.13) and omitting the contribution of transverse shear stresses:

$$G_{3ENF}^{William} = \frac{1}{16E_1'IB}\left[\frac{\frac{P^2}{16}a^2}{\left(\frac{1}{2}\right)^3} + \frac{\frac{P^2}{16}a^2}{\left(\frac{1}{2}\right)^3} - \frac{P^2a^2}{4}\right] = \frac{3P^2a^2}{64E_1'IB} = \frac{9P^2a^2}{16E_1'B^2h^3} \tag{D.11}$$

Davidson method (classical plate theory)

Taking the forces and moments as positive in the directions shown in Figure 2.9, and using the equilibrium equations (2.18) and (2.19):

$$\begin{cases} N_1 = N_2 = 0 \\ M_1 = M_2 = \dfrac{Pa}{4B} \end{cases} \rightarrow \begin{cases} N_3 = 0 \\ M_3 = \dfrac{Pa}{2B} \end{cases} \rightarrow \begin{cases} N_c = \dfrac{-3Pa}{8Bh} \\ M_c = 0 \end{cases} \tag{D.12}$$

Using equation (2.17) and the definitions of the quantities c_1 , c_2 , c_{12} and a_{ij} given in Appendix C:

$$G_{3ENF}^{Davidson} = \frac{1}{2}\left[c_1 \frac{9P^2a^2}{64B^2h^2}\right] \overset{c_1=\frac{8}{h_1E_1'}}{=} \frac{9P^2a^2}{16E_1'B^2h^3} = G_{3ENF}^{William} \tag{D.13}$$

D.4 The AFRMM test specimen

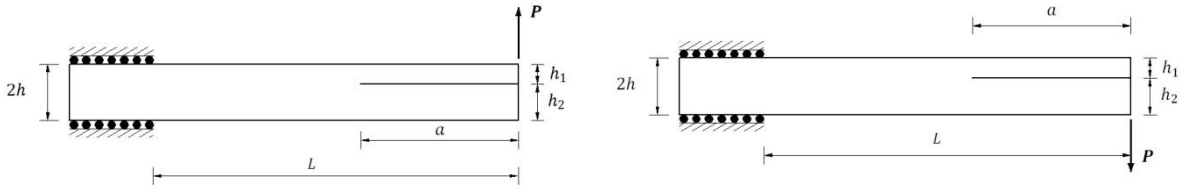

(a) (b)

Figure D. 4. Schematic representation of the AFRMM test specimen (width, B) for the cases in which (a) the upper arm (thickness h_1) is loaded and (b) the bottom arm(thickness h_2) is loaded.

D.4.1 Case I: Upper arm (thickness h_1) loaded

This case is illustrated in Figure D. 4-a:

Williams method (beam analysis)

Taking into account the sign criteria shown in Figure 2.8-b:

$$\begin{cases} N_1 = N_2 = 0 \\ M_1 = -Pa \\ M_2 = 0 \end{cases} \tag{D.14}$$

Using equation (2.13) and omitting transverse shear effects:

$$G_{AFRMM/h_1}^{William} = \frac{1}{16E_1'IB}\left[\frac{P^2a^2}{\xi^3} + P^2a^2\right] = \frac{3P^2a^2}{4E_1'B^2h^3}\left[\frac{1-\xi^3}{\xi^3}\right] \tag{D.15}$$

where ξ is the thickness parameter defined in (2.14)

Davidson method (classical plate theory)

Taking the forces and moments as positive in the directions shown in Figure 2.9, and using the equilibrium equations (2.18) and (2.19):

$$\begin{cases} N_1 = N_2 = M_2 = 0 \\ M_1 = \dfrac{Pa}{B} \end{cases} \rightarrow \begin{cases} N_3 = 0 \\ M_3 = M_1 = \dfrac{Pa}{B} \end{cases} \rightarrow \begin{cases} N_c = a_{12}M_1 \\ M_c = \left(1 + a_{12}\frac{h_1}{2} - a_{22}\right)M_1 \end{cases} \tag{D.16}$$

Using equation (2.17) and the definitions of the quantities c_1, c_2, c_{12} and a_{ij} given in Appendix C (expressed in terms of the thickness ration $\alpha = h_2/h_1$):

$$\begin{cases} N_c = -\dfrac{6\alpha}{(1+\alpha)^3}\dfrac{1}{h_1}\dfrac{Pa}{B} \\ M_c = \cdots = \dfrac{\alpha^2(3+\alpha)}{(1+\alpha)^3}\dfrac{Pa}{B} \end{cases} \tag{D.17}$$

$$G_{AFRMM/h_1}^{Davidson} = \cdots = \frac{6P^2a^2}{E_1'B^2h_1^3}\frac{\alpha}{(1+\alpha)^6}[12(1+\alpha) + (1+\alpha^3)(3+\alpha)^2 - 6(1-\alpha^2)(3+\alpha)] \tag{D.18}$$

Introducing the relationship $h_1 = 2h/(1+\alpha)$, operating and factorizing:

$$\begin{aligned} G_{AFRMM/h_1}^{Davidson} &= \frac{3P^2a^2}{4E_1'B^2h^3}\frac{\alpha}{(1+\alpha)^3}[3 + 12\alpha + 19\alpha^2 + 15\alpha^3 + 6\alpha^4 + \alpha^5] \\ &= \frac{3P^2a^2}{4E_1'B^2h^3}[\alpha(3 + 3\alpha + \alpha^2)] = \frac{3P^2a^2}{4E_1'B^2h^3}[(1+\alpha)^3 - 1] \end{aligned} \tag{D.19}$$

Substituting $1 + \alpha = 1/\xi$ in the last expression and operating:

$$G_{AFRMM/h_1}^{Davidson} = \frac{3P^2a^2}{4E_1'B^2h^3}\left[\frac{1}{\xi^3} - 1\right] = \frac{3P^2a^2}{4E_1'B^2h^3}\left[\frac{1-\xi^3}{\xi^3}\right] = G_{AFRMM/h_1}^{William} \tag{D.20}$$

D.4.2 Case II: Lower arm (thickness h_2) loaded

This case is illustrated in Figure D. 4-b:

Williams method (beam analysis)

Taking into account the sign criteria shown in Figure 2.8-b:

$$\begin{cases} N_1 = N_2 = 0 \\ M_1 = 0 \\ M_2 = Pa \end{cases} \tag{D.21}$$

Using equation (2.13) and omitting the contribution of transverse shear stresses:

$$G_{AFRMM/h_2}^{William} = \frac{1}{16E_1'IB}\left[\frac{P^2a^2}{(1-\xi)^3} + P^2a^2\right] = \frac{3P^2a^2}{4E_1'B^2h^3}\left[\frac{1-(1-\xi)^3}{(1-\xi)^3}\right] \tag{D.22}$$

where ξ is the thickness parameter defined in (2.14)

Davidson method (classical plate theory)

Taking the forces and moments as positive in the directions shown in Figure 2.9, and using the equilibrium equations (2.18) and (2.19):

$$\begin{cases} N_1 = N_2 = M_1 = 0 \\ M_2 = -\dfrac{Pa}{B} \end{cases} \rightarrow \begin{cases} N_3 = 0 \\ M_3 = M_2 = -\dfrac{Pa}{B} \end{cases} \rightarrow \begin{cases} N_c = a_{12}M_2 \\ M_c = \left(a_{12}\frac{h_1}{2} - a_{22}\right)M_2 \end{cases} \tag{D.23}$$

Using equation (2.17) and the definitions of the quantities c_1, c_2, c_{12} and a_{ij} given in Appendix C (expressed in terms of the thickness ration $\alpha = h_2/h_1$):

$$\begin{cases} N_c = \dfrac{6\alpha}{(1+\alpha)^3}\dfrac{1}{h_1}\dfrac{Pa}{B} \\ M_c = \cdots = \dfrac{(1+3\alpha)}{(1+\alpha)^3}\dfrac{Pa}{B} \end{cases} \tag{D.24}$$

$$G_{AFRMM/h_2}^{Davidson} = \frac{6P^2a^2}{E_1'B^2h_1^3}\frac{1}{\alpha^3(1+\alpha)^6}[12\alpha^4(1+\alpha) + (1+\alpha^3)(1+3\alpha)^2 + 6\alpha^2(1-\alpha^2)(1+3\alpha)] \tag{D.25}$$

Introducing the relationship $h_1 = 2h/(1+\alpha)$ in the last expression and operating:

$$G_{AFRMM/h_2}^{Davidson} = \cdots = \frac{3P^2a^2}{4E_1'B^2h^3}\frac{1}{\alpha^3(1+\alpha)^3}[1+6\alpha+15\alpha^2+19\alpha^3+12\alpha^4+3\alpha^5] \quad \text{(D.26)}$$

Noticing that $(1+6\alpha+15\alpha^2+19\alpha^3+12\alpha^4+3\alpha^5)$ can be written as $((1+\alpha)^3-\alpha 31+\alpha 3$ and substituting $\alpha=1-\xi\xi$:

$$G_{AFRMM/h_2}^{Davidson} = \frac{3P^2a^2}{4E_1'B^2h^3}\frac{1}{\alpha^3}[(1+\alpha)^3-\alpha^3] = \cdots = \frac{3P^2a^2}{4E_1'B^2h^3}\left[\frac{1-(1-\xi)^3}{(1-\xi)^3}\right] = G_{AFRMM/h_2}^{William} \quad \text{(D.27)}$$

D.5 The AMMF test specimen

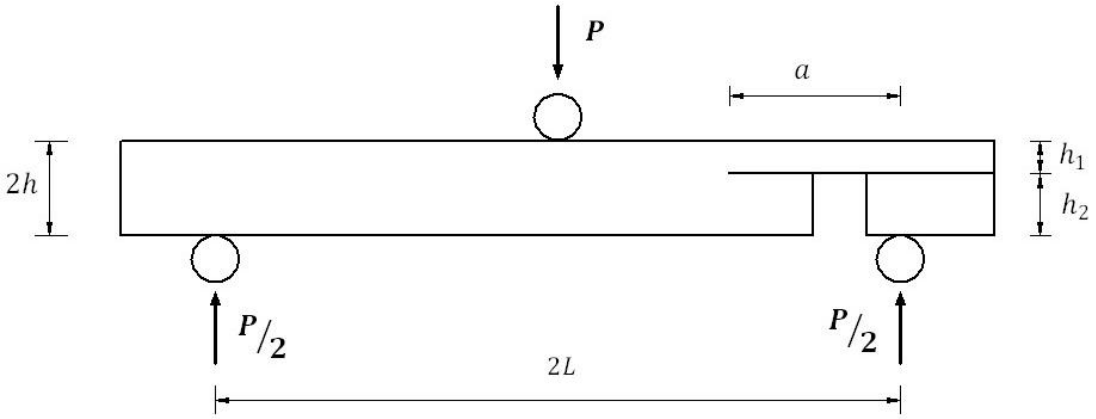

Figure D. 5. Schematic representation of the AMMF test specimen (width, *B*) and its loading conditions.

Williams method (beam analysis)

Taking into account the sign criteria shown in Figure 2.8-b:

$$\begin{cases} N_1 = N_2 = 0 \\ M_1 = -\dfrac{P}{2}a \\ M_2 = 0 \end{cases} \quad \text{(D.28)}$$

Using equation (2.13) and omitting transverse shear effects:

$$G_{AMMF}^{William} = \frac{1}{16E_1'IB}\left[\frac{P^2a^2}{4\xi^3}+\frac{P^2a^2}{4}\right] = \frac{3P^2a^2}{16E_1'B^2h^3}\left[\frac{1-\xi^3}{\xi^3}\right] \quad \text{(D.29)}$$

where ξ is the thickness parameter defined in (2.14)

Davidson method (classical plate theory)

Taking the forces and moments as positive in the directions shown in Figure 2.9, and using the equilibrium equations (2.18) and (2.19):

$$\begin{cases} N_1 = N_2 = M_2 = 0 \\ M_1 = \dfrac{Pa}{2B} \end{cases} \rightarrow \begin{cases} N_3 = 0 \\ M_3 = M_1 = \dfrac{Pa}{2B} \end{cases} \rightarrow \begin{cases} N_c = a_{12} M_1 \\ M_c = \left(1 + a_{12}\frac{h_1}{2} - a_{22}\right) M_1 \end{cases} \tag{D.30}$$

Using equation (2.17) and the definitions of the quantities c_1, c_2, c_{12} and a_{ij} given in Appendix C (expressed in terms of the thickness ration $\alpha = h_2/h_1$):

$$\begin{cases} N_c = -\dfrac{6\alpha}{(1+\alpha)^3}\dfrac{1}{h_1}\dfrac{Pa}{2B} \\ M_c = \cdots = \dfrac{\alpha^2(3+\alpha)}{(1+\alpha)^3}\dfrac{Pa}{2B} \end{cases} \tag{D.31}$$

$$G_{AMMF}^{Davidson} = \cdots = \frac{3P^2a^2}{2E_1'B^2h_1^3}\frac{\alpha}{(1+\alpha)^6}[12(1+\alpha) + (1+\alpha^3)(3+\alpha)^2 - 6(1-\alpha^2)(3+\alpha)] \tag{D.32}$$

Introducing the relationship $h_1 = 2h/(1+\alpha)$, operating and factorizing:

$$\begin{aligned} G_{AMMF}^{Davidson} &= \frac{3P^2a^2}{16E_1'B^2h^3}\frac{\alpha}{(1+\alpha)^3}[3 + 12\alpha + 19\alpha^2 + 15\alpha^3 + 6\alpha^4 + \alpha^5] \\ &= \frac{3P^2a^2}{4E_1'B^2h^3}[\alpha(3 + 3\alpha + \alpha^2)] = \frac{3P^2a^2}{4E_1'B^2h^3}[(1+\alpha)^3 - 1] \end{aligned} \tag{D.33}$$

Substituting $1 + \alpha = 1/\xi$ in the last expression and operating:

$$G_{AMMF}^{Davidson} = \frac{3P^2a^2}{4E_1'B^2h^3}\left[\frac{1}{\xi^3} - 1\right] = \frac{3P^2a^2}{4E_1'B^2h^3}\left[\frac{1-\xi^3}{\xi^3}\right] = G_{AMMF}^{William} \tag{D.34}$$

Appendix E: Correction factors for large displacement (F_v) and end-blocks (N_v)

$$F_v = 1 - \theta_1 \left(\frac{\delta}{L}\right)^2 - \theta_2 \left(\frac{\delta l_1}{L^2}\right) \tag{E.1}$$

$$N_v = 1 - \theta_3 \left(\frac{l_2}{L}\right)^3 - \theta_4 \left(\frac{\delta l_1}{L^2}\right) - \theta_5 \left(\frac{\delta}{L}\right)^2 \tag{E.2}$$

E.1 ADCB Test Specimen

Note that for the ADCB $L = a$, and in the symmetric case $\alpha = 1$.

$$F_v = 1 - \theta_1 \left(\frac{\delta}{a}\right)^2 - \theta_2 \left(\frac{\delta l_1}{a^2}\right) \tag{E.3}$$

$$N_v = 1 - \theta_3 \left(\frac{l_2}{a}\right)^3 - \theta_4 \left(\frac{\delta l_1}{a^2}\right) - \theta_5 \left(\frac{\delta}{a}\right)^2 \tag{E.4}$$

$$\theta_1 = \frac{3}{5}\left[\frac{1+\alpha^6}{(1+\alpha^3)^2}\right] \tag{E.5}$$

$$\theta_2 = \frac{3}{2} \tag{E.6}$$

$$\theta_3 = 1 \tag{E.7}$$

$$\theta_4 = \frac{9}{8}\left[1 - \left(\frac{l_2}{a}\right)^2\right] \tag{E.8}$$

$$\theta_5 = \frac{9}{35} \tag{E.9}$$

E.2 ELS Test Specimen

$$\beta = \frac{(h_1 + h_2)^3}{{h_1}^3 + {h_2}^3} \longrightarrow \text{Symmetric case: } \beta = 4 \tag{E.10}$$

$$\theta_1 = \frac{3}{20}\left[\frac{15 + (20\beta - 30)\left(\frac{a}{L}\right)^2 + (8\beta^2 - 20\beta + 15)\left(\frac{a}{L}\right)^4}{\left(1 + (\beta - 1)\left(\frac{a}{L}\right)^3\right)^2}\right] = \frac{3}{20}\left[\frac{15 + 50\left(\frac{a}{L}\right)^2 + 63\left(\frac{a}{L}\right)^4}{\left(1 + 3\left(\frac{a}{L}\right)^3\right)^2}\right] \tag{E.11}$$

$$\theta_2 = 3\left(\frac{L}{a}\right)\left[\frac{1 + (\beta - 1)\left(\frac{a}{L}\right)^2}{1 + (\beta - 1)\left(\frac{a}{L}\right)^3}\right] = 3\left(\frac{L}{a}\right)\left[\frac{1 + 3\left(\frac{a}{L}\right)^2}{1 + 3\left(\frac{a}{L}\right)^3}\right] \tag{E.12}$$

$$\theta_3 = \frac{\beta}{1 + (\beta - 1)\left(\frac{a}{L}\right)^3} = \frac{4}{1 + 3\left(\frac{a}{L}\right)^3} \tag{E.13}$$

$$\begin{aligned}\theta_4 &= \frac{9}{4}\left[\frac{\left(1 - \left(\frac{a}{L}\right)\right)\left(1 + (\beta - 1)\left(\frac{a}{L}\right)^3\right) + \beta\left(\frac{a}{L}\right)^2\left(1 - \left(\frac{l_2}{a}\right)^2\right)\left(1 + (\beta - 1)\left(\frac{a}{L}\right)^2\right)}{\left(1 + (\beta - 1)\left(\frac{a}{L}\right)^3\right)^2}\right] \\ &= \frac{9}{4}\left[\frac{\left(1 - \left(\frac{a}{L}\right)\right)\left(1 + 3\left(\frac{a}{L}\right)^3\right) + 4\left(\frac{a}{L}\right)^2\left(1 - \left(\frac{l_2}{a}\right)^2\right)\left(1 + 3\left(\frac{a}{L}\right)^2\right)}{\left(1 + 3\left(\frac{a}{L}\right)^3\right)^2}\right]\end{aligned} \tag{E.14}$$

$$\begin{aligned}\theta_5 &= \frac{9}{70}\left[\frac{8 + (\beta - 1)\left(\frac{a}{L}\right)^3\left(35 + 14(2\beta - 3)\left(\frac{a}{L}\right)^2 + (8\beta^2 - 20\beta + 15)\left(\frac{a}{L}\right)^4\right)}{\left(1 + (\beta - 1)\left(\frac{a}{L}\right)^3\right)^3}\right] \\ &= \frac{36}{35}\left[\frac{1 + \frac{3}{8}\left(\frac{a}{L}\right)^3\left(35 + 70\left(\frac{a}{L}\right)^2 + 63\left(\frac{a}{L}\right)^4\right)}{\left(1 + 3\left(\frac{a}{L}\right)^3\right)^3}\right]\end{aligned} \tag{E.15}$$

E.3 ENF Test Specimen

$$\theta_1 = \frac{3}{20}\left[\frac{15\left(1-\left(\frac{a}{L}\right)^3\right)^2 - 40\left(\frac{a}{L}\right)^2\left(1-\left(\frac{a}{L}\right)^3\right) + 48\left(\frac{a}{L}\right)^4}{\left(2+3\left(\frac{a}{L}\right)^3\right)^2}\right] \tag{E.16}$$

$$\theta_2 = \theta_3 = \theta_4 = 0 \tag{E.17}$$

$$\theta_5 = \frac{3}{35}\left[\frac{37+147\left(\frac{a}{L}\right)^3 + 210\left(\frac{a}{L}\right)^6 + 105\left(\frac{a}{L}\right)^9}{\left(2+3\left(\frac{a}{L}\right)^3\right)^3}\right] \tag{E.18}$$

E.4 AFRMM Test Specimen

$$\beta = \frac{(h_1+h_2)^3}{{h_2}^3} \longrightarrow \text{Symmetric case: } \beta = 4 \tag{E.19}$$

$$F_v = 1 - \theta_1\left(\frac{\delta}{L}\right)^2 - \theta_2\left(\frac{\delta l_1}{L^2}\right) \tag{E.20}$$

$$N_v = 1 - \theta_3\left(\frac{l_2}{L}\right)^3 - \theta_4\left(\frac{\delta l_1}{L^2}\right) - \theta_5\left(\frac{\delta}{L}\right)^2 \tag{E.21}$$

$$\theta_1 = \frac{3}{20}\left[\frac{15+(20\beta-30)\left(\frac{a}{L}\right)^2 + (8\beta^2-20\beta+15)\left(\frac{a}{L}\right)^4}{\left(1+(\beta-1)\left(\frac{a}{L}\right)^3\right)^2}\right] = \frac{3}{20}\left[\frac{15+50\left(\frac{a}{L}\right)^2+63\left(\frac{a}{L}\right)^4}{\left(1+3\left(\frac{a}{L}\right)^3\right)^2}\right] \tag{E.22}$$

$$\theta_2 = 3\left(\frac{L}{a}\right)\left[\frac{1+(\beta-1)\left(\frac{a}{L}\right)^2}{1+(\beta-1)\left(\frac{a}{L}\right)^3}\right] = 3\left(\frac{L}{a}\right)\left[\frac{1+3\left(\frac{a}{L}\right)^2}{1+3\left(\frac{a}{L}\right)^3}\right] \tag{E.23}$$

$$\theta_3 = \frac{\beta}{1+(\beta-1)\left(\frac{a}{L}\right)^3} = \frac{4}{1+3\left(\frac{a}{L}\right)^3} \tag{E.24}$$

$$\theta_4 = \frac{9}{4}\left[\frac{\left(1-\left(\frac{a}{L}\right)\right)\left(1+(\beta-1)\left(\frac{a}{L}\right)^3\right)+\beta\left(\frac{a}{L}\right)^2\left(1-\left(\frac{l_2}{a}\right)^2\right)\left(1+(\beta-1)\left(\frac{a}{L}\right)^2\right)}{\left(1+(\beta-1)\left(\frac{a}{L}\right)^3\right)^2}\right]$$
$$= \frac{9}{4}\left[\frac{\left(1-\left(\frac{a}{L}\right)\right)\left(1+3\left(\frac{a}{L}\right)^3\right)+4\left(\frac{a}{L}\right)^2\left(1-\left(\frac{l_2}{a}\right)^2\right)\left(1+3\left(\frac{a}{L}\right)^2\right)}{\left(1+3\left(\frac{a}{L}\right)^3\right)^2}\right] \quad \text{(E.25)}$$

$$\theta_5 = \frac{9}{70}\left[\frac{8+(\beta-1)\left(\frac{a}{L}\right)^3\left(35+14(2\beta-3)\left(\frac{a}{L}\right)^2+(8\beta^2-20\beta+15)\left(\frac{a}{L}\right)^4\right)}{\left(1+(\beta-1)\left(\frac{a}{L}\right)^3\right)^3}\right]$$
$$= \frac{36}{35}\left[\frac{1+\frac{3}{8}\left(\frac{a}{L}\right)^3\left(35+70\left(\frac{a}{L}\right)^2+63\left(\frac{a}{L}\right)^4\right)}{\left(1+3\left(\frac{a}{L}\right)^3\right)^3}\right] \quad \text{(E.26)}$$

Appendix F: Test Results

F.1 Mode I Tests

F.1.1 DCB Test Specimens

Table F. 1. Initiation G_{Ic} values corresponding to the MAX/5% C_0 criterion obtained with the titanium DCB specimens bonded with the supported and unsupported versions of AF-163-2.

SPECIMEN	INITIATION G_{Ic} $(\mathrm{J/m^2})$			
	MAX/5% C_0			
	SBT	CBT	ECM	CBTE
S6 (AF163-2OST)	1389	1666	1759	1772
S7 (AF163-2OST)	1719	1977	2078	2109
S8 (AF163-2OST)	971	1274	1349	1292
W1 (AF163-2OST)	1307	2829	3067	2548
W2 (AF163-2OST)	1332	1716	1816	1883
W4 (AF163-2OST)	1289	1280	1556	1799
Average ± SDV	1335±218	1790±526	1938±553	1900±379
S1U (AF163-2U)	2543	3136	3219	3127
S2U (AF163-2U)	2651	2985	3101	3137
S3U (AF163-2U)	2523	3234	3332	3178
Average ± SDV	2573±56	3118±103	3217±94	3147±22

Table F. 2. Average propagation G_{Ic} values (Plateau) obtained with the titanium DCB specimens bonded with the supported and unsupported versions of AF-163-2.

SPECIMEN	PROPAGATION G_{Ic} $(\mathrm{J/m^2})$			
	PLATEAU			
	SBT	CBT	ECM	CBTE
S6 (AF163-2OST)	2346±113	2605±87	2601±123	2738±93
S7 (AF163-2OST)	2990±173	3068±69	3054±88	3278±83
S8 (AF163-2OST)	2819±104	2910±85	2923±120	3084±95
W1 (AF163-2OST)	2496±231	3030±122	2990±128	3121±144
W2 (AF163-2OST)	2475±268	2792±127	2700±136	3016±111
W4 (AF163-2OST)	2510±327	2667±168	2669±327	3209±138
Average ± SDV	2606±223	2845±173	2823±173	3074±172
S1U (AF163-2U)	3540±91	4013±56	4020±51	4052±50
S2U (AF163-2U)	3878±117	3966±98	3950±143	4187±102
S3U (AF163-2U)	4115±168	4273±101	4249±101	4404±117
Average ± SDV	3845±236	4084±135	4073±128	4214±145

Table F. 3. Initiation G_{Ic} values corresponding to the MAX/5% C_0 criterion obtained with the CFRP DCB specimens bonded with the supported version of AF-163-2 [388].

SPECIMEN	INITIATION G_{Ic} (J/m^2)			
	MAX/5% C_0			
	SBT	CBT	ECM	CBTE
CFRP-W1 (AF163-2OST)	1456	1949	2082	2000
CFRP-W2 (AF163-2OST)	1770	2051	2201	2225
CFRP-W3 (AF163-2OST)	1639	1733	1747	1802
CFRP-W4 (AF163-2OST)	1957	2048	2218	2482
Average ± SDV	1705±183	1945±129	2062±189	2127±254

Table F. 4. Average propagation G_{Ic} values (Plateau) obtained with the CFRP DCB specimens bonded with the supported versions of AF-163-2 [388].

SPECIMEN	PROPAGATION G_{Ic} (J/m^2)			
	PLATEAU			
	SBT	CBT	ECM	CBTE
CFRP-W1 (AF163-2OST)	2620±236	2925±201	2897±190	3026±199
CFRP-W2 (AF163-2OST)	2456±219	2820±215	2836±250	2931±227
CFRP-W3 (AF163-2OST)	2512±183	2727±115	2688±127	2761±121
CFRP-W4 (AF163-2OST)	2713±255	2779±103	2717±165	3157±123
Average ± SDV	2575±114	2813±84	2785±99	2969±167

F.1.2 TDCB Test Specimens

Table F. 5. Initiation G_{Ic} values corresponding to the MAX/5% C_0 criterion obtained for the aluminium alloy TDCB specimens bonded with AF-163-2OST.

SPECIMEN	INITIATION G_{Ic} (J/m^2)		
	MAX/5% C_0		
	SBT	CBT	ECM
T1	2164	2391	2112
T2	1687	1868	1737
T3	1695	1881	1735
T4	1818	2027	1800
T5	1658	1850	1656
Average ± SDV	1804±188	2004±204	1808±159

Table F.1. Average propagation G_{Ic} values (Plateau) obtained with the aluminium TDCB specimens bonded with the supported version of AF-163-2.

SPECIMEN	PROPAGATION G_{Ic} (J/m^2)		
	PLATEAU		
	SBT	CBT	ECM
T1	2625±46	2853±45	2562±45
T2	2621±35	2858±42	2699±36
T3	2621±95	2859±96	2682±97
T4	2467±39	2688±39	2443±38
T5	2725±57	2974±59	2721±57
Average ± SDV	2612±82	2847±91	2622±105

F.2 Mixed Mode I/II Tests

F.2.1 ADCB Test Specimens

Table F. 6. Initiation $G_{I/IIc}$ values corresponding to the MAX/5% C_0 criterion obtained for the CFRP-ADCB specimens bonded with AF-163-2OST.

SPECIMEN	$\alpha = \frac{h_2}{h_1}$	INITIATION $G_{I/IIc}$ (J/m^2)				MIXED MODE RATIO $G_{II}/G = \Phi(\alpha)$		
		MAX/5% C_0						
		SBT	CBT	ECM	CBTE	Williams	CTE/SF	CTE/NSF
CF31	0.470	2805	3174	2732	3274	0	0.1668	0.0558
CF30	0.472	2569	3002	3408	3056	0	0.1655	0.0553
CF32	0.503	2899	3381	2371	3465	0	0.1473	0.0497
CF3	1.111	3102	3248	4760	3414	0	0.005	0.0018
CF27	1.400	1730	2598	1897	2526	0	0.0466	0.0166
CF39	1.970	2030	2229	2177	2341	0	0.1447	0.0489
CF21	2.009	4023	3803	3765	4146	0	0.1503	0.0506
CF23	2.014	3464	3055	3098	3545	0	0.1511	0.0509
CF22	2.015	3605	3604	3431	3825	0	0.1512	0.0509
CF38	2.177	3291	3660	3199	3717	0	0.1728	0.0576

Table F. 7. Propagation $G_{I/IIc}$ values obtained for the CFRP-ADCB specimens bonded with AF-163-2OST.

SPECIMEN	$\alpha = \frac{h_2}{h_1}$	PROPAGATION $G_{I/IIc}$ $(\mathrm{J/m^2})$			
		PLATEAU			
		SBT	CBT	ECM	CBTE
CF31	0.470	3476±97	3920±67	3339±68	3999±24
CF30	0.472	3694±198	3996±208	4489±227	4125±207
CF32	0.503	4016±172	4207±97	2921±63	4427±117
CF3	1.111	3200±49	3367±45	4926±62	3527±39
CF27	1.400	2495±172	3217±81	2320±52	3259±123
CF39	1.970	3683±179	3299±144	3232±130	3631±152
CF21	2.009	4279±56	3933±76	3878±83	4313±69
CF23	2.014	4040±79	3510±46	3505±58	4035±58
CF22	2.015	3996±193	3867±143	3654±128	4118±154
CF38	2.177	4277±193	3582±81	3515±111	4298±98

F.2.2 AFRMM Test Specimens

Table F. 8. Initiation $G_{I/IIc}$ values corresponding to the MAX/5% C_0 criterion obtained for the CFRP-AFRMM specimens bonded with AF163-2OST.

SPECIMEN	$\alpha = \frac{h_2}{h_1}$	INITIATION $G_{I/IIc}$ (J/m^2)				MIXED MODE RATIO $G_{II}/G = \Phi(\alpha)$		
		MAX/5% C_0						
		SBT	CBT	ECM	CBTE	Williams	CTE/SF	CTE/NSF
CF31	0.470	4623	4700	3516	4117	0.0633	0.3905	0.2237
CF30	0.472	5152	5073	4315	4662	0.0643	0.3907	0.2246
CF36	0.484	4557	3512	1045	4681	0.0695	0.3916	0.2294
CF37	0.489	4135	4294	3439	3944	0.0717	0.392	0.2313
CF32	0.503	5315	5497	4073	4672	0.0784	0.3931	0.2371
CF19	0.949	4406	4694	4839	4193	0.4675	0.432	0.4461
CF14	0.972	3860	4110	3766	4175	0.4074	0.4267	0.419
CF4	0.993	3684	3995	3440	3508	0.4236	0.4281	0.4263
CF18	0.995	3613	3939	3635	3435	0.425	0.4283	0.4269
CF20	1.004	3392	3691	3584	3314	0.4314	0.4288	0.4299
CF13	1.005	3462	3772	2597	3755	0.4324	0.4289	0.4303
CF5	1.062	4048	4332	2517	4103	0.4728	0.4325	0.4485
CF3	1.111	5776	6073	5675	5725	0.5062	0.4356	0.4636
CF27	1.400	3080	3481	2303	4078	0.6666	0.4524	0.5407
CF21	2.009	3060	3093	6735	3567	0.8437	0.4807	0.6496
CF23	2.014	2883	2941	2024	3421	0.8446	0.481	0.6503
CF22	2.015	3274	3263	5207	4124	0.8448	0.481	0.6504

Table F. 9. Propagation $G_{I/IIc}$ values obtained for the CFRP-ADCB specimens bonded with AF163-2OST.

SPECIMEN	$\alpha = \frac{h_2}{h_1}$	PROPAGATION $G_{I/IIc}$ (J/m^2)			
		PLATEAU			
		SBT	CBT	ECM	CBTE
CF30	0.472	5280±136	5041±267	4436±112	4554±106
CF36	0.484	5157±254	4873±172	3761±161	4287±139
CF37	0.489	4422±132	4226±186	3633±90	3884±177
CF32	0.503	5406±219	5382±290	4388±175	4725±97
CF19	0.949	6765±152	6846±159	7248±158	6516±156
CF14	0.972	5905±52	6004±51	5613±54	5981±53
CF4	0.993	6026±199	6260±198	6240±213	5733±66
CF18	0.995	5326±200	5576±211	5391±196	5130±157
CF20	1.004	5440±71	5621±88	5615±71	5400±73
CF13	1.005	5380±252	5666±247	3972±187	5461±135
CF5	1.062	5361±78	5596±69	5593±77	5249±85
CF3	1.111	7853±205	7947±187	7658±194	7340±173
CF27	1.400	6026±214	6492±218	4707±171	6817±98
CF23	2.014	10081±262	9021±224	11616±299	11552±162
CF22	2.015	8814±126	7669±98	15416±212	11095±100

Appendix G: Quasi-Static Locus of Failure for Initiation (MAX/5%)

Even though only the propagation fracture criterion was needed for the cohesive element formulation, the initiation loci were also approximated by equations (7.1) to (7.3). In spite of the questions surrounding the physical meaning of the initiation values, the resulting functions could be employed to obtain conservative performance predictions if no propagation data were available or crack growth were simply not permitted. Table G. 1 presents the values of the fitting parameters, calculated in each case via a non-linear least squares analysis.

Figure G. 1 shows the fracture energies for initiation (MAX/5% criterion) obtained for the various fracture mechanics specimens tested quasi-statically. Considered the most accurate data reduction scheme of those investigated, only the results corresponding to the effective crack length approach have been included.

Despite the MAX/5% criterion yielding the most consistent values, the experimental scatter was significant, especially as the shear component increased. The variability under pure mode II conditions was particularly noteworthy, with the ELS results typically lower than those obtained for the ENF joints. Indeed, the uncertainties in the crack length measurements as well as the initial non-linear response observed for the ENF specimens contributed to the problem.

The loci (i.e. plots of G_{Ic}^{mixed} versus G_{IIc}^{mixed}) exhibited a very characteristic shape: after an initial section where the mode I component rose very rapidly from $G_{Ic}$to a maximum value (3500-4500 J/m^2 depending on the decomposition scheme), G_{Ic}^{mixed} then decreased progressively with the mode II component. As discussed in Chapter 6, it is proposed here that the abrupt increase in the mode I component of the fracture energy observed for very small shear contributions (i.e. $G_{Ic}^{mixed} > G_{Ic}$) is partly caused by the carrier mat. The woven mat provides a weak path for crack propagation under pure opening conditions, resulting in an "artificially" low value of G_{Ic}.

Excluding any potential discrepancies with the ADCB results, it seemed that the average initiation values for pure mode II were greater than those corresponding to mode I (i.e. $(G_{IIc})_{initiation} > (G_{Ic})_{initiation}$). Unfortunately, the experimental scatter prevents from stating the relative positions of G_{Ic}, $G_{I/IIc}$ and G_{IIc}.

The three functions considered here were able to model the initial increment observed in G_{Ic}^{mixed} with G_{IIc}^{mixed}. The shapes of the experimental data corresponding to the CTE/NSF and Williams' decompositions were successfully captured by both the 4th order polynomial and the modified B-K criterion, whereas the agreement attained with the bilinear function was somehow poorer due to the limitations of its mathematical formulation. In contrast, they struggled to reproduce some of the local trends exhibited by the singular field locus. Furthermore, in this case the order of the polynomial had to be reduced to cubic to avoid introducing unrealistic undulations.

Table G. 1. Least square curve fit parameters for various initiation criteria. The critical strain energy release rates for pure modes I and II obtained in each case as well as the average values have also been included.

Fracture Criterion	Least Square Fitting Parameters					G_{Ic} (J/m^2)	G_{IIc} (J/m^2)
	α_0	α_1	α_2	α_3	α_4		
INITIATION CRITERION (MAX/5%): Williams (No ADCB)							
Polynomial	2004	38070	-135023	162786	-62593	2004	5244
Modified B-K	-	37.23	1.46	-	-	1946	5130
Bi-Linear	-	8.35	-0.80	-	-	1959	4777
INITIATION CRITERION (MAX/5%): CTE/NSF							
Polynomial	2369	24061	-85156	107102	-42550	2369	5847
Modified B-K	-	8.86	2.67	-	-	2365	5849
Bi-Linear	-	0.55	-0.53	-	-	2816	5580
INITIATION CRITERION (MAX/5%): CTE/SF							
Polynomial	2346	11754	-25236	16423	0	2346	5288
Modified B-K	-	4.33	1.47	-	-	2353	5286
Bi-Linear	-	0.41	-0.59	-	-	2554	5191
Values calculated as average of the DCB and ELS&ENF results:						**1925**	**5290**

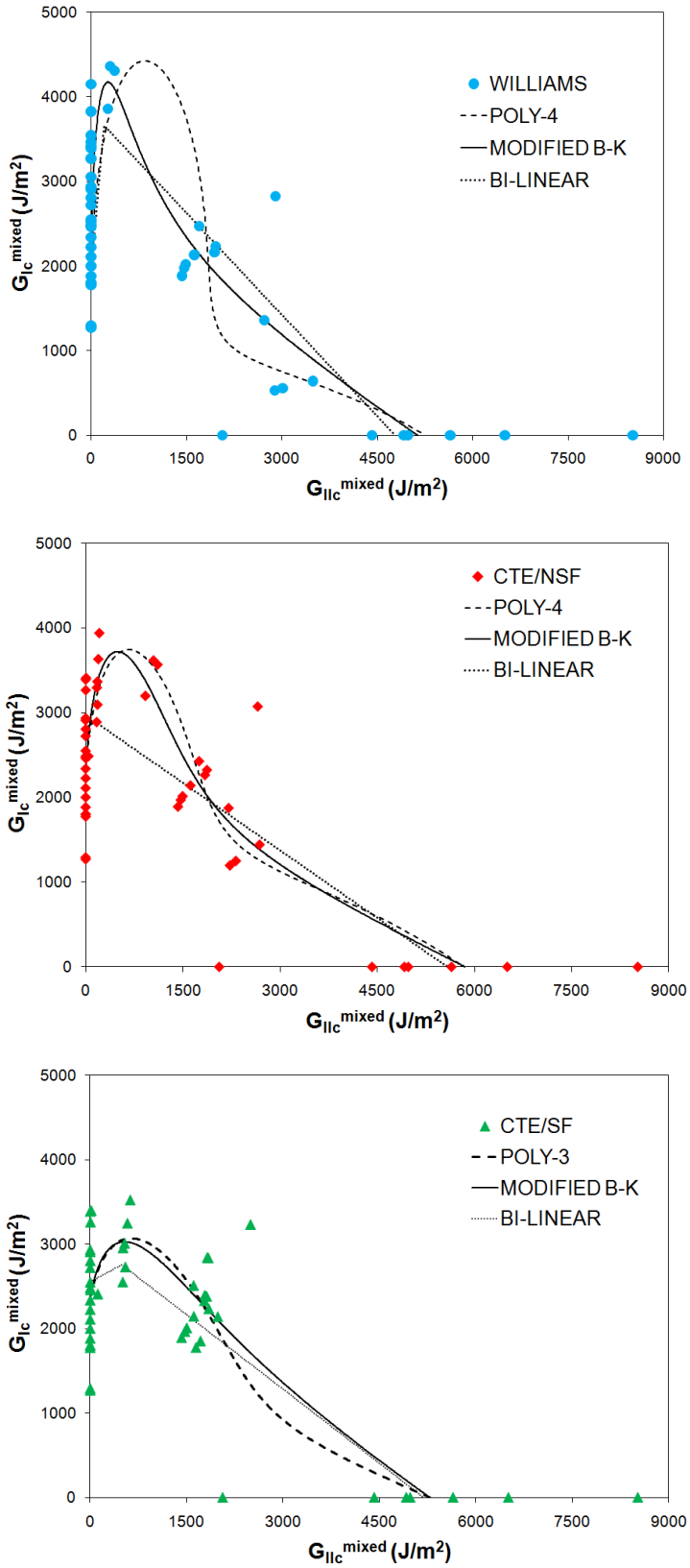

Figure G. 1. Initiation (MAX/5%, CBTE) fracture energies for AF163-2OST corresponding to the various partitioning strategies considered. The experimental data has been approximated by three different functions in each case: a fourth order polynomial, a modified B-K criterion and a bilinear law (equations (7.1), (7.2) and (7.3) respectively).

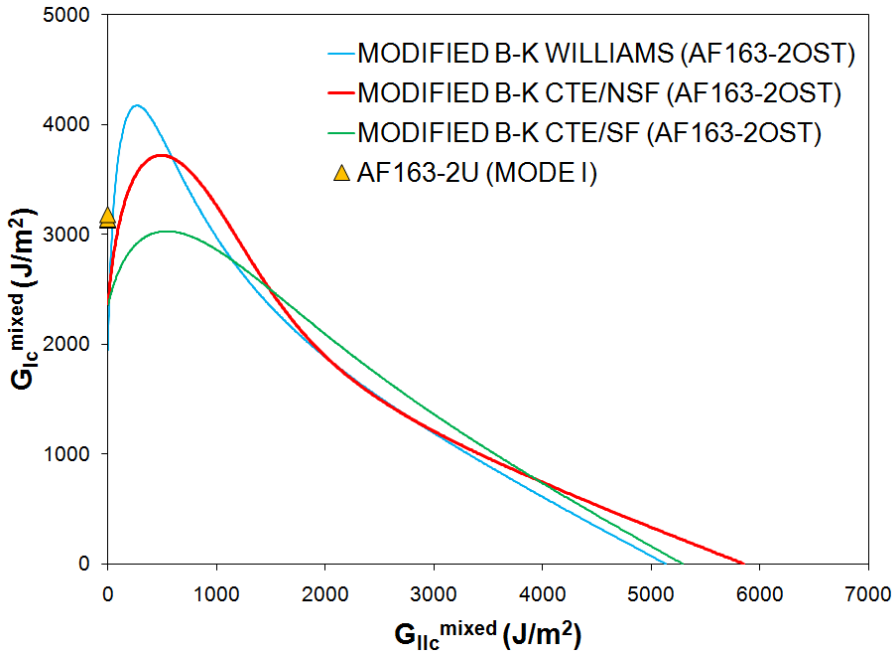

(a)

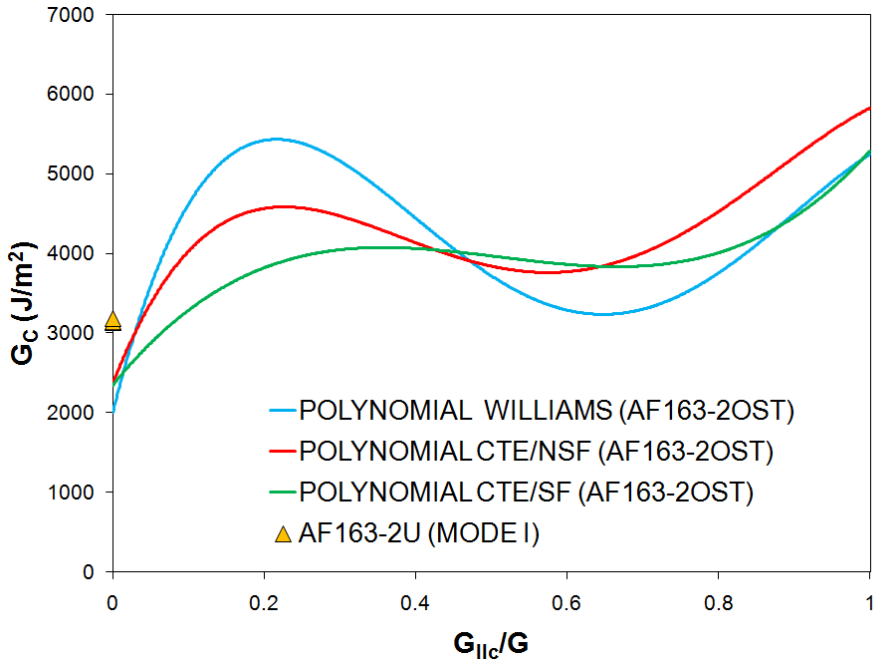

(b)

Figure G. 2. Comparison of the initiation loci corresponding to the various partitioning schemes investigated. (a) The modified B-K functions are shown in the plots of G_{Ic}^{mixed} versus G_{IIc}^{mixed}; (b) The fitted polynomials are illustrated in the plot of G_c versus the mixed mode ratio G_{II}/G.

Appendix H: Verification of the Fatigue Degradation Strategy

The simple model illustrated in Figure H. 1-a was built using a single cohesive element (second order, 30 integration points) in order to study its response to a sinusoidal displacement of constant amplitude, frequency (5Hz) and ratio R ($R = \delta_{min}/\delta_{max} = 0.1$) applied to the top edge. Obviously, since the cohesive formulation employed a jump-cycle strategy, the sinusoidal function was replaced by the envelope of its cyclic variation with time (see Figure H. 1-b) and the simulations were run in Abaqus/Standard.

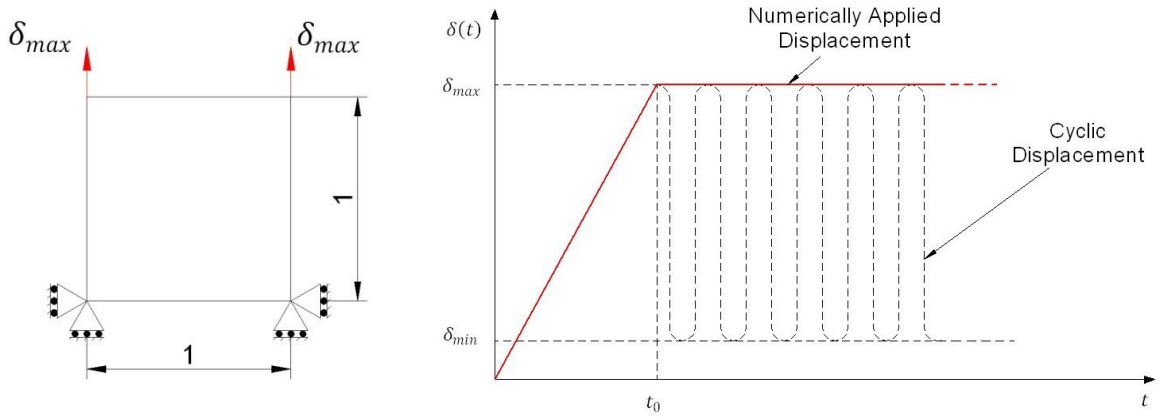

Figure H. 1. (a) Single element model used to verify the fatigue degradation strategy; (b) Schematic representation of the cyclic displacement applied to the structure and the displacement function for which it was substituted in the numerical model.

To demonstrate the response of the user element in the various regions of the fatigue diagram, four different maximum displacements were considered (see Figure H. 2):

$$\begin{cases} \delta_1 = 5{\cdot}10^{-6}\text{m} \;\; \text{so} \;\; \delta_1 < \Delta_I^{th} \\ \delta_2 = 1.2 \cdot 10^{-5}\text{m} \;\; \text{so} \;\; \Delta_I^{th} < \delta_2 < \Delta_I^0 \\ \delta_3 = 5.0{\cdot}10^{-5}\text{m} \;\; \text{so} \;\; \Delta_I^0 < \delta_3 < \Delta_I^f \\ \delta_4 = 2.0{\cdot}10^{-4}\ \text{m} \;\; \text{so} \;\; \delta_4 > \Delta_I^f \end{cases}$$

where Δ_I^0, Δ_I^f and Δ_I^{th} are the displacement jump norms for damage initiation, complete failure and fatigue threshold respectively (see Chapter 3).

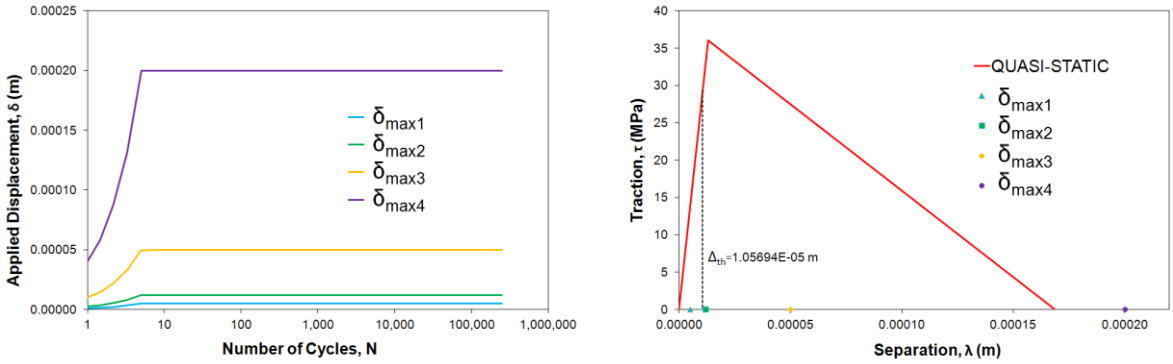

(a) (b)

Figure H. 2. (a) Displacement functions applied to the single element model for the various values of λ and (b) their corresponding relative positions in the traction-separation diagram.

As expected, the cohesive element remained intact below Δ_I^{th}, whereas it followed the quasi-static evolution law for maximum applied displacements greater than Δ_I^f. The latter case, where the element fractured completely during the rising section of the first cycle, would correspond to the rapid growth region of the diagram. Conversely, the element accumulated damage due to the cyclic loading when $\Delta_I^{th}<\lambda<\Delta_I^f$ (even below Δ_I^0), with the degradation rate logically increasing with amplitude of the sinusoidal function (see Figure H. 3).

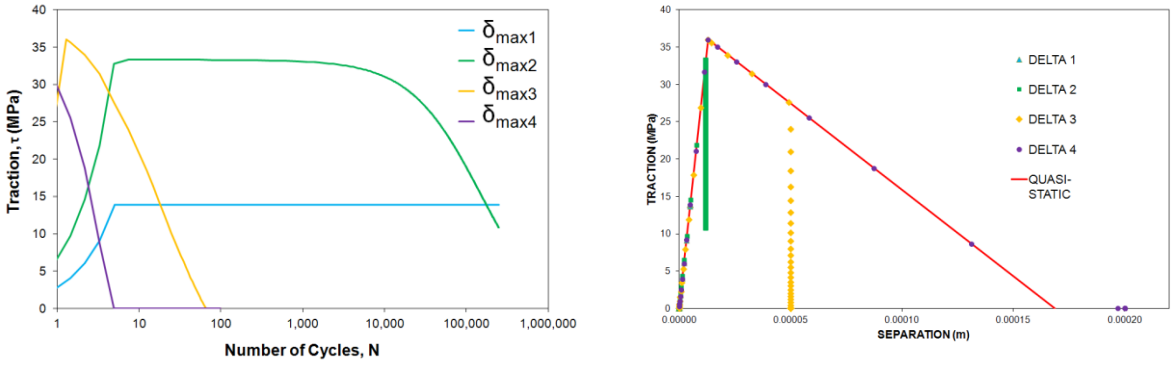

(a) (b)

Figure H. 3. Variation of the traction on the top face of the cohesive element with (a) the number of cycles and (b) the local separation obtained for various values of the maximum applied displacement.